DE-EE0002891

FINAL TECHNICAL REPORT

VOLUME 1: TEST SITE

DeepCwind Consortium Research Program

January 15, 2010 - March 31, 2013

Habib J. Dagher, Ph.D., P.E., University of Maine
Elizabeth Viselli, University of Maine
Damien Brady, Ph.D., University of Maine
Peter Browne, HDR
Heather Deese, Ph.D., Island Institute
Rebecca Holberton, Ph.D., University of Maine
Theresea Johnson, Ph.D., University of Maine
Benjamin Karlson, Sandia
Adrienne Leopold, University of Maine
Linda Magnum, University of Maine
Melissa Maynard, Ph.D., University of Maine
James McCleave, Ph.D., University of Maine
Robert Mizrahi, New Jersey Audubon Society
Andrew Pershing, Ph.D., GMRI
Neal Pettigrew, Ph.D., University of Maine
Andrew Qua, Kleinschmidt Associates
Graham Sherwood, Ph.D., GMRI
Robert Steneck, University of Maine
Jason Stockwell, Ph.D., GMRI
Jeff Thaler, University of Maine
Gayle Zydlewski, Ph.D., University of Maine

1 Introduction

This is Volume 1 of the final technical report for the U.S. Department of Energy-funded program, DE-0002981: DeepCwind Consortium Research Program. The project objective was the partial validation of coupled models and optimization of materials for offshore wind structures.

The DeepCwind Consortium has a 20-year research, education and commercialization plan. The primary objectives in the first two years were to: (1) partially validate coupled aeroelastic-hydrodynamic models for floating offshore wind turbines. This has been a landmark experimental study which serves to advance floating wind turbine modeling, design and reliability; and (2) optimize floating platform designs by integrating more durable, lighter, hybrid composite materials. These advanced composite materials, in combination with conventional materials such as steel and concrete, provide critical enabling technologies that can transform the design of floating wind systems, and reduce deployment and operational and maintenance costs. These material and structure technologies form the core competency of the UMaine Advanced Structures and Composites Center. The 87,000 ft^2 140-employee Center, established by the National Science Foundation in 1996, is a recognized leader in the use of composites in civil infrastructure and marine applications. Integral to the objectives is a deepwater offshore wind education mission that spans the spectrum of high school, community college, university education, and industry outreach.

The DeepCwind Consortium Research Program has focused on the development of floating offshore wind farm technologies, and has provided the following key results which this proposal is founded on:

- **2007-2012: Deepwater Test Site**. Obtained lease for the first deepwater offshore wind test site in the US, off Monhegan Island, Maine. Collected environmental, ecological, geophysical, and metocean data at the site. Obtained a FONSI (Finding of No Significant Impact) for the site.
- **2010: Floating Design Competition.** Completed an international floating wind turbine design competition, in which over 12 designs were received and reviewed by a blue ribbon panel of experts.
- **2010-2011: 1:50 Scale Testing**. Completed the most extensive floating turbine model basin test program ever conducted: Three 5 MW floating turbines were designed (TLP, spar, semi-submersible), scaled to 1:50, constructed fully operational models, and tested each under 60 different metocean conditions.
- **2011-2012: Cost-benefit analysis of floating turbines.** Performed a cost-benefit analysis of various floating turbine designs.
- **2010-2012:** Composite tower designs.
- **2012: Optimize floating turbine design.** Developed the VolturnUS pre-stressed concrete semisubmersible design concept as a low-cost floating turbine system. (Separate funding).
- **2013**: **Deploy a 1:8 Scale VolturnUS** unit off the Maine coast in second quarter 2013. (Separate funding).

To advance the state-of-the-art in deepwater floating offshore wind technology, the University of Maine has identified the need for a robust test and demonstration site for offshore wind technology. The need for such a site has been also identified by several reports on the development of the offshore wind industry, including a recent gap analysis performed by GL

Garrad Hassan.[1] An objective of this program was establishing baseline physical and ecological characteristics of the test site, as well as permit the site, in anticipation of a 1/8-scale model deployment (under separate funding) in 2013.

The University of Maine Deepwater Offshore Wind Test Site at Monhegan Island, Maine, is located in Maine state waters 12 miles off the coast. The site is leased to UMaine and has 9.2 m/s wind at 90 m; 10 years of meteocean data; and preliminary bird and bat, benthic, marine mammal, fish, bottom characterization, and core sample studies. Maine Public Law 270 sets a unique, 60-day limit for new hardware permit review and approval. In 2011, the University of Maine was awarded a Finding of No Significant Impact (FONSI) for a pilot-scale project at the test site, reflecting the quality of environmental data available for the site.

- **Permits:** Leased UMaine site located in state waters. 60-day hardware permits through the state of Maine.
- **Geophysical and geotechnical conditions:** Limited site-specific data and surveys available to facilitate anchoring and foundation designs. A range of geotechnical conditions allowing a variety of anchoring options (drag, suction, rock).
- **Water depths:** Water depths between 300-400 ft. within 3 nautical miles of the coast.
- **Wind resource:** Class 6 and 7 winds—10 years of (10 meter high) wind speed and direction data available. Additional site-specific wind data collection for test site partners, including full wind field characterization, wind shear, and wake measurements. Floating met tower option available.
- **Wave resource:** 10 years of survey data available, including one year of current data.
- **Ecological monitoring and assessment:** Provided ecological baseline data for permitting and ongoing environmental studies.

2 Metocean Data

The metocean conditions at the proposed site have been extensively studied by the University of Maine over the past 10 years. Oceanographic buoys have been deployed since July of 2001 by the University of Maine Physical Oceanography Group (PhOG) within the School of Marine Sciences. Buoy E01 is located less than one nautical mile west from the test site. It collects data on wave heights and periods, wind speeds and directions, temperatures, and current speeds and directions to name a few. Subsequently, an analysis of the data has been completed which complies with the guidelines of the Standard International Electrotechnical Commission 61400- 1 and 61400-3 (IEC): Wind Turbines: Design requirements and design requirements for offshore wind turbines.

Some data required by the IEC and ABS applicable standard are not available from the buoy. Specifically, wave direction and spectra were not available from the PhOG buoys. However, Private and publically available numerical wave hindcast models (Waveclimate) and wind models (AWS Truepower) have been used to supplement the buoy data for this area.

[1] *Gap Analysis of Offshore Demonstration Sites on Behalf of the Crown Estate.* www.thecrownestate.co.uk/…/gap_analysis_executive_summary.pdf

Table 1: Summary of Annual Full-scale Marine Conditions Based on 10 Years of Buoy Data and Hindcast Models

Design Requirement (IEC 61400-3)	**Estimated Design Value**	**Notes and Method of Calculating Value**
Mean Still Water Level (MSWL) (m)	Approx. 60-100	TBD. Buoy E02 depth in test site stated here.
50 year tidal variation (m)	3.57	NOAA extrapolated values[1]. P.O.T using Weibull, P=8 u=10.75
Highest astronomical tide (m)	3.47	Max value of NOAA extrapolated values. Referenced to MLLW
Lowest astronomical tide (m)	-0.58	Minimum values of NOAA extrapolated values. Referenced to MLLW
Highest still water level (m)	Approx. 107.1	TBD.
Lowest still water level (m)	Approx. 103.0	TBD.
50 year significant wave height (m)	10.0	P.O.T using GPD, P=8 u=4
Mean period associated with 50 year sig wave Height (s)	14.0	Joint probability; mean period =1.4186(Hs)^(.7694)+5.66
Extreme 50 year sea current at depths 2,10,30 & 62 m (cm/s)	105/ 105/ 86.6/ 87.5	P.O.T using GPD, P=8 u=29-50
Wave spectrum JONSWAP Factor, (γ)	1.7-2.0 normal conditions. 2.5-3.0 extreme conditions	Estimated from NOAA Buoy 44005
Wind Turbulence intensity at 15m	0.12	Per IEC 61400-1. Assume type C turbulence for offshore.
Annual average wind speed at 4 m / 90 m (m/s)	5.6/ 9.3	Average of 10 min winds speed (adjusted from 8 min).
Wind speed distribution (annual)	$P=1-e^{-(V/6.39)^2}$	Rayleigh for 10 min speeds
Wind Shear Power Law Exponent	0.16	Wind shear exponent calibrated from NREL Resource maps at 90m, ASCE-7, and buoy data at 4m.
Extreme 10 minute average 50 year wind speed at 4m/ Extrapolated to 90 m (m/s)	24.7/ 40.6	P.O.T using GPD with 10 min wind speeds, P=8 u=14.5
Extreme 50 year 5-second gust at 4 m / Extrapolated to 90 m (m/s)	40.6/ 66.8*	P.O.T using GPD, P=8 u=18.5

3 Expedited Permitting Process

Maine Public Law Chapter 270, *An Act to Facilitate Testing and Demonstration of Renewable Ocean Energy Technology*, provides generous permitting guidelines for projects located in the University of Maine Deepwater Wind Test Site, particularly when partnering with the University of Maine for testing purposes. There is a 60-day review period for applications for a general permit for an offshore wind energy demonstration project located in the test site. The review period begins on the date that the department has accepted an application for processing.

For the University of Maine's DOE-funded research at the test site, the National Environmental Policy Act required the DOE to conduct an environmental assessment to consider potential environmental impacts of proposed projects prior to making funding decisions. In accordance with this Act, the DOE completed the Environmental Assessment for the University of Maine's Deepwater Floating Offshore Floating Wind Turbine Demonstration Project in May of 2011. Following the public comment and review period, the University of Maine received a Finding of No Significant Impact from the Department of Energy for the DeepCwind Consortium Research Program's proposed turbine. Although an Environmental Impact Assessment and Record of Decision will be required for this proposed project, the fact that UMaine received a FONSI for a scaled version of this program indicates the strength of the permitting team.

A copy of the FONSI is attached in Appendix.

4 Characterized Ecological Data

The Gulf of Maine is home to an abundance of species, some of which are endangered or threatened and require top consideration in the site selection process. Understanding the importance of protecting the local ecosystem, the University of Maine partnered with key environmental monitoring organizations and state and federal agencies to gather appropriate data at the test site.

The environmental monitoring for this program was designed to deliver information about species of conservation or commercial concern, as well as provide new understanding about the spectrum of potential environmental impacts of deepwater, offshore wind development on marine species, habitats, and ecosystems in the Gulf of Maine. The plan was developed in consultation with the Maine Department of Marine Resources, the U.S. Fish and Wildlife Service, NOAA/NMFS, the Maine Historic Preservation Office, our permitting subcontractors (HDR, James Sewall Company, and Kleinschmidt Associates

Table 2: Summary of Data Collected for Environmental Monitoring for Aqua Ventus I; collaborators include Pacific Northwest National Laboratories and Sandia National Laboratories

Species/Habitat Concern	Data Collected
Bird Studies	One year of radar monitoring, one season of visual surveys (Fall 2011), & literature review of the Gulf of Maine as a migratory bird pathway
Bat Studies	Two periods of pre-deployment monitoring: Paired echolocation detectors at the Monhegan Island Lighthouse in 2011 and on NERACOOS Buoy E off Monhegan Island from April 2012-April 2013.
Visual Impact	SNL produced visual impact simulations used in stakeholder engagement
Hydro-acoustic and Marine Mammal Studies	Visual surveys in Summer 2012 and Fall 2011 and year-round passive acoustic monitoring by Maine DMR
Benthos	Three years of drop camera and remotely operated vehicle (ROV) surveys of the Monhegan Island test site
Fish	Benthic species have been monitored by benthic drop cameras and ROV (Summer 2011-2013). Pelagic species identified by telemetry (year round) of tagged individuals and acoustic surveys (Summer/Fall 2010)

5 Bird and Bat Studies

UMaine and its partners have closely monitored bird and bat activity over the test site over the last year, teaming with the New Jersey Audubon Society to maintain a radar trailer on Monhegan Island, 2-3 miles from the Test Site. The results indicated that 93% of species flying during day and 95% of species flying during night flew at an altitude of 246 feet or higher Figure 1. For the full report, see Appendix. Generally, our results for target passage and passage rates were consistent with respect to Period and Season. We detected significantly more targets during nocturnal compared with diurnal periods across most seasons. Not surprisingly, targets recorded at our Monhegan study site were greater during the Fall/Early season, when the nocturnal migration of passerines and shorebirds is at its peak. Our indices of avian movement was lowest in winter when there is a dearth of avian activity in and around the coastal waters of Maine.

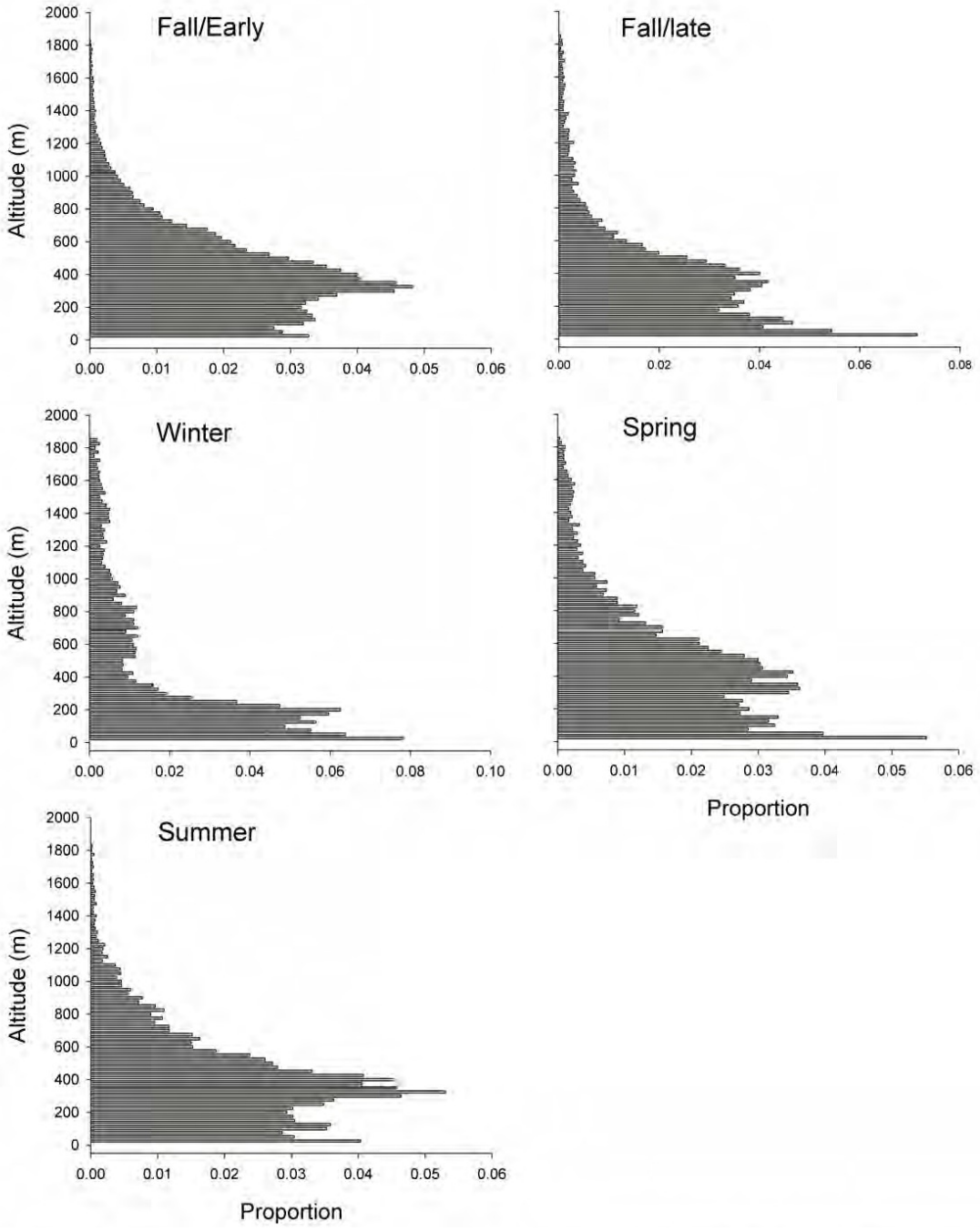

Figure 1: Bat Survey

UMaine also performed passive acoustic survey on Monhegan Island. The monitoring period was late in the migration season for mid-coast Maine. The acoustic monitoring period for land bird migrants at the site on Monhegan Island captured the late passage of only a few warbler species and the majority of sparrows. By the end of the monitoring period, MFCs comprised mostly sparrows, a pattern consistent with other acoustic surveys, banding, and visual observations for the region. While the currently proposed 1/3 scale test turbine is likely to incur little direct collision risk to most land bird migrants under optimal weather conditions, lighting during construction, operation, and removal phases of the proposed small-scale test turbine should be

minimized, particularly during periods of high migration activity and under low visibility conditions.

Finally in September, October, and November, 2011, during the pre-deployment stage of the DeepCwind's deepwater test wind turbine project at the University of Maine's Offshore Wind Test Site off Monhegan Island, boat-based visual surveys gathered data on species of birds and, opportunistically, marine mammals, and turtles, including occurrence and numbers, as well as various bird behaviors, flight direction, and flight heights.

The most numerous of bird species during the entire survey period was by far the migrating flocks of cormorants, with 93% of their numbers counted while in the Control Quadrat. The next five most numerous species, listed by greatest count to lesser, were Herring gull (63% of which occurred in the Test Quadrat), Great shearwater (78% of which occurred in the Control Quadrat), Northern gannets (72% of which occurred in the Control Quadrat), Common eider (all 65 birds counted within the Test Quadrat), and Great black-backed gulls (67% of which occurred in the Test Quadrat). Unidentified "Large" gulls ranked high in numbers as well, with 84% of these counted within the Test Quadrat. The majority of all animals (79%, includes all birds, mammals, fish) sighted were observed in the Control Quadrat. See appendix for full report.

6 Visual Impact

6.1 Marine Mammals

Complete studies were carried out to determine the effect of floating, offshore turbines on existing benthic (seafloor dwellers), demersal (near bottom), and pelagic (away from bottom). These studies included supplemented existing data available from the Maine Department of Marine Resources with physical surveys to monitor the existence and movements of marine species. For the full report, see Appendix.

6.2 Benthos

UMaine has deployed a remotely operated vehicle in order to survey the benthos at the site. The potential deployment area is relatively species depauperate and provides habitat for comparatively low densities of benthic megafauna. Most ecologically and economically valuable species, including American lobster, crabs and pollock all decrease in abundance to zero at 100m depth. Even within the proposed test bed, our ROV surveys confirm that the mud dwelling communities are considerably less diverse than the surrounding ledge habitats. Since mud habitats are so expansive near the deployment area, we conclude that the impacts to valuable species from deployment will likely be minimal within this area. Northern shrimp and Acadian redfish populations do persist within the test bed and control sites. However we do not expect drastic impacts to either of these species, for full report see Appendix.

6.3 Fish

Two methods were implemented to survey fish at the test site. An acoustic receiver was deployed at the site to locate tagged Atlantic salmon, sturgeon and dogfish. Although 4 dogfish, 7 Atlantic sturgeons, and 8 Atlantic salmon were detected at the site, no individual fish spent more than a day at the receiver location.

The second method was an acoustic survey for pelagic fish (mostly herring) with a Simrad EK60 echo sounder. The relative biomass for all sites and all months was quite low with nautical area scattering coefficient (NASC) values of 2000 or less, with the exception of one transect. The control site sampled in September at night had a mean NASC value of 6841, significantly higher than other values. Preliminary analysis showed a consistently higher abundance of targets in the upper water column (0-20m) compared to targets closer to the bottom (80-100m) across all sites and months. The range of target strength values for identified single targets was the same for all

sampling months, with a maximum of -18dB and a minimum of -60dB for July, August and September.

7 Geophysical and Geotechnical Data and Analysis

In 2010, the University of Maine led a research effort to characterize the geophysical and geotechnical conditions of the test site. The surveys performed utilized the best available bathymetric technology to gather a broader view of the distribution of substrates and gain a more detailed picture of the ocean floor to assist developers in selecting the appropriate technologies to employ at the Site. Researchers traveled over the test site performing seismic reflection profiling, side-scan sonar, and multi-beam bathymetry to provide a fully characterized data set for the test site. Characterization of test site properties allows the team to select site that meets criteria of water depths, floor composition, ocean currents, and other properties that affect the performance of offshore structures. Seismic stratigraphy data provide vital inputs to engineering models to determine the appropriate anchoring technology for offshore structures. Digital seismic reflection profiling was performed in conjunction with coring to gather samples and determine the composition and sediment thickness of the test site. As a result, *significant data has already been collected on the site which is critical for the design of the VolturnUS units anchor and mooring systems which will help allow the project move more quickly and more cost effectively*.

Preliminary analyses of seismic reflection data show mainly bedrock outcropping at the seafloor along the eastern half of the test site. Western and central portions of the site contain seafloor areas having variable patterns of north-south oriented bedrock outcrops 100 m to 300 m across that are interspersed with glaciomarine and Holocene mud basins 100 m to 600 m across. The basins are lenticular in shape, pinching out to zero on their margins and may reach a total thickness of up to 35 m along their deepest axes. The majority of the 54 muddy basins identified are less than 5 m in depth, however, 15 of these basins are deep, and up to 35 m in depth.

Core samples were collected and a sample core log maintained. This core, typical of other cores analyzed, is comprised of high plasticity clay. The uppermost meter of sediment has slightly higher water and organics contents and Atterberg limits (plasticity and liquidity indexes) than the deeper sediments, which have average values of 97%, 51, 91 and 6% for water content, plastic limit, liquid limit and organic content, respectively. The in situ vertical effective stress (s'_{v0}) was determined based on the profile of bulk density determined from CRS consolidation specimens at the natural water content.

A geoarchaeological study was also performed.

For the full reports, see Appendix.

Appendix 1

Two-year baseline characterization of benthic and demersal assemblages inside the University of Maine deepwater wind test sites off Monhegan Island, Maine

Prepared for the DeepCwind Consortium
March 2013
Prepared by
Jennifer McHenry, Project Manager
Dr. Robert Steneck, Principle Investigator
University of Maine- Orono, Maine

Introduction

Wind-power development has become cost-competitive in areas with the most favorable wind regimes. However, high transmission costs and concerns for sight and sound disruption make land-based turbine deployment controversial. Offshore wind development in the Gulf of Maine (GoM) could be beneficial to all because the GoM has consistently high wind potential (156 GW) at an optimal distance from coastal residents (Schwartz *et al*. 2010). The University of Maine, as an emergent leader in the engineering of floating offshore wind platforms, seeks to harness this energy by deploying the first operational test-scale turbine by the end of 2013. Yet, offshore wind is just one of many valuable natural resources in the Gulf of Maine.

Organisms living on or near the seafloor are also vitally important to New England. The GoM is a relatively wide, shallow and well-mixed extension of the continental shelf, which sustains high rates of pelagic and benthic primary productivity (Townsend 1991). Since phytodetritus rains to the benthos relatively rapidly, diverse communities of invertebrates proliferate and ultimately support a high carrying capacity for large demersal fishes. Historically, the commercial harvest of these species, including Atlantic cod, haddock and flounder, has provided a livelihood for fishermen and shaped the culture of coastal communities in Maine. In the late 1980's, many demersal, or groundfish, populations in the GoM collapsed from overharvesting, leaving Maine's economy reliant on a few benthic invertebrate species (Steneck *et al.* 2011). In particular, the American lobster now comprises 85% of Maine's harvested marine resource value.

Given the inherent ecological, economic and cultural value of benthic megafauna, the University of Maine-led DeepCwind Consortium considers potential impacts from turbine deployment to be of the highest importance. For this reason, we have undertaken extensive video surveys to quantify patterns of benthic megafaunal abundance before, during and after deployment of the test turbine. In order to evaluate the population densities we observed within the potential deployment area, we also conducted surveys in coastal control sites. These data allow us to evaluate trends in population density, biomass, species diversity and megafauna community structure with distance from shore, depth and substrate type. This report summarizes our results.

Figure 1: Images of drop camera and small remotely operated vehicle (ROV) used in 2010 and 2011, respectively. The drop camera consists of a metal frame and a 500-line resolution camera. The Video Ray is propelled by four thrusters (two horizontal, two vertical), controlled from surface console and collects live video with a 570-line resolution camera. Both units illuminated the seafloor with Halogen lights and allowed us to collect size measurements using a laser-scaling system. Both years, the laser scaling system measured approximately a 10.4 cm diameter.

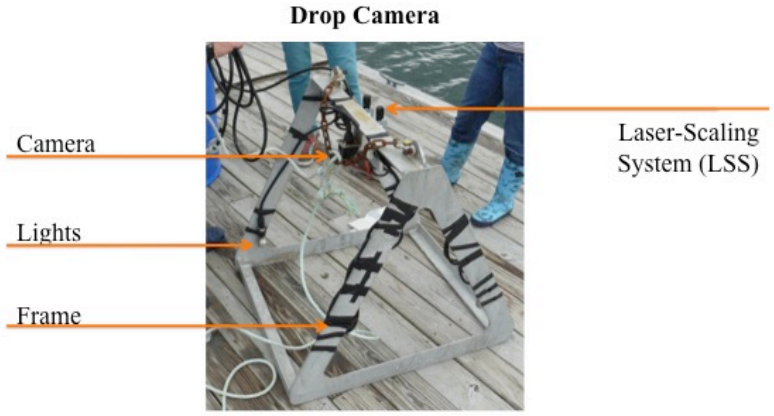

Methods

Survey Methods

During the summer of 2010 and 2011, the Steneck Lab used a drop-camera and a small Videoray Pro 3 remotely operated vehicle (ROV) to characterize bottom habitats and communities in the midcoast Maine region (Figure 1). Initially we intended to collect one year of "before deployment" data and one year of "after deployment" data, but due to delays in deployment we have collected two years of baseline data. During this time, we conducted over 100 geo-referenced, laser-scaled underwater video surveys between the Boothbay and Monhegan Island, Maine (10-100m water depth) (Figure 2). Twenty-seven transects characterize the proposed testbed and two adjacent control sites near Monhegan (a total of 27 transects) prior to turbine deployment and approximately 73 transects (from 28 sites) characterize the benthos from coastal controls sites.

Figure 2: Map of sites surveyed at Mohegan Island (A) and within Midcoast Maine (B). The hash-marked area denotes the area of potential deployment for the University of Maine's test floating offshore wind turbine. Black and red lines denote transects conducted using a drop camera in 2010 and a small Videoray remotely operated vehicle (ROV) in 2011, respectively.

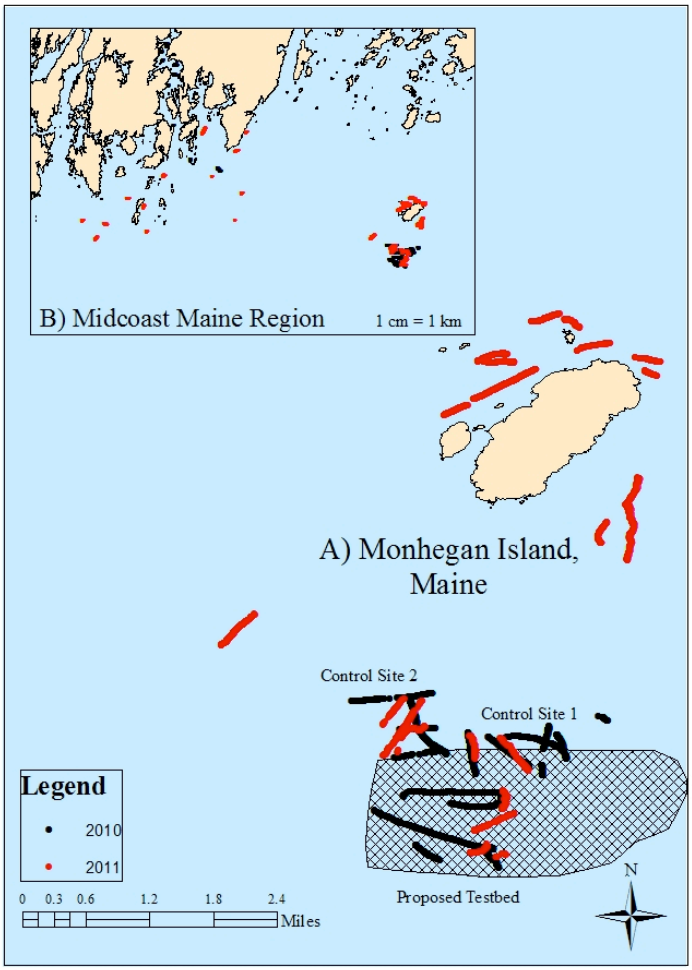

Each transect involved deploying the unit from a small vessel (usually a lobster boat), lowering it to approximately 0.5 to 1m above the seafloor and drifting with the current for 40 to 1000m. The lengths of each transect varied depending on the direction of the currents, the wind speed, and the presence of lobster gear. Where surveys could be completed without obstacles, we surveyed continuously for up to an hour per transect. However in locations where interruptions occurred more frequently, we conducted a higher number of transects for a shorter period of time per transect (usually adding up to one to two hours total).

Video Analyses

In the lab, we reviewed the videos and sub-divided each transect into roughly 50m^2 segments to standardize our dataset. Then, we analyzed each segment to quantify patterns species composition, population density (#/100m^2), dominance, and diversity (Shannon-Weiner Index). We also calculated body sizes for any organisms we observed using the onscreen laser distance. Together, these metrics of benthic community structure and biodiversity allow us to describe baseline communities of invertebrates and groundfishes in the midcoast Maine region. To minimize variance between sites and reveal the habitat preferences of organisms, we stratified our data by depth and substrate type (Table 1).

Table 1: Samples sizes by habitat strata. Video data was collected using a drop camera and a small Videoray Pro3 ROV in 2010 and 2011 from sites across the midcoast Maine region (from Monhegan Island to Boothbay Harbor, Maine.)

HABITAT STRATA							
	Depth (m)						
Substrate Type	*10*	*20*	*30*	*40*	*50*	*60*	*100*
Boulder	x	10	27	10	3	10	x
Cobble	x	4	9	8	7	7	x
Gravel	x	7	23	7	2	4	x
Ledge	10	60	36	10	7	3	17
Mud	20	7	32	12	4	30	142
Sand	2	6	8	x	x	x	x
Silt	x	x	3	x	x	x	x

Results

Area and Habitats Surveyed

Between 2010 and 2011, we characterized a substantial area of the midcoast Maine coastal shelf (i.e. the area between Mohegan, Island and Boothbay Harbor, ME). Within the potential deployment area, we surveyed 4595m^2 of the proposed testbed, as well as 3532m^2 and 3640m^2 of the adjacent control sites, 1 and 2 respectively (a total of 7922 m^2 and 3846m^2 by year) (Figure 2A). We also characterized approximately 18,812 m^2 of benthic habitat across the near shore midcoast region (Figure 2B), allowing us to collect video from a wide array of habitats. From these surveys, we observed that substrate and depth profiles are exceptionally heterogeneous in this area. Near shore and shallow habitats in the region (above 60m) consist predominantly of ledge, boulder and cobble areas with fewer soft-bottom habitats occurring between outcroppings; whereas mud habitat pervasively dominates deeper areas (below 60m) of the coast where the test turbine is proposed for deployment (J. McHenry and R. Steneck, personal observation).

Table 2: List of species identified from the midcoast Maine region (from Monhegan Island to Boothbay Harbor, Maine) from laser-scaled, geo-referenced video surveys conducted in 2010 and 2011. Seventy-one species are presented below by taxonomic grouping.

TAXONOMIC GROUPINGS	SPECIES NAME
Demersal Fishes	Atlantic cod (*Gadus morhua*), pollock (*Pollachius virens*), cusk (*Brosme brosme*), silver hake (*Merluccius bilinearis*), red hake (*Urophycis chuss*), spotted hake (*Urophycis regius*), white hake (*Urophycis tenuis*), cunner (*Tautogolabrus adspersus*), tautog (*Tautoga onitis*), black sea bass (*Centropristis striata*), searobin (*Prionotus evolans*, other *Prionotus* sp.), longhorn sculpin (*Myoxocephalus octodecemspinosus*), shorthorn sculpin (*Myoxocephalus scorpius*), grubby (*Myoxocephalus aenaeus*), Acadian rockfish (*Sebastes fasciatus*), American eel (*Anguilla rostrata*), rock gunnel (*Pholis gunnellus*), Atlantic hagfish (*Myxine glutinosa*), snakeblenny (*Lumpenus lumpretaeformis*), daubed shanny (*Lumpenus maculates*), radiated shanny (*Ulvaria subbifurcata*), winter flounder (*Pseudopleuronectes americanus*), American plaice (*Hippoglossoides platessoides*), summer flounder (*Paralichthys dentatus*), Atlantic halibut (*Hippoglossus hippoglossus*), lumpfish (*Cyclopterus lumpus*), ocean pout (*Zoarces americanus*), and alligator fishes (*Aspidophoroides monopterygius*).
Decapods	Northern shrimp (*Pandalus borealis,* other *Pandalus* sp.), American lobster (*Homarus americanus*), Jonah crab (*Cancer borealis*), Atlantic rock crab (*Cancer irroratus*) and Arctic lyre crab (*Hyas araneus*).
Bivalves	Horse mussel (*Modiolus modiolus*) and giant sea scallop (*Placopectan magellanicus*).
Anemones	Northern cerianthid anemone (*Cerianthus borealis*), northern red anemone (*Urticina felina*), frilled anemone (*Metridium senile*), swimming anemone

	(*Stomphia coccinea*) and rugose anemone (*Hormathia nodosa*).
Echinoderms	Blood seastar (*Henricia sanguinolenta*), northern seastar (*Asterias rubens*), Forbes' seastar (*Asterias forbesi*), spiney sunstar (*Crossaster papposus*), smooth sunstar (*Solaster endeca*), horse seastar (*Hippasteria phrygiana*), common sand dollar *(Echinarachnius parma),* Psolus cucumber (*Psolus fabricii*), orange footed sea cucumber *(Cucumaria frondosa*) and brittle stars *(Ophirudiae sp.)*
Brachiapods	Northern lampshell (*Terebratulina septentrionalis*)
Sponges	Fig sponge (*Suberites ficus*), breadcrumb sponge (*Halichondria panicea*), finger sponge *(Haliclona oculata*), palmate sponge (*Isodictya palmate*), *Iophon sp.,* boring sponge (*Cliona celata*), red beard sponge (*Microciona prolifera*), *Polymastia sp. and* warty sponge *(Melonanchora elliptica*).
Tunicates	Crust (Didemnum spp., Botrylloides diegensis) and solitary tunicates (Mogula sp.)
Polychaetes	Sabellid sp.
Bryozoans	Bugula turrita

Figure 3: Population density (#/100m^2) of dominant organisms broken down by depth and substrate type from the midcoast Maine region from Boothbay to Monhegan Island, Maine. Data was collected using a drop camera and a small Videoray Pro3 ROV in 2010 and 2011. "Hard substrates habitats" include ledge, boulder and cobble areas, while "soft substrates habitats" include silt, mud and sandy areas. Error bars denote +/- 1 standard error.

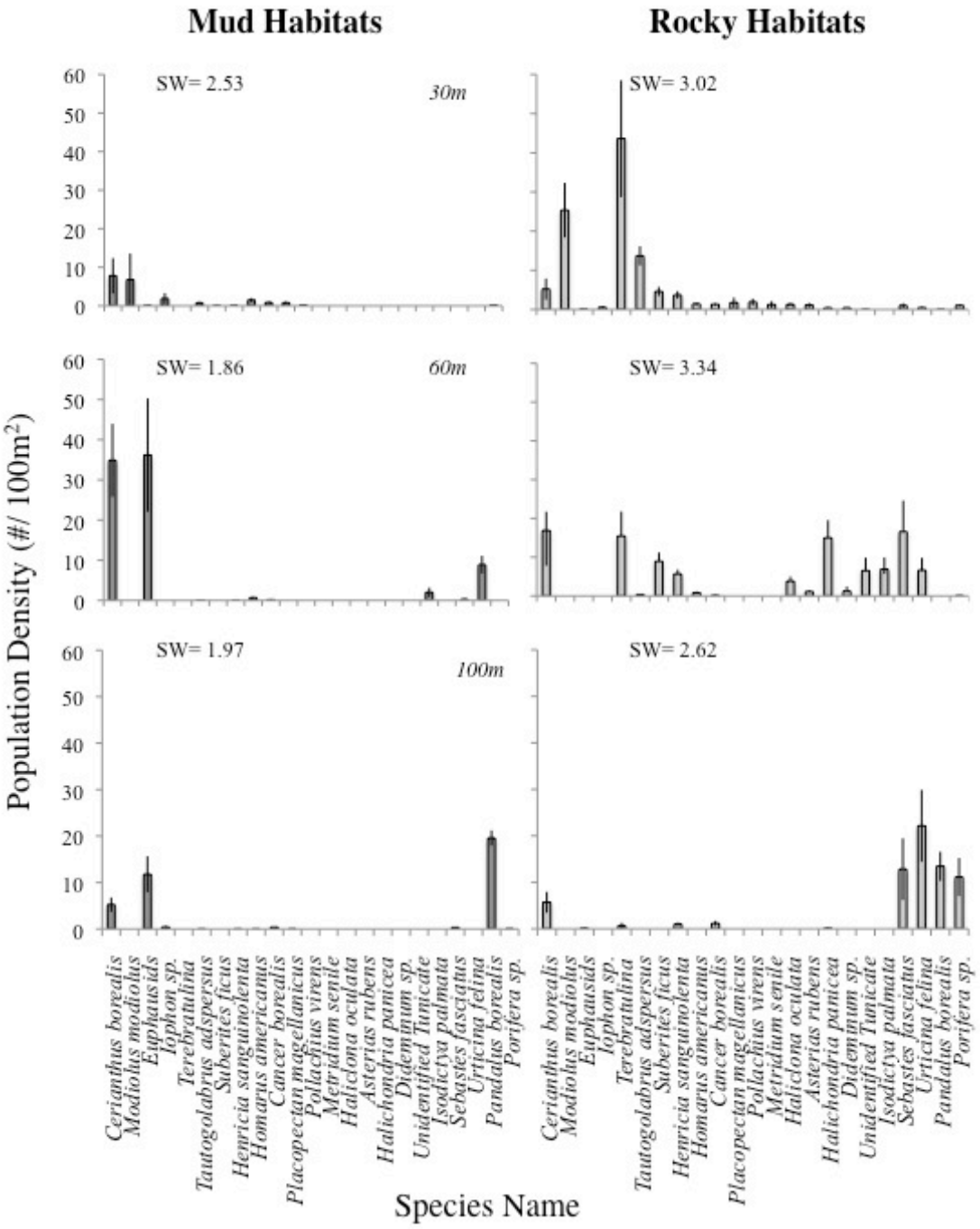

Benthic Assemblages from Coastal Maine to Monhegan Island

From the Boothbay to Monhegan Island, we observed a total of 71 species (Table 2). Throughout the region, we found that the species composition, population densities (#/100m^2) and species diversity of megafaunal communities vary with substrate and depth. Overall, rocky habitats were more diverse and sustained higher population densities than soft bottom habitats (Figure 3). We also found that the species composition and the diversity of communities changed drastically with depth depending on the substrate

type. On soft bottom habitats, assemblages of cerianthid anemones and euphausids dominated the shallow (30m) to intermediate (60m) depth sites, while northern shrimp become more abundant in deeper areas (100m) (Figure 3). However on rocky habitats, average population densities and species diversity for megafauna were highest at intermediate depths (60m). For examples, brachiopods, horse mussels and cunner dominated shallow sites (30m) and Acadian redfish and northern red anemones dominated deep sites (100m). However at intermediate depths (60m), diverse assemblages of Acadian redfish, cunner, northern red anemones, cerianthid anemones, four sponges species and two tunicate species persisted. Lastly, we found that the population densities for many valuable species, including American lobsters, Jonah crabs, northern shrimp, and pollock all decrease from shallow to deeper sites (Figure 4). The only commercially valuables species to increase drastically in abundance near the testbed were Acadian redfish and northern shrimp (Figure 4B).

Figure 4: Average population density (#/100^2) of demersal fishes (A) and decapods (B). Abundance data was collected using a drop camera and a small Videoray Pro3 ROV in 2010 and 2011.

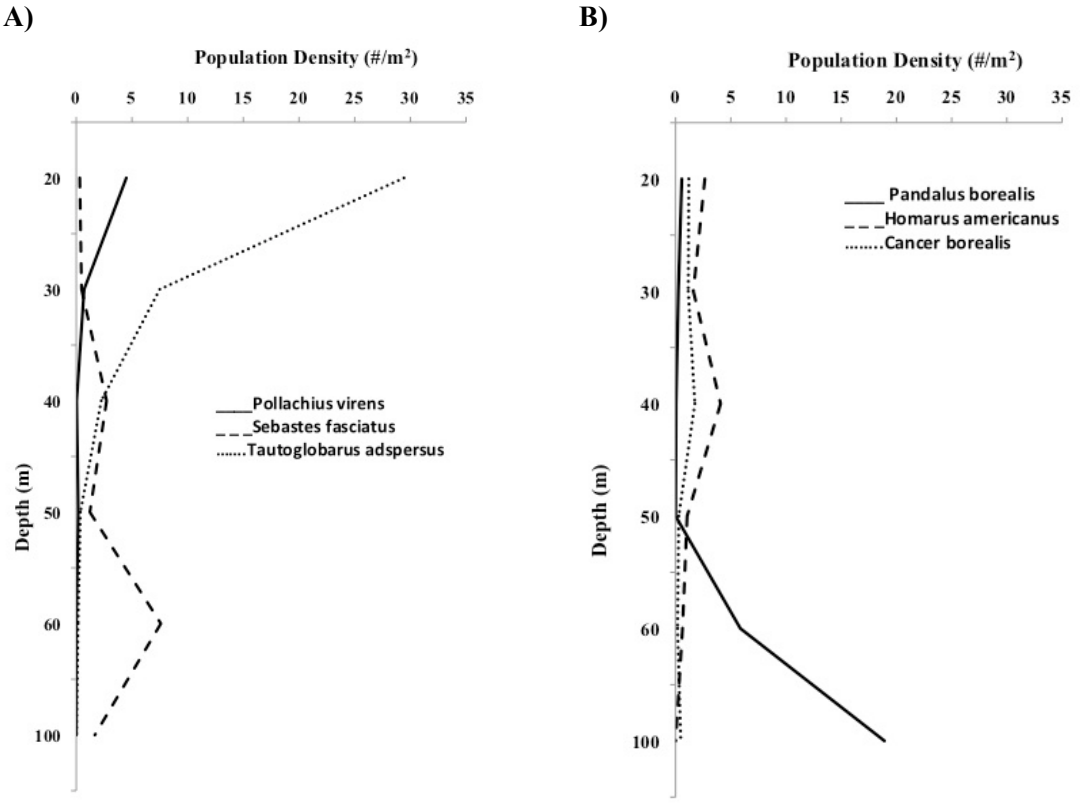

Table 4: List of species identified within the deployment test site and two control sites off of Monhegan, Maine from laser-scaled, geo-referenced

video surveys conducted in 2010 and 2011. Thirty-two species are presented below by taxonomic grouping.

TAXONOMIC GROUPINGS	SPECIES NAME
Demersal Fishes	Silver hake (*Merluccius bilinearis*), red hake (*Urophycis chuss*), spotted hake (*Urophycis reguis*) white hake (*Urophycis tenuis*), cunner (*Tautogolabrus adspersus*), longhorn sculpin (*Myoxocephalus octodecemspinosus*), shorthorn sculpin (*Myoxocephalus scorpius*), Acadian rockfishes (*Sebastes fasciatus*), rock gunnel (*Pholis gunnellus*), Atlantic hagfish (*Myxine glutinosa*), snakeblenny (*Lumpenus lumpretaeformis*), daubed shanny (*Lumpenus maculates*), radiated shanny (*Ulvaria subbifurcata*), winter flounder (*Pseudopleuronectes americanus*), American plaice (*Hippoglossoides platessoides*), summer flounder (*Paralichthys dentatus*), Atlantic halibut (*Hippoglossus hippoglossus*), lumpfish (*Cyclopterus lumpus), ocean pout (Zoarces americanus*) *and* alligatorfish (*Aspidophoroides monopteryguis*).
Decapods	Northern shrimp (*Pandalus borealis*), American lobster (*Homarus americanus*), Jonah crab (*Cancer* borealis) and Arctic lyre crab (*Hyas araneus*).
Bivalves	Giant sea scallop (*Placopectan magellanicus*)
Anemones	Northern cerianthid anemone (*Cerianthus borealis*), northern red anemone (*Urticina felina*), rugose anemone (*Hormathia nodosa*).
Echinoderms	Blood seastar (*Henricia sanguinolenta*)
Brachiapods	Northern lampshell (*Terebratulina septentrionalis*)
Sponges	Breadcrumb sponge (*Halichondria panicea*), *Iophon* sp.

Benthic Assemblages within the Potential Deployment Area

Compared to shallower sites, the potential deployment area at Mohegan Island has only 32 species (Table 3). In 2010 and 2011, benthic assemblages observed in the proposed testbed, control site 1 and control site 2 differed between mud and ledge habitats. As stated above, Acadian redfish and northern red anemones dominate the deeper hard bottom ledge habitats whereas northern shrimp and other panda lid shrimp species dominate the mud areas within the area of potential deployment (Figure 5, Figure 6). Species diversity is also much lower in areas with mud compared to areas with ledge (Table 5).

Discussion and Conclusions

The potential deployment area is relatively species depauperate and provides habitat for comparatively low densities of benthic megafauna. Most ecologically and economically valuable species, including American lobster, crabs and pollock all decrease in abundance to zero at 100m depth. Even within the proposed testbed, our ROV surveys confirm that the mud dwelling communities are considerably less diverse than the surrounding ledge habitats. Since mud habitats are so expansive near the deployment area, we conclude that the impacts to valuable species from deployment will likely be

minimal within this area. Northern shrimp and Acadian redfish populations do persist within the testbed and control sites. However we do not expect drastic impacts to either of these species.

Figure 5: Population density (#/100m^2) of dominant benthic and demersal organisms within the potential deployment area near Monhegan Island, Maine in 2010. Abundance data was collected using a drop camera from mud and ledge habitats at 100m water depth within the proposed deployment site, control site 1 and control site 2. Error bars denote +/- 1 standard error.

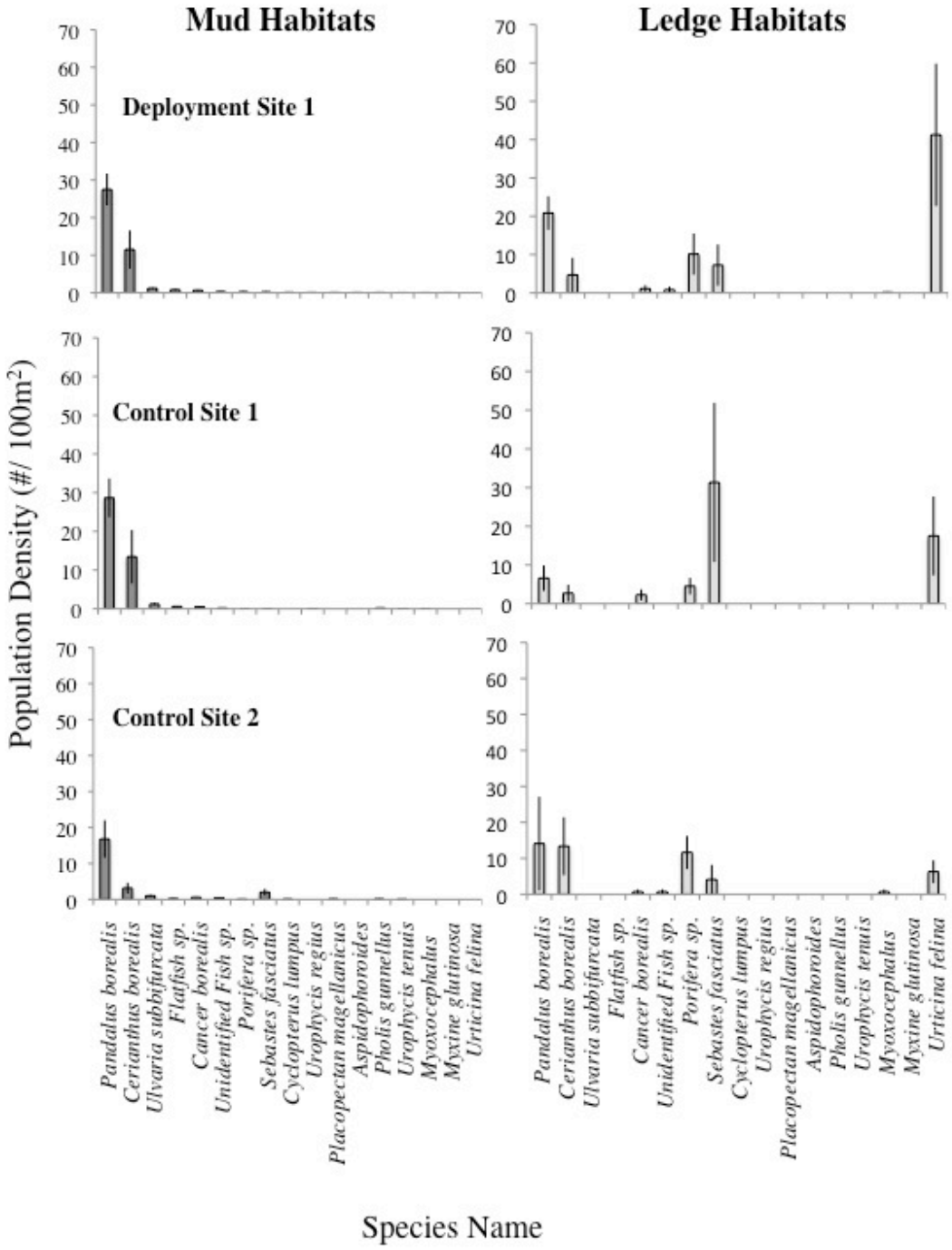

Figure 6: Population density (#/100m^2) of dominant benthic and demersal organisms within the potential deployment area near Monhegan Island, Maine in 2011. Abundance data was collected using a small Videoray Pro 3 ROV from mud and ledge habitats at 100m water depth within the proposed deployment site, control site 1 and control site 2. Error bars denote +/- 1 standard error.

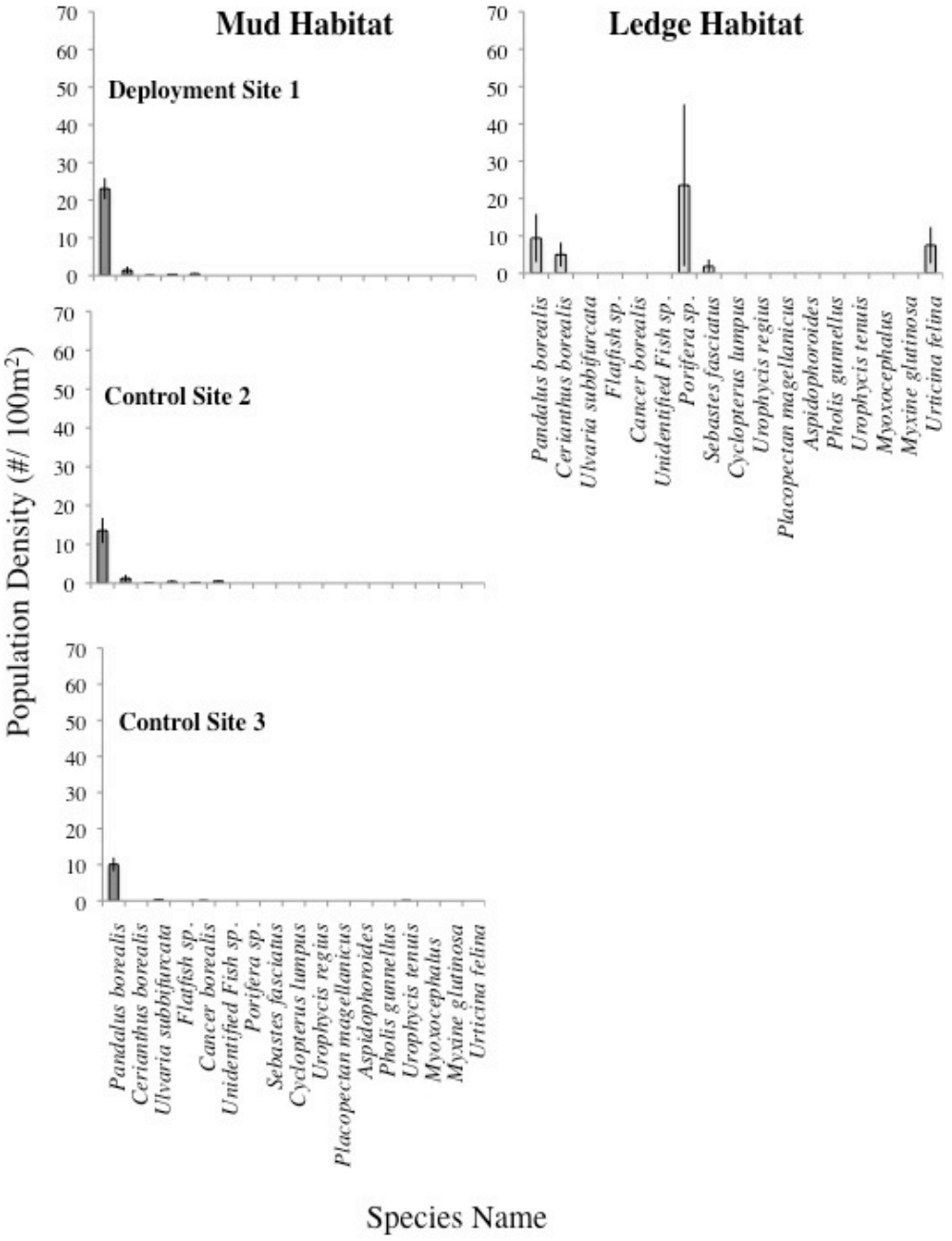

Table 5: Differences in Shannon Weiner species diversity and richness by substrate in the Monhegan testbed and two adjacent controls. Benthic abundance data was collected using a drop camera and a small Videoray Pro3 ROV in 2010 and 2011.

SHANNON WEINER DIVERSITY INDEX FOR MONHEGAN SITES								
	Proposed Testbed		Control Site 1		Control Site 2		Average SW Index	
Year	Ledge	Mud	Ledge	Mud	Ledge	Mud	Ledge	Mud
2010	2.15	1.49	2.06	1.37	2.52	1.69	2.25	1.51
2011	2.36	0.79	-	0.94	-	1.06	2.36	0.93

Future surveys

The next phase of the permitting process will involve siting for subsea transmission lines between Mohegan Island and the cable's point of landfall (a site to be determined). Since population densities and species diversity are relatively higher on hard substrate habitats (i.e. ledge, boulder and cobble) and hard substrate habitats are more common in the near shore area, we will commence extensive ROV surveys between Mohegan Island and land in early 2013. Ecosystem models that incorporate past data from 2010, 2011, 2012 (in prep.) and 2013 will be used to help select the most appropriate path for transmission lines that ensures the lowest impact to benthic communities.

Literature Cited:

1. Schwartz, M., Heimiller, D., Haymes, S., and Musial, W., 2010. Assessment of Offshore Wind Energy Resources for the United States. National Renewable Energy Laboratory (NREL), Technical Report NREL/TP-500-45889.

2. Steneck, R. S., Hughes, T. P., Cinner, J. E., Adger, W. N., Arnold, S. N., Berkes, F., ... & Worm, B. (2011). Creation of a gilded trap by the high economic value of the Maine lobster fishery. Conservation Biology, 25(5), 904-912.

3. Townsend, D. W. (1991). Influences of oceanographic processes on the biological productivity of the Gulf of Maine. Reviews in Aquatic Sciences, 5(3), 211-230.

Results of Abbreviated Passive Acoustic Monitoring of Nocturnal Bird Migration Conducted Near the University of Maine Deepwater Test Site at Monhegan Island During Fall Migration, 2011

a final report prepared for and submitted to the University of Maine and DeepCwind Consortium
June, 2012

by
Rebecca L. Holberton, Ph.D.
and
Wesley A. Wright

Laboratory of Avian Biology
University of Maine
Orono, Maine 04469
207-581-2526; rebecca.holberton@maine.edu

Table of Contents

Figures and Tables

Suggested citation for this report: Holberton, R.L. and Wright, W.A. 2012. *Results of Abbreviated Passive Acoustic Monitoring of Nocturnal Bird Migration Conducted Near the University of Maine Deepwater Test Site at Monhegan Island During Fall Migration, 2011; a report submitted to the University of Maine and DeepCwind Consortium.*

Cover photos: Acoustic recording set-up at Lobster Cove (photo courtesy of David Bridges); spectrogram of White-throated Sparrow migratory flight call; White-throated Sparrow (R. Holberton photos).

Executive Summary – The University of Maine's Laboratory of Avian Biology (hereafter LAB) was contracted to conduct passive acoustic surveys on Monhegan Island, approximately 22 km southwest from Port Clyde on the mainland, at a land-based location nearest to the University of Maine's deepwater offshore wind test site located in state waters within 5 km of the southwest coastline of the island. The main objective of the acoustic survey project was to record flight vocalizations made primarily by nocturnal landbird migrants occurring within the detection area during the period of the calendar year corresponding to the same period in a subsequent year in which a single 1.5 kW test turbine is planned for deployment, sometime from late July through early November 2012 or 2013. The equipment was in place within a week that funds became available. Recording began on the night of 30 September-1 October and continued through the night of 4-5 November, operating 15 hours each night from 1800h to 0900h EDT the following morning to target nocturnal migrants, including those who may be arriving at the site soon after dawn. Only calls characteristic of migratory flight calls, in contrast to alarm calls or songs, were included in analyses and were limited to those in the high frequency range.

The monitoring period was late in the migration season for mid-coast Maine. The acoustic monitoring period for landbird migrants at the site on Monhegan Island captured the late passage of only a few warbler species and the majority of sparrows. By the end of the monitoring period, MFCs comprised mostly sparrows, a pattern consistent with other acoustic surveys, banding, and visual observations for the region. Within-night patterns during the monitoring period revealed that the site is a multi-purpose one at which not only do migrants fly over while aloft, but also depart from soon after sunset, patterns that are congruent with radar collected at this site the previous fall. This area on the island, nearest to the offshore test site, is likely to concentrate migrants not only because it may offer optimal habitat characteristics for foraging and refuge for some species on stopover, but it appears to serve as a strategic departure area for landbird migrants ultimately heading to the mainland. The reverse may be true for migrants in spring. Further, flight altitudes are not only lower as birds ascend or descend, but also during flights over water, along coastlines, and in conditions with poor visibility. While the currently proposed 1/3 scale test turbine is likely to incur little direct collision risk to most landbird migrants under optimal weather conditions, lighting during construction, operation, and removal phases of the proposed small-scale test turbine should be minimized, particularly during periods of high migration activity and under low visibility conditions.

INTRODUCTION

As reviewed by Evans (2005), it has been known for centuries that birds make vocalizations during migratory flights, although the purpose of these calls is still debated. The first electronic recording of night migrants in North America began in the early 1900s and illustrated the wide diversity of sounds birds make when flying aloft (Graber & Cochran 1959, 1960; Evans 2005). These vocalizations, known as 'migratory flight calls', differ from those made in other contexts such as courtship, social interactions, and predator detection primarily by the shifted frequency range, generally short duration, and reduced complexity compared to song or alarm vocalizations.

Technological advances over the past 50 years have improved the quality of flight call recordings and the ability to analyze them, resulting in a growing database of flight call identification. While many flight calls of distinct sound frequency, pattern, and duration can be made by more than one species, most calls have been found to be species-specific. Researchers at Cornell University and elsewhere continue to improve night sampling techniques and flight call identification (Farnsworth et al. 2004; Farnsworth 2005; Farnsworth & Lovette 2005; Lanzone et al. 2009). The ability to document, through the use of 'passive acoustic survey', the temporal and spatial movement patterns of known species or species groups provides much needed information about migration at local as well as broader landscape levels (Evans & Mellinger 1999; Murray 2004; Farnsworth et al. 2004; Farnsworth 2005).

STUDY OBJECTIVES AND DESIGN

Objectives -

The main objective of this preliminary study was to document and characterize nocturnal migrant passage, as detected by vocalizations, during the fall 2011 migration period at a location nearest to the offshore deepwater wind energy test site located approximately 5 km away. Migratory flight calls, hereafter referred to as MFCs, are defined as those made only in the context of migratory flights, with birds aloft at the moment of calling. Thus, one can assume that the detection of MFCs illustrates birds are present and actively in flight at the time of recording. Most migratory landbirds are nocturnal migrants that, at the end of a stopover bout to rest and refuel, resume migration within the first few hours after sunset and end a night's bout of flight before dawn. For birds crossing ecological barriers such as large bodies of water or desert, flights

may continue after sunrise in order to reach an appropriate stopover area (Baird & Nisbet 1960; Gauthreaux 1971; Able 1977). Although not confirmed by direct visual observation in this study, MFCs recorded soon after sunset are interpreted as made from birds that initiated flight at or near the recording site, and that these birds, at the end of the day, are resuming migration after having been on stopover in the local area. Similarly, a concentration of MFCs near the period of sunrise (before and after) are interpreted as made by birds passing by or arriving to land near the recording location, most likely to initiate a stopover period of rest and refueling after a night of migratory flight. MFCs detected at other times within the recording period clearly indicate birds flying over, but could also include those departing from or arriving at the general recording area. Examining temporal patterns of MFC distribution within each night as well as changes in species group composition of MFCs throughout a migration season helps characterize the site. *The extent of acoustic monitoring at this site was limited by when funds became available and for the scope of the proposed activities associated with siting, operating, and removal of a single, small test turbine, described as having a spar no more than approximately 30.5 m above waterline and a rotor diameter of approximately 21.3 m, for a total height of approximately 41.1 m above the water, and deployed only during the July – November, 2012 or 2013 window proposed at the time of the study's initiation.*

Study Design

Recording Site – Monhegan Island (43° 45′ 59″ N, 69° 19′ 5″ W) is approximately 22 km southeast from Port Clyde on the mainland (Fig. 1). Its total land area is about 2.59 km^2 and is dominated by mixed conifer and scrub vegetation ringed by a rocky shoreline. The acoustic equipment (see description below) was set up approximately 25 m above sea level at the southern end of Monhegan Island in an area called "Lobster Cove" (43°45.494' N, 69° 19.284' W) and within 100 m of the site at which, in 2010, the marine surveillance radar was operated by New Jersey Audubon for the University of Maine's DeepCwind deepwater offshore wind energy test project (Fig. 2). This site provided an unobstructed view in the direction of the offshore test project site to the south and of the mainland to the west-southwest (Figs. 1, 2). The buoy deployed by DeepCwind for gathering weather conditions and sea characteristics at the deepwater test site was not collecting data after October 7, 2011. Thus, wind direction and speed data representative of relevant conditions near the monitoring site were obtained from the buoy, LLNR

820, Station 44005 (43° 12' 13"N; 69° 7' 40" W), located 144.5 km east of Portsmouth, NH and operated by the National Data Buoy Center. This buoy provided general weather conditions that would be relevant to not only birds at or near the test site but also for those making trans-Gulf flights from Nova Scotia and New Brunswick.

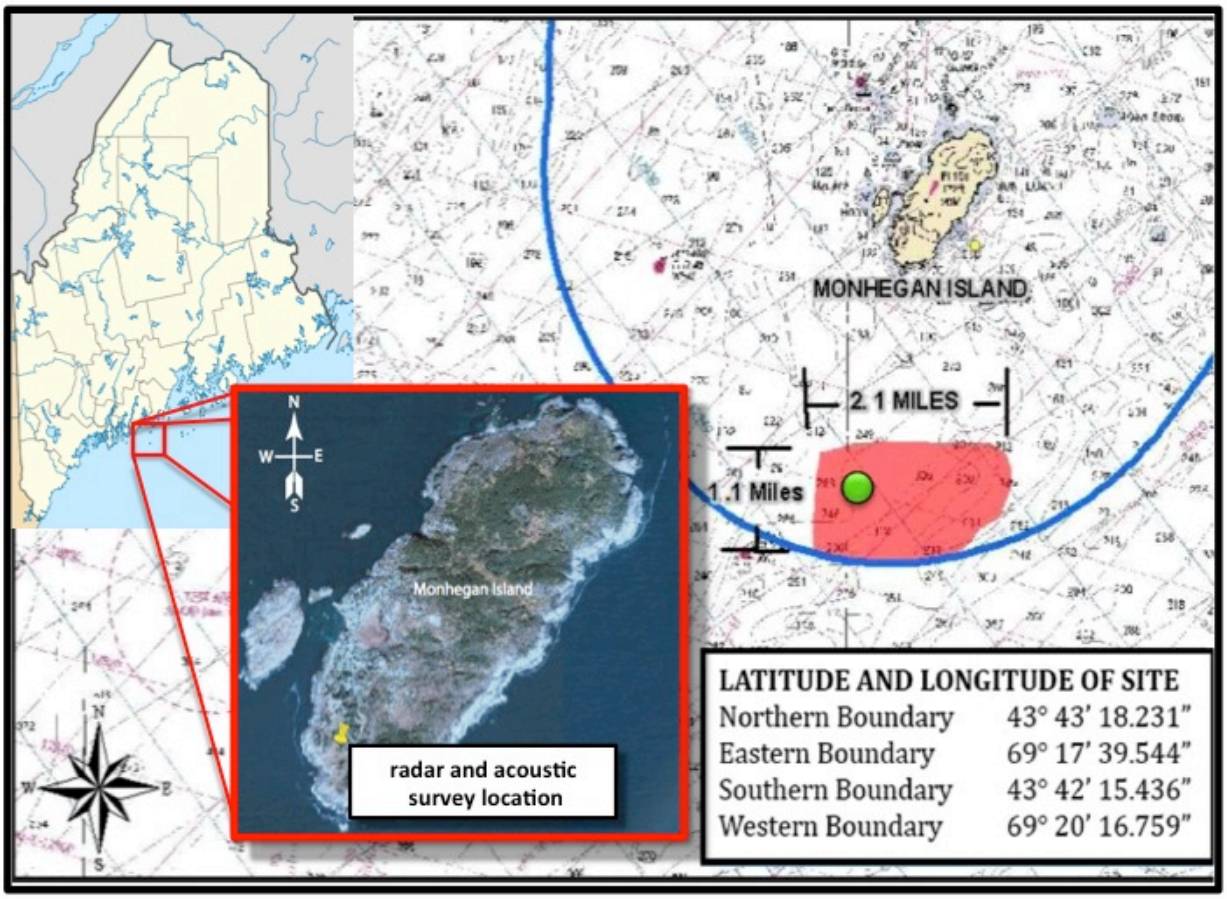

Figure 1. The location of Monhegan Island with respect to the Maine coastline (upper left image from Wikipedia) is shown in a chart illustrating the location of the University of Maine-DeepCwind Consortium's deepwater offshore wind energy test site (shown as green dot within the state-designated test site area noted in red and denoted by the coordinates provided; the blue line indicates the boundary between state and federal waters; image from UMaine-DeepCwind Consortium). The center insert shows the location of the land-based survey site, marked with the yellow pin, at Lobster Cove on the southwest end of Monhegan Island (insert image from Mizrahi, 2010).

Recording Equipment - microphone assembly, recorder, and power supply

Microphone assembly – The microphone assembly was constructed following the general housing design developed by William Evans (Oldbird, Inc., http://oldbird.org/mike_home.htm)

(Figs. 3, 4). The otherwise omnidirectional microphone element (Wildlife Acoustics® SMX-II, reported sensitivity: -36+/- 4 dB (0dB = 1V/pa@1KHz; frequency response: flat 20Hz – 20,000Hz; signal-to-noise ratio: > 62dB, Wildlife Acoustics®, Inc., Concord, MA; www.wildlifeacoustics.com) was adapted for unidirectional recording of sounds originating from above.

Figure 2. View from the acoustic survey/marine surveillance radar survey site looking south-southwest from Lobster Cove (photo courtesy of David Bridges; insert image from Mizrahi, 2010)

The microphone element, with its wind-deterrent foam covering removed (Fig. 3A), was held in place by a heavy marine gasket positioned in the center of a solid plastic plate (approx. 20 cm diameter, Fig. 3B, C). This created a 'pressure-zone' microphone wherein the plate provides a rigid sound boundary directing sound vibrations towards the microphone element. Direct and reflected sound waves reach the microphone element at essentially the same time and, thus,

double in strength the sound pressure (W. Evans, Oldbird, Inc.). The microphone-plate assembly was covered with clear, thin plastic film stretched over the plate to keep moisture out (Fig. 3C, D). The underside of the plate was attached with silicone caulking to the upper rim of a small (~ 15 cm diam.) plastic flowerpot (Fig. 4A) that was then anchored by Velcro® inside a large (46 cm inner diameter) plastic flowerpot (Fig. 4A, B) that funnels and directs sounds generated from above towards the microphone while reducing ambient sounds at or below microphone level. The large flowerpot was lined with a layer of foam padding to reduce ambient noise generated at or below microphone level and to minimize sound distortion. The cables attaching the microphone to the recorder and the recorder to its power source were soundly secured to prevent them from making noise in the wind. The large flowerpot was covered with a thin cotton cloth to keep animals, leaves, and other debris out. Earlier trials conducted showed that neither the plastic film nor the cotton cloth interfered with the microphone element's detectability of avian vocalizations (R. Holberton, unpublished data).

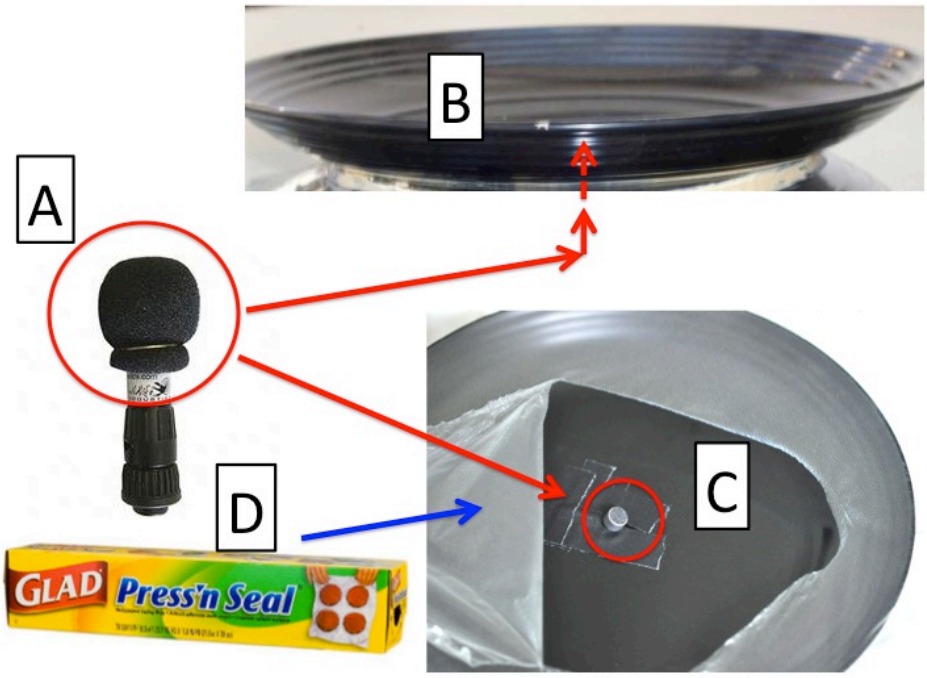

Figure 3. The Wildlife Acoustics® microphone element (A), shown here with foam wind-deterrent cover in place but removed for this study, was inserted up through a hole centered in a rigid plastic plate (B, C). Plastic film (D), shown here partially removed for display (C), protects the microphone element from precipitation.

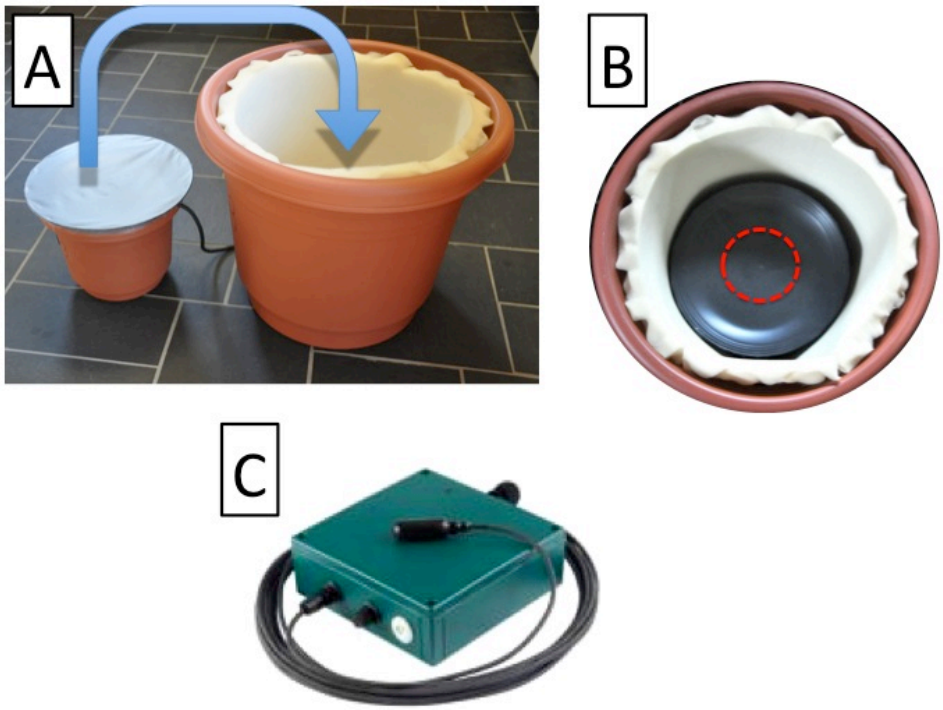

Figure 4. The small flowerpot supporting the microphone element is housed inside the large flowerpot lined with a layer of foam padding (A). The microphone, shown within red-hatched circle under the layer of plastic film (B), is centered within the large flowerpot. The recorder (C) was connected to the microphone assembly by an audio cable.

Recorder and power source – The microphone assembly, pointed skyward, and the recording unit was mounted on a 10-foot ladder anchored with rope and stakes (Fig. 5A, B). The flowerpot microphone assembly, tightly secured to the ladder frame to prevent the unit from rattling in high winds, was connected to a Wildlife Acoustics (WA)® SongMeter™, model SM2 Platform recorder (http://www.wildlifeacoustics.com/products/acoustic-monitoring, Fig. 5A, B). The unit was programed to turn on and off at pre-set times and powered by a 12-V battery charged by a solar panel (Fig. 5C). The recorder held up to four 32 GB SDHC storage discs that stored recordings as WAV format files. The sampling rate was set to 48 kHz, which, in preliminary trials, produced the clearest recordings of avian sounds and covered the frequency range of audible avian flight calls (0-24 kHz).

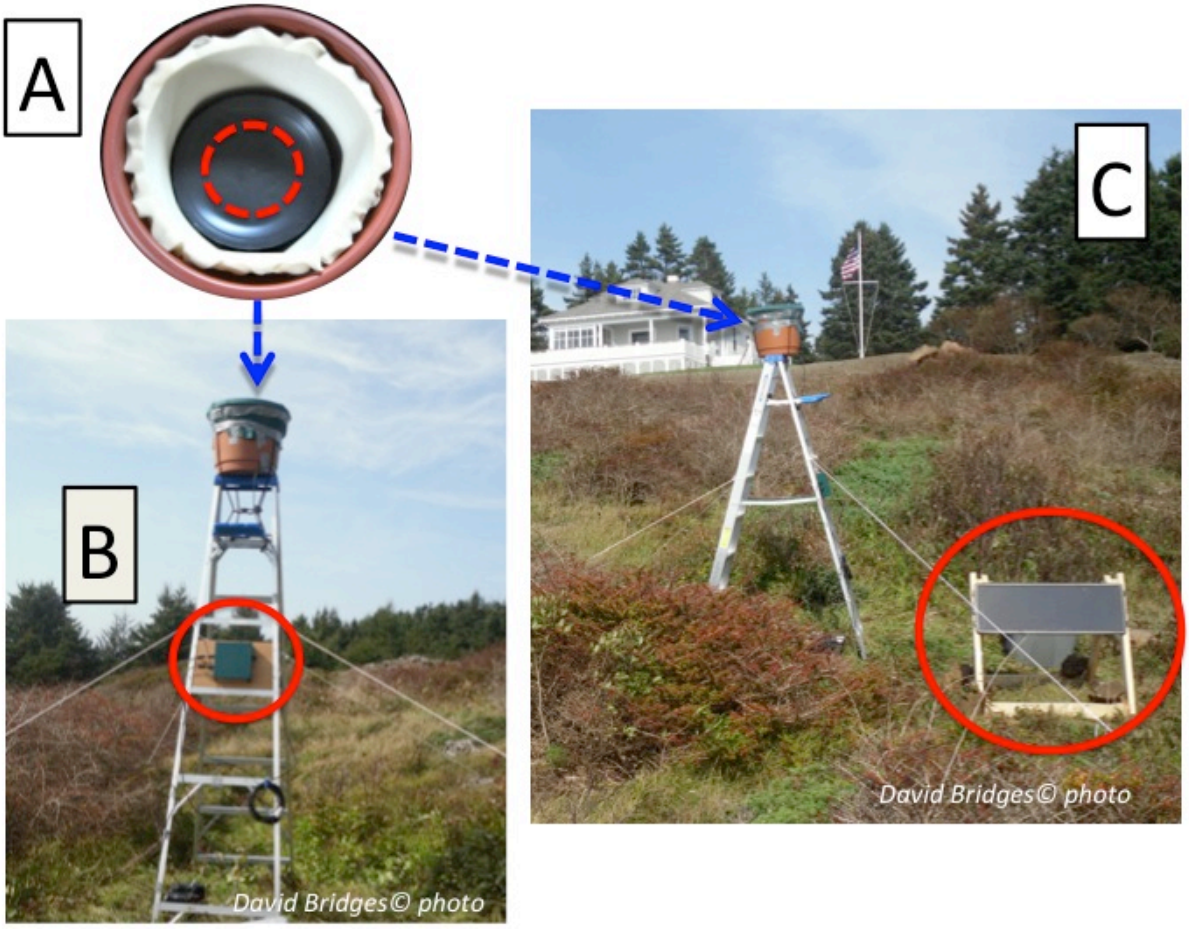

Figure 5. The microphone assembly (A, microphone element noted with red hatched circle) was covered by thin cotton cloth (green, as shown in B), directed skyward, and, along with the Wildlife Acoustics SM2® recorder (shown within the solid red circle in B), was anchored firmly to the stand. A 12-V battery (at base of ladder in B) charged by a solar panel (in solid red circle in C) supplied power.

DATA HANDLING AND ANALYSIS

Data handling – Archived hourly wind direction and wind speed obtained from the buoy (http://www.ndbc.noaa.gov/station_history.php?station=44005) in 2011 were averaged for each 3-h block of time during each night's recording period, creating a total of 75 3-h time periods for the 15 nights analyzed for temporal patterns of HF MFCs. Acoustic sound files were regularly transferred from the SDHC cards, organized into electronic folders labeled for date and time of recording, and stored on external hard drives until processed at the LAB (Fig. 6). All acoustic analyses were done using Cornell's Raven Pro 1.4® software for the Mac® platform, licensed to

the LAB at the University of Maine. The software program, which transduces digital sound into an image that visually portrays the sound's patterns of frequency, intensity, and duration, can be programed to search for desired sound ranges.

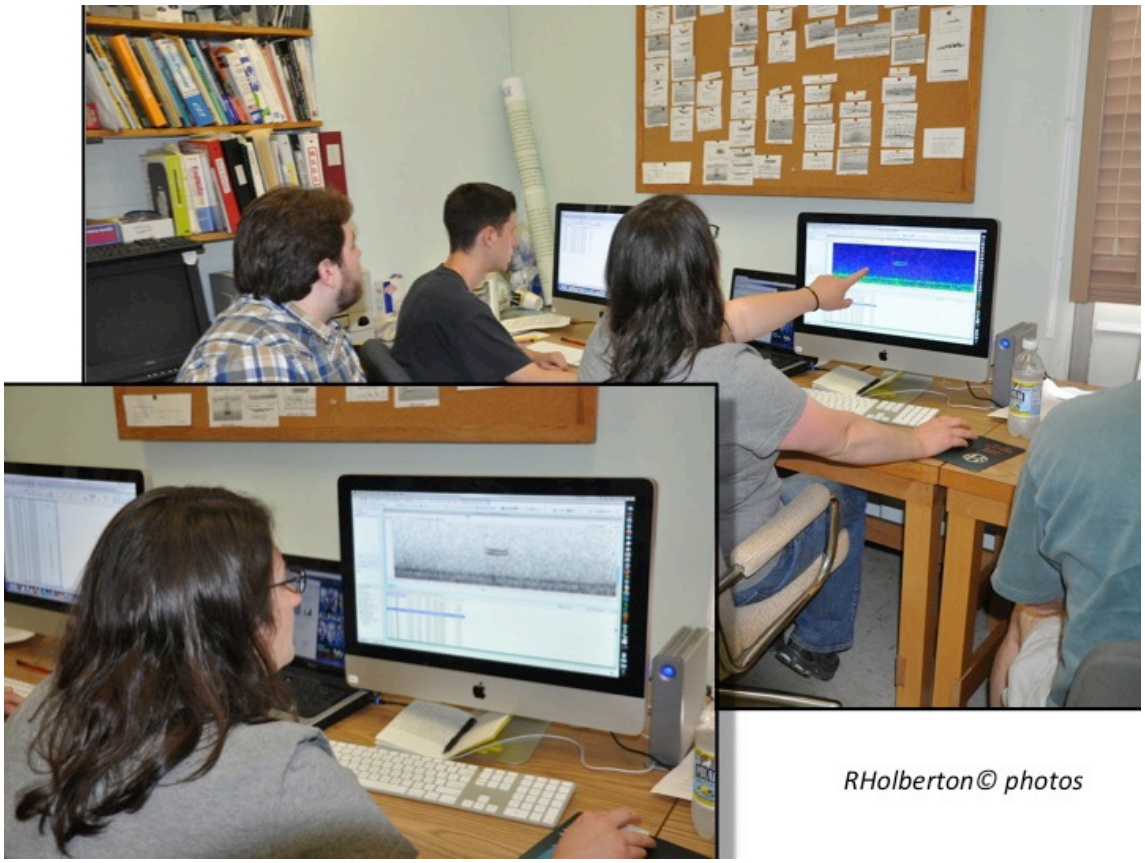

Figure 6. LAB acoustic facilities and technicians (left to right) James Skrabak, David Bridges, and Anne Marchini, supervised by Mr. Wes Wright (partially in photo at right), at work using Cornell's Raven Pro® software program to analyze avian sound files. Insert: Anne Marchini inspecting a sparrow spectrogram.

Avian MFCs normally span the range from 1 to 20 kHz, with flight calls of major bird groups clustered into two general frequency ranges: 'high frequency' (HF) comprising calls that fall mostly within 5-12 kHz (and up to 20 kHz in a few cases), and 'low frequency' (LF) comprising calls typically at or below 4 kHz (Fig. 7). In general, HF calls are short in duration (< 100 msec) and include passerines primarily comprising warblers, kinglets, finches, buntings, and sparrows (see Fig. 7A). In contrast, a few passerines, and all raptors, shorebirds, waders, waterfowl, and seabirds fall within the LF range, tending to be much longer in duration than HF calls (see Fig. 7B). Within the HF call group, different calls may overlap in frequency range

(kHz) but vary in the pattern of sounds made within this range as well as the length (msec) of the entire call (see Fig. 7, for examples). Flight calls within the 1-4 kHz range can be masked by chronic ambient noise, including wind and wind-related vegetation rustling, airplanes, and human conversation.

***Recommendation**: This report only contains information regarding avian MFCs within the HF range (~5-20 kHz) due to sound interference and masking by frequent wind that occurred during the monitoring period. To maximize sound detection and to reduce noise from wind-caused vegetation rustling, which produces low frequency sounds that obscure flight calls at or below 3-4 kHz, units should be situated at least 15-30 m from nearest vegetation (shrubs, trees) that are above 2 meters, and away from objects that make noise, especially during windy conditions (e.g. machinery, flags and lines on flag poles).*

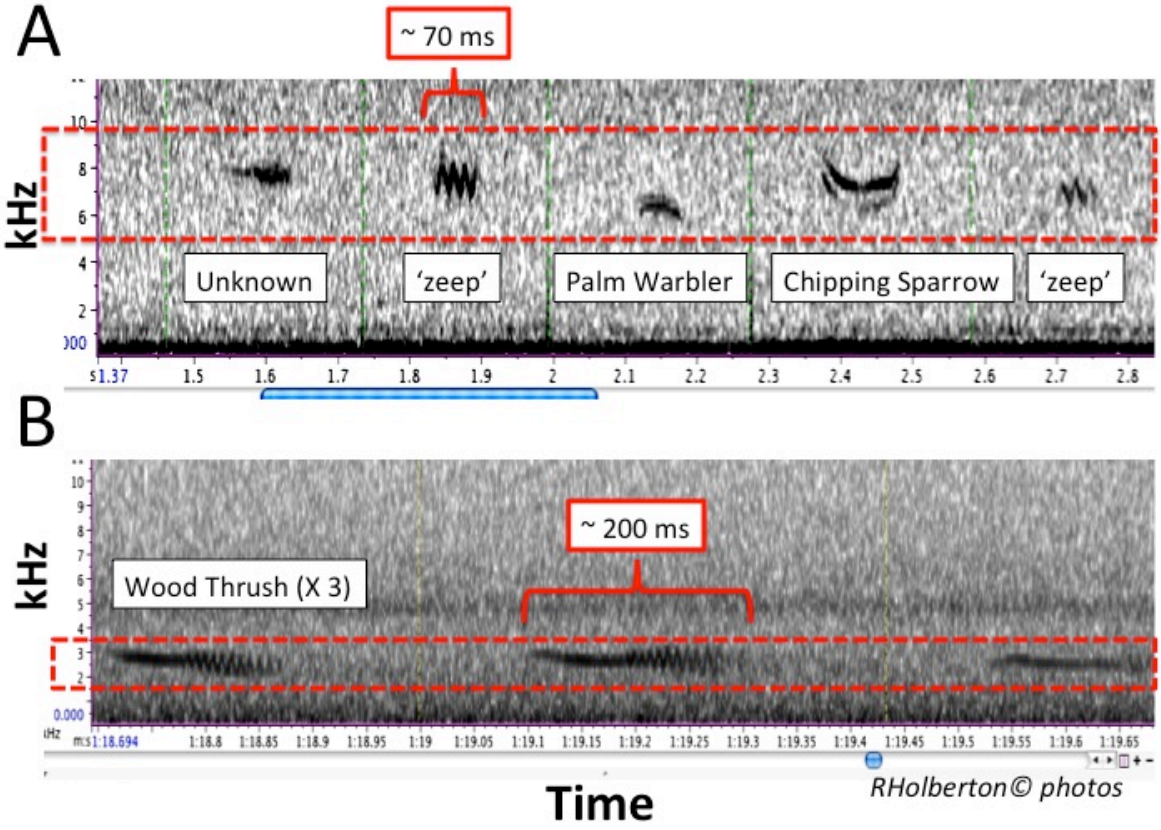

Figure 7. Spectrogram examples of high frequency (A) and low frequency (B) migratory flight calls. Note: time (x-axis) is shown in seconds for upper panel A, and in minutes and seconds for lower panel B. The top figure (A) shows five examples detected with the high frequency detector (see text for details) used to find calls characterized by a frequency range of 5 -10 kHz and < 100 ms in duration. Many calls are species-specific, such as the Palm warbler, *Setophaga palmarum*, and Chipping sparrow, *Spizella passerina* (shown), but several warbler and sparrow species make similar calls, with 3-5 modulations repeated within the same frequency range and time duration. These are collectively grouped as 'zeep' calls. Two examples of slightly different 'zeep' calls are shown in A. Flight calls of Wood Thrush, *Hylocichla mustelina*, (B) and many other species (*Catharus* thrushes, tanagers, shorebirds, etc.) are characterized by lower frequency range (1-4 kHz) and longer duration.

Four steps of acoustic data analysis:
Detector development, data extraction and filtering, call identification, and data collation

Detector development – Before any flight calls could be 'harvested' from sound files, potential MFCs were first 'detected' within each sound file by Raven® so that the potential avian sounds could be isolated from other sounds on the file and then visually examined for further identification. In the initial step, sounds of a particular frequency range and duration of interest were targeted amidst other sounds, including background noise, in the file. A set of "detector" parameters was developed for use by the software program to scan each sound file and to tag sounds that fit the targeted parameters. The best set of detector parameters were those that produced the highest "% extraction efficiency", defined as the maximum number of detections derived from a 30-min file sample from the recording site compared to the number achieved by direct visual inspection of this same sample. Once this was calculated for the Monhegan site, it was checked periodically and adjusted as needed throughout the data extraction process.

Data extraction and filtering –Once a detector searched through a sound file, Raven® was programmed to save a table containing a list of potential calls that corresponded with the composite of individual spectrograms of sounds. Each spectrogram was then visually inspected to first determine if it was a MFC or not. MFCs that could be easily identified to species or species group at this time were noted. A new table was then produced to contain only those sounds designated as MFCs. Each of these spectrograms corresponded to a sound 'snippet' that was individually 'harvested' as a single wav file.

Call identification – Sound snippets were combined to create a single composite sound file, with each snippet separated by 0.1 sec. The composite file containing the harvested but as-yet-unidentified MFCs was brought up in Raven® and each spectrogram was visually inspected. Calls were visually compared to known spectrograms by their characteristics (frequency, pattern, and duration) using a spectrogram library made available by William Evans (Oldbird, Inc., see online examples on http://oldbird.org/Library.htm and CD-ROM "Flight Calls of Migratory Birds: Eastern North American Landbirds", by W.H. Evans and M. O'Brien) and the Cornell Laboratory of Ornithology online library of flight calls, as well as the primary literature (e.g. Evans 1994; Evans & Mellinger 1999; Evans & O'Brien 2002; Murray 2004; Farnsworth et al. 2004;

Farnsworth 2005; Farnsworth & Lovette 2005). Two people independently examined all 'snippet' files to maximize identification accuracy. (It should be noted that the MFCs for many North American species have yet to be identified.)

All indistinct MFC spectrograms were categorized as 'unclear' (UNC). All distinct and intact MFC spectrograms were categorized as either 'unknown' (UNK, clear but not identifiable at this time) or into known categories of species or specific groups, or into a flight call complex. The most common HF flight call complex is 'zeep', a call that is modulated (2-4 undulations) over a fixed frequency range usually between 6-8.5 kHz and with a similar duration (for example, Fig. 6A). Several warbler species, including Magnolia warbler (*Setophaga magnolia*), Blackburnian warbler (*S. fusca*), Blackpoll warbler (*S. striata*), Cape May (*S. tigrina*) and Yellow warbler (*S. petechia*), are known to make 'zeep' flight calls.

Data collation – Once a table comprising UNC, UNK and identified MFCs was made, the list, excluding UNC, was collapsed into three upper level categories comprising "UNK' = unknowns, 'Sparrow' = sparrows of the family Emberizidae and finches of the family Fringillidae; and 'Warblers' = wood warblers of the family Parulidae and Golden-crowned kinglets (*Regulus satrapa*, family Regulidae). These three higher-level categories (UNK, 'Sparrow', and 'Warbler') were used to create nightly pie diagrams depicting the general composition of MFCs detected in the recording area. It is currently believed that Ruby-crowned kinglets, *R. calendula*, do not make MFCs. Nor do vireos (family Vireonidae), which are more closely related to shrikes (family Laniidae) than to warblers. Calls made by shrikes in the context of migratory flight have not been reported and this group may be among those believed not to vocalize in flight during migration.

Note*: Important assumptions in this survey are that all species call at same rate, that each flight call represents a single bird and that each flight call made is independent of calling activity by other birds. However, local weather conditions such as the extent of cloud cover and the height of the cloud ceiling, fog, and precipitation can affect MFC rates (Drost 1960; Graber & Cochran 1960; Evans 2005; Farnsworth 2005; Hüppop & Hilgerloh 2012).*

RESULTS

Recording Effort Summary -

As soon as funding allowed, the recording period began on the night of 30 September-1 October (local sunrise = 0633 EDT; local sunset = 1820 EDT) and continued through the night of 4-5 November (local sunrise = 0716 EDT; local sunset = 1724 EDT). Over the recording period, daylength decreased by a total of 1 h 40 min, with sunrise occurring 44 min later and sunset occurring 56 min earlier by the last night of recording. For each night, recording began at 1800 EDT, within an hour of local sunset and continued for a total of 15 hours. These times targeted the period when the majority of nocturnal landbird migrants initiate a flight, are aloft, or are likely to be arriving at stopover sites along the coast at or after dawn after making over water flights. For all periods, but especially for those around sunrise, only calls characteristic of MFCs, in contrast to songs (e.g., 'dawn chorus') or other diurnal vocalizations, were included in analyses. The total number of nights analyzed for MFCs in this report is less than the total number of nights in which recordings were made (Fig. 8) due to poor weather conditions but this is not likely to have missed many MFCs as most landbird migrants are less likely to fly in heavy precipitation or high winds.

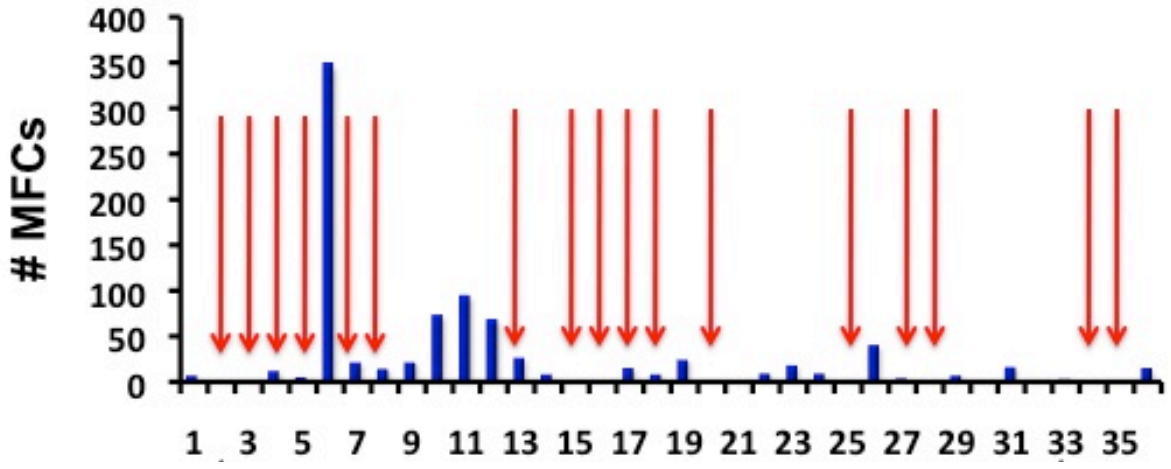

Figure 8. The total number of high frequency (HF) migratory flight calls (# MFCs) for each night (15 hours, from 1800 EDT to 0900 EDT) during the 36-day monitoring period from the night of September 30th to the night of November 4th, 2011, at Monhegan Island. Red arrows point to nights with high winds and/or rain that precluded analysis during the monitoring period.

The first few nights of recording (Sept. 30, Oct. 1, 2, and 4) yielded fewer than 10 HF MFCs not obscured by high winds (example shown in Fig. 9). Only those nights with at least ten

MFCs were analyzed for total number of flight calls (including UNKs), hourly distribution of flight calls, and species group composition.

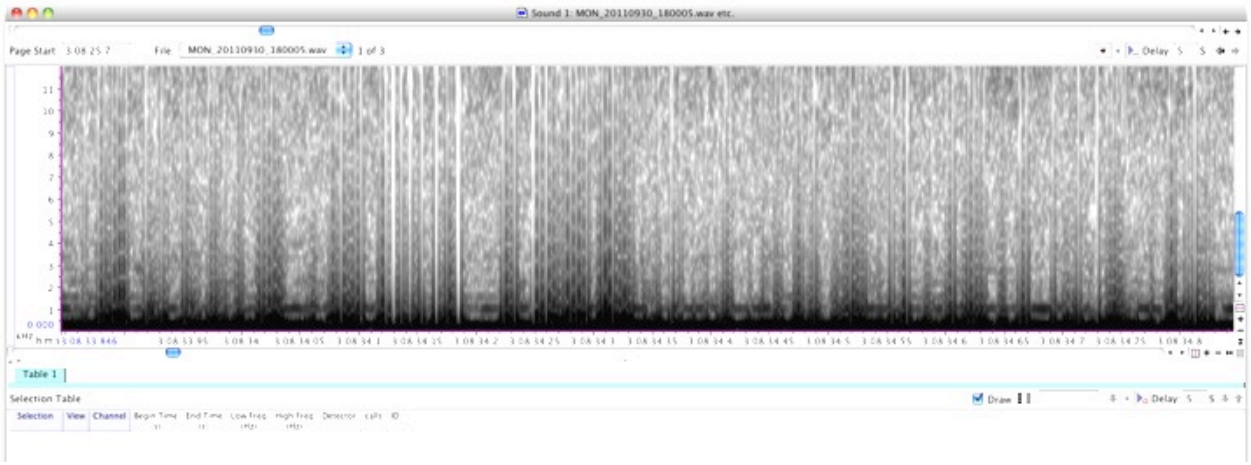

Figure 9. Example of a Raven® spectrogram produced as a result of high winds during acoustic survey recording at Monhegan Island during the night of September 30th. Note that high as well as low frequency sounds are heavily obscured by extensive wind noise.

As expected, the number of flight calls each night declined as the region's landbird migration season was coming to an end (Fig. 8, Figs. 10A,B,C). The proportion of 'warblers' declined and 'sparrows' increased (Figs. 10A,B,C). Table 1 provides a list of the HF MFCs that could be identified to species or species groups. The night of highest MFCs during the recording period occurred on Oct. 5 (Figs. 10A,B,C; shown as 'Day 6' in Fig. 8), which coincided with the onset of a period of high daily bird numbers, primarily characterized as 'late migrants', banded or visually counted at Metinic Island, approximately 18 km northeast of Monhegan (Leppold, 2011).

Within-night temporal patterns of MFCs, surface wind direction and surface wind speed -

Nightly temporal patterns illustrated that not only were birds aloft over the area during the night, but that, on some nights, birds congregated and most likely departed from the stopover site soon after sunset. Further, some birds passed over and/or arrived at the site at or near dawn. As is characteristic for the northeast during late fall migration, the majority (68%) of the 75 3-h blocks of time for which acoustic monitoring occurred for the 15 nights with at least 10 HF MFCs, had surface winds out of the west (18.7%), northwest (12.0%), and north (37.3%) (Fig. 10 A,B,C). Winds out of south or east (southwest = 6.7%; south = 2.7%; southeast = 8.0%; east = 10.7%; northeast = 4.0%) were less frequent. Average surface wind speeds out of the west,

northwest, and north in 3-h blocks in which MFCs were recorded ranged from 7 k/h to 54 k/h (Fig 10A,B,C). On seven of the first ten analyzed nights, (Oct. 3-16, Fig. 10A,B), the majority of MFCs (primarily sparrows) were recorded within the first three hours after sunset, the time period referred to as 'exodus', suggesting that this site serves as a major departure area where birds, including local breeders and those on stopover, may congregate before initiating a bout of migratory flight. Four of these nights occurred while winds were out of the west or northwest while the remainder occurred with winds out of the northeast, east, or southeast.

Three of the 15 nights showed a concentration of MFCs at or near the time of sunrise, suggesting that birds were passing over or arriving at the site with winds more likely to be out of the north or northwest (Fig. 10A,B). The data for the remaining five nights (Oct. 18 – Nov. 4, Fig. 10C), wherein the preponderance of MFCs occurred well after sunset and well before sunrise, illustrate birds aloft, either *en route* in a directed trans-Gulf flight originating in the Canadian Maritimes or northern Maine coastal areas, or in redirected flights back towards the mainland after being blown offshore by strong west and northwest winds. The night of Oct. 5 had the greatest total number of MFCs, which also occurred with the highest average wind speed for each of the 3-h time blocks (35-51 k/h, all out of the north) throughout the night's recording period. Most of these MFCs occurred at or near sunrise, when north winds had decreased.

Figure 10. (BELOW) The temporal distribution of high frequency MFCs (% of night total) for 15 nights in which more than 10 calls were recorded during the 15 hours of recording beginning at local sunset are presented next to a corresponding pie chart for the three main categories of clear high frequency flight calls recorded during each night. The 'Sparrow' category is in red; 'Warbler' is in blue; and 'Unknown' is in green (see text for category descriptions). A) Oct. 3-8; B) Oct. 9-16; C) Oct. 18- Nov. 4. Local sunset occurred 20 min after the onset of recording at the beginning of the monitoring period (Sept. 30) and 36 min before the onset of recording at the end of the monitoring period (Nov. 4). Local sunrise occurred 30 min into the 12th h of recording at the beginning of the monitoring period (Sept. 30) and 18 min into the 13th h of recording at the end of the monitoring period (Nov. 4). Inserted within each graph is the average wind direction and wind speed (k/h) for each 3-h block below for during each night.

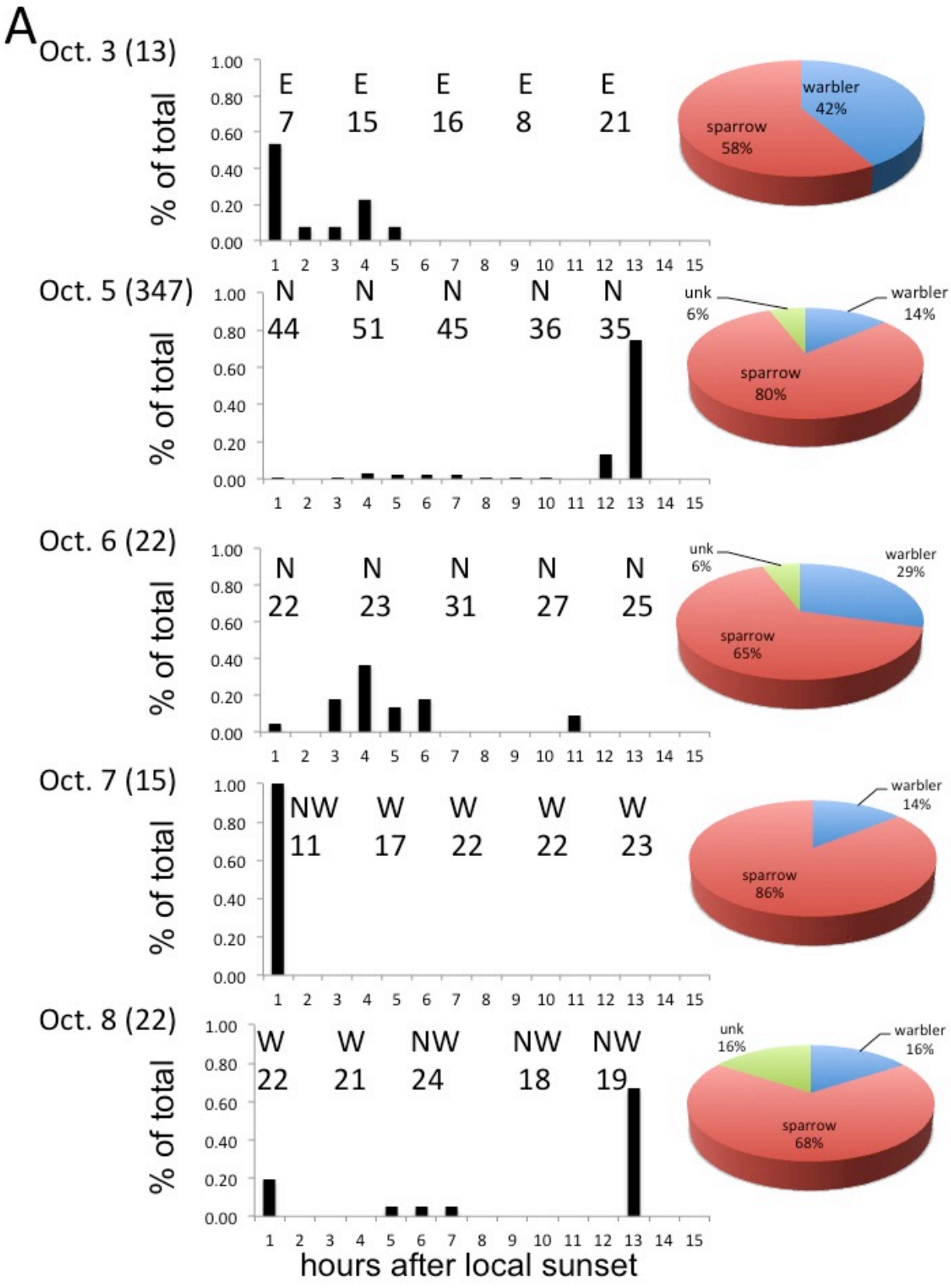
A
Oct. 3 (13)
% of total
E E E E E
7 15 16 8 21
warbler 42%
sparrow 58%
Oct. 5 (347)
% of total
N N N N N
44 51 45 36 35
unk 6%
warbler 14%
sparrow 80%
Oct. 6 (22)
% of total
N N N N N
22 23 31 27 25
unk 6%
warbler 29%
sparrow 65%
Oct. 7 (15)
% of total
NW W W W W
11 17 22 22 23
warbler 14%
sparrow 86%
Oct. 8 (22)
% of total
W W NW NW NW
22 21 24 18 19
unk 16%
warbler 16%
sparrow 68%
hours after local sunset

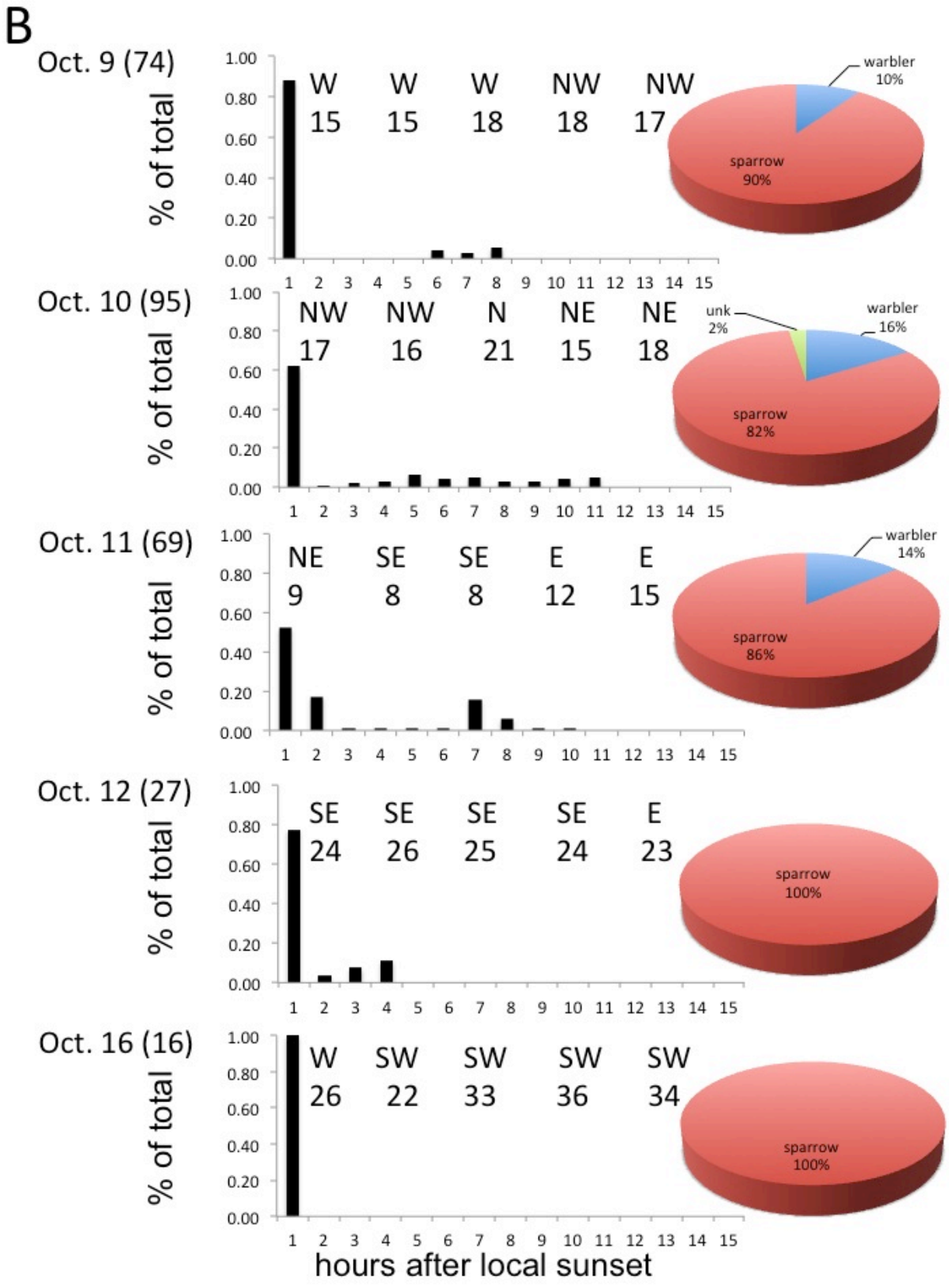
B
Oct. 9 (74)
% of total
W W W NW NW
15 15 18 18 17
warbler 10%
sparrow 90%
Oct. 10 (95)
% of total
NW NW N NE NE
17 16 21 15 18
unk 2%
warbler 16%
sparrow 82%
Oct. 11 (69)
% of total
NE SE SE E E
9 8 8 12 15
warbler 14%
sparrow 86%
Oct. 12 (27)
% of total
SE SE SE SE E
24 26 25 24 23
sparrow 100%
Oct. 16 (16)
% of total
W SW SW SW SW
26 22 33 36 34
sparrow 100%
1.00
0.80
0.60
0.40
0.20
0.00
1 2 3 4 5 6 7 8 9 10 11 12 13 14 15
hours after local sunset

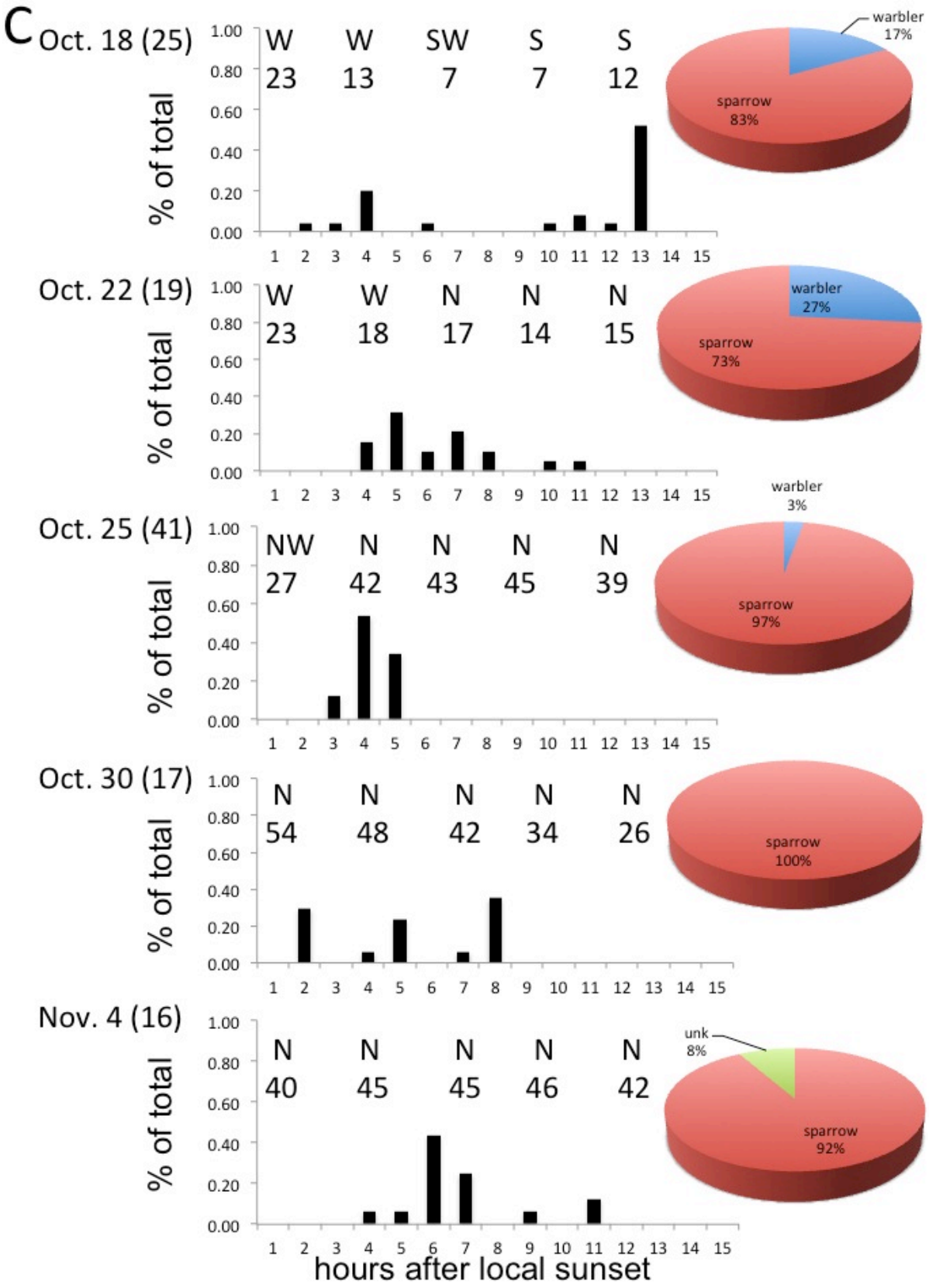
C
Oct. 18 (25)
W W SW S S
23 13 7 7 12
warbler 17%
sparrow 83%
Oct. 22 (19)
W W N N N
23 18 17 14 15
warbler 27%
sparrow 73%
Oct. 25 (41)
NW N N N N
27 42 43 45 39
warbler 3%
sparrow 97%
Oct. 30 (17)
N N N N N
54 48 42 34 26
sparrow 100%
Nov. 4 (16)
N N N N N
40 45 45 46 42
unk 8%
sparrow 92%
% of total
hours after local sunset

SUMMARY AND CONCLUSIONS

Timing and seasonal patterns –

The list (Table 1) of group and species-specific MFCs, including late migrants such as Yellow-rumped warblers, Palm warblers, Blackpoll warblers, and the majority of sparrows that pass through or winter in the area, is congruent with passive acoustic surveys conducted by the LAB and USFWS in the region. This list is also consistent with visual observations recorded during the same period the previous fall on Monhegan Island by Mr. Tom Magerian, an experienced technician hired by New Jersey Audubon to operate the marine surveillance radar unit (included in this report as Appendix I and listed in Appendix A in the 2011 Environmental Assessment, Department of Energy, DOE/EA #1792). However, data from numerous banding and acoustic survey activities, visual observations, and published studies illustrate that the majority of migrants of all major avian taxa begin to pass through the mid-coast Maine region in July and August (e.g., www.mainebirding.net; Cornell's E-BIRD online database, www.ebird.org; multiple banding reports for individual banding stations; references in Morris et al. 1996). Recent passive acoustic surveys conducted by the LAB and USFWS found that median dates of MFC nightly intensity for individual Neotropical warbler species such as Canada warbler, Black-and-white warbler, and Magnolia warbler, occur in mid- to late-August and early September along the northern Maine coast and mid-coast region (Tengeres & Holberton, unpublished data). Thus, the 2011 passive acoustic survey period for the DeepCwind project at Monhegan occurred extremely late in the migration season for this region and, therefore, excluded the preponderance of birds that move through the area each year.

In addition to the limited monitoring period, uncontrolled ambient noise and high winds at the exposed site obscured MFCs across all audible ranges, but particularly those made by shorebirds, waterfowl, wading birds, raptors, and many songbird migrant species. Unfortunately, options for placing the recording equipment at Lobster Cove were limited. It is highly recommended that, when recording at a site in which windy conditions are common, microphones should be placed in a protected location and at a distance from vegetation and other objects that become noisy in moderate to high winds. In spite of the limited recording time and uncontrolled sound interference in this study, however, nightly MFC counts during the recording period at Monhegan Island were within the range of those recorded during fall migration at other coastal

sites in the region (Holberton, 2011; Holberton, unpublished data). Congruent with visual observations, banding activities, and acoustic data recorded at other sites within the region during this and other years (Leppold, 2009, 2010, 2011; Holberton, 2011; Holberton, unpubl data), MFC numbers at Monhegan reflected the seasonal decline in bird numbers and the accompanying change in species group composition towards a sparrow/finch dominated distribution. Some of these late arriving species, such as Song sparrow, White-throated sparrow, and Dark-eyed junco, are facultative migrants that will make initial movements away from the breeding grounds but will remain as far north as possible as long as weather conditions and food availability allow (Holberton 1993 and references therein). Thus, these species can continue to make migratory movements throughout autumn and winter.

Patterns of MFCs, surface wind direction and surface wind speed -

Within-night temporal patterns of MFC distribution at the Monhegan recording location suggest that the site near the offshore deepwater test area is a multi-purpose one. Three basic patterns emerged from this monitoring effort. There were nights in which the majority of MFCs occurred either well after sunset, soon after sunset, or only near dawn. On approximately half of the 15 nights in which more than 10 MFCs were detected, all or almost all MFCs occurred within the first three hours after sunset, the period known as 'exodus' when birds are ascending as they initiate a flight (Able 1973). This pattern of activity soon after sunset is congruent with radar data collected by New Jersey Audubon at this site the previous year: during the last half of the 2010 fall migration season, the rate of radar 'targets' peaked in the second hour after sunset (Mizrahi, 2011). These results collectively suggest that this site serves as a major departure area. As shown in Figure 5, the recording equipment was situated within an area dominated by scrub-shrub habitat that many species including sparrows are readily attracted to on stopover sites. Thus, birds may congregate in this area before initiating a bout of migratory flight. Although surface wind direction can influence when exodus occurs (Gauthreaux & Able, 1970; Able, 1973), flights initiated from Monhegan Island in 2011 occurred regardless of wind direction or wind speed. The survey site, located at the southwest end of the island, offers an unobstructed view of the mainland. This area at Lobster Cove, adjacent to the deepwater test site, is likely to concentrate migrants not only because the habitat there may allow them to replenish energy stores needed to resume migration in a timely fashion but it may also serve as a strategic site for departure to the

mainland (c.f. Covino & Holberton, 2011). This hypothesis is supported by the previous year's radar data in which the mean direction of 'night targets' at this site during late migration (1 October – 30 November) was to the southwest at 232 degrees (Mizrahi, 2010), in the general direction towards the coast, a finding also consistent with the southwest track of radar targets documented by Drury and Nisbet (1964) on a larger scale along the southern Maine coast in autumn.

Areas that concentrate migrants, either because they provide resources such as food availability and refuge from predators or pose topographic features that minimize flight distance to their next destination, should be avoided for placement of structures such as buildings, communication towers, and wind energy turbines. Recent studies have shown that collision risk assessments may underestimate impacts because individual birds on migration often make multiple local flight forays in the departure area soon after sunset before finally departing on migration altogether (Mills et al. 2011; Taylor et al. 2011). These repeated local round-trip forays, often as far as 10 km, are at low altitudes and may be exploratory as birds assess topography and wind conditions before committing to a true departure from the area. The results from Taylor and colleagues (Mills et al. 2011; Taylor et al. 2011) illustrate that collision risk for birds concentrated in departing from an area may be higher than risk assessment models currently estimate because individual birds at stopover sites are likely to eventually spend a significant amount of total time aloft in the area at heights well within the rotor swept zone.

In addition to lower flight heights during ascent and descent during migration (Cooper & Ritchie 1995), radar studies have shown that, for many landbird migrants, maximum flight heights achieved over water are lower than that reported for over land, presumably to take advantage of lower air turbulence and higher, more consistent wind speeds found over the ocean (Hüppop et al. 2006 and references therein). Landbird migrants are also more likely to fly at lower altitudes along coastlines compared to inland sites (Alerstam et al. 1978; Hüppop et al. 2006). Species such as Yellow-rumped warblers and Dark-eyed juncos have been documented flying along the southern New England coast in autumn at altitudes less than 30 m (Baird & Nisbet 1960). These observations are congruent with results of the 2010 marine surveillance radar study at Lobster Cove showing that the proportions of radar targets observed at or below 50 m as well as targets observed between 51 and 100 m above the water's surface were higher during

the late migration season (1 October – 30 November) compared to the earlier fall migration period (Mizrahi, 2011).

Not only are flight heights lower along coastlines and as birds near their destination (Cooper & Ritchie 1995), they can be affected by weather conditions, with birds more likely to fly low in foggy conditions and under the ceiling of heavy cloud cover (Bruderer, 1997; Hüppop & Hilgerloh, 2012). Thus, collision risk for birds along the Gulf of Maine coastal areas may be compounded by the fact that not only do they have a greater tendency to fly at low altitudes under optimal conditions, the region, particularly the coastal waters near the mouth of Penobscot Bay, experiences the highest frequency of days with low visibility, with maximum periods occurring during the early morning hours, just before sunrise, from May to October (Hayes, 2009), causing migrants to further reduce flight heights. Plans for construction as well as operational and maintenance activities associated with coastal land-based, near-shore and deepwater wind energy operations will need to take into consideration the fact that under these conditions artificial illuminations attract nocturnal migrants and may lead to mass collisions with obstacles, particularly where disoriented birds may have no alternatives for landing (Jones & Francis, 2003; Gauthreaux & Belser, 2003, 2006; Evans et al., 2007; Drewitt & Langston, 2008; Hüppop & Hilgerloh, 2012).

Origin of landbird migrants at Monhegan -

In addition to hundreds of thousands of waterfowl, shorebirds, and seabirds that move through the Gulf of Maine coastal areas and offshore islands, the region serves as a major flyway system for as many as a half a million landbird migrants, with birds using a variety of strategies to move along the coast, 'island hop', or make non-stop overwater flights from Nova Scotia and New Brunswick (Drury & Nisbet, 1964; Leppold & Holberton, 2010; Baird & Nisbet, 1960; Nisbet & Drury 1967, 1969; Drury & Keith 1962; Richardson 1972, 1978; Williams et al. 1977, Williams & Williams 1978; Peckford & Taylor 2008; Covino & Holberton 2011). While a preponderance of these birds represent breeding populations in the Canadian Maritimes, Quebec, Ontario, and Maine, stable isotope studies have shown that a significant proportion of migrant songbirds occurring on offshore islands as well as along the Maine coast originate from breeding populations across North America, with some birds coming from as far west as Alaska and western Canada (Holberton 2011, Holberton & Hobson, unpubl data). Under region-wide

weather conditions optimal for flight, major movements of migrants across the Gulf and along the coast are often 'broad front' movements rather than narrow 'corridors'. This is supported by the temporal patterns of daily radar target intensities of radar data collected at Lobster Cove on Monhegan Island in 2010 being positively correlated with temporal patterns of visual counts and banding activity co-occurring on Metinic Island almost 18 km to the northeast of Monhegan Island (Leppold & Holberton 2010). Further, temporal patterns of MFCs during fall migration in 2010 at sites inland (Hampden), on the mainland coast (Petit Manan Point), and on Metinic Island in 2010 showed similar changes in nightly intensity although these sites were more than 90 km apart from each other (Holberton 2011).

Summary -

Over 300 bird species comprising all major avian taxa have been documented in the Gulf of Maine region, and 80% of these are migrants on their way to or from the breeding grounds across the northern regions of North America. Boreal breeding birds, which comprise a significant portion of bird species moving through the Gulf of Maine area are of particular concern as many of these breeding areas are of particular risk from global climate change and populations are experiencing rapid declines (North American Bird Conservation Initiative Canada, 2012). Many of these species are currently state and/or federally listed in Maine (USFWS, 2008; MDIFW, 2011). It is well established that coastal areas concentrate birds during migration (Ralph, 1981), and Maine's coastal areas and islands are not only popular ecotourism sites for seabird viewing during the breeding season, but are major sites for birders throughout both migration periods. Monhegan Island, in particular, is a destination 'hotspot' for commercial bird tours because of the number and diversity of migrant landbirds that occur there during spring and fall migration. More extensive study is needed to fully understand bird activity in the Monhegan Island area.

The limited time period of deployment and the reduced size of the University of Maine-DeepCwind test turbine, as originally described for the deepwater test site at Monhegan Island, is not likely to adversely affect migrant landbird behavior. However, lighting during construction and operation activities for the project should be minimized during nighttime periods at any time of the year, especially when visibility is low. Given how migrant landbirds negotiate the complex topography of this major flyway region, it should be recognized that the current assessments of

potential direct and indirect impacts of land-based and offshore commercial scale wind energy development elsewhere are not likely to be readily extrapolated to the coastal and offshore areas of the Gulf of Maine.

ACKNOWLEDGEMENTS

Doreta Schwier provided much critical logistic support on Monhegan Island throughout the monitoring period. David Bridges helped set up the equipment at the monitoring site and analyzed much of the data. Support was provided by funds from the American Recovery and Reinvestment Act program (U.S. Department of Energy, #DE-EE0002981) awarded to the University of Maine and DeepCwind Consortium.

LITERATURE CITED

Able, K.P. 1973. The role of weather variables and flight direction in determining the magnitude of nocturnal bird migration. Ecology, 54:1031-1041.

Able, K. P. 1977. The orientation of passerine nocturnal migrants following offshore drift. *The Auk* 94:320–330.

Alerstam, T., Enckell, P.H., & Ulfstrand, S. 1978. Current bird migration research-Proceedings of a symposium at Falsterbo, Sweden, Oct. 1977. *Oikos* 30:163-418

Baird, J., & I.C.T. Nisbet. 1960. Northward fall migration on the Atlantic coast and its relation to offshore drift. *The Auk* 77:119–149.

Bruderer, B. 1997. The study of bird migration by radar. Part 2: Major achievements. *Naturwissenschaften* **84**: 45–54.

Cooper, B.A. & R.J. Ritchie. 1995. The altitude of bird migration in east-central Alaska: a radar and visual study. *J. Field Ornithol* 66:590-608.

Covino, K.M. & Holberton, R.L. 2011. The influence of energetic condition on flight initiation and orientation of migratory songbirds in the Gulf of Maine region. *The Auk* 128:313-320.

Drewitt, A.L. & Langston, R.H.W. 2008. Collision effects of wind-power generators and other obstacles on birds. *Ann. N. Y. Acad. Sci.* 1134*:* 233–266.

Drost R. 1960. Über den nächtlichen Vogelzug auf Helgoland. – Proc. XIIth Int. Ornithol. Congr. Helsinki 1958, pp. 178–192.

Drury, W.H., Jr. & Keith, J.A. 1962. Radar studies of songbird migration in coastal New England. *The Ibis* 104: 449-489.

Drury, W.H., Jr. & Nisbet, I.C.T. 1964. Radar studies of orientation of songbird migrants in southeastern New England. *Bird-Banding* 35:69-119.

Environmental Assessment for University of Maine's Deepwater Offshore Floating Wind Turbine Testing and Demonstration Project – DOE/EA #1792. 2011. U.S. DOE, Office of Energy Efficiency and Renewable Energy, Golden Field Office. May 2011.

Evans, W.R. 1994. Nocturnal flight call of Bicknell's Thrush. *Wilson Bull* 106:55-61.

Evans, W.R. 2005. Monitoring avian night flight calls: The new century ahead. *The Passenger Pigeon* 67:15-24.

Evans, W.R. & Mellinger, D.K. 1999. Monitoring grassland birds in nocturnal migration. *Studies in Avian Biology* 19:219-229.

Evans, W.R. & O'Brien, M. 2002. Flight Calls of Migratory Birds - *Eastern North American Landbirds*. Old Bird, Inc. [CD-ROM]

Evans, W.R., Akashi, Y., Altman, N.S. & Manville, A.M. 2007. Response of night-migrating songbirds in cloud to colored and flashing light. *N. Am. Birds* 60*:* 476–488.

Farnsworth, A. 2005. Flight calls and their value for future ornithological studies and conservation research. *The Auk* 122:733-746.

Farnsworth, A. & Lovette, I.J. 2005. Evolution of nocturnal flight calls in migrating wood-warblers: apparent lack of morphological constraints. *J. Avian Biology* 36:337-347.

Farnsworth, A., Gauthreaux, S.A., & van Blaricom, D. 2004. A comparison of nocturnal call counts of migrating birds and reflectivity measurements on Doppler radar. *J. Avian Biology* 35:365-369.

Gauthreaux, Jr., S.A. 1971. A radar and direct visual study of passerine spring migration in southern Louisiana. *The Auk* 88: 343-365.

Gauthreaux, Jr., S.A. & Belser, C.G. 2003. Radar ornithology and biological conservation. *The Auk* 120:266-277.

Gauthreaux S. A. *&* Belser C. 2006. Effects of artificial night lighting on migrating birds. *In:* Rich C. *and* Longcore T. *(eds),* Ecological consequences of artificial night lighting. Island Press, pp. 67–93.

Gauthreaux, Jr., S.A. & Able, K.P. 1970. Wind and the direction of nocturnal songbird migration. *Nature* 228:476-477.

Graber, R.R. & Cochran, W.W. 1959. An audio technique for the study of nocturnal migration of birds. *Wilson Bulletin* 71:220-236.

Graber, R.R. & Cochran, W.W. 1960. Evaluation of an aural record of nocturnal migration. *Wilson Bulletin* 72:252-273.

Hayes, J.C. 2009. An applied climatology of low visibility over the coastal waters of New Hampshire and So. Maine - *Eastern Region Technical Attach No. 2009-04, Dec. 2009*

Holberton, R.L. 1993. An endogenous basis for differential migration in the dark-eyed junco. *Condor* 95:580-587.

Holberton, R.L. 2011. Passive acoustic monitoring during 2010 fall migration. Report to U.S. Fish & Wildlife Service - Maine Coastal Islands National Wildlife Refuge.

Hüppop, O., Dierschke, J., Exo, K-M, Fredrich, E. & Hill, R. 2006. Bird migration studies and potential collision risk with offshore wind turbines. *Ibis* 148:90-109.

Hüppop, O. & Hilgerloh, G. 2012. Flight call rates of migrating thrushes: effects of wind conditions, humidity and time of day at an illuminated offshore platform. *J. Avian Biology* 43:85-90. doi: 10.1111/j.1600-048X.2011.05443.x

Jones, J. & Francis, C.M. 2003. The effects of light characteristics on avian mortality at lighthouses. *J. Avian Biol*. 34*:* 328–333.

Lanzone, M., DeLeon, E., Grove, L., & Farnsworth, A. 2009. Revealing undocumented or poorly known flight calls of warblers (Parulidae) using a novel method of recording birds in captivity. *The Auk* 126:511-519.

Leppold, A.J. 2009. Metinic Island 2009 Fall Migration Monitoring Report. Submitted to U.S. Fish & Wildlife Service - Maine Coastal Islands National Wildlife Refuge.

Leppold, A.J. 2010. Metinic Island Fall 2010 Migration Monitoring Report. Submitted to U.S. Fish & Wildlife Service - Maine Coastal Islands National Wildlife Refuge.

Leppold, A.J. 2011. Metinic Island Fall 2011 Migration Monitoring Report. Submitted to U.S. Fish & Wildlife Service - Maine Coastal Islands National Wildlife Refuge.

Leppold, A.J. & Holberton, R.L. 2010. Gulf of Maine Bird Migration Monitoring – Interim Report for Fall, 2010 Bird Monitoring Activities for the DOE-DeepCwind Consortium Project at Monhegan Island.

Maine Department of Inland Fisheries & Wildlife Species of Special Concern, March 1, 2011.

Mills, A.M., Thurber, B.G., Mackenzie, S.A., & Taylor, P.D. 2011. Passerines use nocturnal flights for landscape scale movements during migratory stopover. *Condor* 113:597-607.

Mizrahi, D. 2011. Radar monitoring of bird and bat movement patterns on Monhegan Island, Maine and its coastal waters – interim report to University of Maine – DeepCwind.

Morris, S.R., Holmes, D. W., & Richmond, M.E. 1996. A ten-year study of the stopover patterns of migratory passerines during fall migration on Appledore Island, Maine. *Condor* 98:395-409.

Murray, J. 2004. Nocturnal flight calls analysis as a method for monitoring density and species composition of migratory songbirds (Order Passeriformes) across southern Vancouver Island, British Columbia in 2004. Report prepared by J. Murray, Rocky Point Bird Observatory for TD The Friends of the Environment Foundation.

Nisbet, I.C.T. & Drury, W.H., Jr. 1967. Orientation of spring migrants studied by Radar. *Bird-Banding* 38: 173-186.

North American Bird Conservation Initiative Canada. 2012. The State of Canada's Birds, 2012. Environment Canada, Ottawa, Canada.

Peckford, M.L. & Taylor, P.D. 2008. Within-night correlations between radar and ground counts of migrating songbirds. *J. Field Ornithol.* 79:207-214.

Ralph, C.J. 1981. Age ratios and their possible use in determining autumn routes of passerine migrants. *Wilson Bulletin* 93:164-188.

Richardson, W.J. 1972. Autumn migration and weather in eastern Canada: a radar study. *Amer. Birds* 26:10-17.

Richardson, W.J. 1978. Timing and amount of bird migration in relation to weather: a review. *Oikos* 30:224-272.

Taylor, P.D., Mackenzie, S.A., Thurber, B.G., Calvert, A.M., Mills, A.M., McGuire, L.P. & Guglielmo, C.G. 2011. Landscape movements of migratory birds and bats reveal an expanded scale of stopover. PLoS ONE 6: e27054. doi:10.1371/journal.pone.0027054

U.S. Fish and Wildlife Service. 2008. Birds of Conservation Concern 2008. United States Department of Interior, Fish and Wildlife Service, Division of Migratory Bird Management, Arlington, Virginia. 85 pp. [http://www.fws.gov/migratorybirds/]

Williams, T.C., Williams, J.M., & Teal, J. M. .1977. Autumnal bird migration over the western North Atlantic Ocean. *Am. Birds 31:251-267.*

Williams, T.C., & Williams, J.M. 1978. Orientation of transatlantic migrants. Pp. 239-251, In: S. Gautheraux (Ed.) *Animal Migration, Orientation, and Homing.* Academic Press. New York, NY.

Table 1. List of landbird migrant bird species or species groups for whom MFC were identified during passive acoustic survey of nocturnal migration at Lobster Cove, Monhegan Island, near the University of Maine Deepwater Offshore Wind Test Site, 30 September – 4 November, 2010. An * indicates the species is listed as 'Species of Concern' by Maine Department of Inland Fisheries and Wildlife (March 1, 2011), and # indicates listed as Birds of Conservation Concern or "Important Neotropical Migrant Species in Maine" by USFWS for Region 5 (Northeast Region BCC, 2008).

Blue Jay, *Cyanocitta cristata*
American Crow, *Corvus brachyrhynchos*
Black-capped Chickadee, *Poecile atricapilla*
Golden-crowned Kinglet, *Regulus satrapa*
American Robin, *Turdus migratorius*
Vermivora spp (all characterized by a 'double up' spectrogram indistinguishable among three possible species within this genus)
- Tennessee warbler, *V. peregrina* *
- Orange-crowned warbler, *V. celata*
- Nashville warbler, *V. ruficapilla*

Northern parula, *Parula americana* #
Black-throated Blue warbler, *Setophaga caerulescens* #
Palm warbler, *Setophaga palmarum*
Common Yellowthroat, *Geothlypis trichas*
American Redstart, *Setophaga ruticilla* *
'Zeep' complex that includes:
- Yellow-rumped warbler, *Setophaga coronata* *
- Blackpoll warbler, *Setophaga striata*
- Yellow warbler, *Setophaga petechia* *
- Magnolia warbler, *Setophaga magnolia*
- Bay-breasted warbler, *Setophaga castenea* #
- Cape May warbler, *Setophaga tigrina*
- Blackburnian warbler, *Setophaga fusca*

Am. Tree Sparrow, *Spizella arborea*
Chipping Sparrow, *Spizella passerina*
Savannah Sparrow, *Passerculus sandwichensis*
Fox Sparrow, *Passerella iliaca* *
Song Sparrow, *Melospiza melodia*
Lincoln's Sparrow, *Melospiza lincolnii*
Swamp Sparrow, *Melospiza georgiana*
White-throated Sparrow, *Zonotrichia leucophrys* *
Dark-eyed Junco, *Junco hyemalis*

BIRD SITINGS OFF MONHEGAN ISLAND'S LOBSTER COVE, JULY 2, 2010 TO OCTOBER 16, 2010

Source: **Maine-birds** *"an email forum devoted to the discussion of birds and birding in the state of Maine. The primary function of the list is to provide an efficient means of reporting wild bird sightings in the state. Including discussions on identification, behavior, conservation, etc."*

Unless otherwise identified, the following bird sitings on Monhegan and in transit to and from the island were made by ornithologist Tom Magarian and submitted by him to the Maine -Bird online forum data archive . They are being forwarded here with his acknowledgement.

References to Lobster Cove are highlighted; the air and water off Lobster Cove are proposed for development of the Deepwater wind turbine test area. Birds using that area would be the ones most likely to be directly impacted by the test windturbines. The following narratives and lists detail birds using the area during the time of year when the proposed prototype turbines would be operating directly offshore.

Tom Magarian tmagarian@alumni.unity.edu is a professional ornithologist who works with New Jersey Audubon. He has been tasked to carry out radar sitings of birds off Lobster Cove, Monhegan. The visual observations recorded below are a supplement to those readings, by this highly qualified individual.

TOM MAGARIAN:

Monhegan July 11, 2010 Today there was a group of about 20 greater shearwaters off from Lobster Cove following a school of fish that were breaking the water after baitfish. Yellow warblers, house wrens, song sparrows, common yellow-throats, common grackles, american robins, cedar waxwings, american goldfinches, and american crows are all making there presence known.
Cheers!
-Tom M.

Monhegan July 11, 2010
Tom M. I just did about an hour of seawatching off Lobster Cove. There were some shearwaters, gulls, and a few terns working over a school of bait that was being pushed up by something. I did not see any whales or dolphins, but did see some big splashes. Puffins were mostly heading out to sea. Some guillemots and eider were in the surf and near the island. Sooty shearwater was most numerous followed by greater, and a couple of cory's were in the mix. Here is the list.
sooty shearwater - 25
greater shearwater - 15
cory's shearwater - 2
wilson's storm-petrel - 10

atlantic puffin - 15
black guillemot - 3
common eider - 5
laughing gull- 13
common tern - 7
unknown large alcid - 2 (most likely puffins)
Cheers!
-Tom M.

Monhegan July 12, 2010

This morning I seawatched at Lobster Cove for 45 min and clinched the fourth species of shearwater in less than 24 hours from shore. The first shearwater was a wonderful looking manx heading east and not all that far out. And then the only other shearwaters were five cory's!
Here is the rest.
common tern - 35
black guillemot - 6
wilson's storm-petrel - 7
arctic tern - 2
roseate tern - 2
laughing gull - 6
common loon - 1
northern gannet - 2
Interesting sighting of 3 meduim sized shorebirds heading south. I got on them heading away and could not put a name to them, one looked different from the other two.
Mid day I walked the trails up to the north end and back and picked three swainson's thrushes, one was singing near Black Head. It was great to hear one again, it has been a to long. There were a handful of black-throated green warblers, a couple of common yellowthroats, one flock of golden crowned kinglets, a couple of singing winter wrens, and a singing brown creeper.

This evening I seawatched again from Lobster Cove for a half as it was getting late and there was a bit of sea mist. I did see one cory's, two greater, and one sooty shearwater. One puffin was heading west. That was about all worth noting here.
Cheers!
-Tom M.

July 14, 2010
Yesterday evening from **Lobster Cove**
northern gannet - 30
atlantic puffin - 16
greater shearwater - 7
cory's shearwater - 16
sooty shearwater - 36
manx shearwater - 1
common tern - 14
black guillemot - 5
wilson's storm-petrel - 11
laughing gull - 18
Cheers!
-Tom M

JULY 15, 2010 one immature sharp-shinned hawk.
The evening of the 15th from Lobster Cove
Black Guillemot - 4
Atlantic Puffin - 22
Sooty Shearwater - 2
Greater Shearwater - 2
Northern Gannet - 39
Laughing Gull - 17
Wilson's Storm-petrel - 3
Common Tern
Harbor seal - 3
Harbor Porpoise - 5
All but one puffin heading west.

July 16, 2010

This evening an hour spent seawatching from Lobster Cove turned up few shearwaters, but was good for gannets and west bound puffins.
black guillemot - 4
atlantic puffin - 22
northern gannet - 39
sooty shearwater - 2
greater shearwater - 2
wilson's storm-petrel - 3

laughing gull - 17
common tern
common eider
double-crested cormorant
harbor seal - 3
harbor porpoise ~5
Cheers!
-Tom M.

July 17, 2010 Morning

In the morning on the 17th from Lobster Cove
Atlantic Puffin - 3
Northern Gannet - 18
Laughing Gull - 13
greater shearwater - 14
Black Guillemot - 4
Razorbill - 1
Wilson's Storm-petrel - 1
Common Tern
Roseate Tern - 1
Arctic Tern - 4

Monhegan July 17, 2010 PM
The evening of the 17th Lobster Cove
Cory's Shearwater - 2
Sooty Shearwater - 5
common Tern
Northern Gannet - 17
Laughing Gull - 6

Monhegan July 18, 2010
On the 9am boat on the 18th
Black Guillemot - 52 (most were at the north end of Manana in two big flocks)
Northern Gannet - 25
Great Cormorant - 1
Common Tern
Arctic Tern - 3
Monarch Butterfly - 1

On the 3pm boat back
Black Guillemot - 8
Great Cormorant - 2
Northern Gannet - 10
Common Tern
Laughing Gull

MONHEGAN July 19, 2010 This morning the 19th
One Semi-palmated Plover heard over the harbor and a female kestrel near Lobster Cove.
Cheers!
-Tom M.

Monhegan July 23, 2010
There have been sporadic migrants the last few days. Eastern phoebe, Short-billed Dowitcher, semi-palmated plover, and a few others.

Today there was a great blue heron on Manana and possibly a turkey vulture (I went out without my bins). Also today there was a male purple finch and a killdeer which were new. Also of note were about 125 wilson's storm-petrels off from Lobster Cove. Also, there are a few carolina wrens on the island. I was not expecting these here. does anyone know how regular they are this far north?
Cheers!
-Tom M.

Monhegan July 24,2010

Today i took the 9am to the mainland and the 3pm back out. They trip in was the better trip. both were fogged in, but it was thicker in the afternoon. the early trip surprised me with all four shearwaters!
am boat
cory's shearwater - 1
greater shearwater - 1
manx shearwater - 1
sooty shearwater - 1
wilson's storm-petrel - 16
black guillemot - 20
northern gannet - 1
arctic tern - 1

pm boat
wilson's storm petrel - 6
black guillemot - 9
Cheers!
-Tom M.

Monhegan July 25, 2010

This morning seawatching from Lobster Cove (for 45mins) again proved worth while. I was also treated to a decent look at a fin whale and saw a distant blow, but was unable to ID that one.
wilson's storm-petrel - 16
northern gannet - 12
sooty shearwater - 3
greater shearwater - 30
black guillemot - 1
common eider
common tern
laughing gull - 13
Other migrants
yellow warbler - 3
yellow-rumped warbler- 1?
This evening a brief watch at Lobster Cove for 15 minutes
atlantic puffin - 3
wilson's storm-petrel - 20
northern gannet - 8
balck guillemot - 2
common eider
common tern
laughing gull - 14
And to end the evening a migranting great blue heron flew south down the island headed for the open sea just before 8pm.
Cheers!
-Tom M

July 30, 2010
This morning from Lobster Cove:
manx shearwater - 1
northern gannet - 5
greater shearwater - 6
wilson's storm-petrel - 8
Some of the above migrants this morning, mostly the shorebirds and

yellow warblers.

But last night was the biggest migration event of the fall so far!!!!!!! And I slept in! Anyways, after missing a great morning and completing some of my duties this afternoon I was all stressed out, but then miraculously, during the height of stress, I hear what sounds like....could it really be? After asking about another southern, but pushing north species and get a lot of feedback. (which I really enjoyed) Carolina wrens are hear this far north.

But white-eyed vireo? I almost blew it off at first. But after listening to the bird sing for 5-10 minutes what else could it be? Oh, and for anyone who did not know the "4 letter code", Richard Crossley's new guide will be a godsend! So, I maybe jumping the gun here, but I am pretty sure that WEVI is not all that common this far north??? Anyways, I have heard plenty to know the song. It was not a mimic (ie thrasher, cat bird, or mocker). Having no seen the bird is suspect i know, but hey, I do not want to piss off the land owners out here.
All I know is when I here "QUICK! waitor, check please, CHECK! that there are not many other songs that compare, but please enlighten me if there are.
Cheers!
-Tom M.

Monhegan AUGUST 3, 2010
Today I spent a half hour seawatching from Lobster Cove and have the following to report
manx shearwater - 1
greater shearwater - 16
sooty - shearwater - 1
wilson's storm petrel - 13
northern gannet - 12
laughing gull - 2
common tern
Then a couple "in passing" sightings from later in the day
1445 - eastern kingbird - 3
1930 - BLACK-LEGGED KITTIWAKE - 1(young bird seen flying around the harbor)
Cheers!
-Tom M.

August 6, 2010

[Today] I hit the mainland and took the 1230 boat to Port Clyde. Three puffins flying out to sea were a real treat and an excellent look as well!
black guillemot - 5
ATLANTIC PUFFIN - 3
sooty shearwater - 1
harbor porpoise and seals were seen.

Yesterday evening in downtown Camden after the heavy rain I was treated to at least seven osprey soaring overhead!

Monhegan August 7, 2010

Today on the 3pm out of Port Clyde
great cormorant - 1 (about a mile or two out on one of the small islands)
black guillemot - 5
northern gannet - 25
greater shearwater - 1
manx shearwater - 1
osprey - 2
harbor porpoise and seals

This evening in the southern part of the village I was treated to a young OLIVE-SIDED FLYCATCHER. I presume that they do not nest on the island, so no doubt that this was a migrant. And then I seawatched for about a half hour from Lobster Cove very late in the day.
black guillemot - 1
greater shearwater - 6
manx shearwater - 1
northern gannet - 48
laughing gull - 1
common tern
Cheers!
-Tom M.

AUGUST 10, 2010

A brief mid morning bit of seawatching was rather uneventful. There was more action in the trees around the village. In the evening seawatching was slightly more fruitful.

am seawatching
northern gannet - 20
laughing gull - 2
common eider
wilson's storm-petrel - 1

Around town
magnolia warbler - 1
northern cardinal
carolina wren
golden-crowned kinglet
blue jay
blackpoll warbler - 1
blackburnian warbler - 1
gray catbird
red-breasted nuthatch
semi-palmated plover - 1

pm seawatching
least sandpiper - 6
tree swallow - 5
northern gannet - 13
CORY'S SHEARWATER - 1
wilson's storm-petrel - 1
mourning dove
Cheers!
-Tom M.

AUGUST 11, 2010

Yesterday the 11th proved to be an excellent morning to be out. There have been a few good migration events out here since mid/late July, but they keep getting better. There were warblers in the air calling and the diversity has increased, however it was hard to see them and I am lacking in the flight call dept, but the bulk of what I heard were yellow warblers. There also seemed to be a good push of red-breasted nuthatches, as their numbers were much higher than any other time I have walked the village, and the season's first "farting" dickcissel was a nice treat!

red-breasted nuthatch - 18
american robin - 4
mourning dove - 4

blue jay - 5
carolinia wren - 7
american crow - 8
american goldfinch - 14
cedar waxwing - 80
northern cardinal - 5
common yellowthroat - 5
herring gull
great black-backed gull
ring-necked pheasant - 4
purple finch - 3
red-winged blackbird - 6
golden-crowned kinglet - 8
song sparrow - 6
northern gannet - 22
double-crested cormorant
black guillemot - 14 (1st juv seen on the water in the harbor)
common eider - 8
laughing gull - 1
black-capped chickadee - 10
house wren - 1
gray catbird - 6
chipping sparrow - 1
lesser yellowlegs - 2
least sandpiper - 30
baltimore oriole - 1
yellow warbler - 20 (definitely a big under count)
blackpoll warbler - 3
semi-palmated plover - 2
DICKCISSEL - 1 (heard in flight over harbor headed south towards
Manana, but never saw it)
semi-palmated sandpiper - 3
mallard
common grackle - 1
bobolink - 3
savannah sparrow - 1
blackburnian warbler - 1
black-throated green warbler - 3
american redstart - 1
black and white warbler - 1
trails flycatcher - 1
barn swallow - 1
downy woodpecker - 1
dark-eyed junco - 2

Cheers!
-Tom M.

AUGUST 16, 2010

I seawatched mid afternoon from Lobster Cove and the change of weather has got the shearwaters moving again. I wish I gotten out there earlier and had more time to spend. Cory's and greaters were pasing by heading NE. Some gannets were in the mix, but mostly headed SW or milling about.

cory's shearwater - 10
greater shearwater 34
northern gannet - 35
black guilliemot - 1
common eider
unidentified shorebird - 2 (heading NE, possibly phalaropes)
Cheers!
-Tom M.

AUGUST 18, 19, 20, 2010

Migration is starting to pickup out here on the island. This morning I saw my first peregrine and osprey, and yesterday my first harrier of the season. Also this morning I heard numerous semi plovers calling as they headed south, mostly single birds I presume. I did see one flock of about four. I heard them as I was getting things together out the window, and the first southbound flock of double-crested cormorants went winging by. Last evening while catching mackerel from the warf after dark I heard a handful of yellow warblers and a few call notes that I did not know. The best was hearing an oystercatcher call twice as it flew by to he west and was headed south! Here are the last few days recap:

AUGUST 18, 2010

solitary sandpiper - 1

On the 9am boat leaving the island

wilson's storm-petrel - 15
black guillemot - 6
laughing gull

common eider
great cormorant - 1 (adult)
northern gannet - 300

On the 3pm boat back
osprey - 1
common eider
black guillemot - 8
common loon - 1
northern gannet - 20

Harbor porpoise and seals were easy to see on both trips.

19 AUG

northern harrier - 1 (imm)
-After sunset-
yellow warbler - 5
AMERICAN OSYTERCATCHER - 1

20 AUG

osprey - 1
northern gannet - 10
peregrine falcon - 1 (imm)
laughing gull - 7
black guillemot - 1
tree swallow - 5
common eider
double-crested cormorant - 50 (one flock headed south of about 40)
Cheers!
Tom M.

--

AUGUST 21, 2010
This morning I got a late start, but still saw some interesting birds. Warblers were hard to come by, I only heard a few call notes that might have been yellows. Red-breasted nuthatches seemed more abundant again this morning. I only birded the south end of town down to Lobster Cove.

red-breasted nuthatch - 6
carolina wren - 2
chipping sparrow - 1
eastern kingbird - 12
purple finch - 4
eastern phoebe - 1
laughing gull - 35
black guillemot - 16
bobolink - 1
double-crested cormorant - 50 (one southbound flock of 20)
common eider - 75 (a couple of decent rafts)
northern gannet - 12
parasitic jaeger - 1 (non-breeding adult chasing a laughing gull, then a herring gull attempted to chase it!)
spotted sandpiper - 6
great cormorant - 1 (adult on one of the rock outcrops)

Cheers!
-Tom

AUGUST 22, 2010
Last night after it got dark I heard a few warblers and one veery while fishing from the wharf for mackerel. This morning i had a flyby pectoral sandpiper and there was a flock of about 50 tree swallows at the same location. Then mid afternoon from Lobster Cove, a brief bit of seawatching turned up three shearwaters.

Last evening at the wharf

veery - 1
yellow warbler - 3
american redstart - 3
unknown warbler - 5

This morning from the wharf

pectoral sandpiper - 1
tree swallow - 50

Seawatching from Lobster Cove

CORY"S SHEARWATER - 1

MANX SHEARWATER - 1
greater shearwater - 3
northern gannet - 25
laughing gull - 10
bonapartes gull - 1
black guillemot - 3
black-bellied plover - 1 (still in alternate plumage)
common eider

Cheers!
-Tom M.

AUGUST 23, THROUGH 27, 2010

Migration seems to be picking out here. There have been a couple of recent days with shearwaters. Waterbirds have started moving down from he north. The warblers are arriving. At night it is quite easy to here call notes. (I wish I knew more of them). The last couple of days I heard dickcissels in the morning and today there may possibly be more than one around. I finally saw one perched a top a spruce across from The Trailing Yew about an hour ago. Here is a recap of the last few days.

23 Aug

northern gannet - 12
greater shearwater - 1
black guillemot - 4
common eider
blue-winged teal - 1
ring-billed gull - 1
belted kingfisher - 1
tree swallow - 30
american redstart - 1
yellow warbler - 1
semi-palmated plover - 7
spotted sandpiper - 1

24 Aug

merlin - 1
peregrine falcon - 1
eastern kingbird - 10

northern gannet - 40
common eider
great blue heron - 1
sharp-shinned hawk - 1

25 Aug

sharp-shinned hawk - 1
northern gannet - 20
black - guillemot - 5
osprey - 1
common raven - 2

26 Aug

DICKCISSEL - 1 (heard from The Trailing Yew while I was eating breakfast, could have been two birds?)
northern gannet - 60
greater shearwater - 21
cory's shearwater - 3
red-necked grebe - 8 (one flock heading NE the same as the shearwaters)
unknown large shearwater - 1
Listening to night migrants:
veery - 2
wood thrush - 1
yellow warbler - 5
american redstart - 2
semi-palmated plover - 1
-numerous other call notes went unidentified

27 Aug

DICKCISSEL - 2? (one heard from The Trailing Yew this morning, one heard further south along the road later, and one heard and seen mid day across from The Trailing Yew)
lesser yellowlegs - 1
bobolink - 7
tree swallow - 25
red-breasted nuthatch - 6
cape may warbler - 1
white-winged scoter - 1
purple finch - 4
eastern kingbird - 2

eastern phoebe - 2
blue-winged teal - 1
wilson's warbler - 3
common raven - 2
red-eyed vireo - 1
merlin - 1
semi-palmated sandpiper - 1

Harbor porpoise - 3
harbor seal - 2
grey seal - 1

Cheers!
-Tom M.

AUGUST 27, 2010

This morning was rather birding on the island. I bumped into a couple birding and they told me I had missed a lark sparrow by minutes by the school house. There were a number of warblers and others around. Another blue-gray gnatcatcher by the Winter Works. It could have been the same as the one the evening before. Here is the tally:

coopers hawk - 1
merlin - 1
sharp-shinned hawk - 1
purple finch - 5
northern gannet - 15
black guillemot - 3
bobolink - 12
black-throated green warbler - 3
yellow warbler - 8
american redstart - 1
BLUE-GRAY GNATCATCHER - 1
baltimore oriole - 7
eastern kingbird - 3
red-eyed vireo - 4
belted kingfisher - 1
blackpoll warbler - 1
northern waterthrush - 4
least sandpiper - 3

Cheers!
-Tom M.

AUGUST 29, 30, 11, 2010

The last few days have been good out on the island. The mornings are relatively birdy. The accipts and falcons are around now. Warblers are about and bobolinks are more common. The seabirding has been slow, but gannets are easy to see. Here is a recap.

29 AUG

northern waterthrush - 1
yellow-rumped warbler - 1
common yellowthroat - 1
red-breatsed nuthatch - 1
carolina wren - 1
bobolink - 1
northern gannet
gray catbird - 1

30 AUG

american kestrel - 2
eastern wood-peewee - 1
sharp-shinned hawk - 3
merl - 1
common eider
northern gannet - 15
black guillemot - 2
eastern kingbird - 2
red-breasted nuthatch - 1
one unidentified medium passerine cam in off the water to Lobster Point from the SW at 0920. It makes you wonder how far offshore it was and how long it had been flying to find land.

31 AUG

downy woodpecker - 1
blue jay - 5
common grackle - 2
red-winged blackbird - 2
purple finch - 5
cape may warbler - 7

red-breasted nuthatch - 10
european starling - 4
cedar waxwing - 100
eastern kingbird - 4
wilson's warbler - 1
american warbler - 17
common yellowthroat - 1
carolina warbler - 2
gray catbird - 1
yellow warbler - 2
yellow-rumped warbler - 2
bobolink - 30
american kestrel - 4
merlin - 3
peregrine falcon - 1
sharp-shinned hawk - 1
black guillemot - 2
northern gannet
unidentified warbler - 15

Cheers!
-Tom M.

AUGUST 31 THROUGH SEPTEMBER 6, 2010
This morning was rather birdy on the island. The last few days have been good for bobolinks. Not to much was blown by the storm. The number of gulls did increase after though. Here is a recap.

31 AUG
chimney swift - 1 (late in the day)

1 SEP (before and after sunset at the wharf while fishing for mackerel)
veery - 1
wilson's snipe - 1
yellow warbler - 3
blackpoll warbler - 1
unknown warbler - 6

2 SEP
purple finch - 8
blue jay - 10

brown-headed cowbird - 1
yellow warbler - 1
eastern kingbird - 13
unknown warbler - 6
carolina wren - 2
bobolink - 3
BLUE-GRAY GNATCATCHER - 1 (by the Trailing Yew)
european starling - 3
red-breasted nuthatch - 1
sharp-shinned hawk - 1
gray catbird - 1
laughing gull - 1
black-crowned night heron - 2 (after sunset)

3 SEP
bobolink - 35
pectoral sandpiper - 2

4 SEP
unknown large shearwater - 1
cory's shearwater - 2
northern gannet - 60
common eider
black guillemot - 1
laughing gull - 12
sterna spp - 4 (common/arctic/roseate/forster's)
ring-billed gull - 1
semi-palmated plover - 1

6 SEP
red-breasted nuthatch - 3
bobolink - 27
LARK SPARROW - 3 (one up the hill from The Novelty, and two together by the Lupine Gallery that flew up to the school house, all immatures)

american robin - 6
carolina wren - 2
semipalmated plover - 1
baltimore oriole - 1
purple finch - 20
purple martin - 1
black guillemot - 7
chipping sparrow - 1
solitary sandpiper - 1

yellow warbler - 1
great blue heron - 1
BLUE-GRAY GNATCATCHER - 1 (by the Trailing Yew)
merlin - 2
eastern kingbird - 1
blackpoll warbler - 3
gray catbird - 2
osprey - 1
great cormorant - 4 (one flock heading south)

Cheers!
-Tom M.

SEPTEMBER 9, 10, 2010
Today was decent with good variety on the island. Yesterday was most likely as good, but I did not get out. I was out both nights and there were numerous flight calls, as well as this evening. These seem to be the best movements of the fall so far. Hopefully, tomorrow will be as good as today!

9 SEP
wilson's snipe - 2 (after sunset)

10 SEP
In the morning

american kestrel - 2
american redstart - 3
greater yellowlegs - 1
common yellowthroat - 2
red-breasted nuthatch - 2
blackpoll warbler - 4
purple finch - 1
blackburnian warbler - 3
black-throated green warbler - 2
red-eyed vireo - 3
chipping sparrow - 1
bobolink - 15
northern parula - 1

common raven - 1
solitary sandpiper - 1
gray catbird - 2

This afternoon

rose-breatsed grosbeak - 1
nashville warbler - 1
american redstart - 3
carolina wren - 3
red-eyed vireo - 5
black -throated green warbler - 1
common yellowthroat - 3
yellow-rumped warbler - 1
northern waterthrush - 1
magnolia warbler - 2
black and white warbler - 2
western palm warbler - 1
merlin - 1
purple finch - 1
brown thrasher - 1
bobolink - 1

Cheers!
-Tom M.

SEPTEMBER 11, 12, 13, 2010
It was a great weekend to be out on the island, just ask the 13 year old kid who must tracked every bird on the island that was present. He reported a handful of philadelphia vireos, a couple of yellow-throated vieros, a few lincoln's sparrows, and a scarlet tanager. He and I saw possible mourning warbler, it was a quick look and fleeting look.

The legendary Tom Martin has arrived on the island. He got settled in on Friday. So the seed is being puy out and he keeping is constant vigil from the porch.

Here is most of what was around, or at least what I saw.

11 SEP

belted kingfisher - 3
blackpoll warbler - 3 (definitely an under count as many zip call notes were heard)
red-breasted nuthatch - 3
purple finch - 22
blue jay - 3
cedar waxwing - 12
merlin - 3
carolina wren - 3
least flycatcher - 2
yellow-rumped warbler - 1
american goldfinch - 12
semi-palmated plover - 1
gray catbird - 7
downy woodpecker - 1
black-capped chickadee - 12
red-eyed vireo - 5
black-throated green warbler - 6
common yellowthroat - 4
ruby-throated hummingbird - 3
bobolink - 15
black guillemot - 11
bald eagle - 3
cooper's hawk - 1
black and white warbler - 3
american black duck - 1
northern harrier - 2
swamp sparrow - 1
canada warbler - 1
chestnut-sided warbler - 1
northern flicker - 1
eastern kingbird - 2
sharp-shinned hawk - 2
ruby-crowned kinglet - 1
rose-breated grosbeak - 1
brown thrasher - 1

12 SEP
american goldfinch - 3
northern flicker - 5
common raven - 2
gray catbird - 3
black-capped chickadee - 6

least flycatcher - 2
red-eyed vireo - 3
black guillemot - 1
american black duck - 1
belted kingfisher - 1
blue jay - 2
baltimore oriole - 3
common yellowthroat - 2
american kestrel - 1
merlin - 2
wilon's snipe - 1
northern harrier - 2
red-breasted nuthatch - 3
purple finch - 4
cedar waxwing - 18
sharp-shinned hawk - 1
canada warbler - 1
cooper's hawk - 1
brown creeper - 1
american robin - 1
semi-palmated plover - 4
northern gannet - 4

13 SEP
northern flicker - 8
blue jay - 9
gray catbird - 6
black-capped chickadee - 19
carolina wren - 2
purple finch - 4
brown thrasher - 1
red-eyed vireo - 6
merlin - 1
red-breasted nuthatch - 6
least flycatcher - 1
white-winged scoter - 2
chestnut-sided warbler - 1
northern parula - 1
american robin - 3
sharp-shinned hawk - 1
carolina wren - 1
belted kingfisher - 1
semi-palmated plover - 1
brown creeper - 1

golden-crowned kinglet - 4
common yellowthroat - 1
whimbrel - 1 (flying NE seen from Hornes Hill)

Cheers!
Tom M.

SEPTEMBER 15, 2010
Hello Maine Birders:
The highs were high and the lows were low out on Monhegan yesterday (9/15/10). It started off really challenging but in the end we all left with big smiles on our faces.
It was painful trying to scare up songbirds. It was the slowest I've seen on my trips to Monhegan (spring or fall). We walked for ten minutes before encountering our first passerine - a chickadee. But there were a few gems to be had. A Blue-gray Gnatcatcher was doing its thing in an apple tree next to the church and the Lark Bunting was very cooperative (thanks Bryan and co.!) at White head.
The non-songbirds were the real highlights. A Blue-winged Teal and a Solitary Sandpiper in the Ice Pond. An American Bittern posed at the edge of the reeds down by the pump house. There was an amazing Northern Gannet show off White Head: 100+ birds soaring and plunging. I could have stayed there all day.
The most dramatic bird activity was the raptors. By mid-morning the NW winds really kicked up and there wasn't a moment after that when you couldn't spot a Sharp-shinned or a Merlin overhead. When we were down at Lobster Cove, 6-10 raptors were in the sky at all times dog-fighting, soaring, and pursuing prey. A few Peregrines, harriers, and Osprey rounded out the species list. A Merlin narrowly missed picking off the Lark Bunting while we watched it.
Good birding,
Eric Hynes

SEPTEMBER 27, 2010

Kristen Lindquist Cold and rainy this afternoon but last night's wind blew in some new birds. We spent this Morning watching a great falcon show (mostly merlins) at Lobster Cove and finding a few more songbirds.

Highlights:

YELLOW-THROATED WARBLER-bright and beautiful amid a plum bush, presumably the one first found on Saturday by

Blair Nikula. Thanks to Doug Hitchcox for pointing it out!
LARK SPARROW-with two dickcissels, chipping sparrows, a clay-colored sparrow, etc. Behind the school.
Baltimore oriole in full summer male plumage.
Lots more palm warblers, including a brown Western palm.
Not seen by me but also here:
WHITE-EYED VIREO-found by Derek Lovitch near the Ice Pond the morning.
Derek also had a marsh wren and a Canada warbler on the way to Lobster Cove this morning.
Sora in the Meadow.
BLUE GROSBEAK-found by Eric Hynes in the Meadow.
And lots of other stuff despite the weather!
Kristen

SEPTEMBER 30. 2010
Robin Robinson
This morning had a 'Get-Your-Hard-Hat" massive fall out on the leading edge of the storm. mild breeze about 5mph

at the time, overcast and warm. Lasted 45 min, then fog bank rolled in and rain. Birches referenced are off a deck, two of them which seem to catch lots of passerines
Numbers of warbs are conservative. Got lots of pics, always fun! Robin Robinson
http://robins-chaos.blogspot.com

- Show quoted text -
Then, I went to Lobster Cove:
Snowies 2
GHB 1
GLOSSY IBIS!!! 1
Greater Yellow Legs, 1 hanging with above
more Yellow rumps, 5
Flickers 3
Kingfisher 1
Marsh Cove Rd
Wild turkies 3
Wat'ah Lake/Sebasco resort
Canadas 100
Herring gulls
RT Hummer zoomed by
GBH 1
Crazy day!

Robin Robinson

OCTOBER 7, 2010
Now that most of the birders are gone I will resume my posts. They did a much better job of searching the island than I do. Today had a few birds still kicking around, but a lot have moved along.

magnolia warbler - 1
golden-crowned kinglet - numerous
white-throated sparrow - numerous
yellow-rumped warbler - numerous
northern flicker - 2
yellow-bellied sapsucker - 2
red-breasted nuthatch - numerous
red-eyed vireo - 2
black and white warbler - 2
brown creeper - 4
purple finch
baltimore oriole - 1
osprey - 2
merlin - 2
peregrine falcon - 2
ruby-crowned kinglet - 1
black duck - 3
white-crowned sparrow - 2
clay-colored sparrow - 2
common yellowthroat - 1
yellow palm warbler - 2

cheers!
Tom M.

OCTOBER 8, 2010

This morning there were a smattering of interesting birds around. Most noteworthy was a WORM-EATING WARBLER that came into my pishing after viewing a chat briefly. This was just up the hill from the Trailing Yew. I watched it for five minutes or so, then it disappeared back into the brush.

red-bellied woodpecker - 1
yellow-rumped warbler

red-breasted nuthatch - 8
baltimore oriole - 2
ruby-crowned kinglet - 3
northern flicker - 6
golden-crowned kinglet
brown thrasher - 1
osprey - 1
white-throated sparrow
sharp-shinned hawk - 2
winter wren - 1
brown creeper - 2
red-eyed vireo - 4
swamp sparrow - 2
peregrine falcon - 5
black duck - 4
black-throated green warbler - 1
wilson's warbler - 1
yellow-bellied sapsucker - 2
chipping sparrow - 6
white-crowned sparrow - 4
pine siskin - 2
northern gannet
merlin - 2
pine warbler - 2
blackpoll warbler - 2
great blue heron - 1
palm warbler - 2
yellow-breasted chat - 1
WORM-EATING WARBLER - 1

Cheers!
-Tom M.

OCTOBER 8, 2010 #2
Paul Corcoran
Oct 9, 7:43 am
Yesterday I went over to Monhegan Island for the first time. The wind was blowing 15 to 20 mph. I was joined by Jonathan, Ellen and Bryce. We had 49 species by lunch and then added guillemot in the afternoon. We went to Lobster Cove and then continued past the ship wreck to the back side of the island. We were treated to 450+ Northern Gannets they were diving repeatedly.
Paul from Bangor

OCTOBER 16, 2010

There have been some good birds around this week. It seems a lot have left the island with the strong winds. Warblers and vireos are getting scarce. I saw only one red-eyed vireo today. The yellow-rumps are way down, and the blackpolls were almost as numerous. The 14th was a good day all around, as you will see. A few black-throated-blue and green-warblers were seen on the 14th as well as a few common yellowthroats, and northern waterthrush was a surprise. Today I saw my first orange-crowned warbler. Palm warblers were less scarce today. Only yellows were present, the westerns were most abundant on 14th. I heard a chat on the 14th. On the 12th I saw a scarlet tananger. One blue headed vireo on the 13th.

The sparrows were very abundant since the 12th with the 14th seeming to be the peak. Today there were many less white-throats. There was however a nice lark sparrow coming to the seed in Tom's yard. A field sparrow has been seen the last few days. White-crowned sparrows peaked on the 14th with 17 being seen. My first fox sparrow was on the 14th, and a lincoln's was seen on the also.

Pine siskins were in good numbers on the 14th. Three wood ducks were on Ice Pond on the 14th, as well as a mallard/black duck hybrid, which is hanging with black ducks. Baltimore orioles were seen up til the yesterday. Four rusty blackbirds were seen on the 14th. A lone yellow-billed cuckoo was seen on the 14h and I found feathers of a yellow-billed in the same area today, so I fear it has come the way of the hooded warbler. Both kinglets are less numerous and I only turned up one sapsucker today. Great cormorants are picking up though. Peregrines and merlins are still terrorizing the skies.

All and all it is still relatively birdy and the time is here for any wayward vagrant to show. Who will come out find them?

Cheers!
-Tom M.

END

Cultural Resource Management Assessment for the UMaine Deepwater Offshore Wind Test Site: Pre-Columbian Cultural Resource Evaluation

Prepared for

DeepCwind Consortium

November 19, 2010

Prepared by

Alice R. Kelley, Ph.D.

Department of Earth Sciences, Climate Change Institute, and Department of Anthropology,

University of Maine, Orono, Maine 04469

Reviewed by

Melissa Landon Maynard

Dept. Civil & Environmental Engineering

Table of Contents

Table of Figures

Introduction

The cultural resource assessment of the UMaine Deepwater Offshore Wind Test Site (Figure 1, Figure 2) is being carried out to satisfy the requirements of Section 106 of the National Historic Preservation Act. The Act requires the identification of significant pre-Columbian or historic cultural resources within the study area, so that that potential project impact can be assessed and plans to avoid, minimize or mitigate adverse affects be implemented.

Maine's complex sea level history and long history of fishing and maritime commerce creates the potential for both pre-Columbian and historic cultural resources within State offshore waters. Glaciation and deglaciation of the New England/Maritime region associated with the Laurentide Ice Sheet resulted in postglacial subaerial exposure of offshore regions between the modern day coast and depths of 60 m between 13,000 and 5,000 years ago (Barnhardt et al., 1995, Belknap et al., 2005). All of coastal Maine and much of central Maine was inundated by marine waters prior to 15,000 years ago, as the Laurentide Ice Sheet retreated across the glacially depressed landscape. Between 15,000 and 12,000 years ago the land surface rebounded as a result of the removal of the weight of the ice, and fell to a lowstand of 60 meters below present day sea level. As world-wide sea level rose, this subaerially exposed region was once again inundated. This sea level rise occurred rapidly at first, reached a significantly lower rate from 11,000 to 8,000 years ago and then rose steadily to its current elevation. Human occupation of this area is documented in Maine's nearshore region, with most time-diagnostic artifacts representing the time period of slow sea-level rise from 11,000 to 8,000 years ago (Kelley et al., 2010; Price and Spiess 2007; Crock et al., 2003).

1 Archaeological Assessment Methods

The cultural resources of the UMaine Deepwater Offshore Wind Test Site are currently under evaluation. Multibeam bathymetry, seismic reflection, and side scan sonar survey information acquired by Drs. Daniel F. Belknap and Joseph T. Kelley of the University of Maine Department of Earth Sciences (Belknap et al 2010) was analyzed with the goal of identifying high potential areas for pre-Columbian archaeological remains and exposed historic shipwrecks. Details regarding these surveys are described below. Side scan sonar images of the ocean bottoms were reviewed for evidence of submerged historic material. Seismic reflection information was combined with side scan sonar images to evaluate the pre-Columbian archaeological potential of the area. While this type of geophysical data cannot be used to identify individual artifacts or

pre-Columbian archaeological sites, it is possible to identify geomorphic settings have a high potential for preservation of cultural resources based on terrestrial settlement/preservation models. These models, when applied to the coastal zone suggest that shell midden sites are most likely to be located on shorelines with south to southeastern exposures adjacent to tidal flats (Kellogg 1987) or on beaches or other coastal landforms adjacent to freshwater (Kelley et al., 2010). Investigations of New England interior sites has indicated that occupation locations associated with the earliest occupants of the region (Paleoindians) are most frequently located on high, sandy geomorphic features with a broad view of the landscape, and access to water (Spiess et al., 1988) or on thoroughfares between large bodies of water (Kelley 2006). Sites from 9,000 years ago to European contact are frequently positioned at the margins of wetlands (Almquist-Jacobson and Sanger 1995; Kelley 2006) and on rivers at tributary mouths (Sanger et al., 1991; Kelley 2006). Thus, geomorphic analysis of geophysical data involves establishing the position of earlier, below present shorelines and the geomorphology of terrestrial settings that are anticipated to contain cultural remains.

1.1 Geophysical Surveys

The following described the geophysical surveys conducted within the entire bounds of the University of Maine Deepwater Offshore Wind Test site. The following summaries are extracted from Belknap et al., (2010).

1.1.1 Sidescan Sonar

Digital sidescan sonar profiling was conducted from the *R/V Friendship* on June 17 and 18, 2010. An EdgeTech DF2000 fish was towed from the center block of the A-frame at a layback of approximately 39 m, at a speed of 4-5 knots. Survey lines were laid out in an E-W orientation with an approximate N-S 200 m spacing. The scale was set at 200 m to port and starboard, giving theoretical 100% overlap of the mosaic. Data were collected with the Triton-Elics (TEI) topside system, which provides a real-time "waterfall display" of the imagery. Each sidescan ping (1 per second) was electronically tied to a differential global positioning system (DGPS) navigation point for complete georectification on processing. In addition, manual records were logged approximately every 5 minutes for a backup summary navigation. In the laboratory, lines were replayed to find the best compromise for the automatic bottom-tracking feature to display a slant-range, along-track and georectified image. Unfortunately, the sea state (a range of choppy to

calm) and water-column stratification forced a combination of fixed-depth and rapid manual readjustments during playback to achieve a reasonable final image. The georectified images were then combined in local examples and an overall mosaic of the UMaine Deepwater Offshore Wind Test Site. Data are displayed in the overall mosaic emphasize the E-W lines, as the data become severely distorted during short turns. The southern two profiles are no longer available, either improperly recorded in the field, or subsequently lost. In spite of these difficulties in creating the mosaic, the native playback lines provide the best imagery for location of artifacts such as cables, shipwrecks, or other unnatural features. No significant historic or prehistoric artifacts were found in the sidescan sonar survey. There were numerous lines or cables, and individual lobster traps visible in several basins.

Interpretation of sidescan imagery is based on intensity of backscattered sound, generally shown as gray-scale values, on pixels of 0.25 m square in the native data. Mosaicing requires massive data files, and thus is generally reduced to 1 m resolution or less. Figure 3 is a mosaic at 1 m resolution of the E-W lines in the survey area. The digital corrections for slant range and speed result in a true-scale image similar to a surficial photograph (ideally), such that bedrock structure, rippled sand fields, artifacts, etc. are noticed easily. More subtle are the distinctions among gray scales on relative smooth surfaces that may represent changes from mud (low backscatter), sandy mud (intermediate), sand (medium backscatter) and gravel (high backscatter) on the basis of surface roughness and hardness. It is also possible to image individual cobbles and boulders at the 100 m and 200 m range scales. A second control on backscatter is the angle of the surface toward or away from the towfish, which increases or decreases the reflection intensity. Large objects such as bedrock ridges may give a strong proximal return, but their opposite side is completely acoustically shadowed, giving no return. Sidescan sonar displays may be customized in several ways, but our convention is that a strong return is dark and a low return is light in color, analogous to seismic data. Finally, interpretation of any sidescan mosaic requires understanding that the sonar source travels along the trackline pinging to port and starboard, with reflections coming back to that centerline. Thus, an object ensonified on alternative passes may switch from "shadowed" to "strong" return depending on the geometry.

1.1.2 Seismic Reflection Profiling

Digital seismic reflection profiling was conducted from the *R/V Friendship* on June 15 and 16, 2010, and supplementary lines associated with coring from the *R/V ARGO Maine* on July 7

and 8, 2010. Seismic lines were laid out E-W at a spacing approximately 100 m apart N-S, with supplementary lines diagonally across encountered basins, and to tie in proposed sediment coring locations. The single-beam seismic reflection system source was an Applied Acoustics Engineering (AAE) "boomer" with peak acoustic power at 1.5 kHz, powered at 105 Joules, firing every 0.25 seconds. The two-way travel time of the source sound at a velocity of 1500 m/s corresponds to a total water depth and sediment thickness of 187.5 m. This provides an appropriate compromise of resolution and penetration in the expected water depths and sediment thicknesses, based on decades of prior experience in the Maine nearshore (e.g., Belknap and Shipp, 1991; Kelley and Belknap 1991; Barnhardt et al., 1997). Adjustments for increased acoustic velocity in sediments can be made after measurements from core samples, but this is not generally necessary for the Holocene and glaciomarine muds (Belknap and Shipp, 1991). The boomer was towed on a catamaran float at the water surface several meters outside of the vessel wake.

Reflections were received by a 20-element AAE hydrophone, and digitized and amplified by the TEI topside system. The hydrophone was towed 0-0.5 m below the surface at the same distance behind the ship as the catamaran on the opposite side of the wake and at a spacing of 5-7 m. Seismic shots (4 per second) were automatically matched with DGPS navigation data for sub-5 m positioning accuracy. As with the sidescan data, supplementary manual navigation notes were kept approximately every 5 minutes. A raw readout available at collection time and as the base playback record provided guidance for adjustments to deployment and track lines. Filtering was adjusted to 600-2400 Hz for this project. The data were then replayed in the laboratory to create a georectified profile of seismic reflection 2-way travel time versus horizontal distance traveled. Subsequent analysis included digitization of the bathymetric surface within the TEI software, and export of the line image for manual interpretation in a graphics program (Canvas10). Digitized x, y, z data were subsequently corrected for tidal variation. No Pythagorean correction for towing geometry was thought to be necessary in the 60-100 m water depth. All lines were georectified, except short inter-line turns, which often are compromised by changing towing geometry.

Conditions during seismic profiling were optimal for equipment performance in terms of weather and sea state for the majority of the cruise, resulting in clear records. A few internal problems in the TEI topside system hardware and/or software resulted in short-term glitches,

resulting in the irregular auto-numbering system of lines and a few time gaps. However, there is near full areal coverage of the UMaine Deepwater Offshore Wind Test Site (Figure 4).

1.1.3 Multibeam Bathymetric Survey

The system used is comprised of a WASSP pole-mounted multibeam swath bathymetric survey transducer with real-time DGPS navigation and correction for pitch, yaw and roll and an Olex topside receiver that integrates data to produce a real-time image of bathymetry, hardness, or other sea-floor conditions. The WASSP-Olex system is unique in not just "painting over" previous swaths like a typical sidescan system, but in selecting the best data for true depth based on geometry of beam angles. In addition, the Olex system makes corrections for speed of sound and tidal elevation in real time. The survey was conducted on October 12, 2010. Sea state varied during data collection from greater than 1 m short-period waves, to less than 0.5 m waves by the end of data collection, which the WASSP-Olex system compensated for in data processing. Figure 5 provides survey results, which are being analyzed in greater detail currently.

2 Results

Areas of interest for potential development were chosen based on the presence of both rock and mud substrate for a widest range of anchoring possibilities. These are shown in Figure 6. Analysis of the bathymetric, seismic reflection and side scan sonar surveys indicate no areas of high potential for pre-Columbian archaeological remains in the recommended development areas, Areas 1 and 2 in the western and central portions of the test area (Figure 6). The bathymetry of these areas is below 60.6 m (200 ft.), and thus they were not subaerially exposed since the last glaciation of the region. As a result, this area was not available for occupation by pre-Columbian inhabitants, even during the brief sea-level lowstand approximately 12,000 years ago.

The only region that would have been subaerially exposed at the maximum of the sea-level lowstand is located in the northeastern portion of the UMaine Deepwater Offshore Wind Test Site, and has been precluded from development on the basis of extensive rock outcrops with limited sediment accumulations (Figure 1, Figure 6). This area is also identified as having little potential for intact archaeological remains. Bathymetric data shows this region to be at the tip of an elongate southwest/northeast trending underwater peninsula, with maximum elevations just over 60.6 m (200 ft.) below sea level in the test site area. Seismic reflection profiles and side

scan surveys of the area showed a predominately rocky bottom with the areas of highest elevation above the seafloor associated with rock outcrops. This area was briefly subaerially exposed, and then inundated during the rapid sea-level rise at 12,000 years ago. During subaerial exposure, this rocky, higher relief area probably had little original sedimentary cover to host archaeological remains, and what was present was most likely removed by wave activity as it passed through the surf zone during sea level rise. It is important to note that in most archaeological sites from this time period in Maine terrestrial locations, materials are typically found in shallow settings, within the upper 510 mm (20 in.) of the soil column, after 10,000 years or more of biological and mineralogical additions to the ground surface. It is highly unlikely that deposits of this time period would be preserved on the exposed tip of a bedrock peninsula with thin surficial deposits that experienced wave action generated in the Gulf of Maine.

Analysis of detailed side scan sonar images showed no intact shipwrecks on the ocean bottom. Figure 8, Figure 9 and Figure 10 show representative results from the sidescan sonar survey. The location of these images is shown on Figure 7. Figure 8 is a detail from line 169-1209, and shows an isolated outcrop of steeply dipping bedrock surrounded by fine-grained sediments. The very dark portions of the outcrop are steeply dipping beds facing the source of acoustic energy directed from the right hand portion of the image, with lighter portions being bedrock that received less energy. The white/light area to the left of the outcrop is an acoustic shadow, created by a blockage of sound energy by the higher bedrock exposure. This is very characteristic of the general bottom morphology in the region. Figure 9 is a detail from line 169-1259, and shows an elongate bedrock body suggestive of the outline of a shipwreck. However, note that the darkest portions of the feature are on trend with the adjacent bedrock outcrop. The white/light area ringing the left portion of the feature is an acoustic shadow created by the outcrop blocking the acoustic energy coming from the right hand portion of the image. A string of lobster traps are located on the bottom near the bedrock outcrop and on the right hand portion of the image. An elongate feature is identified as a log. Figure 10 is also a detail from line 169-1259, and shows a bedrock outcrop surrounded by fine-grained sediments with a cable and net or other gear. This may represent fishing equipment lost, perhaps, by snagging on the protruding bedrock.

3 Conclusions

All areas with water depth greater than 60 m within the UMaine Deepwater Offshore Wind Test Site have no potential for pre-Columbian cultural resources, as these areas were not subaerially exposed since the last glaciation of the region. This includes Area 1 and Area 2 (Figure 6), which have been pre-selected for potential development. Only a small area located within the northeastern portion of the UMaine Deepwater Offshore Wind Test Site has been identified to have extremely limited potential for pre-Columbian occupation or use, as water depths are just less than 60 m below sea level. This area was subaerially exposed for an extremely short period of time, and is characterized by exposures of bare rock, suggesting that it has experienced significant wave erosion as the area passed through the surf zone during sea level rise. However, if this area was used by the earliest pre-Columbian inhabitants in the region, preservation of a site or of intact archaeological material within this area is extremely unlikely. Note that this area is not being considered for development due to the limited nature of the gravel and rock substrates present at the seabed.

Visual analysis of side scan sonar image data has shown that no intact shipwrecks are exposed on the ocean bottom. However, at the request of the Maine State Historic Planning Office, all areas of planned bottom and sub-bottom disturbance will be examined in more detail using a marine magnetometer survey to identify the presence of potential shipwrecks and eliminate the potential for damage to these by avoidance of these areas.

4 Recommendations

Pre-Columbian resources have not been identified through sidescan sonar image analysis at the UMaine Deepwater Offshore Wind Test Site, including within the pre-selected development areas (Area 1 and Area 2). No further investigation or monitoring with respect to pre-Columbian archaeological remains is needed. However, as a precaution, any work in sediment rich areas of the northeastern portion of the test area should include monitoring for the recovery of pre-Columbian archaeological remains or buried shipwrecks. It is anticipated that any recovered materials will have been removed from their original location of deposition by wave action as sea level rose in the area.

5 References

Almquist-Jacobson, H. and Sanger, D., (1995). "Holocene climate and vegetation in the Milford drainage basin, Maine, USA, and their implications for human history, *Vegetation History and Archeobotany,* 4:211-222.

Barnhardt, W.A., Belknap, D.F. and Kelley, J.T., (1997). "Stratigraphic evolution of the inner continental shelf in response to late Quaternary relative sea-level change, northwestern Gulf of Maine," *Geological Society of America Bulletin*, 109:612-630.

Barnhardt, W.A., Gehrels, W.R., Belknap, D.F., and Kelley, J.T., (1995). "Late Quaternary relative sea-level change in the western Gulf of Maine: Evidence for a migrating glacial forebulge," *Geology*, 23:317-320.

Belknap, D.F., Kelley, J.T., Kelley, A.R., (2010). "Report on Geophysical Surveys Conducted June through October, 2010, University of Maine Deepwater Offshore Wind Test Site, Offshore Monhegan Island, Maine," Unpublished Report submitted October 22 2010, University of Maine, 41p.

Belknap, D.F., Gontz, A.M., and Kelley, J.T., (2005) "Paleodeltas and preservation potential on a paraglacial coast: evolution of eastern Penobscot Bay, Maine", High Resolution Morphodynamics and Sedimentary Evolution of Estuaries, FitzGerald, D.M. and Knight, J., Eds., Springer, 335-360.

Belknap, D.F. and Shipp, R.C., (1991). "Seismic stratigraphy of glacial-marine units, Maine inner shelf." *Glacial-Marine Sedimentation; Paleoclimatic significance*, J.B. Anderson and G.M. Ashley, eds., Geological Society of America Special Paper 261, 137-157.

Crock, J. G., Petersen, J. B., and Anderson, R. M. (1993). "Scalloping for artifacts: A biface and plummet from eastern Blue Hill Bay, Maine," *Archaeology of Eastern North America*, 21:179-192.

Kelley, J.T., Belknap, D., Clausen, S., (2010) "A drowned, coastal deposits with associated archaeological remains from a sea-level "slowstand": Northwestern Gulf of Maine" *Geology*, 38:695-698.

Kelley, J.T. and Belknap, D.F., (1991). "Physiography, surficial sediments and Quaternary stratigraphy of the inner continental shelf and nearshore region of central Maine, United States of America." *Continental Shelf Research*, 11:1265-1283.

Kelley, A.R., (2006). Archaeological Geology and Postglacial Development of the Central Penobscot River Valley, Maine (USA), University of Maine Ph.D. Dissertation, 327 p.

Kellogg, D.C., (1994). "Why did they choose to live here? Ceramic Period settlement in the Boothbay Maine Region," *Northeast Anthropology,* 48: 25-60.

Kellogg, D.C., (1987). "Statistical relevance and site locational data," *American Antiquity.* 52:143-150.

Maynard, M.L., (2010). Recommended Areas for Study and Development in the UMaine Deepwater Offshore Wind Test Site. Unpublished report submitted July 2010, updated August 2010.

Price, F. and Spiess, A. (2007). "A new submerged prehistoric site." *Maine Archaeological Society Bulletin*, 47:21-35.

Sanger, D., Belcher, W.R., and Kellogg, D.C. (1991), "Early Holocene occupation at the Blackman Stream site, Central Maine," Early Holocene Occupation in Northern New England, B.S. Robinson, J.P. Petersen and A.K. Robinson, Eds, Maine Archaeological Society, Augusta, ME, 149-162.

Spiess, A., Wilson, D. and Brady, J., (1998). "Paleoindian occupation in the New England-Maritimes Region: Beyond cultural ecology," *Archaeology of Eastern North America*, 26:201-264.

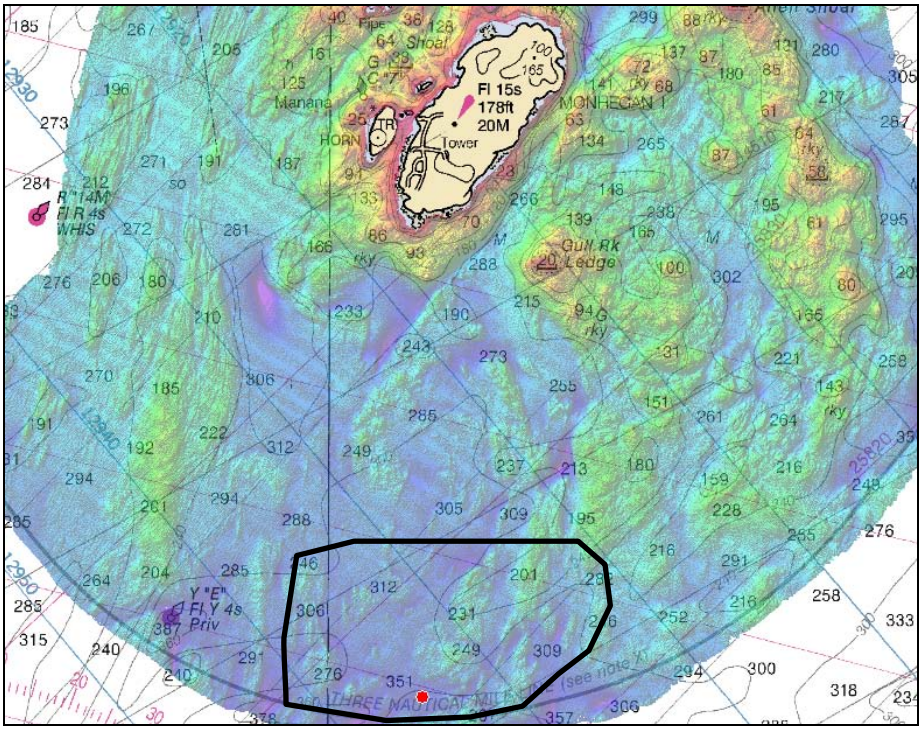

Figure 1: UMaine Deepwater Offshore Wind Test Site outline with mulitbeam bathymetry data courtesy of Maine Department of Marine Resources (from Maynard 2010). Color scale illustrates depth: red is shallow, dark blue is deep.

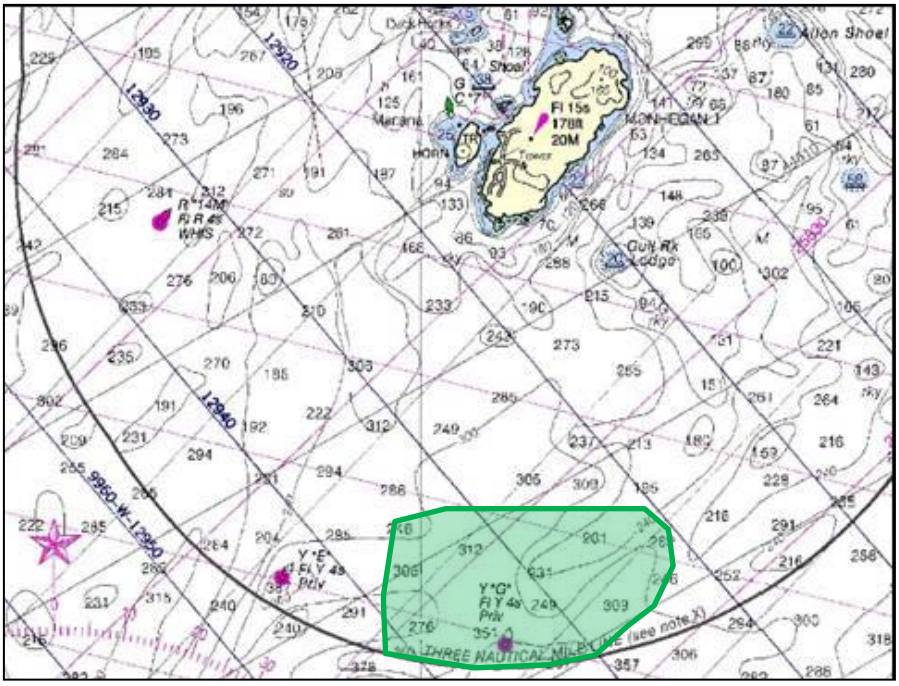

Figure 2: UMaine Deepwater Offshore Wind Test Site outline overlying NOAA Coastal Navigation Chart. Depths shown in feet (from Maynard 2010).

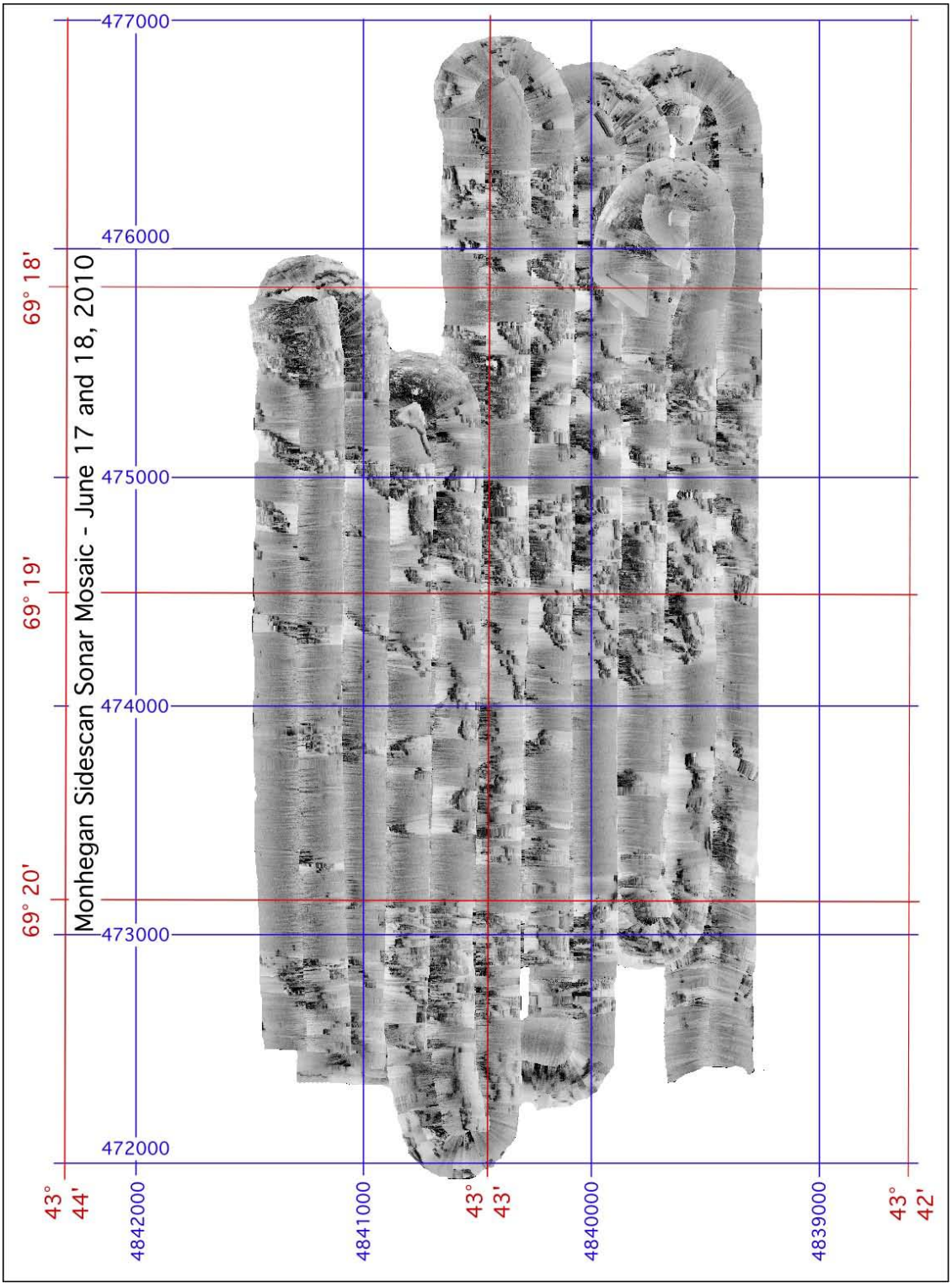

Figure 3: Sidescan sonar mosaic over the UMaine Deepwater Offshore Wind Test Site at 1 m resolution. Grids are both latitude-longitude and UTM grid points (WGS 84 datum) (from Belknap et al., 2010).

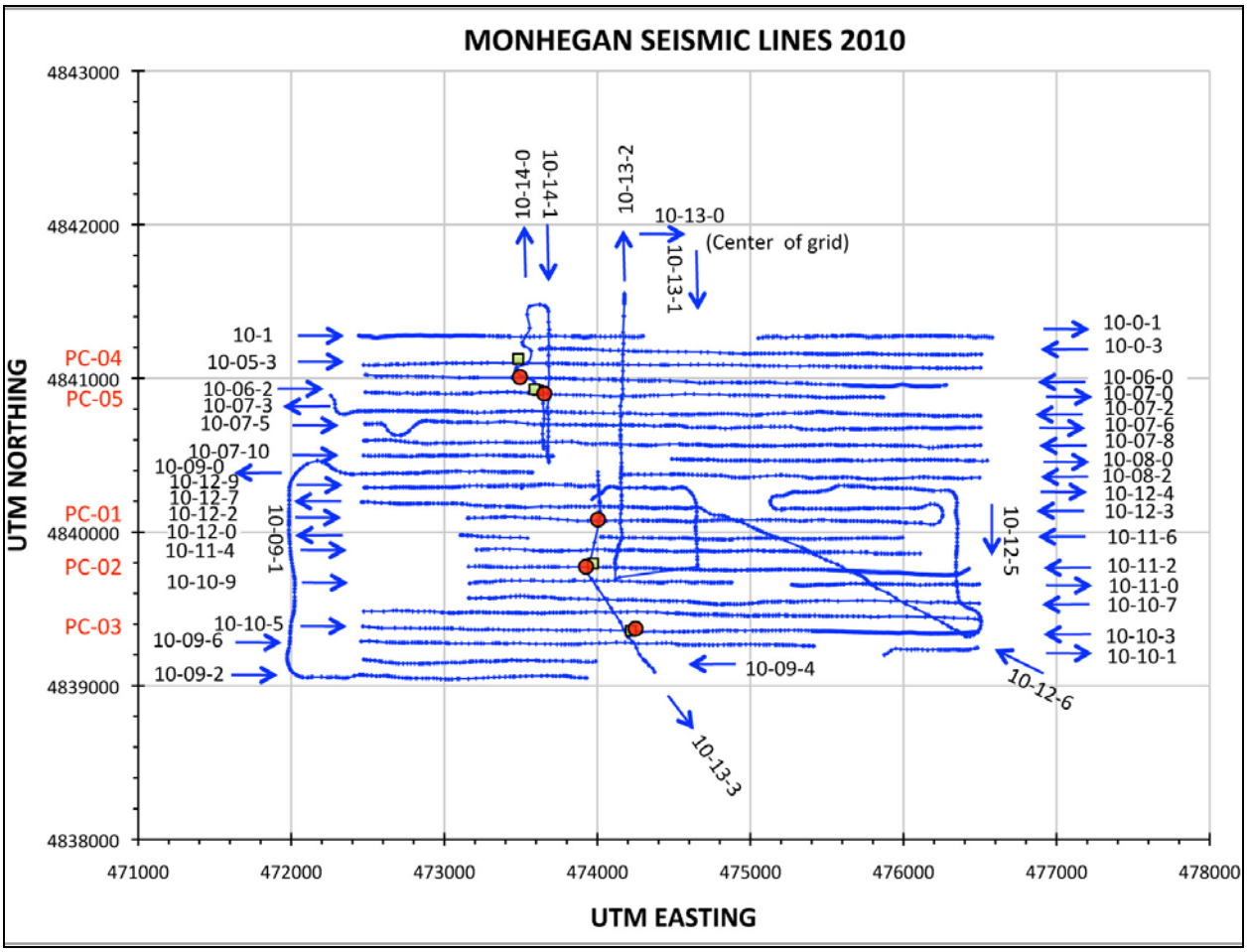

Figure 4: Seismic reflection profiles from the UMaine Deepwater Offshore Wind Test Site, June 15 - 16, 2010, and during the coring cruise July 7-8, 2010 (lines 10-13-3, 10-14-0 and 10-14-1). Most short turns are numbered, but not shown. The complicated line numbering is from an automatic software incrementation and some irregular data holidays. Line directions are indicated by blue arrows. The five piston core (red dot) and four box core (green square) locations. (From Belknap et al., 2010).

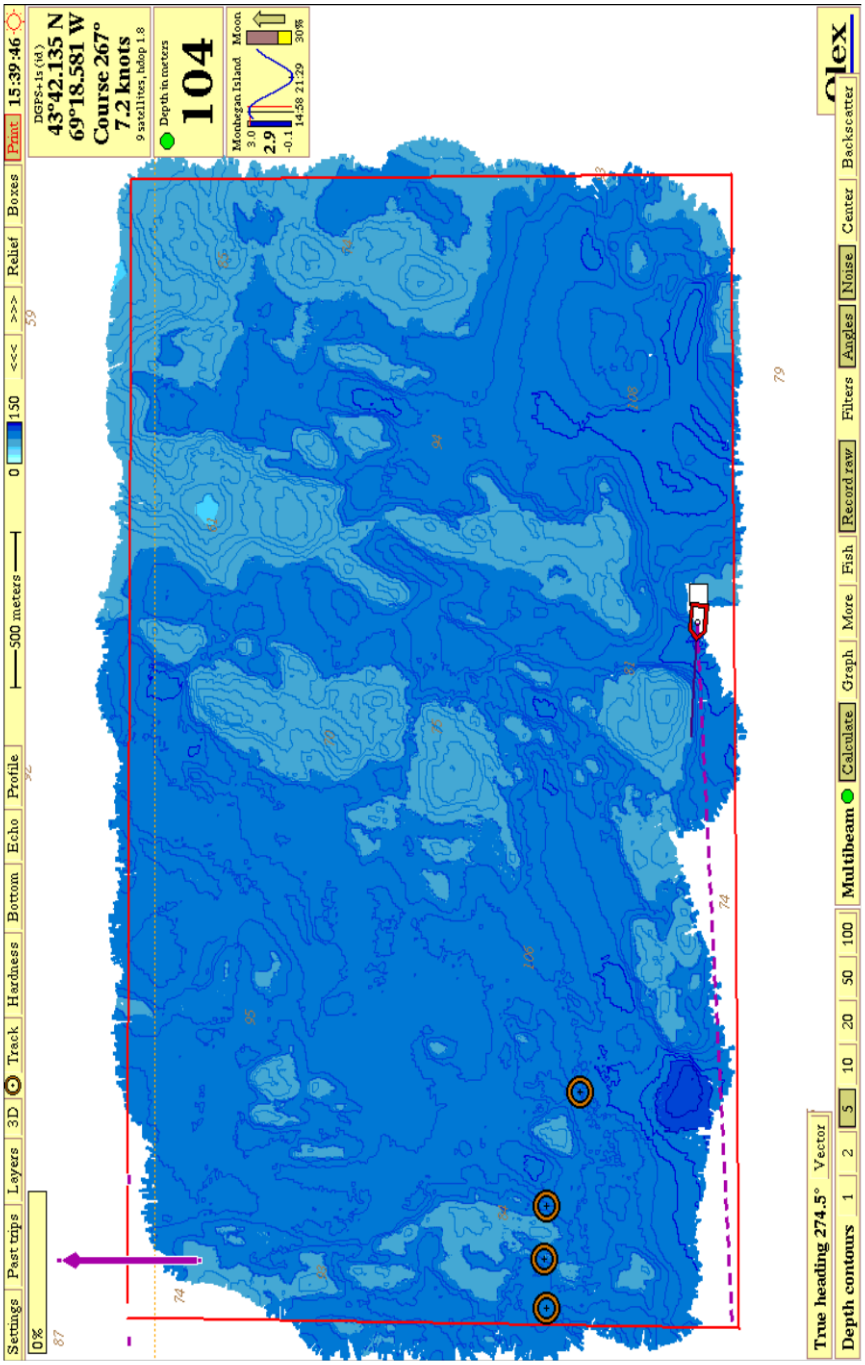

Figure 5: Preliminary bathymetric map of the study area from the WASSP-Olex system completed October 12, 2010. Darker colors correspond with greater depths. This screen-grab image is backed up by full x,y,z files that are currently being processed (from Belknap et al., 2010).

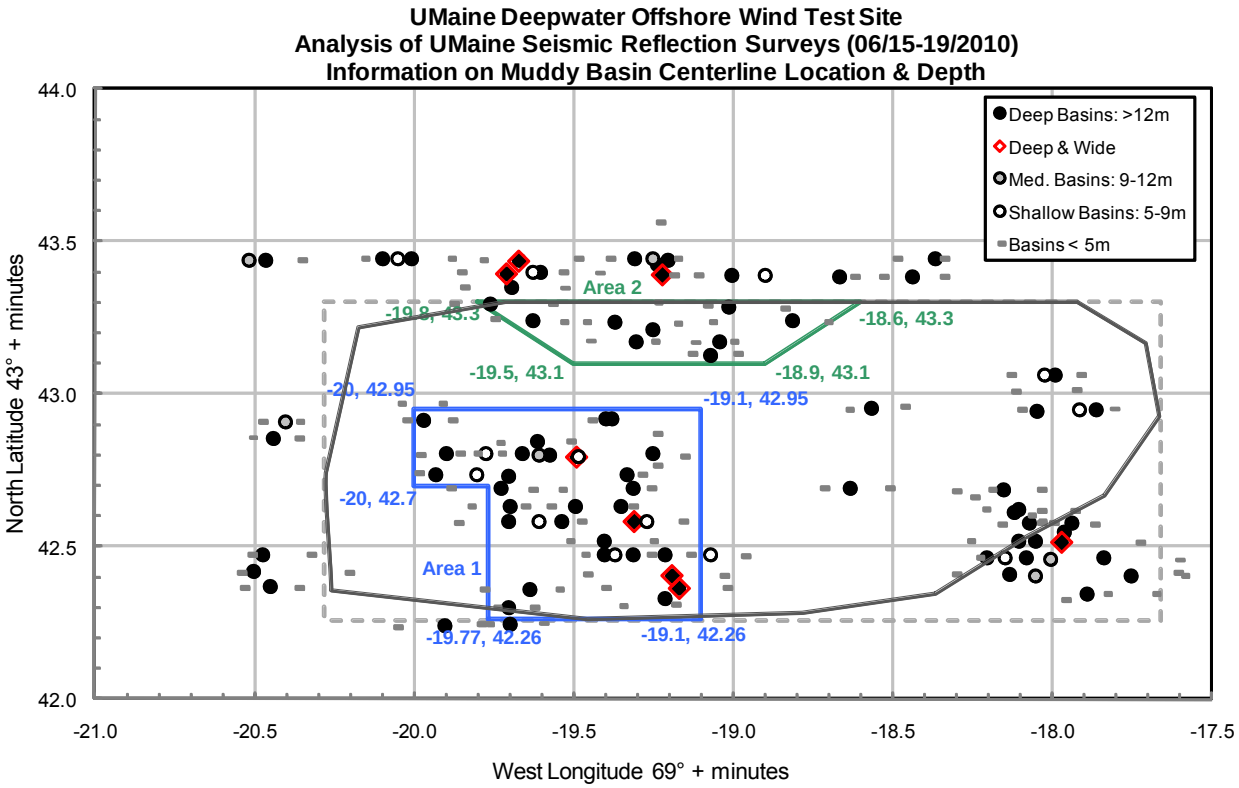

Figure 6: Locations of turbine anchoring areas of interest (from Maynard 2010).

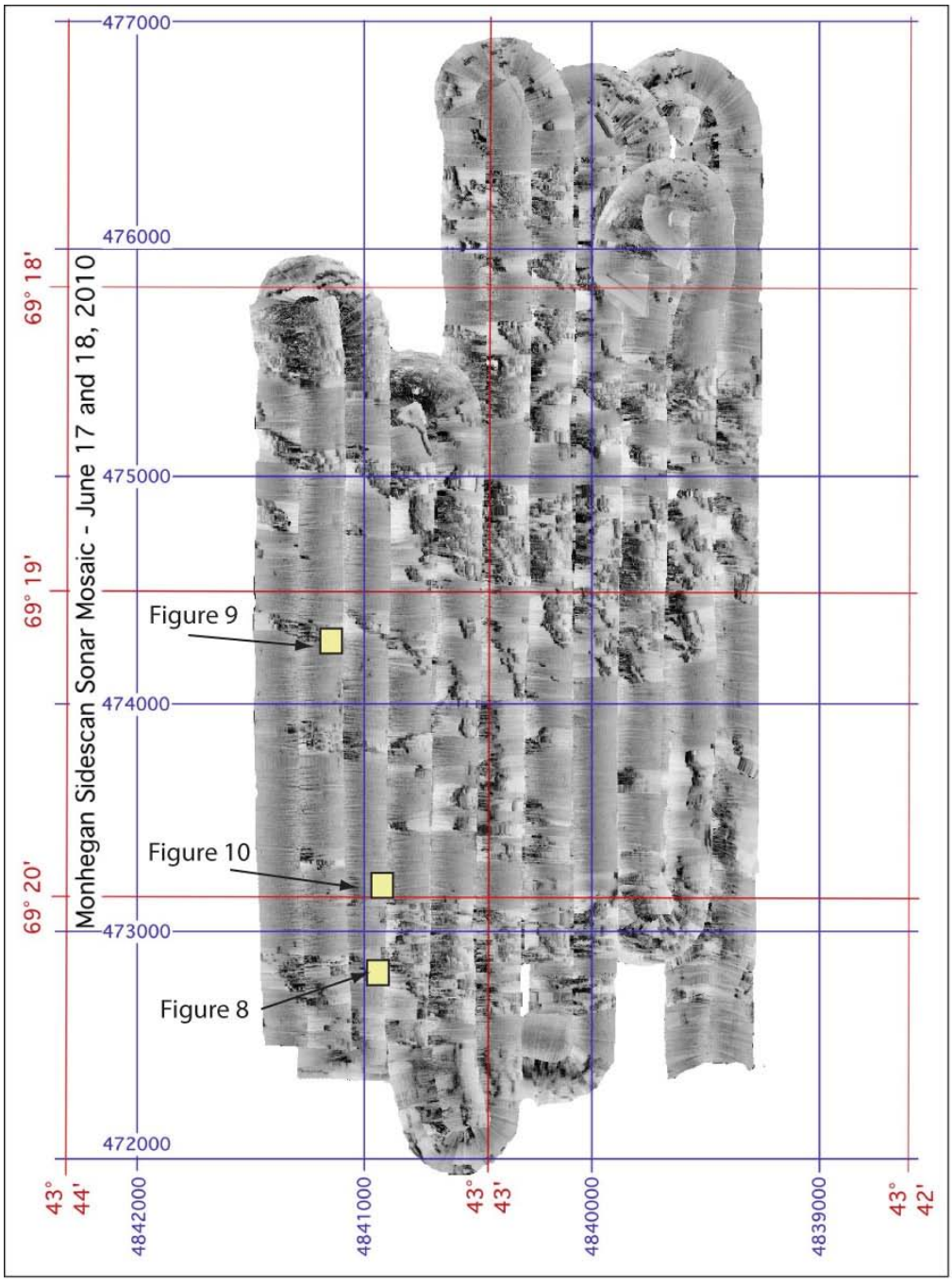

Figure 7: Approximate location of detailed sidescan sonar images in Figures 8,9 and 10. Grids are both latitude-longitude and UTM grid points (WGS 84 datum) (Modified from Belknap et al., 2010).

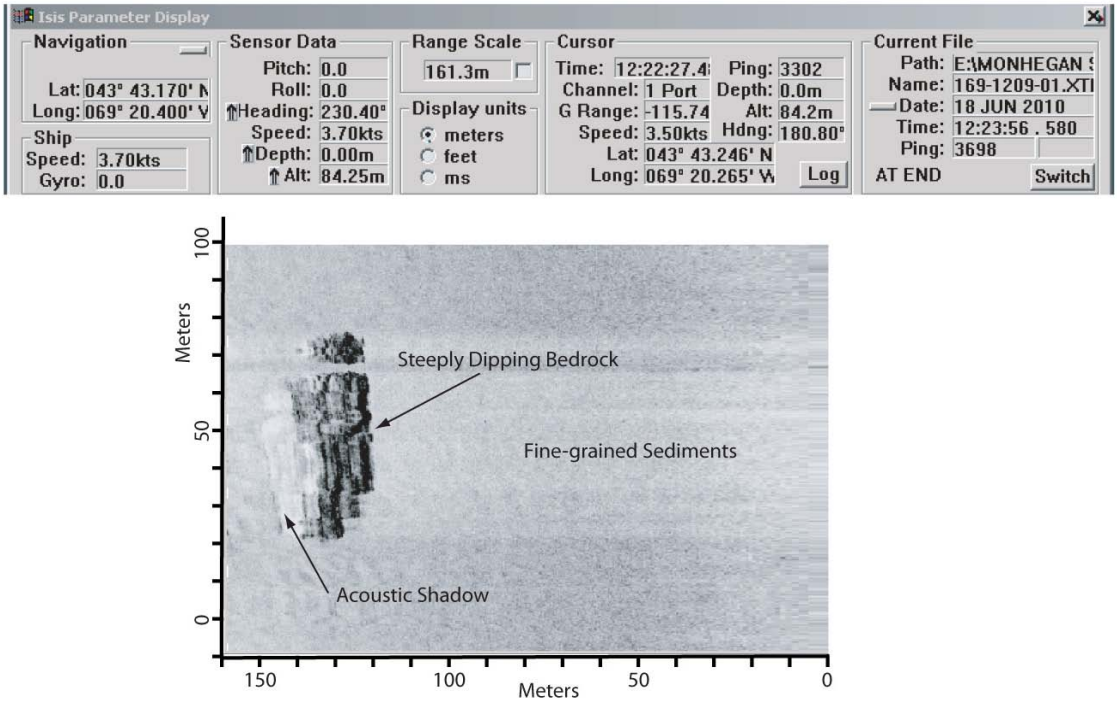

Figure 8: Detail of a sidescan sonar image showing a bedrock outcrop surrounded by fine grained sediments.

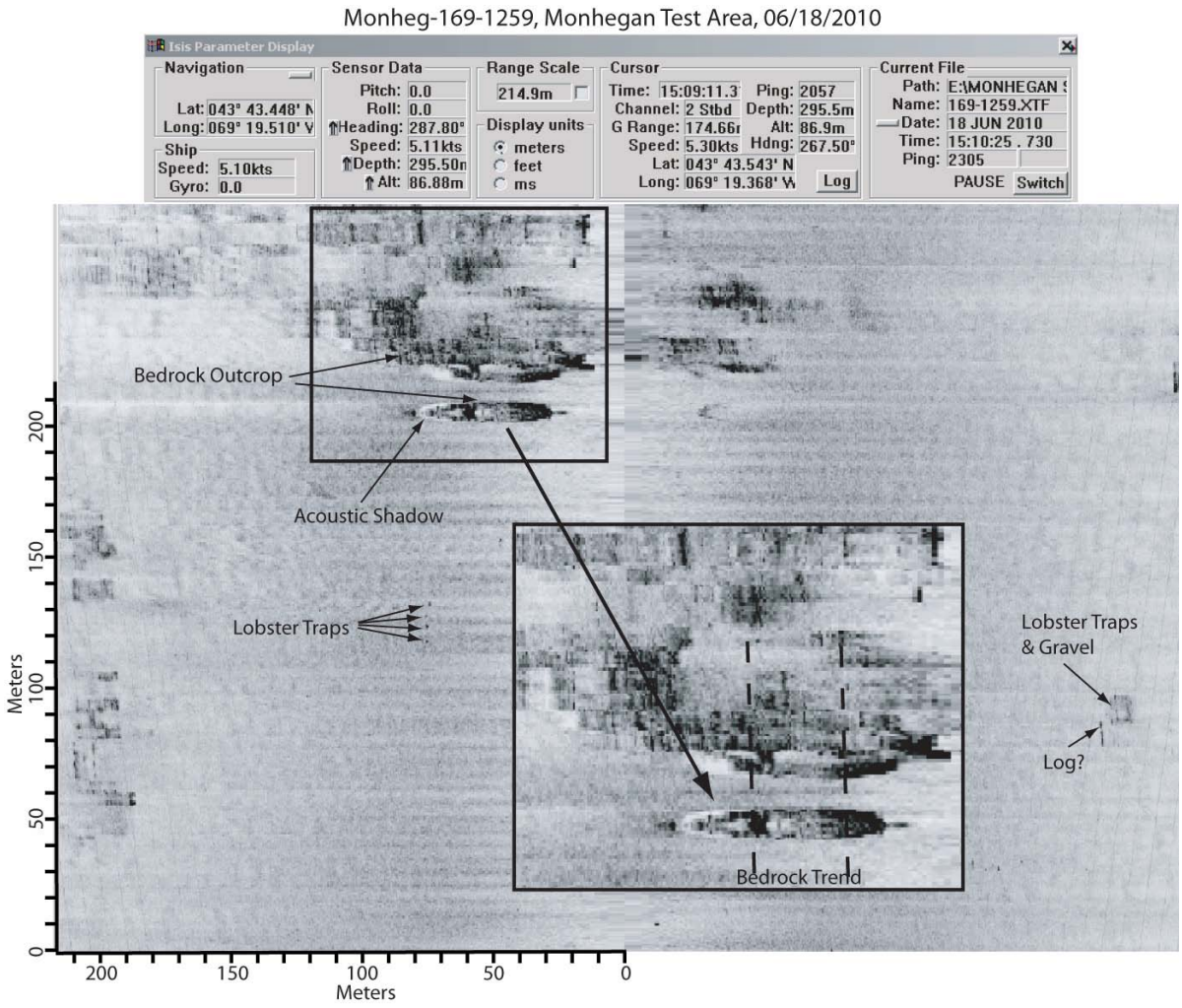

Figure 9: Detail of a sidescan sonar image showing bedrock outcrops, lobster traps and a log. A small bedrock outcrop has a shipwreck-like appearance; however examination of the feature shows high and low areas match the adjacent bedrock trend.

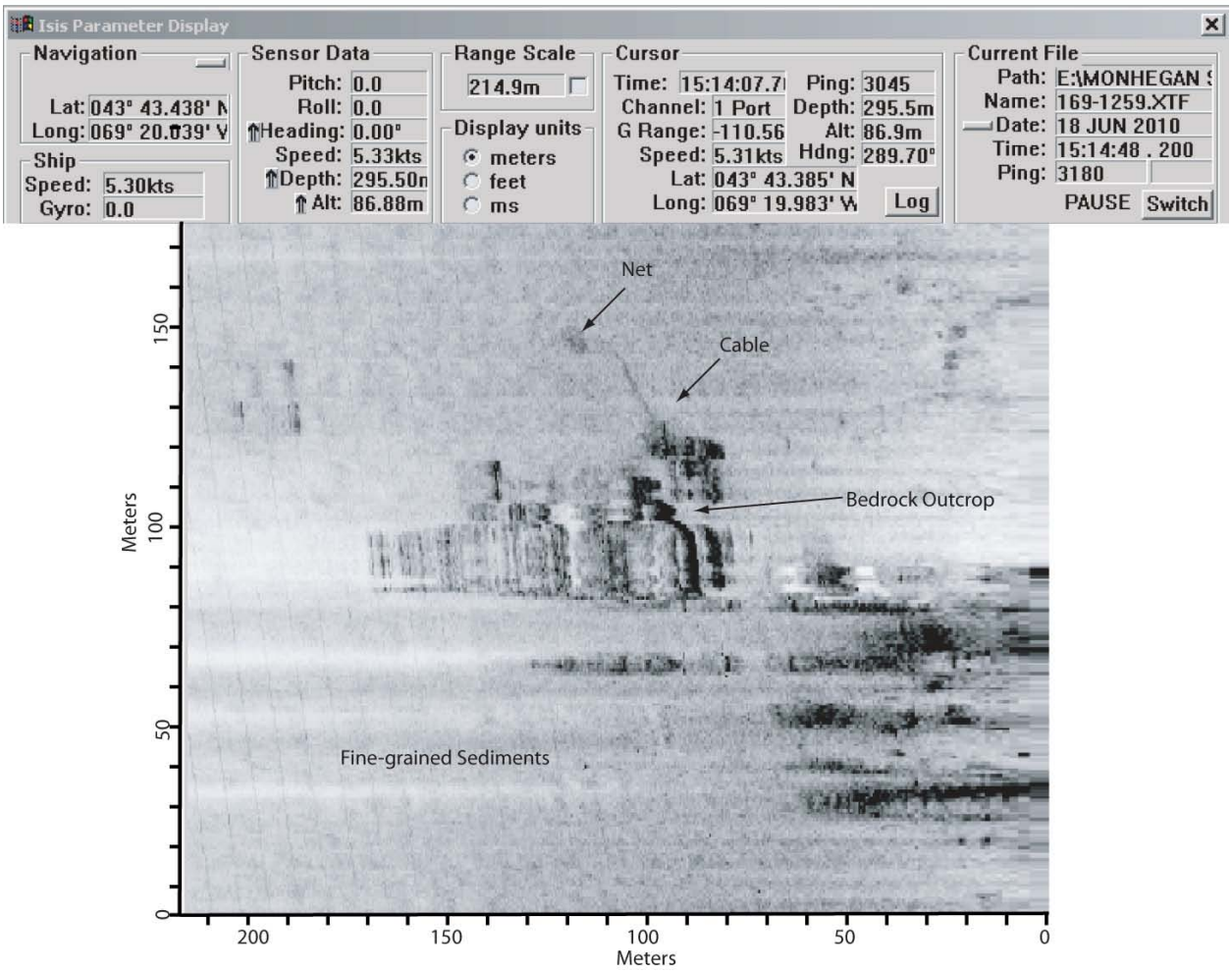

Figure 10: Detail of a sidescan sonar image showing a bedrock outcrop surrounded by fine-grained sediment, a cable and a net.

Visualization Study for a 1/3 Scale Floating Wind Turbine Platform for the DeepCwind Consortium

Benjamin Karlson
Wind & Water Power Technologies
Sandia National Laboratories

January 2011

Prepared by
Sandia National Laboratories
Albuquerque, New Mexico 87185 and Livermore, California 94550

Sandia is a multiprogram laboratory operated by Sandia Corporation,
a Lockheed Martin Company, for the United States Department of Energy's
National Nuclear Security Administration under Contract DE-AC04-94AL85000.

CONTENTS

FIGURES

TABLES

1. INTRODUCTION

Sandia National Laboratories was asked to perform a wind visualization study for the proposed 1/3 scale floating wind turbine platform development off of Monhegan Island in Maine as part of the DeepCwind Consortium work funded by the Department of Energy. It is anticipated that additional visualization studies will be needed to support the next phases of the DeepCwind Consortium plan, including the 25 MW deepwater offshore wind farm that is currently the topic of a Request for Proposal released on September 1, 2010 by the Maine Public Utilities Commission.

This visualization study for a 1/3 scale floating wind turbine platform is a compilation of photo simulations of a 100 kW Northwind Turbine located in the center of the test site location at various locations on Monhegan Island and Pemaquid Point, Maine. The specifications for this particular turbine are given in Table 1. For purposes of this study the 30 m hub height was selected.

Table 1 – Northwind 100 Turbine Specifications[1]

GENERAL CONFIGURATION	DESCRIPTION
Model	Northwind 100
Design Life	20 years
Hub Height	37 m (121 ft) / 30 m (98 ft)
Tower Type	Tubular steel monopole
Orientation	Upwind
Rotor Diameter	21 m (69 ft)

The University of Maine Deepwater Offshore Wind Test Site is located in state waters approximately 2.5 miles south of Monhegan Island, Maine. Water depths in the area are variable, ranging up to 140 m. The site is approximately 1.1 miles wide and 2.1 miles long, and is bounded at the southern edge by the 3 nm line indicating the extent of Maine state waters. The boundary coordinates are shown below in Figure 1. The coordinates giving the location for the Northwind 100 turbine are 43°42'46.86"N by 69°18'58.17"W. This essentially simulates the turbine at the center of the test site. Further investigation will be warranted to determine the exact location of the turbine placement. However, given the nature of the proposal, the location of the turbine placement will not be determined by terrain affects but more likely by bathymetry. Thus, selecting the center of the test site as the location for turbine simulation is a reasonable place to assess the visual impacts.

This study will attempt to quantify the visual impacts of a medium size, offshore wind turbine as seen from Monhegan Island, the closest island to the test site location, and Pemaquid Point, the nearest mainland point. It should be noted that any visualization is accompanied with an element of subjective interpretation.

[1] http://www.northernpower.com/pdf/specsheet-northwind100-us.pdf

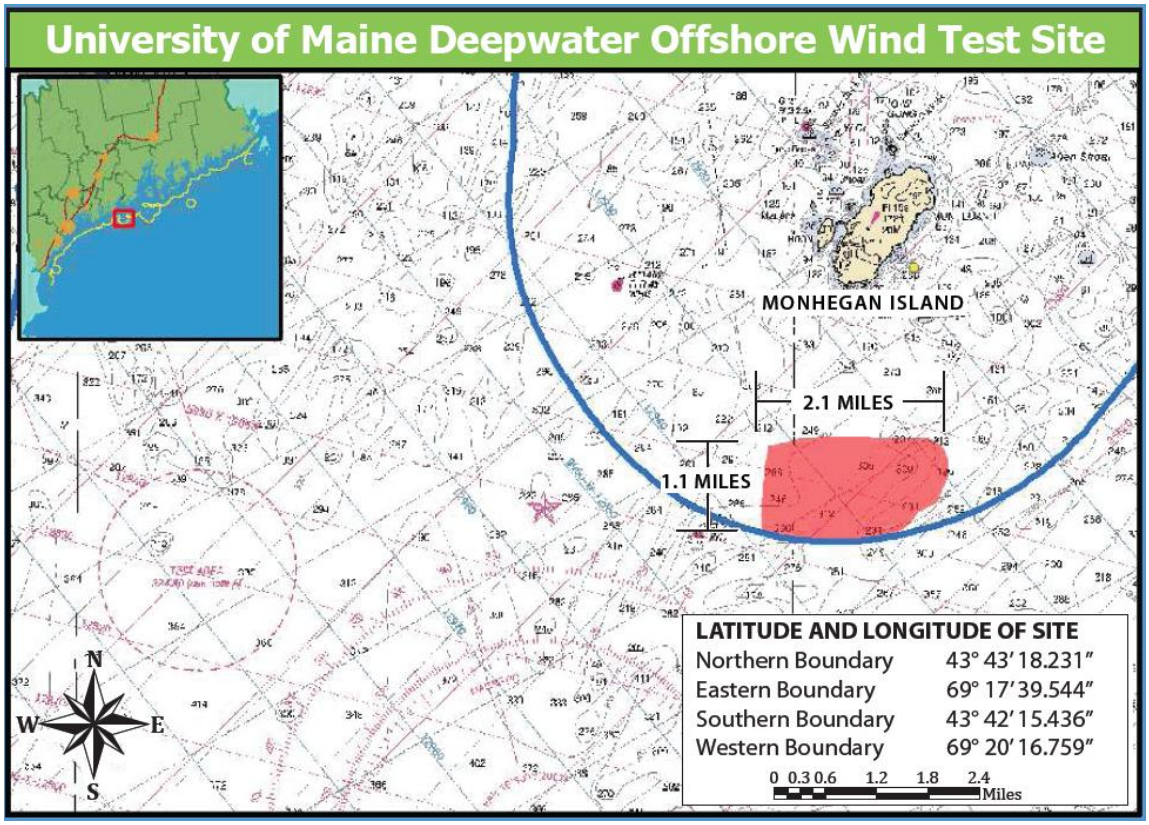

Figure 1 – University of Maine Deepwater Offshore Wind Test Site

2. DISCUSSION OF PHOTOS

The photographs taken from the various locations on Monhegan Island were taken with a Canon Power Shot SD750 digital camera. The location of each viewpoint is listed in Table 2 with the latitude and longitude, distance to the turbine, and elevation above sea level. Figure 2 is a map of Monhegan Island with the locations marked.

Table 2 – Locations of photos from Monhegan Island

VIEWPOINT	LATITUDE	LONGITUDE	DISTANCE TO TURBINE (Mi)	ELEVATION (FT)	DESCRIPTION
1	43°45'27.72"N	69°19'22.62"W	3.10	48	Lobster Cove
2	43°45'21.06"N	69°19'17.70"W	2.96	34	Shipwreck
3	43°45'22.08"N	69°19'11.22"W	2.97	53	Christmas Cove
4	43°45'25.14"N	69°18'50.94"W	3.03	76	Gull Rock
5	43°45'33.30"N	69°18'49.02"W	3.19	13	Burnt Head
6	43°45'40.98"N	69°18'37.98"W	3.34	37	Gull Cove
7	43°45'46.62"N	69°18'28.32"W	3.47	159	White Head
8	43°45'54.00"N	69°18'21.66"W	3.62	68	Little White Head
9	43°46'1.74"N	69°18'16.86"W	3.78	15	Squeaker Cove
10	43°46'8.28"N	69°18'5.70"W	3.92	156	Black Head

Figure 2 – Monhegan Island with Photo Locations

All photos taken on Monhegan Island were taken in the direction of true south. Two sets of photos were taken; the first set used a normal photo setting on the camera and the second set utilized a three times zoom.

The photographs taken from the locations on Pemaquid Point, Maine were taken with a Canon Power Shot A1000IS digital camera. The location of each viewpoint is listed in Table 3 with the latitude and longitude, distance to the turbine, and elevation above sea level. Figure 3 is a map of Pemaquid Point with the location of where the photographs were taken marked. All photographs taken at Pemaquid Point were shot using the landscape setting on normal zoom.

Table 3 – Locations of photos taken from Pemaquid Point

VIEWPOINT	LATITUDE	LONGITUDE	DISTANCE TO TURBINE (Mi)	ELEVATION (FT)
1	43°50'12.60"N	69°30'21.47"W	12.76	93
2	43°50'12.66"N	69°30'21.96"W	12.77	91

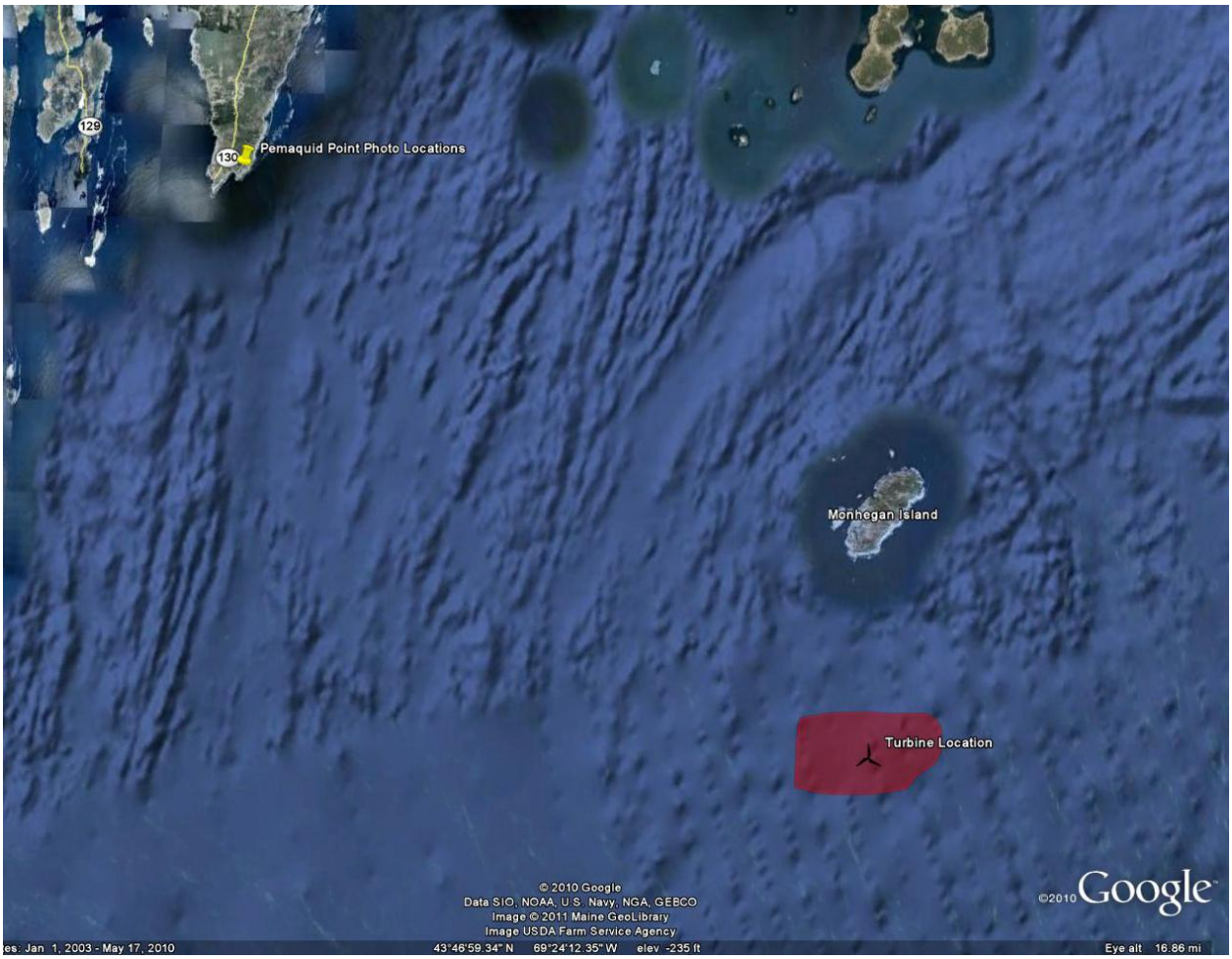

Figure 3 – Location of Pemaquid Point with relation to turbine location

3. MODELING OF THE TURBINE

Photo visualizations were completed using Google Earth Pro and Google SketchUp. In order to accurately simulate the visual impacts of the turbine, a representative model was needed. A valid Northwind 100 wind turbine model was available in the Google SketchUp Library[2]. Figure 4 shows two viewpoints of the Northwind 100 turbine model from Google SketchUp. Google Earth Pro then allows the user to enter the necessary information about the photos and models to be displayed in the 3D viewer and thus, creates the photo simulations to scale.

[2] Google SketchUp model can be found at:
http://sketchup.google.com/3dwarehouse/details?mid=225922eded527e58b74a9ec7ca778b5a&prevstart=0

Figure 4 – Google SketchUp Model of the Northwind 100 Wind Turbine

4. DISCUSSION OF SIMULATION RESULTS

The twenty seven (27) photo simulations were created to show visual approximations of how the turbine will appear from the various locations on Monhegan Island and Pemaquid Point. As shown in Table 2 the distance from the location of the photos on Monhegan Island to the turbine ranges from about 3 miles to 4 miles. The distance from the location of the photos from Pemaquid Point to the turbine is about 12.77 miles.

When discussing the visual impacts of a wind turbine offshore and 3 miles to the closest island and over 12 miles to the mainland, it is important to understand the factors that can impair natural visibility, i.e. the impacts that atmospheric conditions, meteorology, and the curvature of the earth can have on natural visibility. Visibility impairment is caused by light scattering and light absorption from particles in the atmosphere. The range of natural visibility will vary with the season, daily meteorology, and time of day. The pictures used for this study were taken on clear days with relatively low humidity.

With regard to the curvature of the earth, a quick investigation into visibility distances at sea reveals that the geographical range of visibility is dependent on the height of the viewer, the height of the object to be viewed, and atmospheric conditions. Geographical range of visibility in nautical miles for a lighthouse is calculated as 1.144 times the root of the height of the lighthouse[3]. A 50 foot lighthouse has an 8.1 nm geographical range. According to the Navigation Safety Plan[4] the height of the lighting on the turbine is 20 feet, which gives a 5.1 nm range of geographical visibility. The photos taken at Pemaquid Point were from an elevation of approximately 90 feet, giving a range of 10.8 nm. Summing the two ranges of visibility equates to a total range of 15.9 nm. Given that the distance from Pemaquid Point to the turbine location is about 11.10 nm, the tower lighting should just barely be visible above the horizon.

4.1 Monhegan Island Photos

The Northwind 100 wind turbine is visible in all photos taken from Monhegan Island. Again, the actual visibility is dependent on a number of local factors that may limit range of visibility from the island. The photos taken at dusk when the turbine tower light will be illuminated shows that the light will be visible from the island.

4.2 Pemaquid Point Photos

From Pemaquid Point, the turbine becomes difficult to discern on the horizon. It's not until the photo is magnified that the turbine can be seen and even then it is difficult to distinguish it from the background.

[3] Rousmaniere, J., Smith, M., *The Annapolis Book of Seamanship*
[4] Cpt. Chase, A.G., "Navigation Safety Plan For the UMaine Deepwater Offshore Wind Test Site," Maine Maritime Academy

Visual Observations for Birds, Turtles, and Marine Mammals at the University of Maine Test Site off Monhegan Island

a report prepared for and
submitted to the Maine State Planning Office
and the DeepCwind Consortium
January, 2012
by

LAURA KENNEDY, MS
Lubird Kennedy Environmental Services
Bar Harbor, Maine
lubirdkennedy@yahoo.com
918-549-5625

and

Dr. Rebecca L. Holberton
Laboratory of Avian Biology-University of Maine
rebecca.holberton@maine.edu

TABLE OF CONTENTS

Tables:

Maps:

Figures:

Appendices:

Public Use Statement

This report contains data collected through federal funds provided by the Maine State Planning Office through a cooperative agreement with the University of Maine (Ct-07B-20111024*2017). While the information provided in this report is meant for public access, permission is required to reproduce figures, tables, and any other product contained within this report without the express permission of the Maine State Planning Office or the Laboratory of Avian Biology at the University of Maine.

Suggested citation for this report: Kennedy, L. & Holberton, R.L. 2012. "Visual Observations for Birds, Turtles, and Marine Mammals at the University of Maine Test Site off Monhegan Island, a report submitted to the Maine State Planning Office and University of Maine. "

[0]

INTRODUCTION

More than 300 bird species representing all major avian taxa have been documented in the Gulf of Maine region. In addition to those species that breed or spend the winter there, millions of songbirds, shorebirds, wading birds, waterfowl, and raptors (birds of prey) that breed throughout the Arctic, sub-Arctic, and boreal regions use the Gulf of Maine as a major corridor in spring and fall to reach their destinations. Resource agencies such as the Maine Department of Inland Fisheries and Wildlife and the United States Fish and Wildlife Service consider monitoring bird activity with respect to offshore wind development a high priority. However, originally, visual observations for bird use of the test site, and interactions with the test turbine and anchoring system proposed by the University of Maine-DeepCwind Consortium for use at the University's Monhegan Offshore Wind Test Site were not components of the earlier DeepCwind Draft Fish and Wildlife Monitoring Plan, but have been added to it in response to agency comments. In particular, specific information about species identities, flight heights, and behaviors is needed in order to better understand the birds' relationship to the site (e.g., feeding, resting, passing through the area) and to assess potential risk as a result of human activities associated with the siting, construction, operation, and removal of turbine structures.

The main objectives of the activities covered in this report include 1) to assess the abundance of birds and species composition that may occur in the vicinity of the DeepCwind's test and control site for the proposed initial test turbine project, and 2) to record the behaviors (feeding versus flying, direction of movements) of birds observed at the two sites in order to assess potential risk of collision with above surface and subsurface structures such as blades and spar (e.g. 'rotor swept zone') and platform anchoring lines.

This report includes observations made only during the pre-deployment period that corresponded with the proposed calendar period of installation and operation. Additional observations will be needed once the project, including installation and operation, begins, and if any substantial changes are made to the proposed structures. At-sea survey protocols vary across different studies and are dependent on the study objectives. The proposed project, as initially described, is small in scale and temporary, but it is planned to occur during a period (breeding and migration) of high species abundance and diversity in the Gulf of Maine. The survey design developed for this project and interpretation of the results are limited to the temporary and short-term activities described in the initial DeepCwind's proposal for a single 1.5 kW test turbine at the University of Maine's

Monhegan Offshore Wind Test Site to be deployed sometime during the period from late July through early November.

METHODS

Visual boat-based observations were conducted at the University of Maine's Monhegan Offshore Wind Test Site, located within 3 miles of Monhegan Island, a small rocky island located about 12 miles (19.3 km) out of Port Clyde, Maine (Map 1), to assess species composition and occurrence during the pre-deployment phase of the project. Ferry service and private charter out of Port Clyde provide access to Monhegan Island. At-sea surveys occurred within an area located three miles south of the island, consisting of a two-square mile section (5.18 km^2, centered at approximately N 43.719° W 69.333°) further divided into two separate survey quadrats, one each for the "Test" and "Control" sites, designated as such by the DeepCwind Environmental Task group for all related monitoring activities (Map 1 Inset). To prevent confusion, the distinction of "Monhegan Test Site" refers to the full two-square mile area, and the smaller individual quadrats that lie within this larger area will be hereafter called the "Test" and "Control" sites, or quadrats. Map 2 shows the Monhegan Test Site area and the generalized tracks used for conducting these surveys.

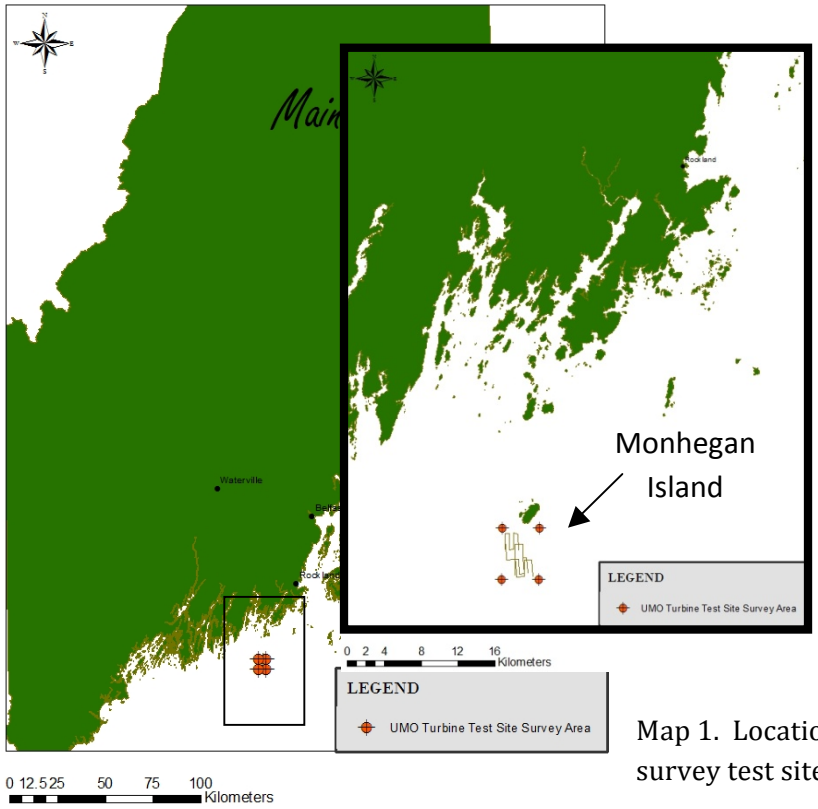

Map 1. Location of Monhegan Island and survey test site (inset map).

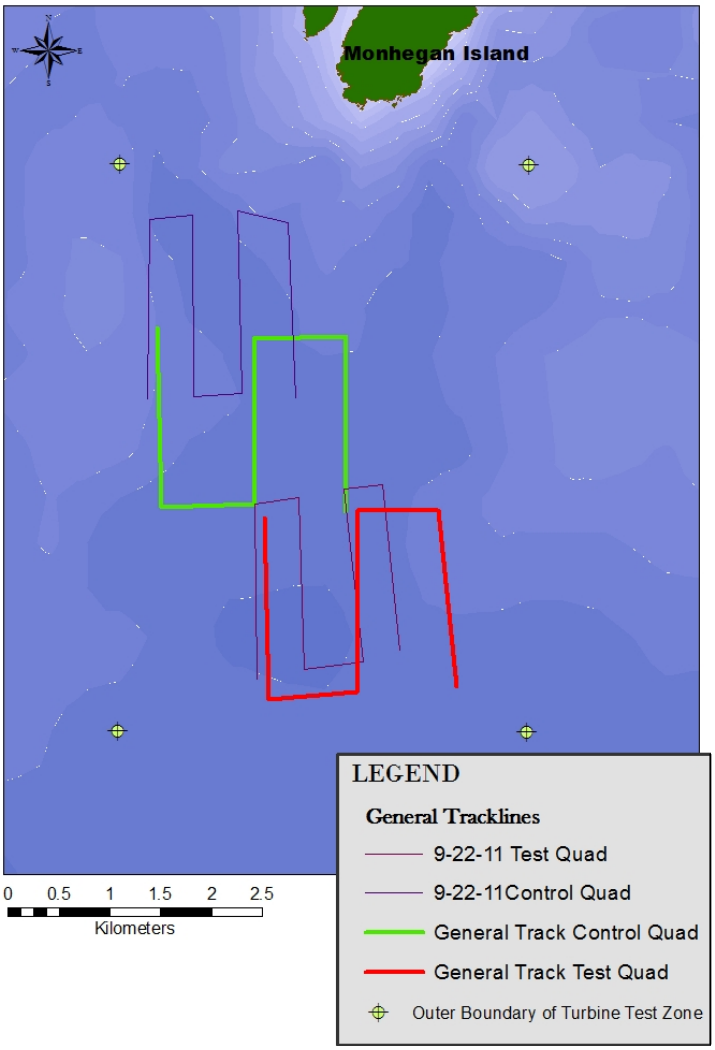

Map 2. Location of University of Maine Test Site off Monhegan Island with "Test" (red, south-eastern grid) and "Control" (green, north-western grid) quadrats showing transect pathways.

Each quadrat measured roughly one nautical mile by one nautical mile (~1850 m X 1850 m square) and transects were performed with the vessel running at an average speed of 7 knots (12.96 k/h) for 2,000 m beginning in a N-S direction and documenting all birds, mammals, and other wildlife observed on both sides of the boat and out to a distance of 500 m. At the end of this run, surveying would stop and the boat would turn 90˚ along an E-W line and motor to the next waypoint located 1,000 m away. After arriving at this next position and turning again 90˚, surveying would resume for the next 2,000 m as mentioned previously, heading in the N-S direction. This pattern was repeated a third time, totaling a survey area of five square kilometers. Immediately following the Test quadrat, the boat was repositioned in the Control area, located adjacent to and slightly to the north and west of the Test site, and the procedure was repeated.

Surveys were conducted aboard the F/V *Priscilla Earl*, a 38-ft Osmond Beal monohull boat used for lobster fishing and captained by Christina Cash. Observations were conducted from either the bow or stern, depending on sea conditions and safety concerns for that particular day, using binoculars and unaided vision. Height from which observations were made averaged 1.5 m above sea level. All data were recorded into an RCA digital voice recorder, synchronized with time on a Garmin GPS unit that simultaneously logged the boat's tracks and waypoints at the beginning and end of each transect line. Codes used to document species behaviors and other observation and weather conditions followed Gould & Forsell (1989) and Tasker et al. (1984). Examples of common bird behaviors include but are not limited to sitting on the water, flying in direct and consistent headings, flying with changing directions, and feeding at the water's surface. See Appendix 1 for a complete list of behaviors. Brief descriptions are provided below. Other information included flight height, recorded in single meters when under five meters high or otherwise compartmentalized into five meter bins (10, 15, 20, 25, etc.) up to 50 m. Observations were documented as "> 50 m" for all those above 50 m. The number of birds, species, gender and age (if known), and flight direction (see details below) were recorded. The data were transcribed into Excel and mapped with ArcMap software.

Maps and tables summarize species and behaviors observed during the six pelagic surveys at the Monhegan Test Site during the 2011 survey period are provided. The tables below explain bird and other marine animal behavior (numerical) codes used in the tables summarizing each survey. Some of the most common behaviors documented have lengthy definitions; therefore a shortened descriptive behavior term is used in the following sections (Table 1). These include the following: code #20, described as "flying in a direct and consistent heading" but hereafter shortened to "direct flight"; #35, described as "flying, milling or circling" which typically involves flight associated with foraging behavior and is erratic in height and location, hereafter called "milling"; #48, described as "flying, meandering" which involves indirect flight that changes direction but not necessarily height, hereafter called "meandering"; #61, described as "feeding at or near the surface while flying (dipping or pattering)" which typically describes scavenging or the act of picking food from the water's surface, hereafter called "dipping"; #66, described as "feeding at or near surface, not diving or flying (surface seizing)" which differs from dipping in that the bird is sitting in the water while foraging, hereafter called "surface seizing"; and #71, described as "feeding below surface (plunge diving)" which involves the bird plunging into the water from a defined height, as if to glean food under the water's surface, hereafter called "plunge diving." (In most cases, the bird that was recorded as plunge diving was previously flying either direct flight or milling, but after one plunge into the water, it was recorded once and repeated plunges were not typically observed due to the need to scan the horizon for other activities by birds and other wildlife as the transect continued.)

Table 1. Codes used to document behaviors observed during transects. (Gould & Forsell 1989)

Bird Behavior
01 = Sitting on water
20 = Flying in direct and consistent heading
31 = Flying, circling ship
32 = Flying, following ship
35 = Flying, milling or circling (foraging)
48 = Flying, meandering
61 = Feeding at or near surface while flying (dipping or pattering)
66 = Feeding at or near surface, not diving or flying (surface seizing)
71 = Feeding below surface (plunge diving)

Mammal & Fish Behavior
00 = Undetermined
01 = Leaping
02 = Feeding
08 = Sleeping

At the top of each survey days' section (below), a list of the species and numbers observed for that day, separated into Test and Control Quadrats, is presented. Four-letter species "alpha" codes are also used in the following tables to simplify table content (see Appendix 2 for species codes and common and scientific names). Flight directions, given in cardinal direction such as NE, SW, WNW, represent the direction in which the bird was flying at the time of observation.

RESULTS

Approval for the project was not given until mid-September, 2011. Funding did not become available until early December, 2011. Surveys were conducted six days throughout the months of September, October, and November. Three surveys (50%) occurred in the morning hours and the remaining three occurred in the afternoon. Throughout October, numerous and often successive days of severe weather conditions, combined with scheduling conflicts, hampered efforts to perform more than one survey during that month. Table 2 provides the breakdown of surveys by date, time of day, and weather conditions.

Table 2. Surveys by time of day and corresponding weather conditions.

	TIME OF DAY		SURVEY CONDITIONS			
MONTH	AM	PM	sea ht (ft)	wind dir	wind (kt)	sky
Sept						
22		X	1.8	S	2 to 5	rain
27		X	1.8	NE	3 to 8	clear
28	X		2.5	E	11 to 12	clear
Oct						
11	X		1.7	NE	11 to 12	partly cloudy
Nov						
9	X		2.6	S	10 to 11	clear
16		X	4	S	7 to 8	partly cloudy

The initial, trial, survey on September 22, used a slightly different survey pattern but covered almost the same region within the Test quadrat and a quarter of the Control quadrat used in the remaining five surveys. Survey protocol on this day varied in the following ways: surveys on September 22 were conducted only off one side of the vessel and out to 300 m, instead of both sides and out to 500 m; four transect lines were utilized, but while also measuring 2,000 m long, the lines were only 500 m apart instead of three lines that measured 1,000 m apart. The total survey area covered for each quadrat on September 22 equaled 4.2 km^2 each with the vessel traveling an average distance of 6.95 km. The remaining surveys quadrats equaled 5 km^2 each, with an average of 8.3 km traveled *per* survey. Location of general track lines for the four versions of quadrats surveyed can be seen in Map 2. All surveys were assessed equally while using the corresponding total survey area for the analysis of the species composition, location, and behaviors observed in the Test and Control quadrats within the Monhegan Test Site.

Within the 2 mi^2 (5.2 km^2) Offshore Wind Test Site, the Test and Control survey quadrats each covered an average of 4.8 km^2 and the vessel traveled an average direct linear distance of 6.9 km while conducting the transects, except for the first surveys on September 22, when, as noted, the vessel traveled an average of 8.75 km and covered 3.5 km^2. Half of the surveys were conducted in the morning and half in the afternoon in order to gain a more comprehensive temporal picture of wildlife activity within the Monhegan Test Site. In addition to the sixteen bird species identified, the presence of tuna, Harbor seals, and Harbor porpoise was also noted during these surveys (Appendix 2).

SEPTEMBER 22, 2011 AFTERNOON SURVEY (12:54 PM)

Table 3. Numbers of species observed during the afternoon survey on September 22, 2011.

Num/spp	Quadrat		
Species	**Test**	**Control**	**Total**
Great black-backed gull	2	6	8
Herring gull	15	11	26
Unidentified "large" gull	1	0	1
Great shearwater	2	11	13
Sooty shearwater	1	1	2
Northern fulmar	0	1	1
Northern gannet	3	10	13
Pomarine jaeger	0	1	1
Harbor seal	0	2	2
Total	**24**	**43**	**67**

Test Quadrat

On September 22, the Test survey grid covered an area of 3.5 km^2 for a total linear distance of 8.6 km. Seas averaged 1.8 ft (0.55 m), with winds from the south at two - five knots and light intermittent rain. Map 3 shows the survey track area of this day's transects and all species observed along it. The Test Quadrat is in the lower right location and the Control Quadrat is in the upper left. Five identified species were included Great black-backed (*Larus marinus,* coded as GBBH) and Herring gulls (*L. argentatus,* HERG), Great (*Puffinus gravis*, GRSH) and Sooty (*P. griseus*, SOSH) shearwaters, and Northern gannets (*Morus bassanus*, NOGA) (Table 3). Their behaviors included sitting on water (two Herring gulls), direct flight (18 birds of multiple species types), one Northern gannet milling at a height of three meters, one Herring gull meandering at 25 m, one Northern gannet plunge diving from an initial height of two meters, and a Great black-backed gull from an initial height of one meter landing on the water to surface seize food (Table 4). The heights of the 18 total birds in direct flight varied, with both Great and Sooty shearwaters flying one meter above the surface, one gannet at 35 m, and 12 gulls flew at heights from five to 50 m. The most common heights flown by gulls were 15 m and 30 m.

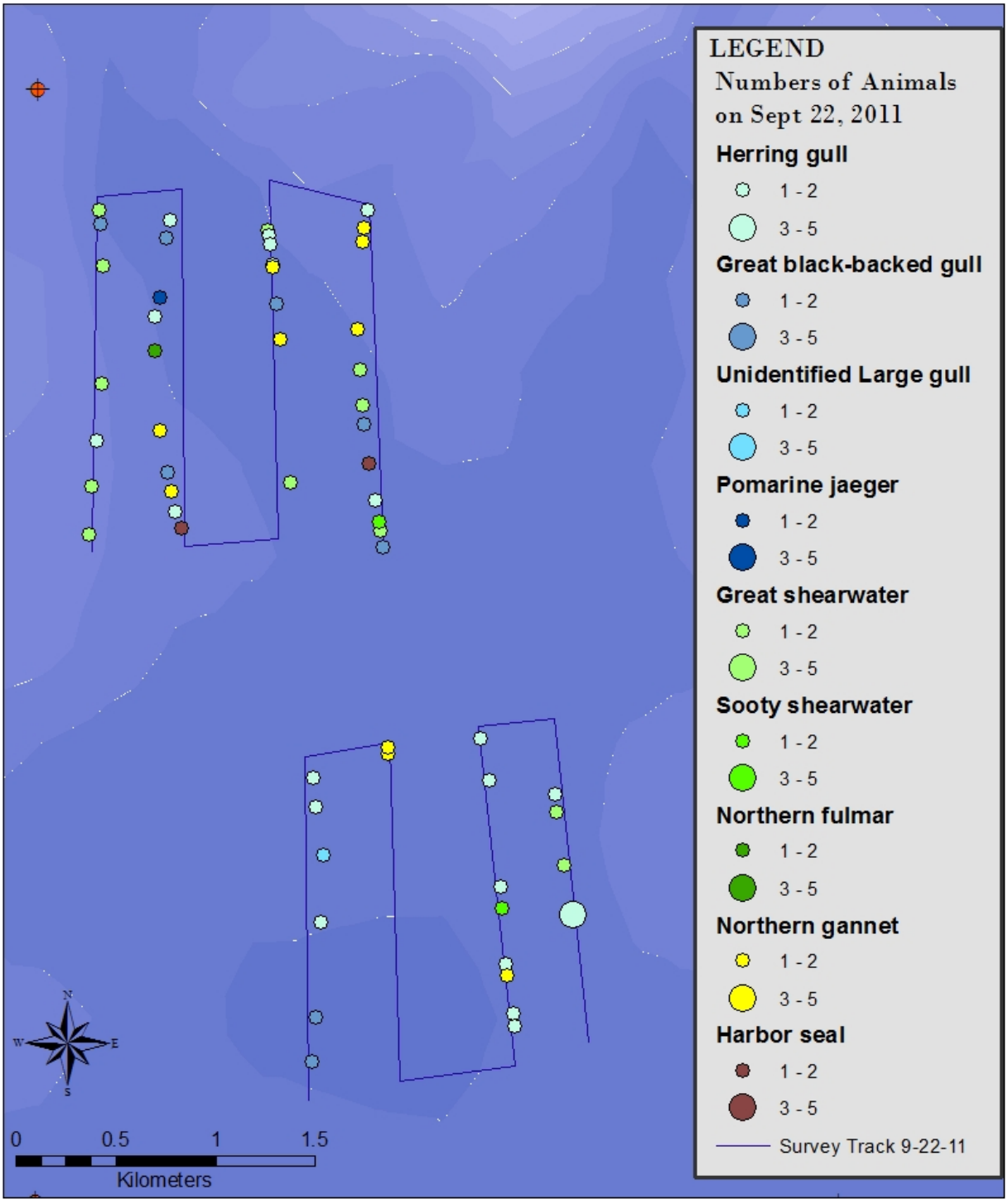

Map 3. Survey track, species, and numbers observed in both survey quadrats on September 22.

Table 4. Numbers of observations for each behavior (codes from left to right across table), flight height categories (meters) above sea surface, and flight direction (N = North, etc., where relevant) for each species (total # observations/species) in the Test Quadrat on September 22, 2011.

Behavior code:	**01**	**20**								**35**	**48**	**66**	**71**	**#/Spp Total**
Meters	**0**	**1**	**5**	**15**	**20**	**30**	**35**	**40**	**50**	**3**	**25**	**1**	**2**	
GBBG						**1**						**1**		**2**
N												1		1
(none)						1								1
HERG	**2**		**1**	**5**	**1**	**3**		**1**	**1**		**1**			**15**
N						2			1					3
NNW								1			1			2
SSW				5										5
SW					1									1
(none)	2		1			1								4
UNLG						**1**								**1**
(none)						1								1
GRSH		**2**												**2**
NE		2												2
SOSH		**1**												**1**
S		1												1
NOGA							**1**			**1**			**1**	**3**
NNW							1							1
(none)										1			1	2
Total	**2**	**3**	**1**	**5**	**1**	**5**	**1**	**1**	**1**	**1**	**1**	**1**	**1**	**24**

Control Quadrat

On September 22, the "Control" survey grid also covered an area of 3.5 km^2 for a total linear distance of 8.9 km (Map 3). Eight different species were identified using the Control area, consisting of gulls, shearwaters, one Northern fulmar (*Fulmarus glacialis*, NOFU), gannets, one Pomarine jaeger (*Stercorarius pomarinus*, POJA), and two harbor seals (*Phoca vitulina*, Hseal) (Table 3). Behaviors for the gull species included three sitting on the water, and eight in direct flight with single observations noted at the 20, 35, 40, and >50 m heights, and two observations each at 30 m and 50 m (Table 5). Three gulls were milling at three meters, and one milling gull each recorded at 20, 30, and 40 m. From an initial height of one meter a Great black-backed gull landed on the water to surface seize food. At one meter high, seven Great shearwaters flew in a direct flight, three flew meandering, and one landed on the water to surface seize food. One Sooty shearwater also

flew meandering at one meter high. One Northern fulmar was observed sitting on the water, and two Harbor seals were observed with one appearing to sleep. Seven gannets were recorded sitting on the water, two flew direct while at 5m, and one flew direct while at 30 m.

Table 5. Numbers of observations for each behavior (codes from left to right across table), flight height categories (meters) above sea surface, and flight direction (N = North, etc., where relevant) for each species (total # of observations/species) in the Control Quadrat on September 22, 2011.

Behavior Code:	**0**	**1**	**8**	**20**								**35**				**48**	**66**	**#/Spp Total**
Meters	**0**	**0**	**0**	**1**	**5**	**20**	**30**	**35**	**40**	**50**	**70**	**3**	**20**	**30**	**40**	**1**	**1**	
GBBG		**3**					**1**		**1**									**6**
NE							1		1									2
(none)		3															1	4
HERG						**1**	**1**	**1**		**2**	**1**	**2**	**1**	**1**	**1**			**11**
E							1											1
ESE								1										1
NE										2								2
NNE											1				1			2
SSE						1												1
(none)												2	1	1				4
GRSH				**7**												**3**	**1**	**11**
ENE																2		2
N				1														1
NE																1		1
NNW				2														2
SW				1														1
WNW				2														2
WSW				1														1
(none)																	1	1
SOSH																**1**		**1**
NE																1		1
NOFU		**1**																**1**
(none)		1																1
NOGA		**7**			**2**		**1**											**10**
SW					2		1											3
(none)		7																7
POJA						**1**												**1**
S						1												1
Hseal	**1**		**1**															**2**
(none)	1		1															2
Total	**1**	**11**	**1**	**7**	**2**	**2**	**3**	**1**	**1**	**2**	**1**	**2**	**1**	**1**	**1**	**4**	**2**	**43**

SEPTEMBER 27, 2011 AFTERNOON SURVEY (2:04 PM)

Table 6. Numbers of species observed during the afternoon survey on September 27, 2011.

Num/spp	Quadrat		
	Test	Control	Spp Total
Unidentified Duck species	0	1	1
Double-crested cormorant	0	1500	1500
Unidentified cormorant	0	22	22
Great black-backed gull	12	1	13
Herring gull	21	3	24
Great shearwater	4	4	8
Sooty shearwater	1	0	1
Northern gannet	18	17	35
Harbor seal	1	1	2
Tuna	2	4	6
Grand Total	**59**	**1553**	**1612**

Test Quadrat

On September 27, the seas were 1.8 ft (0.55 m) with winds NE three to eight knots and clear skies. The total area surveyed was 5 km^2 and the boat traveled a total linear distance of 7.2 km. Map 4 shows the survey tracks of this day's surveys, which span the most ideal locations for the Test and Control Quadrats, and vary slightly from the surveys on September 22. As stated earlier, the remaining surveys follow the quadrat locations established on this survey day, September 27. Five bird species, one Harbor seal, and two feeding tuna (family Scombridae) were observed at the survey site (Table 6). Ten Great black-backed gulls and 17 Herring gulls were sitting on the water, as were three Great shearwaters and six Northern gannets. Direct flight was observed in two gulls and two shearwaters: one gull at three meters and one at five meters, with both shearwaters flying one meter high. Three herring gulls circled at variable heights above a working lobster boat within the survey area. One gull with milling behavior flew five meters high and one gannet milled at 10 m and two more gannets milled at 30 m. Eight gannets were observed plunge diving within this survey quadrat, with initial dive heights ranging from three to 25 m (Table 7). Three of these observations occurred in the same vicinity as the feeding and leaping tuna.

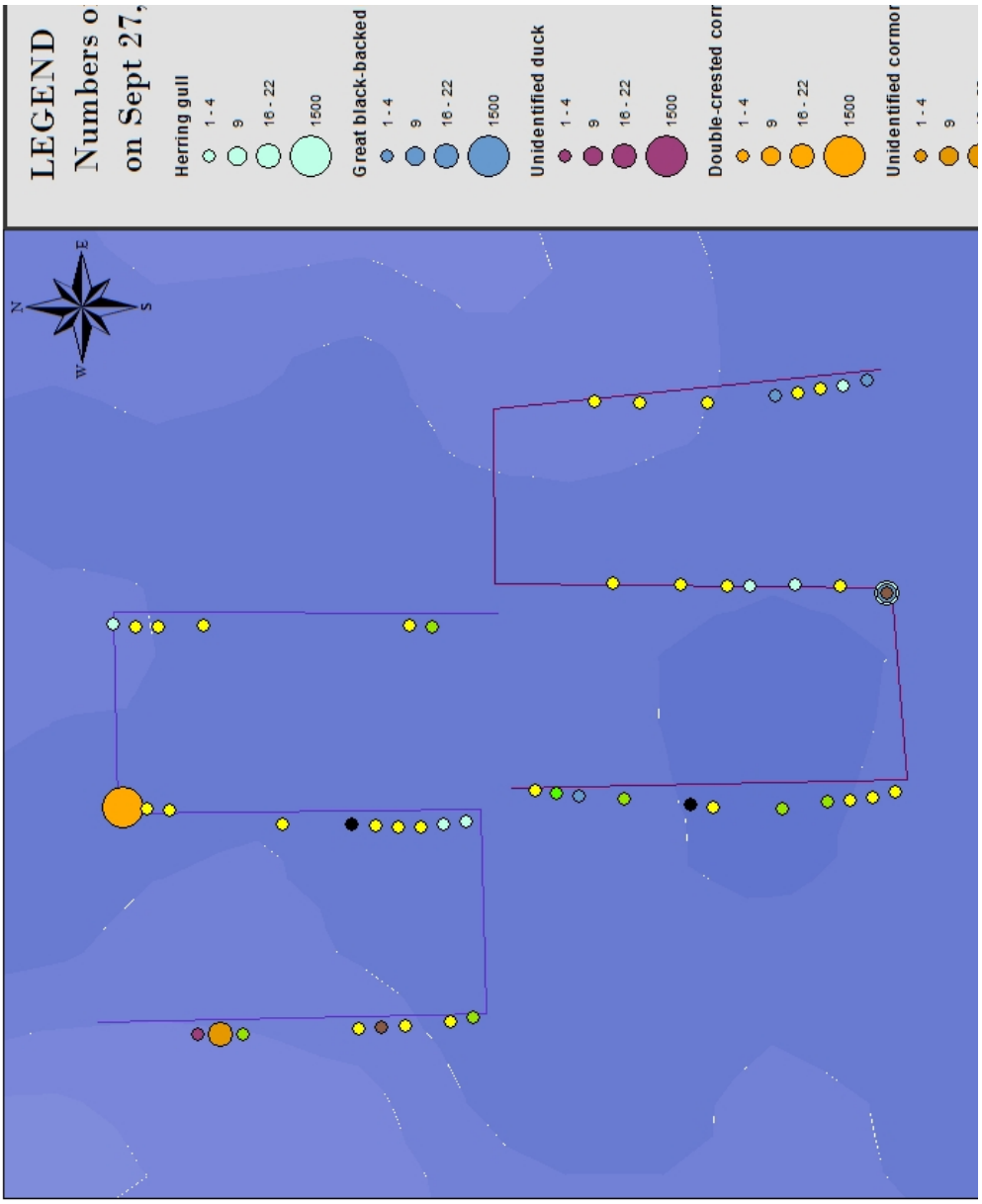
LEGEND
Herring gull
1 - 4
9
16 - 22
1500
Great black-backed
1 - 4
9
16 - 22
1500
Unidentified duck
1 - 4
9
16 - 22
1500
Double-crested corm
1 - 4
9
16 - 22
1500
Unidentified cormor
1 - 4
9
N
E
S
W

Table 7. Numbers of observations for each behavior (codes from left to right across table), flight height categories (meters) above sea surface, and flight direction (N = North, etc., where relevant) for each species (total # of observations/species) in the Test Quadrat on Sept. 27, 2011.

Behavior Code:	0	1	2	20			31	35			71					#/Spp Total
Meters	0	0	0	1	2	5	10	5	10	30	3	5	10	15	25	
GBBG		10				1		1								12
WSW						1										1
(none)		10						1								11
HERG		17			1		3									21
NNW					1											1
(none)		17					3									20
GRSH		3		1												4
(none)		3		1												4
SOSH				1												1
SW				1												1
NOGA		6							1	2	1	2	3	2	1	18
E												1				1
(none)		6							1	2	1	1	3	2	1	17
Hseal	1															1
(none)	1															1
TUNA			2													2
(none)			2													2
Total	1	36	2	2	1	1	3	1	1	2	1	2	3	2	1	59

Control Quadrat

The Control quadrat on September 27 covered 5 km^2 and the boat traveled a total linear distance of 7.04 km. Six bird species, four feeding tuna, and one Harbor seal were observed (Map 4 and Table 6). Three Great shearwaters and eight gannets were sitting in the water. Four gulls were flying direct, with two recorded at 20 m and two at 35 m above the surface. One Great shearwater flew direct at one meter high, while two gannets with direct flight flew at five m and one gannet flew at 20 m above the surface. Six more gannets were observed milling, ranging from three to 15 m high. One unidentified duck species was observed flying straight west at a height above 50 m and two large flocks consisting of Double-crested cormorants (*Phalacrocorax auritus*, DCCO) and another unidentified group of cormorants with direct flight also flew over 50 m above the water's surface (Table 8).

Table 8. Numbers of observations for each behavior (codes from left to right across table), flight height categories (meters) above sea surface, and flight direction (N = North, etc., where relevant) for each species (total # of observations/species) in the Control Quadrat on Sept. 27, 2011..

Behavior Code:	**0**	**1**	**2**	**20**					**35**			**#/Spp Total**
Meters	**0**	**0**	**0**	**1**	**5**	**20**	**35**	**>50**	**3**	**5**	**15**	
UNDU								**1**				**1**
W								1				1
DCCO								**1500**				**1500**
SW								1500				1500
UNCO								**22**				**22**
W								22				22
GBBG							**1**					**1**
S							1					1
HERG						**2**	**1**					**3**
S						1						1
SSW							1					1
WNW						1						1
GRSH		**3**		**1**								**4**
NE				1								1
(none)		3										3
NOGA		**8**			**2**	**1**			**2**	**3**	**1**	**17**
N						1						1
SE					2							2
(none)		8							2	3	1	14
Hseal	**1**											**1**
(none)	1											1
TUNA			**4**									**4**
(none)			4									4
Total	**1**	**11**	**4**	**1**	**2**	**3**	**2**	**1523**	**2**	**3**	**1**	**1553**

Prior to the start of the test and control surveys, two general observations worthy of note were two large flocks of unidentified cormorants or geese flying 45 m to over 50 m above the water's surface, with direct flight. These flocks, ranging from 70 – 1,500 birds, flew due west and passed through the area between Monhegan Island and the Monhegan Test Site at distances of ¾ miles (1.2 km) and 1.5 miles (2.4 km) from the island.

SEPTEMBER 28, 2011 MORNING SURVEY (7:09AM)

Table 9. Numbers of species observed during the afternoon survey on September 27, 2011.

Num/spp	Quadrat		
	Test	Control	Spp Total
Red-necked phalarope	0	1	1
Common eider	19	0	19
Unidentified Duck species	0	2	2
Common loon	9	2	11
Double-crested cormorant	106	22	128
Unidentified cormorant	7	0	7
Great black-backed gull	11	4	15
Herring gull	25	14	39
Unidentified "large" gull	1	6	7
Great shearwater	6	17	23
Unidentified shearwater	1	0	1
Northern gannet	1	11	12
Grand Total	**186**	**79**	**265**

Test Quadrat

On September 28, the morning survey had seas with an average of 2.5 ft (0.76 m), and east winds at 11 - 12 kts. The vessel traveled a total linear distance of 6.8 km covering a total area of 4.7 km^2, and documented seven bird species (Map 5 and Table 9). Eight gulls and two Great shearwaters were recorded sitting on the water. Many larger flocks of birds were observed in direct flight heading due west: ten Common eider (*Somateria mollissima*, COEI) flew five meters high, five Common loons (*Gavia immer*, COLO) flew at 20 m, and another flock of four loons (unidentified spp.) flew at 35 m. Other large flocks with direct flight flew southwest: a flock of nine Common eider flew one meter high, a single Double-crested cormorant flew 10 m high and flocks of 25, seven, 30, and 50 cormorants flew from 15 m, 40 m, 50 m, and greater than 50 m high, respectively. Seventeen gulls with direct flight were recorded across a spread of heights from one meter to 35 m, with the most common height (three Herring gulls) averaging 25 m above the surface. Three Great black-backed gulls meandered at five meters, whereas six Herring gulls meandered at heights varying from one to 15 m. Two Herring gulls were observed feeding at the surface, but one was dipping (in flight) and the other was surface seizing while sitting in the water at the time. Two Great shearwaters in direct flight heading southwest flew one meter high and one other shearwater flew direct at three meters. One Great shearwater meandered at three meters high and one unidentified shearwater meandered at two meters high. Only one Northern gannet was observed in direct flight at 10 m high in this quadrat (Table 10).

Table 10. Numbers of observations for each behavior (codes from left to right across table), flight height categories (meters) above sea surface, and flight direction (N = North, etc., where relevant) for each species (total # of observations/species) in the Test Quadrat on Sept. 28, 2011.

Behavior Code:	**1**	**20**													**48**						**61**	**66**	**#/ Spp Total**
Meters	**0**	**1**	**3**	**5**	**7**	**10**	**15**	**20**	**25**	**30**	**35**	**40**	**50**	**>50**	**1**	**2**	**3**	**5**	**12**	**15**	**1**	**1**	
COEI		**9**		**10**																			**19**
SW		9																					9
W				10																			10
COLO								**5**			**4**												**9**
W								5			4												9
DCCO						**1**	**25**						**30**	**50**									**106**
SW						1	25						30	50									106
UNCO												**7**											**7**
SW												7											7
GBBG	**3**				**1**	**1**	**1**			**1**	**1**							**3**					**11**
S						1	1																2
SE										1													1
SW											1												1
(none)	3				1													3					7
HERG	**5**	**1**		**2**	**1**	**1**	**2**		**3**	**2**					**1**		**2**		**2**	**1**	**1**	**1**	**25**
N																	1						1
NNW										1													1
S		1				1	1		1														4
SSE				1																			1
SSW									2														2
W				1	1		1																3
(none)	5									1					1		1		2	1	1	1	13
UNLG												**1**											**1**
S												1											1
GRSH	**2**	**2**	**1**														**1**						**6**
SW		2																					2
(none)	2		1														1						4
UNSH																**1**							**1**
(none)																1							1
NOGA						**1**																	**1**
(none)						1																	1
Total	**10**	**12**	**1**	**12**	**2**	**4**	**28**	**5**	**3**	**3**	**5**	**8**	**30**	**50**	**1**	**1**	**3**	**3**	**2**	**1**	**1**	**1**	**186**

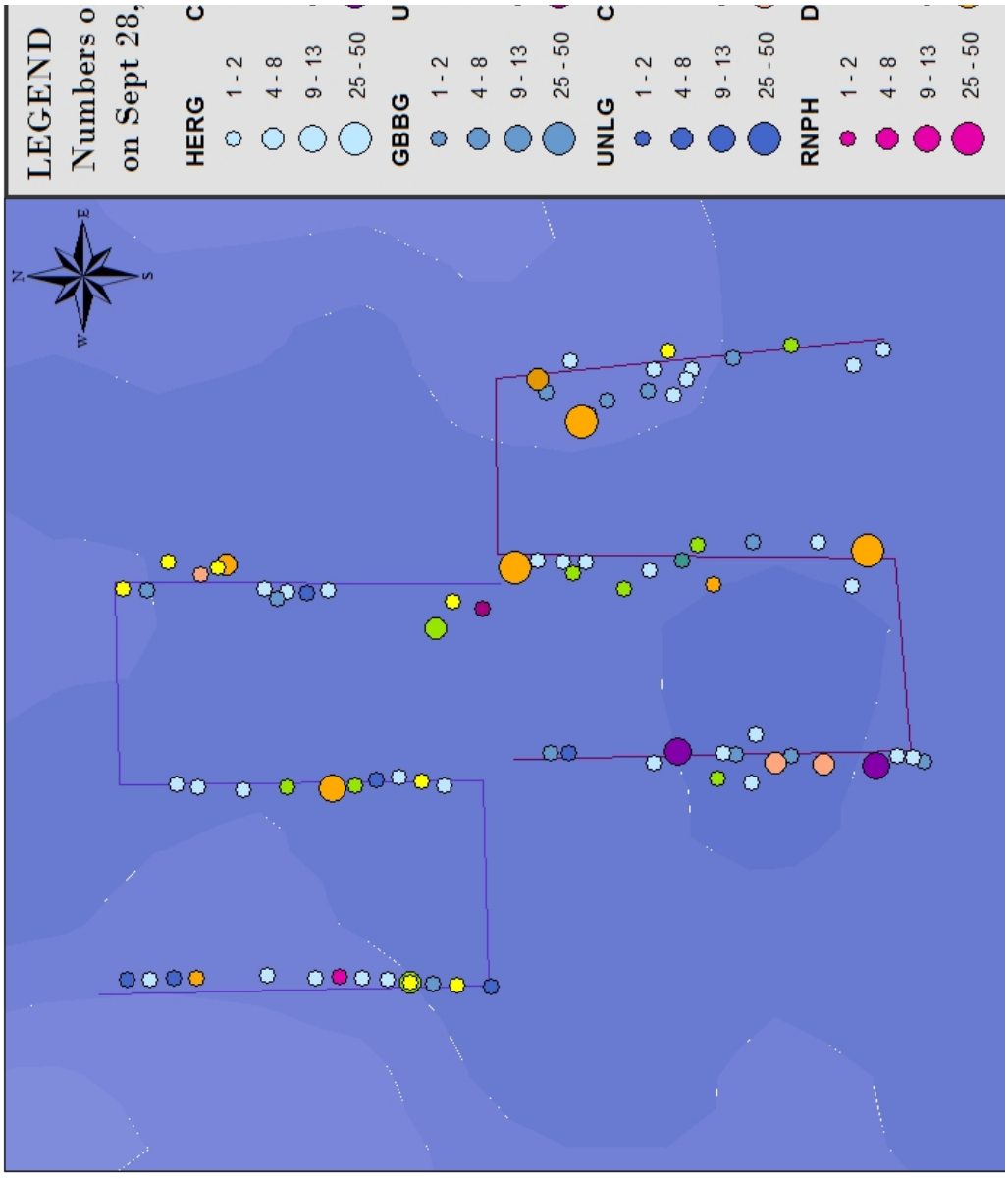
LEGEND
Numbers o
on Sept 28,
HERG
1 - 2
4 - 8
9 - 13
25 - 50
GBBG
1 - 2
4 - 8
9 - 13
25 - 50
UNLG
1 - 2
4 - 8
9 - 13
25 - 50
RNPH
1 - 2
4 - 8
9 - 13
25 - 50
N
E
S
W

Control Quadrat

The Control quadrat on September 28 covered 4.5 km^2 and the vessel traveled a total linear distance of 6.7 km (Map 5). Eight bird species were identified (Table 9), including one Red-necked phalarope (*Phalaropus lobatus*, RNPH) sitting in the water and one unidentified duck (UNDU) flying due west at two meters high. Two Common loons flew direct, heading SSW at a height of 30 m, and three separate observations of double-crested cormorants flew direct in flocks of seven, 13, and two at heights from five to 10 m, respectively. Gulls were observed in direct flight at heights from 5 to 30 m, with the most common height for both species being 15 m. One subadult and one juvenile Herring gull flew following our survey vessel at heights of five and eight meters, while two adult Herring gulls were milling at heights of five and 10 m, and one Great black-backed gull meandered at 20 m. Seven Great shearwaters sat on the water, one each flew due south at one meter and three meters high, while eight more flew SSW at three meters high. Two Northern gannets sat on the water, three flew direct at 20 m high, and one meandered at one meter above the water's surface. Four gannets milled about from heights of three, five, and 15 m, and one other gannet plunge dived from an initial height of three meters (Table 11).

Table 11. Numbers of observations for each behavior (codes from left to right across table), flight height categories (meters) above sea surface, and flight direction (N = North, etc., where relevant) for each species (total # of observations/species) in the Control Quadrat on Sept. 28, 2011..

Behavior Code:	**1**	**20**											**32**		**35**				**48**		**71**	**#/Spp Total**
Meters	**0**	**1**	**2**	**3**	**5**	**8**	**10**	**12**	**15**	**20**	**25**	**30**	**5**	**8**	**3**	**5**	**10**	**15**	**1**	**20**	**3**	
RNPH	**1**																					**1**
(none)	1																					1
UNDU			**2**																			**2**
W			2																			2
COLO												**2**										**2**
SSW												2										2
DCCO					**7**	**13**	**2**															**22**
NNE							2															2
S					7																	7
WNW						13																13
GBBG									**2**		**1**									**1**		**4**
NNW									1													1
SSW																				1		1
SW									1		1											2
HERG							**1**	**1**	**5**	**1**	**2**		**1**	**1**		**1**	**1**					**14**
N									1													1
NE									1													1
S							1	1														2
SW									1		2			1								4
W										1												1
WSW									2													2
(none)													1			1	1					3
UNLG		**1**			**1**					**2**		**2**										**6**
S					1							2										3
WSW										2												2
(none)		1																				1
GRSH	**7**	**1**		**9**																		**17**
S		1		1																		2
SSW				8																		8
(none)	7																					7
NOGA	**2**									**3**					**1**	**1**		**2**	**1**		**1**	**11**
N																		1	1			2
NW										1												1
WSW										2												2
(none)	2														1	1		1			1	6
Total	**10**	**2**	**2**	**9**	**8**	**13**	**3**	**1**	**7**	**6**	**3**	**4**	**1**	**1**	**1**	**2**	**1**	**2**	**1**	**1**	**1**	**79**

OCTOBER 11, 2011 MORNING SURVEY (9:57AM)

Table 12. Numbers of species observed during the morning survey on October 11, 2011.

Sum of num	Test	Control	Grand Total
Canada goose	1	0	1
Common eider	4	0	4
Unidentified Duck species	0	3	3
Common loon	1	2	3
Double-crested cormorant	16	4	20
Great black-backed gull	1	1	2
Herring gull	25	11	36
Unidentified "Large" gull	42	0	42
Unidentified shearwater	0	1	1
Northern gannet	2	13	15
Grand Total	**92**	**35**	**127**

Test Quadrat

On October 11, the seas were 1.7 ft (0.52 m) with NE winds 11 - 12 knots and partly cloudy skies. Seven bird species were identified in the Test Quadrat, which covered 4.5 $km^{2,}$ and the vessel traveled a total linear distance of 6.8 km (Map 6 and Table 12). One Canada goose (*Branta canadensis*, CANG) flew 10 m high with direct flight to the SE, a flock of four Common eider flew direct to the NE at five meters high, one Common loon flew due west at 15 m high, and a flock of 16 Double-crested cormorants flew 30 m high directly to the SSW. One working lobster boat within the survey area incited activity by various large gulls, with 30 sitting in the water next to the boat and 10 gulls circling the boat at heights averaging five meters. Nine more gulls flew in a direct SSW and SW path at 20 m high towards this lobster boat and the ongoing activity, and two Northern gannets flew directly SW at 15 m high also in the direction towards this boat. Seventeen gulls were documented in direct flight ranging from two to 20 m high, with the most common heights flown at two meters (seven birds flying SSW) and five meters (five birds). Two additional working lobster boats were observed in the survey area and one Herring gull milled 15 m high near the vessel and one gull landed on the water to surface seize a food item, having initially been flying at 5 m high (Table 13). An incidental observation by the survey vessel's Captain Chris Cash occurred on October 10 between the hours of 10:30 and 11:00 am while she was lobster fishing within the Test Quadrat. A small songbird with "a little yellow on it" landed on her boat to rest. The weather conditions that day were seven-knot winds from the west and seas were less than one foot (0.3 m).

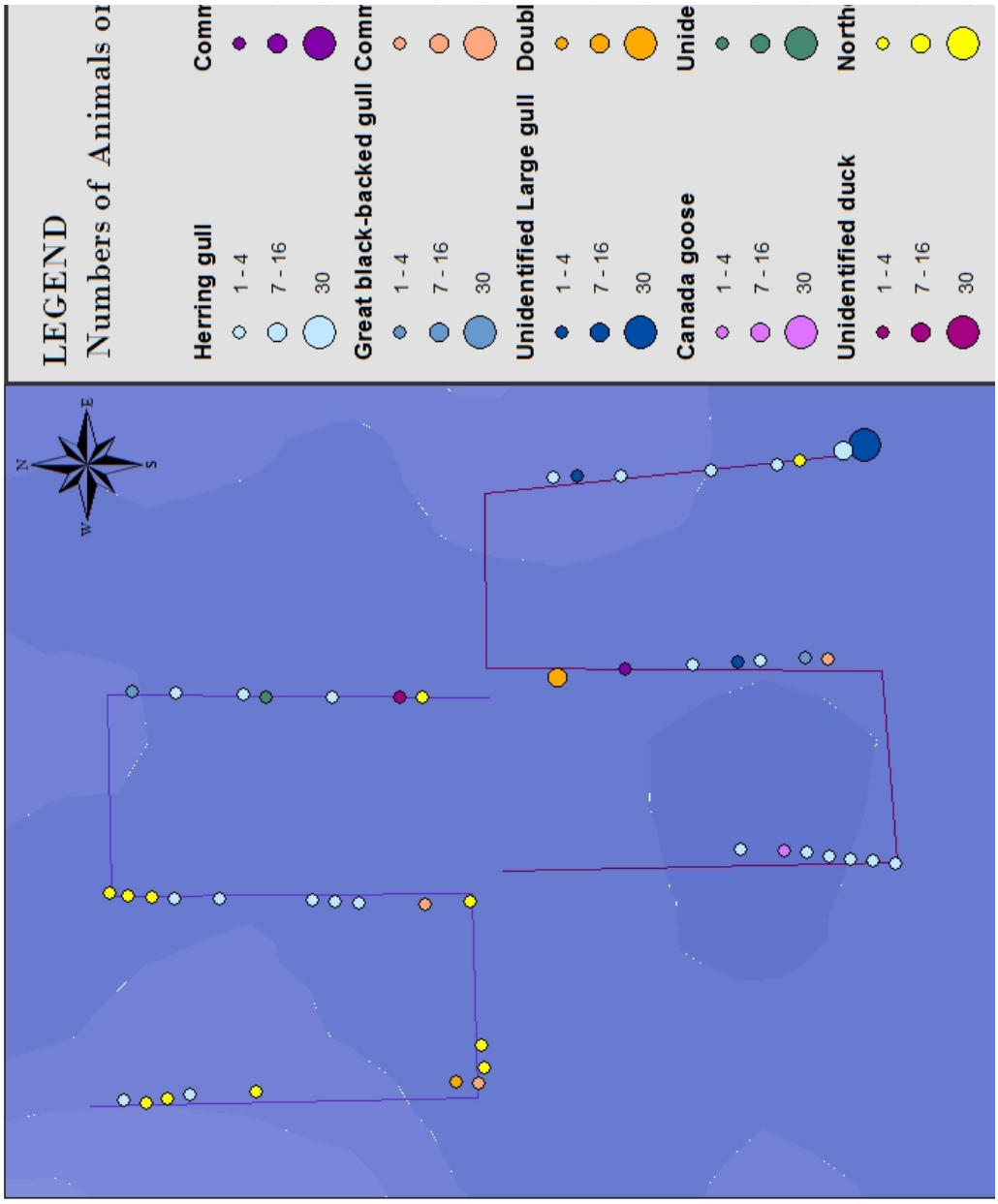
LEGEND
Numbers of Animals or
Herring gull
Comm
1 - 4
7 - 16
30
Great black-backed gull
Comm
1 - 4
7 - 16
30
Unidentified Large gull
Doubl
1 - 4
7 - 16
30
Canada goose
Unide
1 - 4
7 - 16
30
Unidentified duck
North
1 - 4
7 - 16
30
N
E
S
W

Table 13. Numbers of observations for each behavior (codes from left to right across table), flight height categories (meters) above sea surface, and flight direction (N = North, etc., where relevant) for each species (total # of observations/species) in the Test Quadrat on Oct. 11, 2011.

Behavior Code:	**1**	**20**						**31**	**35**	**66**	**#/Spp Total**
Meters	**0**	**2**	**5**	**10**	**15**	**20**	**30**	**5**	**15**	**5**	
CANG				**1**							**1**
SE				1							1
COEI			**4**								**4**
NE			4								4
COLO					**1**						**1**
W					1						1
DCCO							**16**				**16**
SSW							16				16
GBBG				**1**							**1**
E				1							1
HERG	**8**	**7**	**5**	**2**		**1**			**1**	**1**	**25**
E			4								4
SSE						1					1
SSW		7		1					1		9
SW				1							1
W			1								1
(none)	8									1	9
UNLG	**30**			**1**				**11**			**42**
N				1							1
(none)	30							11			41
NOGA					**2**						**2**
SW					2						2
Total	**38**	**7**	**9**	**5**	**3**	**1**	**16**	**11**	**1**	**1**	**92**

Control Quadrat

The Control Quadrat on October 11 covered 4.6 km^2 and the vessel traveled a total linear distance of 6.9 km (Map 6). Seven bird species were identified including three unidentified ducks (UNDU) flying due south at two meters high (Table 12). Two Common loons were documented with direct flight, one heading SW at 10 m high and one flying NW at 40 m high. Four Double-crested cormorants flew directly NNE at one meter high and one unidentified shearwater species flew three meters high heading directly NW. Six gulls with direct flight ranged in heights from three to 12m, two Herring gulls milled at 10 m, one milled at 15 m, and one meandered at 10 m. Two Herring gulls surface seized food while

sitting in the water after landing from an initial height of one meter. Thirteen total gannets were observed, with seven of these in direct flight from five meters to greater than 50 m, one sat in the water, four milled from five to seven meters, and one meandered at two meters high (Table 14).

Table 14. Numbers of observations for each behavior (codes from left to right across table), flight height categories (meters) above sea surface, and flight direction (N = North, etc., where relevant) for each species (total # of observations/species) in the Control Quadrat on Oct. 11, 2011.

Behavior Code:	**1**	**20**										**35**				**48**		**66**	**#/ Spp Total**
Meters	**0**	**1**	**2**	**3**	**5**	**10**	**12**	**15**	**20**	**40**	**>50**	**5**	**7**	**10**	**15**	**2**	**10**	**1**	
UNDU			**3**																**3**
S			3																3
COLO						**1**				**1**									**2**
NW										1									1
SW						1													1
DCCO		**4**																	**4**
NNE		4																	4
GBBG						**1**													**1**
N						1													1
HERG				**1**	**1**	**2**	**1**							**2**	**1**		**1**	**2**	**11**
NE					1														1
NNW						1													1
S				1															1
SSW																	1		1
SW						1													1
W							1												1
(none)														2	1			2	5
UNSH			**1**																**1**
NW			1																1
NOGA	**1**				**1**			**2**	**1**	**1**	**2**	**3**	**1**			**1**			**13**
SE											2								2
SSW								1		1									2
SW								1	1										2
W					1														1
(none)	1											3	1			1			6
Total	**1**	**4**	**4**	**1**	**2**	**4**	**1**	**2**	**1**	**2**	**2**	**3**	**1**	**2**	**1**	**1**	**1**	**2**	**35**

NOVEMBER 9, 2011 MORNING SURVEY (8:19AM)

Table 15. Numbers of species observed during the morning survey on November 9, 2011.

Num/spp	Test	Control	Spp Total
Black-legged kittiwake	0	2	2
Bonaparte's gull	1	0	1
Unidentified "Small" gull	0	1	1
Common eider	2	0	2
Surf scoter	0	1	1
Common loon	1	1	2
Great black-backed gull	1	1	2
Herring gull	8	11	19
Unidentified "Large" gull	25	0	25
Great shearwater	21	84	105
Sooty shearwater	0	1	1
Unidentified shearwater	1	1	2
Northern fulmar	1	0	1
Northern gannet	1	6	7
Razorbill	2	2	4
Harbor seal	1	0	1
Harbor porpoise	10	0	10
Grand Total	**75**	**111**	**186**

Test Quadrat

On November 9, the seas were 2.6 ft (0.79 m) and the wind was from the south at 10 - 11 knots, with clear skies. The Test Quadrat on November 9 covered 4.9 km^2 and the vessel traveled a total linear distance of 6.9 km (Map 7). Nine bird species were identified and two marine mammals were also observed in the Test Quadrat (Table 15). One Harbor seal was documented and a pod of about 10 Harbor porpoise (*Phocoena phocoena*, HAPO) were porpoising. Two Common eider in direct flight headed SW at one meter above the water and one Common loon flew due west at three meters high. The season's first Bonaparte's gull (*Chroicocephalus philadelphia*, BOGU) was observed in meandering flight at five meters. Two separate lobster boats working in the survey area each attracted flocks of 10 and 15 large gulls that were sitting in the water around the vessels. At another separate occasion, two large gulls sat in the water (no boat association) while one gull flew direct at four meters high and two flew due north at 10 m high. Four Herring gulls milled from eight to 10 m high, and one Great shearwater was also observed milling one meter above the water. Two shearwaters sat in the water, and a total of 19 shearwaters with direct flight and one with milling flight were observed flying one meter above the water. One Northern fulmar surface seized food while sitting in the water, one gannet with direct flight at one meter high was observed, and the first two Razorbills (*Alca torda*, RAZO) of the season's surveys were observed sitting in the water (Table 16).

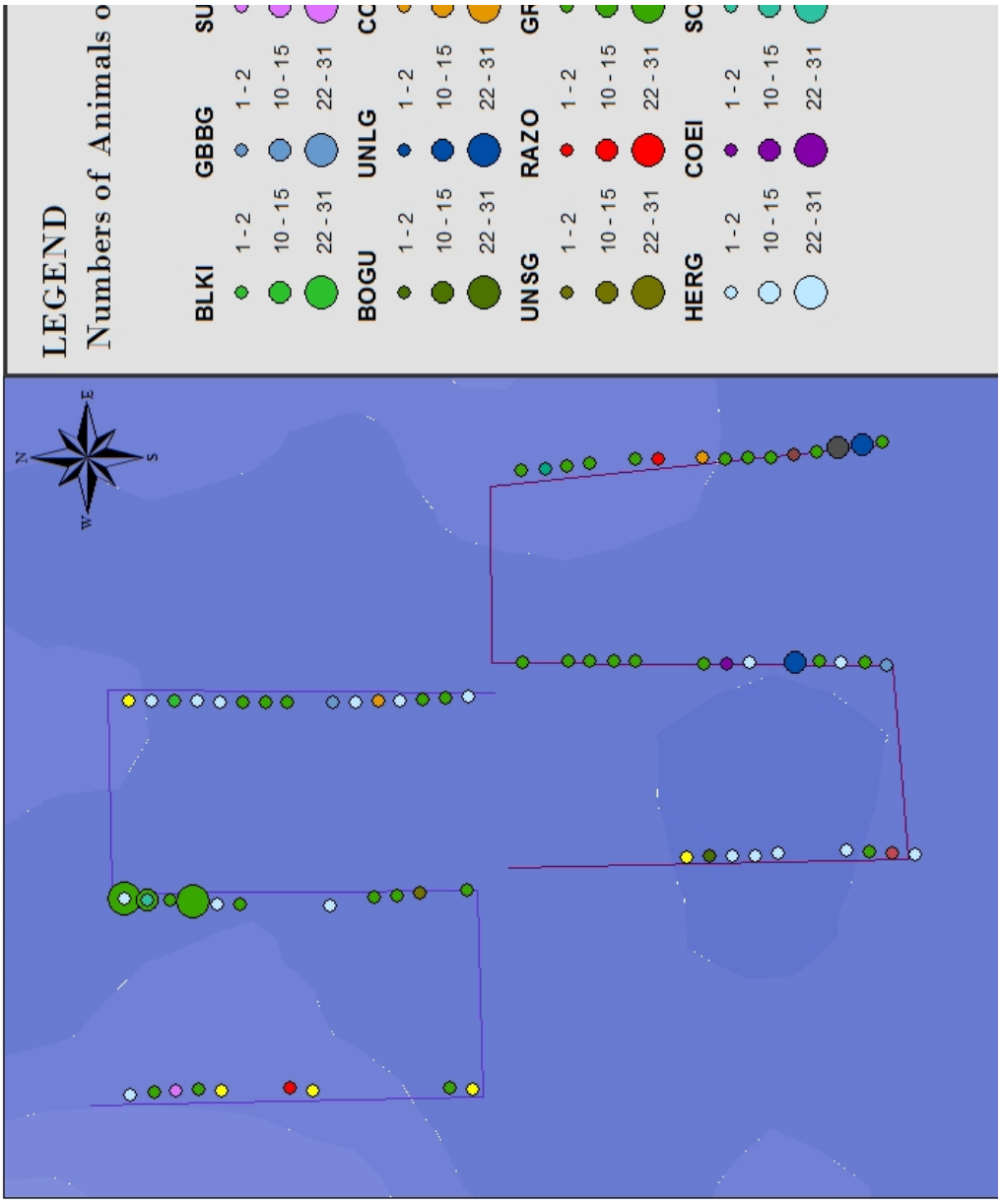
LEGEND
Numbers of Animals o
BLKI
GBBG
BOGU
UNLG
UNSG
RAZO
HERG
COEI
1 - 2
10 - 15
22 - 31
N
E
S
W

Table 16. Numbers of observations for each behavior (codes from left to right across table), flight height categories (meters) above sea surface, and flight direction (N = North, etc., where relevant) for each species (total # observations/species) observed in the Test Quadrat on Nov. 9, 2011.

Behavior Code:	**0**	**1**	**6**	**20**				**35**			**48**	**66**	**#/Spp Total**
Meters	**0**	**0**	**0**	**1**	**3**	**4**	**10**	**1**	**8**	**10**	**5**	**0**	
BOGU											**1**		**1**
(none)											1		1
COEI				**2**									**2**
SW				2									2
COLO					**1**								**1**
W					1								1
GBBG		**1**											**1**
(none)		1											1
HERG		**1**				**1**	**2**		**1**	**3**			**8**
N							1						1
S						1							1
W							1						1
(none)		1							1	3			5
UNLG		**25**											**25**
(none)		25											25
GRSH		**2**		**18**				**1**					**21**
E				2									2
ENE				1									1
ESE				2									2
SE				7									7
SSW				3				1					4
SW				2									2
W				1									1
(none)		2											2
UNSH				**1**									**1**
E				1									1
NOFU												**1**	**1**
(none)												1	1
NOGA				**1**									**1**
W				1									1
RAZO		**2**											**2**
(none)		2											2
Hseal	**1**												**1**
(none)	1												1
HAPO			**10**										**10**
(none)			10										10
Total	**1**	**31**	**10**	**22**	**1**	**1**	**2**	**1**	**1**	**3**	**1**	**1**	**75**

Control Quadrat

The Control Quadrat on November 9 covered 4.9 km^2 and the vessel traveled a total linear distance of 6.9 km (Map 7). Nine bird species were identified (Table 15), including the season's first Black-legged kittiwake (Rissa tridactyla, BLKI), observed in direct flight heading due west at 10 m above the surface. One unidentified "small" gull (UNSG) meandered at five meters high, one male Surf scoter (*Melanitta perspicillata*, SUSC) flew west in direct flight at one meter high, and one Common loon flew directly SSW seven meters above the water. A Great black-backed gull landed on the water to surface seize, from an initial height of 10 m, and in separate observations, two Herring gulls were sitting on the water. Eight Herring gulls with direct flight ranged in flight heights from five to 30 m, with the majority at 10 m, and another gull meandered at 15 m above the surface. Three large rafts of Great shearwaters sitting in the water were documented, with 31, 15, and 22 birds in each, but four other single shearwaters were also observed sitting in the water. In the first group of 31 Great shearwaters, one unidentified shearwater (UNSH) also slept, head tucked into its back, but was slightly larger than the others, suggesting the potential to be another species of shearwater (such as Cory's shearwater *Calonectris diomedea*, which regularly occurs in the area) or large petrel. Twelve Great shearwaters and one Sooty shearwater flew direct at one meter above the water. Two Northern gannets at two meters and four more at 10 m flew in direct headings (Table 17).

Two other noteworthy observations occurred only 2 mi south of Monhegan on our drive to the survey area and are not included in the total numbers for this report. November 9 had a substantial number of shearwaters, with a total of 105 Great shearwaters, one Sooty shearwater, and two unidentified shearwaters documented within the entire Monhegan Test Site. However, not inside the survey quadrats were approximately 15 shearwaters (species not identified) displaying direct and meandering flight at one meter above the water. Four Razorbills were documented inside the Monhegan Test Site on this date, but one additional Razorbill was also observed sitting in the water just north of the Control Quadrat.

Table 17. Numbers of observations for each behavior (codes from left to right across table), flight height categories (meters) above sea surface, and flight direction (N = North, etc., where relevant) for each species (total # of observations/species) in the Control Quadrat on Nov. 9, 2011.

Behavior Code:	**1**	**20**						**48**		**66**	**#/Spp Total**
Meters	**0**	**1**	**2**	**5**	**7**	**10**	**30**	**5**	**15**	**10**	
BLKI						**2**					**2**
W						2					2
UNSG								**1**			**1**
(none)								1			1
SUSC		**1**									**1**
W		1									1
COLO					**1**						**1**
SSW					1						1
GBBG										**1**	**1**
(none)										1	1
HERG	**2**			**1**		**5**	**2**		**1**		**11**
NW						1					1
SSW						1					1
SW							1				1
WNW						2					2
WSW				1		1	1				3
(none)	2								1		3
GRSH	**72**	**12**									**84**
ESE		2									2
SE		8									8
SSE		1									1
W		1									1
(none)	72										72
SOSH		**1**									**1**
NE		1									1
UNSH	**1**										**1**
(none)	1										1
NOGA			**2**			**4**					**6**
NW						1					1
SW			2			1					3
W						1					1
WNW						1					1
RAZO	**2**										**2**
(none)	2										2
Total	**77**	**14**	**2**	**1**	**1**	**11**	**2**	**1**	**1**	**1**	**111**

NOVEMBER 16, 2011 AFTERNOON SURVEY (12:00PM)

Table 18. Numbers of species observed during the afternoon survey on November 16, 2011.

Num/spp	Test	Control	Spp Total
Black-legged kittiwake	0	1	1
Unidentified "Small" gull	2	0	2
Common eider	40	0	40
Common loon	0	1	1
Great black-backed gull	2	1	3
Herring gull	18	17	35
Unidentified "Large" gull	0	7	7
Great shearwater	0	3	3
Sooty shearwater	0	1	1
Northern gannet	1	9	10
Unidentified jaeger	0	1	1
Razorbill	0	1	1
Unidentified alcid	1	0	1
Tuna	1	0	1
Grand Total	**65**	**42**	**107**

Test Quadrat

On November 16, the seas were four feet (1.2 m) and the wind was seven to eight knots from the south. The survey covered 5 km^2 and the vessel traveled a total linear distance of 7.1 km (Map 8). Six bird species were identified while in the Test Quadrat and one tuna was also observed (Table 18). Two unidentified small gulls (UNSG) in direct flight flew at 10 m and 30 m and one raft of both male and female Common eiders sat on the water. Nine Herring gulls were observed sitting in the water throughout the survey area, as were two lobster boats, but none of these appeared to have an association with each. Five other Herring gulls with direct flight flew at heights from five meters to 30 m. Two gulls milled about in the area near our survey vessel at five meters high and then eventually landed on the water, whereas one other gull, while still flying, dipped food from an initial height of two meters and another gull landed on the water to surface seize, from an initial height of one meter. One Northern gannet milled about at a height of one meter, and an unidentified alcid (UNAL) flew due west at two meters high (Table 19).

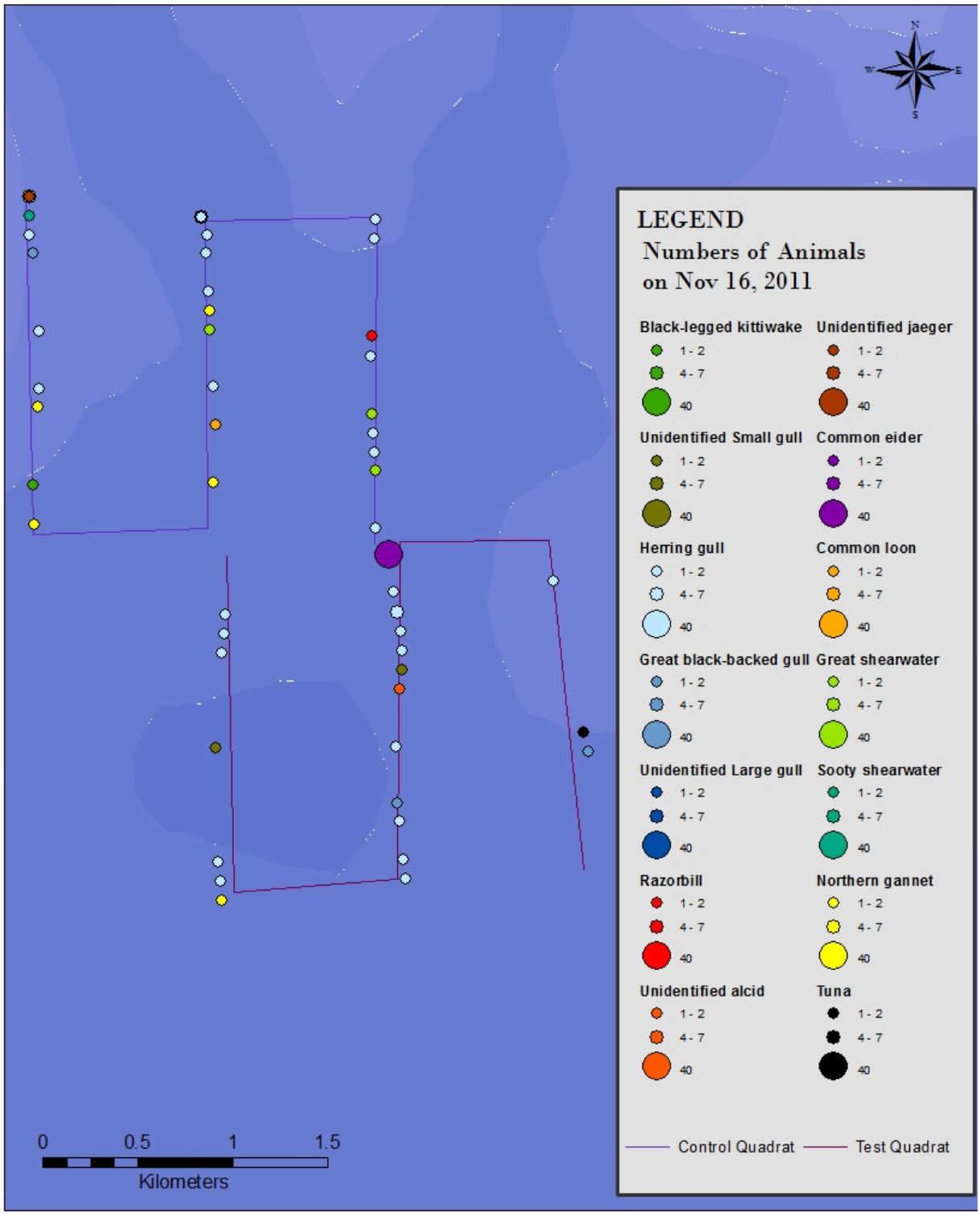

Map 8. Survey track, species, and numbers observed in both survey quadrats on November 16.

Table 19. Numbers of observations for each behavior (codes from left to right across table), flight height categories (meters) above sea surface, and flight direction (N = North, etc., where relevant) for each species (total # of observations/species) in the Test Quadrat on Nov. 16, 2011.

Behavior Code:	**1**	**20**							**35**		**61**	**66**	**#/Spp Total**
Meters	**0**	**2**	**5**	**7**	**10**	**15**	**30**	**>50**	**1**	**5**	**2**	**1**	
UNSG					**1**		**1**						**2**
NE					1								1
NNW							1						1
COEI	**40**												**40**
(none)	40												40
GBBG							**1**	**1**					**2**
ESE							1						1
SW								1					1
HERG	**9**		**1**	**1**		**2**	**1**			**2**	**1**	**1**	**18**
ESE						1							1
N			1										1
NW				1									1
SSW											1		1
WNW						1							1
(none)	9						1			2		1	13
NOGA									**1**				**1**
(none)									1				1
UNAL		**1**											**1**
W		1											1
TUNA	**1**												**1**
(none)	1												1
Total	**50**	**1**	**1**	**1**	**1**	**2**	**3**	**1**	**1**	**2**	**1**	**1**	**65**

Control Quadrat

On November 16, the survey area covered 4.9 km^2 and the vessel traveled 7.1 km (Map 8). Nine bird species were identified in the Control Quadrat (Table 18), including one Black-legged kittiwake in direct flight at 10 m high heading NE, one Common loon in direct flight heading SW at one meter high, and one unidentified subadult jaeger (UNJA) flying due south at two meters high. Twelve large gulls (UNLG) in direct flight flew at heights ranging from one meter to 35m, with 50% (six birds) flying at 10m. Seven various large gulls (UNLG) were surface seizing food while sitting next to a working lobster boat. Four other separate observations recorded gulls at initial heights from one to 10m landing on the water to surface seize food items. One Great shearwater and two Northern gannets were sitting in the water, while two shearwaters flew direct at one meter high and one meandered one meter high. Five Northern gannets flew direct at heights of two meters or

under, while one milled at one meter high and one meandered at two meters high. One Razorbill flew directly SW at two meters high (Table 20).

Table 20. Numbers of observations for each behavior (codes from left to right across table), flight height categories (meters) above sea surface, and flight direction (N = North, etc., where relevant) for each species (total # of observations/species) in the Control Quadrat on Nov. 16, 2011.

Behavior Code:	**1**	**20**								**35**		**48**		**66**					**#/Spp Total**
Meters	**0**	**1**	**2**	**5**	**7**	**10**	**25**	**35**		**1**	**5**	**1**	**2**	**0**	**1**	**2**	**5**	**10**	
BLKI						**1**													**1**
NE						1													1
COLO		**1**																	**1**
SW		1																	1
GBBG		**1**																	**1**
SW		1																	1
HERG				**2**	**1**	**6**	**1**	**1**			**2**				**1**	**1**	**1**	**1**	**17**
E				1															1
ENE						2													2
N								1											1
NNW						2													2
NW							1												1
S					1														1
SE						1													1
SW				1															1
W						1													1
(none)											2				1	1	1	1	6
UNLG														**7**					**7**
(none)														7					7
GRSH	**1**	**1**										**1**							**3**
SSE		1																	1
(none)	1											1							2
SOSH		**1**																	**1**
SSE		1																	1
NOGA	**2**	**1**	**4**							**1**			**1**						**9**
N		1																	1
WSW			4										1						5
(none)	2									1									3
UNJA			**1**																**1**
S			1																1
RAZO			**1**																**1**
SW			1																1
Total	**3**	**5**	**6**	**2**	**1**	**7**	**1**	**1**		**1**	**2**	**1**	**1**	**7**	**1**	**1**	**1**	**1**	**42**

BEHAVIOR CATEGORIES

Non-bird Species Summary

A complete list of all species observed is provided in Appendices 2, 3, and 4, summarizing the species and the dates on which they were documented. No turtles were observed during these surveys, but on two of the six survey days tuna were observed. Three days produced Harbor seals, and on only one day were Harbor porpoise observed. Table 21 summarizes the tuna, harbor porpoise, and harbor seal numbers by date observed in the Test and Control survey quadrats. Both tuna and harbor seals were recorded in both quadrats, but only one pod of porpoise was documented in the Test Quadrat.

Table 21. Numbers of non-bird species observed in the Test and Control Quadrats, by date.

		22-Sep	27-Sep	28-Sep	11-Oct	9-Nov	16-Nov
Test	Tuna		2				1
	Harbor seal		1			1	
	Harbor porpoise					10	
Control	Tuna		4				
	Harbor seal	2	1				
	Harbor porpoise						

To further discuss the bird observations during these surveys, bird species will be grouped by a taxonomical classification at the Order level. Five orders within the Class Aves comprise the seabirds and waterfowl that commonly utilize this Northeastern Atlantic region and they are as follows:

-Order Charadriiformes (large and small gulls, kittiwakes, razorbills and other alcids, phalarope, jaegers)
-Order Procellariformes (fulmar, shearwaters, and other petrels)
-Order Suliformes (gannets, cormorants)
-Order Gaviiformes (loons)
-Order Anseriformes (ducks, geese, eider, scoters)

Flight height and behavior were recorded in the Test and Control Quadrats, and the following figures will show flight height within the three most common flight behavior categories (direct flight, milling, and meandering) while grouping the observed species into four categories and a fifth category of "All Birds." The groups are as follows: 1) Anseriformes (ex., ducks, geese, swans), 2) Charadriiformes (ex., shorebirds, terns, gulls, alcids), 3) Procellariformes (ex., shearwaters, petrels), 4) Suliformes (ex., gannets) & Gaviiformes (ex., cormorants, gannets,

and loons), and 5) All Birds. Further discussion regarding the other observed behaviors of the bird species will follow.

Directional Flight: Flying in a Direct and Consistent Heading (Behavior code #20)

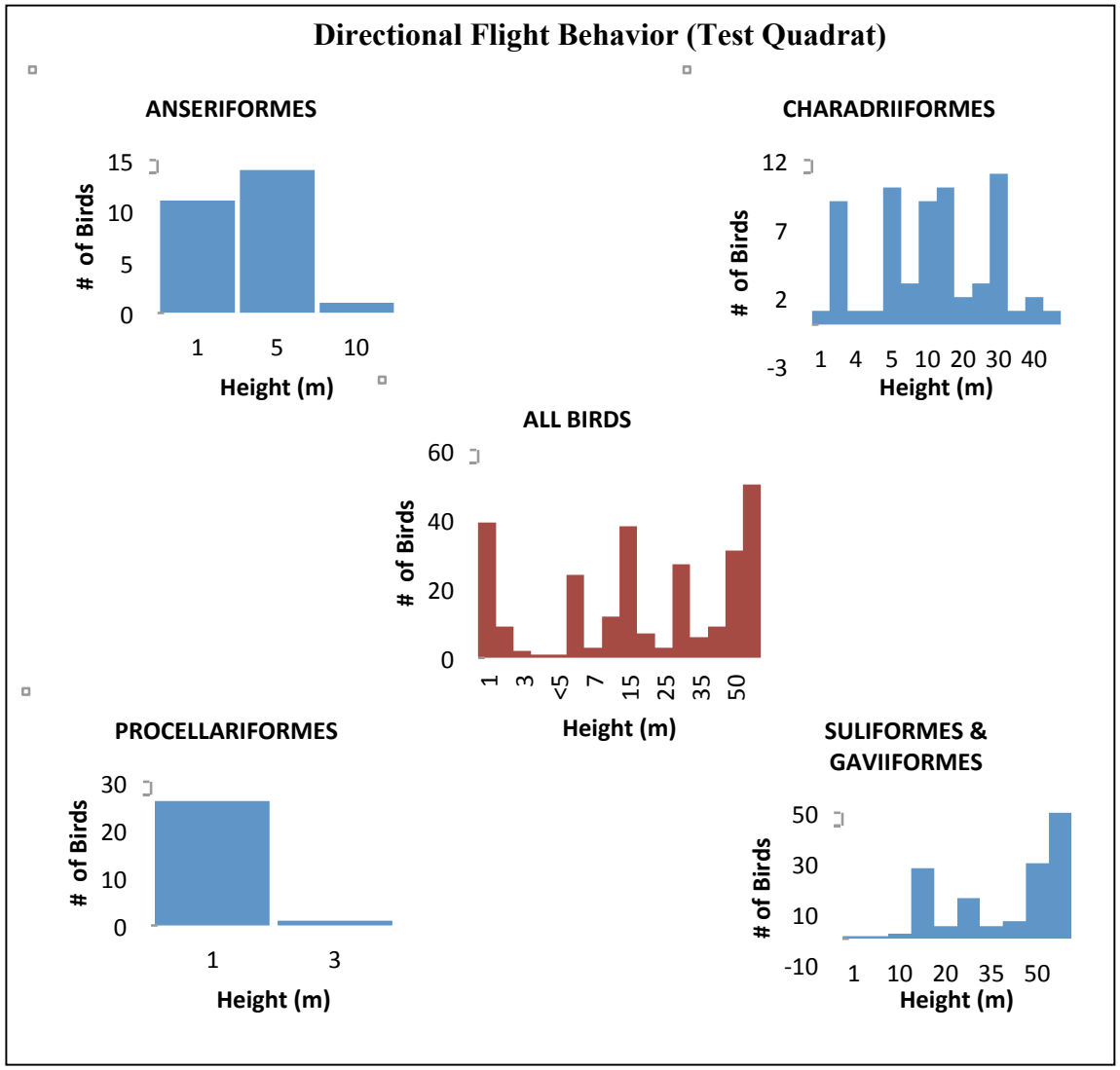

Figure 1. Test Quadrat flight heights of birds by group, observed in directional flight behavior.

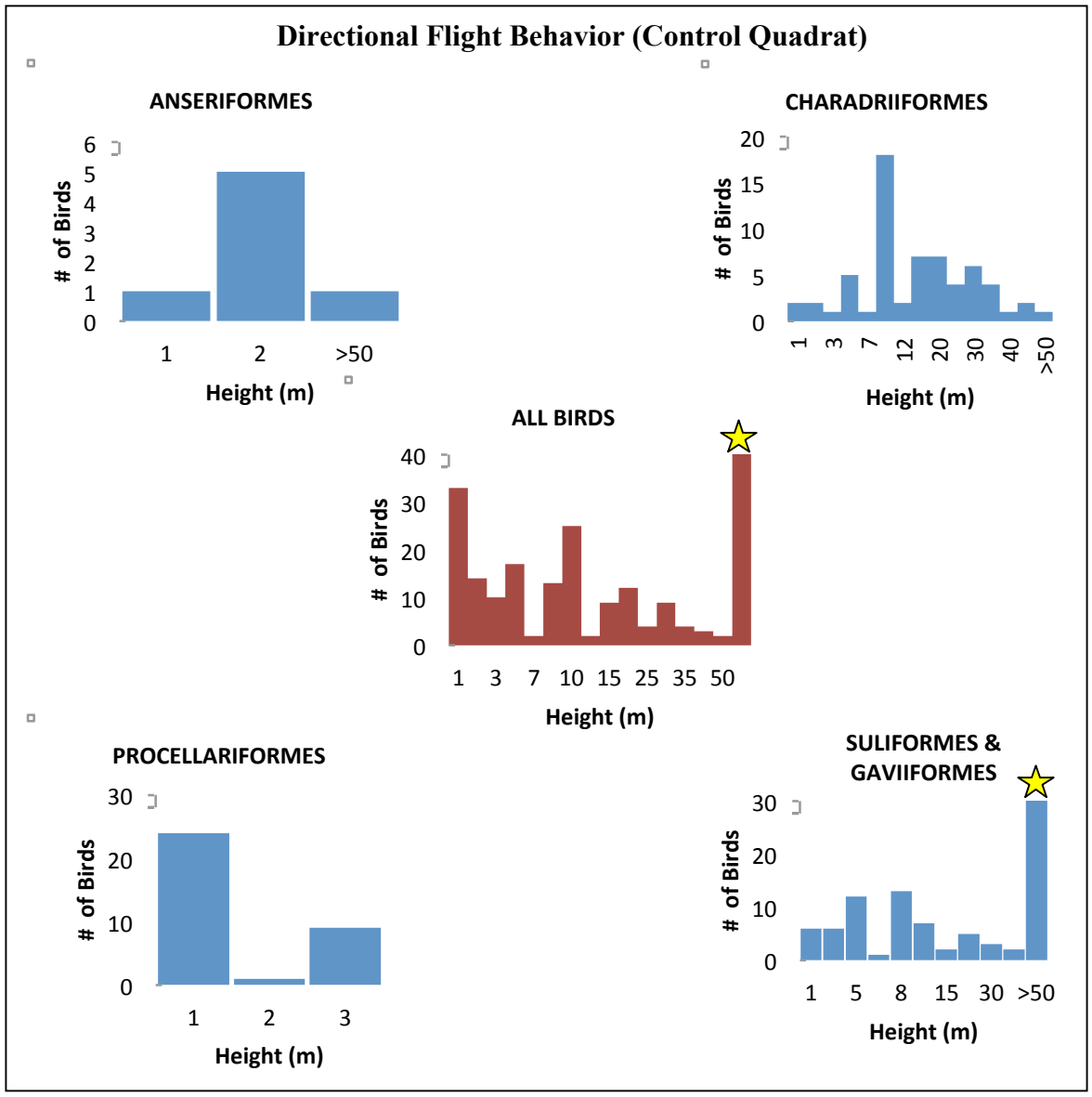

Figure 2. Control Quadrat flight heights of birds by group, observed in directional flight behavior. The two yellow stars indicate a height value of 1,524 cormorants in the Order Suliformes and 1,526 total birds in the All Birds chart, both recorded at the >50 m flight height.

Figures 1 and 2 show the behavioral data with species grouped by Order, displaying only behavior determined to be direct flight. Direct flight is described as a bird flying consistently through the area, not actively involved in foraging or other activities. The designation of this behavior during the survey is taken at the precise moment it is noticed by the surveyor. When in direct flight, the majority of Anseriformes (geese, ducks, eider, and scoters) flew at or below five meters above the surface in both the Test (96%) and

Control Quadrats (86%). One unidentified duck flew >50 m high through the Control Quadrat on September 22, heading due west.

Within the Charadriiformes (gulls, razorbills, jaegers, etc.), the majority of birds (~10 birds in each height category) flew from three meters to 30 m high through the Test Quadrat, while 18 birds in the Control Quadrat flew 10 m and seven birds each flew at the 15 m and 20 m height, and four flew at 30m. All of the alcids, including the three (two Razorbills and one unidentified) in the Test Quadrat and the two razorbills in the Control flew at two meters above the water's surface.

In both Quadrats, the majority of the Procellariformes (shearwaters and fulmars) flew one meter above the water (96% in Test and 71% in Control), with 26% of these birds flying three meters high and only one bird was observed flying at two meters high through the Control Quadrat.

Most (78%) of the birds grouped in the Orders of Suliformes and Gaviiformes (cormorants, gannets, and loons) flew at the 15, 30, and 50 m heights above the surface in the Test Quadrat; however, in the Control Quadrat most birds (74%) flew at or below 10 m (excluding the single large flock of over 1,500 cormorants flying to the southwest on September 27). The gannets and the cormorants were observed at all heights, whereas most of the loons were seen to fly at 10 m high or higher.

Summary of direct flight behaviors for all birds observed in the two survey quadrats –

Figure 1 for the Test Quadrat surveys shows relatively even distribution across the height divisions from one meter high to 50 or more meters above the water's surface for birds (species pooled) flying through the area in a direct and consistent heading. Figure 2 shows the data collected in the Control Quadrat surveys, in which the height of directed flight for most of the birds (species pooled, and not including the large flock noted) was observed to occur at or below 10 m. The single large flock of 1,500 cormorants flying through the Control Quadrat was recorded as >50 m. In general, for both areas, gulls and terns in direct flight were likely to be observed across all heights; ducks, geese, and shearwaters in direct flight were more likely to be at or below five meters. Loons and gannets in direct flight tended to be at or above 50 m above the surface. Two additional sightings outside of the survey area 1.2 - 2.4 km north of the Control Quadrat included two large flocks comprising 70 and 1,500 geese or cormorants each, direct flying west at heights between 45 m and 50 m and above. *These observations made during the migration period suggest that, regardless of location within the University of Maine's Monhegan Offshore Wind development site, this area is well within the migratory pathway of a wide variety of species that fly at a wide range of heights above the water.*

Meandering Flight (Behavior Code #48)

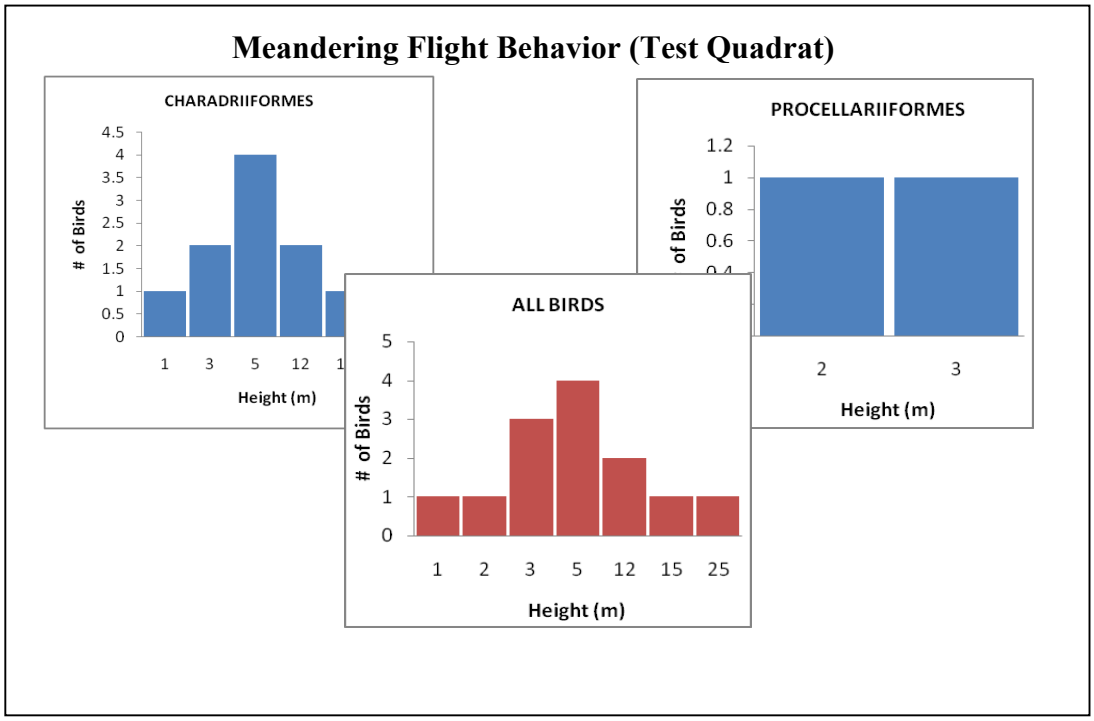

Figure 3. Test Quadrat flight heights of birds by group, observed in meandering flight behavior.

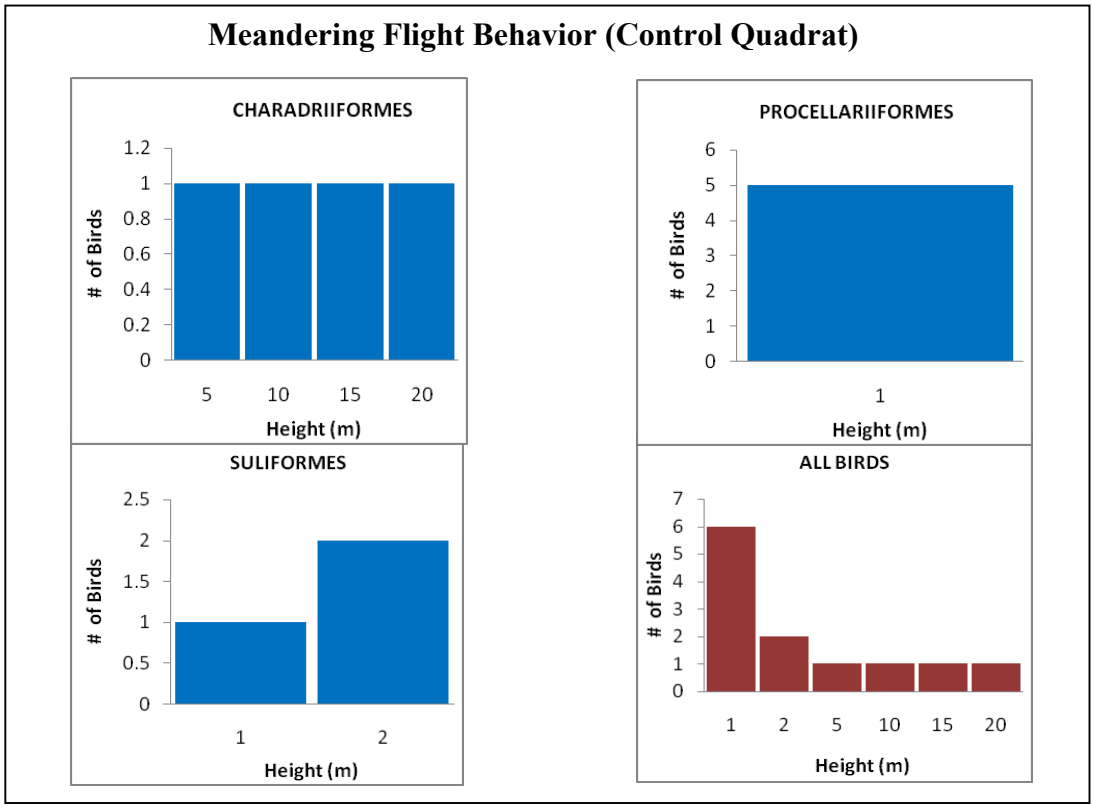

Figure 4. Control Quadrat flight heights of birds by group, observed in meandering flight behavior.

Figures 3 and 4 show the meandering flight behavior of species grouped by Order. Meandering flight is defined here as a bird flying in 'wandering' manner, not directly feeding or moving in a direct manner in a particular direction. Flight direction constantly changes, thus no flight direction is noted in the survey data for these birds. Only two Orders of birds were represented in the Test Quadrat for this behavior type, whereas three were represented in the Control, with the third Order comprising only the Suliformes (Northern gannets). No Gaviiformes were observed in meandering flight behavior. In general, 'meandering' represents food searching behavior as these species rely not only on vision but also olfaction to find food, and moving over the water's surface helps them detect and respond to a gradient of smells as well as to search for prey.

Most of the Charadriiformes meandering within the Test Quadrat were at the five-meter height (36%), with two birds (18%) each at three and 12 m above the surface. Single birds were observed from one meter up to 25 m. In the Control Quadrat, a total of four gulls was observed, one gull each meandering at heights from five to 20 m.

Of the Procellariiformes, one shearwater each meandered at two and three meters high in the Test Quadrat, whereas five shearwaters all meandered at only one meter above the water throughout the Control Quadrat.

Only three Northern gannets were observed meandering through the Control Quadrat, one bird at one meter and two birds at two meters above the water. No other Suliformes or Gaviiformes were observed with this flight behavior at the Control Quadrat site.

Summary of meandering behaviors for all birds observed in the two survey quadrats –

Too few data preclude statistical comparisons in the incidence of meandering behavior across species and flight heights between both sites. Overall, the Test Quadrat site had the majority (54%) of the birds exhibiting meandering flight at three to five meters above the water (for all bird species combined), whereas the majority (67%) of all birds (species pooled) meandered through the Control Quadrat at or below one meter above the water. *Regardless of height, these results illustrate that these seabird species actively forage in the general area, regardless of location within the University of Maine's Monhegan Offshore Wind development site.*

Milling Flight: Flying, milling or circling (Behavior Code #35)

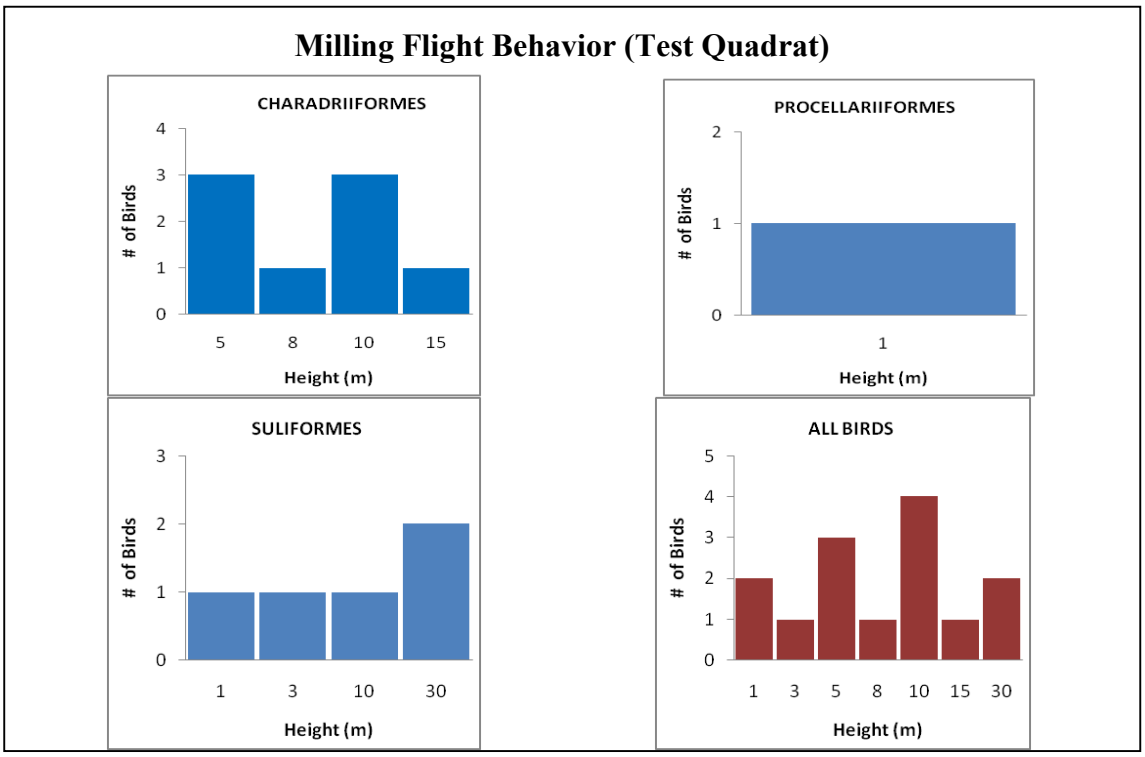

Figure 5. Test Quadrat flight heights of birds by group, observed in milling flight behavior.

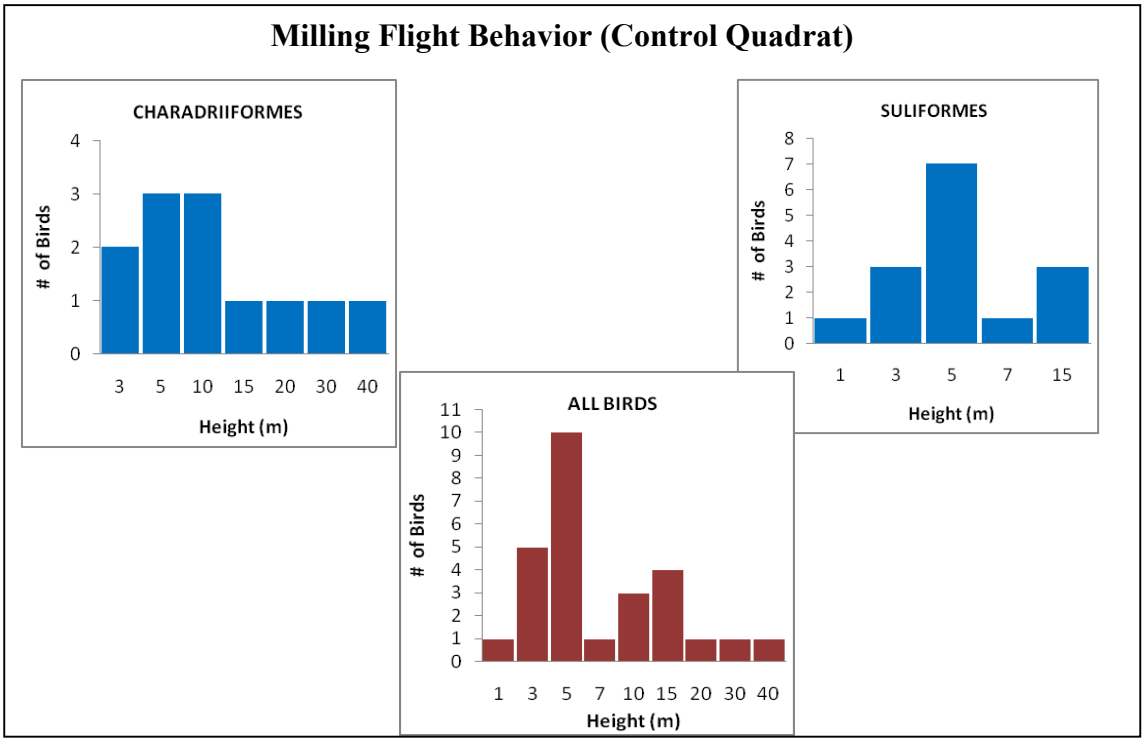

Figure 6. Control Quadrat flight heights of birds by group, observed in milling flight behavior.

Figures 5 and 6 show milling behavior data with species grouped by Order. Milling flight is described as a bird flying in a more distinct circling or milling path that is usually associated with foraging search patterns, as mentioned above for meandering behavior. Similar to meandering flight, general direction of milling flight constantly changes, thus flight direction is rarely noted in the survey data for these birds. Three Orders of seabirds, which rely on olfaction as well as sight for finding food, displayed milling behavior in the Test Quadrat (as above, Gaviiformes are not part of the third Order/group because no birds displayed milling behavior), and only two Orders displayed milling behavior in the Control Quadrat.

The Charadriiformes observed in the Test Quadrat displayed milling behavior from five to 15 m above the surface, with most of the birds concentrating around the five and 10 m heights (37% each). In the Control Quadrat, most of the birds milled around these heights, although the majority (67%) flew at three, five, and 10 m high, with some individual birds observed from 15 m to 40 m heights.

Only one shearwater in the Procellariiformes group was observed milling at one meter above the water within the Test Quadrat and none were observed in the Control Quadrat.

Two Northern gannets milled 30 m above the water surface in the Test Quadrat, and three additional birds each milled at the one, three, and 10 m height. A total of 15 gannets milled throughout the Control Quadrat, with most of the birds observed at five meters above the water (47%). Three gannets also milled at three meters and three more were flying at 15 m.

Summary of milling behaviors for all birds observed in the two survey quadrats – Overall, both the Test and Control Quadrats, pooled, revealed most milling flight occurring between three and 30 m above the water: 57% were milling from five to ten m in the Test Quadrat whereas 56% were found milling at three to five meters in the Control. *As noted above, these results illustrate that these seabird species actively forage in these areas, regardless of location within the University of Maine's Monhegan Offshore Wind development site.*

Other Behaviors Observed

Herring gulls, Great black-backed gulls, and other large gull species commonly search for easy, reliable foraging opportunities and therefore are attracted to vessels that commonly discard offal or bycatch (Garthe & Scherp 2003). Starting in late September every year, the

winter lobster season begins at Monhegan and fishermen toss their bait bag discards as they reset their lobster traps. It is well-known that vessels, particularly fishing vessels attract birds, as was the case in the Control Quadrat, when two Herring gulls, consisting of one juvenile and one subadult, appeared attracted to the slow-moving survey vessel (following ship, behavior code #32) and followed the boat for a short period of time. While surveying in the Test Quadrat, a total of 14 gulls were observed circling working lobster boats (behavior code #31), and on one occasion on November 16, in the Control Quadrat, a group of seven large gulls were eating (surface seizing) while sitting in the water next to a working lobster vessel. Numerous other occasions occurred where birds, mostly large gulls, were documented consuming food items while sitting in the water surface seizing (16 birds in Control Quadrat, five in Test Quadrat) or dipping while in flight (two birds, Test Quadrat only).

Plunge diving is a common foraging activity by birds in the Order Suliformes. Northern gannets will survey an area until a school of fish below the surface is spotted. They will then perform a steep plunge, often at heights of 20-30 m above the surface (Sibley 2001), into the water with their wings held back against the body and, with pointed bill and streamlined body, pierce the water to pursue food. During these surveys, 91% of plunge diving activity occurred in the Test Quadrat, with only one bird observed plunge diving, from 1 m, in the Control Quadrat (Fig. 7). The remaining 10 gannets (30%) dove from 10 m above the water's surface. Figure 7 summarizes the plunge diving- initial heights of all 11 Northern gannets observed during the survey period.

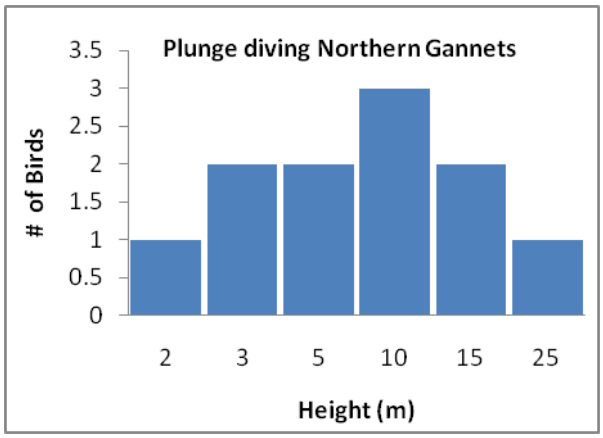

Figure 7. Initial height of plunge diving behavior by all northern gannets in both quadrats.

Throughout the surveys, numerous birds were observed sitting in the water, which is a behavior category not meant to suggest or exclude feeding activity. Behaviors described as 'sitting' may include sleeping or resting. Table 22 shows the total numbers of

birds by species, separated into the Test and Control Quadrats, pooled for all six surveys. Fifty-nine percent of all sitting birds were recorded in the Test Quadrat. The raft of 40 Common eider, comprising males and females, was a single observation on November 16 in the Test Quadrat. On October 11, a group of 30 gulls (mixed species) were sitting near a working lobster boat and, again on November 9, two groups of 10 and 15 gulls sat next to a lobster boat. Three separate rafts of shearwaters were recorded on November 9 consisting of 32, 15, and 22 birds in each. In the Test Quadrat, six gannets sat on the water on September 27, while in the Control Quadrat on September 22, seven gannets were recorded sitting, while and eight birds were sitting on the water in the Test Quadrat area on September 27.

Table 22.Total numbers of birds by Quadrat sitting on the water.

Num/spp	Test	Control	Spp Total
Red-necked phalarope	0	1	1
Common eider	40	0	40
Great black-backed gull	14	3	17
Herring gull	42	2	44
Unidentified Large gull	55	0	55
Great shearwater	7	83	90
Unidentified shearwater	0	1	1
Northern fulmar	0	1	1
Northern gannet	6	20	26
Razorbill	2	2	4
Grand Total	**166**	**113**	**279**

SUMMARY

In September, October, and November, 2011, during the pre-deployment stage of the DeepCwind's deepwater test wind turbine project at the University of Maine's Offshore Wind Test Site off Monhegan Island, boat-based visual surveys gathered data on species of birds and, opportunistically, marine mammals, and turtles, including occurrence and numbers, as well as various bird behaviors, flight direction, and flight heights.

The most numerous of bird species during the entire survey period was by far the migrating flocks of cormorants, with 93% of their numbers counted while in the Control Quadrat. The next five most numerous species, listed by greatest count to lesser, were Herring gull (63% of which occurred in the Test Quadrat), Great shearwater (78% of which occurred in the Control Quadrat), Northern gannets (72% of which occurred in the Control

Quadrat), Common eider (all 65 birds counted within the Test Quadrat), and Great black-backed gulls (67% of which occurred in the Test Quadrat). Unidentified "Large" gulls ranked high in numbers as well, with 84% of these counted within the Test Quadrat. The majority of all animals (79%, includes all birds, mammals, fish) sighted were observed in the Control Quadrat (see Appendices 3, 4; Map 9).

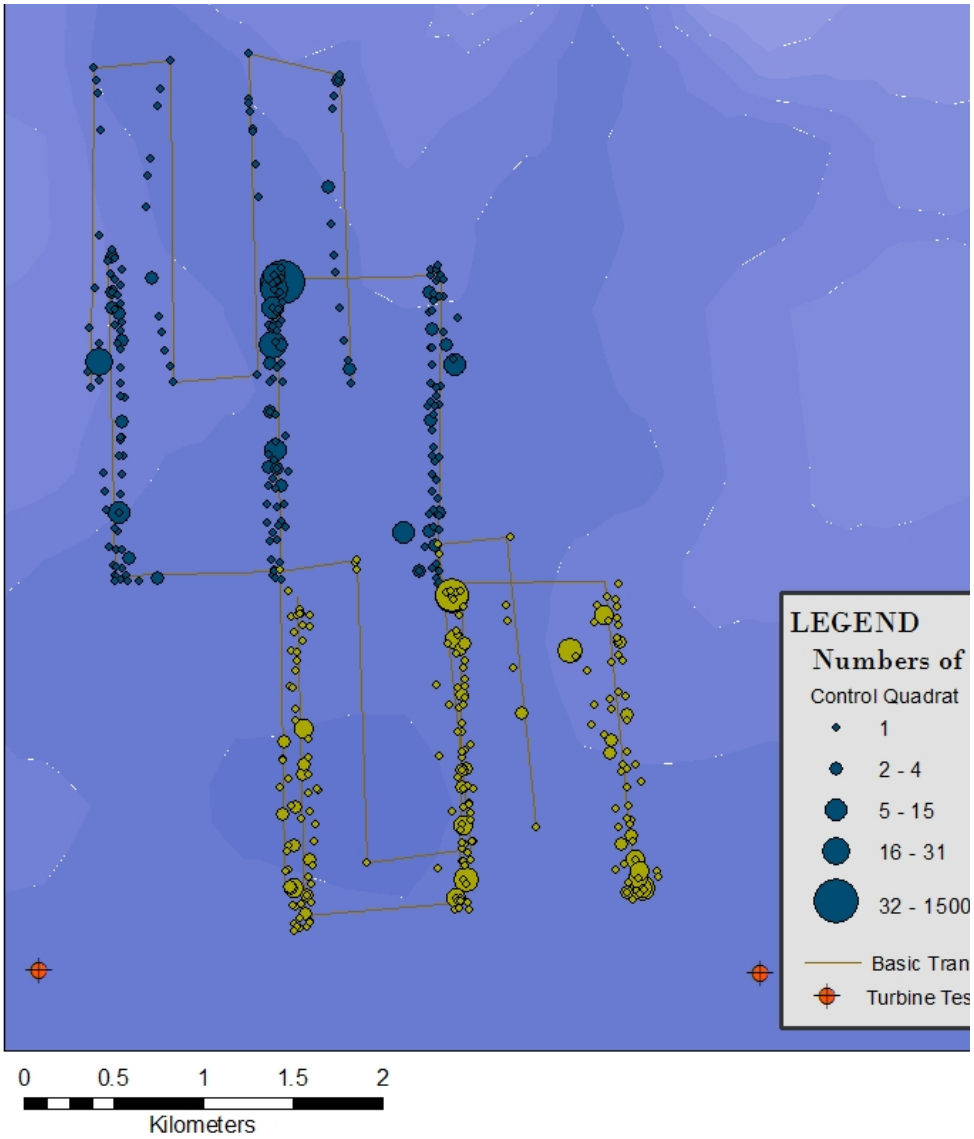

Map 9. Total numbers of animals observed in the Control and Test Quadrant across al

Percentages of most common behaviors were equal across the Test and Control Quadrats, with the majority of birds in direct flight (56% and 91%, respectively). The second most common behavior observed was sitting in the water (35% and 6%), followed by milling, then meandering. Figures 8 and 9 summarize total flight heights in the Test and Control Quadrats for all bird behaviors (direct flight, meandering, milling, sitting, etc.) observed. The large numbers of birds in the "0-m" height were those sitting on the water. For actual flying height comparison, the Test Quadrat had the most birds flying from 15 m and higher, whereas the Control Quadrat appears skewed to the 10m and lower, except for the 1,500 cormorants flying >50 m. As mentioned previously for the September 27 survey summary, the additional non-survey observations outside of the Control Quadrat consisting of over 1,500 migrating birds at 45 m and higher indicate that this area between the Control Quadrat area and the region just south of Monhegan Island is an important migration corridor and should be closely examined in that context.

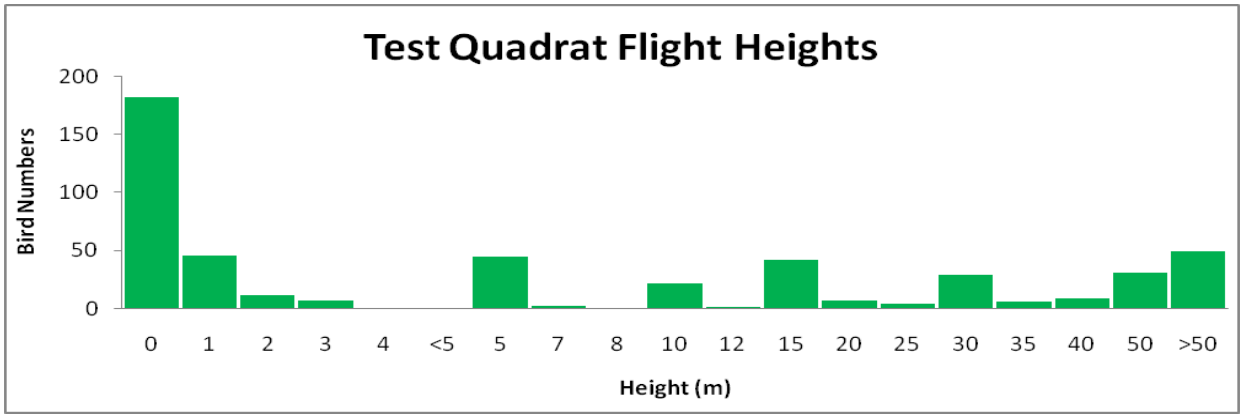

Figure 8. Total flight heights for all bird behaviors observed within the Test Quadrat.

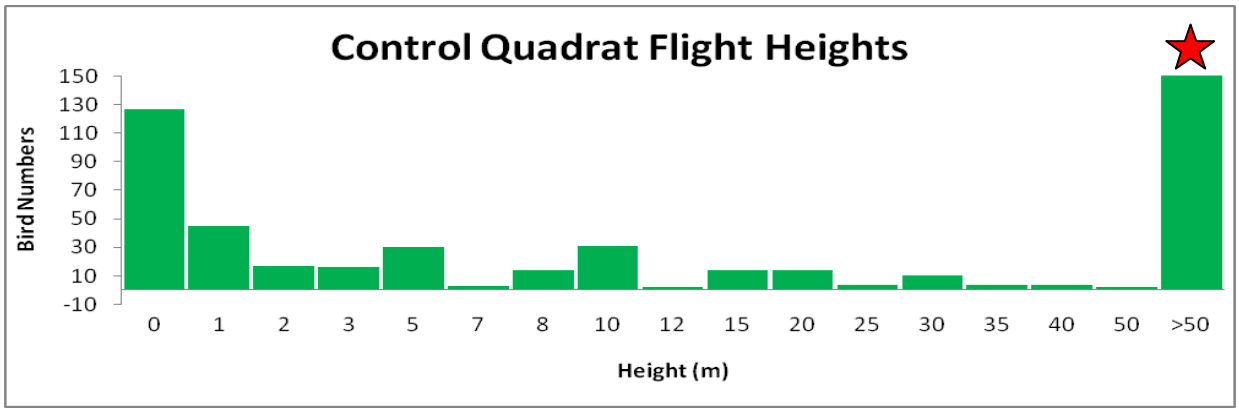

Figure 9. Total flight heights for all bird behaviors observed within the Control Quadrat. The red star indicates a value total of 1,526 birds.

The results of the six surveys described in this report provide an initial, albeit incomplete, baseline inventory of birds. Caution should be noted in that the area of interest was surveyed only six times during a three month period that comprises autumn migration, an extremely active time in that several million birds of all kinds move in the Gulf of Maine region. The six surveys focused exclusively on seabirds and were not designed to include landbirds that have been extensively documented making nocturnal as well as diurnal migratory flights across and along the Gulf of Maine. Monhegan, in particular, is a well-established 'hotspot' for observing migratory landbirds in both spring and fall. *Future at-sea surveys will need to take into account other groups of birds known to occur in the Monhegan Island area, particularly during the periods of spring and fall migration. Further, at-sea visual surveys are usually limited to fairly ideal weather conditions (high visibility, relatively calm seas) needed for safety as well as visibility. However, birds of all taxa can be active under most weather conditions making extrapolation from surveys conducted under ideal conditions to a robust assessment of bird activity and potential risk potentially problematic. More frequent surveys and the use of other methods are strongly encouraged in future assessments of bird activities for offshore wind development.*

The surveys described in this report documented birds not only passing through the area, but also those that were foraging and resting there. This area, therefore, is congruent with much of the Gulf of Maine in that it provides an array of resources (food, rest) for a diversity of seabird species. Of particular note during the surveys were the repeated observations of the birds' attraction to anthropogenic activities, in this case, fishing boats, which caused temporary concentrations of gulls, terns, and diving birds such as gannets, in near the boats. *As documented in these surveys, foraging and feeding behaviors (milling, meandering, and diving), whether for naturally occurring food or in response to fishing activity, occurred at heights characteristically within the rotor swept zone of proposed test as well as commercial scale turbines. The potential for fishing activities near offshore wind farms to concentrate seabirds and, thus, increase collision risk beyond naturally occurring conditions should be considered when developing policy regarding fishing activities.*

In summary, direct flights and foraging (food searching and feeding) behaviors occurred across a wide spectrum of heights, including those proposed for experimental test as well as full-scale commercial turbines. Clearly, in contrast to collision risk associated with bird movements in the context of migration (primarily characterized by direct flight) at land-based wind energy facilities, the types of movements (e.g. milling, meandering, dive plunging, etc.) made by seabirds in addition to directed flight, may pose greater risk for them because these types of movements are highly localized in response to ephemeral resources, and result in an individual remaining in and moving repeatedly about an area for extended periods of time, as compared to direct flight. Thus, risk assessment based on land-based wind energy activities may have limited applicability to birds adapted to and dependent on the marine

environment. Further, it should be noted that the Razorbill, which is currently state listed as 'threatened', Bonaparte's gull and Red-necked phalarope, which are both currently state listed as 'Species of Special Concern', and Great Shearwater, federally listed as a Species of Conservation Concern, were observed in the survey areas. Much more information is needed about the occurrence of these and other species in the area. Finally, as previously stated, these surveys took place over a short period of time and only with the intent of occurring within the initially proposed deployment period for DeepCwind's small 1.5 kW test turbine. The results from this work are, therefore, applicable only to this period and are limited to the context as described in this report.

ACKNOWLEDGEMENTS – Captain Christina Cash provided exceptional service in operating the F/V Priscilla Earl. Her efforts throughout this project were valuable. Mr. Wesley Wright's logistic support was much appreciated.

APPENDIX 1
SURVEY CODES
(Gould & Forsell 1989)

Code 2. Survey Type (15)
1 = General observations: These are records of large flocks, rare or unusual sightings, transects that cannot be used to derive density indexes, or any record that will not fit another format.
7 = Station count: The criteria for a station count are that the platform is stationary and that all birds are counted in a 360° circle from the platform.
9 = Ocean transect: The criteria for a transect are a visibility of at least 1,000m and a moving platform with a constant speed and direction. An oceanic-transect is conducted outside well-defined headlands.

Code 3. Observation Conditions (75)
1 = Bad (general observations only)
2 = Poor (no quantitative analysis)
3 = Fair
4 = Average
5 = Good
6 = Excellent
7 = Maximum

Code 5. Sea State (49)
0 = Calm
1 = Rippled (0.0 1-0.25 ft)
2 = Wavelet (0.26-2.0 ft)
3 = Slight (2-4 ft)
4 = Moderate (4-8 ft)
5 = Rough (8-13 ft)
6 = Very rough (13-20 ft)
7 = High (20-30 ft)
8 = Over 30 ft

Code 6. Weather (55-56)
00 = Clear to partly cloudy (0-50% cloud cover)
03 = Cloudy to overcast (51-100% cloud cover)
41 = Fog (patchy)
43 = Fog (solid)
68 = Rain
71 = Snow
87 = Hail

Code 14. Age (32)
P = Pullus (flightless young)
J = Hatching year (hatching date to spring molt: a bird capable of sustained flight)
S = Subadult (last year before adult plumage)
A = Adult

Code 17. Bird Behavior (56-57)
00 = Undetermined
01 = Sitting on water
10 = Sitting on floating object
15 = Sitting on land
20 = Flying in direct & consistent heading
29 = Flying, height variable
31 = Flying, circling ship
32 = Flying, following ship
34 = Flying, being pirated
35 = Flying, milling or circling (foraging)
48 = Flying, meandering
61 = Feeding at or near surface while flying (dipping or pattering)
65 = Feeding at surface (scavenging)
66 = Feeding at or near surface, not diving or flying (surface seizing)
70 = Feeding below surface (pursuit diving)
71 = Feeding below surface (plunge diving)
82 = Feeding above surface (pirating)
90 = Courtship display
98 = Dead

Code 18. Mammal Behavior (56-57)
00 = Undetermined
01 = Leaping
02 = Feeding
03 = Mother with young
04 = Synchronous diving
05 = Bow riding
06 = Porpoising
07 = Hauled out
08 = Sleeping
09 = Avoidance
14 = Curious/following
15 = Cetacea/pinniped association
16 = Pinniped/bird association
17 = Cetacea/bird association
18 = Breeding/copulation
19 = Moribund/dead

APPENDIX 2

All observed species with code, common name, scientific name, and dates sighted.

Species Code	Common name	Scientific name	Sep 22	Sep 27	Sep 28	Oct 11	Nov 9	Nov 16
BLKI	Black-legged kittiwake	*Rissa tridactyla*					X	X
BOGU	Bonaparte's gull	*Larus philadelphia*					X	
CANG	Canada goose	*Branta canadensis*				X		
COEI	Common eider	*Somateria mollissima*			X	X	X	X
COLO	Common loon	*Gavia immer*			X	X	X	X
DCCO	Double-crested cormorant	*Phalacrocorax auritus*		X	X	X		
GBBG	Great black-backed gull	*Larus marinus*	X	X	X	X	X	X
GRSH	Great shearwater	*Puffinus gravis*	X	X	X		X	X
HERG	Herring gull	*Larus argentatus*	X	X	X	X	X	X
NOFU	Northern fulmar	*Fulmarus glacialis*		X			X	
NOGA	Northern gannet	*Morus bassanus*	X	X	X	X	X	
POJA	Pomarine jaeger	*Stercorarius pomarinus*	X					
RAZO	Razorbill	*Alca torda*					X	X
RNPH	Red-necked phalarope	*Phalaropus lobatus*			X			
SOSH	Sooty shearwater	*Puffinus griseus*	X	X			X	X
SUSC	Surf scoter	*Melanitta perspicillata*					X	
UNAL	unidentified alcid							X
UNCO	unidentified cormorant			X	X			
UNDU	unidentified duck species			X	X	X		
UNJA	unidentified jaeger							X
UNLG	unidentified "large" gull		X		X	X	X	X
UNSG	unidentified "small" gull						X	X
UNSH	unidentified shearwater				X	X	X	
TUNA	Tuna species	*Thunnus spp.*		X				X
Hseal	Harbor seal	*Phoca vitulina*	X	X			X	
HAPO	Harbor porpoise	*Phocoena phocoena*					X	

APPENDIX 3. Test quadrat survey results by species and numbers observed per transect strip.

Num/ Spp																								
	SEP													OCT				NOV							
	22				22 Total	27			27 Total	28			28 Total	11			11 Total	9			9 Total	16			16 Tota
	T1	T2	T3	T4		T1	T2	T3		T1	T2	T3		T1	T2	T3		T1	T2	T3		T1	T2	T3	
BOGU																				1	1			
UNSG																							1	1
CANG																1	1							
COEI												19	19		4		4		2		2		40		4
COLO												9	9		1		1	1			1				
DCCO										30	76		106		16		16								
UNCO										7			7												
GBBG				2	2	2	9	1	12	5	1	5	11		1		1		1		1	1	1		
HERG	6	6		3	15	1	20		21	11	7	7	25	11	2	12	25		2	6	8	1	11	6	1
UNLG				1	1							1	1	41	1		42	10	15		25				
GRSH	2				2			4	4	1	3	2	6					11	9	1	21				
SOSH		1			1			1	1																
UNSH											1		1					1			1				
NOFU																				1	1				
NOGA		1	2		3	7	4	7	18	1			1	2			2			1	1			1	
RAZO																		2			2				
UNAL																							1		
Hseal							1		1									1			1				

APPENDIX 4. Control quadrat survey results by species and numbers observed per transect strip.

Num/ Spp	SEP													OCT				NOV							
	22				22 Total	27			27 Total	28			28 Total	11			11 Total	9			9 Total	16			16 Tota
	C1	C2	C3	C4		C1	C2	C3		C1	C2	C3		C1	C2	C3		C1	C2	C3		C1	C2	C3	
BLKI																		2			2			1	1
UNSG																			1		1				
RNPH												1	1												
SUSC																				1	1				
UNDU								1	1	2			2	3			3								
COLO										2			2		1	1	2	1			1		1		1
DCCO							1500		1500	7	13	2	22			4	4								
UNCO								22	22																
GBBG	2	1	2	1	6		1		1	3		1	4	1			1	1			1			1	1
HERG	4	3	3	1	11	1	2		3	3	5	6	14	3	6	2	11	6	4	1	11	6	6	5	17
UNLG										1	2	3	6										7		7
GRSH	4	2		5	11	2		2	4	8	2	7	17					7	73	4	84	2	1		3
SOSH	1				1														1		1			1	1
UNSH														1			1		1		1				
NOFU			1		1																				
NOGA	5	2	3		10	5	8	4	17	4	4	3	11	1	5	7	13	1	2	3	6		2	7	9
POJA			1		1																				
UNJA																								1	1
RAZO																				2	2	1			1

LITERATURE CITED

Garthe, S. & B. Scherp. 2003. Utilization of discards and offal from commercial fisheries by seabirds in the Baltic Sea. *ICES Journal of Marine Sciences* 60 (5): 980-989.

Gould, P.J. & D.J. Forsell. 1989. Techniques for shipboard surveys of marine birds. U.S. Fish & Wildlife Service, *Fish & Wildl. Technical Report* 25, 22 pp.

Tasker, M.L., P.H. Jones, T. Dixon, & B.F. Blake. 1984. Counting seabirds at sea from ships: A review of methods employed and a suggestion for a standardized approach. *The Auk* 101: 567-577.

U.S. Fish & Wildlife Service 2008. *Birds of Conservation Concern. 2008.* United States Department of Interior, Fish and Wildlife Service, Division of Migratory Bird Management, Arlington, Virginia. 85 pp. [Online version available at <http://www.fws.gov/migratorybirds/>]

Sibley, D.A. 2001. The Sibley Guide to Bird Life and Behavior. C. Elphick, J.B. Dunning, Jr., & D.A. Sibley, Eds. Alfred A. Knopf Publisher, New York.

DeepCWind Year 1 Report

Pelagic Community Acoustic Monitoring

Graham Sherwood, Adam Baukus, Gulf of Maine Research Institute

Background

The goal of this study was to assess the pelagic ecosystem in the test and control sites identified by the DeepCWind project. Acoustic equipment with multiple frequencies was used in order to estimate biomass of pelagic species such as herring, mackerel, squid and zooplankton. Determining the biomass and distribution patterns of these species would help define the importance of this habitat to local fauna and potentially aid in choosing a wind turbine test site that has minimal biological impact. The offshore pelagic zone is a rapidly changing environment, and would require thorough investigation to assess its utilization, which was beyond the scale of this project. However, other goals of this survey included gaining insight into which tools would be most appropriate to effectively identify local species and estimate biomass, determining the extent of sampling which might be necessary to assess this system, and learning about challenges of this particular field site such as island access, and facilities for calibration.

Methods

Three sites were sampled day and night on three occasions in 2010. Sampling dates were July 7, August 11, and September 9. The first two sites are potential areas for deployment of a floating test wind turbine, the third site is a control site. Figure 1 shows the survey transects. Table 1 shows the locations of the corners of the three sites, dimensions, and sampling dates and times. Each site was sampled using a systematic grid with approximately 0.25 km spacing between transects, at a maximum survey speed of 7 knots to keep bow wave and vibration of side mounted equipment to a reasonable level (figure 2) . Day sampling was conducted between sunrise and sunset and night sampling was conducted between evening and morning astronomical twilight. The order of sampling the three sites within each photoperiod (day and night) and month was determined randomly, as was the direction of sampling along the grids (east to west or west to east).

Sampling was done from a Monhegan Island based lobster boat, the F/V Seldom Seen, captained by Matt Weber. Acoustic instruments were mounted on a steel pole bolted to the side rail (figure 3). On July 7, we used a Simrad EK60 echosounder with a 38-kHz split-beam transducer that had a 12˚ circular beam. We set pulse duration to 1.024 ms, transmit power to 1,000 W, and ping rate to 1/sec. On August 11, we also sampled with a Simrad EK60 echosounder with a 120-kHz split-beam transducer that had a 7˚ circular beam. Pulse duration and ping rate were identical to the 38-kHz system, but transmit power was set to 500 W. The September 9 sampling was done with only the 120 kHz system due to technical issues with the 38 kHz system. We calibrated the EK60 echosounders on July 9, August 12, and September 9, immediately before or after sampling, using standard protocols and a 38.1 mm tungsten carbide sphere. Temperature, salinity, and depth profiles were collected with a SeaBird 19 plus CTD. Casts were made at the center of each sampling site just prior to day sampling.

Acoustic analysis was a multi-step process using the EchoView software. First, visual inspection isolated biological targets and removed interference signals. Next, a bottom choosing algorithm was applied to define the lower boundary of the data. Relative biomass estimates were then calculated and expressed in nautical area scattering coefficient (NASC). NASC is a measure of backscattering energy in a known area that is scaled to a nautical mile (m^2/nmi^2). The NASC value was calculated for each leg of a transect and averaged to calculate a single mean NASC value for the entire transect. EchoView software was also used to identify single targets in the acoustic data. This feature identifies acoustic echoes attributable to a single backscattering target detected within the beam of the echosounder and then calculates the target strength in dB and displays the distributions of the target depths in the water column. CTD data were downloaded from the instrument and profiles of depth, temperature and salinity values were created in Microsoft Excel.

Results

Calibration

Estimated target strength of sphere was within 0.59 dB of expected target strength and transducer gain was 22.25 dB for the 38-kHz transducer, for the 120 kHz transducer the target strength was within 0.00 dB of expected and the transducer gain was 25.13 dB.

Biomass and Target Strength

The relative biomass for all sites and all months was quite low with NASC values of 2000 or less (figure 4), with the exception of one transect. The control site sampled in September at night had a mean NASC value of 6841, significantly higher than other values (figure 5). Preliminary analysis showed a consistently higher abundance of targets in the upper water column (0-20m) compared to targets closer to the bottom (80-100m) across all sites and months. The range of target strength values for identified single targets was the same for all sampling months, with a maximum of -18dB and a minimum of -60dB for July (figure 6), August (figures 7) and September (figure 8).

Temperature and Salinity Profiles

Temperature and salinity profiles did not vary substantially among the three sites in July (Figure 9). Sampling in August and September showed very similar profiles to July. Temperatures ranged from 5 to 15 degrees Celsius, with the thermocline located at 15 to 20 m depth, and salinity values approximately 32 ppm.

Discussion and Future Work

The dynamic nature of the pelagic ecosystem requires consistent monitoring to establish a baseline of utilization by pelagic species. It may also require a variety of tools in order to properly identify and quantify different species that may be encountered. This project gave us insight into the pros and cons of certain tools and what extent of man power might be necessary to monitor the pelagic ecosystem in this environment. Deployment of acoustic instruments on smaller boats and on side/pole mounted as opposed to hull mounted is more affordable and reusable, but offers added logistical

challenges as we learned from instrument damage (waves splashing over side rail onto equipment and strain on transducer wires causing them to break). The low overall biomass may indicate this habitat is not critical for pelagic species. Note that large herring schools typically have NASC values of 10,000 or more which was not seen in this study; the control site approached this value in September at night (figure 4) which is consistent with the time of year that herring may be migrating through the area. But to gain a sense of the frequency of use and importance of this area for herring and other pelagics more comprehensive sampling would be necessary. The target strengths seen in this study are suggestive of a mix of pelagic species like herring (~40 dB), squid (~60 dB) and a variety of zooplankton species like pteropods, mysids, and krill (~80 dB). Specifically examining the larger biomass event in September the targets seem to be clustered near thermocline at around 20m, which might suggest they are dense accumulations of zooplankton species, since they are often aggregated at the thermocline by current flows. More extensive sampling and ground truthing would be necessary to verify species identifications; this could be done using various nets or cameras. The acoustic data from both frequencies was very similar, but this was most likely due to the low number of targets seen in this study. In future work it would be advantageous to have a mulitbeam acoustic transducer that would allow data collection off the side of the boat, perpendicular to the path of travel as well as directly underneath. In addition to the wider area of coverage this tool may allow us to address the issue of vessel avoidance, which could be a factor in the lack of pelagic targets seen in this study. The consistent conditions seen in the CTD data suggests that monthly sampling was adequate to resolve hydrographic changes in this area.

Table 1. Location, area, and dates/times of sampling. Times are local.

Site	Lat/Long	Area (km^2)	Date	Day	Night
Test Site 1	43.725 -69.336	2.98 km^2	7 July 2010	17:02 – 18:17	21:46* – 22:46
	43.720-69.320		11 Aug 2010	14:31 – 15:32	22:58 – 00:01
	43.700 -69.336		9 Sept 2010	14:16 – 15:16	23:06 – 00:04
	43.700 -69.320				
Test Site 2	43.725 -69.336	2.72 km^2	7 July 2010	18:34 – 19:27	22:56 – 23:48
	43.724 -69.306		11 Aug 2010	13:36 – 14:28	21:44 – 22:37
	43.729 -69.336		9 Sept 2010	13:06 – 13:56	22:08 – 22:56
	43.718 -69.307				
Ctrl Site 1	43.744 -69.350	3.71 km^2	7 July 2010	19:54 – 20:58#	23:59 – 01:01
	43.744 -69.327		11 Aug 2010	12:08 – 13:05	00:29 – 01:25
	43.731 -60.345		9 Sept 2010	11:43 – 12:44	21:00 – 22:00
	43.731 -69.325				

*Sampling began after nautical twilight.

#Sampling extended past sunset by 37 minutes.

Figure 1. GIS map of survey transect

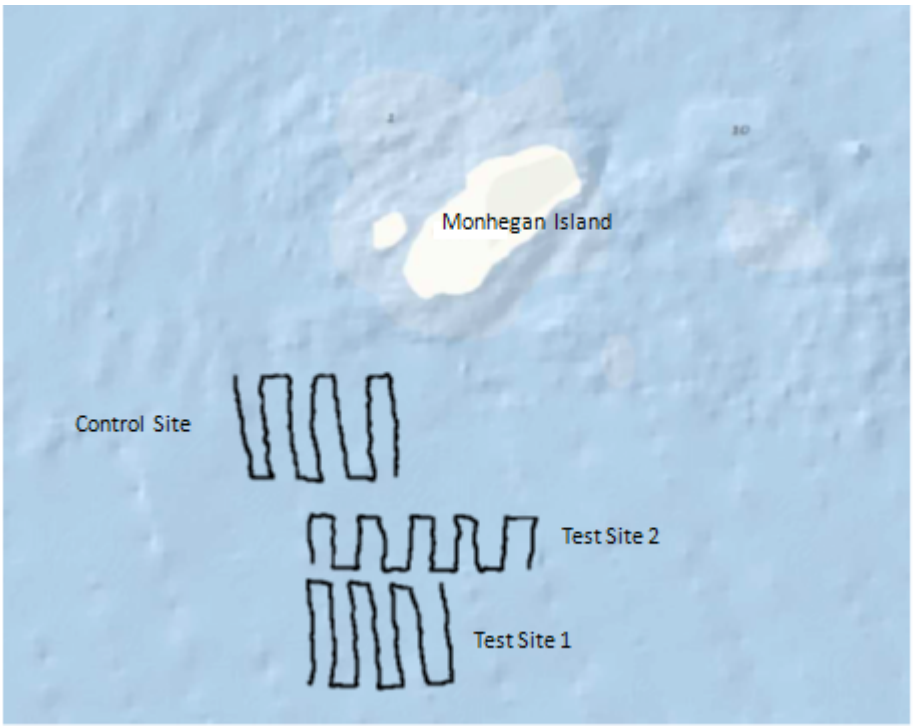

Figure 2. Daytime acoustic survey underway at 7 knots

Figure 3. Mounting of acoustic equipment to survey vessel – F/V Seldom Seen

Figure 4. Relative biomass values (Nautical Area Scattering Coefficient) for all sites in July, August and September.

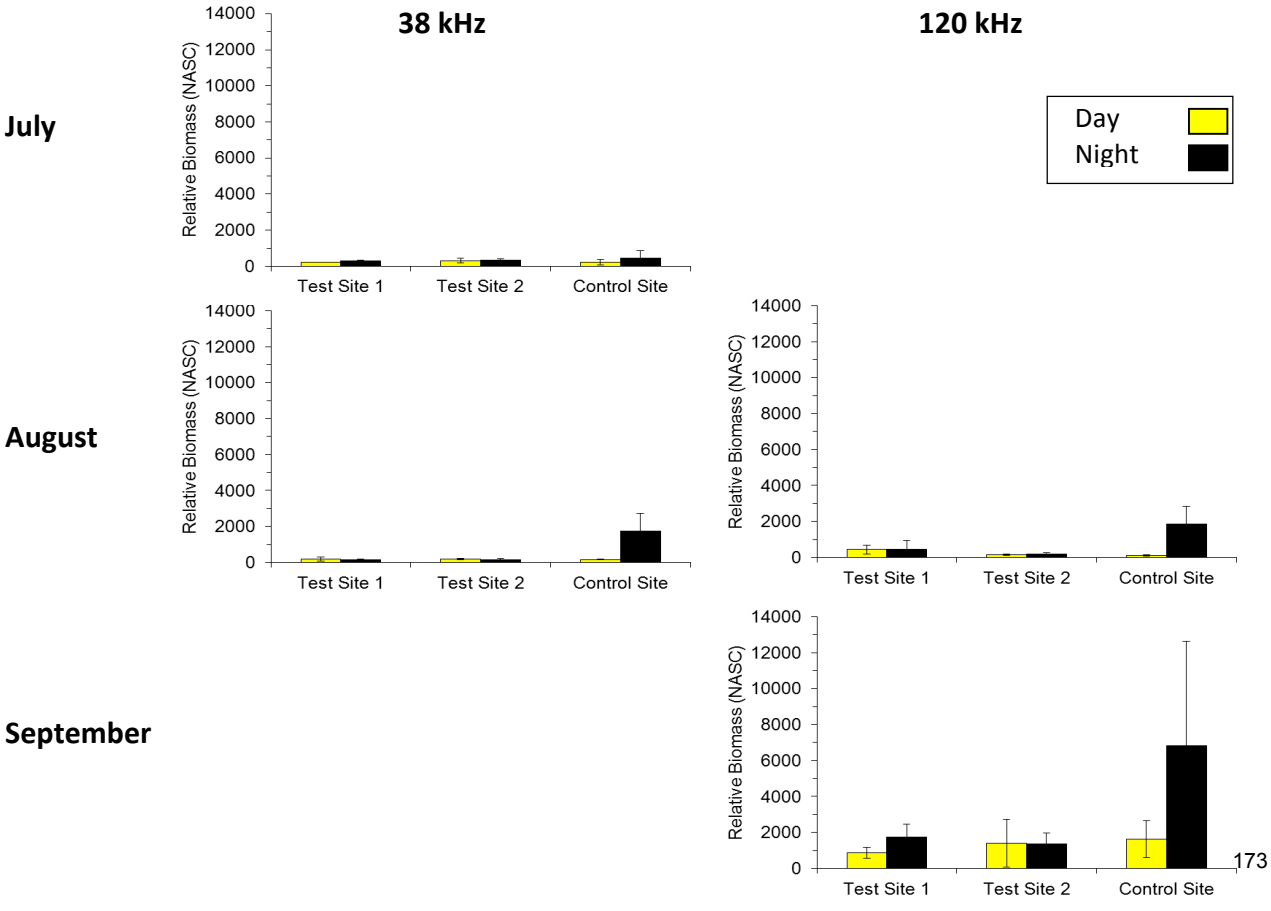

Figure 5. Acoustic data from 120 kHz transducer September 9, 2010, Control site night sampling. Data shows strong scattering around the thermocline (~20m) repetitive blue lines are from interference from other equipment.

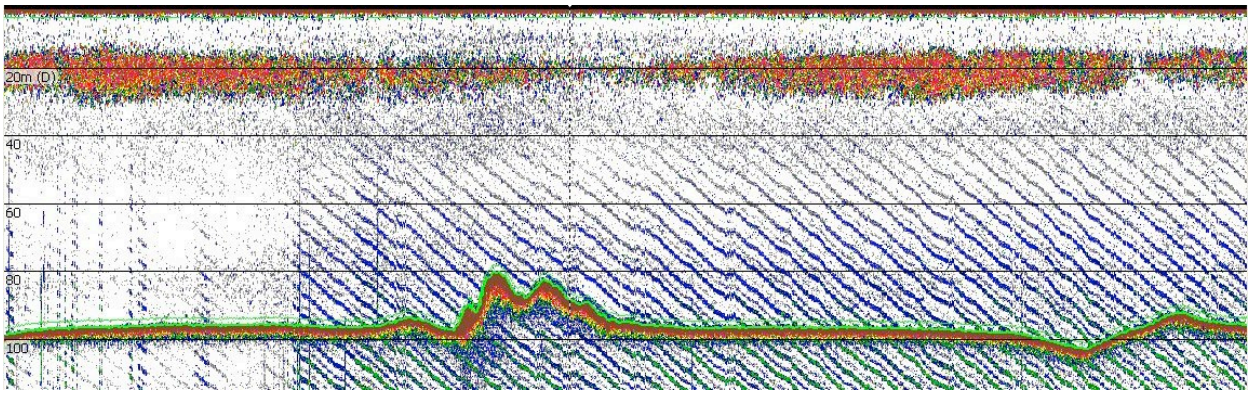

Figure 6. July 38kHz Target Strength values from single target analysis for Test Site 1 (A), Test Site 2 (B), and Control Site (C). Test sites 1 and 2 had no targets identified during daytime sampling.

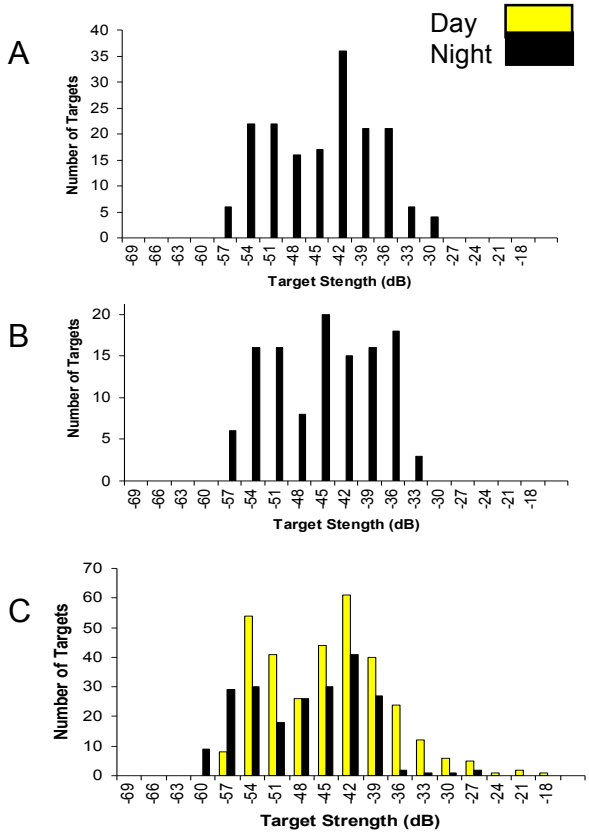

Figure 7. August Target Strength values from single target analysis. Test Site 1 values from 38 kHz (A) and 120 kHz (D), Test Site 2 values from 38 kHz (B) and 120 kHz (E), and Control Site values from 38 kHz (C) and 120 kHz (F).

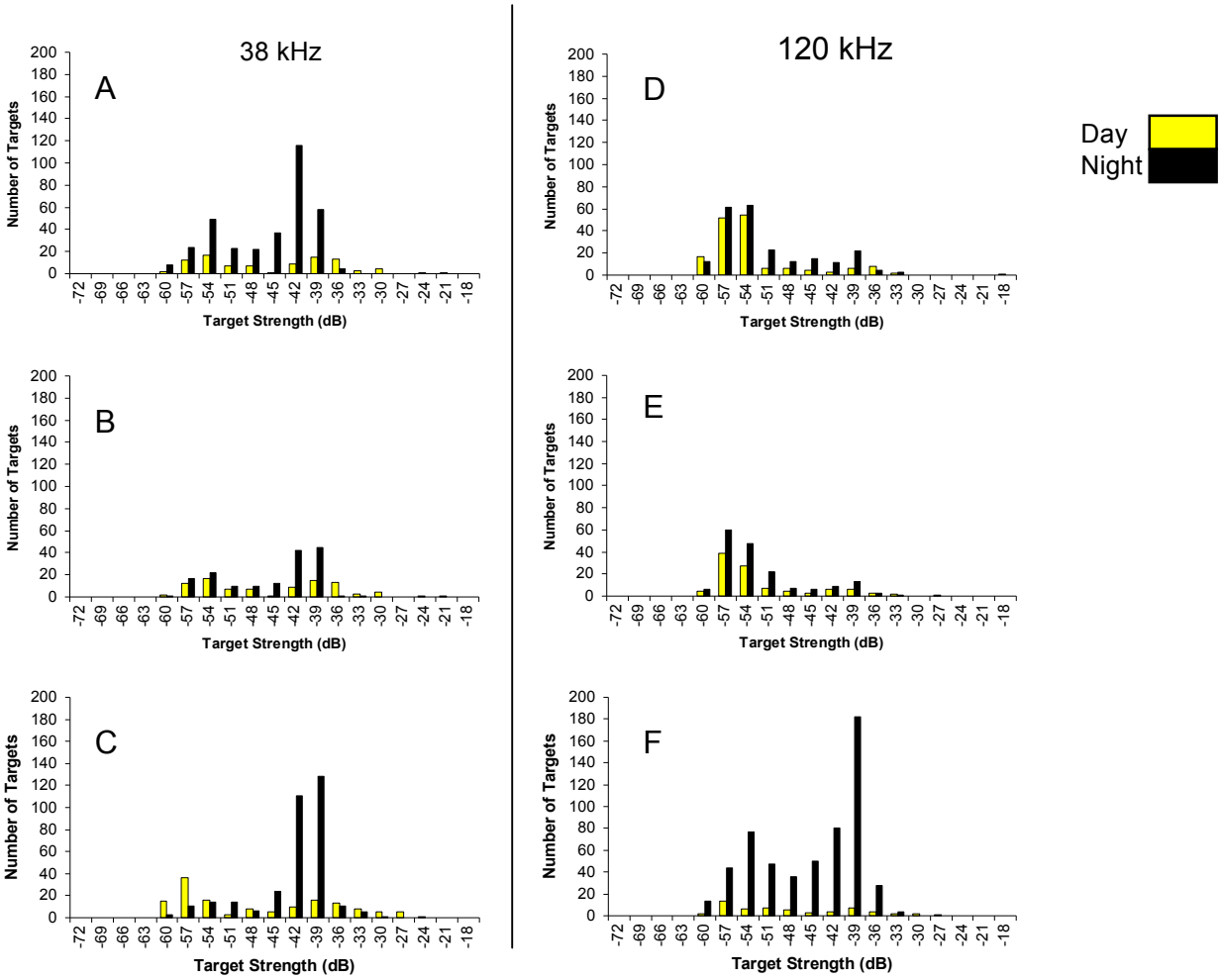

Figure 8. September 120 kHz Target Strength values from single target analysis, for Test Site 1 (A), Test Site 2 (B), and Control Site (C).

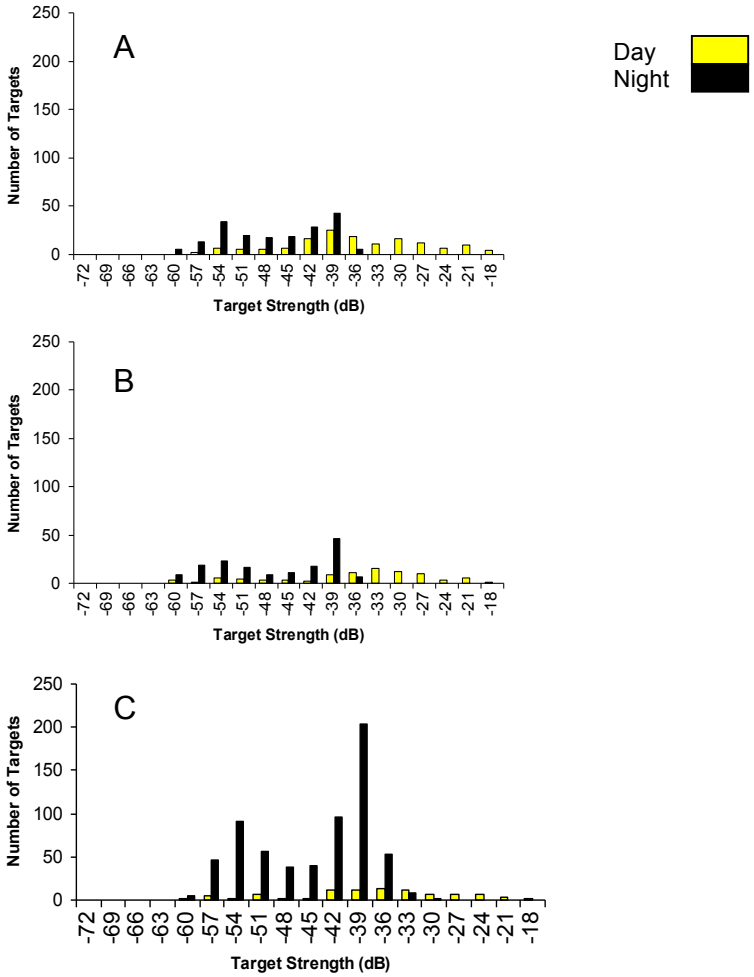

Figure 9. Temperature (solid line) and salinity (dashed line) profiles of Test Site 1 (A), Test Site 2 (B), and Control Site (C) on July 7, 2010.

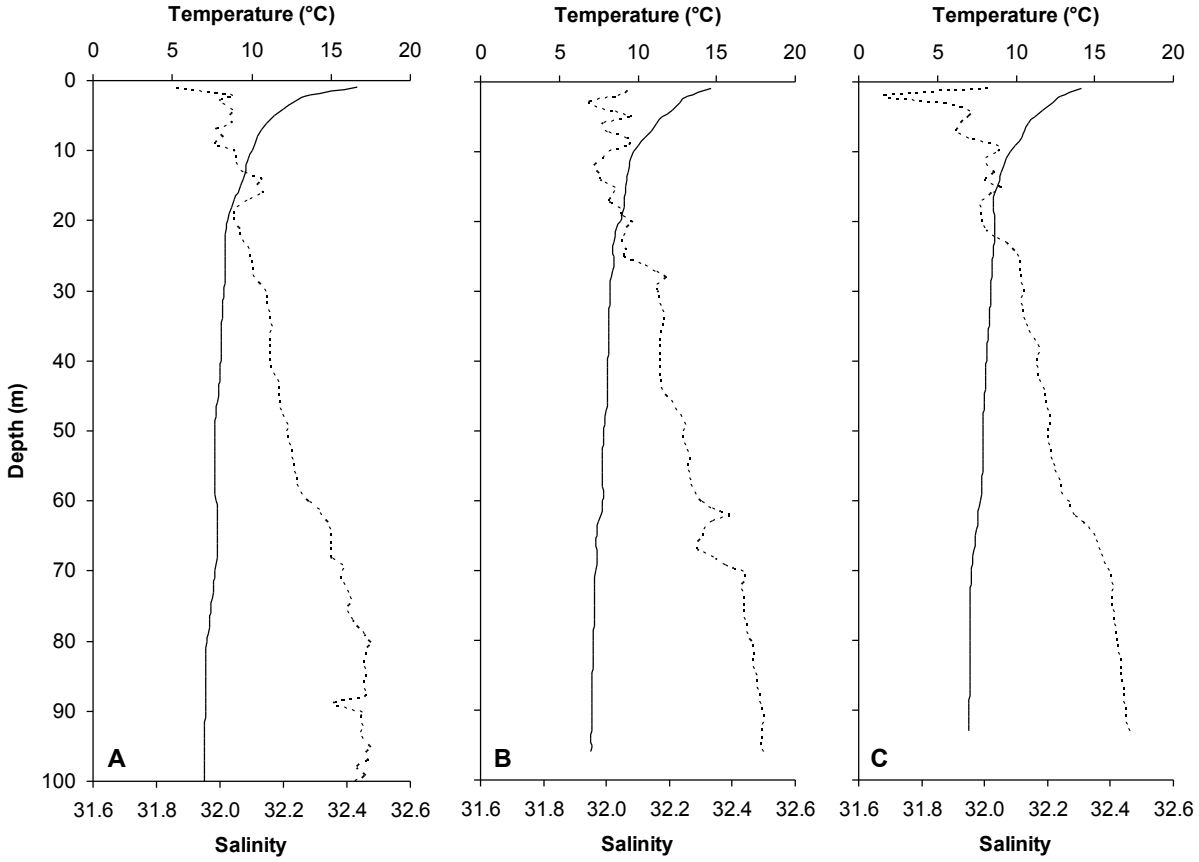

Report on Geophysical Surveys Conducted June through October, 2010
University of Maine Deepwater Offshore Wind Test Site
Offshore Monhegan Island, Maine

Prepared for

DeepCwind Consortium

October 22, 2010

Prepared by

Daniel F. Belknap

Joseph T. Kelley

Alice R. Kelley

Dept. Earth Sciences

Reviewed by:

Melissa Landon Maynard

Dept. Civil & Environmental Engineering

University of Maine - Orono, Maine

Table of Contents

1 Introduction

Digital seismic reflection profiling, sidescan sonar, and multibeam bathymetery data were collected within the bounds of the University of Maine Deepwater Offshore Wind Test Site during 2010. These new data extend the regional data and limited specific coverage discussed in the pre-cruise report (Belknap et al., 2010) on existing 1987 data. Data are archived as digital files in the Triton-Elics (TEI) and standard formats such as SEG-Y, XTF and others. Navigation files are integral to the georeferenced data, but subsequent digitization summaries are listed in x-y-z data bases. The specific lines used as examples in the report below are only examples of the full data set, which remains available in raw and processed forms. Detailed examination of specific stretches of seismic lines or areas of sidescan coverage can be extended as a specific site is selected.

2 Sidescan Sonar Survey

Prior results from the Monhegan area were reported in Kelley and Belknap (1988, 1991), Barnhardt et al., (1996) and the pre-cruise report for this project (Belknap et al., 2010). Those data were collected using methods that differed substantially from those of this project in terms of equipment and navigation, but provide a general framework for interpretation of seafloor imagery.

2.1 Methods

Digital sidescan sonar profiling was conducted from the *R/V Friendship* on June 17 and 18, 2010. The EdgeTech DF2000 fish was towed from the center block of the A-frame at a layback of approximately 39 m, at a speed of 4-5 knots. Sea states varied from choppy and difficult on the morning of June 17, to relatively calm the rest of the cruise. However, the extensive cable layback and ship motion by following swells created a difficult yawing of the towfish. In addition, water-column stratification made automatic bottom tracking extremely problematical.

Data were collected with the Triton-Elics (TEI) topside system, which provides a real-time “waterfall display” of the imagery. Each sidescan ping (1 per second) was electronically tied to a differential global positioning system (DGPS) navigation point for complete georectification on processing. In addition, manual records were logged approximately every 5 minutes for a backup summary navigation file (Appendix A), as shown in Figure 2.1. In the laboratory, lines were

replayed to find the best compromise for the automatic bottom-tracking feature to display a slant-range, along-track and georectified image. Unfortunately, the sea state and water-column stratification forced a combination of fixed-depth and rapid manual readjustments during playback to achieve a reasonable final image. The georectified images were then combined in local examples and an overall mosaic of the UMaine Deepwater Offshore Wind Test Site. The southern two profiles are no longer available, either improperly recorded in the field, or subsequently lost. In spite of these difficulties in creating the mosaic, the native playback lines provide the best imagery for location of artifacts such as cables, shipwrecks, or other unnatural features. A complete scan of the records was conducted to identify the presence of such features.

Sidescan sonar lines were laid out along E-W lines approximately 200 m spacing N-S (Figure 2.1). The scale was set at 200 m to port and starboard, giving theoretical 100% overlap of the mosaic. Data displayed in the overall mosaic emphasize the E-W lines, as the data become severely distorted during short turns. As the survey continued, the intention to concentrate on sedimentary basins rather than continuous bedrock outcrop led to changes in choices for beginning and ending points of lines, in the interest of completing the survey in the time available.

Interpretation of sidescan imagery is based on intensity of backscattered sound, generally shown as gray-scale values, on pixels of 0.25 m square in the native data. Mosaicing requires massive data files, and thus is generally reduced to 1 m resolution or less. The digital corrections for slant range and speed result in a true-scale image similar to a surficial photograph (ideally), such that bedrock structure, rippled sand fields, artifacts, etc. are noticed easily. More subtle are the distinctions among gray scales on relative smooth surfaces that may represent changes from mud (low backscatter), sandy mud (intermediate), sand (medium backscatter) and gravel (high backscatter) on the basis of surface roughness and hardness. It is also possible to image individual cobbles and boulders at the 100 m and 200 m range scales. A second control on backscatter is the angle of the surface toward or away from the towfish, which increases or decreases the reflection intensity. Large objects such as bedrock ridges may give a strong proximal return, but their opposite side is completely acoustically shadowed, giving no return. Sidescan sonar displays may be customized in several ways, but our convention is that a strong return is dark and a low return is light in color, analogous to seismic data. Note that the U.S. Geological Survey (USGS) and other agencies use the "flashlight" convention with reversed

polarity. Finally, interpretation of any sidescan mosaic requires understanding that the sonar source travels along the trackline pinging to port and starboard, with reflections coming back to that centerline. Thus, an object ensonified on alternative passes may switch from “shadowed” to “strong” return depending on the geometry.

2.2 Sidescan Sonar Facies Analysis

Barnhardt et al. (1996, 1998) developed a four-element grid terminology for sidescan sonar units in the inner Gulf of Maine. Those four end members of a square were: Rock, Gravel, Sand and Mud, with sub-unit combinations, such as muddy gravel, gravelly sand, gravelly rock, etc. also shown on the nearshore atlas sheets (Barnhardt et al., 1996). These image interpretations were supported by numerous grab samples, vibracores, ROV and even manned-submersible observations to support the facies assignments. For the purposes of this study, and the limited range of units found at the UMaine Deepwater Offshore Wind Test Site, the mapping was reduced to three simple units: rock (bedrock), sand and gravel, and mud.

BR: bedrock outcrop. This unit is characterized by intense backscatter with more-or-less regularly aligned variations, reflecting individual foliated ridges and swales. The unit is often very sharp edged, and preferentially aligned. The unit is often steep and tall enough to cause complete acoustic shadows behind the peaks.

SG: sand and gravel. This unit is characterized by a medium backscatter intensity, sometimes with individual higher intensity bipolar features (dark proximal and acoustic shadow) consistent with boulders or cobbles. The edges of the unit may be sharp or transitional. In other settings, sedimentary bedforms have been observed in this facies, but these were not seen in the current study.

M: Holocene mud. This unit has a light backscatter intensity, with a uniform texture interrupted only by artifacts such as lobster traps. It has generally transitional contracts with SG, or sharply abuts BR.

2.3 Results

No significant historic or prehistoric artifacts were found in the sidescan sonar survey. There were numerous lines or cables, and individual lobster traps visible in several basins. A more detailed report on cultural and historic will be presented separately after completion of a supplemental magnetometer survey by an outside contractor.

Figure 2.2 is a mosaic at 1 m resolution of the E-W lines in the survey area. Turns have been left off or masked because of the distortions they introduced. Note, however, that some smearing due to yaw and poor bottom tracking remain in the image. Dark mottled patches are bedrock, intermediate backscatter around the bedrock is sand and gravel and the even moderate gray represents Holocene basin mud. The lightest returns are from acoustic shadows as well as data smear caused by yawing of the towfish. Yaw also tends to produce artificially rectangular appearances to the bedrock. The un-interpreted image still provides a general sense of the separation of the UMaine Deepwater Offshore Wind Test Site into numerous small muddy basins interrupted by bedrock ridges generally trending NNE-SSW. This is consistent with the existing bathymetric charts in the area, which were used to initially guide layout of this survey.

Figure 2.3 is an interpretation of the sidescan backscatter imagery, also informed by the seismic data. Note that the SG unit generally surrounds larger groups of bedrock ridges, with few isolated patches. Some bedrock ridges appear to arise abruptly from muddy basins. The muddy basins occur in three types: 1) more-or-less continuous basins hemmed in by parallel bedrock ridges, 2) embayed basins that terminate against sand and gravel basins or bedrock, and 3) a few isolated muddy basins interior to bedrock ridges. The overall complexity of basin and ridge geometry is among the most irregular sites that we have studied in the Gulf of Maine, tempered mainly by the underlying NNE-SSW bedrock structural trend. On the other hand, the consistency of the orientation raises confidence in correlation of seismic reflection profiling transects across lines (N-S).

Figure 2.4 is a more detailed sidescan sonar map over sediment core sites 4 and 5 in the northwestern portion of the site within Basin A. Cores MON-PC-10-04 and MON-PC-10-05 are shown within a relatively broad muddy basin with isolated bedrock outcrops around its edges. Basin A should be considered a prime target for consideration if a smooth muddy basin site is required for wind turbine anchoring.

Figure 2.5 shows a similar detailed sidescan sonar map within Basin B over cores sites 1, 2 and 3 in the west-central portion of the study area. As for Basin A, Basin B is broad and generally continuous between cores 1, 2 and 3, although a few possible small obstructions exist to the NW of core site 3. This too should be considered a prime target area for turbine anchoring.

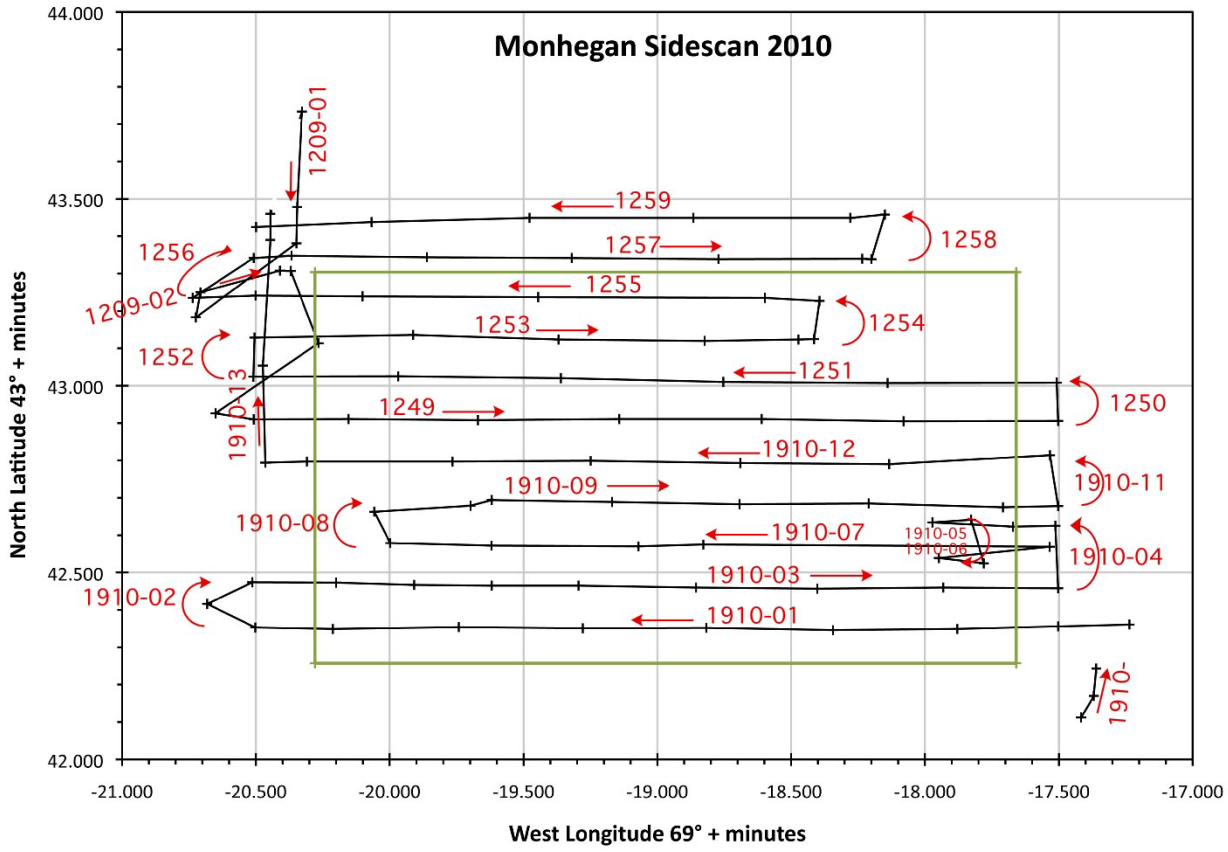

Figure 2.1: Sidescan sonar tracklines, summary navigation points from June 17 - 18, 2010. The green box represents the limits the UMaine Deepwater Offshore Wind Test Site (MDOC 2009). Navigation data are located in Appendix A.

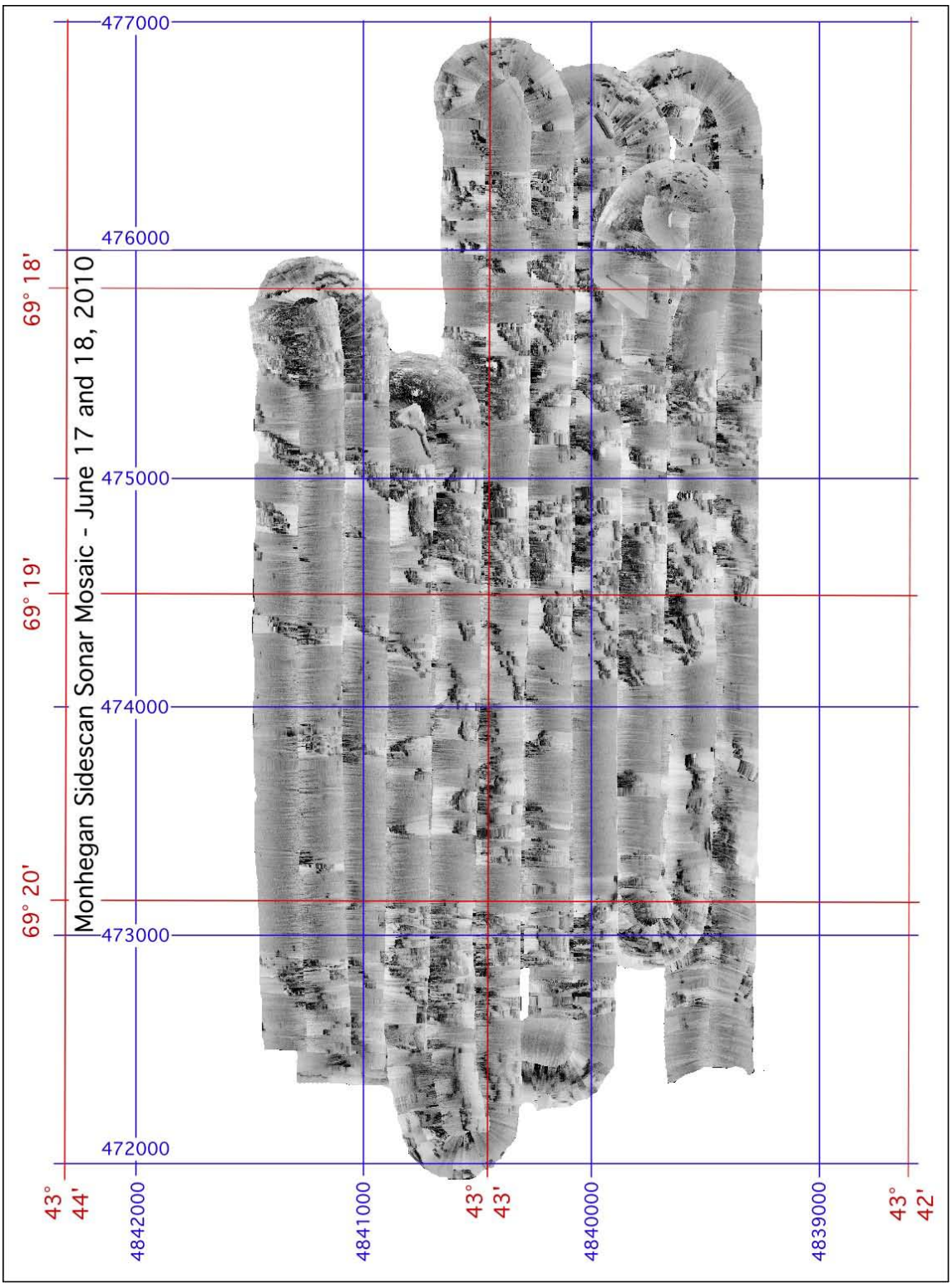

Figure 2.2: Sidescan sonar mosaic over the UMaine Deepwater Offshore Wind Test Site at 1 m resolution. Grids are both latitude – longitude and UTM grid points (WGS 84 datum).

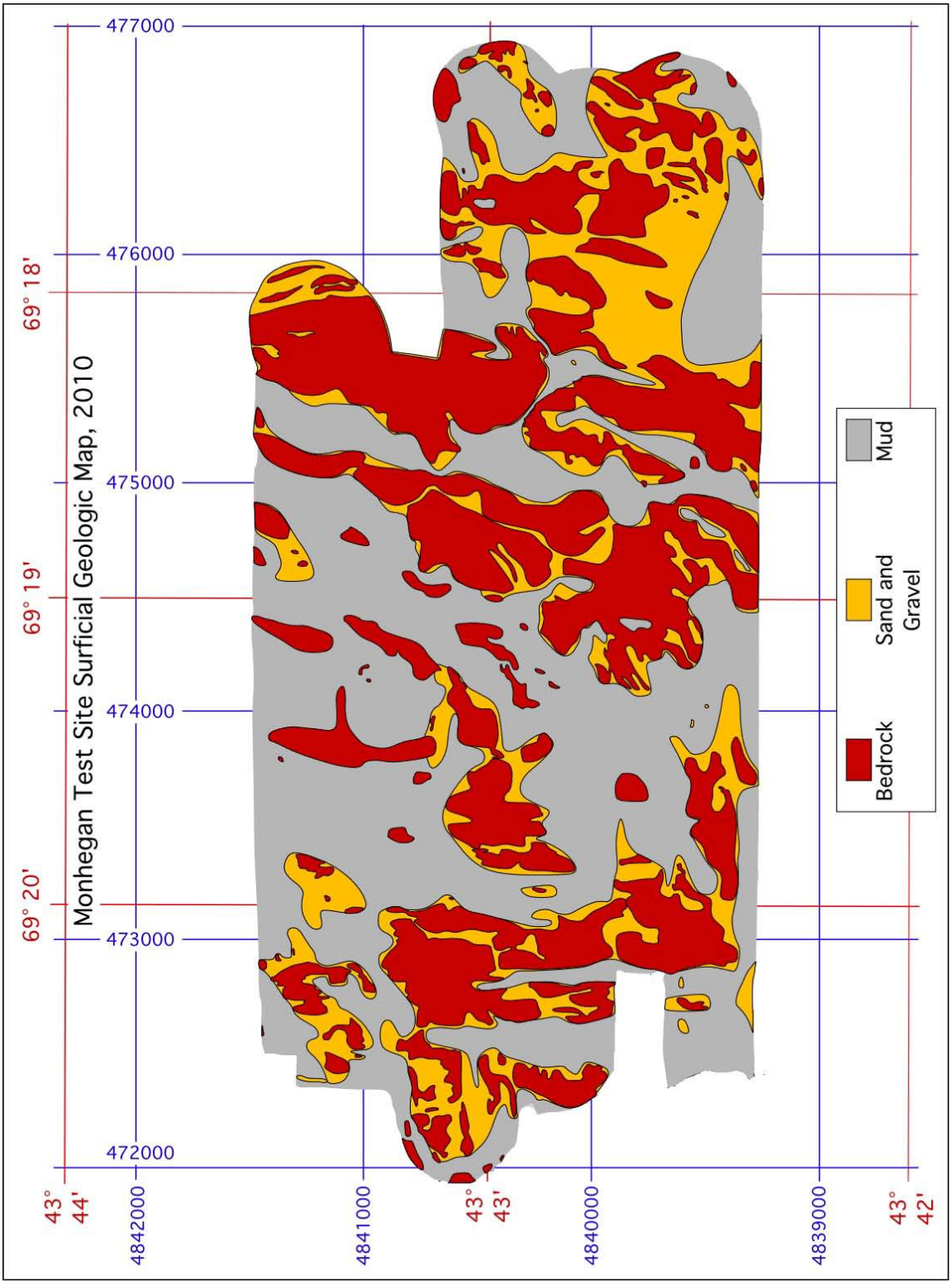

Figure 2.3: Generalized surficial geologic map of the UMaine Deepwater Offshore Wind Test Site based primarily on sidescan sonar mapping.

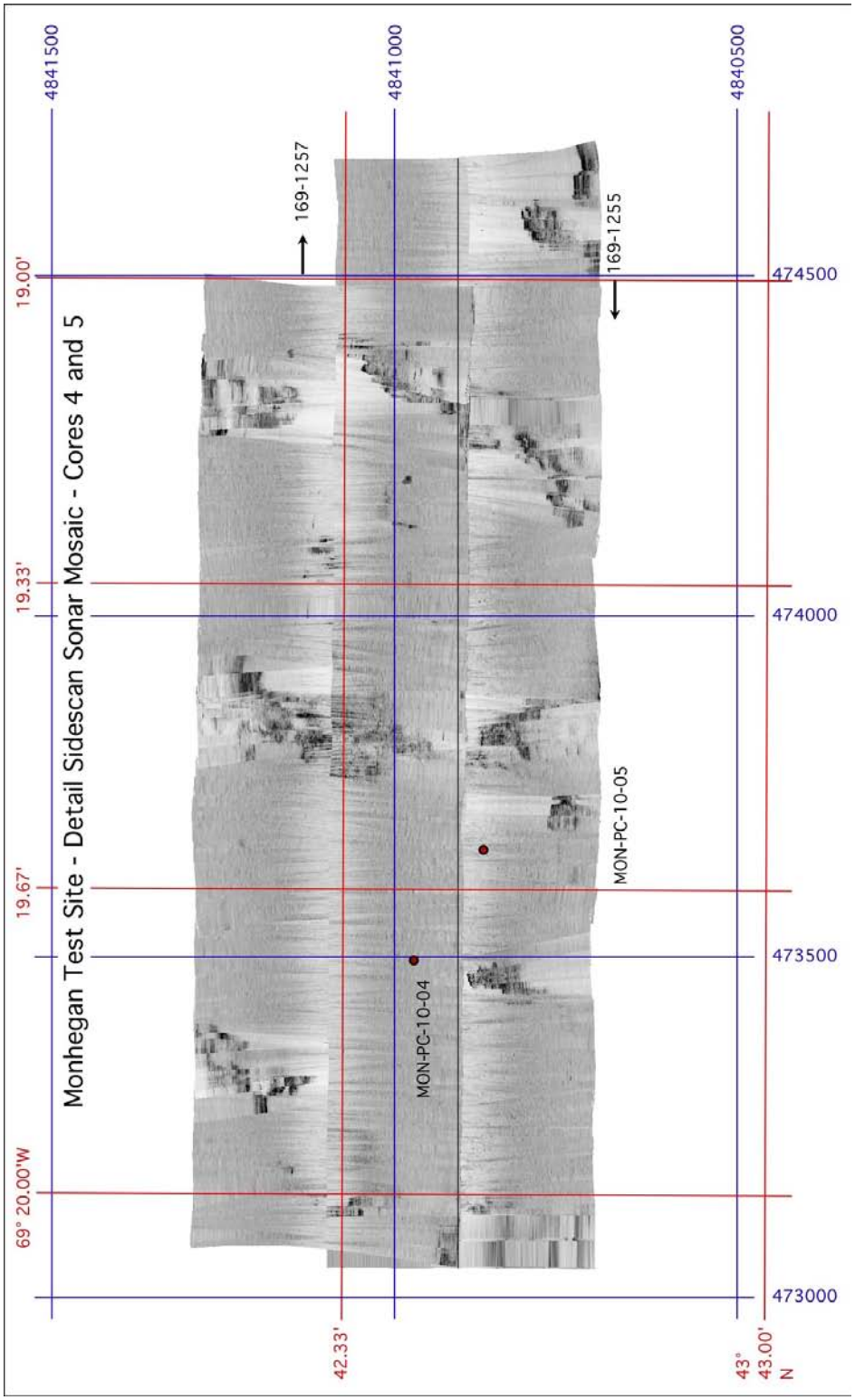

Figure 2.4: Mosaic of portions of sidescan sonar tracks 169-1255 and 169-1257 (the full name of the track includes the Julian day 169 for June 18). Locations of core sites MON-PC-10-04 and 10-05 are shown by the red dots.

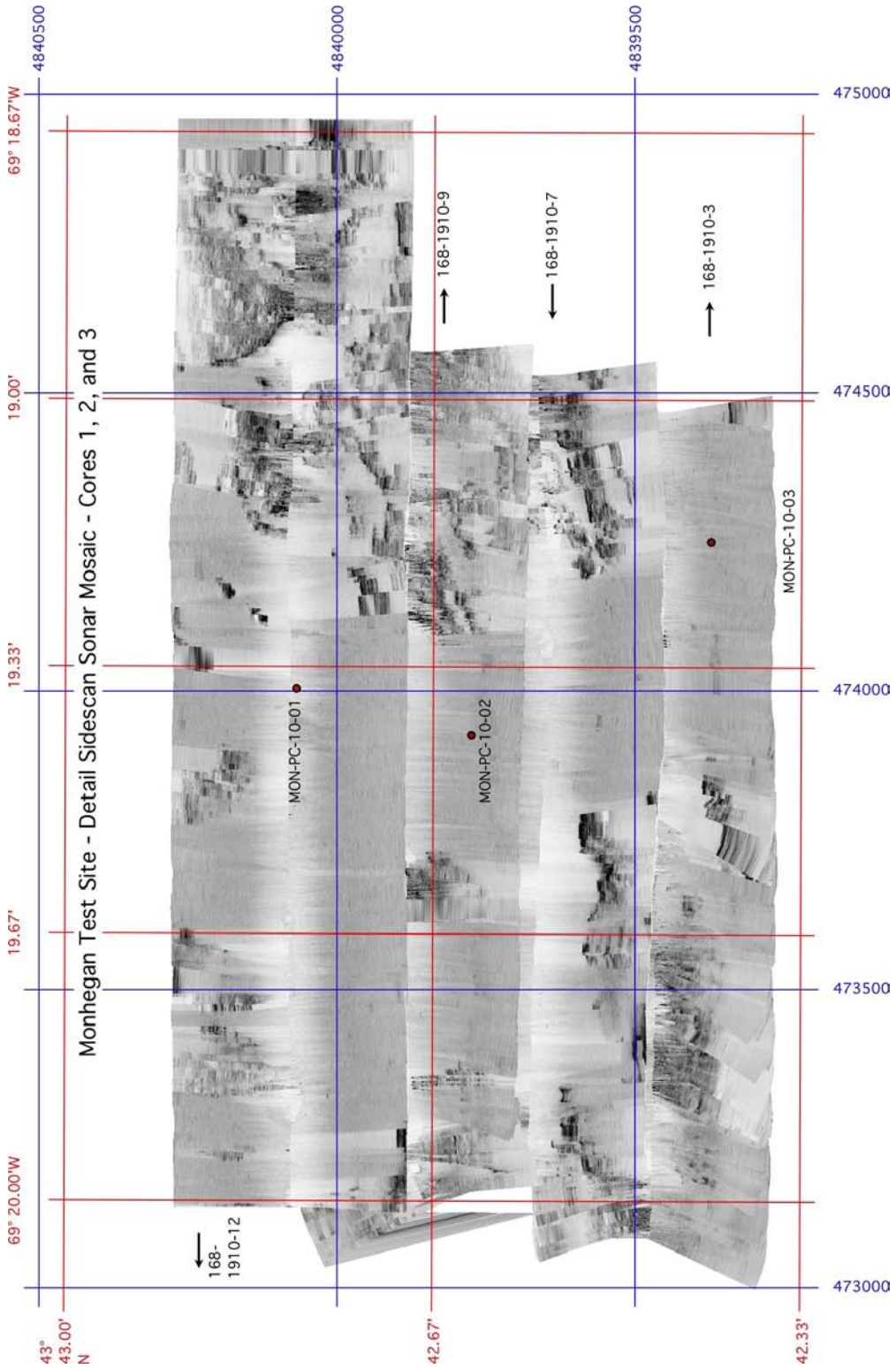

Figure 2.5: Mosaic of portions of sidescan sonar tracks 168-1910-3, 168-1910-7, 168-1910-9 and 168-1910-12 (the full name of the track includes the Julian day 168 for June 17). Locations of core sites MON-PC-10-01, 10-02 and 10-03 are shown by the red dots.

3 Seismic Reflection Profiling

Prior results from the Monhegan area were reported in Kelley and Belknap (1991) and the pre-cruise report for this project (Belknap et al., 2010). Those data were collected using methods similar to the present cruise, with the major difference that navigation was by Loran-C, and thus not directly comparable to the new data set. However, seismic stratigraphy is identical, and the regional trends identified by Belknap et al. (2010) have been confirmed in detail.

3.1 Methods

Digital seismic reflection profiling was conducted from the *R/V Friendship* on June 15 and 16, 2010, and supplementary lines associated with coring from the *R/V ARGO Maine* on July 7 and 8, 2010. The single-beam seismic reflection system source was an Applied Acoustics Engineering (AAE) "boomer" with peak acoustic power at 1.5 kHz, powered at 105 Joules, firing every 0.25 seconds. The two-way travel time of the source sound at a velocity of 1500 m/s corresponds to a total water depth and sediment thickness of 187.5 m. This provides an appropriate compromise of resolution and penetration in the expected water depths and sediment thicknesses, based on decades of prior experience in the Maine nearshore (e.g., Belknap and Shipp, 1991; Kelley and Belknap 1991; Barnhardt et al., 1997). Adjustments for increased acoustic velocity in sediments can be made after measurements from core samples, but this is not generally necessary for the Holocene and glaciomarine muds (Belknap and Shipp, 1991). The boomer was towed on a catamaran float at the water surface several meters outside of the vessel wake.

Reflections were received by a 20-element AAE hydrophone, and digitized and amplified by the TEI topside system. The hydrophone was towed 0-0.5 m below the surface at the same distance behind the ship as the catamaran on the opposite side of the wake and at a spacing of 5-7 m. Seismic shots (4 per second) were automatically matched with DGPS navigation data for sub-5 m positioning accuracy. As with the sidescan data, supplementary manual navigation notes were kept approximately every 5 minutes (Appendix A). A raw readout available at collection time and as the base playback record provided guidance for adjustments to deployment and tracklines. Filtering was adjusted to 600-2400 Hz for this project. The data were then replayed in the laboratory to create a georectified profile of seismic reflection 2-way travel time versus horizontal distance traveled. Subsequent analysis included digitization of the bathymetric surface within the TEI software, and export of the line image for manual interpretation in a graphics

program (Canvas10). Digitized x, y, z data were subsequently corrected for tidal variation (Appendix B). No Pythagorean correction for towing geometry was thought to be necessary in the 60-100 m water depth (a few decimeters at most). All lines were georectified, except short inter-line turns, which often are compromised by changing towing geometry. Lines across subsequent cores sites were interpreted for the purposes of this report.

Conditions during seismic profiling were optimal for equipment performance in terms of weather and sea state for the majority of the cruise, resulting in clear records. A few internal problems in the TEI topside system hardware and/or software resulted in short-term glitches, resulting in the irregular auto-numbering system of lines (e.g., 10-10-9 followed by 10-11, etc.) and a few time gaps. However, there is near full areal coverage of the UMaine Deepwater Offshore Wind Test Site. Seismic lines were laid out E-W at a spacing approximately 100 m apart N-S, with supplementary lines diagonally across encountered basins, and to tie in proposed sediment coring locations (Figure 3.1).

3.2 Seismic Facies Analysis

Seismic facies are defined on the basis of intensity of acoustic impedance contrast at surfaces, character and geometry of internal reflectors, geometry of external shape, and stratigraphic position (e.g., Mitchum et al., 1977a; 1977b). This seismic facies analysis then is placed in the context of seismic stratigraphy, to reconstruct the sequence of depositional and erosional events within a basin or a region. Ground-truthing of interpretations is based on outcrops, grab samples, cores, and in the case of the Maine case, several dozen submersible and SCUBA dives. The seismic facies and stratigraphy for coastal Maine were worked out in detail by Belknap et al. (1987, 1989), Belknap and Shipp (1991), Kelley and Belknap (1991), and Barnhardt et al. (1997). Offshore Gulf of Maine units have similar glacial and post-glacial facies, and a wealth of deep core information (Bacchus, 1993; Bacchus and Belknap, 1997; Schnitker et al., 2001). The descriptions that follow are based on those publications and our later refinements of observations in the region. New data collected in 2010 are consistent with existing seismic facies models.

BR: Seismic facies BR is identified by strong acoustic contrast at the surface with a highly variable external geometry and no coherent internal reflectors. Numerous hyperbolic returns near the surface indicate point source or sharp reflections. Apparent internal reflections are actually side echoes, especially evident in deeper water. BR is always the stratigraphically lowest unit.

The interpretation of BR is **bedrock,** as confirmed at shorelines and submerged outcrops (submersible and remotely operated vehicle [ROV]) and the distinct images of foliation and structure present on sidescan sonar images.

T: Seismic facies T is identified by strong acoustic contrast at the surface, with a hummocky or mounded external geometry. Internal reflections are chaotic or weakly layered. T overlies BR, along a contact that may have low contrast, and in fact may be difficult to discern. T is interpreted as **till**, as confirmed by direct and sidescan sonar imaging of dense matrix and abundant cobbles and boulders. Till occurs either as a widespread thin (several meters thick) cover or as distinct individual moraines up to 10-20 m thick.

GM-P: Seismic facies GM-P is a well-stratified unit with moderate surface contrast, and a distinctly conformable, draping geometry. Internal reflections are more or less parallel, and may correlate for hundreds of meters. GM-P overlies either T or BR and is up to 10-15 m thick in the study area. GM-P is interpreted as **glaciomarine mud, proximal** to original glacial sources. Offshore cores and coastal bluff outcrops demonstrate that GM-P is a mix of moderately stiff mud with variable sand and even gravel layers (Schnitker et al., 2001), with water contents from 15 to 20 percent wet weight. This unit was deposited immediately as the Laurentide ice was retreating from the coast ca. 16 cal. ka (i.e, circa 16 calibrated thousand years before present), in a deep pro-glacial marine setting with rapid deposition rates.

Reflector α is the contact between GM-P and GM-D. It usually has moderate acoustic contrast and separates the well-stratified GM-P from the more weakly stratified GM-D. Reflector α is conformable (i.e., strata parallel without interruption), and is interpreted as a relatively abrupt change in pro-glacial marine environments without erosion or break in sedimentation. It may correspond with a change from a calving ice front nearby to later terrestrially ground ice with meltwater streams leading to the adjacent ocean, ca. 15-14 cal. ka.

GM-D: Seismic facies GM-D is a moderately to weakly stratified unit with moderate to weak acoustic contrast at its surface in shallow water, or a more gradual disconformable surface in present water depths greater than 60 m. GM-D overlies GM-P or deeper units in a draping geometry that is modified by some ponding in paleo-depressions and thinning over paleo-shoals. GM-D is up to 20 m thick in the study area. GM-D is interpreted as glaciomarine mud, distal to glacial sources, and not necessarily in direct contact with floating glacial ice, ca. 14-12.5 cal. ka. The ponded geometry reflects a slower accumulation rate and more reworking by waves and

currents (e.g., Piper et al., 1993; Shipp, 1989; Belknap et al., 1987b, 1989). Offshore cores and coastal outcrops reveal a mud (silt plus clay) composition with up to several percent of sand both dispersed and in millimeter-thick layers. Water content is 40 to 50 percent wet weight, and the plastic mud may stiffen only gradually with depth.

Reflector β is the contact between GM-D and overlying M or other units. In water shallower than 60 m present water depth, this reflector is distinct and may manifest as an angular unconformity (Belknap and Shipp, 1991, Fig. 10). In water deeper than 60-70 m, Reflector β is conformable with a gradual change in acoustic contrast and degree of stratification (Belknap and Shipp, 1991, Fig. 11). When near the sediment surface, "ringing" acoustic artifacts and other noise may obscure this interface. Placement of this interface with seismic data alone is sometimes challenging, and even in cores may be seen only as a gradual change in water content or sediment texture. The significance of the depth control is that local relative sea level, which was constrained by both isostatic rebound and eustatic changes, reached a lowstand at 60-65 m ca. 12.5 cal ka (Belknap et al., 1987a; Barnhardt et al., 1995; Belknap et al., 2002). Above this level, littoral and terrestrial erosion removed earlier deposits and incised paleo-valleys into the glaciomarine mud and allowed dewatering, compaction and oxidation. Below present water depths of 60-70 m, deposition was more-or-less continuous.

M: Seismic facies M is weakly to non-stratified with a moderate to weak acoustic contrast at the modern seafloor. Facies M is ponded in basins directly over Reflector β or may slightly drape bedrock and other units. Facies M may be "moated" around bedrock and till highs, indicating shear stress that prevents deposition or creates erosion. Seismic facies M is interpreted as Holocene (last 11.5 thousand calendar years) marine **mud** in the study area, although estuarine mud found in nearshore embayments has an identical character. This interpretation is confirmed by sidescan sonar, coring, bottom sampling, and direct observations. Marine and estuarine muds in the region contain 50% to greater than 70% water by wet weight, and in coring studies demonstrate a very loosely consolidated material in the top several decimeters to a plastic mud gradually stiffening with depth that gives firm resistance when cutting cores with a knife.

SG: Seismic facies SG is strongly reflecting and variable in stratification. It occurs in two geometries: either a thin blanket surface lag on GM and other units, or wedge-shaped units interfingering with T and GM (Belknap and Shipp, 1991, Fig. 7). Facies SG is not extensive in

the study area. Facies SG is interpreted as sand and gravel on the basis of grab samples and cores, sonar imagery of a darker but smooth or wave-rippled surface, and direct observation.

NG: Seismic facies NG has a strong but diffuse surface acoustic impedance contrast, and no internal stratification. It often exhibits a convex up or flat-topped geometry with sides that spread as sections of hyperbolae. It obscures deeper units either partially or completely, and inhibits multiples. Unlike the stratified sedimentary facies described above, NG cross-cuts earlier stratification, but the top is most common at the base of M (or possibly the top of GM-D) in the deep basins around Monhegan Island. Seismic facies NG is interpreted as **natural gas** bubbles that create an acoustically turbid curtain that disperses initial seismic pulses and obscures deeper reflectors. NG has been sampled in cores in other locations where the methane gas composition has been confirmed by ignition. The methane is probably sourced by beds of organic-rich sediments in deeper basins above Reflector β (e.g., Rogers et al., 2006). Reaction of natural gas pockets to disturbances is unpredictable, but definitely a geohazard well understood in the petroleum industry, and implicated in the formation of large fields of pockmarks (craters) in Maine embayments.

The seismic facies are presented on the diagrams that follow in a consistent color scheme and geometry, as shown in the legend, Figure 3.2. Also noted are water-bottom multiples in some lines that can be distracting. However, water depth here is such that they are always below the basins of interest. In addition to the main facies color, a few interpretive lines are shown in blue for major reflectors within the GM-P and GM-D facies. These may represent times of change in sediment type (sand or gravel layers in a generally muddy matrix), or short-term hiatuses and erosion in a sedimentary sequence. These additional reflector lines are not comprehensive, but representative of a wealth of details too fine to present in the summary diagram.

3.3 Results

A series of tracklines from north to south across the study area (Figure 3.1) demonstrates seismic stratigraphy and basin geometry. The major tracklines are tied to vibracores and box cores collected in July, 2010. The expectation is that these are likely areas for anchoring. They are not unique, but in fact demonstrate a consistent stratigraphy and geometry that is found in most of the tracklines. The basins are generally small and interspersed among bedrock outcrops that generally trend NNE-SSW. All seismic line interpretations are presented in a similar layout,

with georectified distance along the x-axis, 2-way travel time in milliseconds on the right axis, and depth below water surface in meters, assuming 1500 m/s seismic velocity, and not corrected for tidal elevation. Data were adjusted to a consisted 8x vertical exaggeration maintained throughout this report, to simplify comparison of lines. Note the consistent exaggeration results in variable track lengths. Raw data are presented above, and a colored interpretation (leaving out much of the water column) is shown below. The abbreviations and colors correspond to the legend shown in Figure 3.2.

Line MONHEG-10-06-0 crosses piston core site MON-PC-10-4 in Basin A (Figure 3.3). Bedrock crops out along much of the line, but Basin A is underlain by glaciomarine mud up to 25 m thick, and Holocene shelf mud up to 5 m thick. At this water depth, below the local post-glacial lowstand depth, the disconformity (reflector β) is subtle and subject to alternate interpretations. The same goes for all the profiles presented in this report. The disconformity (reflector α) between GM-P and GM-D is generally sharp and distinguished by transition from a strongly draped, even thickness below to a more ponded geometry above. This is interpreted as a decrease in sedimentation rates and trend to less of a blanketed drape to more basin-focused accumulation. Total sediment thickness in the center of the basin, just west of the core site, approaches 30 m.

A more detailed view of the core site is provided in Figure 3.4. This is an extract of the same data as in Figure 3.3, but showing a close-up on Basin A.

Each of the next four profiles show overall geometry and seismic stratigraphy similar to Figure 3.3, differing only in detail from the first. MONHEG-10-06-2 crosses piston core site MON-PC-10-05 (Figure 3.5), with up to 13 m of glaciomarine mud and 4 m of Holocene mud in the basin (Figure 3.6). A new component of the stratigraphy is thin till above the bedrock at the base of the basins.

Seismic line MONHEG-10-12-2 crosses piston core site MON-PC-10-01 in Basin B (Figure 3.7). The stratigraphy is the same as MONHEG-10-06-2 including a broader blanket of till at the base of the basin. Basin B is more complexly segmented than appears on the smooth muddy surface. The sediment fill is a maximum 17 m of glaciomarine and 4 m of Holocene mud over the till (Figure 3.8). This thickest section is within 100 m east of the piston core site.

Seismic line MONHEG-10-11-2 crosses piston core site MON-PC-10-02 in the central part of Basin B (Figure 3.9). New stratigraphic components include a lag of sand and gravel on the

bedrock peaks at the eastern end of the profile, as well as a small plume of natural gas interpreted in the center of the small eastern basin. At the site of PC-10-02, Basin B is relatively shallow, and the core may sample deeper into the glaciomarine mud (Figure 3.10). The glaciomarine mud is 12 to 16 m thick, and the Holocene mud is less than 4 m thick.

Seismic line MONHEG-10-10-3 crosses piston core site MON-PC-10-03 in the southern portion of Basin B (Figure 3.11). Similar to previous lines, Basin B appears to contain a larger plume of natural gas near its deepest point. An alternate explanation would be a side-echo off of a bedrock ridge out of the plane of the profile, especially since there appears to be little masking of underlying units. This portion of Basin B (Figure 3.12) contains over 30 m of glaciomarine mud and 4 m of Holocene mud at its deepest point 50 m W of piston core PC-10-03.

It is useful to compare these cored basins along alternate directions, to check for continuity of the basins and consistency of stratigraphic correlation. North-south and diagonal lines were collected in final preparation for piston and box coring, and these lines provide the comparisons. Figure 3.13 depicts seismic line MONHEG-10-13-3, which passes through the three southern piston cores sites, PC-10-01, 02, and 03. This line confirms that Basin B is more-or-less continuous in a N-S direction, however bedrock basement depth and thus basin fill thickness varies considerably. This also represents the largest continuous basin wholly within the confines of the survey area. North-south seismic line MONHEG-10-14-1 (Figure 3.14) passes over MON-PC-10-05, and approximately 190 m east of MON-PC-10-04. This crossing line shows a setting for Basin A similar to that of Basin B, but the two piston cores are nearer to the southern end of the basin than its center.

Compilation of all the seismic lines to identify basins (Appendix C) resulted in a map of edges and deepest centers of the basins across the study area (Figure 3.15). Comparison of these mapped basins with the surficial geologic map shows a clear correlation of the stratigraphically deep basins with the broad muddy expanses at the sea floor. Interpolation between seismic lines spaced only 100 m apart is clearly justified by this three-dimensional arrangement, and confirmed in the cases where N-S and diagonal crossing lines are available to check the correlation. Nevertheless, the complexity of the bedrock configuration and rapid lateral changes in stratigraphic thicknesses suggest caution in placement of anchors in locations tests not directly imaged with the seismic profiles.

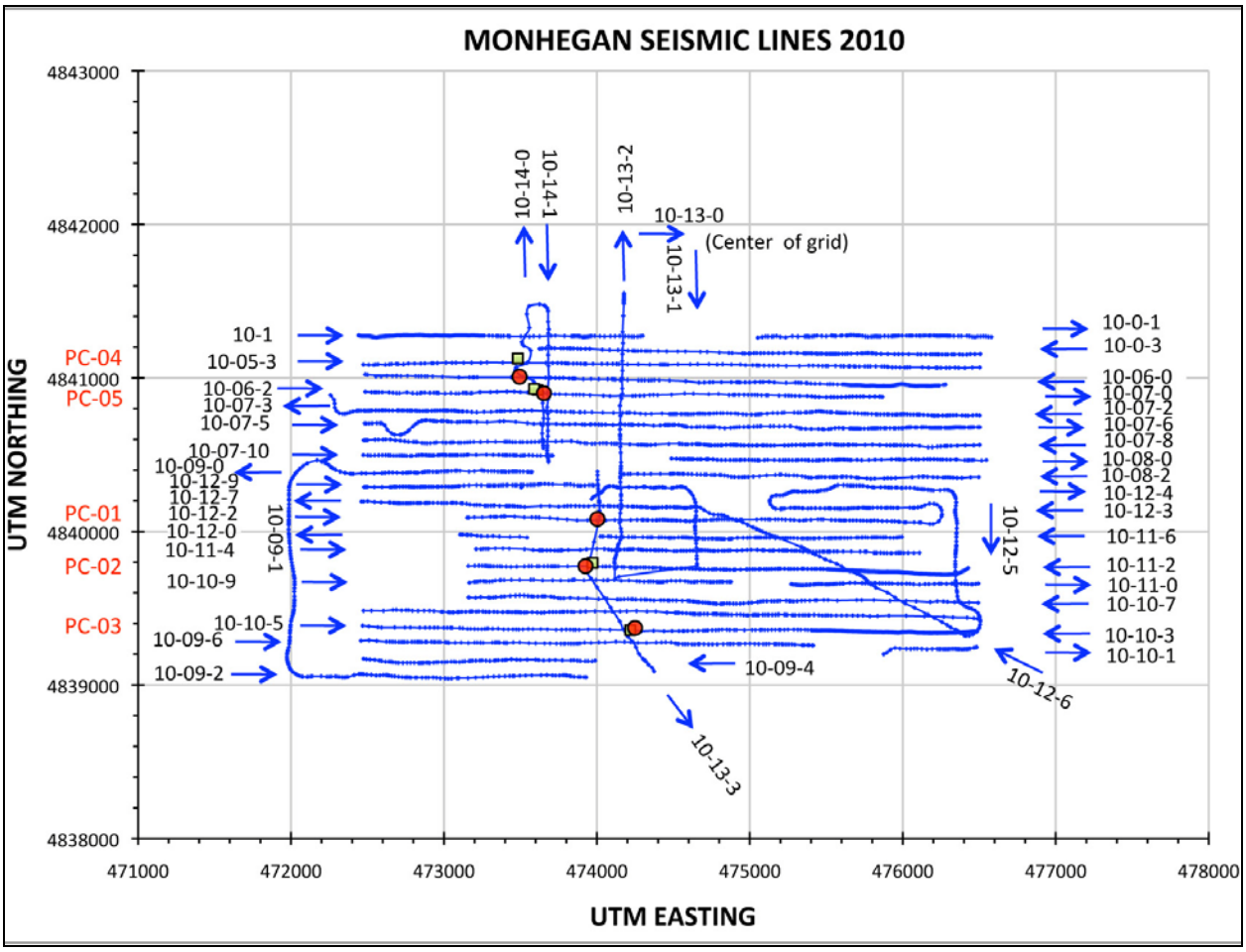

Figure 3.1: Seismic reflection profiles from the UMaine Deepwater Offshore Wind Test Site, June 15 - 16, 2010, and during the coring cruise July 7-8, 2010 (lines 10-13-3, 10-14-0 and 10-14-1). Most short turns are numbered, but not shown. The complicated line numbering is from an automatic software incrementation and some irregular data holidays. Line directions are indicated by blue arrows. The five piston core (red dot) and four box core (green square) locations are also shown (Appendix A).

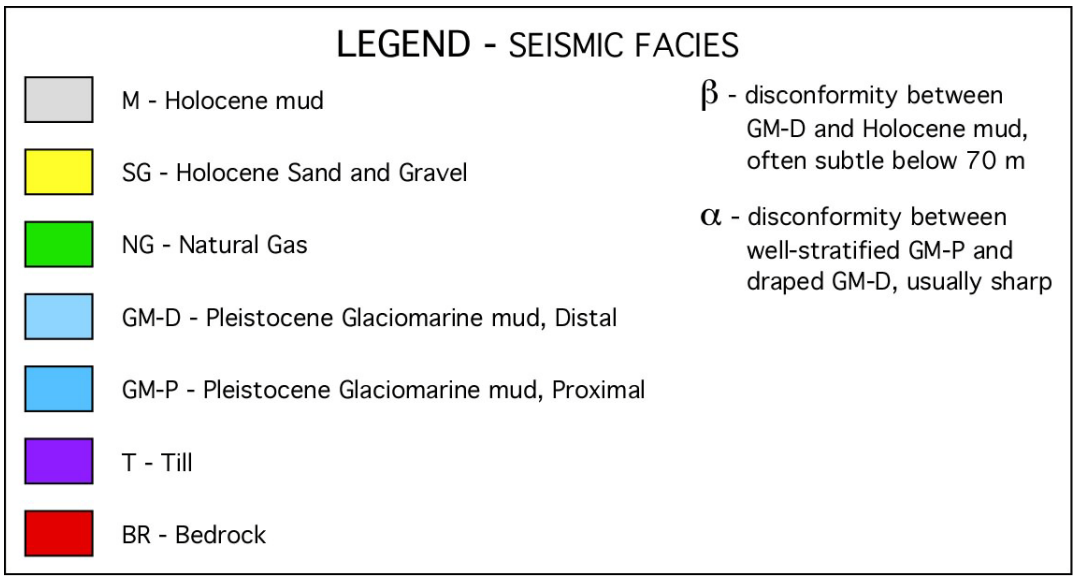

Figure 3.2: Legend for use with seismic reflection profiles.

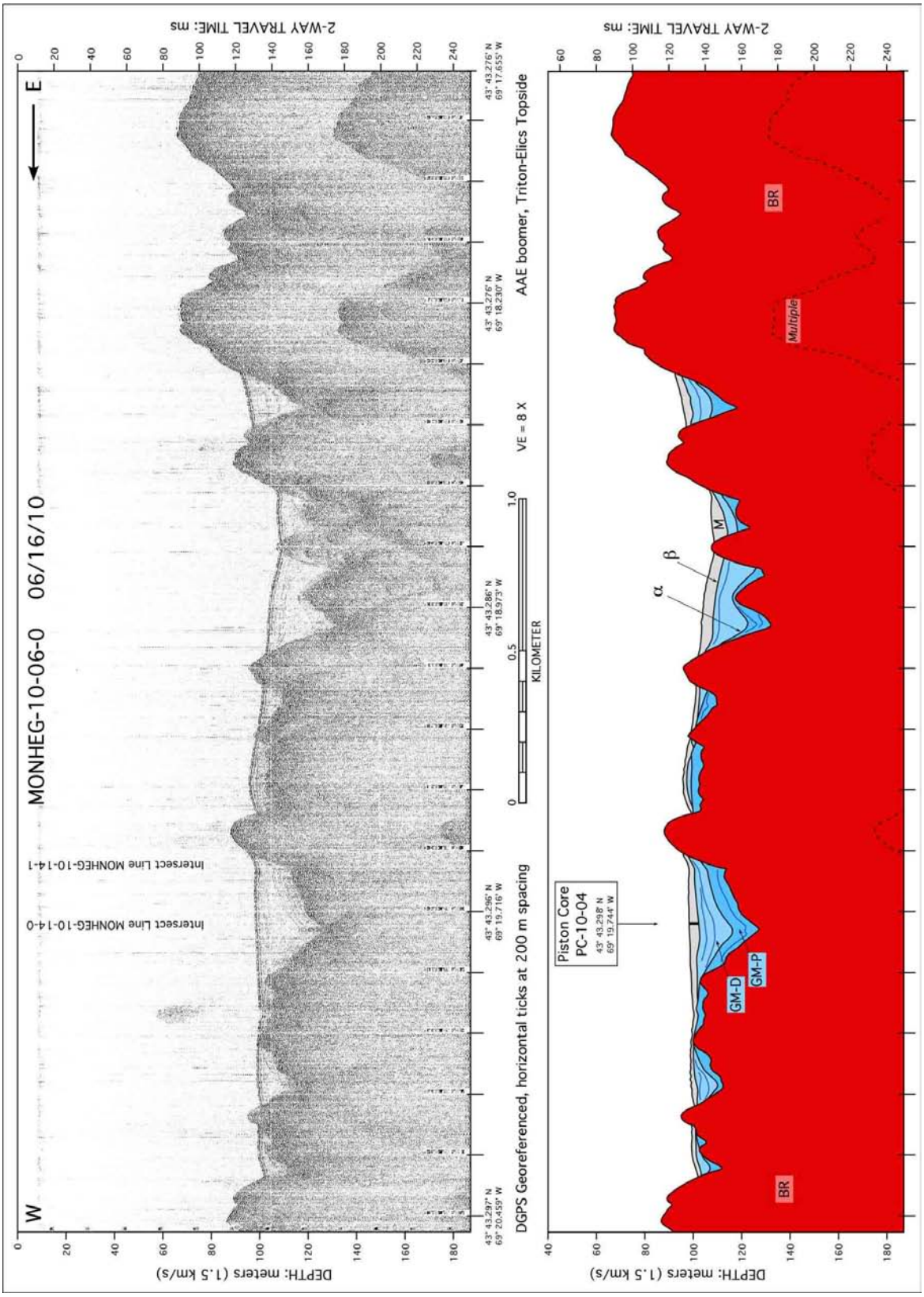

Figure 3.3: Seismic reflection profile MONHEG-10-06-0, crossing core site 10-04 (Basin A).

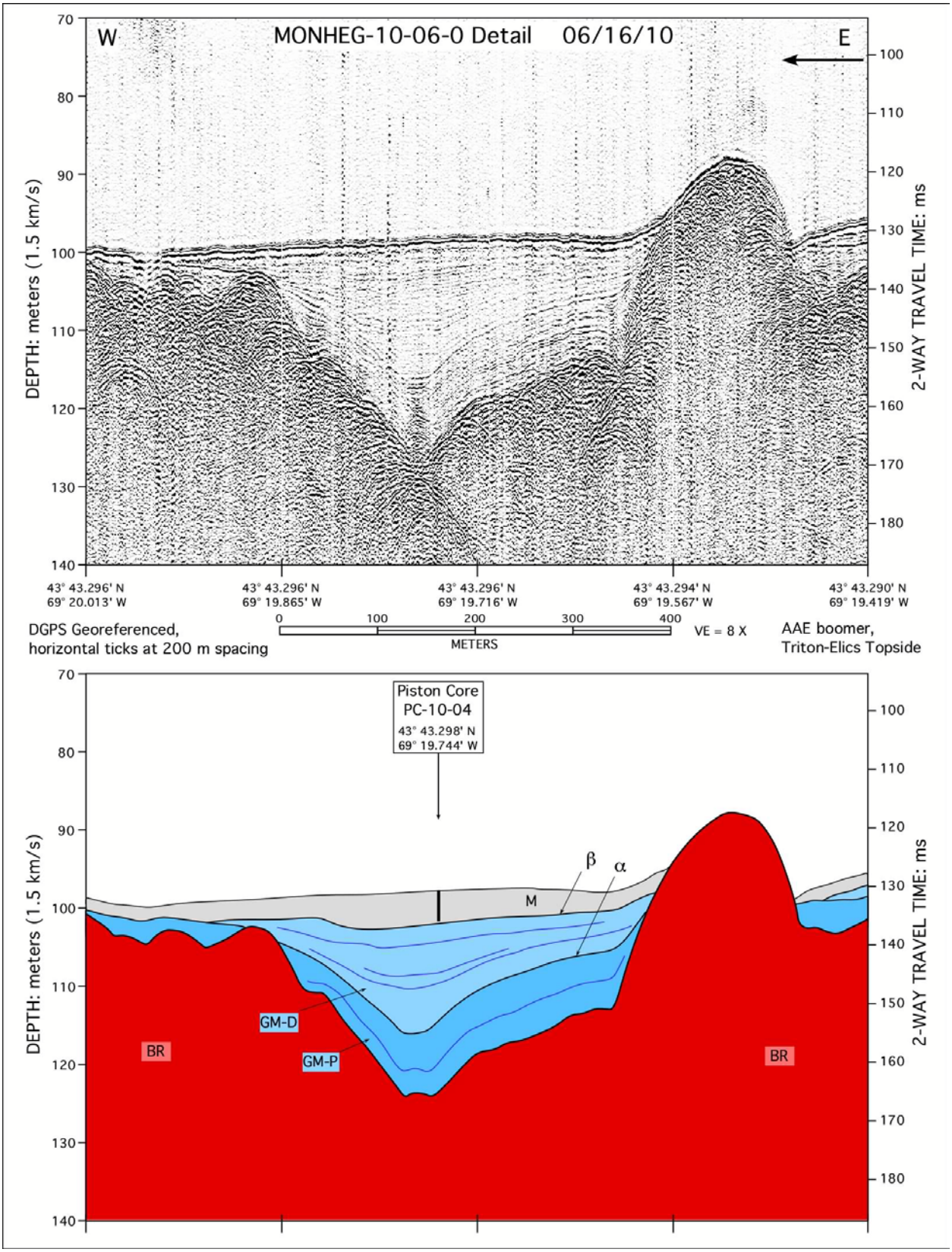

Figure 3.4: Detail of seismic profile 10-06-0 over core site PC-10-04, in Basin A.

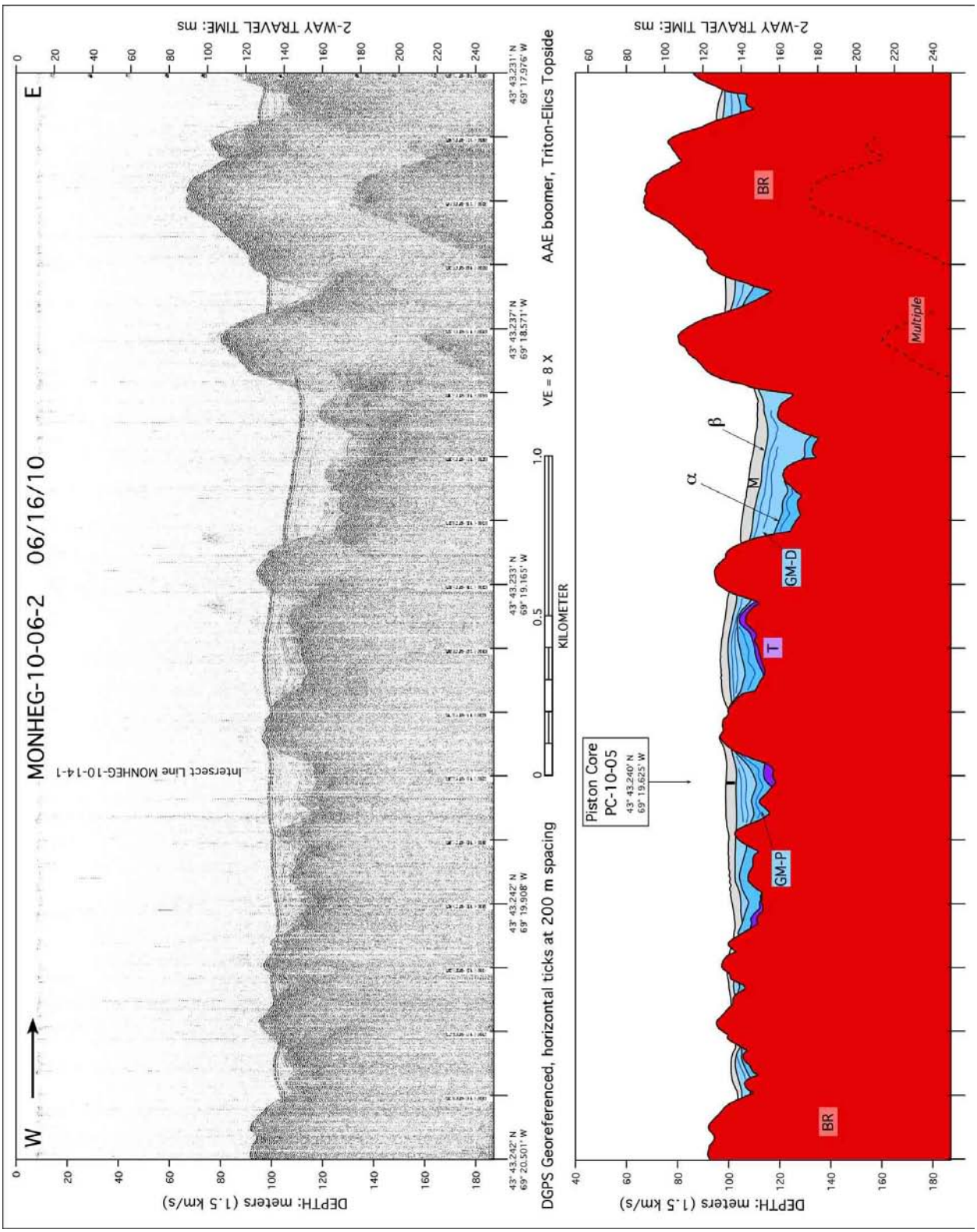

Figure 3.5: Seismic profile MONHEG-10-06-2, crossing core site MON-PC-10-05 in Basin A. The deeper basin 1 kilometer east contains slightly thicker sediments.

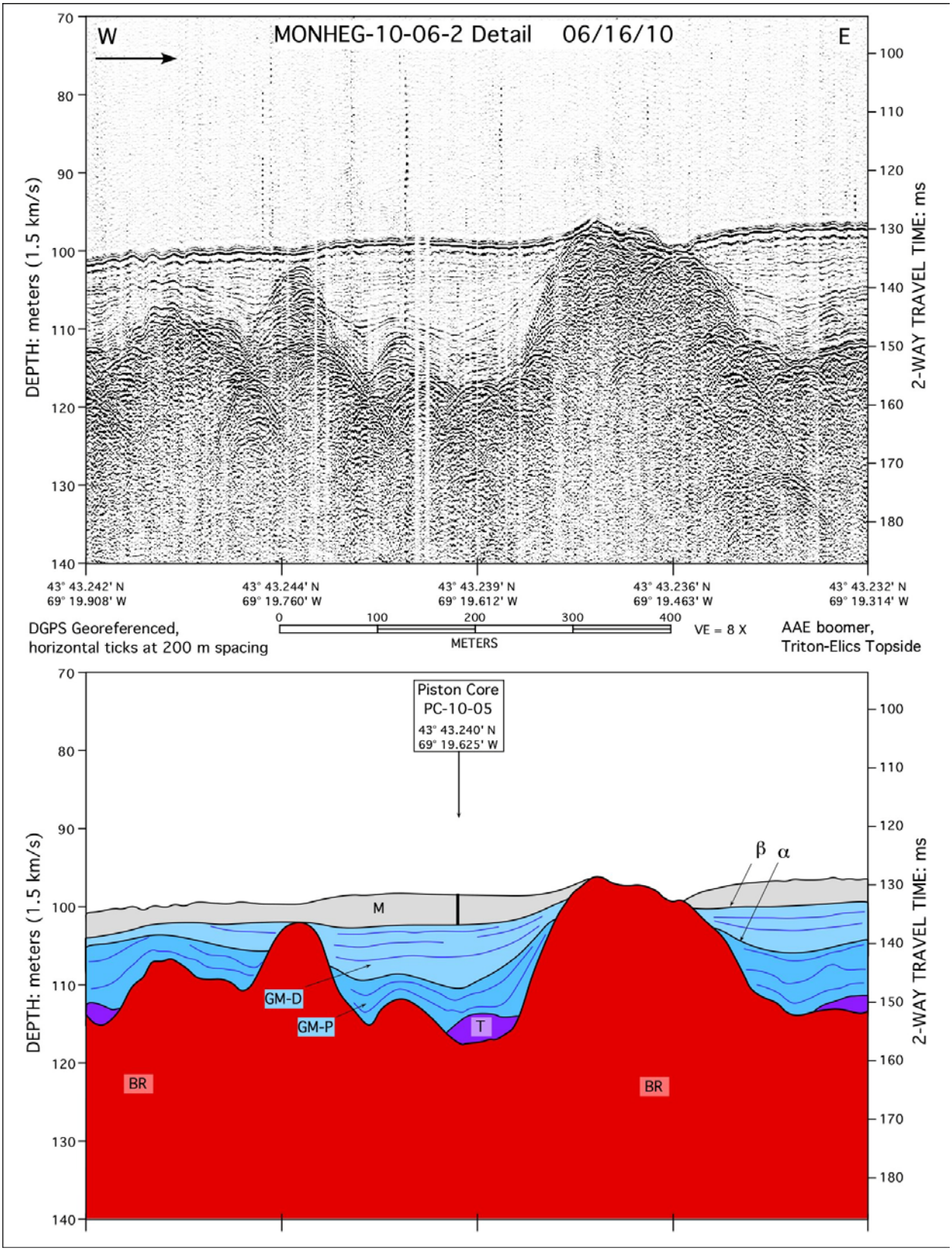

Figure 3.6: Detail of seismic profile 10-06-2 over core site PC-10-04, in Basin A.

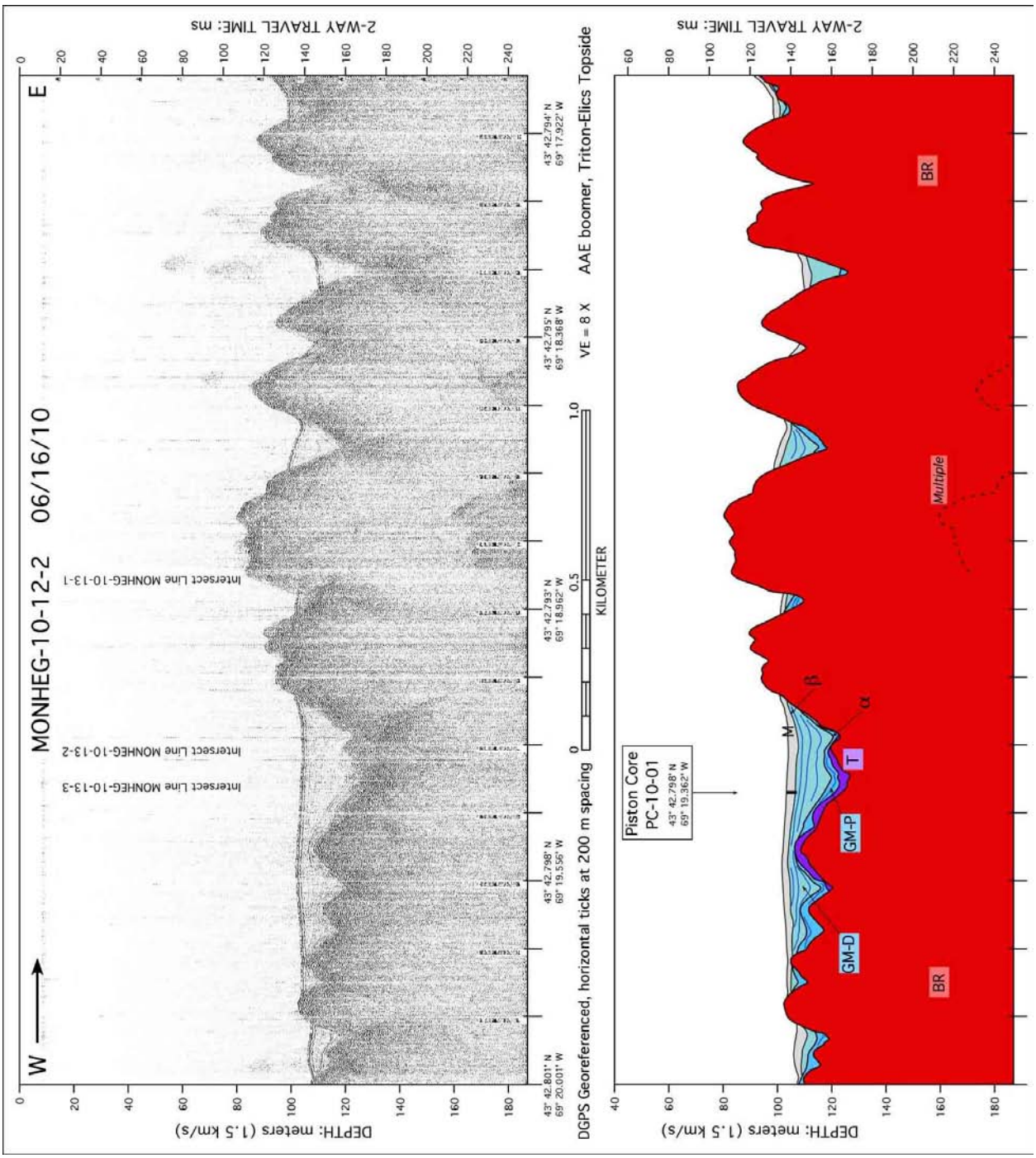

Figure 3.7: Seismic profile MONHEG-10-12-2, crossing core site MON-PC-10-01 in Basin B. The basin is complexly segmented below the deceivingly smooth muddy surface.

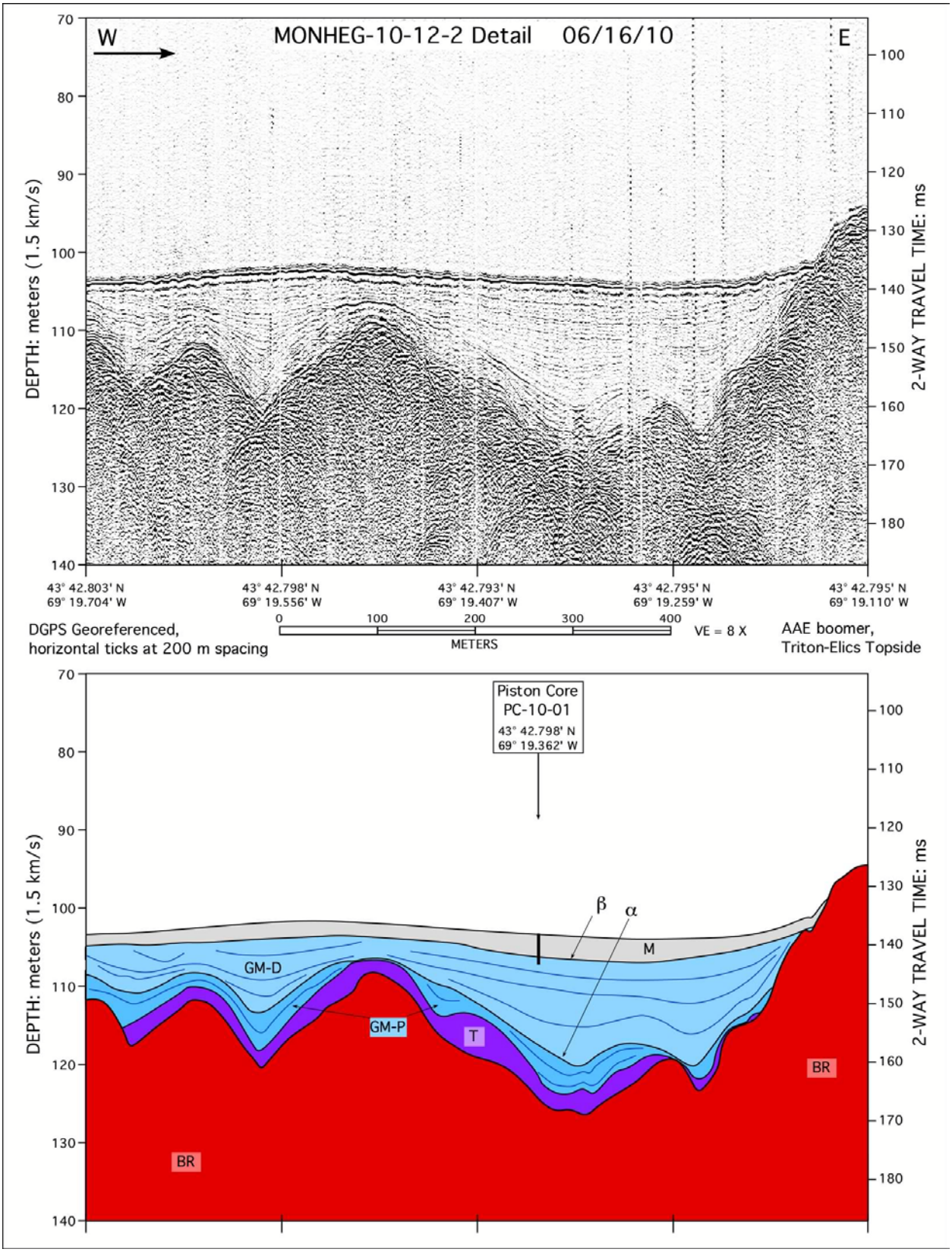

Figure 3.8: Detail of seismic profile 10-12-2 over core site PC-10-01, in Basin B.

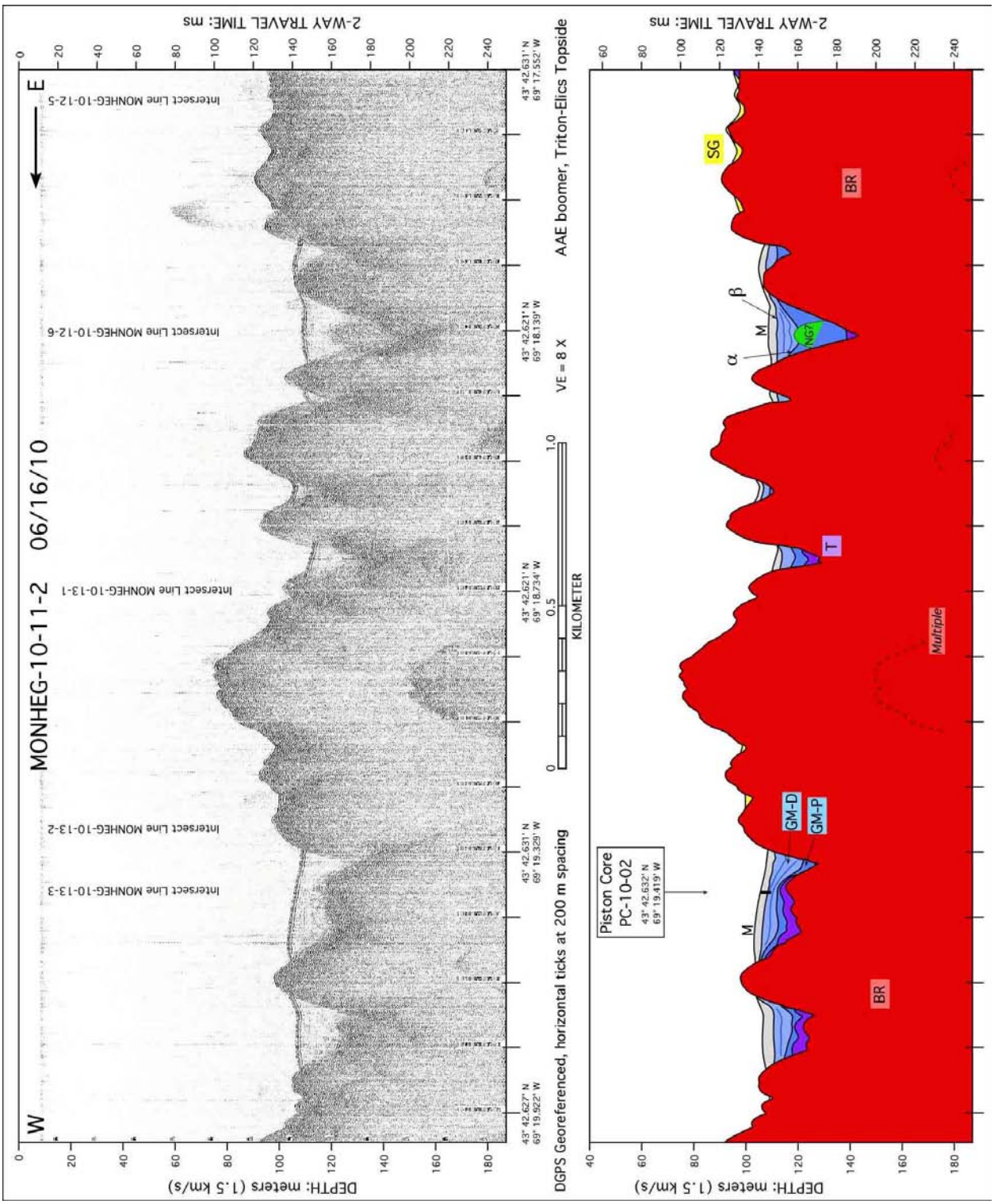

Figure 3.9: Seismic profile MONHEG-10-11-2, crossing core site MON-PC-10-02 in Basin B.

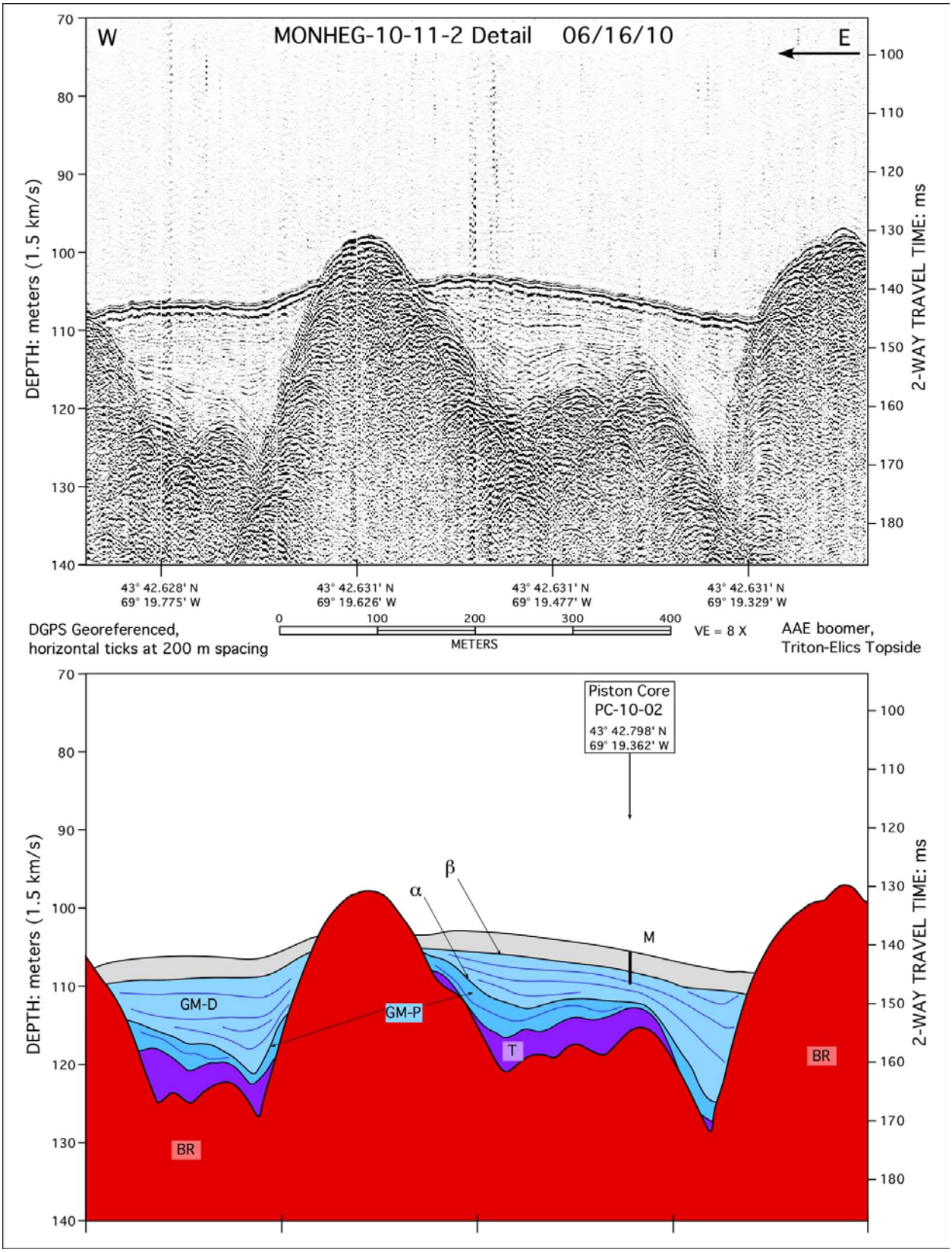

Figure 3.10: Detail of seismic profile 10-11-2 over core site PC-10-02, in Basin B.

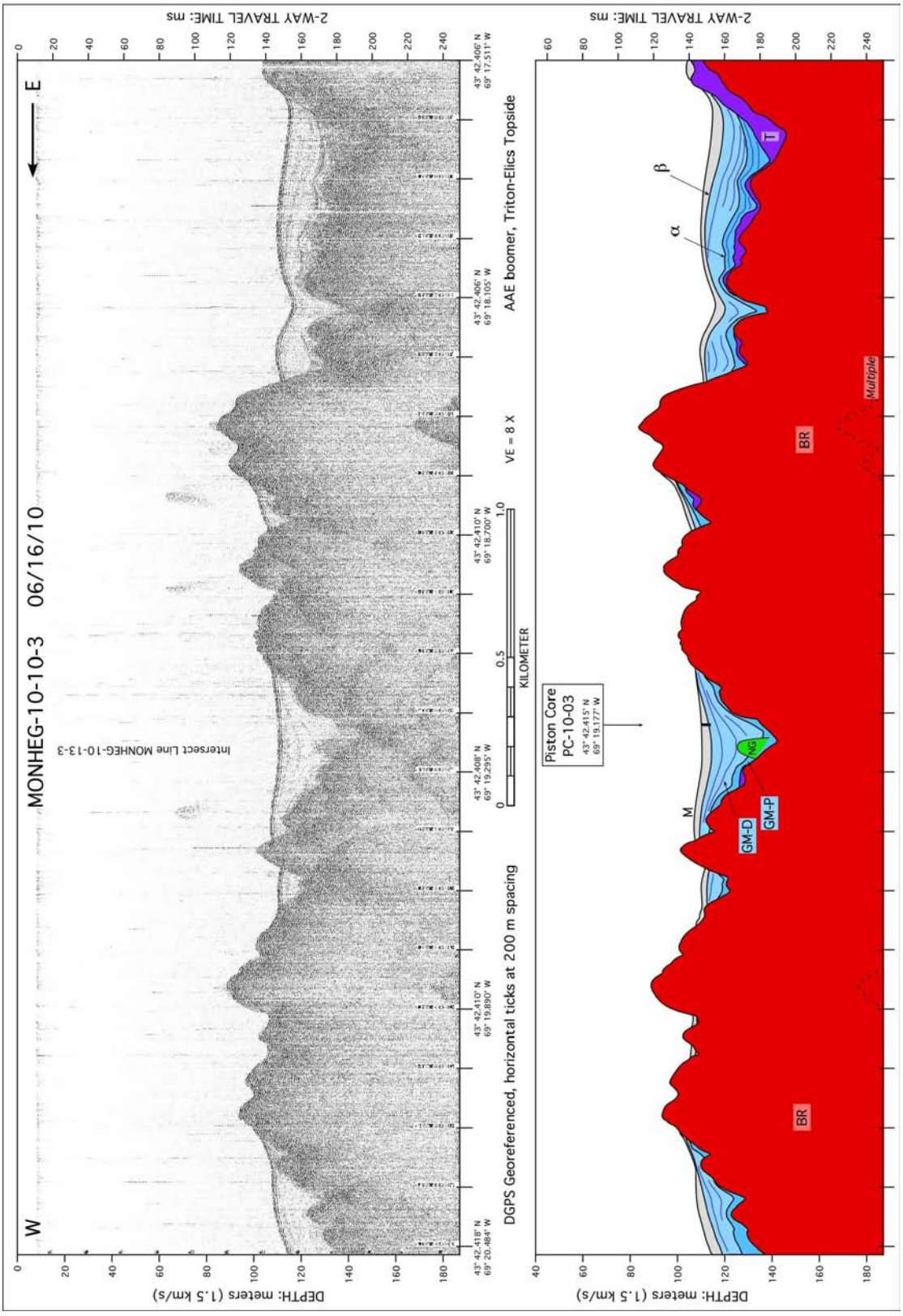

Figure 3.11: Seismic profile MONHEG-10-10-3, crossing core site MON-PC-10-03 in Basin B.

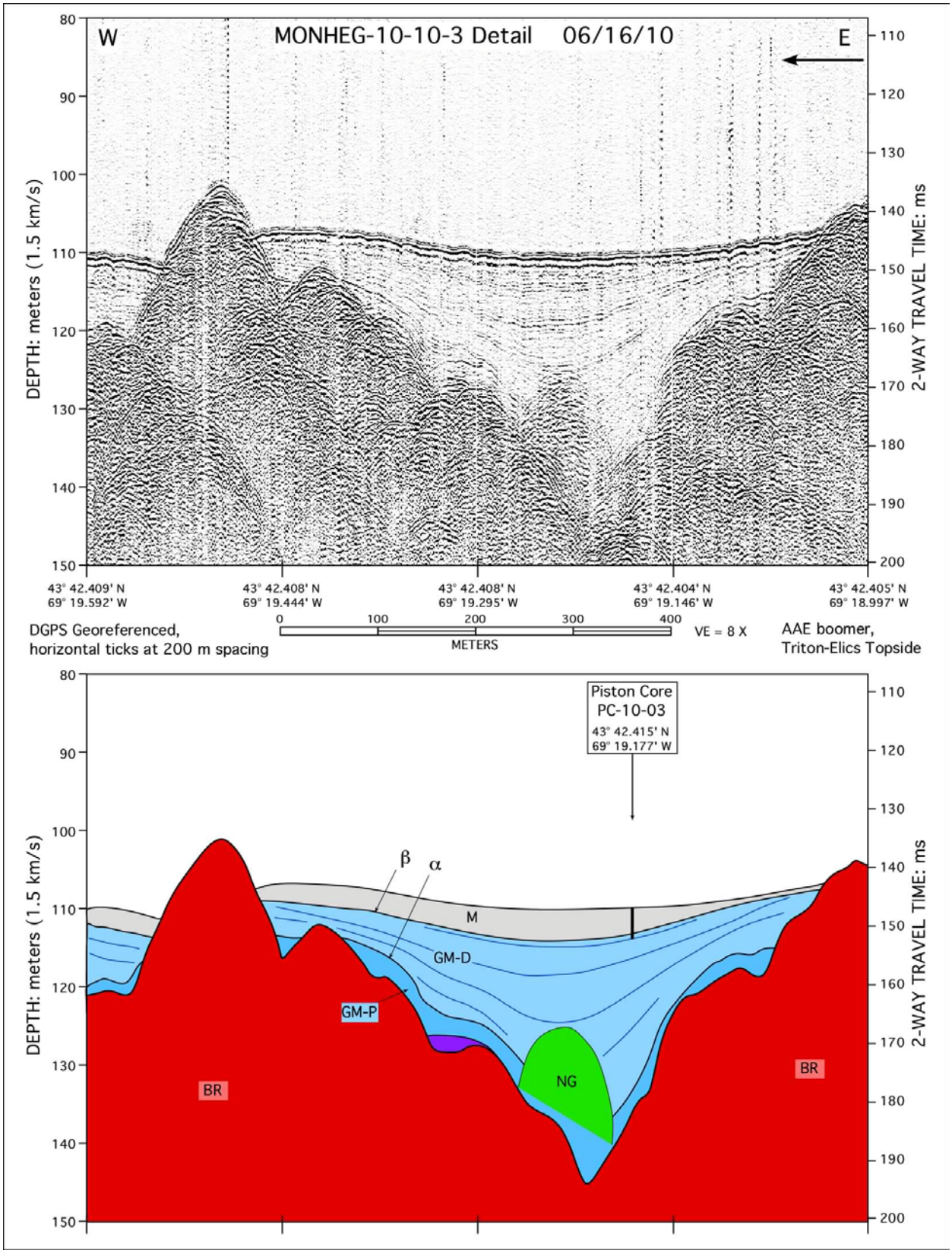

Figure 3.12: Detail of seismic profile 10-10-3 over core site PC-10-01, in Basin B.

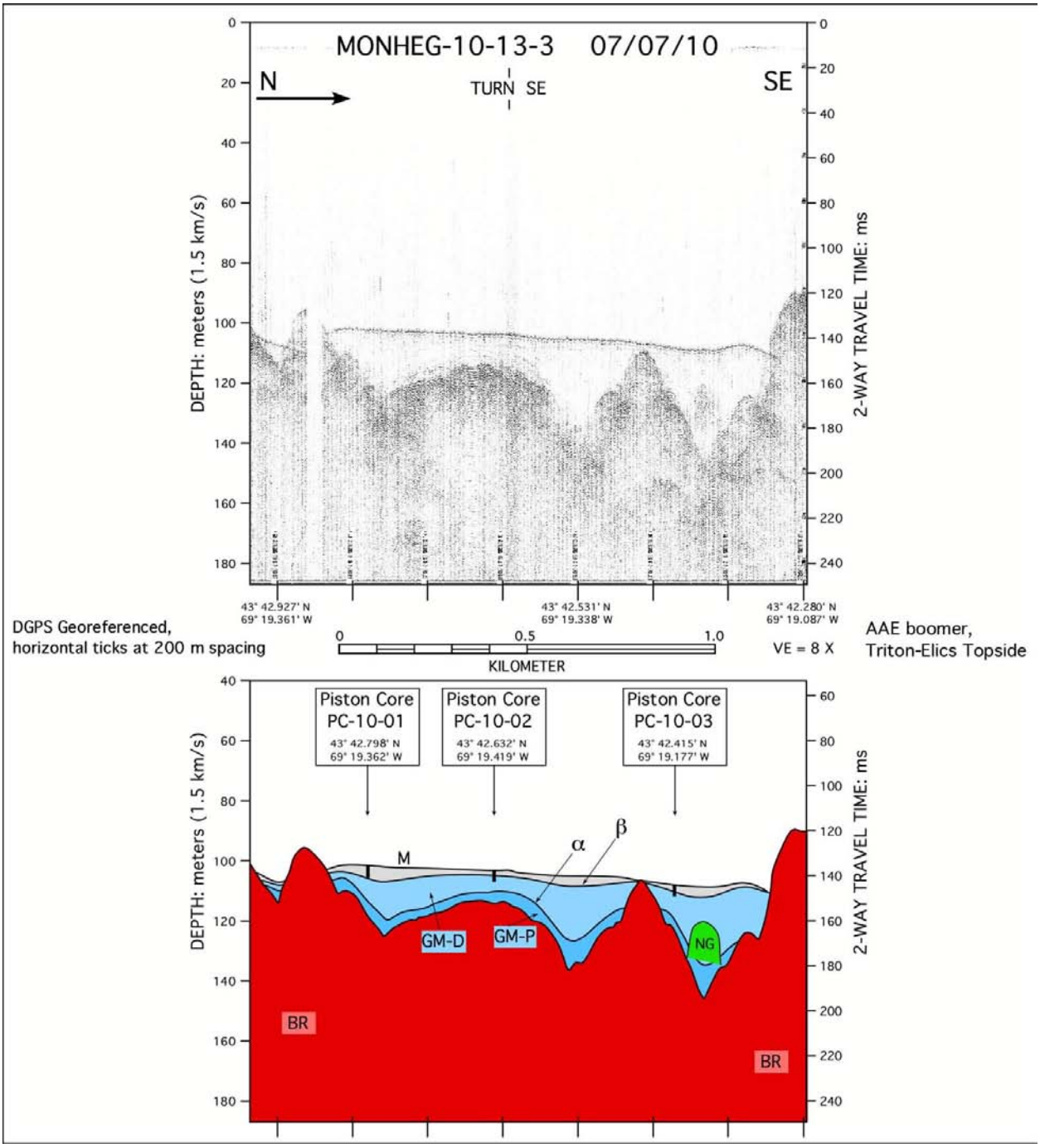

Figure 3.13: Seismic profile MONHEG-10-13-3, crossing core sites MON-PC-10-01, 02, and 03 along the axis of Basin B.

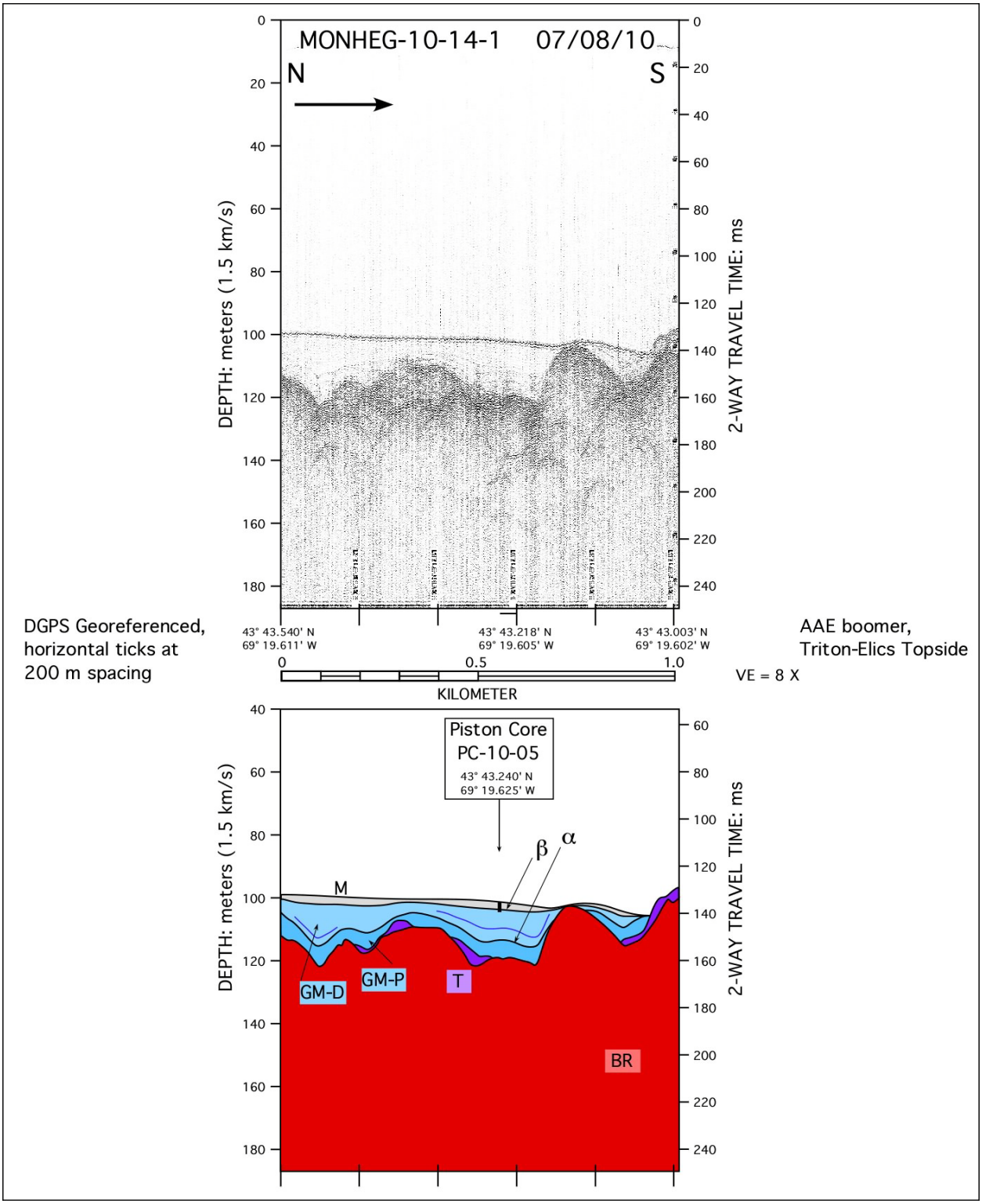

Figure 3.14: Seismic profile MONHEG-10-14-1, crossing core site MON-PC-10-05 along the axis of Basin A. Core site MON-PC-10-04 is approximately 190 m to the west of this line, in Basin A, with a stratigraphy similar to that of core 10-05 (Figure 3.3, Figure 3.4).

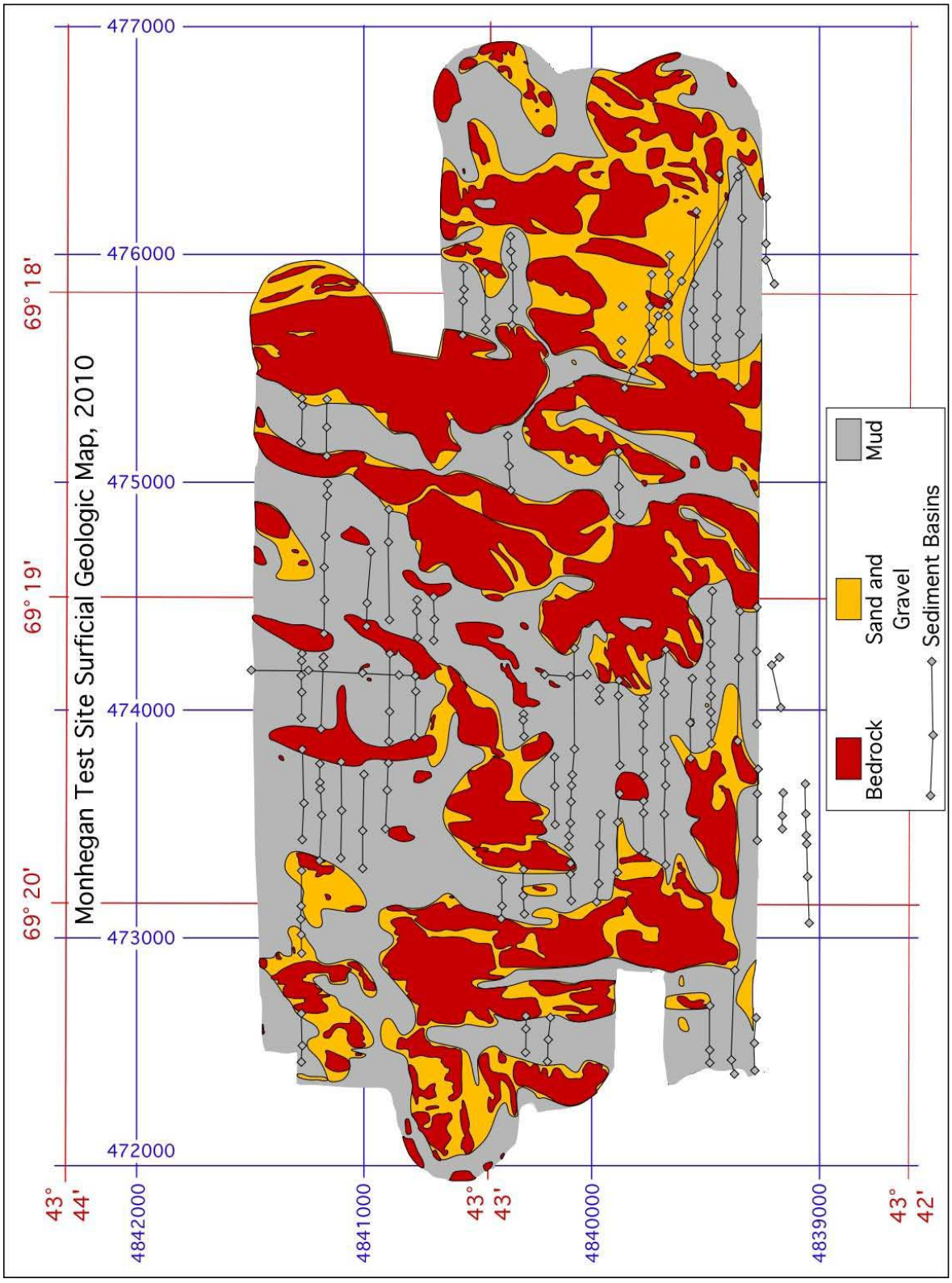

Figure 3.15: Sedimentary basins in the study area, compiled from seismic reflection profile data, and plotted on the surficial geologic map. Grey diamonds represent start, deep point, and end of each basin, with some more complex basins having multiple deep sub-basins.

4 Multibeam Bathymetric Survey

Prior results from the Monhegan area were reported in our pre-cruise report (Belknap et al., 2010), a swath bathymetry image of the waters around Monhegan Island collected for Maine Department of Marine Resources in 2009 (Carl Wilson, personal comm., 2009). Other sporadic efforts in collection of multibeam swath bathymetry include our collaborations with DMR north of Monhegan Island, off Saco Bay, and elsewhere in coastal Maine. A recent report on surveys in Penobscot Bay (Andrews et al., 2010) discusses the potential for this work, especially for repeat surveys in areas of possible sea-floor change.

4.1 Methods

Our present system is a WASSP pole-mounted multibeam swath bathymetric survey transducer with real-time DGPS navigation and correction for pitch, yaw and roll. These data are integrated into the Olex topside receiver, to produce a real-time image of bathymetry, hardness, or other sea-floor conditions. The WASSP-Olex system is unique in not just “painting over” previous swaths like a typical sidescan system, but in selecting the best data for true depth based on geometry of beam angles. In addition, the Olex system makes corrections for speed of sound and tidal elevation in real time. Thus, unlike the majority of multibeam surveys, there is no need for post-processing of data. The University of Maine and the Maine Department of Marine Resources acquired identical units this summer. Because of ship availability and minor delays in equipment completion, the DMR unit was used to acquire the new data on October 12, 2010. Sea state varied during data collection from greater than 1 m short-period waves at the beginning, to less than 0.5 m by the end of data collection. The WASSP-Olex system seems to have compensated for this moderate sea. One output available from the Olex system is a bathymetric map with contours and shaded relief (Figure 4.1). This is a preliminary image taken from the field, but data are also available as a georeferenced x, y, z file that is currently being processed. These data are a significant improvement on the existing swath bathymetry image for the region.

Another option available within the Olex sytem is an internally-calibrated (arbitrary scale) map of hardness of the seafloor, based on reflection intensity calibrated for beam angle. Figure 4.2 shows the same area as Figure 4.1, but as hardness parameter. The shallow features are clearly hard, corresponding to bedrock as seem in seismic profiles and sidescan sonar images. The deep basins are clearly soft, corresponding to watery mud, as seen in seismic profiles, piston

cores, and sidescan sonar images. Other available features of the Olex system include maps of discrete depth points, the ability to draw profiles, and three-dimensional displays at various angles.

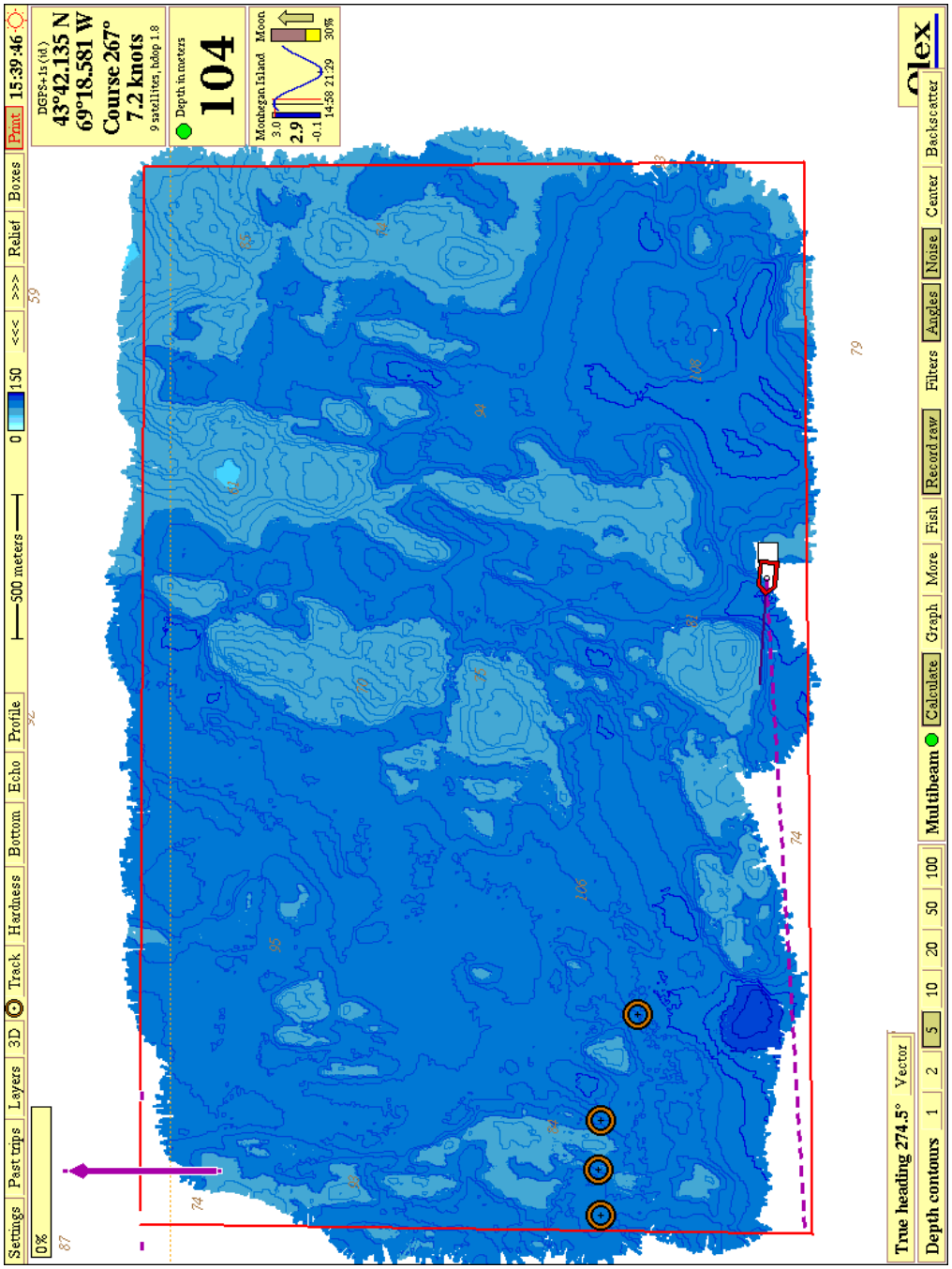

Figure 4.1: Preliminary bathymetric map of the study area from the WASSP-Olex system completed October 12, 2010. Darker colors correspond with greater depths. This screen-grab image is backed up by full x,y,z files that are currently being processed.

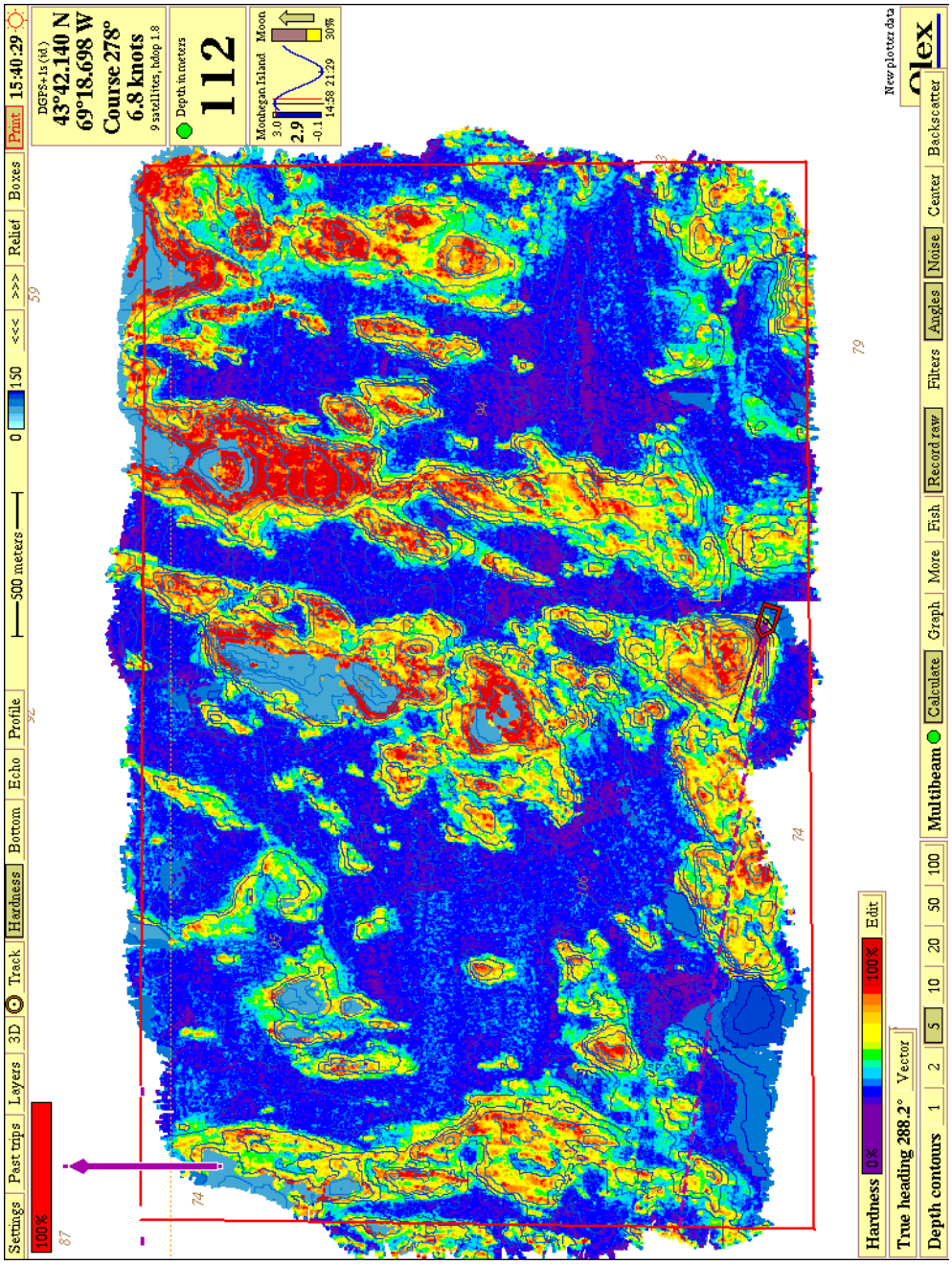

Figure 4.2: Preliminary hardness map of the study area from the WASSP-Olex system completed October, 12, 2010. Hotter colors correspond greater reflectivity (bottom hardness) on an arbitrary scale. Shallow bathymetry clearly corresponds with hard bedrock, while deeper basins are filled with soft sediment.

5 Conclusions

Examination of the UMaine Deepwater Offshore Wind Test Site with various geophysical and coring techniques has produced a broader view of the distribution of substrates than any individual technique could. The multibeam data provide the best available bathymetry for the survey area. Although the multibeam provides a backscatter image, generally displayed as hardness, it does not have the detailed imaging capability of sidescan sonar. Thus, direct images of bedrock structures and surrounding sedimentary environments support and expand the bathymetry. Conversely, sidescan sonar data is not easily related to bathymetry except directly below the towfish, and thus interpretation of imagery can be ambiguous without the bathymetric component such as the multibeam supplies. Each of these tools is strictly limited to the surface of the seafloor. Seismic reflection profiling provides the third dimension of depth to bedrock and sediment thickness, as well as identification of materials by seismic facies analysis. These data are correlated to existing seismic facies models backed up by examination of surface samples and cores. The final piece of the multi-dimensional puzzle is local coring. The piston cores and box cores provide confirmation of geophysical interpretations, but of course are also used for more detailed analysis of geotechnical properties.

This preliminary report is supported by extensive electronic files of original and interpreted data. Selection of a final turbine location can be refined by more detailed investigations using the techniques applied above in more specific locations.

6 References Cited

Andrews, B.D., Brothers, L.D. and Barnhardt, W.A., 2010, Automated feature extraction and spatial organization of seafloor pockmarks, Belfast Bay, Maine, USA: Geomorphology, v. 124, p. 55-64.

Bacchus, T.S., 1993, Late Quaternary Stratigraphy and Evolution of the Eastern Gulf of Maine: Ph.D. Dissertation, Dept. Oceanography, University of Maine, Orono, 347 pp.

Bacchus, T.S. and Belknap, D.F., 1997, Glacigenic features and shelf basin stratigraphy of the eastern Gulf of Maine: In: Davis T.A., Bell, T., Cooper, A.K., Josenhans, H., Polyak, L., Solheim, A., Stoker, M.S. and Stravers, J.A., eds., Glaciated Continental Margins: An Atlas of Acoustic Images, Chapman-Hall Pub. Co., New York, p. 213-216.

Barnhardt, W.A., Belknap, D.F. and Kelley, J.T., 1997, Stratigraphic evolution of the inner continental shelf in response to late Quaternary relative sea-level change, northwestern Gulf of Maine: Geological Society of America Bulletin, v. 109, p. 612-630.

Barnhardt, W.A., Belknap, D.F., Kelley, A.R., Kelley, J.T., and, Dickson, S.M., 1996, Surficial geology of the Maine inner continental shelf: Boothbay Harbor to North Haven, Maine, Geologic Map No. 96-10, Maine Geological Survey, Augusta, ME, 1:100,000.

Barnhardt, W.A., Gehrels, W.R., Belknap, D.F. and Kelley, J.T., 1995, Late Quaternary relative sea-level change in the western Gulf of Maine: evidence for a migrating glacial forebulge: Geology, v. 23, p. 317-320.

Barnhardt, W.A., Kelley, J.T., Dickson, S.M. and Belknap, D.F., 1998, Mapping the Gulf of Maine with side-scan sonar: a new bottom-type classification for complex seafloors: Journal of Coastal Research, v. 14, p. 646-659.

Belknap, D.F., Andersen, B.G., Anderson, R.S., Anderson, W.A., Borns, H.W., Jr., Jacobson, G., Jr., Kelley, J.T., Shipp, R.C., Smith, D.C., Stuckenrath, R. Jr., Thompson, W.B., and Tyler, D.A., 1987a, Late Quaternary sea-level changes in Maine: In: D. Nummedal, O.H. Pilkey, Jr. and J.D. Howard, eds., Sea-Level Fluctuation and Coastal Evolution, Society of Economic Paleontologists and Mineralogists Special Pub. 41, p. 71-85.

Belknap, D.F., Kelley, J.T. and Kelley, A.R., 2010, Monhegan Island Offshore wind turbine test site, Report on existing seismic reflection data, unpub. report, Dept., Earth Sci., Univ. Maine, 19 pp.

Belknap, D.F., Kelley, J.T. and Gontz, A.M., 2002, Evolution of the glaciated shelf and coastline of the northern Gulf of Maine, USA: Journal of Coastal Research Special Issue 36, p. 37-55.

Belknap, D.F., Kelley, J.T. and Shipp, R.C., 1987b, Quaternary stratigraphy of representative Maine estuaries: initial examination by high-resolution seismic reflection profiling: In: D.M. FitzGerald and P.S. Rosen, eds. Glaciated Coasts, Academic Press, San Diego p. 177-207.

Belknap, D.F. and Shipp, R.C., 1991, Seismic stratigraphy of glacial-marine units, Maine inner shelf: In: J.B. Anderson and G.M. Ashley, eds., Glacial-Marine Sedimentation; Paleoclimatic significance, Geological Society of America Special Paper 261, p. 137-157.

Belknap, D.F., Shipp, R.C., Kelley, J.T. and Schnitker, D., 1989, Depositional sequence modeling of late Quaternary geologic history, west-central Maine coast: In: R.D. Tucker and R.G. Marvinney, eds., Studies in Maine Geology - Vol. 5: Quaternary Geology, Maine Geological Survey, Augusta, p. 29-46.

Kelley, J.T. and Belknap, D.F., 1988, Geomorphology and sedimentary framework of the inner continental shelf of central Maine: Open File Report 88-6, Maine Geological Survey, Augusta, 51 pp.

Kelley, J.T. and Belknap, 1991, Physiography, surficial sediments and Quaternary stratigraphy of the inner continental shelf and nearshore region of central Maine, United States of America: Continental Shelf Research, v. 11, p. 1265-1283.

Maine Department of Conservation, Testing Ocean Energy (accessed 2009), http://www.maine.gov/doc/initiatives/oceanenergy/oceanenergy.shtml

Mitchum, R.M., Jr., Vail, P.R. and Thompson, S., III, 1977a, Seismic stratigraphy and global changes of sea level, Part 2: The depositional sequence as a basic unit for stratigraphic analysis: *in:* C.E. Payton, ed: Seismic Stratigraphy - applications to hydrocarbon exploration: AAPG Memoir 26, Tulsa, OK, p. 53-62.

Mitchum, R.M., Jr., Vail, P.R. and Sangree, J.B., 1977b, Seismic stratigraphy and global changes of sea level, Part 6: Stratigraphic interpretation of seismic reflection patterns in depositional sequences: *in:* C.E. Payton, ed: Seismic Stratigraphy - applications to hydrocarbon exploration: AAPG Memoir 26, Tulsa, OK, p. 117-133.

Piper, D.J.W., Letson, J.R.J., DeIure, A.M., and Barrier, C.Q., 1983, Sediment accumulation in low sedimentation, wave dominated, glaciated inlets: Sedimentary Geology, v. 36, p. 195-215.

Rogers, J.N., Kelley, J.T., Belknap, D.F., Gontz, A.M. and Barnhardt, W.A., 2006, Shallow-water pockmark formation in temperate estuaries: a consideration of origins in the western Gulf of Maine with special focus on Belfast Bay: Marine Geology, v. 225, p. 45-62.

Schnitker, D., Belknap, D.F., Bacchus, T.S., Friez, J.K., Lusardi, B.A. and Popek, D.M., 2001, Deglaciation of the Gulf of Maine, In: Weddle, T.K. and Retelle, M.J., eds., Deglacial History and Relative Sea-Level Changes, Northern New England and Adjacent Canada, Boulder Colorado, Geological Society of America Paper 351, p. 9-34.

Shipp, R.C., 1989, Late Quaternary sea-level fluctuations and geologic evolution of four embayments and adjacent inner shelf along the northwestern Gulf of Maine: Ph.D. Dissertation, Oceanography Program, Univ. of Maine, 832 pp.

Shipp, R.C., Belknap, D.F., and Kelley, J.T., 1991, Seismic-stratigraphic and geomorphic evidence for a post-glacial sea-level lowstand in the northern Gulf of Maine: Journal of Coastal Research, v. 7, p. 341-364.

APPENDICES – attached digital files.

Appendix A – Digital .xls file of supplementary field navigation notes, for seismic, sidescan and coring cruises. [APPDX A Navigation2010.xls]

Layout of this file is:

Nav Data: date, time, latitude and longitude, line number and field notes

Chart 1: generalized seismic line navigation (manual points only)

Chart 2: generalized sidescan sonar line navigation (manual points only)

Appendix B – Digital .xls file of digitized bathymetry and geographic coordinates (x, y, z) for seismic reflection profiles (neglecting short turns). [APPDX B Seismic Line Digit.xls]

Layout of this file is:

Input Text files: raw text files of digitized lines

Clean Data: converted to navigation and depth.

Column A – UTM Easting

Column B – UTM Northing

Column F – tidally corrected depth w.r.t. MHW (using columns C, D, E)

Nav Plot: navigation plot using Clean Data UTM eastings and northings

Bathy10-6-0 etc.: individual bathymetric profiles (incomplete)

Appendix C – Digital .xls file of basins compiled from seismic reflection profiles (neglecting short turns). [APPDX C Basins.xls]. This file includes start and end of basins, with thickness of sediments at deepest and some intermediate points.

MONHEGAN ISLAND
OFFSHORE WIND TURBINE TEST SITE

DeepCWind
2009-2010

Report on Existing Seismic Reflection Data:
January 6, 2010

Daniel F. Belknap

Joseph T. Kelley

Alice R. Kelley

Dept. Earth Sciences
University of Maine
Orono, ME

INTRODUCTION

Seismic reflection profiling data were collected in Muscongus Bay, Maine in 1987 (Figure 1) as part of a survey for sediment and bottom characteristics of the Maine inner shelf, funded by the U.S. Minerals Management Service. These high-resolution analogue seismic data were collected simultaneously with digitally rectified, analogue paper-recorded sidescan sonar data of moderate quality. These results were summarized in Kelley and Belknap (1988) and some excellent records were also used in Belknap and Shipp (1991) as type sections for the seismic stratigraphy of the Maine shelf. Also available is a collection of bottom grab sample data within the study area (Kelley and Belknap, 1988). All these data were compiled into a geologic atlas sheet for the west-central Maine shelf by Barnhardt et al. (1996). It should be noted that these techniques involve outmoded analogue systems and navigation that we have now replaced with digital seismic and sidescan acquisition, differential GPS navigation, and realtime plotting and trackline navigation. Nevertheless, these archived data remain highly useful.

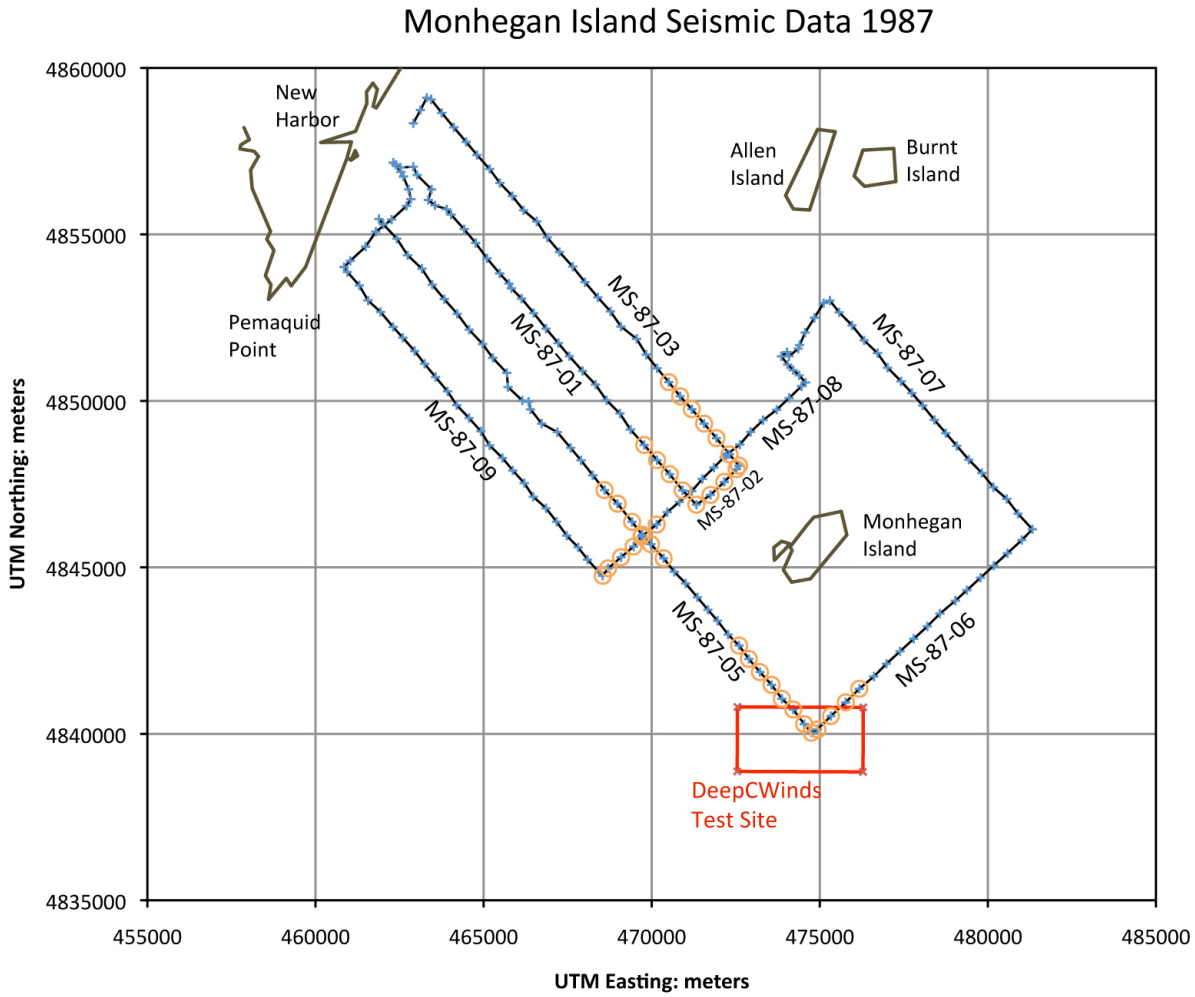

Figure 1 – Seismic reflection data tracklines (blue) with 5-minute position fixes, within Muscongus Bay and around Monhegan Island. Positions fixes from example records (Appendix 1) are emphasized in gold. Trackline identifiers as MS (MuScongus Bay)-year 1987-sequential profile number. The proposed UMaine offshore wind turbine test site is approximated by the red box.

Data exist as original 9" seismic paper rolls, and the examples shown have been scanned and interpreted for this report. These data provide a preliminary record of sediment thickness and composition within the northern portion of the proposed test site, as well as a more general stratigraphic setting from nearby basins.

METHODS

High-resolution seismic reflection profiles were collected July 13 and 14, 1987, from the UMaine Darling Marine Center vessel *R/V Miss Bess*. This closed cabin lobster boat, 12 m in length, provided a stable, weather-sheltered platform for the electronics, and working space for deploying and towing over-side gear, including a small A-frame for the Sidescan sheave block. Captain Mike Dunn of the UMaine Darling center was in command of the *Miss Bess* and maintained the course suggested by the science crew. Principal Investigators Dan Belknap and Joe Kelley were assisted by students Don Robbins, Louise McGarry and Stephanie Staples. The weather was remarkably calm for these exposed waters throughout most of the survey, with 30-60 cm seas that allowed excellent data collection. This began to degrade with seas building to 1 to 1.5 m in the afternoon of July 14, on the end of line 8 and into line 9 resulting in readable, but lower quality records. Vessel speed averaged 3-4 knots throughout the survey.

Navigation was collected as Loran-C with the 9960-W line (numbers in the 12000's) and 9960-X (numbers in the 25000's), with fixes recorded approximately every 5 minutes. These data are highly repeatable (18-91 m), but should not be considered accurate to better than 0.10 to 0.25 nautical miles (185-463 m) in true geographic coordinates, depending on locality (http://en.wikipedia.org/wiki/LORAN). The Muscongus Bay W-X pair are optimal, crossing at about 90 degrees, and readings were not affected by weather or terrain interference, so we feel the smaller values for accuracy most likely apply. The tracklines were laid out along Loran lines to aid in the consistent manual steering of the vessel. Although they are actually segments of hyperbolae, for all practical purposes these tracklines are straight in this region. The Loran-C pairs were plotted as near to real time as possible on paper chart NOAA-NOS 13288 (Monhegan Island to Cape Elizabeth, 1:80,000), and later transferred to 13301 (Muscongus Bay, 1:40,000). In 2009 these positions were converted to latitudes and longitudes using the U.S. Coast Guard POSAID2.1 program (U.S. Coast Guard, 1995). Latitudes and longitudes were also calculated to UTM coordinates using a conversion program written by Steven Dutch (2005).

High-resolution seismic reflection data were collected with an ORE-Geopulse boomer at an output power 105 J with a peak output at 1500 Hz, filtered in the frequency range from 600-2000 Hz. Reflections were received with an ORE 12-element hydrophone. Data were amplified and filtered using the ORE topside acquisition system and recorded on an EG&G 9" paper chart recorder. All settings for power, frequency, gain, etc. were established manually in the field for this analogue system. Data were not electronically recorded for later playback. Sweep was maintained at 1/8 second (125 ms 2-way travel time) to obtain the highest resolution available. At a nominal speed of sound in water of 1500 m/s, this corresponds to a full scale of 93.75 m water depth. Deeper sections were collected by inputting a delay into the recording at 10 ms intervals (7.5 m equivalent), as indicated on the records (Appendix 1). The ORE system also contains a Time Variable Gain (TVG) that can be manually set as to onset (delay) and rate of increase in gain. The onset is seen on the vertical time marks as a horizontal bar. One unfortunate aspect of the TVG is if the operator looses concentration, a rapidly shallowing bottom may be clipped by the TVG onset (as is seen in MS-87-03 at time 17:38.

The representative lines were scanned in December, 2009 using a Canon CanoScan 4400F page-size scanner at 400 dpi. Image segments were then rotated and adjusted using Adobe Photoshop CS3 software. Using a custom UMaine spreadsheet (Belknap, unpublished) vector distances were calculated between UTM coordinate navigation fixes. These distances were the basis for "rubber-sheeting" the images within Canvas X to obtain a more uniform scale. These images were then interpreted using seismic facies analysis (described below), producing a raw and interpreted image for each segment (Appendix 1).

At the same time that the seismic data were collected, we towed an EG&G SMS-260 Seafloor Mapping System (sidescan sonar). This system uses a hybrid of analogue signal with digital rectification of the slant range distortion and along-course speed variations to produce a rectified image, which is produced on an analogue paper recorder. Data were not taped, so as with the seismic data, the record originals are irreplaceable. Through-the-water speed was established with a towed speed log, or adjusted with navigational information. The sidescan data were compromised by electronic interference with the seismic system, a problem rectified in later studies. The sidescan data provide the basis for the seafloor mapping (Barnhardt et al., 1996), and provide clues to interpretation of seismic facies (for example, boulders on top of till, as opposed to bedrock, or distinction between gravel, sand and mud on the basis of image darkness and texture). Barnhardt et al. (1998) detail the mapping criteria, and the final interpretation based on a four-end-member spectrum of rock, gravel, sand an much. Intergradations result in 16 mapping classes (e.g., gravelly sand, mud and rock, etc.). The final atlas sheets are a compilation of all the available Sidescan and seismic data, seismic profiles, and grab samples, with additional information on shipwrecks, undersea cables, and boundaries. Figure 2 is a detail of the Muscongus Bay sheet in the region south of Monhegan Island, as compared to the test site planning locations.

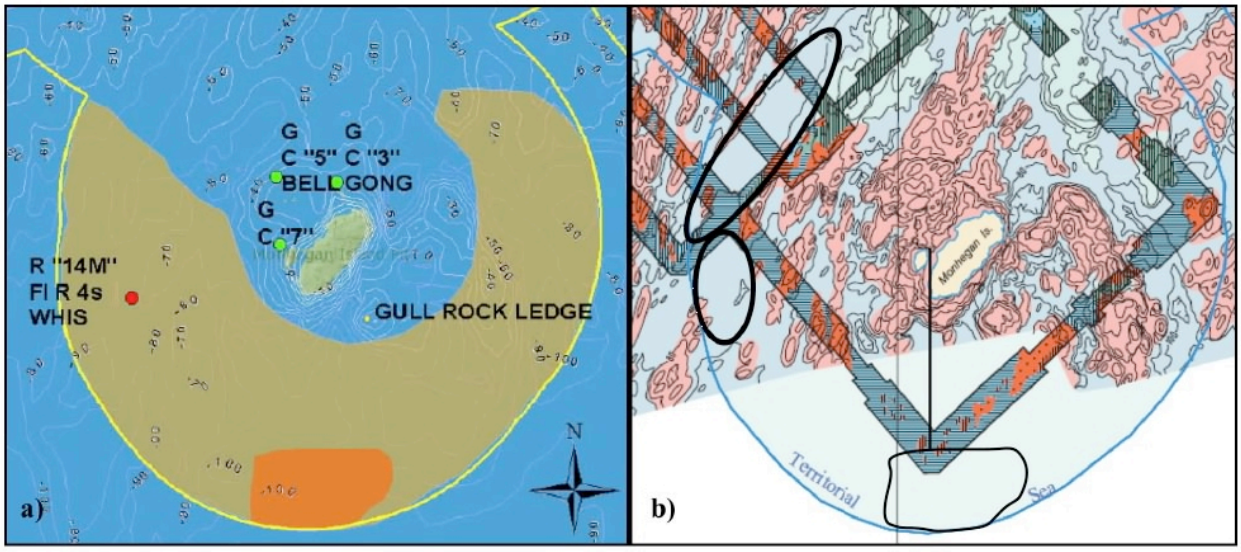

Figure 2 – Monhegan Island Draft Energy Demonstration Area: a) Planning area (brown) and draft demonstration site (orange) (Maine Department of Conservation, 2009), and b) Surficial materials map based on sidescan, seismic, and bottom samples (Barnhardt et al., 1996). Darker colors and lines identify detail surveys and verified sediments: red = rock, green = gravel, yellow = sand, blue = mud. Dark ellipses are deeper basins, discussed in the text.

Bottom grab samples (Kelley and Belknap, 1988) provide spot confirmation of surface sediment composition, in many cases on the same track lines. In addition, two manned submersible dives were conducted 5 km north of Monhegan Island in 1998 (Belknap, 1998 unpublished), near the intersections of lines MS-87-07 and -08. These dive observations provide further "ground truth" for seismic facies and sidescan sonar interpretations in the area.

SEISMIC FACIES ANALYSIS

Seismic facies are defined on the basis of intensity of acoustic impedance contrast at surfaces, character and geometry of internal reflectors, geometry of external shape, and stratigraphic position (e.g., Mitchum et al., 1977a,b). This seismic facies analysis then is placed in the context of seismic stratigraphy to reconstruct the sequence of depositional and erosional events within a basin or a region. Ground-truthing of interpretations is based on outcrops, grab samples, cores, and in the case of the Maine case, several dozen submersible and SCUBA dives. The seismic facies and stratigraphy for coastal Maine were worked out in detail by Belknap et al. (1987, 1989), Belknap and Shipp (1991), and Barnhardt et al. (1997). Offshore Gulf of Maine units have similar glacial and post-glacial facies, and a wealth of deep core information (Bacchus, 1993; Bacchus and Belknap, 1997; Schnitker et al., 2001). The descriptions that follow are based on those publications and our later refinements of observations in the region.

BR – Seismic facies BR is identified by strong acoustic contrast at the surface with a highly variable external geometry and no coherent internal reflectors. Numerous hyperbolic returns near the surface indicate point source or sharp reflections. Apparent internal reflections are actually side echoes, especially evident in deeper water. BR is always the stratigraphically lowest unit. The interpretation of BR is **bedrock,** as confirmed at shorelines and submerged outcrops (submersible and ROV) and the distinct images of foliation and structure present on sidescan sonar images.

T – Seismic facies T is identified by strong acoustic contrast at the surface, with a hummocky or mounded external geometry. Internal reflections are chaotic or weakly layered. T overlies BR, along a contact that may have low contrast, and in fact may be difficult to discern. T is interpreted as **till**, as confirmed by direct and sidescan sonar imaging of dense matrix and abundant cobbles and boulders. Till occurs either as a widespread thin (several meters thick) cover or as distinct individual moraines up to 10-20 m thick.

GM-P – Seismic facies GM-P is a well-stratified unit with moderate surface contrast, and a distinctly conformable, draping geometry. Internal reflections are more or less parallel, and may correlate for hundreds of meters. GM-P overlies either T or BR and is up to 10-15 m thick in the study area. GM-P is interpreted as **glaciomarine mud, proximal** to original glacial sources. Offshore cores and coastal bluff outcrops demonstrate that GM-P is a mix of moderately stiff mud with variable sand and even gravel layers (Schnitker et al., 2001), with water contents from 15 to 20 percent wet weight. This unit was deposited immediately as the Laurentide ice was retreating from the coast ca 16 cal. ka, in deep pro-glacial marine setting with rapid deposition rates.

Reflector α is the contact between GM-P and GM-D. It usually has moderate acoustic contrast and separates the well-stratified GM-P from the more weakly stratified GM-D. Reflector α is conformable, and is interpreted as a relatively abrupt change in pro-glacial marine environments

without erosion or break in sedimentation. It may correspond with a change from a calving ice front nearby to later terrestrially ground ice with meltwater streams leading to the adjacent ocean, ca. 15-14 cal. ka.

GM-D – Seismic facies GM-D is a moderately to weakly stratified unit with moderate to weak acoustic contrast at its surface in shallow water, or a more gradual disconformable surface in present water depths greater than 60 m. GM-D overlies GM-P or deeper units in a draping geometry that is modified by some ponding in paleo-depressions and thinning over paleo-shoals. GM-D is up to 20 m thick in the study area. GM-D is interpreted as glaciomarine mud, distal to glacial sources, and not necessarily in direct contact with floating glacial ice, ca. 14-12.5 cal. ka. The ponded geometry reflects a slower accumulation rate and more reworking by waves and currents (e.g., Piper et al., 1993; Shipp, 1989; Belknap et al., 1989). Offshore cores and coastal outcrops reveal a mud (silt plus clay) composition with up to several percent of sand both dispersed and in millimeter-thick layers. Water content is 40 to 50 percent wet weight, and the plastic mud may stiffen only gradually with depth.

Reflector β is the contact between GM-D and overlying M or other units. In water shallower than 60 m present water depth this reflector is distinct and may manifest as an angular unconformity (Belknap and Shipp, 1991, Fig. 10). In water deeper than 60-70 m Reflector β is conformable with a gradual change in acoustic contrast and degree of stratification (Belknap and Shipp, 1991, Fig. 11); see also MS-87-05 11:25 in Appendix 1. Where near the sediment surface "ringing" acoustic artifacts and other noise may obscure this interface. Placement of this interface with seismic data alone is sometimes challenging, and even in cores may be seen only as a gradual change in water content or sediment texture. The significance of the depth control is that local relative sea level, which was constrained by both isostatic rebound and eustatic changes, reached a lowstand at 60-65 m ca. 12.5 cal ka (Belknap et al., 1987; Barnhardt et al., 1995; Belknap et al., 2002). Above this level littoral and terrestrial erosion removed earlier deposits and incised paleovalleys into the glaciomarine mud, and allowed dewatering, compaction, and oxidation. Below present water depths of 60-70 m deposition was more-or-less continuous.

M – Seismic facies M is weakly to non-stratified with a moderate to weak acoustic contrast at the modern seafloor. Facies M is ponded in basins directly over Reflector β or may slightly drape bedrock and other units. Facies M may be "moated" around bedrock and till highs, indicating shear stress that prevents deposition or creates erosion. Seismic facies M is interpreted as Holocene (last 11.5 thousand calendar years) marine **mud** in the study area, although estuarine mud found in nearshore embayments has an identical character. This interpretation is confirmed by sidescan sonar, coring, bottom sampling, and direct observations. Marine and estuarine muds in the region contain water of 50 to >70% wet weight, and in coring studies demonstrate a very loosely consolidated material in the top several decimeters, that will not maintain a fixed shape, to a gradually stiffening plastic mud as depth increases that gives firm resistance when cutting cores with a knife.

SG – Seismic facies SG is strongly reflecting and variable in stratification. It occurs in two geometries: either a thin blanket surface lag on GM and other units, or wedge-shaped units interfingering with T and GM (Belknap and Shipp, 1991, Fig. 7). Facies SG is not extensive in the study area, but a good example is found on MS-87-0 (Appendix 1). Facies SG is interpreted as sand and gravel on the basis of grab samples and cores, sonar imagery of a darker but smooth

or wave-rippled surface, and direct observation. The example in MS-87-02 at time 17:06 is interpreted as a surface lag of coarse sediment on a lowstand shoreline terrace (e.g., Shipp et al., 1991). The wedge-shaped units are interpreted as outwash associated with till at former grounding-line moraines in Muscongus Bay (Belknap and Shipp, 1991, Fig. 7) and elsewhere along the coast.

NG – Seismic facies NG has a strong but diffuse surface acoustic impedance contrast, and no internal stratification. It often exhibits a convex up or flat-topped geometry with sides that spread as sections of hyperbolae. It obscures deeper units either partially or completely, and inhibits multiples. Unlike the stratified sedimentary facies described above, NG cross-cuts earlier stratification, but the top is most common at the base of M (or possibly the top of GM-D) in the deep basins around Monhegan Island. Seismic facies NG is interpreted as **natural gas** bubbles that create an acoustically turbid curtain that disperses initial seismic pulses and obscures deeper reflectors. NG has been sampled in cores and the methane gas composition has been confirmed by ignition. The methane is probably sourced by beds of organic-rich sediments in deeper basins above Reflector β (e.g., Rogers et al., 2006). Reaction of natural gas pockets to disturbances is unpredictable, but definitely a geohazard well understood in the petroleum industry, and implicated in the formation of large fields of pockmarks (craters) in Maine embayments.

RESULTS

Eight seismic reflection profile segments are shown in Appendix 1 as examples of the seismic stratigraphy of the Muscongus Bay and Monhegan Island region. Line MS-87-05-11:40 and MS-87-06 directly cross into the proposed final test area (Figure 1), while others as shown as examples of the regional setting. The sections of lines 05 and 06 in the test area show variable patterns of bedrock outcrops 100-300 m across, interspersed with basins of glaciomarine and Holocene mud 100-600 m across. The basins are lenticular in shape, pinching out to zero on their margins and reaching a total thickness of up to 30 m in their deepest axes. A test mooring in the center of one of the larger basins would encounter gradually stiffening mud with variable but small amounts of sand to at least 20 m, with a possibly sandier and gravelly unit that would be more difficult to penetrate in the GM-P. It is likely that there are larger basins south of these two tracklines, but new survey is required to confirm the inferences based solely on bathymetry. Interestingly, just outside the test area to the NW along line MS-87-05-11:25 (Appendix 1) the "Manana Shelf Basin" (Kelley and Belknap, 1988) is 1 km across and has a total post-till and bedrock sediment thickness of up to 45 m. One possible hazard, however is a large natural gas deposit at time mark 11:31-11:32.

Other lines cross major basin lacking obstructions (other than central pockets of NG). Appendix 1 contains interpreted segments of MS-87-01, MS-87-02, MS-87-03, MS-87-05-10:25, and MS-87-08. Each of these cross over the broad and extensive "25860 Basin" (informally named for the Loran C X-ray line that runs through it). The "25860 Basin" (Figure 1, black ellipses) would be an ideal site for test operations, if not precluded but the selection process. It remains a useful backup that should be considered if the surveys of the approved test site do to reveal amenable conditions.

CONCLUSIONS

Existing seismic reflection profiling and sidescan sonar data are limited within the accepted test site, but do show small but adequate locations. A more general review of the surrounding areas demonstrates abundant potential sites and provides a firm basis for interpretation of stratigraphy and material compositions. Continuity in interpretations is assured by the continuation of the same PI's from the 1987 survey on the new project. New studies in the test site will be improved by our more advanced digital seismic and sidescan sonar equipment, links to a full digital multibeam bathymetric survey, and analysis of geo-referenced digital data in a GIS framework.

REFERENCES CITED

Bacchus, T.S., 1993, Late Quaternary Stratigraphy and Evolution of the Eastern Gulf of Maine: Ph.D. Dissertation, Dept. Oceanography, University of Maine, Orono, 347 pp.

Bacchus, T.S. and Belknap, D.F., 1997, Glacigenic features and shelf basin stratigraphy of the eastern Gulf of Maine: In: Davis T.A., Bell, T., Cooper, A.K., Josenhans, H., Polyak, L., Solheim, A., Stoker, M.S. and Stravers, J.A., eds., Glaciated Continental Margins: An Atlas of Acoustic Images, Chapman-Hall Pub. Co., New York, p. 213-216.

Barnhardt, W.A., Belknap, D.F. and Kelley, J.T., 1997, Stratigraphic evolution of the inner continental shelf in response to late Quaternary relative sea-level change, northwestern Gulf of Maine: Geological Society of America Bulletin, v. 109, p. 612-630.

Barnhardt, W.A., Belknap, D.F., Kelley, A.R., Kelley, J.T., and, Dickson, S.M., 1996, Surficial geology of the Maine inner continental shelf: Boothbay Harbor to North Haven, Maine, Geologic Map No. 96-10, Maine Geological Survey, Augusta, ME, 1:100,000.

Barnhardt, W.A., Gehrels, W.R., Belknap, D.F. and Kelley, J.T., 1995, Late Quaternary relative sea-level change in the western Gulf of Maine: evidence for a migrating glacial forebulge: Geology, v. 23, p. 317-320.

Barnhardt, W.A., Kelley, J.T., Dickson, S.M. and Belknap, D.F., 1998, Mapping the Gulf of Maine with side-scan sonar: a new bottom-type classification for complex seafloors: Journal of Coastal Research, v. 14, p. 646-659.

Belknap, D.F., 1998 unpublished, Cruise Report, Muscongus Bay, part of project "Coarse Gravel in the Gulf of Maine: an Under-explored Essential Fish Habitat," by R.A. Wahle and D.F. Belknap, funded by National Undersea Research Center, University of Connecticut, Avery Point. NURP dives aboard submersible "Clelia" NAGL-98-04, NAGL-98-05, 08/31/98.

Belknap, D.F., Andersen, B.G., Anderson, R.S., Anderson, W.A., Borns, H.W., Jr., Jacobson, G., Jr., Kelley, J.T., Shipp, R.C., Smith, D.C., Stuckenrath, R. Jr., Thompson, W.B., and Tyler, D.A., 1987, Late Quaternary sea-level changes in Maine: In: D. Nummedal, O.H. Pilkey, Jr. and J.D. Howard, eds., Sea-Level Fluctuation and Coastal Evolution, Society of Economic Paleontologists and Mineralogists Special Pub. 41, p. 71-85.

Belknap, D.F., Kelley, J.T. and Gontz, A.M., 2002, Evolution of the glaciated shelf and coastline of the northern Gulf of Maine, USA: Journal of Coastal Research Special Issue 36, p. 37-55.

Belknap, D.F., Kelley, J.T. and Shipp, R.C., 1987, Quaternary stratigraphy of representative Maine estuaries: initial examination by high-resolution seismic reflection profiling: In: D.M. FitzGerald and P.S. Rosen, eds. Glaciated Coasts, Academic Press, San Diego p. 177-207.

Belknap, D.F. and Shipp, R.C., 1991, Seismic stratigraphy of glacial-marine units, Maine inner shelf: In: J.B. Anderson and G.M. Ashley, eds., Glacial-Marine Sedimentation; Paleoclimatic significance, Geological Society of America Special Paper 261, p. 137-157.

Belknap, D.F., Shipp, R.C., Kelley, J.T. and Schnitker, D., 1989, Depositional sequence modeling of late Quaternary geologic history, west-central Maine coast: In: R.D. Tucker and R.G. Marvinney, eds., Studies in Maine Geology - Vol. 5: Quaternary Geology, Maine Geological Survey, Augusta, p. 29-46.

Dutch, S., 2005, Spreadsheet for converting UTM to Latitude and Longitude (and Vice Versa), UTM Batch Conversion WGS84. Natural and Applied Sciences Center, University of Wisconsin – Green Bay. http://www.uwgb.edu/dutchs/UsefulData/HowUseExcel.HTM,

Kelley, J.T. and Belknap, D.F., 1988, Geomorphology and sedimentary framework of the inner continental shelf of central Maine: Open File Report 88-6, Maine Geological Survey, Augusta, 51 pp.

Maine Department of Conservation, Testing Ocean Energy (accessed 2009), http://www.maine.gov/doc/initiatives/oceanenergy/oceanenergy.shtml

Mitchum, R.M., Jr., Vail, P.R. and Thompson, S., III, 1977a, Seismic stratigraphy and global changes of sea level, Part 2: The depositional sequence as a basic unit for stratigraphic analysis: *in:* C.E. Payton, ed: Seismic Stratigraphy - applications to hydrocarbon exploration: AAPG Memoir 26, Tulsa, OK, p. 53-62.

Mitchum, R.M., Jr., Vail, P.R. and Sangree, J.B., 1977b, Seismic stratigraphy and global changes of sea level, Part 6: Stratigraphic interpretation of seismic reflection patterns in depositional sequences: *in:* C.E. Payton, ed: Seismic Stratigraphy - applications to hydrocarbon exploration: AAPG Memoir 26, Tulsa, OK, p. 117-133.

Piper, D.J.W., Letson, J.R.J., DeIure, A.M., and Barrier, C.Q., 1983, Sediment accumulation in low sedimentation, wave dominated, glaciated inlets: Sedimentary Geology, v. 36, p. 195-215.

Rogers, J.N., Kelley, J.T., Belknap, D.F., Gontz, A.M. and Barnhardt, W.A., 2006, Shallow-water pockmark formation in temperate estuaries: a consideration of origins in the western Gulf of Maine with special focus on Belfast Bay: Marine Geology, v. 225, p. 45-62.

Schnitker, D., Belknap, D.F., Bacchus, T.S., Friez, J.K., Lusardi, B.A. and Popek, D.M., 2001, Deglaciation of the Gulf of Maine, In: Weddle, T.K. and Retelle, M.J., eds., Deglacial History and Relative Sea-Level Changes, Northern New England and Adjacent Canada, Boulder Colorado, Geological Society of America Paper 351, p. 9-34.

Shipp, R.C., 1989, Late Quaternary sea-level fluctuations and geologic evolution of four embayments and adjacent inner shelf along the northwestern Gulf of Maine: Ph.D. Dissertation, Oceanography Program, Univ. of Maine, 832 pp.

Shipp, R.C., Belknap, D.F., and Kelley, J.T., 1991, Seismic-stratigraphic and geomorphic evidence for a post-glacial sea-level lowstand in the northern Gulf of Maine: Journal of Coastal Research, v. 7, p. 341-364.

U.S. Coast Guard Research and Development Center, 1995, Positioning Aid 2.1: USCG-R&D, Avery Point, Groton, CT, 06340-6096. http://www.uscg.mil/hq/cg9/rdc/default.asp?page=misc/posaid.asp

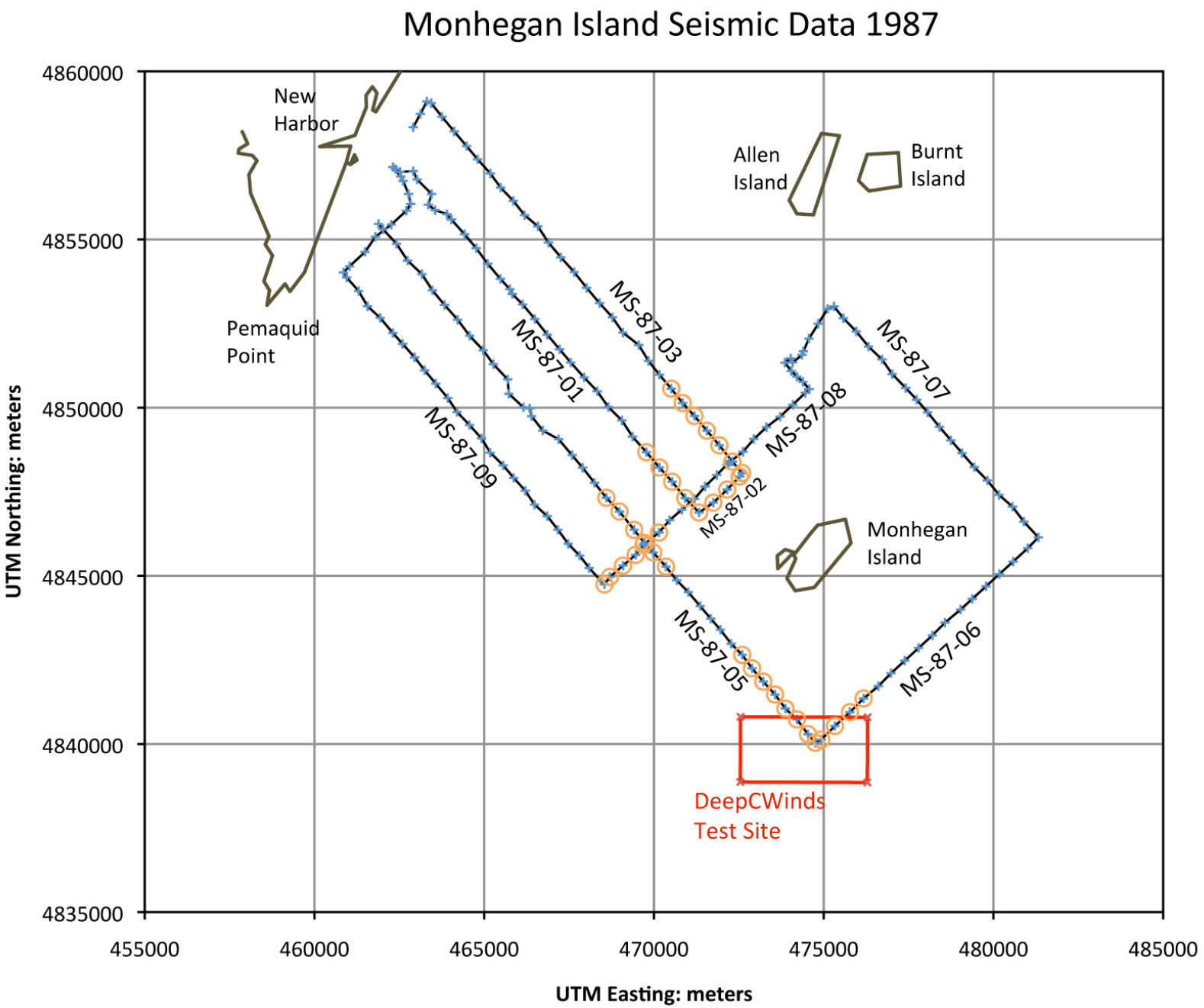
Monhegan Island Seismic Data 1987
New Harbor
Pemaquid Point
Allen Island
Burnt Island
Monhegan Island
MS-87-01
MS-87-02
MS-87-03
MS-87-05
MS-87-06
MS-87-07
MS-87-08
MS-87-09
DeepCWinds Test Site
UTM Northing: meters
UTM Easting: meters
4860000
4855000
4850000
4845000
4840000
4835000
455000
460000
465000
470000
475000
480000
485000

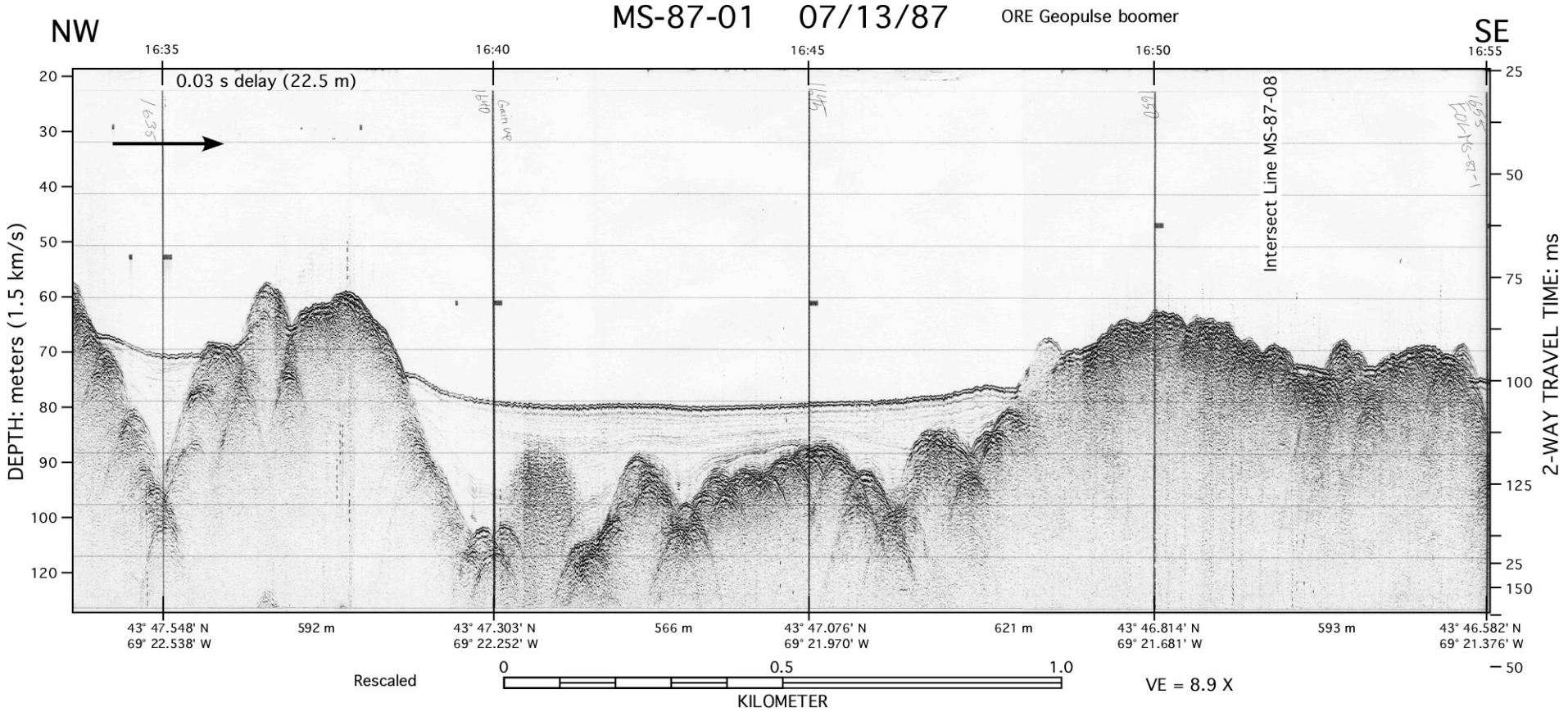
MS-87-01 07/13/87
ORE Geopulse boomer
NW
SE
16:35
16:40
16:45
16:50
16:55
0.03 s delay (22.5 m)
Intersect Line MS-87-08
DEPTH: meters (1.5 km/s)
2-WAY TRAVEL TIME: ms
43° 47.548' N
69° 22.538' W
592 m
43° 47.303' N
69° 22.252' W
566 m
43° 47.076' N
69° 21.970' W
621 m
43° 46.814' N
69° 21.681' W
593 m
43° 46.582' N
69° 21.376' W
Rescaled
0
0.5
1.0
KILOMETER
VE = 8.9 X

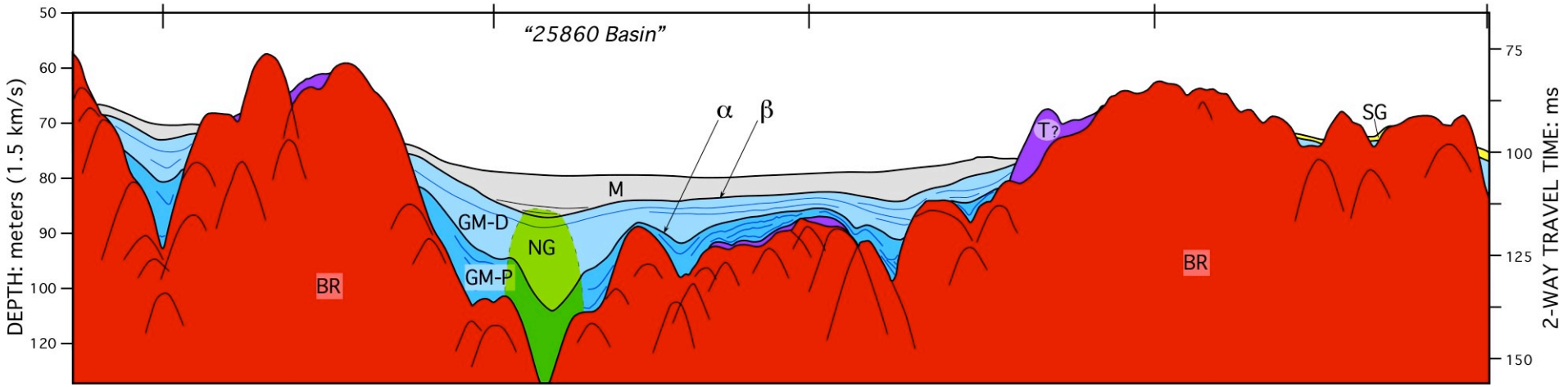
"25860 Basin"
DEPTH: meters (1.5 km/s)
2-WAY TRAVEL TIME: ms
α
β
M
GM-D
NG
GM-P
BR
BR
T?
SG

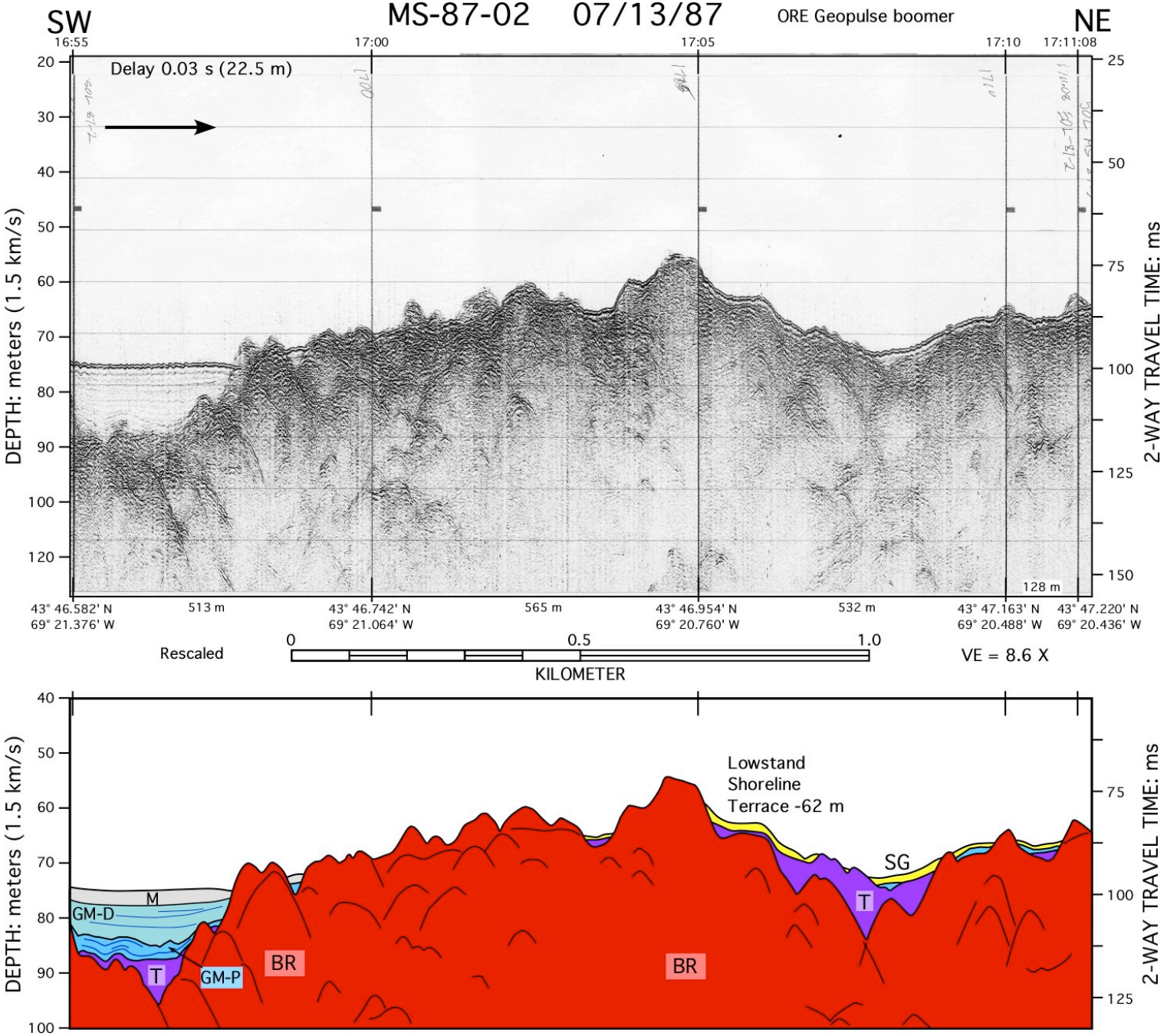
SW
MS-87-02 07/13/87
ORE Geopulse boomer
NE
16:55
17:00
17:05
17:10
17:11:08
Delay 0.03 s (22.5 m)
DEPTH: meters (1.5 km/s)
2-WAY TRAVEL TIME: ms
128 m
43° 46.582' N
69° 21.376' W
513 m
43° 46.742' N
69° 21.064' W
565 m
43° 46.954' N
69° 20.760' W
532 m
43° 47.163' N
69° 20.488' W
43° 47.220' N
69° 20.436' W
Rescaled
0
0.5
1.0
KILOMETER
VE = 8.6 X
Lowstand
Shoreline
Terrace -62 m
SG
M
GM-D
T
GM-P
BR
BR
T

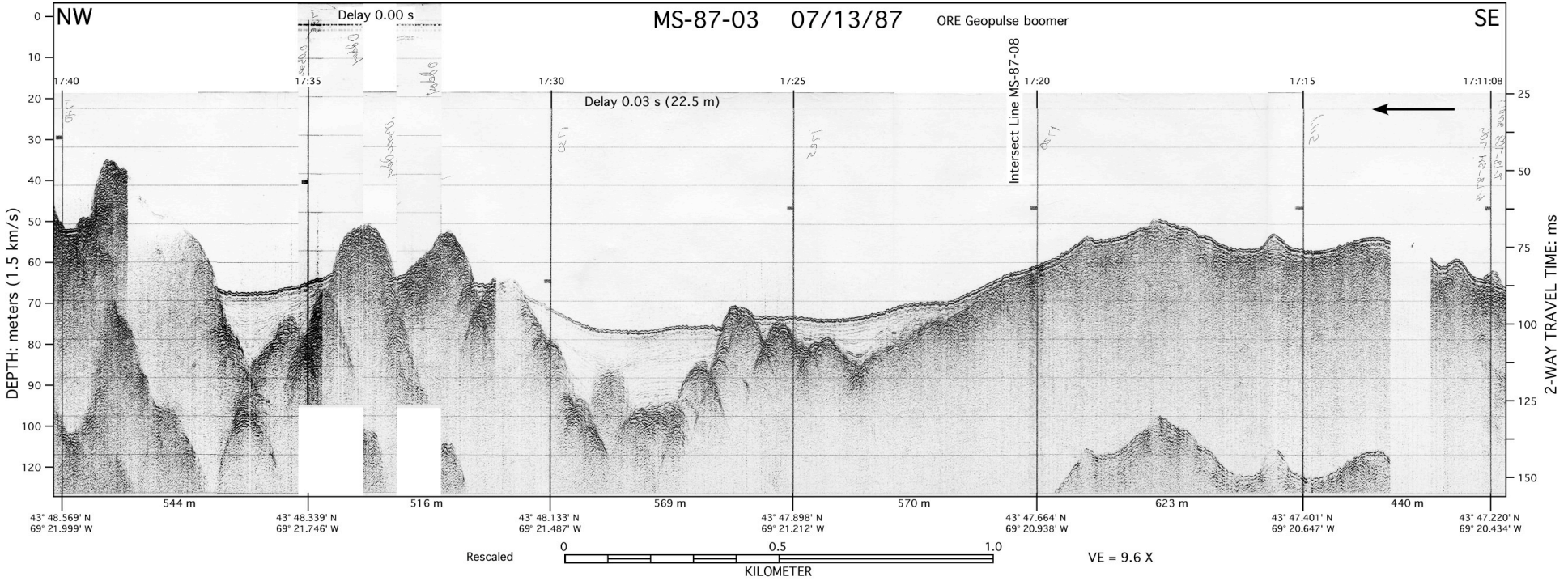
NW
SE
MS-87-03 07/13/87
ORE Geopulse boomer
Delay 0.00 s
Delay 0.03 s (22.5 m)
Intersect Line MS-87-08
17:40
17:35
17:30
17:25
17:20
17:15
17:11:08
DEPTH: meters (1.5 km/s)
2-WAY TRAVEL TIME: ms
544 m
516 m
569 m
570 m
623 m
440 m
43° 48.569' N 69° 21.999' W
43° 48.339' N 69° 21.746' W
43° 48.133' N 69° 21.487' W
43° 47.898' N 69° 21.212' W
43° 47.664' N 69° 20.938' W
43° 47.401' N 69° 20.647' W
43° 47.220' N 69° 20.434' W
Rescaled
0
0.5
1.0
KILOMETER
VE = 9.6 X

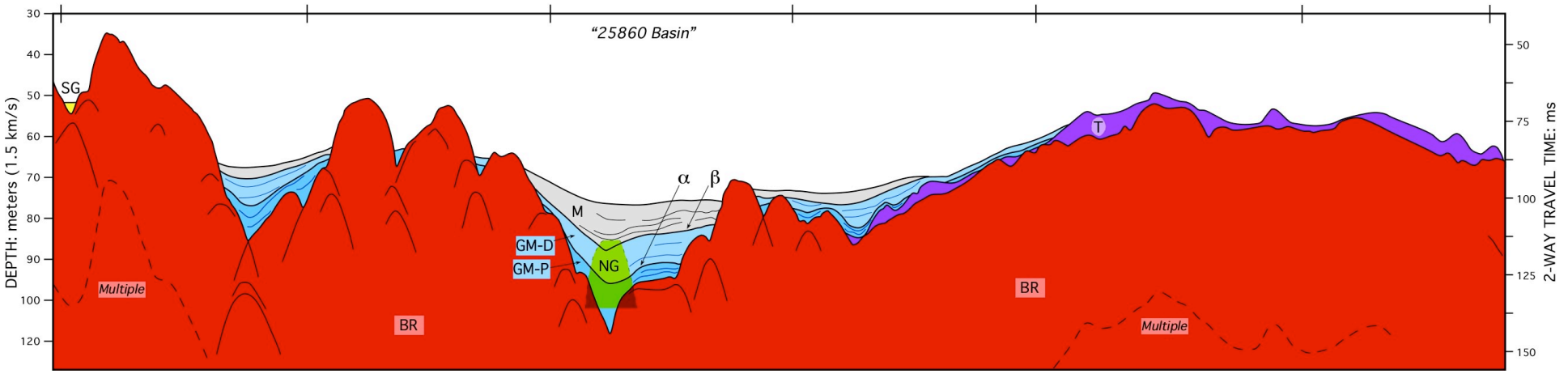
"25860 Basin"
DEPTH: meters (1.5 km/s)
2-WAY TRAVEL TIME: ms
SG
Multiple
BR
GM-D
GM-P
M
NG
α
β
T
BR
Multiple

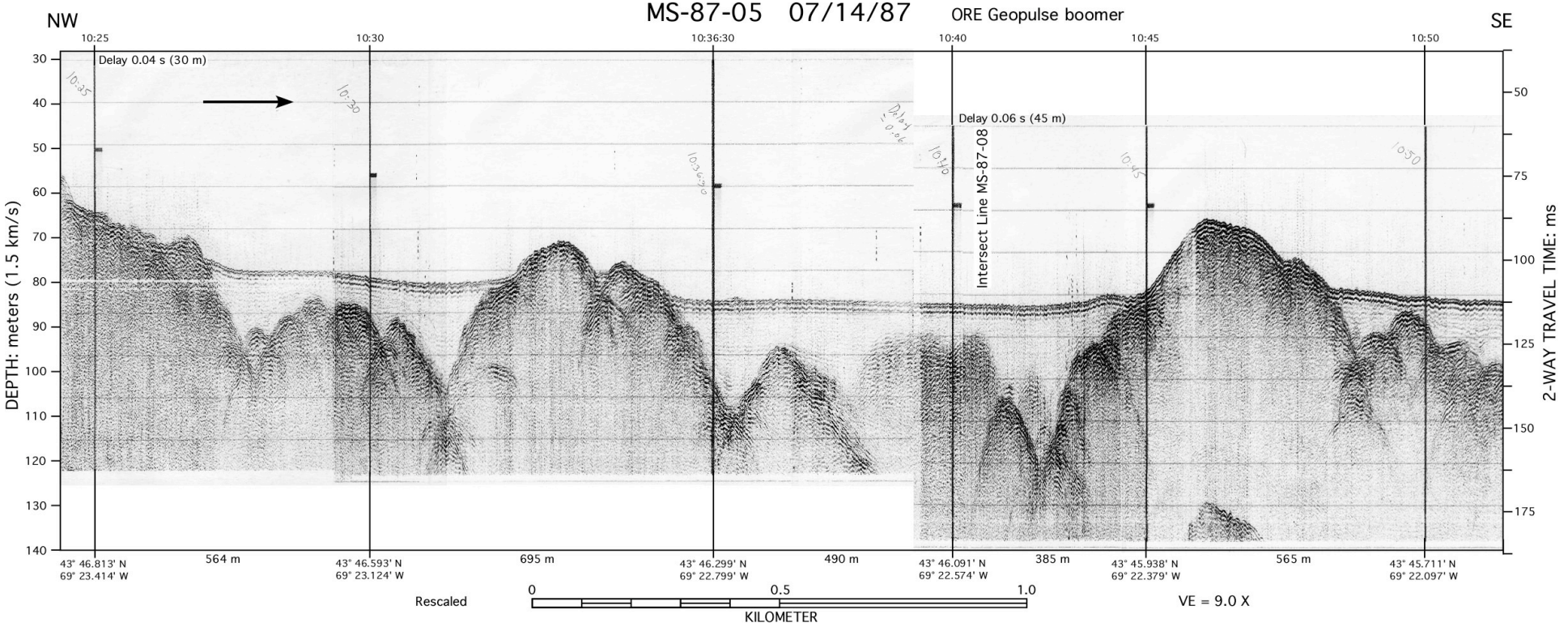
MS-87-05 07/14/87 ORE Geopulse boomer
NW
SE
10:25
10:30
10:36:30
10:40
10:45
10:50
Delay 0.04 s (30 m)
Delay 0.06 s (45 m)
Intersect Line MS-87-08
DEPTH: meters (1.5 km/s)
2-WAY TRAVEL TIME: ms
43° 46.813' N
69° 23.414' W
564 m
43° 46.593' N
69° 23.124' W
695 m
43° 46.299' N
69° 22.799' W
490 m
43° 46.091' N
69° 22.574' W
385 m
43° 45.938' N
69° 22.379' W
565 m
43° 45.711' N
69° 22.097' W
Rescaled
0
0.5
1.0
KILOMETER
VE = 9.0 X

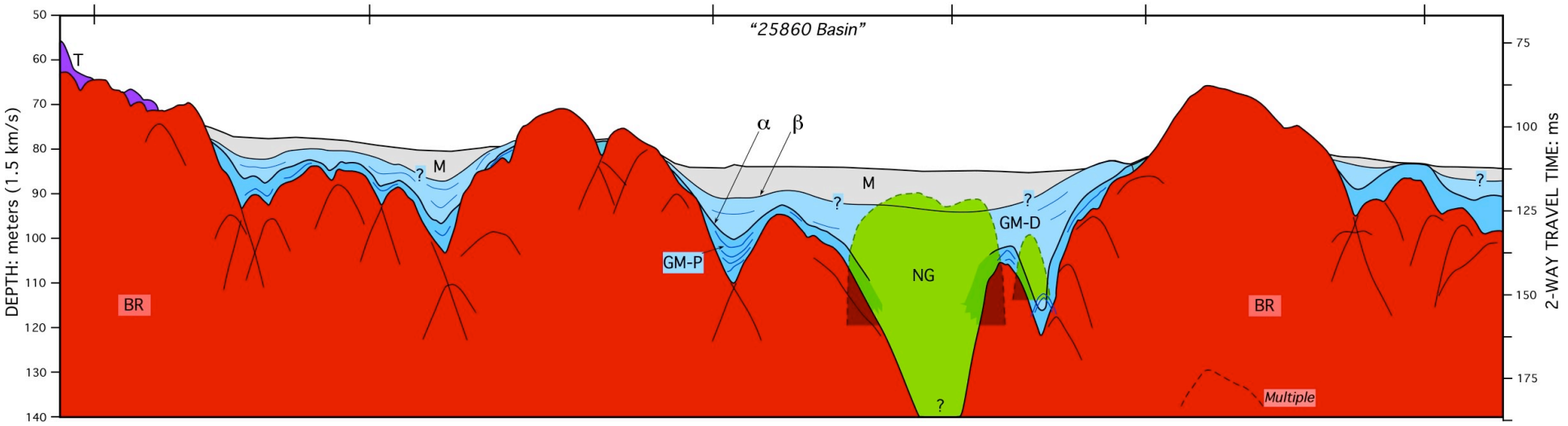
"25860 Basin"
DEPTH: meters (1.5 km/s)
2-WAY TRAVEL TIME: ms
T
M
α
β
GM-P
NG
GM-D
BR
BR
Multiple

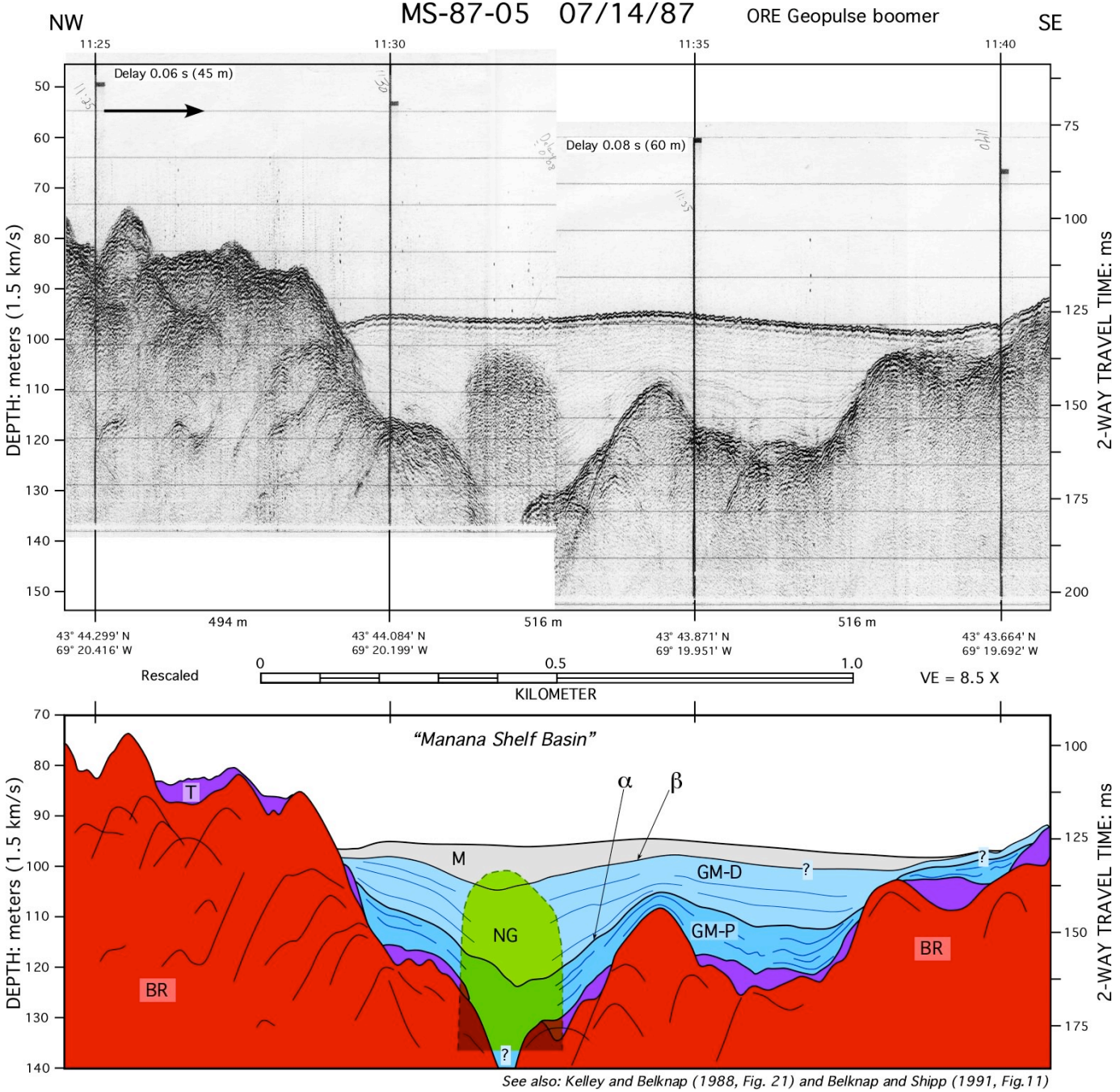

See also: Kelley and Belknap (1988, Fig. 21) and Belknap and Shipp (1991, Fig.11)

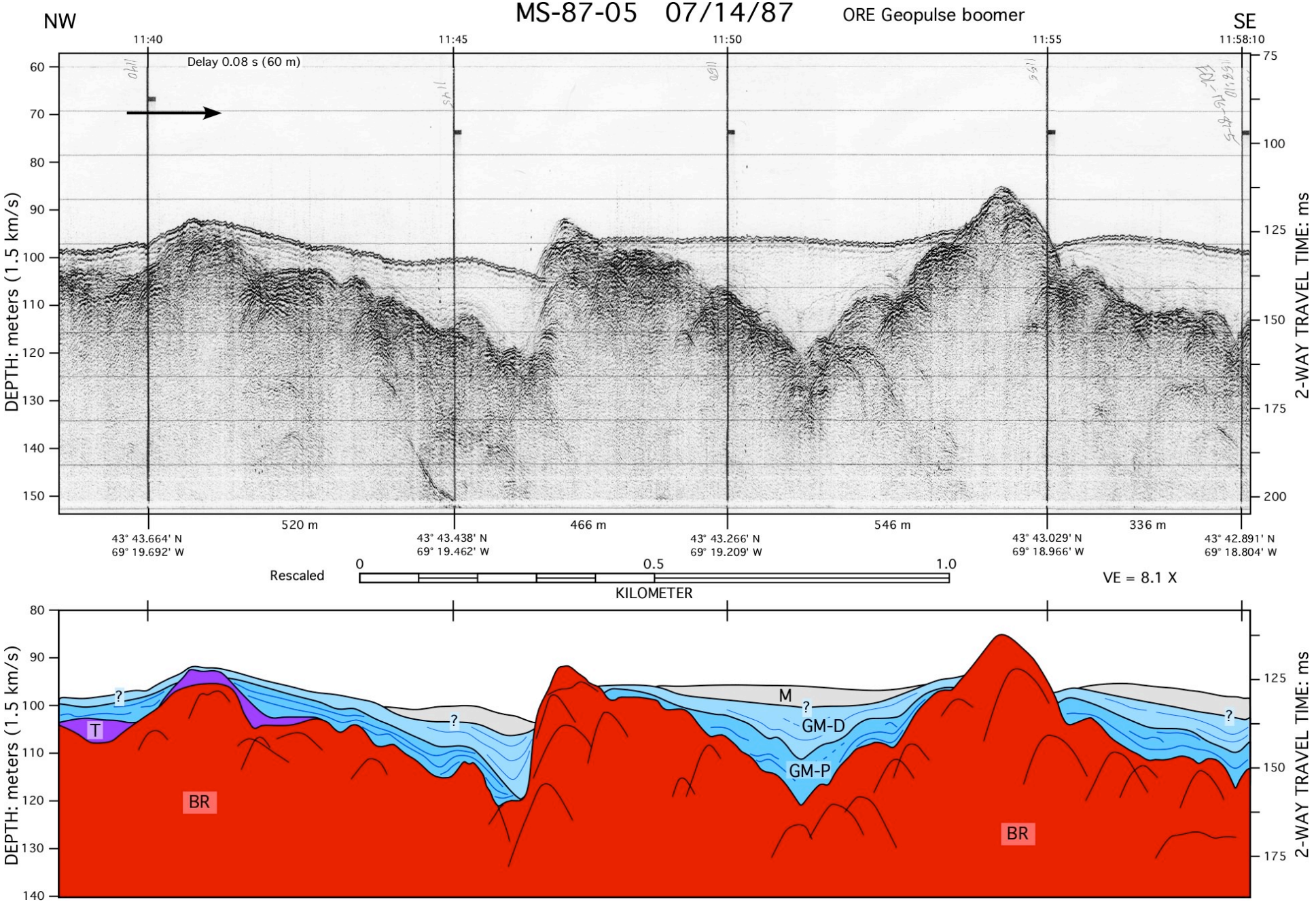
MS-87-05 07/14/87
ORE Geopulse boomer
NW
SE
11:40
11:45
11:50
11:55
11:58:10
Delay 0.08 s (60 m)
DEPTH: meters (1.5 km/s)
2-WAY TRAVEL TIME: ms
520 m
466 m
546 m
336 m
43° 43.664' N
69° 19.692' W
43° 43.438' N
69° 19.462' W
43° 43.266' N
69° 19.209' W
43° 43.029' N
69° 18.966' W
43° 42.891' N
69° 18.804' W
Rescaled
0
0.5
1.0
KILOMETER
VE = 8.1 X
T
BR
M
GM-D
GM-P
BR

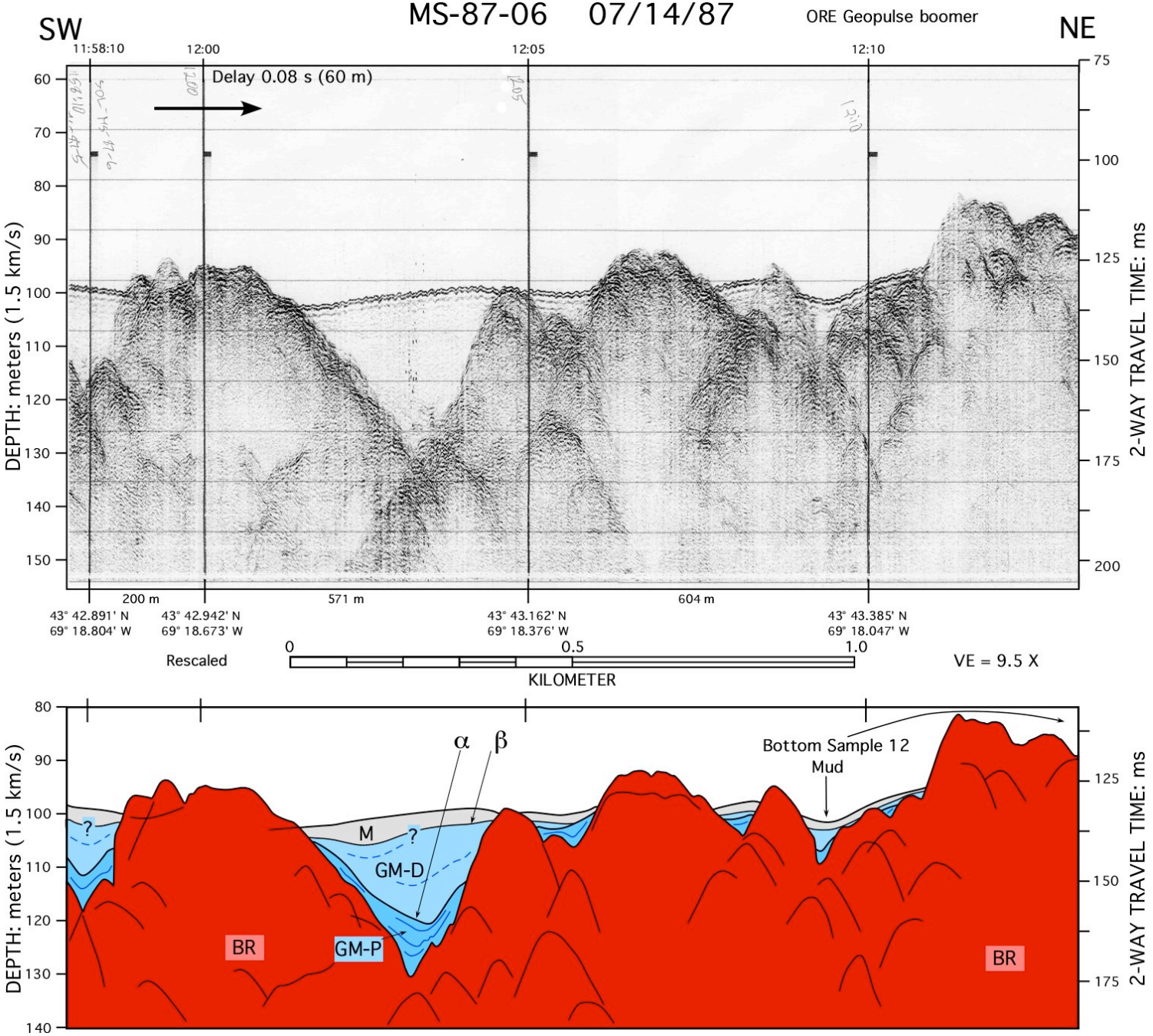
MS-87-06 07/14/87
ORE Geopulse boomer
SW
NE
11:58:10
12:00
12:05
12:10
Delay 0.08 s (60 m)
DEPTH: meters (1.5 km/s)
2-WAY TRAVEL TIME: ms
200 m
571 m
604 m
43° 42.891' N
69° 18.804' W
43° 42.942' N
69° 18.673' W
43° 43.162' N
69° 18.376' W
43° 43.385' N
69° 18.047' W
Rescaled
0
0.5
1.0
KILOMETER
VE = 9.5 X
α
β
Bottom Sample 12
Mud
M
GM-D
GM-P
BR
BR

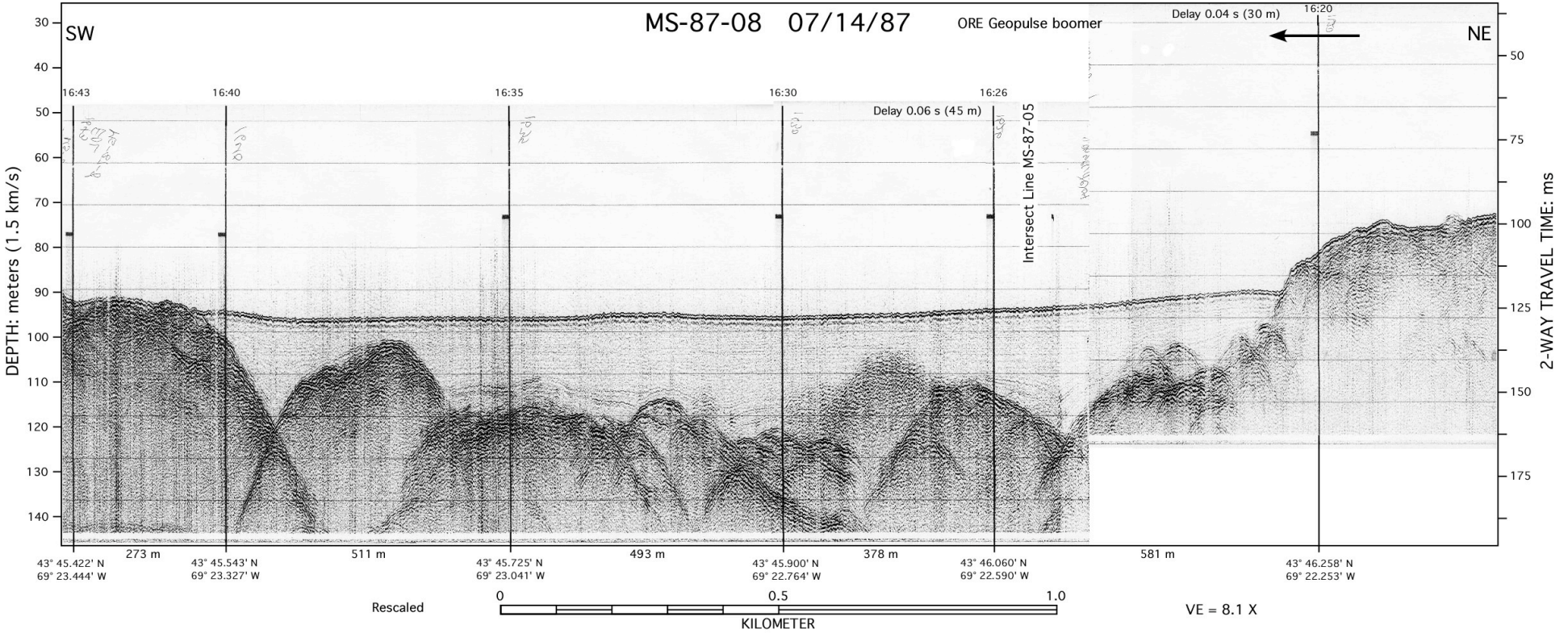
MS-87-08 07/14/87
ORE Geopulse boomer
SW
NE
Delay 0.04 s (30 m)
Delay 0.06 s (45 m)
Intersect Line MS-87-05
DEPTH: meters (1.5 km/s)
2-WAY TRAVEL TIME: ms
16:43
16:40
16:35
16:30
16:26
16:20
273 m
511 m
493 m
378 m
581 m
43° 45.422' N
69° 23.444' W
43° 45.543' N
69° 23.327' W
43° 45.725' N
69° 23.041' W
43° 45.900' N
69° 22.764' W
43° 46.060' N
69° 22.590' W
43° 46.258' N
69° 22.253' W
Rescaled
KILOMETER
VE = 8.1 X

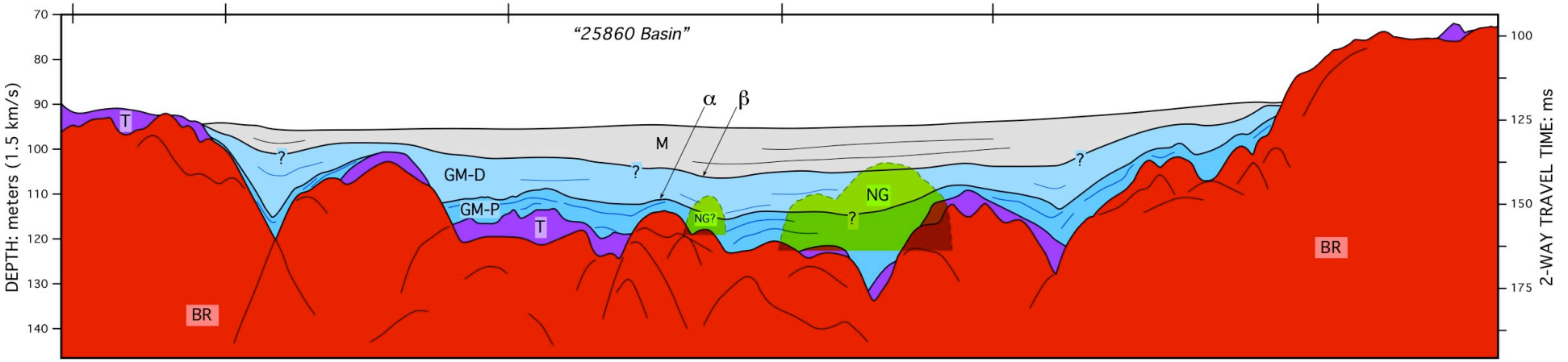
"25860 Basin"
DEPTH: meters (1.5 km/s)
2-WAY TRAVEL TIME: ms
T
M
GM-D
GM-P
NG
NG?
BR
α
β

Table 11. Regressions of log_{10} transformed adjusted numbers of fishes per tow on depth (m) and Pearson correlation coefficients among the transformed numbers, depth, and year from regions 2 and 3 from autumn 2000 through spring 2010, with seasons combined. Regression model is: log_{10} adjusted number per tow = constant + coefficient x depth. Italics = *p* values >0.05 (not significant). Listed in order of decreasing adjusted r^2. Only positive tows included.

Species	N	Regression coefficient (log_{10})	*p* value	Adjusted r^2	Correlation: log_{10} of adjusted number and depth	Correlation: log_{10} of adjusted number and year	Correlation: log_{10} of depth and year
Winter flounder	592	-0.0131	0.0000	0.4206	-0.6493	-0.0240	0.0117
Silver hake	664	0.0170	0.0000	0.3463	0.5893	-0.1183	0.0579
Atlantic herring	665	-0.0186	0.0000	0.2873	-0.5370	0.0228	0.0544
Rainbow smelt	229	-0.0216	0.0000	0.2776	-0.5298	-0.1137	0.0335
American plaice	575	0.0105	0.0000	0.2315	0.4826	0.1979	0.0256
Witch flounder[1]	273	0.0129	0.0000	0.2073	0.4585	-0.0766	0.1159
Witch flounder[2]	272	0.0132	0.0000	0.2033	0.4541	-0.0744	0.1274
Fourbeard rockling	323	0.0054	0.0000	0.1440	0.3830	0.1360	0.1188
Red hake	606	0.0058	0.0000	0.1109	0.3352	0.0518	0.0494
Spiny dogfish	135	0.0083	0.0002	0.0919	0.3141	-0.0156	0.2884
Haddock	141	-0.0042	0.0002	0.0865	-0.3050	-0.1878	0.3265
American sand lance	19	0.0427	*0.1350*	0.0752	-0.1178	0.3557	-0.2432
Atlantic cod	249	-0.0024	0.0001	0.0529	-0.2382	-0.1854	0.2010
Butterfish	269	-0.0057	0.0001	0.0495	-0.2303	0.3263	-0.0507
White hake	583	0.0038	0.0000	0.0437	0.2131	0.1050	0.0656
Scup[1]	38	-0.0063	*0.1607*	0.0276	-0.2322	-0.1870	-0.4941
Scup[4]	37	-0.0034	*0.3869*	0.0000	-0.1465	-0.2603	-0.4947
Goosefish	374	0.0024	0.0011	0.0258	0.1686	-0.3406	0.3227
Atlantic mackerel	121	-0.0039	*0.0604*	0.0212	-0.1712	0.0003	-0.0587
Windowpane	539	-0.0021	0.0035	0.0139	-0.1256	-0.0562	0.1013
Blueback herring	393	-0.0020	0.0398	0.0082	-0.1037	-0.1371	0.0783
Acadian redfish	373	0.0022	0.0463	0.0080	0.1032	0.0980	0.0376
Alewife	734	-0.0019	0.0157	0.0066	-0.0891	0.1140	0.0673
Atlantic menhaden	59	-0.0054	*0.2556*	0.0055	-0.1504	-0.0714	0.0706
American shad[1]	312	-0.0013	*0.1278*	0.0043	-0.0864	0.0109	0.1612
American shad[3]	310	-0.0005	*0.5277*	0.0000	-0.0364	0.0167	0.1605
Longhorn sculpin	591	-0.0013	*0.1304*	0.0022	-0.0623	-0.1791	0.1310

[1]One outlier included. [2]One outlier omitted. Made little difference. [3]Two outliers omitted. Made some difference; raised *p* value.
[4]One outlier omitted. Made some difference; raised *p* value, lowered explained variance.

Table 12. Regressions of $\log_{10}$ transformed adjusted numbers of macroinvertebrates per tow on depth (m) and Pearson correlation coefficients among the transformed numbers, depth, and year from regions 2 and 3 from autumn 2000 through spring 2010, with seasons combined. Regression model is: $\log_{10}$ adjusted number per tow = constant + coefficient x depth. Italics = *p* values >0.05 (non significant). Listed in order of decreasing adjusted r^2. Only positive tows included.

Species	N	Regression Coefficient ($\log_{10}$)	*p* value	Adjusted r^2	Correlation: $\log_{10}$ of adjusted number and depth	Correlation: $\log_{10}$ of adjusted number and year	Correlation: depth and year
Northern shrimp	460	0.0223	0.0000	0.3471	0.5904	0.3473	0.0002
American lobster	694	-0.0135	0.0000	0.2931	-0.5423	0.0871	0.0652
Bristled longbeak	684	0.0122	0.0000	0.2315	0.4824	-0.0047	0.0415
Krill	189	0.0021	0.0000	0.1479	0.3905	0.1166	0.0618
Shortfin squid[3]	168	0.0076	0.0002	0.0728	0.2799	0.6298	0.2115
Shortfin squid[1]	170	0.0076	0.0004	0.0672	0.2697	0.6362	0.2176
Sevenspine bay shrimp	321	-0.0060	0.0000	0.0480	-0.2257	0.1875	0.0441
Aesop shrimp	635	0.0042	0.0002	0.0201	0.1470	0.3220	0.0167
Jonah crab	478	0.0020	0.0018	0.0183	0.1425	-0.1833	0.0420
Atlantic rock crab	291	-0.0028	0.0173	0.0160	-0.1394	-0.0768	-0.2103
Brittle stars[4]	170	0.0025	*0.0551*	0.0159	0.1474	0.2186	0.2398
Sea scallop	264	0.0016	*0.2255*	0.0018	0.0748	-0.2881	0.1949
Waved astarte[1]	81	0.0029	*0.3767*	0.0000	0.0995	-0.3135	0.1129
Waved astarte[2]	78	0.0022	*0.3969*	0.0000	0.0973	-0.2598	0.1191
Longfin squid	264	-0.0011	*0.3791*	0.0000	-0.0543	0.0556	0.1520
Brittle stars[5]	161	-0.0001	*0.9353*	0.0000	-0.0064	0.1372	0.2093
Northern cyclocardia[6]	41	0.0005	*0.9118*	0.0000	0.0178	-0.2503	0.1827
Northern cyclocardia[7]	35	0.0005	*0.4091*	0.0000	-0.1440	0.1404	0.2180

[1]One outlier included. [2]Three outliers omitted. Made little difference. [3]Two outliers omitted. Made little difference. [4]Five outliers included. [5]Nine outliers omitted. Made some difference toward more conservative results. [6]Four outliers included. [7]Six outliers omitted. Made some difference.

DeepCWind Test Site Monitoring for Tagged Fish

2010 – 2011

Information compile by: Gayle Zydlewski, University of Maine

Fish detections made possible by those who tagged these fish:

Dogfish: Roger Rulifson and Jennifer Cudney, East Carolina University
Atlantic Sturgeon: Gayle Zydlewski and Mike Kinnison, University of Maine
James Sulikowski, University of New England
Atlantic salmon: Joseph Zydlewski and Dan Stich, USGS Cooperative Fish and Wildlife Research Unit

Reference as: Zydlewski, Rulifson, Cudney, Kinnison, Sulikowski, Zydlewski and Stich, unpublished data

Total time monitored: June 2010 – August 2011

Approximate detection range: ~ 0.8 km for all tag types listed below

Total number of individuals detected: 19

- 4 dogfish (Summer)
- 7 Atlantic sturgeon (primarily winter, one in summer)
- 8 Atlantic salmon (spring – May)

Dogfish

Release Date	Release Location	Last Detect Date PRIOR to buoy detect	Last Detect Location PRIOR to buoy detect	Detect season	Date Detect @ buoy	Time (in min) at buoy (# of detects)	Last Detect Date AFTER buoy detect	Last Detect Location AFTER buoy detect
1/15/2010	Oregon Inlet to Hatteras			summer	8/2/2010	17 (4)	10/12/2010	Cape Cod
1/15/2010	Oregon Inlet to Hatteras			summer	8/3/2010	18 (4)	10/24/2010	Cape Cod
1/15/2010	Oregon Inlet to Hatteras	10/1/2010	Cape Cod	summer	8/6/2011	61 (46)		
1/15/2010	Oregon Inlet to Hatteras	2/1/2011	North Carolina	summer	8/18/2011	16 (7)		

Notes

- Unsure of total number tagged East coast-wide (estimate: 100)
- 9 other individuals detected on buoys A and B
- Usual to have long-distance migrations
    - *Much of the population travels north in the spring and summer and south in the fall and winter. Some spiny dogfish remain in northern waters throughout the year and move offshore during the winter* (NOAA, NEFSC Resource Evaluation and Assessment Division; relevant publication: Jensen 1965).

Atlantic salmon: only in 2011 (deployment in 2010 did not cover the migratory season)

Release Date	Release Location	Last Detect Date PRIOR to buoy detect	Last Detect Location PRIOR to buoy detect	Detect season	Date Detect @ buoy	Time (in min) at buoy (# of detects)	Last Detect Date AFTER buoy detect	Last Detect Location AFTER buoy detect
4/25/2011	Penobscot River (Milo)	5/13/2011	Penobscot Bay	spring	5/18/2011	25 (44)		
4/25/2011	Penobscot River (Milo)	5/14/2011	Penobscot Bay	spring	5/18/2011	15 (21)	6/18/2011	Halifax, NS
4/27/2011	Penobscot River (Passadumkeag)	5/13/2011	Penobscot River (estuary)	spring	5/18/2011	16 (15)		
4/25/2011	Penobscot River (Milo)	5/16/2011	Penobscot Bay	spring	5/20/2011	10 (15)	6/7/2011	Halifax, NS
5/12/2011	Penobscot River (Abbot) - WILD	5/19/2011	Penobscot Bay	spring	5/21/2011	1 (1, but both receivers)		
4/27/2011	Penobscot River (Passadumkeag)	5/17/2011	Penobscot Bay	spring	5/25/2011	34 (26)	6/10/2011	Halifax, NS
4/27/2011	Penobscot River (Passadumkeag)	5/15/2011	Penobscot Bay	spring	5/27/2011	22 (25)	6/22/2011	Halifax, NS
5/12/2011	Penobscot Bay	5/16/2011	Penobscot Bay	spring	5/28/2011	31 (43)		

Notes

- 381 tagged in the Penobscot, expect 224 survived to the ocean (Stich unpublished)
- No detections on other GoMOOS buoys with receivers
- Likely a migration pathway for Atlantic salmon smolts

Atlantic sturgeon

Release Date	Release Location	Last Detect Date PRIOR to buoy detect	Last Detect Location PRIOR to buoy detect	Detect season	Date Detect @ buoy	Time (in min) at buoy (# of detects)	Last Detect Date AFTER buoy detect	Last Detect Location AFTER buoy detect
10/9/2010	Saco River	10/9/2009	Saco River	winter	1/1/2011	26 (4)	10/5/2011	Saco Bay
8/26/2010	Saco River	8/26/2010	Saco River	winter	1/11/2011	39 (9)	10/12/2011	Saco Bay
8/26/2010	Saco River	8/26/2010	Saco River	winter	2/10/2011*	32(7)	11/6/2011	Saco River
6/9/2010	Penobscot River (estuary)	10/18/2010	Penobscot Bay	winter	2/11/2011	40 (16)	6/19/2011	Union River
7/31/2009	Saco River	7/31/2009	Saco River	winter	2/14/2011	1 (1)	10/19/2011	Saco Bay
10/9/2010	Saco River	10/9/2009	Saco River	winter	2/16/2011**	12 (44)	9/22/2011	Saco Bay
8/2/2010	Penobscot River (estuary)	6/26/2011	Penobscot River (estuary)	summer	7/23/2011	11 (18)	7/25/2011	Kennebec River

Notes

- ~100 tagged in the GOM
- 2 other unique Atlantic sturgeon detected on Buoys A, B, E
- Detections of these individuals on other GoMOOS buoys with receivers (A, B, E):
    - *: detected on Buoy E same day
    - **: detected on Buoy E next day
- Likely a migration pathway

DE-EE0002891

FINAL TECHNICAL REPORT

VOLUME 2: COUPLED MODELS

DeepCwind Consortium Research Program

January 15, 2010 – March 31, 2013

Habib J. Dagher, Ph.D., P.E., University of Maine
James Browning, University of Colorado
Alexander J. Coulling, University of Maine
Matthew J. Fowler, University of Maine
Andrew J. Goupee, Ph.D., University of Maine
Anant Jain, Intertek
Jason M. Jonkman, National Renewable Energy Laboratory
Richard W. Kimball, Ph.D., Maine Maritime Academy
Bonjun Koo, Ph.D., Technip
Matthew Lackner, Ph.D., University of Massachusetts
Kostas Lambrakos, Ph.D., Technip
Ho-Joon Lim, Technip
Heather R. Martin, University of Maine
Marco Masciola , National Renewable Energy Laboratory
Paul Molta, National Renewable Energy Laboratory
Ian Prowell, MMI Engineering
Amy N. Robertson, National Renewable Energy Laboratory
Gordon Stewart, University of Massachusetts
Andrew H. P. Swift , Ph.D., P.E., Texas Tech University
Dale A. Thomas III, Maine Maritime Academy
Anthony M. Viselli, P.E., University of Maine

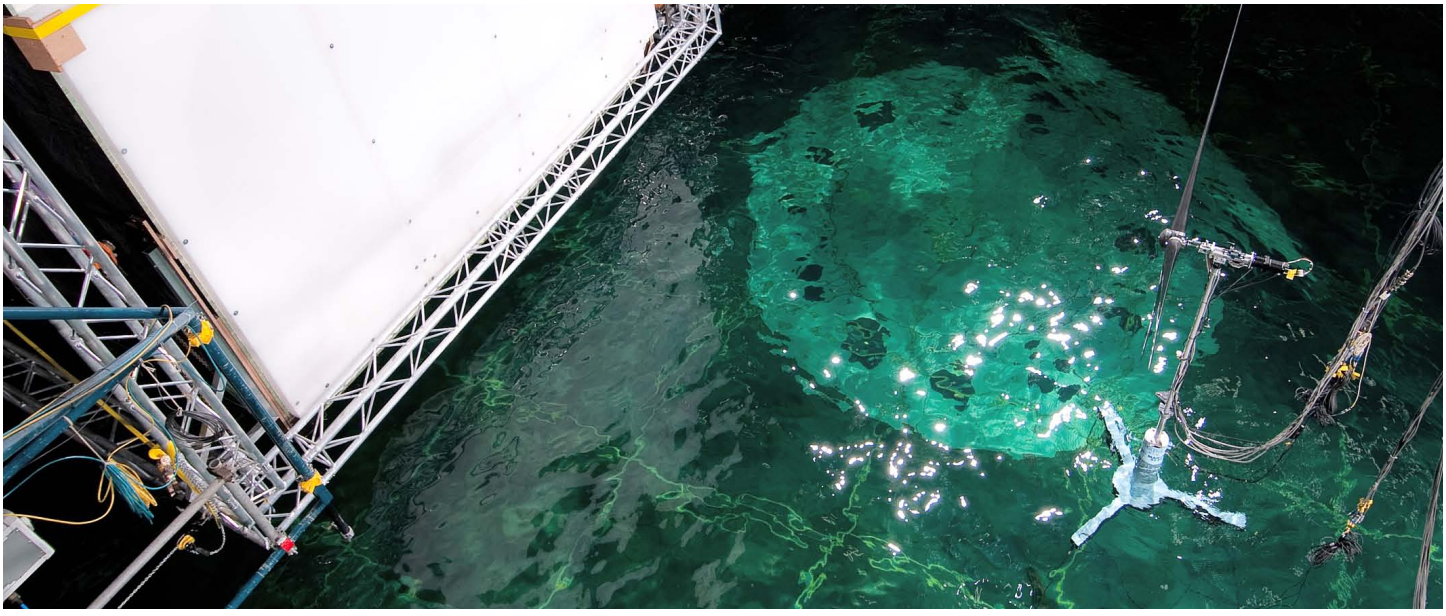

1 Introduction

The United States has a great opportunity to harness an indigenous abundant renewable energy resource: offshore wind. In 2010, the National Renewable Energy Laboratory (NREL) estimated there to be over 4,000 GW of potential offshore wind energy found within 50 nautical miles of the US coastlines (Musial and Ram, 2010). The US Energy Information Administration reported the total annual US electric energy generation in 2010 was 4,120 billion kilowatt-hours (equivalent to 470 GW) (US EIA, 2011), slightly more than 10% of the potential offshore wind resource. In addition, deep water offshore wind is the dominant US ocean energy resource available comprising 75% of the total assessed ocean energy resource as compared to wave and tidal resources (Musial, 2008). Through these assessments it is clear offshore wind can be a major contributor to US energy supplies.

The caveat to capturing offshore wind along many parts of the US coast is deep water. Nearly 60%, or 2,450 GW, of the estimated US offshore wind resource is located in water depths of 60 m or more (Musial and Ram, 2010). At water depths over 60 m building fixed offshore wind turbine foundations, such as those found in Europe, is likely economically infeasible (Musial *et al.*, 2006). Therefore floating wind turbine technology is seen as the best option for extracting a majority of the US offshore wind energy resource.

1.1 Motivation

In order to pursue commercial development of floating wind turbine technology a validated aero-hydro-servo-elastic numerical model is needed to accurately predict the dynamic system behavior during the design and optimization process. Currently, there are very few publicly available coupled numerical models for simulating the performance of floating wind turbines. These codes, such as the NREL's FAST (Jonkman and Buhl, 2005; Jonkman, 2007), have yet to be fully validated against real data as little published information of this type currently exists.

As of the writing of this report, there exists only two commercial scale floating wind turbines in the world: the Hywind by Statoil (Neville, 2009) and the WindFloat by Principle Power (Aubault *et al.*, 2009; Cermelli *et al.*, 2009; Roddier *et al.*, 2009) . The Hywind spar-buoy design supports a 2.3 MW horizontal axis wind turbine and is instrumented to capture key performance data. The WindFloat concept supports a 2 MW horizontal axis wind turbine mounted to a three column semi-submersible and is also instrumented to capture coupled aero-hydro-servo-elastic data. For both of these prototypes, however, the collected information is confidential and is not available to the public. Therefore, this information is inaccessible for many of the parties interested in calibrating and validating numerical analysis codes for offshore floating wind turbines.

Other limited sources of data do exist from the scale model testing of floating wind turbine concepts in a wave basin. Froude scale basin model testing is a refined science and is commonly used to test designs of large scale offshore vessels and structures by the oil and gas industry, military, and marine industries (*e.g.* see Chakrabarti, 1994). A basin model test requires less time, resources and risk than a full scale test while providing real and accurate data for model validation. Protocol for properly modeling the coupled wind and wave loads on a floating wind turbine in a wave basin test environment, however, have not been established. The diverse loads experienced by a floating wind turbine are characterized by dynamic wind spectra, irregular wave loads and many other complex factors. These varied environmental loads combined with challenging fluid-structure interaction, turbine performance and flexible member structural dynamics phenomena make the prospect of performing an accurate scale model test a challenging one. Despite the aforementioned difficulty, a select few floating wind turbine model tests have been performed in wave basins. These include efforts by Principle Power Inc. (Roddier *et al.*, 2010), Hydro Oil & Energy (Skaare *et al.*, 2007) and WindSea AS (Windsea, 2012). However, these tests

only cover select floating wind turbine concepts and report only limited to modest information regarding the scaling methodologies and testing techniques employed. In addition, the differing methods utilized in the aforementioned model tests make it difficult to directly compare the relative performance of the various floating wind turbine concepts considered. Therefore, it is clear that a comprehensive, high-quality data set of several floating wind turbine concepts is needed for the continued development and validation of coupled floating wind turbine simulators.

1.2 Objectives

The primary goal of the basin model test program discussed herein is to properly scale and accurately capture physical data of the rigid body motions, accelerations and loads for different floating wind turbine platform technologies. The intended use for this data is for performing comparisons with predictions from various aero-hydro-servo-elastic floating wind turbine simulators for calibration and validation. Of particular interest is validating the floating offshore wind turbine simulation capabilities of NREL's FAST open-source simulation tool. Once the validation process is complete, coupled simulators such as FAST can be used with a much greater degree of confidence in design processes for commercial development of floating offshore wind turbines.

The test program subsequently described in this report was performed at MARIN (Maritime Research Institute Netherlands) in Wageningen, the Netherlands. The models considered consisted of the horizontal axis, NREL 5 MW Reference Wind Turbine (Jonkman *et al.*, 2009) with a flexible tower affixed atop three distinct platforms: a tension leg platform (TLP), a spar-buoy modeled after the OC3 Hywind (Jonkman, 2010) and a semi-submersible. The three generic platform designs were intended to cover the spectrum of currently investigated concepts, each based on proven floating offshore structure technology. The models were tested under Froude scale wind and wave loads. The high-quality wind environments, unique to these tests, were realized in the offshore basin via a novel wind machine which exhibits negligible swirl and low turbulence intensity in the flow field. Recorded data from the floating wind turbine models included rotor torque and position, tower top and base forces and moments, mooring line tensions, six-axis platform motions and accelerations at key locations on the nacelle, tower, and platform. A large number of tests were performed ranging from simple free-decay tests to complex operating conditions with irregular sea states and dynamic winds.

With the data in hand, analysis of the floating wind turbine responses revealed several of the unique dynamic behaviors of the various floating wind turbine concepts. In particular, the tests highlighted the interplay of the combined wind and wave forcing on floating wind turbine motions and structural load behavior. After analyzing the response of the floating wind turbine concepts, the data was used to validate the floating wind turbine simulator FAST through correlation of the numerical simulation output and test data for the three floating wind turbine types. In addition, validation of coupled simulators other than FAST was also undertaken. A much greater understanding of the strengths and weaknesses of the FAST tool was established through these efforts. In addition to the validation of FAST, several other simulators were investigated many of which utilized more sophisticated hydrodynamics and mooring modules than the standard FAST tools. These efforts were quite helpful in providing suggested improvements for addressing the shortcomings of FAST's fluid-structure interaction calculations. An additional benefit of the validation exercises was the identification of several possibilities for improving model testing procedures for future floating wind turbine wind/wave basin model tests.

1.3 Report Layout

The remainder of this report is organized as follows. In Section 2, an overview of the floating wind turbine model test scaling methods developed for this program are presented. In addition, Section 2 also covers a verification of the scaling laws using FAST simulations in addition to a discussion of Reynolds number effects and their impact on obtaining the correct wind turbine performance in a Froude-scaled

experiment. In Section 3, the technical specifications for three floating wind turbines, in addition to the model instrumentation and test matrix, are presented. For Section 4, select test data is analyzed and the unique dynamic behaviors of each of the three systems is discussed. In Section 5, the model test data is used to calibrate and subsequently validate FAST models of each of the three floating wind turbine systems considered in this report. In addition, Section 5 also investigates the predicative capabilities of improved versions of FAST using the model test data. Afterward, Section 6 presents improved model wind turbine design methodologies and accompanying test data for use in future floating wind turbine wind/wave basin model tests. This is followed by Section 7, which summarizes the conclusions of this report and suggests options for future work.

2 Scaling Methods

Basin model testing is a refined science and is commonly used to test designs of large scale offshore vessels and structures by the oil and gas industry, military, and marine industries (e.g. see (Chakrabarti, 1994)). A basin model test is ideal as it requires less time, resources and risk than a full scale test while providing real and accurate data for system global response. However, even though wave basin testing is well refined for many types of offshore configurations, protocol for properly modeling coupled wind and wave loads on a floating wind turbine in a wave basin test environment has not been established.

Floating wind turbines are complex structures with numerous variables contributing to their complicated dynamic behavior. Simultaneous wind and wave loading, turbine aerodynamics and flexible towers make execution of an accurate scale model test a significant challenge. Despite the aforementioned difficulties, a few select floating wind turbine basin model tests have been performed. Principle Power Inc. tested a $1/67^{th}$ scale semi-submersible wind turbine platform, WindFloat (Roddier *et al.*, 2010). In 2006, Hydro Oil & Energy conducted a $1/47^{th}$ scale model test of a 5 MW spar-buoy floating wind turbine at Marintek's Ocean Basin Laboratory in Trondheim, Norway (Skaare *et al.*, 2007). Another basin test by WindSea of Norway was performed under wind and wave environments at Force Technology on a $1/64^{th}$ scale tri-wind turbine semi-submersible platform (Windsea, 2012). These model tests provided valuable information to respective stake holders and advanced knowledge of floating wind turbine dynamics. However, the methodologies and techniques used during these model tests differed significantly and not all details of the tests have been thoroughly presented in the public domain. Therefore, there is a clear need for a comprehensive, unified model testing methodology for Froude scale testing of floating wind turbines.

In light of this need, this section presents a method for performing combined wind/wave model testing of floating wind turbines under Froude scale conditions. Topics covered include scaling relationships, wind generation techniques and issues concerning the strong dependence of wind turbine aerodynamic behavior on Reynolds number. The method verified using FAST simulations and is demonstrated using results of combined wind/wave $1/50^{th}$ scale model testing performed at MARIN on three floating horizontal axis wind turbine concepts each supporting a model of the 5 MW, 126 m rotor diameter horizontal axis NREL Reference Wind Turbine (Jonkman *et al.*, 2009). The results and corresponding analysis demonstrate that the issues resulting from aerodynamic Reynolds number dissimilitude do not hamper the ability to capture quality global response data for floating wind turbines.

2.1 Overview of Scaling Methods for Floating Wind Turbines

In order to establish a scaling methodology, a particular set of rules and constraints must be selected. The suggested scaling relationships employed for modeling of floating offshore wind turbines are as follows:

1. *Froude number similitude is employed from prototype to scale model.* Offshore platform wave basin tests are typically scaled using Froude number and geometric similarity. Although a Froude model does not scale all parameters properly the dominant factors in the hydrodynamic problem, gravity and inertia,

are properly scaled (Chakrabarti, 1994). For a floating wind turbine, this covers most properties of interest which influence the global dynamic response of the system, excepting the aerodynamic wind forces. Employing a Reynolds number scaling scheme, common for model aerodynamic experiments, is impractical for a floating body subjected to wave forcing. Therefore, Froude scaling is best suited for model testing of floating wind turbines. The Froude number for a free surface wave is

$$Fr_{wave} = C/\sqrt{gL},$$

where C is the wave celerity, or propagation speed, g is the local acceleration due to gravity and L is a characteristic length. The scaling relationship maintained from model scale to the full scale prototype is expressed as

$$Fr_p = Fr_m,$$

where p and m stand for prototype and model, respectively.

2. *Froude scaled wind is employed during basin model testing.* If aerodynamic turbine features are insensitive to Reynolds number, then the wind force to wave force ratio from prototype to model scale is maintained by utilizing Froude scaled wind, defined as

$$Fr_{wind} = U/\sqrt{gL},$$

where U is the wind inflow velocity. Note that the characteristic length L is the same for both the wind and wave Froude numbers. An alternative, yet consistent, way to represent Froude scaled wind is by maintaining the ratio of wind speed to wave celerity from model to full scale. This ratio is identified by the variable Q and represented as

$$Q = U/C.$$

3. *The wind turbine tip speed ratio, TSR, is to be maintained from prototype to scale model. TSR* is computed as

$$TSR = \Omega r/U,$$

where Ω is the rotor rotational speed and r is the blade tip radius. Maintaining *TSR* between the prototype and model is performed by satisfying the relationship

$$TSR_p = TSR_m.$$

Maintaining *TSR* ensures that the turbine rotational speed as well as any system excitation frequencies resulting from rotor imbalance or aerodynamic interaction with the tower will possess the correct frequency. In addition, maintaining *TSR* will yield properly scaled turbine thrust forces and rotor torque in conjunction with a Froude scaled wind environment, assuming a low dependence on Reynolds number for the wind turbine airfoil section lift and drag coefficients. The impact of Reynolds dependent wind blade lift and drag coefficients is discussed in a later section.

While not discussed at length here, it is also important to note that scaling of current loads requires additional measures to accommodate for the mismatch in model and prototype Reynolds numbers (e.g. see (Chakrabarti, 1994) for suggested methods). That stated, the preceding scaling relationships are utilized to obtain the scale factors shown in Table 1 for characterizing a scaled floating wind turbine.

Table 1: Scaling factors for floating wind turbine model testing

Parameter	Scale Factor
Length (e.g. displacement, wave height)	λ
Area	λ^2

Volume	λ^3
Angle	1
Density	1
Mass	λ^3
Time (e.g. wave period)	$\lambda^{0.5}$
Frequency (e.g. rotor rotational speed)	$\lambda^{-0.5}$
Velocity (e.g. wind speed, wave celerity)	$\lambda^{0.5}$
Acceleration	1
Force (e.g. wind, wave, structural)	λ^3
Moment (e.g. structural, rotor torque)	λ^4
Power	$\lambda^{3.5}$
Young's Modulus	λ
Stress	λ
Mass Moment of Inertia	λ^5
Area Moment of Inertia	λ^4

The scale factors are a function of the scale parameter λ which is defined as the ratio of length scales between the prototype and model. With the scale parameter defined, the model value of a desired parameter is obtained by dividing the prototype quantity by the appropriate scale factor in Table 1. For example, if the scale parameter is $\lambda = 50$ and the prototype rotor speed is 10 rpm, then the model rotor speed is equal to $10/50^{-0.5}$, or 70.7 rpm.

To demonstrate some of the practical challenges with constructing a scale model wind turbine, the scale factors in Table 1 are employed to create model specifications for the NREL 5 MW Reference Wind Turbine and OC3 Hywind tower (Jonkman 2010) used for model testing with $\lambda = 50$. The specifications for the various wind turbine and tower components are listed in Table 2. As can be seen in the table, the rated power of the machine is quite low, nearly one millionth the prototype value. In addition, the rotor speed is significantly higher and the wind speed environment, much lower. From a practical standpoint, these quantities do not provide major challenges when constructing a physical model or its accompanying environment. The mass of the components, such as the blade and nacelle, however, are a different matter.

Table 2: Prototype and model specifications for the NREL 5 MW Reference Wind Turbine and OC3 Hywind Tower with scaling parameter $\lambda = 50$

Property	**Prototype**	**Model**
Rated Power	5 MW	5.7 W
Rated Rotor Speed	12.1 rpm	85.6 rpm
Rated Wind Speed	11.4 m/s	1.6 m/s
Blade Mass	17,740 kg	0.14 kg
Blade Length	61.5 m	1.23 m
Hub Mass	56,780 kg	0.45 kg
Nacelle Mass	240,000 kg	1.92 kg
Tower Mass	249,718 kg	1.998 kg
Tower Length	77.6 m	1.55 m
Tower Base Stiffness	6.04×10^{11} N·m^2	1.93×10^{3} N·m^2

This fact is illustrated by the model blade which must be over a meter in length and possess a mass of only 0.14 kg. These blade parameters are necessary in order to correctly model the wind turbine gyroscopic moments. Simultaneously creating an accurate representation of the prototype blade geometry and achieving the mass target is not a simple endeavor. To accomplish this task for the model testing considered here, model wind turbine blades are manufactured from two thin layers of woven carbon fiber

epoxy composite material in a bladder molding process. An image of a completed blade is shown in Figure 1.

Figure 1: Lightweight 1/50th scale carbon fiber epoxy composite model wind turbine blade.

Meeting the mass targets for other tower top components which together impact the tower bending natural frequency, such as the hub and nacelle, also requires careful engineering and design, especially in order to accommodate instrumentation for measuring rotor position, rotor torque, nacelle accelerations, etc. Other creative measures are necessary to meet additional model requirements. For example, to achieve the correct tower bending stiffness to properly emulate the fundamental tower bending frequency, perfectly scaling the material stiffness and tower geometry may be difficult, or even unrealistic as no suitable material may exist. Therefore, it is suggested that the material choice and geometry be tuned together to obtain the desired stiffness, even if neither quantity in and of itself represents the desired model value based on the prototype specifications. For example, the model turbine employed in this study utilizes a tower crafted from two common size hollow aluminum rod sections tailored in length, inner and outer diameter such that the tower mass target and overall tower bending stiffness is achieved. The tower, while not strictly Froude-scaled, yields the correct fundamental tower bending frequencies. An image of the model wind turbine mounted to a semi-submersible platform (a spar-buoy and a TLP were also tested) is shown in Figure 2.

An additional practical challenge outside of creating a functional model wind turbine at such a small scale is the issue of manufacturing a quality Froude scale wind environment for the wind turbine to operate in. The wind environment should be of a high quality with little evidence of fan generated swirl and low turbulence intensity. This requires a dedicated wind generator consisting of a series of fans, screens, as well as a contracting nozzle.

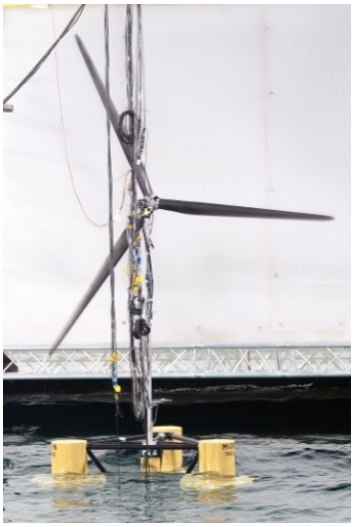

Figure 2: 1/50th scale model NREL 5 MW Reference Wind Turbine mounted to a semi-submersible platform.

In addition, the output area of the nozzle should cover the entire wind turbine rotor in quality wind even as the floating system moves through its expected range of motion. Therefore, a large wind generation system is ideal. However, too large a system is impractical as it will be very costly to build, maintain and

operate. Therefore, a balance must be struck in choosing a model wind turbine size, and hence λ. Ideally the size will be small enough to reduce wind generator requirements, but large enough to yield achievable weight targets for the wind turbine components. Development efforts from the multi-platform floating wind turbine model test program and accompanying wind machine, a schematic of which is shown in Figure 3, suggest a scale parameter λ of approximately 50 is well suited for floating wind turbine experiments of commercial machines.

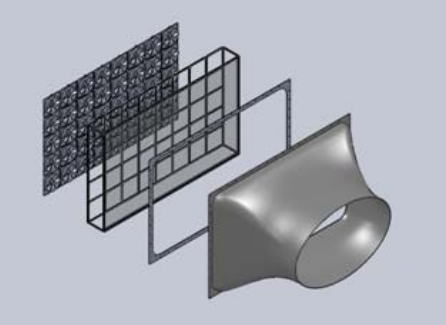

Figure 3: Exploded view of wind generation machine for floating wind turbine wind/wave basin experiments showing, from left to right, a fan bank, screens and a contracting nozzle.

By employing the scaling factors in Table 1 as well as the various recommendations in this section, an adequate floating wind turbine model can be constructed for wind/wave basin testing. However the aerodynamic properties of a typical commercial scale wind turbine rotor are sensitive to Reynolds number, unlike the hydrodynamic properties of the floating platform which possess a weaker dependence on Reynolds number. This scenario creates difficulties in achieving the correct wind forcing from a Froude scale wind turbine and corresponding wind environment. A discussion of the implications of testing a prototype rotor that possesses a strong dependence on Reynolds number will be presented in a later section.

2.2 Verification of Scaling Laws Using FAST

To examine the scaling laws used by DeepCwind, we have conducted a research study to verify them using FAST (Jonkman et. al, 2005). The process, as described in this section, examines if there are any differences between the system responses obtained from full-scale and model-scale simulations in FAST. This assessment is important because all of the results of the tests at MARIN were converted to full scale for reporting purposes. Our verification strategy in this report section is based only on the scaling laws from the previous section and does not include any comparison of actual results from the DeepCwind wind/wave basin experiments. The scaling laws are investigated using two floating offshore wind turbine models, a modified version of the OC3 Hywind and the MIT/NREL TLP. These models are not the exact ones tested in the wave basin, but are sufficient for examining the validity of the scaling approach used for the DeepCwind model tests. The remainder of this section describes the verification procedure, system configurations studied, assumptions and results.

2.2.1 Scaling Law Verification Procedure

This section gives an overview of the FAST code verification and testing process for scaling laws that interlink the full scale and model scale parameters. The process used for verification is described as follows (and depicted in Figure 4):

1. Full-scale FAST models of the two floating offshore wind systems to be examined are modeled.
2. Using the scaling laws, the FAST models are converted to model scale.
3. Simulations are performed at model scale for a variety of load cases.
4. The outputs obtained from the model-scale simulations (forces, displacements) are scaled back up to full scale using the same scaling laws.
5. Simulations are performed using the full-scale model for a variety of load cases.

6. The simulations results from the up-scaled model are then compared to the simulation results from the full-scale model. If the scaling laws are consistent, these results should be the same.

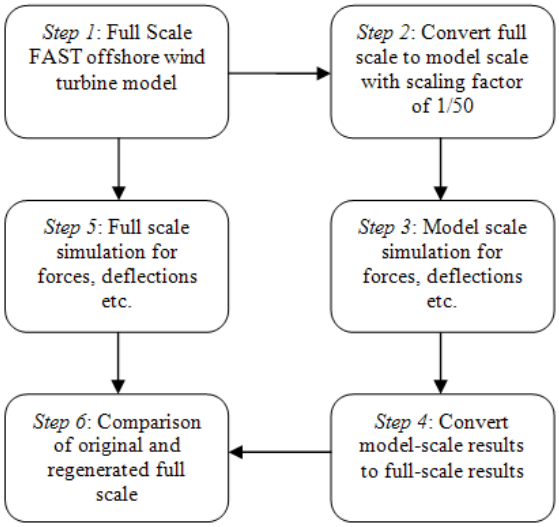

Figure 4: Flowchart for scaling simulation procedure.

2.2.2 System Configurations: Turbine, Platforms, Wind and Wave Specifications

To examine the similarity in system performance between full scale and model scale, simulations are conducted with a variety of loading conditions. Verification of the scaling law accuracy is accomplished through the analysis of two different platform configurations: a modified version of the OC3-Hywind spar buoy and the MIT/NREL TLP. These systems are chosen due to the diversity in design and mooring configuration, and therefore response characteristics.

The turbine used for this research is a 5-MW reference wind turbine (onshore and offshore) from NREL, which is a three-bladed, upwind turbine with rated power of 5 MW. The design of this turbine is a reinvention inspired from the technical specifications of Multibrid M5000, REpower 5M, WindPACT, RECOFF and DOWEC wind turbines (Jonkman et. al., 2009). Some of the properties of the turbine are stated below:

Table 3: Structural and aerodynamic properties of 5-MW wind turbine

Structural and Aerodynamic Properties	Numerical Value
Tip radius	63 m
Hub radius	1.5 m
Tower Height	87.6 m
Rotor Pre-cone angle	2.5 deg
Nacelle Mass	240000 kg
Hub Mass	56780 kg
Air Density	1.225 kg/m^3
Kinematic Viscosity	0.00001464 m^2/sec

The two platform configurations incorporated and compared in this research for various wind and wave loading tests include: the OC3-Hywind spar buoy (Jonkman, 2010) and the NREL/MIT tension leg platform (TLP) (Matha, 2010) configuration. Details on design specifications for these platforms are given below in Table 4 and Figure 5:

Table 4: Structural and hydrodynamic properties of platform configurations

Properties	TLP	Spar-buoy
Tower Draft from MSL	0	-10 m
Center of Moment (Platform) from MSL	40.612 m	89.9155 m
Platform Mass	8600410 kg	7466330 kg
Water displaced in a still water condition	12179.60 m^3	8029.21 m^3
Platform Diameter	18 m	6.5 m
Coefficient of Drag	0.6	0.6

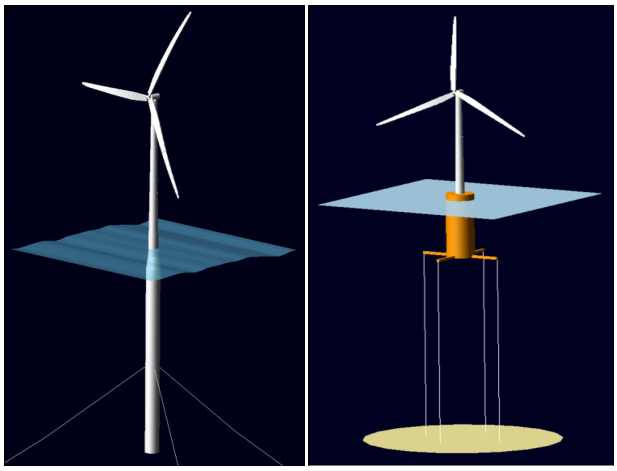

Figure 5: Sketches of OC3-Hywind spar buoy (left) and NREL/MIT TLP (right).

Simulated wind files are generated by using NREL's TurbSim code (B.J. Jonkman, 2009), which generates turbulent wind files to evaluate turbine response in various wind conditions. Wave effects are simulated using HydroDyn (Jonkman, 2007) which generates the hydrodynamic forces and loads using WAMIT (WAMIT Inc., 1998) as a pre-processor for defining the hydrodynamic coefficients of the platform. HydroDyn simulates loads and forces for periodic (consistent amplitude and frequency) and irregular waves. Periodic waves are simulated by using Airy wave theory and non-periodic waves are generated according to JONSWAP/Pierson-Moskowitz spectra (Jonkman, 2007). Predetermined wave conditions for these functions are defined in input files in terms of water density, water depth, significant wave height, peak spectral period and wave direction.

When these scaling laws are applied to the existing wind turbine and offshore floating platform designs, new input files are created for FAST using MATLAB scripts for maintaining accuracy and consistency. FAST v7.00.01a-bjj is applied in all simulations (Jonkman et. al., 2005).

2.2.3 Assumptions

For standardization of scaling laws simulations, we have created and followed few assumptions which are applied to all test procedures demonstrated in this report. These conditions are described below:

1. Fluid properties such as kinematic viscosity for full scale and model scale are constant.
2. Blade airfoil schedule and corresponding coefficients of lift and drag are not scaled for model tests.
3. The generator is prescribed to rotate at a constant speed.

4. Blade and tower vibration modes are constant for full scale and model scale.
5. Control module is inactive in the simulations. Therefore, control algorithm bound parameters such as pitch and yaw angle are either zero or maintained at a constant value for different wind and wave loading conditions.
6. Standard simulation time is assumed to be 630 seconds.
7. The wind and waves are aligned.

2.2.4 Results

The simulations (conducted for both platform configurations) are divided into six categories, as described below:

1. *Static analysis:* The first simulation that was performed is a static analysis to ensure that the mass, buoyancy and mooring pretension of the system are balanced, and therefore are scaled appropriately.
2. *Free-decay tests with initial offsets*: In these tests, the decay pattern is examined to compare structural frequencies and damping characteristics of the systems. Wind and waves are not used in these simulations.
3. *Steady wind and still water:* These tests are conducted to characterize structural response of the system from wind loads only. Wave conditions are ignored in this category. A steady wind at 8 m/s and 1.13 m/s for full scale and model scale, respectively is used with zero vertical and horizontal wind shear. In addition to wind speed, rotor speed is set at 9 rpm and 63.63 rpm for full scale and model scale respectively, according to specifications given for 5-MW wind turbine design.
4. *Still air and periodic waves:* These tests are conducted for assessment of system response from wave-induced loads only. Wind conditions are ignored in this category. Periodic wave conditions such as significant wave height, is 6 m and 0.12 m for full scale and model scale, respectively.
5. *Steady wind and periodic waves*: In these tests, both aerodynamic and hydrodynamic excitations are included in the simulations. The significant wave height is 6 m and 0.12 m for full scale and model scale, respectively. Rotor angular speed is maintained at a constant 9 rpm and 63.63 rpm for full scale and model scale respectively.
6. *Turbulent wind and irregular wave*s: This category of tests is very significant to analyze system response as it represents an extreme stochastic wind/wave loading schedule. The turbulent wind is averaged at 8 m/s at full scale and 1.13 m/s at model scale; with a turbulence intensity of 40%. The waves are irregular with a mean significant wave height of 6 m and 0.12 m for full scale and model scale respectively. As stated earlier, the rotor rpm is kept consistent at 9 rpm and 63.63 rpm for full scale and model scale respectively, with stochastic wind and wave loads.

These tests are conducted independently on both full scale and scale models. The output parameters calculated by FAST are very extensive and therefore only a limited number of parameters are analyzed to ensure the results are similar. The output parameters analyzed include:

1. *Blades*: loads at the base and in-plane and out-of-plane deflections at the tip;
2. *Tower*: tower-top shear, axial force and bending moments
3. *Platf*orm: 6-DOF motion of the platform and loads at the connection point between the platform and tower (tower base)
4. *Mooring Lines*: fairlead and anchor tensions

The scaling laws applied to the above mentioned output parameters that are used to analyze the full scale and model scale compliance are given in Table 5. These laws are also based on Froude scaling regime.

Table 5: Scaling laws for relevant output parameters in FAST code

Output Parameter	Scaling Law
Blade tip deflections	λ
Tower Shear Forces	λ^3
Tower Bending Moments	λ^4
Platform Translational Displacements	λ
Mooring Line Tensions	λ

The output parameters from simulation at both scales and for both platform configurations are shown in Figure 6, Figure 8, Figure 10 and Figure 12 for the spar-buoy platform and Figure 7, Figure 9, Figure 11 and Figure 13 for the TLP. In all these tests, the full-scale and model-scale results are in excellent compliance. But for this report, we have selected only certain test conditions that represent a higher intensity of stochastic wind and wave loads i.e. turbulent wind and non-periodic wave load tests; and different output parameters pertaining to major wind turbine structural components. The following set of figures describe blade tip deflections, tower-top shear forces and bending moments, platform rotational and translational motions, and mooring line fairlead and anchor tensions for spar-buoy and tension-leg platforms. Full-scale and model-scale results are plotted together by blue and red lines and vice-versa for spar buoy and TLP, respectively. In Figure 6 and Figure 7, it is shown that the out of plane and in plane blade tip deflections perfectly coincide with each other. Because Reynolds number is maintained, we have assumed that the airfoil definitions and coefficients of lift and drag of full-scale and model-scale blades are exactly similar, we can conclude that the Froude scaling is capable of scaling the boundary layer flow around an airfoil, under controlled and consistent aerodynamic conditions. Since the aerodynamic conditions for the rotor on both the platform configurations are similar, the simulated tip deflections graphs show good alignment for both cases. On the other hand, the shear and axial forces and bending moment trends for tower top/yaw bearing are quite different among the selected platform configurations.

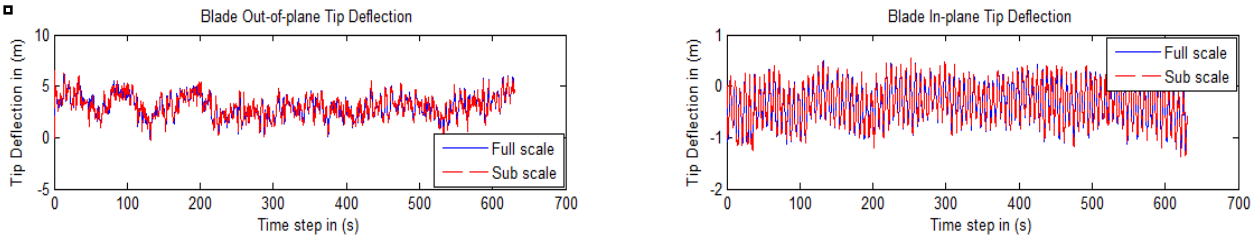

Figure 6: Time history of blade tip out of plane and in plane deflection for a turbine supported by OC3 Hywind spar-buoy platform.

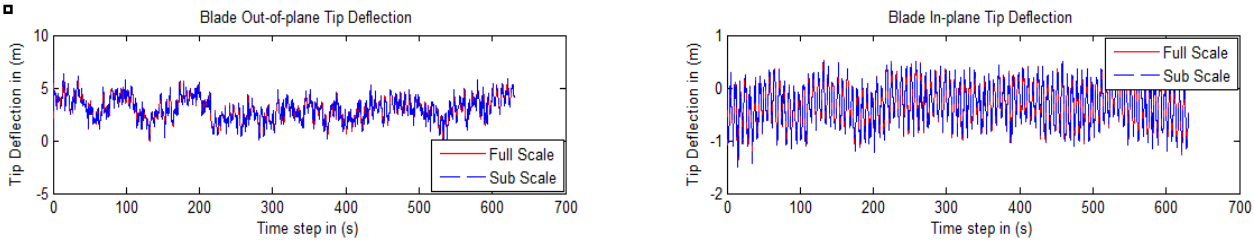

Figure 7: Time history of blade tip out of plane and in plane deflection for a turbine supported by MIT/NREL TLP system.

In Figure 8 (spar-buoy configuration), it is observed that tower top fore-aft shear force reaches to a maximum of approximately 1600N while the same shear force regime is limited to 1200N roughly for a TLP configuration (Figure 9). Similar differences have been observed for side-to-side and vertical force between spar-buoy and TLP systems, where TLP systems have more constrained displacements and rotations as compared to spar-buoy platform. It is important to note here that although the system properties (Table 3 and Table 4) are completely different for both configurations; their structural response is very much consistent when compared between a full-scale and a model-scale system. Moreover, the wind and wave loading regime is required to be similar to obtain such results.

The platform translational and rotational motions are further analyzed to ensure hydrodynamic similitude between the full scale and model scale system. In Figure 10 and Figure 11, it can be observed that surge, sway and heave displacements for spar-buoy platform are much higher in magnitude when compared to a TLP system. A similar pattern is documented for differences between the rotational displacements of the two platform configurations. The explanation for this restricted displacement characteristics is the added pretension in the mooring lines of a TLP system which is not present in the slack mooring lines of a spar-buoy system. This reasoning is further endorsed by the elevated mooring line tensions up to 6000N for a TLP system shown in Figure 13 with higher frequency of perturbations as compared to spar-buoy system (Figure 12). Moreover, the underlying fact that can be summarized from these results is that the hydrodynamic similitude requirements of different platform systems have been met by the scaling laws applied in this research.

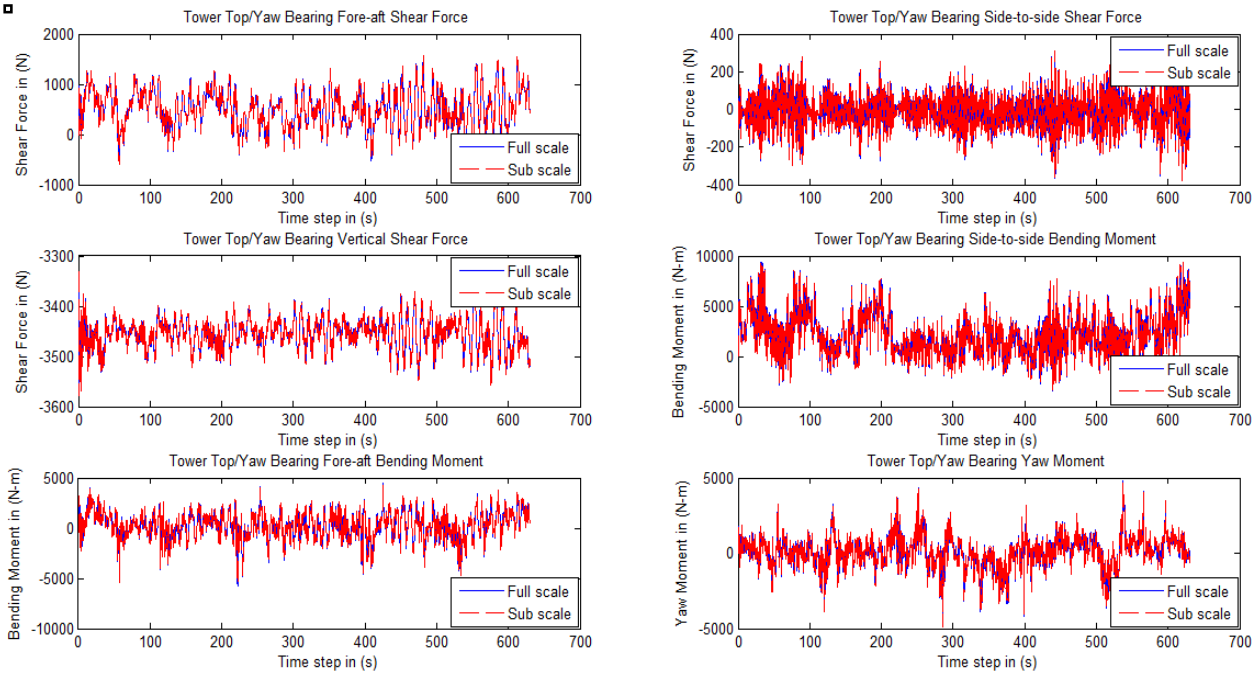

Figure 8: Time history of tower top/yaw bearing shear and axial forces; and bending moments for OC3 Hywind spar-buoy platform.

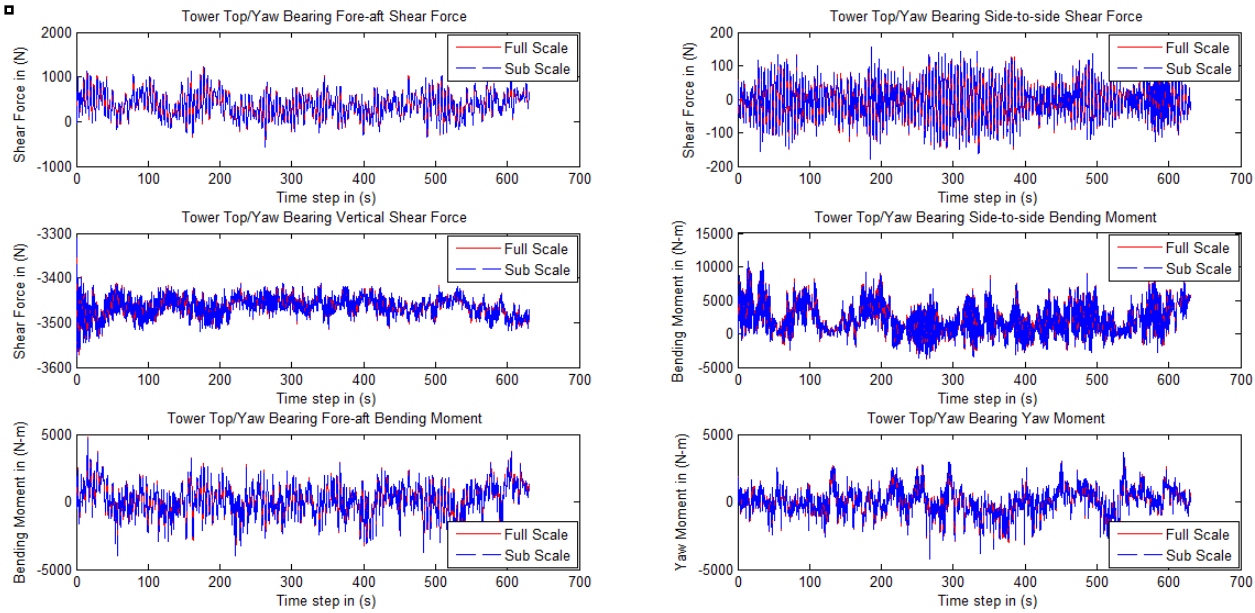

Figure 9: Time history of tower top/yaw bearing shear and axial forces; and bending moments for MIT/NREL TLP system.

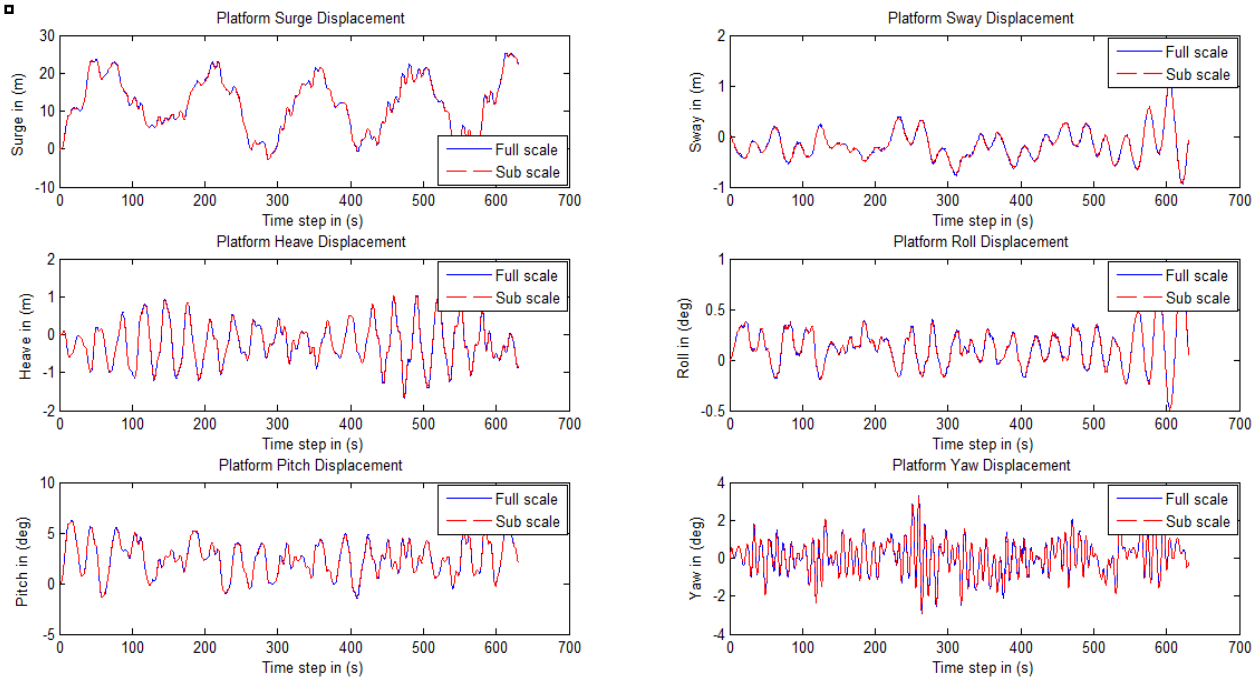

Figure 10: Time history of platform translational and rotational motions for OC3 Hywind spar-buoy platform.

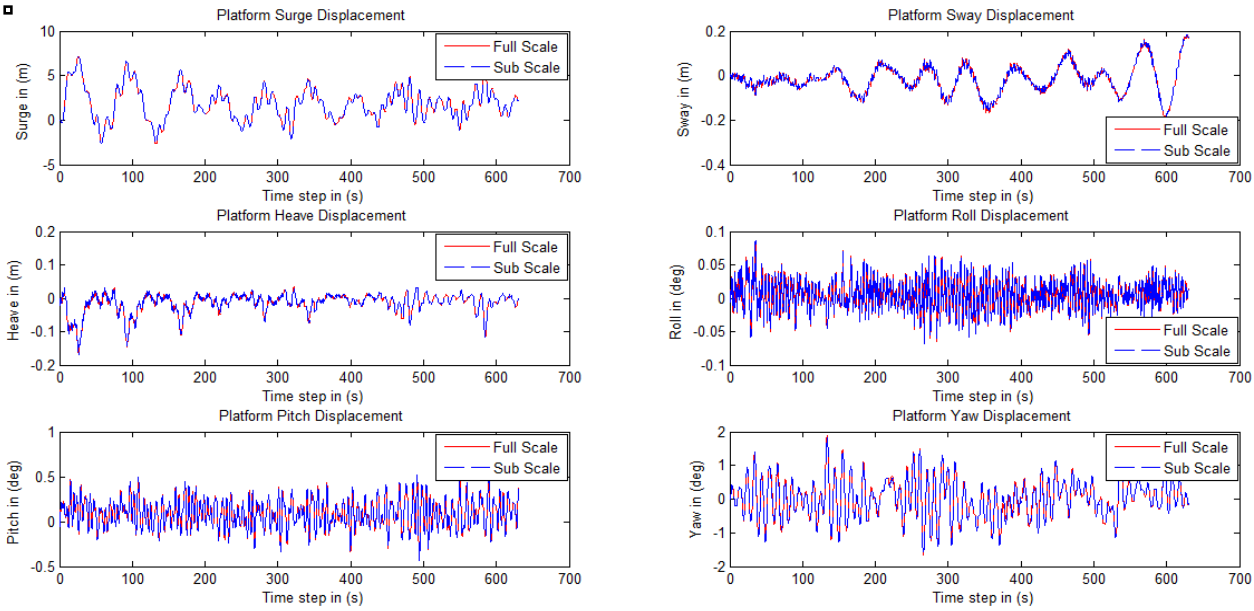

Figure 11: Time history of platform translational and rotational motions for MIT/NREL TLP system.

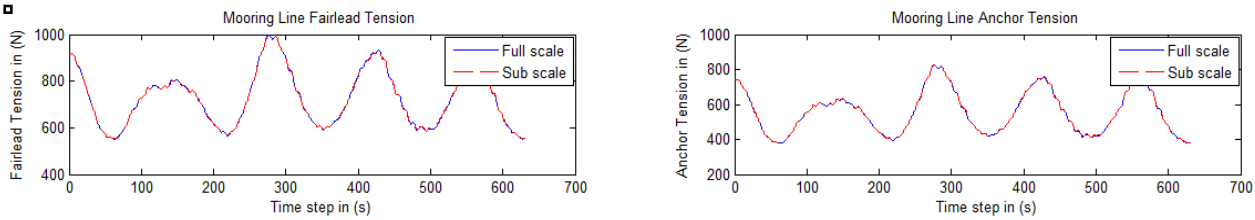

Figure 12: Time history of mooring line fairlead and anchor tension for OC3-Hywind spar-buoy platform.

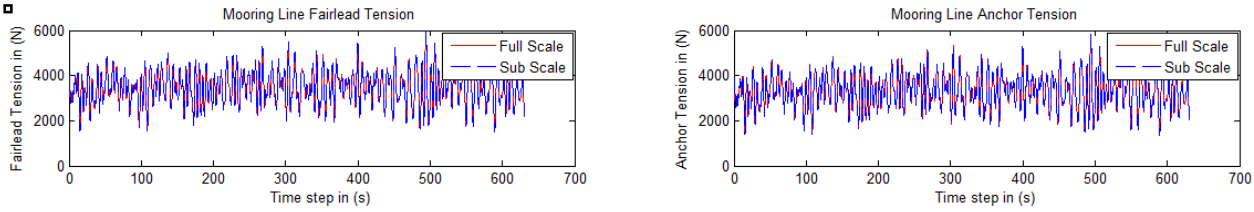

Figure 13: Time history of mooring line fairlead and anchor tension for MIT/NREL TLP system.

In Figure 14, we have shown time histories of wind speed and wave elevation. These parameters are helpful to understand the perturbations related to forces, moments, and motions of different structural components shown in the results of this section. The wind speed reaches to a highest value of 17 m/s for full scale and 2.4 m/s for model scale, respectively. The wave elevation which is measured from a platform reference point attained a maximum value of 5 m above and below the platform. These conditions are quite turbulent and represent a rigorous wind wave loading schedule which is very appropriate for scaling laws verification.

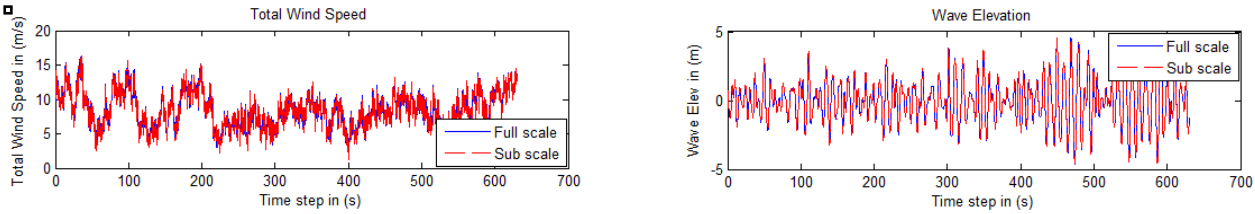

Figure 14: Time History of wind speed and significant wave height for both OC3 Hywind and MIT/NREL TLP system.

For the analyses in this section, the time histories of all the displacements, forces and deflections are not damped with increasing time, which is happening due to the continuous excitation by turbulent wind at a mean value of 8 m/s (full scale) and 1.13m/s (model scale); and irregular wave with a peak spectral period of 10 s and 1.41 s and a significant wave height of 6 m and 0.12 m at full scale and model scale, respectively.

When the output parameters for both platform configurations are compared, it is found that all the full-scale and model-scale quantities are in excellent agreement with the scaling laws. The reason behind the excellent agreement between full-scale and model-scale results is the parallel existence of Froude and Reynolds similitude. Such similarities are impossible to achieve in practical tests and a larger scaling factor between full scale and model scale further adds to the challenges because Reynolds number distortion increases with increasing fundamental scaling factor, by an exponential factor. These Reynolds-number associated difficulties form the basis of the discussion in the following section.

2.3 Reynolds Number Effects on Model Wind Turbine Performance

In this section, the impact of Reynolds number on properly scaling wind turbine thrust and torque are discussed. To illustrate this point, a combination of analysis and model wind turbine test data is employed.

As a fundamental step in the floating wind turbine model testing program, fixed base testing of the scale model wind turbine is performed in order to characterize the aerodynamic behavior of the model NREL 5MW Reference Wind Turbine in a Froude scale environment. The blades, shown in Figure 1 and documented in (Martin, 2011) accurately represent the NREL turbine geometry. The Froude scale environment the rotor is subjected to exhibits no swirl, a turbulence intensity of 4% at the hub location and possesses a mean wind speed of 20.8 m/s. The performance of the turbine is characterized by two parameters: the power coefficient, C_P, and thrust coefficient, C_T. These non-dimensional quantities are computed as

$$C_P = \frac{P}{\frac{1}{2}\rho U^3 A}, \quad C_T = \frac{T}{\frac{1}{2}\rho U^2 A},$$

where P is the rotor power, T is the rotor torque, r is the density of the air and A is swept area of the rotor. To obtain the C_P and C_T test data, the rotor power and torque are measured from the model at various rotor speeds, and hence, TSRs. The results of the testing, in addition to the theoretical full scale performance as computed from NREL's coupled aero-hydro-servo-elastic wind turbine simulator, FAST (e.g. see (Jonkman and Buhl, 2005), is given in Figure 15. As is evident from the figure, the model rotor aerodynamic performance is markedly lower than the theoretical prototype performance, particularly for the performance coefficient.

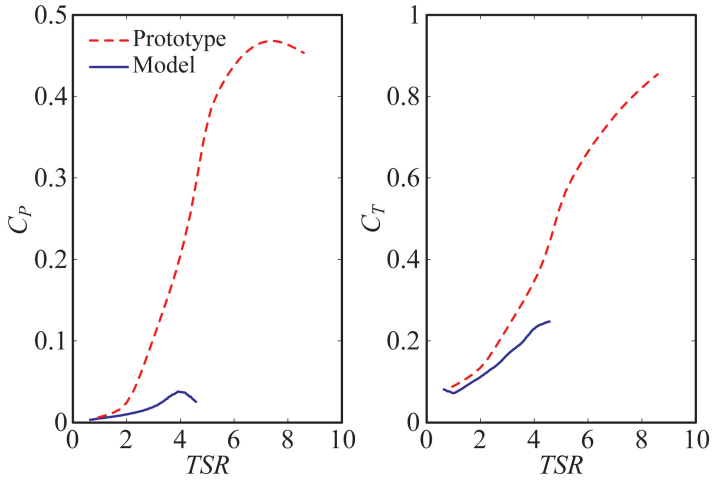

Figure 15: Comparison of ideal prototype rotor aerodynamic performance and realized model rotor aerodynamic performance.

For the model rotor, the peak performance coefficient of 0.04 is achieved at a *TSR* of 3.91 using a collective rotor pitch angle of 6.4°. For comparison's sake, the maximum C_P for the prototype rotor is 0.47 at a *TSR* of 7.5 while employing a collective blade pitch angle of 0.0°. The performance of the λ = 50 NREL rotor is an order of magnitude less than the prototype, with peak performance occurring at approximately half of the expected optimum *TSR*. Generally speaking, the lack of expected model performance is attributable to Reynolds number dissimilitude between the prototype and model scales. The specific impacts of the Reynolds number mismatch are discussed next.

To begin, it is noted that the Reynolds number quantifies the relationship between viscous and inertial qualities of a fluid flow. The Reynolds number, *Re*, is computed as

$$Re = \rho VL/\mu,$$

where L is a characteristic length, V is a characteristic velocity and m is the dynamic viscosity of the fluid. In the process of maintaining the Froude number for the floating wind turbine system and its accompanying environment, the Reynolds number for the hydrodynamic and aerodynamic flows are greatly diminished for the model. For floating body fluid-structure interaction flows, this is not a major concern as evidenced by the common practice of employing Froude scaling to conduct accurate floating body model tests that carefully emulate the full scale behavior. For wind turbines, the drastic reduction in Reynolds number yields a major impact on wind turbine performance. This influence is realized in major alterations to the lift coefficient C_L and drag coefficient C_D of the airfoil sections comprising the wind turbine blade. These coefficients are a key component of the distributed lift force F_L and distributed drag force F_D of the airfoil section. These distributed forces are determined from the relationships

$$F_L = \frac{1}{2}\rho V^2 c C_L, \quad F_D = \frac{1}{2}\rho V^2 c C_D,$$

where V is the actual wind inflow magnitude experienced by the airfoil and c is the chord length of the airfoil. Note that C_L and C_D are functions of the angle of attack a which is determined by the direction of the velocity vector V relative to the chord length axis. To illustrate the factors which influence the magnitude and direction of V, the relationship between the direction of the incoming velocity and the lift and drag forces, and finally, the contributions from the lift and drag forces to the overall rotor thrust and torque, a generic wind turbine airfoil force diagram is shown in Figure 16.

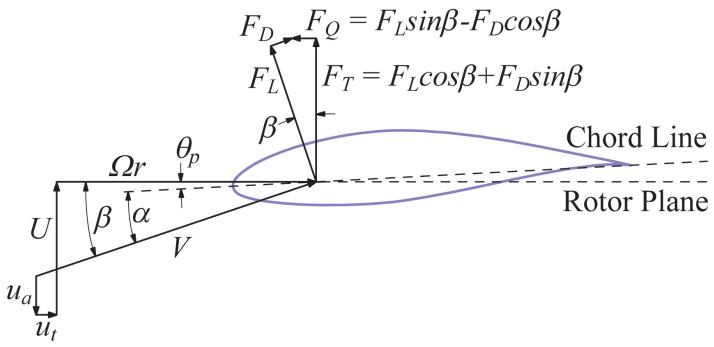

Figure 16: Generic wind turbine airfoil force diagram.

First, the velocity vector V is influenced by many factors. Contributions to the quantity include the incoming wind inflow U, the blade section tangential velocity Wr, and the axial and tangential induced velocities u_a and u_t. The induced velocities result from the wind turbine rotor's wake of shed vorticity. The sum effect of all the vorticity in the wake modifies the flow field in the rotor plane and must be accounted for in order to properly compute the magnitude and direction of V. In numerical aerodynamic simulations of wind turbines, the induced velocities are often calculated using the blade element momentum theory (e.g. see (Leishman, 2000)), however, other possibilities do exist (e.g. see (Peters and He, 1991; Glauert, 1926)). Once V is established, the angle of attack a is determined from the angle between V and the rotor plane, b, and the blade pitch angle q_p, as shown in Figure 16. With a established, the coefficients C_L and C_D can be determined and the distributed forces F_L and F_D computed. Note that the lift force is perpendicular to V, whereas the drag force is parallel to V. As shown in Figure 16, the components of F_L and F_D perpendicular to the rotor plane are both positive and contribute to the total rotor thrust, with F_L being the largest contributor. The thrust contribution from airfoil section is denoted F_T. The force component contributing to rotor torque is labeled F_Q in Figure 16. The positive contribution to F_Q arises from the component of F_L in the direction of the foil tangential motion, which is not very large relative to the magnitude of the lift force. The largest component of the drag force F_D lies in the rotor plane and opposes the motion of the airfoil section, therefore detracting from the net force available for producing torque, F_Q. With these observations in mind, it is evident that the rotor torque, and hence power, is severely impacted by modest increases in drag force. In addition, any reductions in the lift force will only diminish the already small positive contributions to torque production. For the thick airfoil sections typically found on commercial scale wind turbines, reductions in Reynolds number typically diminish C_L and increase C_D, resulting in reduced rotor thrust and torque.

To better understand the reductions in rotor performance due to Reynolds number dissimilitude, the coefficients C_L and C_D are computed as a function of angle of attack a for the NACA 64-618 airfoil section located at 70% of the blade radius for both the prototype and model Reynolds numbers. For this particular section on the model blade, a 20.8 m/s inflow wind speed, 12.7 rpm rotor speed and airfoil chord length of 3.04 m (2.94 m/s, 90.0 rpm and 0.061 m at model scale) yields a Reynolds number of 35.7×10^3. For the prototype at a wind speed of 11.4 m/s and a slightly lower rotor speed of 12.1 rpm, the Reynolds number is orders of magnitude larger at 11.5×10^6. The reason for the differing operational conditions will become apparent in the subsequent section, but it will suffice to state that these two conditions yield similar thrust performance for the model and the prototype. This stated, the coefficients are computed using XFOIL (Drela, 1989), a higher-order panel code incorporating a fully-coupled viscous/inviscid interaction method designed specifically for airfoil analysis. The XFOIL analyses employ the aforementioned Reynolds numbers and a standard laminar to transition effect log factor, N_{crit}, of 9 (Drela and Giles, 1987). The results of the analyses are shown in Figure 17.

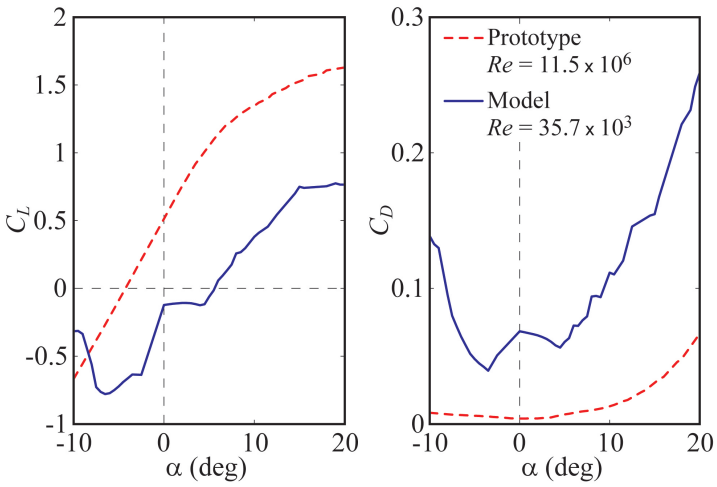

Figure 17: Lift and drag curve coefficients for the NACA 64-618 airfoil at prototype and model Reynolds numbers of 11.5×10^6 and 35.7×10^3, respectively.

The trends in Figure 17 clearly demonstrate that the lower Reynolds number of the model severely affect the performance of the airfoil, drastically reducing the lift coefficient and severely increasing the drag coefficient for the angles of attack shown, these angles covering the typical range of operational *a* for an airfoil. Further analysis with XFOIL indicates that the NACA 64-618 airfoil at the model Reynolds number undergoes laminar separation resulting in the altered coefficients of Figure 6. This stated, it must be noted that XFOIL analysis results in separated flows should be considered more qualitative than quantitative here as the predicted coefficients are likely not accurate. Nonetheless, thick foils, such as the NACA 64-618, are prone to laminar separation at low Reynolds numbers degrading airfoil performance. The NACA 64-618 foil possesses a thickness equal to 18% of its chord length, this being the thinnest airfoil in the NREL 5 MW Reference Wind Turbine blade shown in Figure 1. Sections near the root of this particular blade are even more prone to laminar separation as these airfoils approach a 1 to 1 ratio of thickness to chord length. These sections are necessary to achieve adequate structural bending stiffness for commercial wind blades which are large, heavy, slender structures. This is not a concern at prototype Reynolds numbers, however, as these thick airfoils possess small boundary layers and an organized flow around the foils resulting in high lift and low drag coefficients.

With lower lift coefficients and higher drag coefficients for the airfoils at lower Reynolds numbers, the result, understandably, is diminished airfoil lift forces and drastically increased airfoil drag forces for the various blade sections. This combination, as supported by Figure 16, results in a lower rotor C_T and lower rotor C_P. The extremely low rotor performance in Figure 15 is not surprising given the approximately tenfold increase in drag coefficient estimated for the model airfoil shown in Figure 17. This large increase in drag force for the outer foil sections, which generate most of the power, detracts greatly from the marginal lift force component in the rotor plane, yielding a very low net torque. The larger model drag force quickly overwhelms the positive lift force contribution to torque as *TSR* increases. This is due to the reduction in angle of attack, and hence lift force component in the rotor plane, as the rotor speed increases for a constant wind speed. This is the cause for the peak C_P occurring at much lower *TSR* for the model as compared to the prototype. The smaller model airfoil lift coefficient resulting from the lower Reynolds number is the main contributor to the lower observed C_T. However, the C_T disparity between the model and prototype is not as bad due to the larger positive contribution to thrust loading from the bigger model airfoil drag force.

While the present analysis may explain the poor turbine performance in Figure 15, the severe reduction in wind turbine performance is not ideal for a Froude scale experiment. The results of Figure 15 clearly indicate that a strictly Froude scaled model wind turbine of commercial design will produce too little thrust, and not nearly enough power, when subjected to Froude scale winds. Therefore, to conduct a proper Froude scale floating wind turbine experiment, alterations to the wind turbine and/or environment are required to achieve the appropriate aerodynamic forces that strongly influence the coupled response of a floating wind turbine system. Suggested corrective measures and the shortcomings of these measures are presented in the next section.

2.4 Analysis of Model Testing Wind Turbine Thrust Correction Methods

Previous analysis demonstrates that a model wind turbine with thick commercial airfoil sections and an accompanying wind environment which adheres strictly to the scaling protocol listed in Table 1 will not perform adequately for a proper experiment. Therefore, adjustments must be made to achieve the desired model turbine forces. The key forces the turbine transmits to the floating system include gyroscopic moments, rotor torque and rotor thrust. The first, the gyroscopic moment, is properly maintained by creating a model turbine with the correct Froude scale mass properties and operating the turbine at the correct Froude scale rotor speed. The second two forces, torque and thrust, are not maintained as previously mentioned. It is unlikely that any alterations will give rise to a scenario in which both forces are maintained exactly as one would desire. Therefore, a prioritization of the two forces is required. Setting this priority is rather straightforward since the overturning moment created by the thrust force and opposing mooring reaction is typically an order of magnitude greater than the overturning moment due to the aerodynamic rotor torque from which power is extracted. For the semi-submersible system of Figure 2, the overturning moment due to torque is less than 5% of the overturning moment due to thrust for a typical operating condition. With the priority established, possible methods for achieving the correct model thrust force include the following:

1. Increase the model wind speed to compensate for the low model C_T and achieve the correct prototype thrust forces. *TSR* between the prototype and model will not be maintained.
2. Roughen the leading edge of the model blade to trip the boundary layer transition from laminar to turbulent flow around the airfoil, reattaching the flow and improving the airfoil's lift and drag coefficients at model scale.
3. Design a low-Reynolds number specific model wind turbine blade geometry that, while may not resemble the prototype blade with regard to surface geometry, will yield appropriate thrust performance when subjected to an unmodified Froude scale environment.

In addition to these suggestions, one may implement combinations of the above methods to achieve the desired thrust forcing for the model.

With the suggested corrective measures outlined, the focus will now turn to the implementation of these measures and their associated shortcomings. The first suggestion, increasing the wind speed, is relatively straightforward to implement. For the model testing of the system in Figure 2, the wind speed is raised from 11.4 m/s to 20.8 m/s to achieve the desired thrust forces. For the various tests performed under steady winds, the increase in wind speed to 20.8 m/s yields mean thrust values ranging from 91-105% of the desired prototype value at the rated wind speed of 11.4 m/s during testing, this being 827 kN. The fact that these two conditions yield similar performance was alluded to in the previous section, and thus, is the reason for using these two distinct wind speeds in the Reynolds number dissimilitude analysis. That stated, adjusting the wind speed only maintains the mean thrust force for the model and does not necessarily capture all the sensitivities of the thrust force due to changes in various field variables. For example, this method does not inherently imply proper simulation of the variations in thrust force due to changes in inflow wind speed, changes in relative wind speed resulting from structure motion and

changes in blade pitch angle, this last being critical for studies which aim to investigate the impact of active blade pitch damping on the global motions of the system. While no active blade pitch testing is performed during the model test program, tests are conducted which can help assess the impact of matching thrust via an increase in mean wind speed on the aerodynamic damping provided by the turbine, and hence, the measured global response of the floating system.

To begin this assessment, the global motion response of floating system most affected by aerodynamic wind turbine damping is first identified. This region of altered response will be identified using Figure 18 which compares two model tests of the floating semi-submersible floating wind turbine system, one with an operating wind turbine subjected to wind loading and the other without.

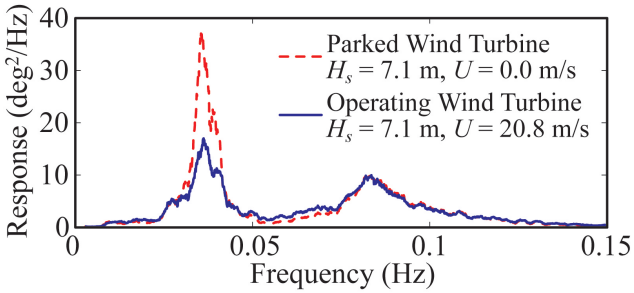

Figure 18: Comparison of floating semi-submersible wind turbine pitch motion response for the same sea state with and without an operating wind turbine.

The figure, which shows the frequency domain pitch motion response, displays cases that both experience a sea state consisting of an H_s = 7.1 m significant wave height with a peak spectral period of 12.1 s. The distinction between the two cases is that the first possesses a parked turbine with no wind, while the second has an operating wind turbine at 12.7 rpm under steady, 20.8 m/s winds. As can be seen in the figure, the response for the two conditions is nearly identical in the wave energy frequency range, this being greater than 0.05 Hz. The second-order difference frequency response, which is greatest near the floating turbine natural rigid body pitch frequency of 0.037 Hz, is significantly damped by the operating wind turbine. While this is only a single example, the trend of damping the low frequency second-order response of the system illustrated in Figure 18 is consistent with observations in similar tests. Therefore, assuming that this trend would still hold if the turbine performance properly emulated the prototype, further investigation will focus solely on the wind turbine aerodynamic motion damping of the natural rigid body pitching motion of a floating wind turbine system.

To assess the shortcomings of the increased wind speed method on global response, the focus will now turn to pitch motion free decay tests and simulations for the semi-submersible floating system, these tests being characterized by floating system motion at the natural rigid body pitch motion frequency. The results of the model tests, as well as simulations from FAST, are given in Figure 19.

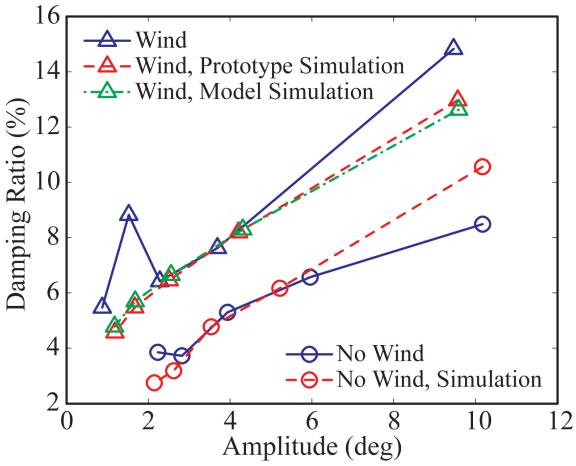

Figure 19: Damping ratio as a function amplitude for the floating semi-submersible wind turbine from model tests and simulations.

The figure displays the damping ratio as a function of amplitude for all of the cases analyzed. The figure displays five scenarios; two without wind and three with wind. The two without wind include model test data and a FAST simulation, each denoted with circular markers. As can be seen in the figure, the curves are very similar indicating that the FAST simulation hydrodynamic damping accurately represents physical reality, especially for modest motion amplitudes. It should be noted that the FAST simulator employed included modifications to allow for the inclusion of custom drag elements. This stated, the remaining three curves in Figure 19 each correspond to a free decay test with an operating wind turbine, which as observed from the figure, results in a considerable increase in pitch motion damping at the natural pitch frequency. For the model test, the wind turbine operates at 7.8 rpm and is subjected to steady 10.7 m/s winds. The same case is simulated with FAST using a numerical model of the physical model wind turbine. A comparison of the numerical model wind turbine and the measured model performance data is shown in Figure 20.

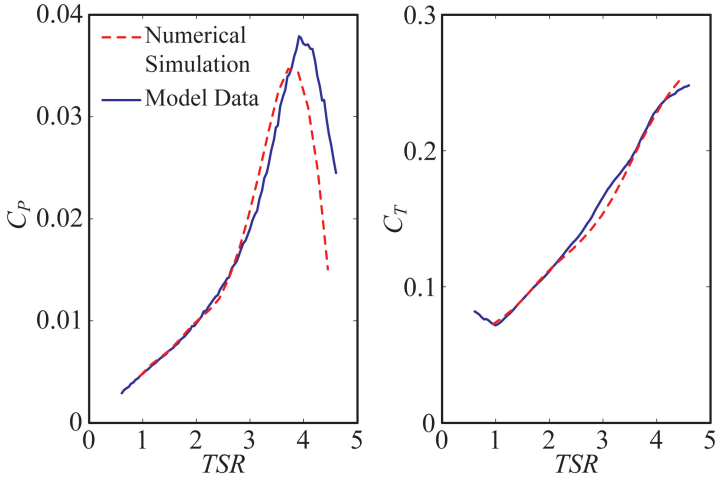

Figure 20: Comparison of numerical model and measured test performance data for the model wind turbine.

The numerical model, which is obtained by parameterizing XFOIL derived lift and drag coefficients and then optimizing the parameters via a genetic algorithm to minimize the error between the numerical

model prediction and data for C_P and C_T, is a fair representation of the actual model wind turbine performance. That aside, the comparison between the free decay test results with an operating turbine and the corresponding simulations results shown in Figure 19 agree fairly well. To assess if the poorly performing model wind turbine subjected to increased wind speeds accurately portrays the full scale response, an additional simulation is performed using a numerical model of the prototype 5 MW turbine, the performance and thrust curves of which are shown in Figure 15. The operating and environmental conditions for this simulation were set such that the mean thrust on the wind turbine for the prototype simulation is similar to the model simulation, and hence, the test data. Due to the prototype's larger thrust coefficient, the prototype requires a lower steady wind speed of 5.9 m/s and a rotor speed of 7.9 rpm to obtain the same thrust force as the model. After running the simulation, Figure 20 clearly indicates that the additional aerodynamic damping provided by the model and prototype wind turbines is nearly identical despite the large discrepancies in C_T and mean wind speed. Both systems appear to increase the damping ratio by an additional 2-3%, regardless of amplitude, with the prototype simulation exhibiting a slightly stronger increase in damping force with rising amplitude. Nonetheless, these results indicate that matching of the mean thrust through increased wind speed for a poorly performing model wind turbine does not necessarily compromise the wind turbine aerodynamic damping effect.

To better understand why this is so, a Taylor series expansion of the wind turbine thrust force T for a fixed speed, fixed blade pitch wind turbine is taken about the mean wind speed U_M, yielding

$$T(U) \approx \tfrac{1}{2}\rho A[C_T(U_M)U_M^2 + \left\{2C_T(U_M)U_M + \frac{\partial C_T(U_M)}{\partial U}U_M^2\right\}\Delta U] + O(\Delta U^2),$$

where $DU = U\text{-}U_m$ is the change in the relative wind velocity, either due to motion of the rotor or a change in wind inflow speed. In most realistic operating cases, the change in velocity is small relative to the mean wind speed, and hence, the terms associated with DU^2 are considered negligible here. In addition, the constant term involving the $C_T(U_M)U_M^2$ product is the same for both the model and prototype as a result of matching the mean thrust through increasing the inflow wind speed for the model relative to the prototype. The end result is that the second term characterizes the wind turbine damping, this term being proportional to DU. For the aforementioned free decay tests under steady wind, DU is controlled by the natural pitch period of the floating wind turbine structure, this being the same for both the model and the prototype. The lone discrepancy between the two scales is the term pre-multiplying DU, the damping coefficient, comprised of the sum of the $rAC_T(U_M)U_M$ product and the $r\,A(\partial C_T(U_M)/\partial U)U_M^2/2$ product. The first and dominant term, is larger for the prototype by a factor of 1.7 for this example. However, the second product, which contributes negatively to the sum as the partial derivative is negative, is also larger in magnitude for the prototype by a factor of 1.5 yielding comparable damping coefficients for the two scales. The end result is similar wind turbine motion damping for the prototype and the model despite the fact that the model wind speed is 81% larger than the prototype.

As noted earlier in this section, an additional measure which may be taken to improve model wind turbine thrust forces in a Froude scale experiment is to roughen the leading edges of the blade sections. To help quantify the effect of this correction, performance tests are conducted for the model wind turbine with a 25 mm wide strip of 250-290 mm calibrated sand applied to the leading edge of the turbine blades, as shown in Figure 21.

Figure 21: Image of roughened leading edge of model wind turbine blade.

These particular values are selected based on MARIN experience and preferred protocol (e.g. see (van Walree and Yamaguchi, 1993)). The wind conditions for the roughened blade performance tests are identical to earlier turbine testing with a 20.8 m/s wind inflow speed. The results for C_P and C_T as a function of *TSR* for the roughened edge blade, as well as the results for the original untreated blades, are shown in Figure 22.

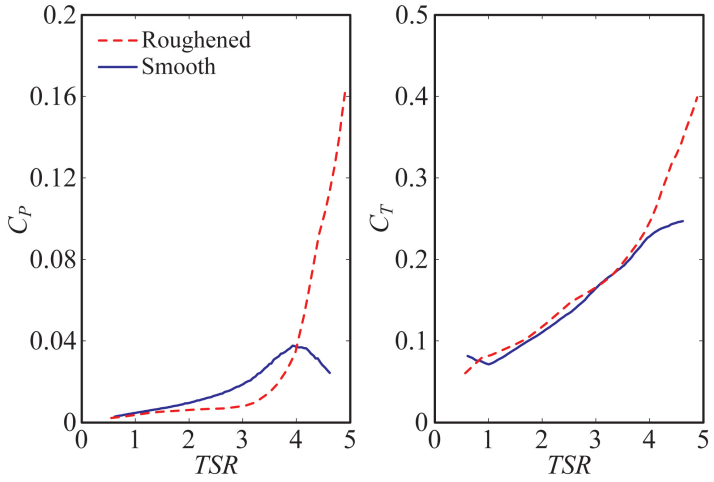

Figure 22: Comparison of model wind turbine performance with and without roughness on the wind blade leading edge.

As can be seen in the figure, the performance and thrust coefficients improve greatly once the TSR exceeds a value of roughly 4. At this point, the combination of a roughened leading edge and large enough rotor speed trip the transition from laminar to turbulent boundary layer flow, eliminating the laminar stall condition of the thick untreated blades depicted in Figure 1. As a result, the airfoil begins producing significantly improved lift forces evidenced by the increased C_P and C_T responses.

While the performance improves from this treatment, there are some important points worth mentioning. First, the wind turbine performance is not sufficiently improved to the point of being comparable with the prototype. Therefore, thrust matching of a treated model wind turbine with commercial scale geometry would still require increased wind speeds. Second, the peak performance coefficient is not obtained for the roughened blades in Figure 22 as sufficiently large TSR values cannot be achieved with the model wind turbine employed for testing here. This is due to a combination of wind turbine rotor speed safety limitations, and the fairly high 20.8 m/s wind speed used to generate the curves. At lower wind speeds, and even for lower rotor speeds for the 20.8 m/s wind case, the transition from laminar to turbulent flow of the boundary layer does not occur, and thus, performance is not improved. In addition to the airfoils still experiencing laminar separation in these cases, there also exists added drag due to the leading edge roughness producing even poorer performance than if the blade is left untreated. Also, it is observed during the testing that the transition out of laminar stall for the turbine blades is fairly dramatic, leading to sudden increases in rotor thrust force despite only small changes in rotor speed. This situation, of course, is not representative of the prototype's response and is not ideal for model testing. In short, it is recommended that leading edge roughness be employed carefully, ideally as a small tuning adjustment and not as the sole means to emulate the prototype turbine response.

The final recommended practice for matching aerodynamic rotor thrust forces for floating wind turbines is to design a rotor using low Reynolds number airfoil sections that properly mimics the prototype thrust

coefficient curves when subjected to Froude scale winds. If properly designed, the airfoil will not need to employ much, if any, leading edge roughness preventing the possibility of the aforementioned erratic rotor performance. Also, a properly designed low Reynolds number specific blade will not need to rely on increased wind speeds, as the C_T for model and prototype will be the same. This will in turn yield a model turbine that better captures the aerodynamic damping of the prototype, not only due to motion of the floating structure at its natural period, but also due to other changes such as variations in the inflow wind speed. This is a result of the similarity between the model and prototype terms, such as U_M and $C_T(U_M)$, in the Taylor series expansion equation. A final important note is that such a turbine will be best suited for blade pitch control studies. When an airfoil is performing correctly in its operational range, the variation of the lift coefficient is nearly proportional to the angle of attack, a, this variable being determined in part by the blade pitch angle. In addition, the lift force F_L is proportional to the product of the chord length c, square of the apparent velocity V^2 and the lift coefficient C_L. A model that minimizes the distortion of the airfoil apparent velocity, C_L curve slope and airfoil chord length will be best suited for blade pitch studies as it will preserve the sensitivity of the blade lift forces to changes in blade pitch angle.

To complete this section, an example of a redesigned low Reynolds number model blade is given. A redesigned turbine should employ low Reynolds number specific airfoils throughout the rotor, and no thick airfoils should be included as is common on commercial machines. An example of such a foil, the Drela AG04, is given in Figure 23. Thin Airfoils of

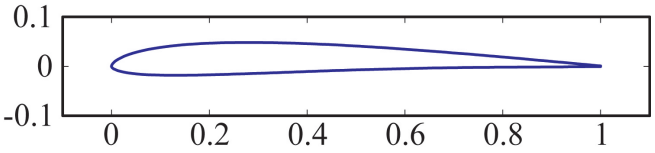

Figure 23: Drela AG04 low-Reynolds number airfoil.

this type are not as susceptible to the laminar separation problem of the thick airfoils employed on commercial machines at the low Reynolds numbers of the Froude scale environment. This is evidenced by the improved lift and drag coefficient behavior of the Drela AG04 airfoil at low Reynolds numbers as compared to the NACA 64-618 used in the outer portion of the NREL 5 MW Reference wind turbine. The comparison of the NACA 64-618 airfoil from Figure 17 and the XFOIL predicted performance of the Drela AG04 airfoil is shown in Figure 24. At the low model Reynolds number, the Drela AG04 greatly outperforms the NACA 64-618 with much larger lift coefficients and significantly reduced drag coefficients due to a lack of separation at low a. In addition, the Drela AG04 airfoil performance is moderately representative of the prototype Reynolds number performance of the NACA 64-618 for small angles of attack, which is desirable.

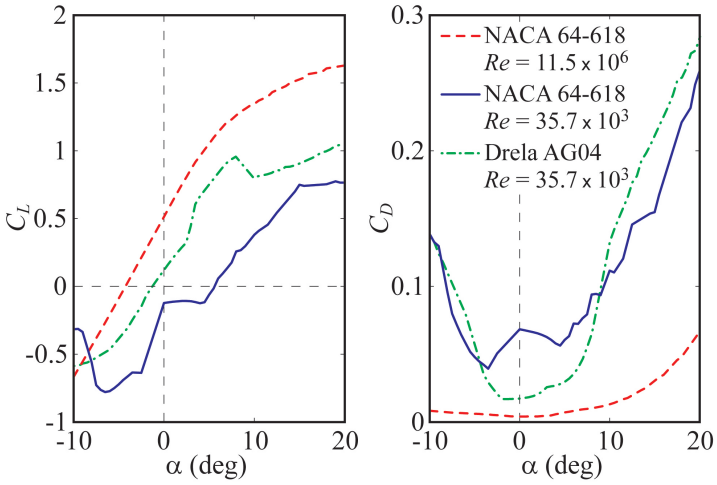

Figure 24: Lift and drag coefficients of the NACA 64-618 airfoil under high and low-Reynolds number conditions and of the Drela AG04 airfoil under low-Reynolds number conditions.

To redesign the blade, the Drela AG04 airfoil is employed over the complete length of the blade. In addition, the structural twist of the NREL 5 MW Reference Wind Turbine blade is mimicked, with the exception of the root sections which more closely follow an ideal twist distribution (e.g. see (Manwell *et al.*, 2009)). The relative chord distribution is maintained from the NREL machine, but the chord length is uniformly increased by 25% in order to compensate for the slightly lower lift coefficient allowing for production of the appropriate thrust forces under unaltered Froude scale winds. Ideally, the chord lengths of the airfoils should be as close to the prototype as possible in order to preserve the sensitivity of the thrust force to blade pitch angle. That said, an analysis of this blade using the lift and drag coefficients of Figure 24 with FAST yields the non-dimensional performance curves shown in Figure 25.

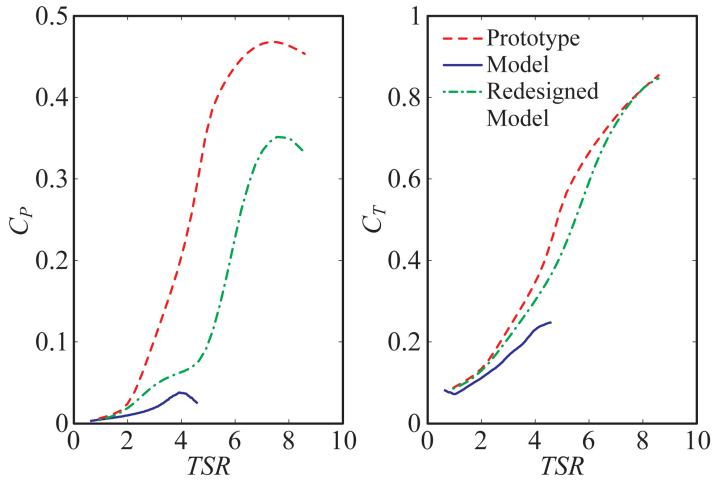

Figure 25: Power and thrust coefficient curves for the prototype, original model, and redesigned model rotor.

As can be seen in the figure, the performance is markedly better than the original model. The C_T response is nearly the same as the prototype, and the less important power coefficient, while not ideal, is drastically improved. In short, the low-Reynolds number specific blade design presented here would perform admirably when subjected to Froude scale winds, yielding correct thrust forces, modest power output and

aerodynamic damping very similar to the prototype as a result of preserving the terms laid out in Taylor series expansion equation of this section.

While the three corrective measures outlined in this section all possess some potential for improving the thrust scaling problem, the option for increasing the wind speed was selected as the turbine blade could not be modified once the testing had begun and the addition of leading edge roughness lead to erratic wind turbine performance. However, as demonstrated in this section, this choice does not appear to severely hamper the value of the test data as the dynamic wind response of the floating wind turbine is very similar for both the prototype and poorly-performing model-scale wind turbine for comparable mean thrust conditions. Regarding the redesigned wind turbine option, this scenario will be investigated further in a later section in this report.

3 Test Program Overview

In this section, an overview of the floating wind turbine model test program performed at MARIN is given. Topics covered include descriptions of the floating wind turbine models, instrumentation and lastly, the matrix for the floating wind turbine model tests.

3.1 Definition of Floating Wind Turbine Systems

For the model tests, the horizontal axis wind turbine chosen for scale model construction is the NREL designed 5 MW Reference Wind Turbine (Jonkman *et al.*, 2009). An image of the wind turbine is shown in Figure 26.

Figure 26: Wind turbine model.

The wind turbine possesses a 126 m rotor diameter and is located with a hub height of 90 m above the still water line (SWL). The flexible tower, which begins 10 m above SWL, is designed to emulate the fundamental bending frequency of the OC3 Hywind tower (Jonkman, 2010). The wind turbine deviates from the standard NREL 5 MW Reference Wind Turbine in a few notable areas (Martin, 2011). For the model wind turbine, the shaft tilt is 0°, the blade precone is 0° and the blades are rigid. The last difference is the result of two factors. First, fabricating the 17.7 mt blades at 1/50th scale requires a very light woven carbon fiber construction which is inherently stiff. Second, eliminating the added aeroelastic dynamic phenomena associated with a flexible rotor is deemed to be desirable as these effects are perceived as being beyond the scope of these tests. To mimic the first bending frequency of the OC3 Hywind tower, the tower is constructed from specifically sized aluminum tubing. Furthermore, the lower 11.3 m of the tower is of a larger diameter than the remainder of the tower in order to more closely match the OC3 Hywind tower center of gravity and fundamental bending mode shape. The total topside mass,

which includes the wind turbine, tower and all accompanying instrumentation, is 699.4 mt. This value is 16.6% larger than the standard specifications for the NREL 5 MW Reference Wind Turbine and OC3 Hywind tower.

While most floating wind turbine concepts under consideration employ a horizontal axis wind turbine, the platforms employed in current concepts vary widely. Therefore, to make the test results useful to as broad an audience as possible, the previously described wind turbine and tower is tested atop three different floating platforms. The platforms, each modeled after viable offshore oil and gas platform technology, derive stability from differing mechanisms. The platforms consist of a TLP (mooring stabilized), a spar-buoy (ballast stabilized) and a semi-submersible (buoyancy stabilized). Images of the platforms employed during testing, including the wind turbine, are shown in Figure 27.

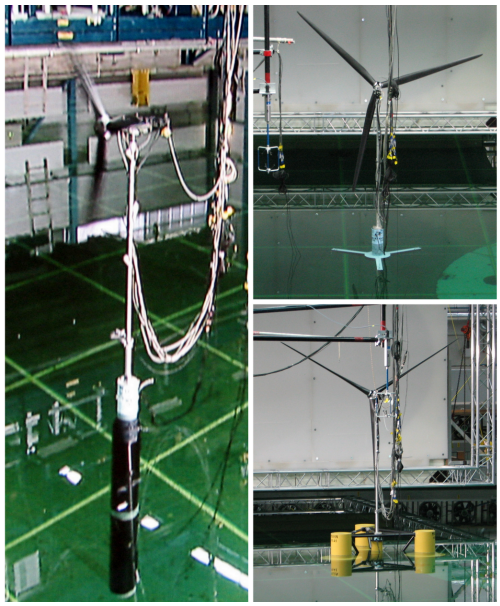

Figure 27: Clockwise from left: spar-buoy, TLP and semi-submersible floating wind turbines utilized in model testing.

Like the blades, each platform is designed to be rigid to eliminate the added complexity of a flexible platform. Each of the designs is tested in a water depth of 200 m. The first design, the TLP, is restrained by three stiff vertical tendons. The spar-buoy is moored by a spread mooring consisting of taught lines attached to the spar-buoy via a delta connection similar in nature to the type employed on the actual Statoil Hywind (Jonkman, 2010). The last design, the semi-submersible, is restrained by three slack catenary lines with fairlead attachments located at the top of the lower bases. Images of the floating foundations alone are given in Figure 28. The principle dimensions of the spar-buoy, TLP and semi-submersible are given in Figure 29, Figure 30 and Figure 31, respectively.

Figure 28: Selected floating platforms.

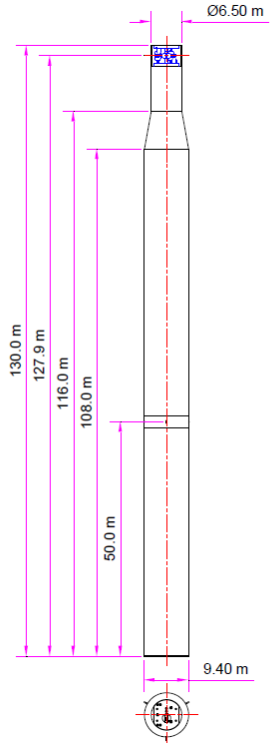

Figure 29: Principal dimensions of the spar-buoy.

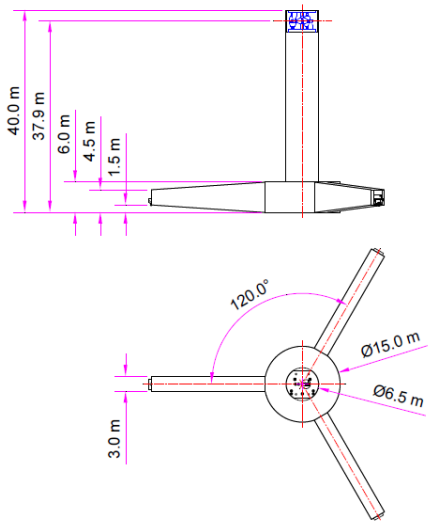

Figure 30: Principal dimensions of the TLP

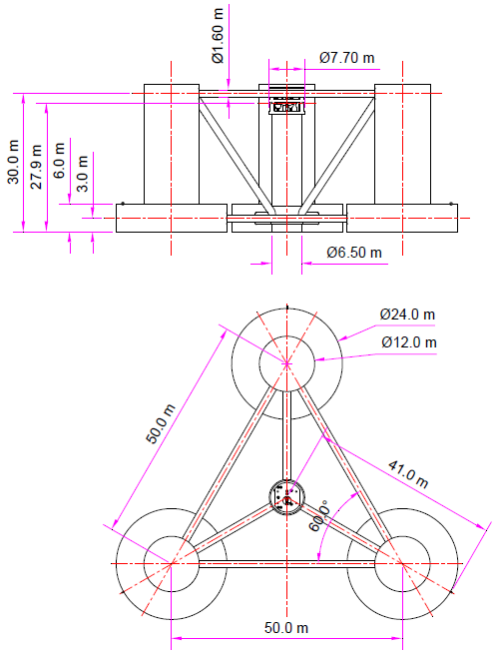

Figure 31: Principal dimensions of the semi-submersible.

Key features of the three designs, inclusive of the wind turbine, are shown in Table 6 including draft, displacement and mooring spread diameter. The mooring details are specified in

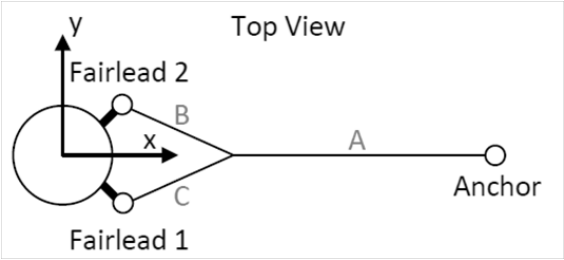

Figure 32: Delta connection and taught mooring line.

Table 7,

Table 8 and Table 9 for the spar-buoy, semi-submersible and TLP, respectively. A depiction of the delta connection employed for the taut mooring system of the spar-buoy is shown in Figure 32.

Table 6: Select specifications for each of the platforms tested

Platform Type	TLP	Spar	Semi
Mass w/ Turbine (mt)	1361	7980	14040
Displacement (mt)	2840	8230	14265
Draft (m)	30	120	20
CG Above Keel (m)	64.1	43.7	10.1
Mooring Spread Diameter (m)	60	890	1675
Roll Radius of Gyration (m)	52.6	53.5	31.6
Pitch Radius of Gyration (m)	52.7	53.6	32.3
Natural Surge Period (s)	39.3	43.0	107
Natural Sway Period (s)	39.3	42.8	112
Natural Heave Period (s)	1.25	28.1	17.5
Natural Roll Period (s)	3.7	32.0	26.9
Natural Pitch Period (s)	3.7	31.5	26.8
Natural Yaw Period (s)	18.2	5.5	82.3
Tower Fore-Aft Fundamental Bending Frequency (Hz)	0.28	0.43	0.35
Tower Side-Side Fundamental Bending Frequency (Hz)	0.29	0.44	0.38

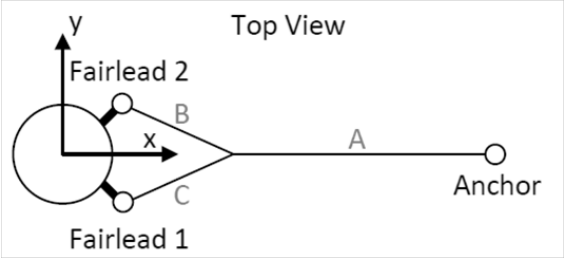

Figure 32: Delta connection and taught mooring line.

Table 7: Taut mooring system properties (spar-buoy)

Item	Unit	Designations
Anchor Radius	(m)	445.0
Anchor Depth	(m)	200.0
Radius of Fairlead	(m)	5.2
Fairlead Depth	(m)	70.0
Unstretched Line Length A	(m)	424.35
Unstretched Line Length B & C	(m)	30.0
Line A Diameter	(m)	0.167
Line B & C Diameter	(m)	0.125
Mass per Length Line A (dry)	(kg/m)	22.5
Mass per Length Line B & C (dry)	(kg/m)	12.6
Mass per Length Line A,B & C (wet)	(kg/m)	0.0
Axial Stiffness Line A (EA)	(MN)	121.0
Axial Stiffness Line B & C (EA)	(MN)	68.0

Table 8: Catenary mooring system properties (semi-submersible)

Item	Unit	Designations
Anchor Radius	(m)	837.6
Anchor Depth	(m)	200.0
Radius of Fairlead	(m)	40.9
Fairlead Depth	(m)	14
Unstretched Line Length	(m)	835.5
Line Diameter	(m)	0.0766
Mass per Length (dry)	(kg/m)	113.35
Mass per Length (wet)	(kg/m)	108.63
Axial Stiffness(EA)	(MN)	753.6

Table 9: TLP tendon properties

Item	Unit	Designations
Anchor Radius	(m)	30.0
Anchor Depth	(m)	200.0
Radius of Fairlead	(m)	30.0
Tendon Porch Depth	(m)	28.5
Unstretched Tendon Length	(m)	171.39
Tendon Diameter	(m)	0.6
Mass per Length (dry)	(kg/m)	289.8
Mass per Length (wet)	(kg/m)	0.0
Axial Stiffness (EA)	(MN)	7430.0

For each design, the freeboard at the tower base is 10 m. As can be seen in the table, the TLP is by far the smallest of the designs with the semi-submersible being the largest. Note, however, that these structures are generic, not optimized and are intended to exhibit the main characteristics of each concept. In addition, the TLP system does not contain any ballast unlike the other two designs. As can be seen in Table 6, the primary mass properties and motion characteristics for each of the designs, including a mounted wind turbine and tower, are also given. Examining the table, the natural periods of roll, pitch and heave motion for the moored structures indicate that the TLP system is very stiff as opposed to the spar-buoy and semi-submersible systems. In all cases, however, the natural periods of motion for these noted rigid body modes do not lie in the range of typical wave energy peak spectral periods, these being from approximately 5 to 17 seconds. Lastly, the fundamental tower bending frequencies in the fore-aft (surge) and side-side (sway) directions are also given for the three designs. It is evident from Table 6 that floating platform characteristics significantly influence the bending frequencies, with the foundations stiffer in pitch and roll exhibiting a lower bending frequency than the compliant foundations. This is not unexpected as stiffer foundations are more representative of a fixed boundary condition for the base of the tower, while the softer foundations are more akin to a free condition at the tower base (e.g. see (Rao, 2004)).

3.2 Instrumentation

In order to measure loads and motions of the floating wind turbines, a total of about 40 to 50 channels were used in the model tests depending on the floater. The six DOF motions of the floating wind turbine were measured by the optical tracking system. Three accelerometers were located at the base, middle and top of the turbine tower to measure accelerations. The structural mode shapes and natural periods of the wind turbine tower were derived from these accelerometers. The nacelle was connected to the tower by

means of a six component load cell that measured the six DOF forces and moments between the tower and nacelle. The global connection loads between the wind turbine and the platform were measured by another six component load cell between the tower base and platform top. The turbine performance was measured by the torque sensor between the motor and the blades. Figure 33 and Figure 34 show instrumentation for the wind turbine and floating platform. The mooring top tension was measured by a ring type transducer at the fairlead location. A z-shaped strain gauge was installed at each tendon porch to measure tendon top tensions.

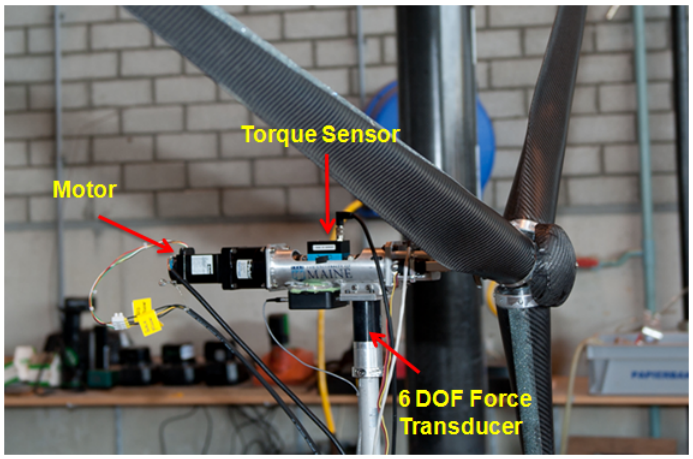

Figure 33: Instrumentation on wind turbine.

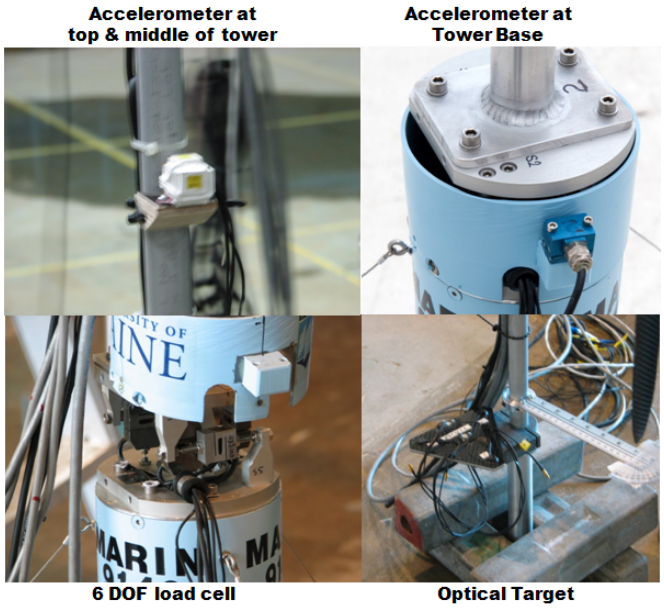

Figure 34: Instrumentation on turbine tower and floating platform.

A total of three calibration probes and two reference probes were used for the wave calibration tests. The reference wave probes remained in place throughout the tests to ensure repeatability of the wave generation. A total of three ADVs were used for the wind calibration tests. During the tests, two reference ADVs were also deployed to measure the tested wind. Table 10 gives the summary of the test measurements.

Table 10: Instrumentation list

Item	Channel	Remark
Ref. wave probes (2)	2	
Ref. ADV (2)	6	Three Axes
Optical Measuring	6	
Accelerometer Top	3	below nacelle
Accelerometer Mid	2	middle at tower
Accelerometer Low	3	bottom at tower
6 DOF Load Cell Low	6	at base of tower
6 DOF Load Cell High	6	at nacelle
Mooring – Semi	3	3 mooring lines
Tendon – TLP	3	3 tendons
Mooring - Spar	9	3 mooring line + 6 delta connections
Rotor Speed	1	
Torque sensor	1	at main rotor shaft

3.3 Test Matrix

In this section, an overview of the test matrix is presented. First, details including the wind and wave environments are discussed. Subsequently, the calibration of these environments is presented. Lastly, the test procedures and matrix of tests is covered.

3.3.1 Environments

The wind speeds were selected from the NREL 5 MW wind turbine power curve. Figure 35 shows the power curve of the full-scale NREL 5 MW wind turbine.

Table 11 lists the tested wind speeds. During the model tests, six steady wind conditions were simulated. The steady wind speeds are defined at hub height (i.e. 90m above MWL) of the wind turbine. In addition to steady wind conditions, three dynamic wind conditions were also simulated to test realistic ocean wind conditions. The API (i.e. NPD) wind spectrum was used for the dynamic wind simulations (API, 2000). The dynamic wind speeds are defined at 10m above MWL.

Table 12 summarizes the tested wave conditions. Three wave conditions were selected based on 9 years worth of data measurement from the NERACOOS floating buoy system in offshore Gulf of Maine. In addition to wind driven wave conditions, one swell condition was also selected to simulate a bi-directional sea state. The bi-directional sea state was simulated by superposing the operational wave condition 2 from head seas (= 180 deg) and the swell waves from quartering seas (= 225 deg).

Table 11: Selected wind conditions

	Velocity (m/s)	Rotor rpm	Remarks
Steady Wind 1	7.0	4.95	
Steady Wind 2	9.0	5.66	
Steady Wind 3	11.4	7.78	Rated Wind
Steady Wind 4	16.0	9.19	
Steady Wind 5	21.0	12.73	Design Maximum
Steady Wind 6	30.5	-*	Survival
Dynamic Wind 1	9.5	7.78	API Spectrum
Dynamic Wind 2	17.0	12.73	API Spectrum
Dynamic wind 3	24.0	-*	API Spectrum

*feathered turbine

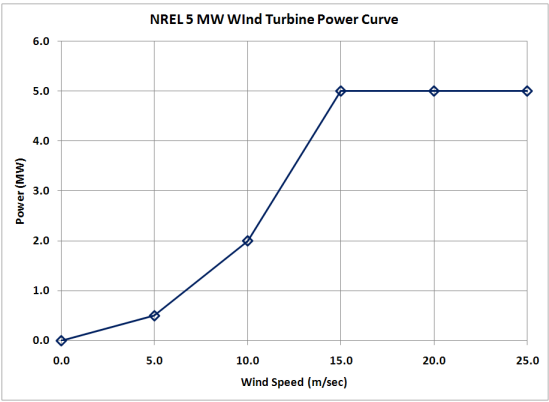

Figure 35: NREL 5 MW wind turbine performance curve.

Table 12: Selected wave conditions (JONSWAP spectrum)

	Hs (m)	Tp (sec)	Gamma	Remarks
Operation 1	2.0	7.5	2.0	
Operation 2	7.1	12.1	2.2	1 Year
Design	10.5	14.3	3.0	100 Year
Bi-directional	7.1/3.6	12.0/17.0	2.2/6.0	

3.3.2 Calibration of wind and wave environments.

Extensive wind calibrations were conducted of the wind generation machine. An image of the custom wind generation machine, unique to these model tests, is shown in Figure 36. Three Acoustic Doppler Volocimeters (ADV) were used for wind calibrations. Each ADV measures velocity in three directions. The wind calibration procedure is summarized as follows:

1. Determine spatial distribution over a calibration grid
2. Calibrate all steady wind speeds
3. Calibrate dynamic wind velocity spectrum

The wind field measurement range and locations are shown in Figure 37, and wind field measurement results are shown in Figure 38.

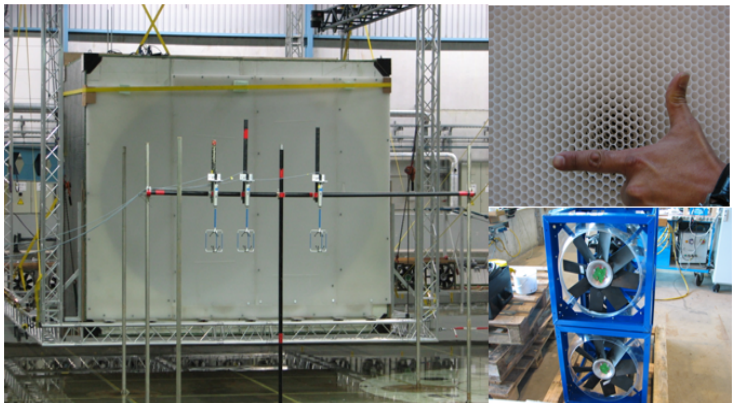

Figure 36: Wind generator.

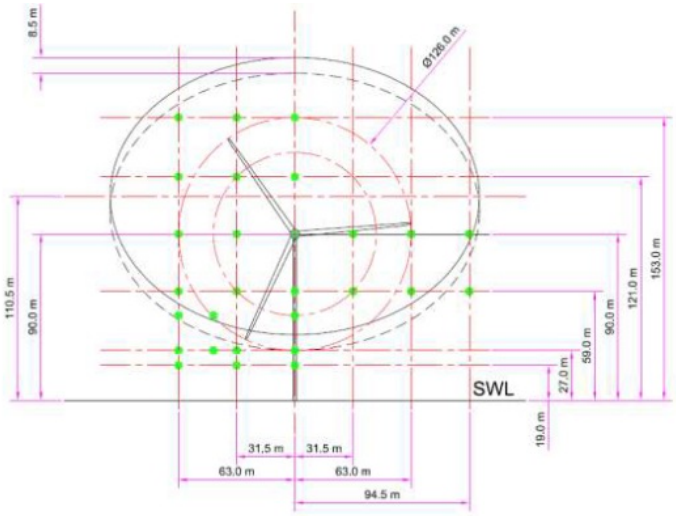

Figure 37: Wind field measurement locations.

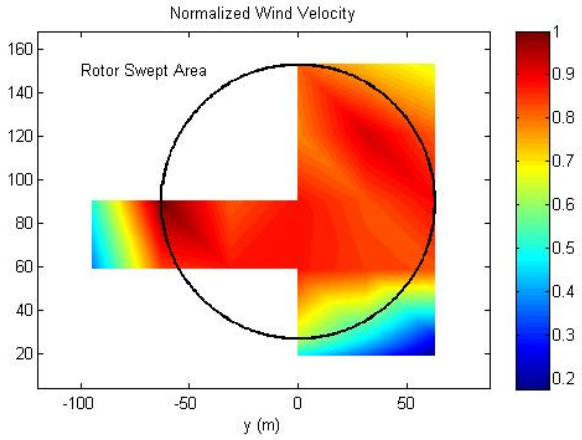

Figure 38: Wind field measurement results.

The waves were calibrated prior to installation of the model in the basin. The wave heights were measured at the location where the wind turbines will be located. In addition to calibration probe, two more wave probes were deployed at expected mean offset positions (i.e. 9m and 18m) of the floating wind turbines. Two additional reference probes were also deployed. The calibration results show that the maximum difference in standard deviation between the target waves and measured waves was less than 3%. Table 13 summarizes comparison results between target waves and measured waves. As shown in Figure 39, the basin generated wave spectra shows good agreement with the theoretical JONSWAP spectrum.

Table 13: Comparisons between target and measured waves

		Target	Measured	Diff. (%)
Operation 1	STD (m)	0.50	0.49	2.34
	Tz (sec)	5.74	6.16	7.43
Operation 2	STD (m)	1.79	1.77	1.15
	Tz (sec)	9.18	9.72	5.81
Design	STD (m)	2.62	2.62	0.21
	Tz (sec)	11.09	11.56	4.31
Swell	STD (m)	0.88	0.91	2.84
	Tz (sec)	13.83	12.9	6.75

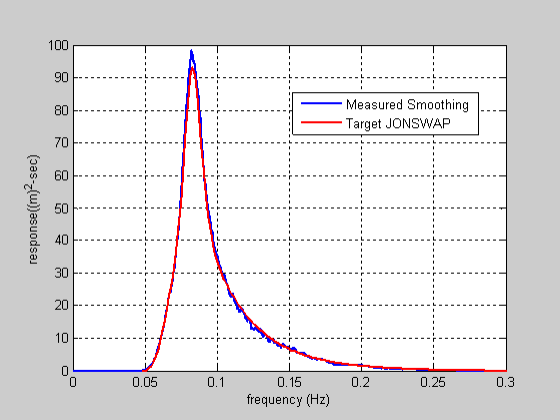

Figure 39: Operational wave 2 comparisons (measured Vs theory).

3.3.3 Test Procedures

The model tests started with calibration of the selected environmental conditions. After completing the calibration tests, the system identification tests were conducted. The purposes of the system identification tests are to verify physical properties such as system stiffness, natural periods, total system damping, and linear (RAOs) and non-linear (low & high frequency) response characteristics of the floating wind turbine models. Table 14 summarizes the system identification tests.

After the system identification tests, the station keeping tests were carried out. In order to identify coupling between the wind turbine and the floating platform, four different in-place test phases were conducted.

Table 14: Summary of system identification tests

Test Types	Measurements
Hammer Tests	Structural natural periods
Static Offset Tests	Mooring stiffness
Free Decay Tests	System natural periods and total damping
Free Decay + Steady Wind	Damping contribution from wind
Regular Wave Tests	Linear response characteristics (RAOs)
Regular Wave + Steady Wind	Linear response characteristics include wind
White Noise Wave Tests	Linear response characteristics (RAOs) & Non-linear response characteristics (low frequency & high frequency)
White Noise Wave + Steady Wind	Wind damping contribution on system response

After the system identification tests, the station keeping tests were carried out. In order to identify coupling between the wind turbine and the floating platform, four different in-place test phases were conducted.

The first phase was wind only tests for the fixed wind turbine configuration. These tests served as benchmark for calibrating and verifying the aerodynamic load coefficients such as drag (C_D), lift (C_L), thrust, and torque of the wind turbine model.

The second phase was wind only tests for the floating wind turbine configuration. In this phase, the wind turbine was responding to wind and to “calm” water. The test isolated the wind effects on the floating wind turbine response.

The third phase was wave only tests for the floating wind turbine configuration. This phase served as benchmark for calibrating and verifying the hydrodynamic coefficients and station keeping characteristics of the floating wind turbines. The final phase was wind and wave tests. These tests were carried out with steady and dynamic winds, and regular and random wave environments. The station keeping test types and load cases are summarized in Table 15 and

Table 16, respectively. Since the current speed is low in Gulf of Maine, currents were not simulated in these tests.

Table 15: Summary of station keeping test types

Test Types	Test Description
Wind only	Wind tests for fixed wind turbine
	Wind tests for floating wind turbines
Wave only	Head seas
	Oblique seas
	Bi-directional seas (swell & local waves)
Wind & Wave	Operation wave with wind speed 1,2 & 3
	1year storm wave with wind speed 3,4 & 5
	100 year storm wave with wind speed 5
	100 year storm wave and wind speed 6
	Bi-directional wave + steady wind 5
	Bi-directional wave + dynamic wind 2

Table 16: Summary of load cases

	Operational Wave 1	Operational Wave 2	Design Wave	Bi-Directional
Steady Wind 1	Operation Low 1			
Steady Wind 2	Operation Low 2			
Steady Wind 3	Operation Low 3	Operation High 1		
Steady Wind 4		Operation High 2		
Steady Wind 5		Operation High 3	Design	Swell 1
Steady Wind 6			Survival	
Dynamic Wind 1		Operation High 1		
Dynamic Wind 2		Operation High 2	Design	Swell 2
Dynamic Wind 3		Operation High 3	Survival	

4 Experimental Comparison of the Three Floating Wind Turbine Systems

In this section, the experimental data for the three floating wind turbine systems is investigated. First, data pertaining to the system identification tests will be discussed. The system identification tests outline key characteristics of the floating wind turbine systems, such as non-dimensional wind turbine performance, tower bending natural frequencies, mooring restoring forces, motion natural periods and response amplitude operators (RAOs). Subsequently, the performance of the three floating wind turbines in several coupled wind and wave environments is analyzed and the results presented.

4.1 System Identification of the Floating Wind Turbine Systems

The first system identification test performed was a fixed-base test of the wind turbine under steady winds. During these tests, a sweep through various rotor speeds at a fixed wind speed was conducted to measure the variation of performance coefficient and thrust coefficient as a function of tip speed ratio. The results of the tests are given in Figure 40.

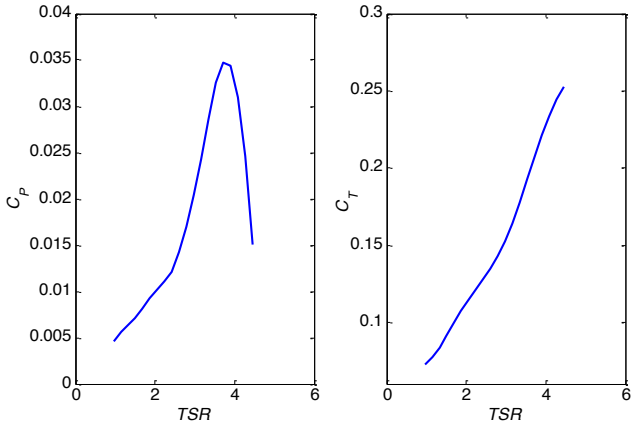

Figure 40: Performance coefficient and thrust coefficient as a function of tip-speed ratio for the wind turbine used in the model test program.

The turbine tower structural natural periods were measured with hammer tests. Hammer tests were executed by exciting the model with an impulse forces. Hammer test results are summarized and shown in Table 17 and Figure 41. The hammer test results show that the floating platform characteristics significantly influence the bending frequencies of the turbine tower. As expected, the stiffer foundation such as a TLP provides lower tower bending natural frequency than the compliant foundations such as a Spar-Buoy and Semisubmersible. The stiffer foundations represent free-fixed boundary condition such as cantilever beam, while softer foundation represents free-free boundary condition at the tower base.

The total stiffness of the mooring system was measured by the static offset tests. Static offset test results are shown in Figure 42. As expected, softening was observed with the synthetic mooring system. On the other hand, hardening was observed with the catenary mooring system. The tendon system shows a linear stiffness trend. Set down of the TLP was also measured during the horizontal static offset tests. Figure 43 shows set down measurement of the TLP.

Table 17: Measured tower bending natural frequencies

	Natural Frequency (Hz)		
	1st FA*	1st SS**	2nd FA*
Fixed Turbine	0.29	0.29	1.24
TLP	0.28	0.29	1.16
Spar-Buoy	0.43	0.44	1.29
Semi-Submersible	0.35	0.38	1.26

*fore - after mode
**side - side mode

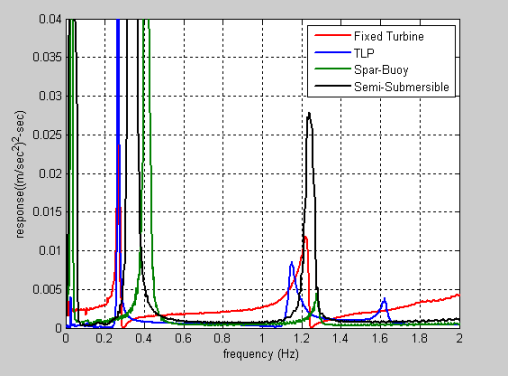

Figure 41: Hammer test results.

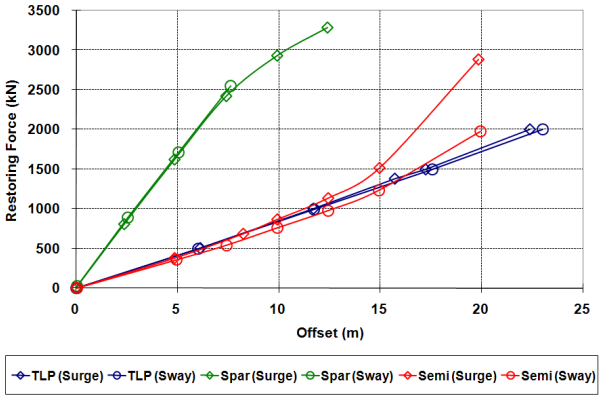

Figure 42: Comparison of static offset test results.

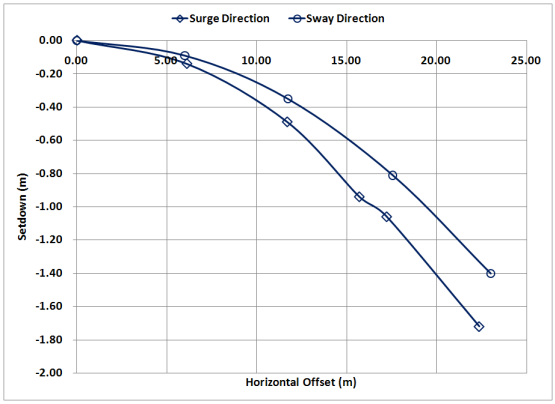

Figure 43: TLP set down.

Table 18: Comparisons of natural periods

DOF	Unit (sec)		
	TLP		
	Measured	Measured	Predicted
	No wind	Steady wind	No wind
Surge	39.30	39.48	40.2
Sway	39.30	-	40.2
Heave	1.25	-	1.05
Roll	3.70	-	3.11
Pitch	3.70	-	3.08
Yaw	18.20	-	16.8
DOF	Spar – Buoy		
	Measured	Measured	Predicted
	No wind	Steady wind	No wind
Surge	43.0	42.6	41.3
Sway	42.8	42.8	41.3
Heave	28.1	-	28.4
Roll	32.0	-	30.4
Pitch	31.5	31.2	30.4
Yaw	5.5	-	8.1
DOF	Semi-Submersible		
	Measured	Measured	Predicted
	No wind	Steady wind	No wind
Surge	107.0	102.0	107.5
Sway	112.0	-	107.5
Heave	17.5	-	17.2
Roll	26.9	-	26.6
Pitch	26.8	26.9	26.6
Yaw	82.3	-	84.3

The natural periods and total damping of the floating platform system were obtained from free decay tests. In order to measure damping for the floating wind turbines, two types of free decay tests were carried out. The first type was calm water free decay test that measures system natural periods and hydrodynamic damping. The second type was free decay test with steady wind that measures aerodynamic damping from the wind turbine. The six DOF natural periods of the floating wind turbines are listed in Table 18.

Damping ratios with respect to motion amplitudes for all three floating wind turbines are shown in Figure 44, Figure 45 and Figure 46. Damping analysis results show that steady wind substantially increases pitch damping of the Spar-buoy and Semi-submersible. Due to slender and deep draft shape, relatively low heave, roll and pitch damping were measured with the Spar-buoy.

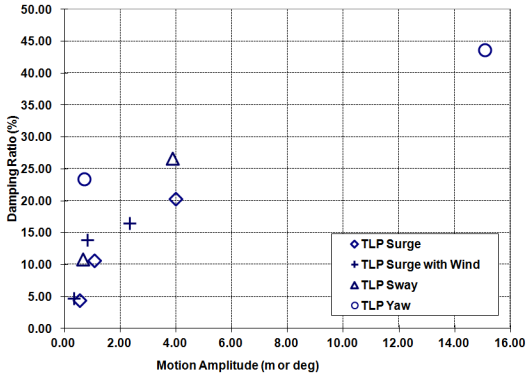

Figure 44: Comparisons of damping ratios (TLP).

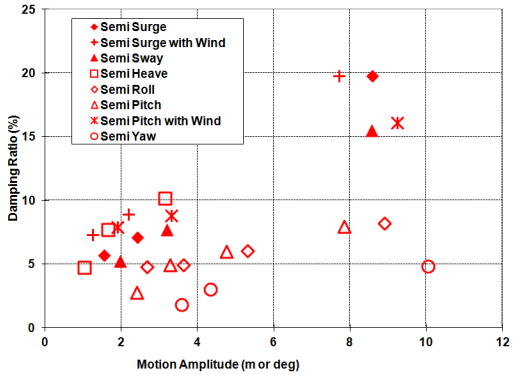

Figure 45: Comparisons of damping ratios (semi-submersible).

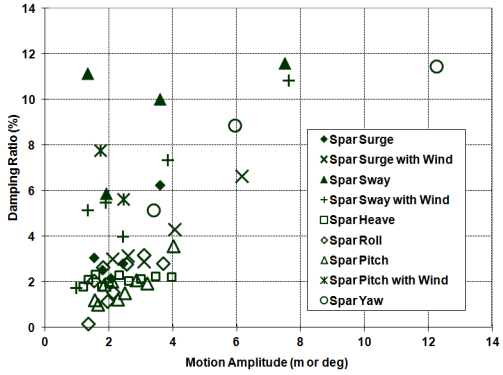

Figure 46: Comparisons of damping ratios (spar-buoy).

The linear and nonlinear wave response characteristics of the floating wind turbines were measured by the regular and white noise wave tests. In order to identify wind effects on the global performance of the floating wind turbines, the regular wave and white noise tests were conducted with and without steady wind.

4.1.1 TLP Response Amplitude Operators

Figure 47 shows surge RAOs of the TLP. The surge natural period of the TLP is longer than the linear wave frequency range, and therefore the damping effect from wind is not shown in the surge RAO.

However, as shown in Figure 48, the response spectra comparisons clearly show wind damping effect at the TLP surge natural period (= 39.3 sec) response.

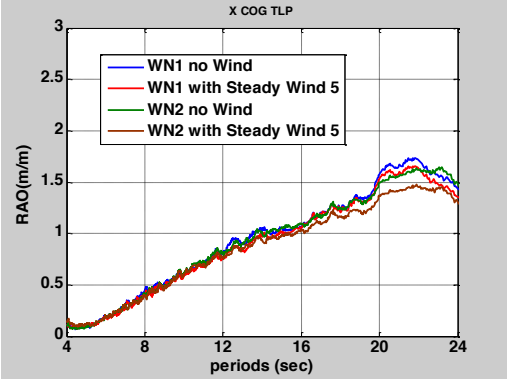

Figure 47: Surge RAOs of the TLP.

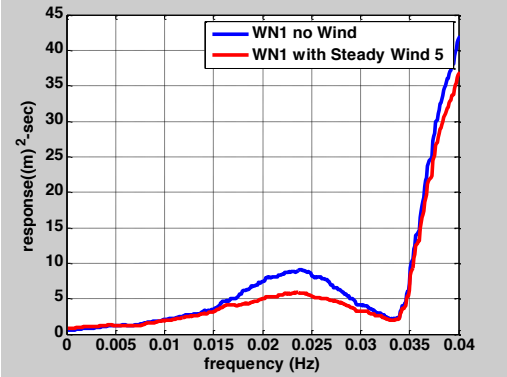

Figure 48: TLP Surge response spectra.

Figure 49 shows pitch RAOs of the TLP. Since pitch natural period of the TLP is near the linear wave excitation periods, the RAOs clearly show wind damping effects on the TLP pitch response. As shown in Figure 50, the response spectra comparison clearly shows reduction of the TLP pitch natural period motion.

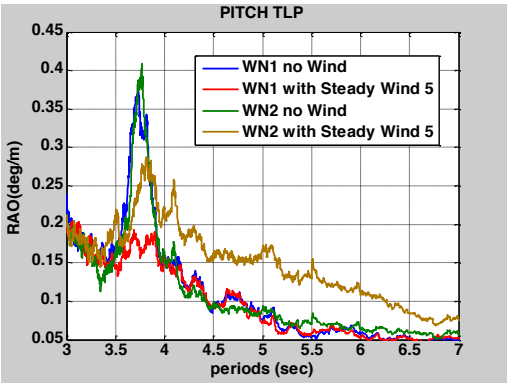

Figure 49: Pitch RAOs of the TLP.

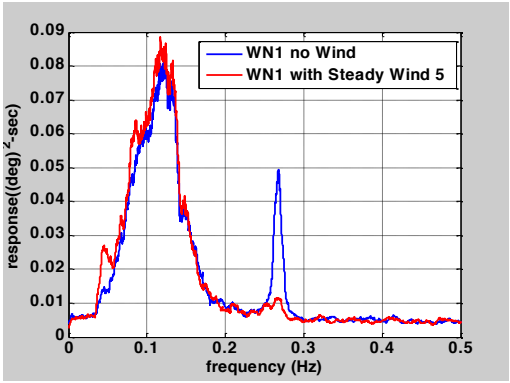

Figure 50: Pitch responses of the TLP.

4.1.2 Spar-buoy Response Amplitude Operators

Figure 51, Figure 52 and Figure 53 show the surge, heave and pitch RAOs of the Spar-Buoy, respectively. Since all six DOF motion natural periods of the Spar-buoy are longer than linear wave excitation period range, the damping effect from wind is not shown in the RAOs. On the other hand, Figure 54 and Figure 55 show response spectra of the Spar-Buoy, and both surge and pitch responses show that the wind reduces the surge and pitch responses at the natural periods, while the wind increases the linear wave frequency responses of the Spar-Buoy in surge and pitch modes.

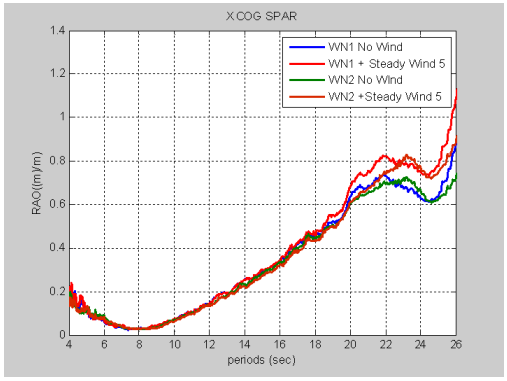

Figure 51: Surge RAOs of the spar-buoy.

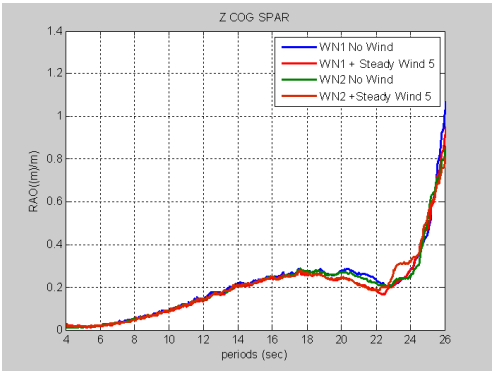

Figure 52: Heave RAOs of the spar-buoy.

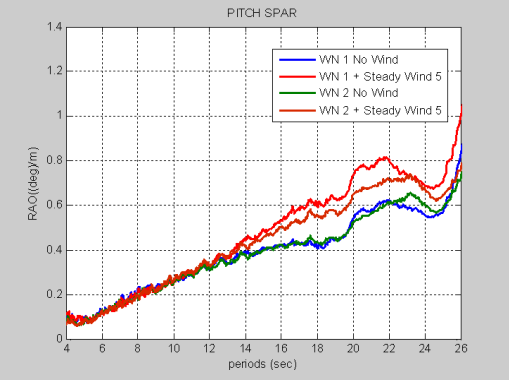

Figure 53: Pitch RAOs of the spar-buoy.

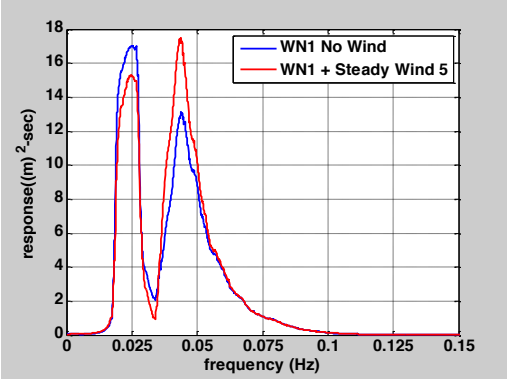

Figure 54: Surge response of the spar-buoy.

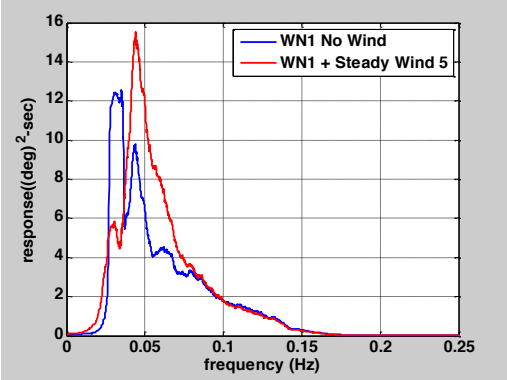

Figure 55: Pitch response of the spar-buoy.

4.1.3 Semi-submersible Response Amplitude Operators

Figure 56, Figure 57, and Figure 58 show the RAOs of the Semi-submersible. Since the heave natural period of the semi-submersible is close to linear wave energy, the heave RAO comparisons show nonlinear damping effect near the heave natural period (= 17.5 sec).

Figure 59 and Figure 60 show the surge and pitch response spectra of the semi-submersible. It is interesting to note that the surge and pitch linear wave frequency responses remained same for both with and without wind, while the steady wind reduces the low frequency surge and pitch responses.

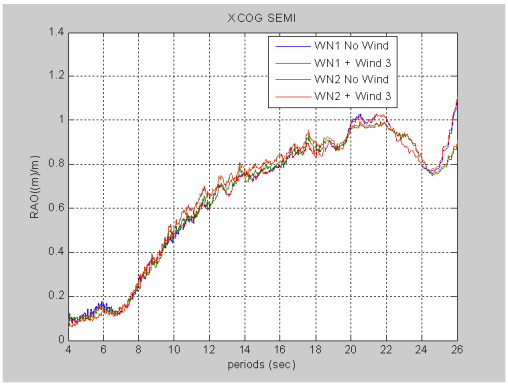

Figure 56: Surge RAOs of the semi-submersible.

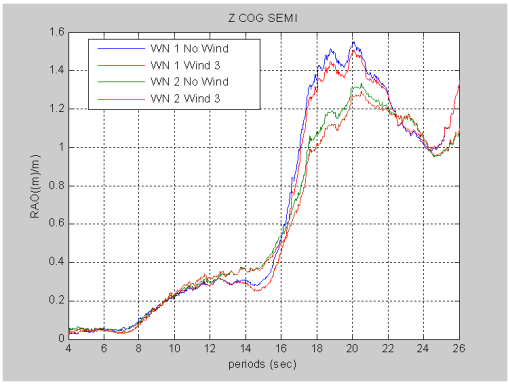

Figure 57: Heave RAOs of the semi-submersible.

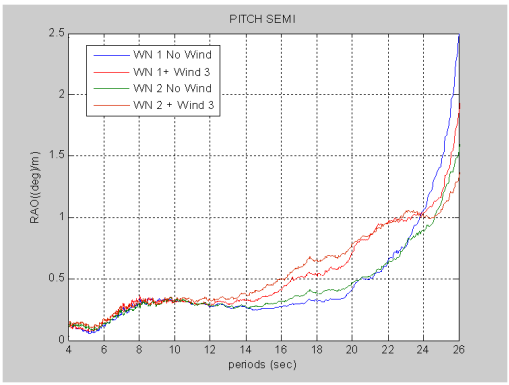

Figure 58: Pitch RAOs of the semi-submersible.

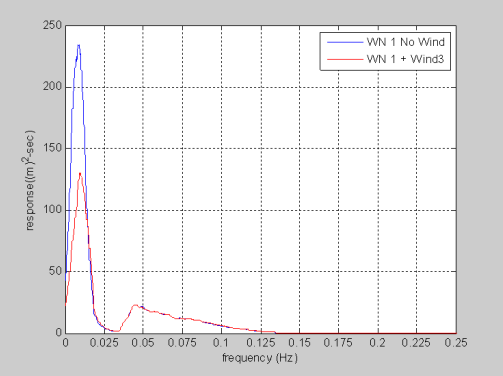

Figure 59: Surge response of the semi-submersible.

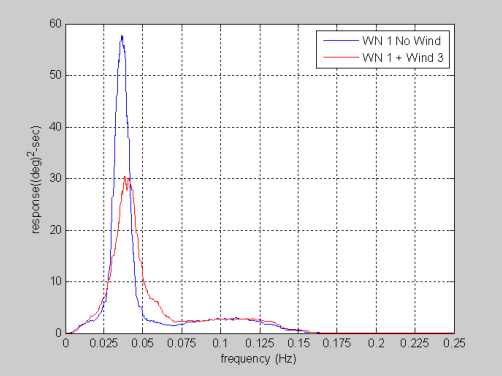

Figure 60: Pitch response of the semi-submersible

4.2 Performance of the Floating Wind Turbine Systems in Dynamic Winds and Irregular Waves

As noted earlier, the floating wind turbine test program covers a large number of tests ranging from basic system identification to complex, coupled wind/wave tests. With these system identification tests already covered, this section only presents results for the three systems subjected to combined wind and irregular wave loading. Also, as there were numerous combinations of wind and wave environments studied, this report focuses on only a select set of environmental conditions that yield interesting results. As such, the next section will outline the specific wind and wave environmental conditions employed throughout this section. Subsequently, the response of the three floating wind turbine systems to these environments will be discussed.

4.2.1 Environmental Conditions

The metocean conditions employed during the tests are based on measurements made from the Gulf of Maine NERACOOS floating buoy system. The wind environment during testing is created via a novel wind machine suspended above the water which produces near spatially uniform winds with a turbulence intensity at hub height of 4%. Multiple steady and dynamic winds are tested that cover a majority of the wind turbine operational wind speeds in addition to extreme, 100 year winds. However, only results using two steady winds and two temporally dynamic, NPD spectrum winds (NPD, 1992) are presented in the results section. The steady winds possess mean wind speeds at the 90 m hub height of U_m = 11.2 and 21.8 m/s. The NPD spectrum winds exhibit mean wind speeds of U_{10} = 17.0 and 24.0 m/s at the NPD specification height of 10 m above SWL. All winds are directed at 180 degrees and last for 3 hours. A depiction of the orientations and degrees of freedom (DOF) employed during model testing is shown in Figure 61.

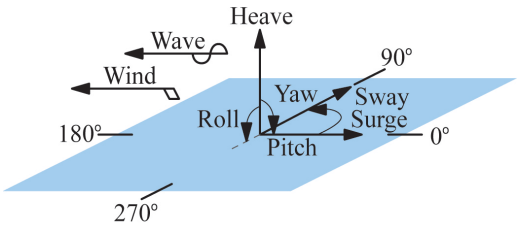

Figure 61: Orientations and degrees of freedom used during model testing.

The wind turbine operates at a rotor speed of 7.8 rpm for the U_m = 11.2 m/s condition and at a speed of 12.7 rpm for the steady U_m = 21.8 m/s and U_{10} = 17.0 m/s NPD winds. For the higher NPD wind speed, U_{10} = 24.0 m/s, the rotor is parked (0 rpm) with the blades feathered to minimize the aerodynamic drag loads. No active blade pitch control schemes are attempted and all tests utilize a fixed blade pitch setting in order to keep the number of variables that influence the global response of the floating wind turbine systems to a manageable level. For the dynamic winds, a comparison of the theoretical and obtained wind spectrums is shown in Figure 62. As can be seen in the figure, the match between the theoretical and measured spectra is quite good. The hub height statistics for the two dynamic winds are displayed in Table 19. For each of the steady and dynamic wind cases, the primary aerodynamic load contributing to global motion, thrust, varies significantly. The average thrust force for all three structures from wind only testing is found in Table 20. Note that even though the U_{10} = 24.0 m/s wind possesses the largest mean wind speed of all the winds presented, the average thrust load is the least due to the drag reducing effect of parking the turbine rotor and feathering the blades.

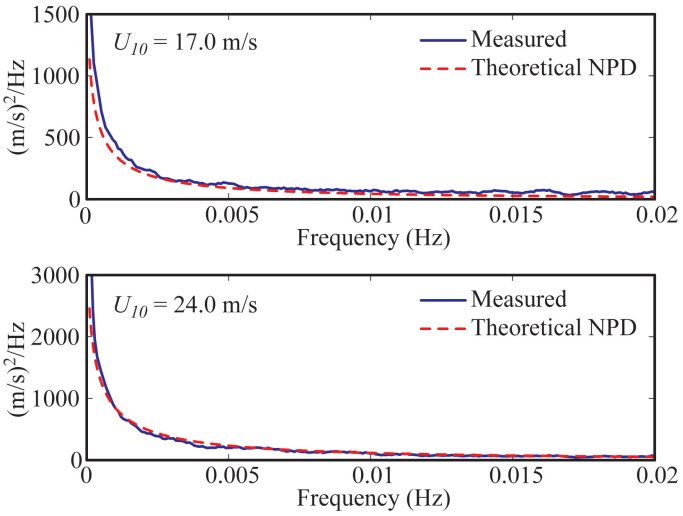

Figure 62: Theoretical and measured spectra for the U_{10} = 17.0 and 24.0 m/s NPD dynamic winds.

Table 19: Hub height (90 m) statistics for the U_{10} = 17.0 and 24.0 m/s NPD dynamic winds

U_{10} (m/s)	Mean (m/s)	Std (m/s)	Max (m/s)	Min (m/s)
17.0	20.7	2.04	28.7	12.9
24.0	30.1	2.71	41.3	20.4

Table 20: Average thrust forces from wind only tests

Wind Case	TLP (kN)	Spar (kN)	Semi (kN)
U_m = 11.2 m/s	263	255	203
U_m = 21.8 m/s	775	870	749
U_{10} = 17.0 m/s	642	755	683
U_{10} = 24.0 m/s	171	190	202

Similar to the winds, multiple regular and irregular waves are tested during the model floating wind turbine experiment. However, this section presents data from only three unidirectional irregular waves. The waves follow a JONSWAP spectrum (IEC, 2009) with significant wave heights of H_s = 2.0, 7.1 and 10.5 m. The peak spectral periods for these waves are T_p = 7.5, 12.1 and 14.3 s, respectively. Each of these waves is applied at 180 degrees, and thus, is aligned with the wind direction. All of these irregular waves are 3 hours in length. A comparison of the theoretical and measured spectra is shown in Figure 63.

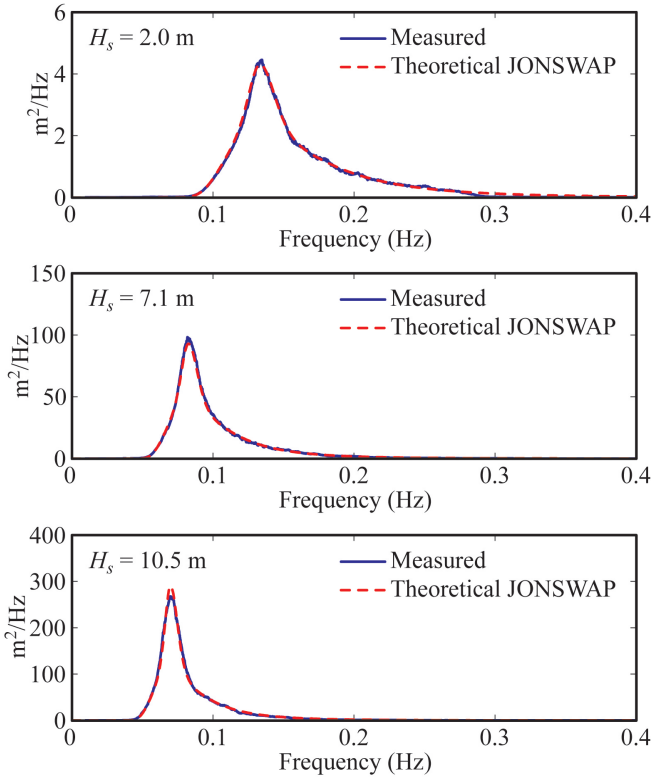

Figure 63: Theoretical and measured spectra for the H_s = 2.0, 7.1 and 10.5 m JONSWAP irregular waves.

Similar to the dynamic wind results, the comparisons shown in Figure 63 show a very good agreement between the theoretical and measured spectra. The statistics for the three irregular waves, consisting of standard deviation, maximum crest height, minimum trough and maximum wave height, are shown in Table 21. As can be seen in the table, the maximum crest heights are slightly larger than the value of H_s, while the maximum wave heights are roughly double H_s for each of the waves shown.

Table 21: Statistics for the H_s = 2.0, 7.1 and 10.5 m JONSWAP irregular waves

H_s (m)	T_p (s)	Std (m)	Max Crest (m)	Min Trough (m)	Max Wave (m)
2.0	7.5	0.49	2.14	1.87	3.64
7.1	12.1	1.79	7.20	6.37	13.58
10.5	14.3	2.62	13.59	9.58	22.01

4.2.2 Wave Only Performance Comparison

In this section, a performance comparison of the three floating wind turbine systems is presented in wave only conditions. Response spectra and statistical surge and pitch results are provided for the systems subjected to each of the three, aforementioned irregular waves to illustrate the relative motion performance of the three floating systems in irregular seas. To begin, the response spectra for the surge DOF is shown in Figure 64. The surge coordinate is reported at the structure center of gravity (CG) for all three systems, as this location provides greater physical understanding of the system translational motion.

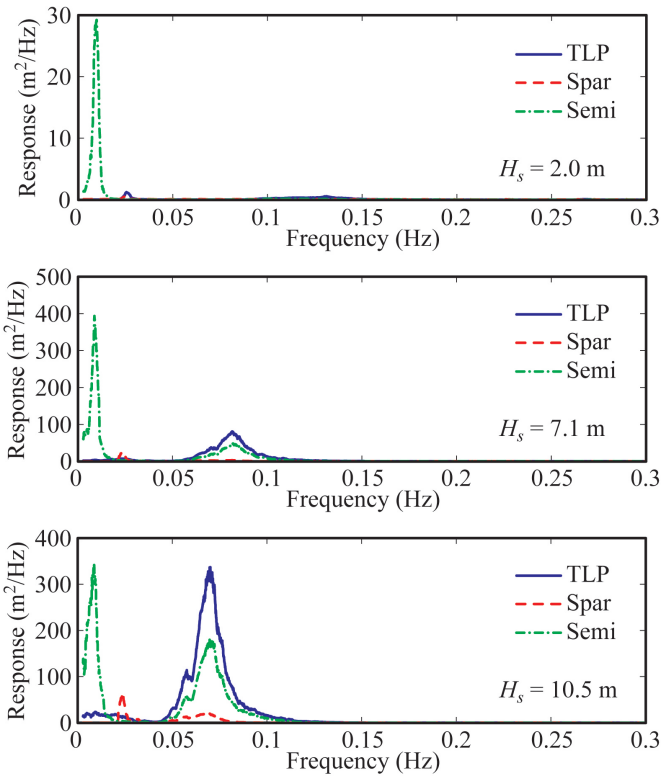

Figure 64: Surge response spectra for all three systems under wave only loading.

As can be seen in Figure 64, the TLP exhibits the greatest surge response in the wave energy range (0.05 to 0.15 Hz) about its CG for the three systems. The spar-buoy response is the least of the three, however, this is due in large part to the fact that the CG is very low on the structure and does not move much relative to the portion of the structure located near the waterline. The semi-submersible response is slightly less than the TLP in the wave energy range, but the semi-submersible exhibits by far the largest second-order difference-frequency associated surge motion of any of three floating turbine systems as evidenced by the significant response near the surge natural frequency of 0.009 Hz.

The second wave only comparison presented is the response spectra for the pitch motion of the structures, given in Figure 65. As one would expect, the stiff pitch restoring stiffness of the TLP is evidenced by the very low response of this system compared to the other two. Comparing the other two systems, the response is greatest for the spar-buoy in the wave energy regime, excepting the H_s = 2.0 m sea state where the semi response is slightly greater. The second-order difference-frequency response is once again greatest for the semi-submersible, with the disparity between the spar-buoy and semi-submersible being greatest as the sea state is diminished.

To complete the wave only comparison, the statistics for the surge and pitch motion are presented in Table 22. Many of the previous observations made from the frequency domain results are reinforced by the statistics of Table 22. The TLP and semi-submersible exhibit the largest minimum and maximum surge motions, with the TLP possessing the largest maximum surge for any design, 6.91 m, and the semi-submersible, the largest magnitude minimum for any of the designs, -13.72 m.

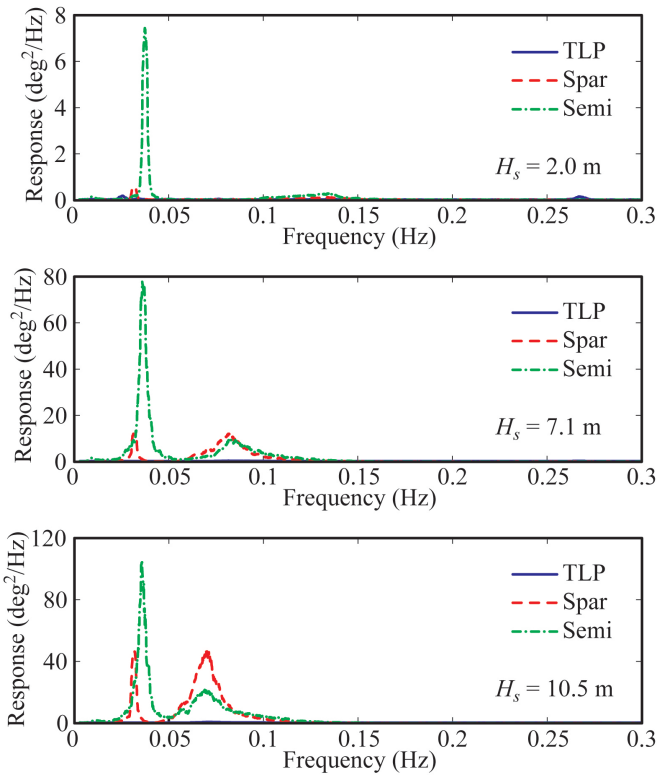

Figure 65: Pitch response spectra for all three systems under wave only loading.

Table 22: Statistics for the surge and pitch motion for the TLP, spar-buoy and semi-submersible

DOF	H_s	Mean	Std	Max	Min
TLP					
Surge (m)	2.0 m	0.07	0.21	0.86	-0.70
Pitch (deg)	2.0 m	-0.20	0.19	0.24	-0.67
Surge (m)	7.1 m	-0.11	1.37	4.49	-8.22
Pitch (deg)	7.1 m	-0.18	0.15	0.42	-0.81
Surge (m)	10.5 m	-0.33	2.53	6.91	-12.73
Pitch (deg)	10.5 m	-0.18	0.16	0.64	-1.37
Spar-buoy					
Surge (m)	2.0 m	0.18	0.21	0.97	-0.50
Pitch (deg)	2.0 m	-0.11	0.13	0.42	-0.61
Surge (m)	7.1 m	0.17	0.45	2.00	-1.87
Pitch (deg)	7.1 m	-0.12	0.57	2.13	-2.54
Surge (m)	10.5 m	0.16	0.81	3.13	-3.42
Pitch (deg)	10.5 m	-0.13	1.01	-3.65	-5.43
Semi-submersible					
Surge (m)	2.0 m	-0.73	0.38	0.70	-2.36
Pitch (deg)	2.0 m	0.05	0.24	0.97	-0.90
Surge (m)	7.1 m	-1.83	1.71	3.44	-9.68
Pitch (deg)	7.1 m	0.06	0.86	3.35	-3.92
Surge (m)	10.5 m	-2.38	2.41	5.16	-13.72
Pitch (deg)	10.5 m	0.06	1.11	4.27	-4.71

Uniquely enough, the mean surge value for the TLP is quite small for all the environments, while the mean surge value for the semi-submersible grows modestly as the structure is subjected to increasing sea states. For the pitch motion, the TLP motion is by far the smallest of the three, as expected. For the other two systems, the pitch response range of the semi-submersible is largest in the H_s = 7.1 m sea state, as is the pitch standard deviation. In the H_s = 10.5 m condition, the spar-buoy and semi-submersible pitch ranges are nearly identical (approximately 9 degrees) with a slightly larger pitch standard deviation for the semi-submersible as opposed to the spar-buoy.

4.2.3 Effect of Wind on Global Performance

In this section, the effect of wind turbine aerodynamic loading on the global motion of the three structures is investigated. For all three structures, the response spectra and statistics of the surge and pitch DOF are investigated for three cases with an H_s = 10.5 m sea state: no wind, an operating turbine subjected to a U_{10} = 17.0 m/s wind and a parked and feathered turbine subjected to U_{10} = 24.0 m/s winds.

4.2.3.1 TLP

The response of the TLP floating wind turbine in these three conditions is investigated first. The response spectra for the surge and pitch DOF for the three cases are given in Figure 66. For both DOF, the response of the no wind and U_{10} = 24.0 m/s cases are very similar. This indicates that even under high wind speeds, a parked and feathered rotor minimizes the impact of the wind loading on the structure's response.

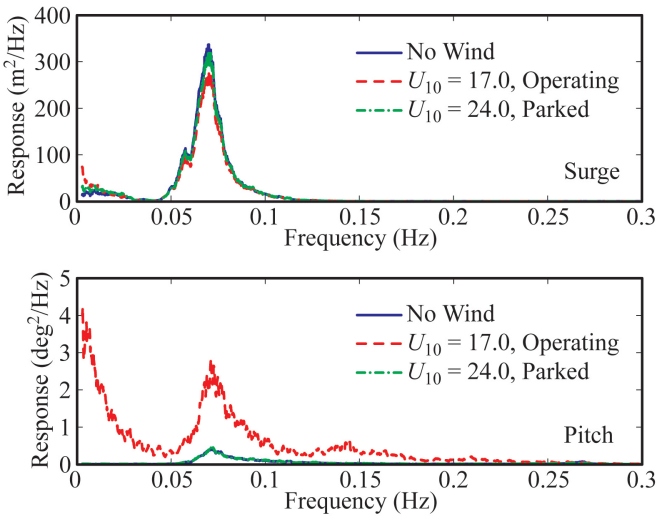

Figure 66: TLP surge and pitch response spectra for an H_s = 10.5 m sea state with three different wind conditions.

When the turbine is operating and the thrust loads are high in the U_{10} = 17.0 m/s case, the surge DOF exhibits increased response in the wind energy frequency range (<0.02 Hz) and is slightly damped in the wave frequency range (0.05 to 0.1 Hz). For the pitch response, the operating turbine increases the pitch response over all frequencies shown, with the greatest increases near the wind and wave energy frequencies. This is due to the fact that the TLP employed during model testing is of a small design and is not large enough to support the large overturning moment created by the thrust of the operating wind turbine in high seas, resulting in multiple slack line events. These slack line events result in infrequent, but violent pitch motions that excite a broad range of structural vibrations as evidenced by the increased pitch response shown in Figure 66. It should be noted though, that the TLP pitch response is very small, and hence, the disparity between the TLP pitch response curves in Figure 66 does not represent a great deal of energy. The statistics for the three cases are given in Table 23. For the no wind and U_{10} = 24.0 m/s cases, the statistics are very similar, with the U_{10} = 24.0 m/s case yielding a larger magnitude mean surge and on average slightly larger magnitude extreme statistics.

Table 23: TLP surge and pitch statistics for an H_s = 10.5 m sea state with three different wind conditions

DOF	U_{10}	Mean	Std	Max	Min
Surge (m)	0.0 m/s	-0.33	2.53	6.91	-12.73
Pitch (deg)	0.0 m/s	-0.18	0.16	0.64	-1.37
Surge (m)	17.0 m/s	-11.03	2.46	-3.62	-22.21
Pitch (deg)	17.0 m/s	-0.52	0.41	1.48	-6.86
Surge (m)	24.0 m/s	-3.23	2.52	4.31	-15.75
Pitch (deg)	24.0 m/s	0.28	0.16	1.44	-1.72

For the U_{10} = 17.0 m/s scenario, the mean value for surge is increased, but the standard deviation is similar to the other cases. The evidence for the slack tendon in the operating turbine case is the minimum pitch value of -6.86 degrees, this being abnormally large pitch motion for a TLP platform. If the TLP were of a sufficiently large size to prevent slack tendons, than the minimum pitch value for the U_{10} = 17.0 m/s scenario would likely decrease in magnitude by a significant amount.

4.2.3.2 Spar-buoy

Next, the results for the spar-buoy floating wind turbine are discussed. The response spectra for the surge and pitch DOF are displayed in Figure 67. For both surge and pitch DOF, the no wind and parked wind turbine cases are quite similar. As seen in Figure 67, the operating turbine increases only the second-order difference-frequency surge response of the spar-buoy, this being near the spar surge natural frequency of 0.023 Hz.

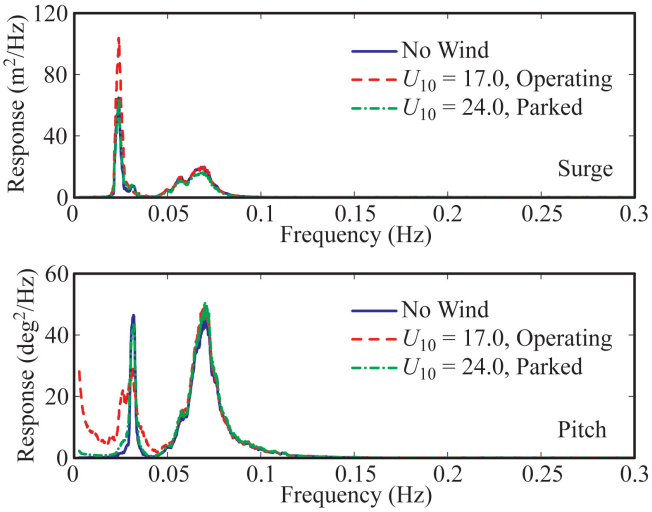

Figure 67: Spar-buoy surge and pitch response spectra for an H_s = 10.5 m sea state with three different wind conditions.

The pitch response, however, is increased significantly in the wind energy frequency range, with the sole exception being some damping of the pitch second-order difference-frequency response, near 0.032 Hz. The spar-buoy statistics for the two DOF for all three environments are given in Table 24.

Table 24: Spar-buoy surge and pitch statistics for an H_s = 10.5 m sea state with three different wind conditions

DOF	U_{10}	Mean	Std	Max	Min
Surge (m)	0.0 m/s	0.16	0.81	3.13	-3.42
Pitch (deg)	0.0 m/s	-0.13	1.01	3.65	-5.43
Surge (m)	17.0 m/s	0.14	0.92	11.23	-4.41
Pitch (deg)	17.0 m/s	-4.36	1.25	0.04	-15.26
Surge (m)	24.0 m/s	-0.08	0.76	2.93	-3.48
Pitch (deg)	24.0 m/s	-1.25	1.07	2.39	-6.13

The statistics for the surge DOF for all three conditions are very similar with the lone exception being a larger range of motion for the U_{10} = 17.0 m/s case than the other two conditions. For the pitch motion, the mean value is much larger for the operating turbine than the no wind and parked turbine cases, as expected. The range of motion is also increased, however, the standard deviation is only 17% larger than the parked and feathered rotor subjected to U_{10} = 24.0 m/s winds.

4.2.3.3 Semi-submersible

Finally, the surge and pitch response spectra for the semi-submersible floating wind turbine are presented in Figure 68.

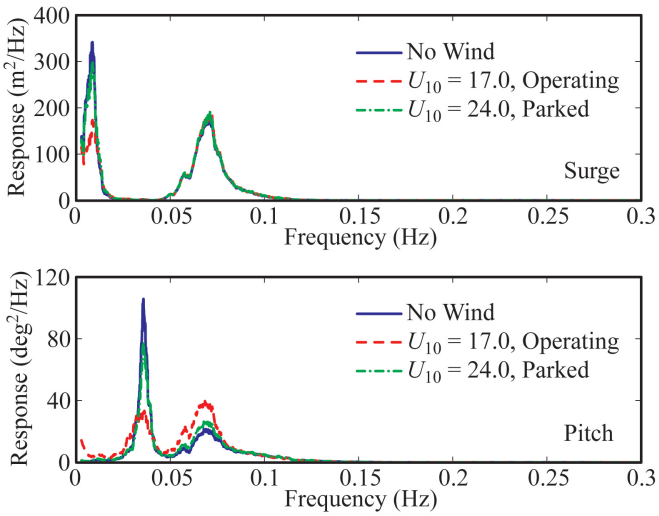

Figure 68: Semi-submersible surge and pitch response spectra for an H_s = 10.5 m sea with three different wind conditions.

Observing the figure, the parked wind turbine under U_{10} = 24.0 m/s winds provides marginal damping of the second-order difference-frequency response (0.009 Hz surge, 0.037 Hz pitch), and marginal excitation of the wave energy frequency response for pitch motion. The operating wind turbine case significantly damps the second-order response in surge and pitch, but noticeably amplifies the response in the wind and wave energy frequency ranges for pitch motion. The statistics for the cases shown in Figure 68 are given in Table 25.

Table 25: Semi-submersible surge and pitch statistics for an H_s = 10.5 m sea state with three different wind conditions

DOF	U_{10}	Mean	Std	Max	Min
Surge (m)	0.0 m/s	-2.38	2.41	5.16	-16.72
Pitch (deg)	0.0 m/s	0.06	1.11	4.27	-4.71
Surge (m)	17.0 m/s	-9.28	2.30	-2.31	-22.28
Pitch (deg)	17.0 m/s	-3.48	1.25	1.55	-8.91
Surge (m)	24.0 m/s	-4.61	2.41	2.99	-17.78
Pitch (deg)	24.0 m/s	-0.69	1.12	3.73	-5.69

Similar to the other two floating wind turbine systems, the statistics are very similar for the no wind and parked turbine cases. The operating turbine case exhibits the largest magnitude mean pitch and surge values in Table 25, but the ranges of motion for both DOF are quite similar to the no wind and parked rotor cases.

4.2.4 Nacelle Acceleration

In this section, a study of the relative performance of the three floating wind turbine systems as measured by the nacelle surge acceleration is presented. The nacelle acceleration, which is a function of platform motion and flexible tower dynamics, is of great interest as it is indicative of the inertial loading that the wind turbine gearbox, bearings, and other complex parts will experience. For the comparison, the nacelle surge acceleration measured at 88.25 m above SWL is investigated for all three floating wind turbine systems under three distinct environmental conditions. The environmental conditions consist of H_s = 2.0, 7.1 and 10.5 m irregular sea states, each with an operating wind turbine. The H_s = 2.0, 7.1 m sea states are subjected to steady U_m = 11.2 m/s winds while the H_s = 10.5 m sea state case is subjected to U_m = 21.8

m/s steady winds. The response spectra for all three systems in each of the three conditions are displayed in Figure 69. There are several noteworthy observations to be made from the results shown in Figure 69. First, for the modest, H_s = 2.0 m sea state environment, the performance of the three systems is very similar in the wave energy frequency range (0.1 to 0.2 Hz). However, the TLP exhibits significant response at frequencies larger than the wave energy, which the other two systems do not. This energy is associated with the TLP coupled platform pitch/tower bending frequency of 0.28 Hz which is excited by the second-order sum-frequency wave loading from the small, T_p = 7.5 s sea state. While the response of all three systems is quite low in energy for the H_s = 2.0 m sea state, the prevalence of these mild sea environments indicates that this TLP may be prone to greater wind turbine and tower fatigue issues than the other systems.

Moving to the intermediate sea state of H_s = 7.1 m, the figure shows that the performance of the three systems are quite distinct. The spar-buoy system possesses the maximum peak response of the three systems with a peak that is nearly double that of the second most excited system, the TLP. While the TLP motion is primarily pure surge translation, the spar pivots about a point located low on the spar, near the CG, translating modest wave induced motions at the water line into large translational motions at the nacelle location. The result is the large nacelle surge accelerations seen in Figure 69 for this environmental condition. Surprisingly for this environment, the semi-submersible system nacelle surge acceleration response is greatly diminished to negligible levels over most of the wave energy range (0.05 Hz to 0.2 Hz). This is unexpected as the platform motion is substantial for this sea state with motion similar to the responses given in Figure 64 and Figure 65. The low surge acceleration at the nacelle location is a result of the unique interplay of the surge and pitch motion characteristics for this semi-submersible in the H_s = 7.1 m environment.

The nacelle surge acceleration response comparison for the most severe environment in Figure 69, H_s = 10.5 m, shows that the response of the semi-submersible is once again the smallest, albeit only slightly less than the TLP floating wind turbine system. The spar-buoy floating wind turbine exhibits the largest response of the three, with a peak response in the frequency domain of approximately three times the TLP and semi-submersible. The reasons for the large response are similar to those identified for the H_s = 7.1 m condition, only magnified.

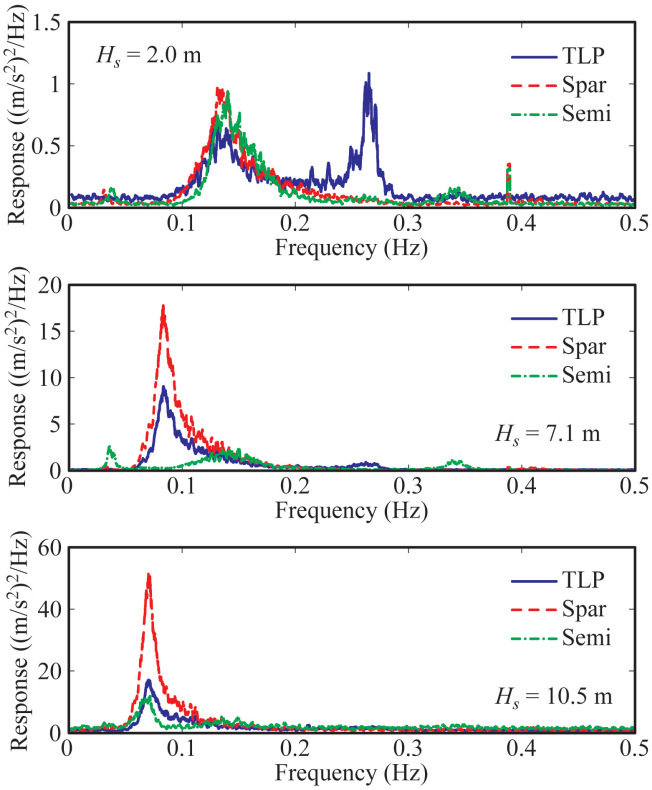

Figure 69: Nacelle surge acceleration spectra for all three systems under three distinct environmental conditions.

4.2.5 System Loads Comparison

In this section, a comparison of a few of the floating wind turbine system loads is presented. First, the tower base bending moment about the sway axis (pitch DOF) is presented for two different environments. This bending moment is the largest moment induced in the tower and is major design driver in the sizing of the tower. The second comparison involves the mooring line tensions for each of the designs subjected to the same wind and wave loading. These loads will indicate the relative demands of the floating wind turbine systems on the mooring and anchoring systems.

4.2.5.1 Tower Loads

For the comparison of the tower base bending moment, two environments are considered, both with an operating wind turbine subjected to a U_{10} = 17.0 m/s dynamic wind. The first possesses an H_s = 2.0 m irregular sea while the second consists of an H_s = 10.5 m sea state. The response spectra for the two conditions are shown in Figure 70. For the low energy sea state, all three systems exhibit a moderate response in the wave energy frequency regime (0.1 to 0.2 Hz), with the semi possessing the greatest response and the TLP the least. The largest discrepancy in the three systems is the response in the frequency ranges above and below the wave energy frequency range. For low frequencies in the wind energy regime, the TLP exhibits very little response, unlike the spar-buoy and semi-submersible. The wind loading excites the rigid body pitching motion of these two systems which in turn induces significant moments at the base of the tower as a result of supporting the large nacelle and rotor weight on a tilted tower. As can be seen in Figure 70, the response at the spar-buoy and semi-submersible natural pitch frequencies (0.032 And 0.037 Hz, respectively) is quite prominent as a result of this phenomenon.

At frequencies above the wave energy range, the TLP shows by far the greatest response. The response, located near the coupled platform pitch/tower bending frequency of 0.28 Hz, is excited primarily by the second-order sum-frequency wave loading of the TLP platform. The spar-buoy and semi-submersible also exhibit some tower base bending energy at their respective tower bending frequencies of 0.43 and 0.35 Hz, albeit, at a much reduced level as compared to the TLP. A final note for this condition is that the stiff TLP system allows transmission of the turbine's once per revolutions excitation at 12.7 rpm (0.21 Hz) all the way down the tower, as evidenced by the strong peak in the signal at this frequency.

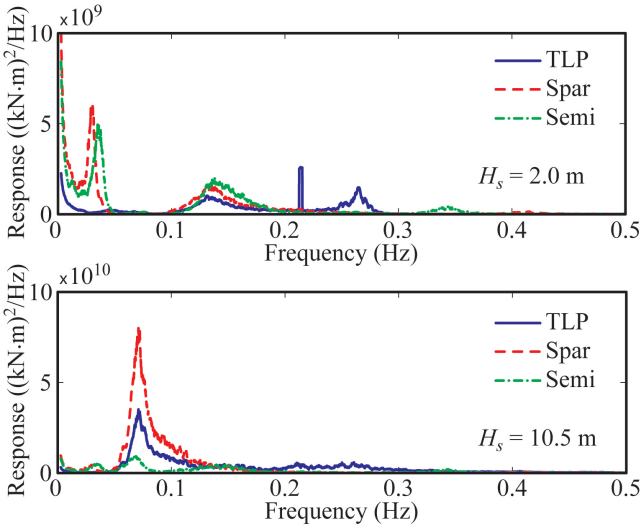

Figure 70: Tower base bending moment spectra for all three systems for two combined wind/wave loading conditions.

Moving to the environment with the larger H_s = 10.5 m sea state, it is evident from Figure 70 that the majority of the response for all three systems is in the wave energy frequency range (0.05 to 0.1 Hz). The spar-buoy possesses the most energy in the tower base bending, with the semi-submersible the least. Since the inertial forces created by motion of the nacelle and rotor contribute greatly to the tower base moment, it is not surprising that the response trends for this sea state are similar to the Figure 69 trends for the nacelle surge acceleration in the H_s = 10.5 sea.

To complete the moment comparison, the statistics for the two conditions for all three systems are shown in Table 26: Tower base bending moment statistics for all three systems for two combined wind/wave loading conditions. It should be noted that the extreme minimum and maximum values for the TLP system in the H_s = 10.5 m condition are the result of tendon snapping events which cause violent pitch motions of the TLP floating wind turbine.

Table 26: Tower base bending moment statistics for all three systems for two combined wind/wave loading conditions

H_s	Mean (kN)	Std (kN)	Max (kn)	Min (kN)
TLP				
2.0	-73,922	10,731	-23,047	-121,784
10.5	-74,291	38,757	356,510	-301,933
Spar-buoy				
2.0	-87,468	15,990	-27,787	-156,258
10.5	-79,064	45,332	91,815	-301,657
Semi-submersible				
2.0	-86,929	15,804	-28,538	-161,873
10.5	-84,358	24,572	53,555	-221,031

For a properly sized (i.e., larger) TLP platform, the extreme values for the TLP system in large seas would be significantly smaller, likely less than the spar-buoy and semi-submersible. This stated, the TLP has the smallest magnitude mean, standard deviation, minimum and maximum for the H_s = 2.0 m condition. While more severe, the moment statistics for the other two systems are very similar in the smaller energy environment. For the larger sea state, the TLP appears to be the poorest performer, again, as a result of the slack tendon events encountered during testing for this TLP design. For the other two systems, the spar-buoy has a moderately larger magnitude standard deviation, minimum and maximum bending moment due mostly to the larger variations in pitch angle of the structure as displayed in Table 23, Table 24 and Table 25.

4.2.5.2 Mooring Loads

To complete the loads comparison, the fairlead mooring line tensions for the three designs is investigated next. Note that for the spar-buoy system, only the main mooring lines are shown and the lines comprising the delta connection are omitted here. The environment investigated consists of U_{10} = 17.0 m/s winds and H_s = 2.0 m seas. The response spectra for the three mooring lines per design, denoted by orientation in degrees, are shown in Figure 71. From the figure, it is clear to see that the energy in the response of the TLP tendons is an order of magnitude greater than the response for the other two systems. This is not entirely unexpected as the TLP system gains its stability from highly loaded, stiff mooring tendons. For the spar-buoy, the mooring load response is tied closely to the surge natural period, as is the peak response of the semi-submersible. The TLP, on the other hand, exhibits significant response at frequencies associated with the wind energy, wave energy, and platform pitch/tower bending natural frequency. Surprisingly, all three TLP tendons also display a sharp response at the once per revolution rotor excitation frequency of 12.7 rpm (0.21 Hz). This is likely a result of the vertically stiff and lightweight nature of the floating TLP wind turbine system tested here.

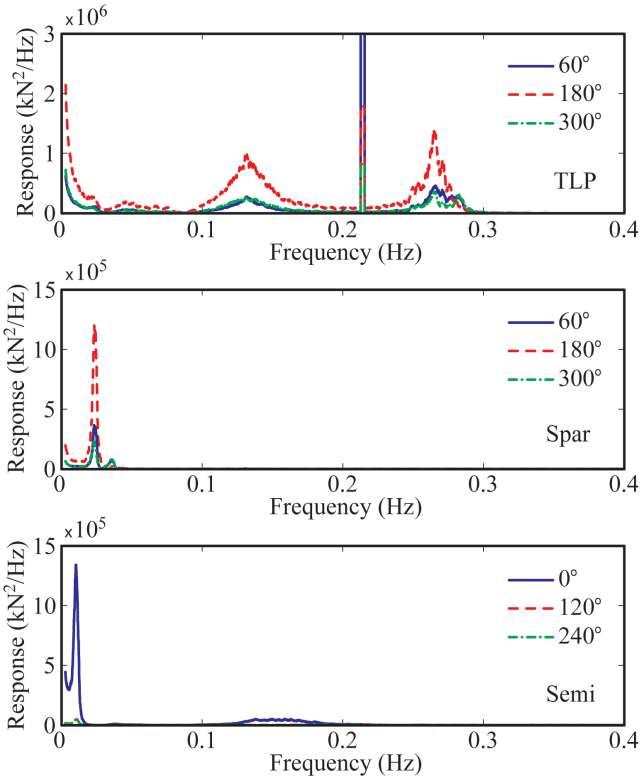

Figure 71: Fairlead mooring tension response spectra for all three systems in a combined wind and wave environment.

5 Calibration and Validation of Floating Wind Turbine Numerical Simulators Using Model Test Data

In this section, the calibration and validation of FAST models of the three floating wind turbine models is presented. First, the calibration of the wind turbine model as well as the coupled semi-submersible floating wind model is presented. Subsequently, the calibration and validation of the tension-leg platform floating wind turbine is discussed. Next, the calibration and validation of the spar-buoy floating wind turbine is reviewed. Lastly, a discussion is given presenting various improvements to FAST's hydrodynamic and mooring simulation capabilities.

5.1 Calibration and Validation of a Semi-submersible Floating Wind Turbine Model

5.1.1 Model Description

In this section, a description of the DeepCwind semi-submersible floating wind turbine is presented. Froude scaling was used to create the 1/50th-scale model, shown in Figure 72, and a variety of corresponding 1/50th-scale environmental loading conditions.

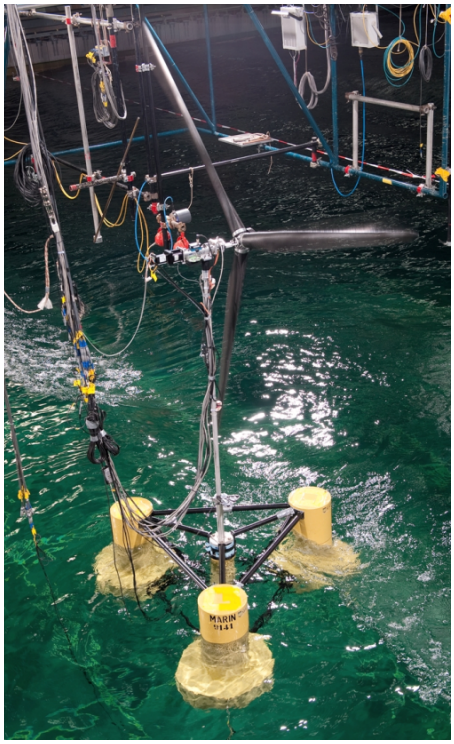

Figure 72: Image of the 1/50th-scale DeepCwind semi-submersible floating wind turbine.

Descriptions of pertinent system properties will be given for the wind turbine, tower, floating platform, and mooring system. The properties, which will include mass, elastic, aerodynamic and hydrodynamic quantities, are all presented at full-scale. It should also be noted that all test data and validation work is also presented at full-scale, as is customary for Froude-scale wave basin model testing. For more information regarding the scaling methods utilized to present the model test data at full-scale, please see the works of (Jain *et al.*, 2012) and (Martin *et al.*, 2012).

5.1.1.1 Wind Turbine

This subsection describes pertinent properties of the rotor blades, hub, nacelle, and control system. The rotor diameter and hub height dimensions are identical to the NREL 5-MW reference wind turbine at 126.0 m and 90.0 m above the still water line (SWL), respectively. However, the wind turbine tower top mass is larger than the NREL turbine by 13.47%. This resulted from physical design constraints when producing the scale model, which necessitated a significant amount of electronic and instrumentation gear to be housed inside the nacelle (Martin, 2011). After final design, accommodation of this equipment required a top-side mass of 397,160 kg, a total in excess of the desired 350,000-kg original target specification from the NREL 5-MW reference wind turbine. The gross properties of the model wind turbine are given in Table 27.

Table 27: Wind turbine gross properties

Rotor Orientation, Configuration	Upwind, 3 Blades
Rotor, Hub Diameter	126.0 m, 3.0 m
Hub Height Above SWL	90.0 m
Height of Tower-Top Flange Above SWL	87.6 m
Overhang, Shaft Tilt, Precone	10.58 m, 0°, 0°
Vertical Distance Along Tower Centerline Between Tower Top and Shaft	2.4 m
Total Tower-Top Mass	397,160 kg

Table 28: Hub and nacelle gross properties

Nacelle Mass	274,940 kg
Nacelle Center of Mass (Above Tower)	2.4 m
Nacelle Center of Mass (Downwind)	4.56 m
Nacelle Roll Inertia	284,100 kgm^2
Nacelle Pitch Inertia	22,440,000 kgm^2
Nacelle Yaw Inertia	22,440,000 kgm^2
Hub Mass	72,870 kg
Hub Inertia About Rotor Axis	Negligible (0)

In Table 28, additional details for the hub and nacelle required for generating a FAST numerical model are given. Note that the hub inertia about the rotor shaft axis is a very small contribution to the total rotor inertia and is taken to be zero. The experimentally derived rotor inertia and the total rotor inertia about the rotor axis utilized in the FAST model compare extremely well. A final detail worth noting is that the shaft tilt and blade precone are eliminated from both the physical and numerical models.

For the model tests, the rotor blades were designed to closely emulate the geometry of the NREL 5-MW reference wind turbine as is typical of a Froude-scaled model (Martin, 2011). In addition, the total mass of the blade was targeted to be roughly equal to the NREL 5-MW reference wind turbine. However, the wind turbine blades were designed to be nearly rigid to eliminate the aeroelastic complexities resulting from flexible blades. As a result, the nine degrees of freedom (DOF) associated with blade flexibility in FAST are turned off for all calibration and validation efforts in this work. The gross wind blade properties are given in Table 29 and the distributed blade mass properties employed in the analyses are given in Table 30.

Table 29: Blade gross properties

Blade Length	61.5 m
Blade Mass	16,450 kg
Location of Blade Center of Mass (Measured from Blade Root)	23.4 m
Blade First Mass Moment of Inertia	385,150 kgm
Blade Second Mass Moment of Inertia	13,940,000 kgm^2

Moving to Table 31, details concerning the wind blade aerodynamics are presented, including blade twist, chord length, and airfoil designation. It is important to note that while the information in Table 31 is nearly identical to that for the NREL 5-MW reference wind turbine, the airfoil performance of the Froude-scaled blade geometry was significantly altered. This is because Froude scaling produces aerodynamic Reynolds numbers much smaller than what would be seen in a full-scale system. As such, new airfoil lift and drag coefficients were created for the model-scale wind turbine through a calibration process that employed model test wind turbine performance data. The details of this procedure are outlined in the calibration section of this section.

Table 30: Blade-distributed mass properties

Radius (m)	Structural Twist (°)	Aerodynamic Center (-)	Mass (kg/m)
1.50	13.308	0.250	5868.9
1.95	13.308	0.250	350.1
3.40	13.308	0.228	345.9
5.54	13.308	0.199	338.7
8.63	13.308	0.173	334.5
11.78	13.308	0.125	337.8
15.88	11.480	0.125	331.2
19.97	10.162	0.125	309.7
24.07	9.011	0.125	289.8
28.16	7.795	0.125	270.8
32.26	6.544	0.125	251.4
36.35	5.361	0.125	233.3
10.45	4.188	0.125	215.7
44.54	3.125	0.125	198.1
48.64	2.319	0.125	182.0
52.73	1.526	0.125	165.8
56.20	0.863	0.125	152.3
58.91	0.370	0.125	137.3
61.61	0.106	0.125	93.4
63.00	0.000	0.125	13.2

Table 31: Blade-distributed aerodynamic properties

Node Radius (m)	Aerodynamic Twist (°)	Chord Length (m)	Airfoil Designation*
2.867	13.308	3.542	Cylinder
5.600	13.308	3.854	Cylinder
8.333	13.308	4.167	Cylinder
11.750	13.308	4.557	DU 40
15.850	11.480	4.652	DU 35
19.950	10.162	4.458	DU 35
24.050	9.011	4.249	DU 30
28.150	7.795	4.007	DU 25
32.250	6.544	3.748	DU 25
36.350	5.361	3.502	DU 21
40.450	4.188	3.256	DU 21
44.550	3.125	3.010	NACA 64-618
48.650	2.319	2.764	NACA 64-618
52.750	1.526	2.518	NACA 64-618
56.167	0.863	2.313	NACA 64-618
58.900	0.370	2.086	NACA 64-618
61.633	0.106	1.419	NACA 64-618

*DU = Delft University, NACA = National Advisory Committee for Aeronautics

Moving to the operating details of the wind turbine, the control system used for the model wind turbine was very basic compared to the variable-speed, active blade-pitch systems encountered in many existing commercial-scale wind turbines. The tested system did not use variable-speed control or active pitch control in an effort to manage the complexity of the model testing campaign. In operational test modes, the blades on the turbine were each fixed at a collective pitch of 6.4° and in parked test modes the blades were each fixed at 85°. Because of the aforementioned altered airfoil performance of the wind blades, the collective blade-pitch values utilized for operating and feathered modes differ from those employed in (Jonkman *et al*., 2007). During each test, the rotor speed was held constant, although the speed did change from test to test. Table 32 shows the various environmental and operating conditions for the model wind turbine studied in this work. Aside from a range of environments with an operating wind turbine, this work considered one extreme environment with a parked wind turbine and a mean wind speed of 30.5 m/s corresponding to a 100-year event in the Gulf of Maine (University of Maine, 2011).

Table 32: Wind turbine operating parameters

Mean Wind Speed (m/s)	Reference Height (m)	Wind Condition	Rotor Speed (RPM)	Collective Blade Pitch Angle (°)
7.32	90.0	Steady	4.95	6.4
8.94	90.0	Steady	5.66	6.4
11.23	90.0	Steady	7.78	6.4
16.11	90.0	Steady	9.19	6.4
21.80	90.0	Steady	12.73	6.4
30.50	90.0	Steady	0.0	85.0
16.98 (20.60)	10.0 (90.0)	Dynamic	12.73	6.4

5.1.1.2 Tower

The tower for the DeepCwind semi-submersible platform was designed to emulate the fundamental bending frequencies of the OC3-Hywind tower (Jonkman, 2010) when supporting the previously described wind turbine mounted atop the OC3-Hywind spar-buoy. Successful achievement of this target is demonstrated in (Martin, 2011).

The mass and stiffness properties of the tower were calculated using the tower geometry and material properties of aluminum, of which the tower is made. As can be seen in Figure 72, there was a significant bundle of instrumentation cables that runs along a majority of the tower for the physically tested model. The weight of these cables that the floating platform had to support was calculated during testing, and this additional mass was evenly distributed along the entire length of the tower for numerical modeling. The cables were assumed to add negligible bending stiffness to the tower. The gross properties of the tower are given in Table 33 and the distributed properties are found in Table 34. Note that Table 34 only provides bending stiffness and excludes tower torsional and extensional stiffnesses as these quantities are not utilized by the FAST code.

Table 33: Gross tower properties

Tower Height	77.6 m
Tower Base Elevation Above SWL	10.0 m
Tower Top Elevation Above SWL	87.6 m
Total Mass	302,240 kg
Center of Mass Above SWL	44.6 m

Table 34: Tower distributed properties

Elevation (m)	Mass (kg/m)	Fore-aft Stiffness (Nm^2)	Side-side Stiffness (Nm^2)
10.00-10.31	55,671.5	1.123×10^{12}	1.123×10^{12}
10.31-18.54	4599.0	1.123×10^{12}	1.123×10^{12}
18.54-21.56	5808.1	1.371×10^{12}	1.371×10^{12}
21.56-22.26	16,044.3	1.371×10^{12}	1.371×10^{12}
22.26-81.63	2982.9	2.485×10^{11}	2.485×10^{11}
81.63-82.87	5128.5	2.485×10^{11}	2.485×10^{11}
82.87-83.49	11,821.4	2.485×10^{11}	2.485×10^{11}
83.49-84.42	10,433.7	2.485×10^{11}	2.485×10^{11}
84.42-87.60	5710.8	1.104×10^{12}	1.104×10^{12}

In addition to distributed properties, FAST also requires the first two modes of vibration for both fore-aft and side-side bending as well as modal damping quantities. The generation of mode shapes, estimation of modal damping, and reconciliation of FAST tower response with test data will be covered in the calibration section of this work.

5.1.1.3 Floating Platform

The floating platform for this model is a semi-submersible. It is considered to be buoyancy-stabilized because rotational displacements induce large buoyant-restoring forces from the volumes of water that are displaced. Dimensioned drawings of the DeepCwind semi-submersible platform are given in Figure 73 along with the coordinate system employed in this study.

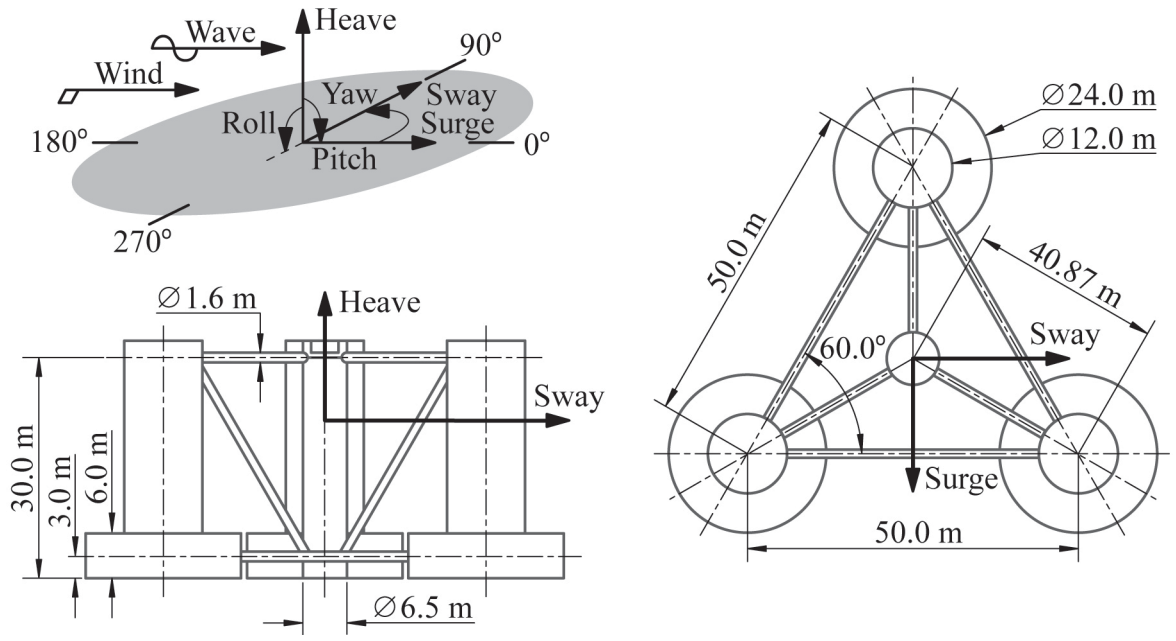

Figure 73: Coordinate system and dimensions of the DeepCwind semi-submersible platform.

The platform is made up of three offset columns with larger diameter lower bases, one center support column for the turbine, and a series of horizontal and diagonal cross bracing. The 1.6-m-diameter cross bracing consists of two sets of three pontoons connecting the outer columns with each other, two sets of three pontoons connecting the outer columns to the center column and three diagonal braces connecting the top of the outer column to the bottom of the center column. An overview of the full-scale dimensions and gross properties of the platform are given in Table 35. Concerning platform flexibility, the 1/50th-scale platform was designed to be very stiff and was assumed to be rigid for the analyses conducted in this work.

Table 35: Platform gross properties

Depth to Platform Base Below SWL (Total Draft)	20.0 m
Elevation to Platform Top (Tower Base) Above SWL	10.0 m
Platform Mass, Including Ballast	13,444,000 kg
Displacement	13,986.8 m^3
Center of Mass (CM) Location Below SWL Along Platform Centerline	14.4 m
Platform Roll Inertia About CM	8.011×10^9 kgm^2
Platform Pitch Inertia About CM	8.011×10^9 kgm^2
Platform Yaw Inertia About Platform Centerline	1.391×10^{10} kgm^2

This is consistent with the modeling approach employed in FAST.[2] A full-scale platform built with these dimensions would likely have some compliance and therefore require larger bracing components to be considered rigid. It is important to note that the model tests performed were intended to capture the global performance characteristics of a generic semi-submersible platform, not to analyze an optimal design. Certainly more efficient semi-submersible designs can be created through optimization.

Regarding hydrodynamics, FAST implements a linear, time-domain formulation in which the problem is separated into three separate problems: hydrostatics, diffraction, and radiation (Jonkman, 2007; Faltinsen,

1990, Newman, 1997). The quantities required for executing the time-domain hydrodynamic load simulation are obtained from WAMIT (Lee and Newman, 2006), a three-dimensional frequency-domain potential-flow numerical panel method. For WAMIT analysis, a higher-order representation geometric description file for the DeepCwind semi-submersible platform was created using MultiSurf (MultiSurf, 2011). In the higher-order geometric description, the velocity potential on the body surface is represented using B-splines. One geometric plane of symmetry was exploited in the analysis, and the average panel size utilized was 2.0 m. To further improve the accuracy of the WAMIT results, options were selected to integrate the logarithmic singularity analytically, solve the linear system of equations using a direct solver, and remove the effects of irregular frequencies by manually paneling the free surface. These settings were beneficial because of the requirement for high-frequency output for time-domain analysis. The semi-submersible platform was analyzed in its un-displaced position and with a water depth of 200.0 m. The origin for the analysis was taken to be the intersection of the platform centerline and waterline because this point coincides with the location of FAST platform DOF. As such, all hydrodynamic quantities in this section are referenced from this point.

With the numerical solution parameters established, the output of the WAMIT analysis is now presented and discussed. The linear hydrostatic restoring forces account for contributions due to system weight and center of gravity location, buoyancy and center of buoyancy location, and lastly, water plane stiffness. In FAST, the contribution due to weight is handled separately and the hydrostatic restoring force is characterized via a stiffness matrix, C_{ij}^{H}, which includes only buoyancy and water plane effects. The hydrostatic forces F_i^H are computed as

$$F_i^H = \rho g V_o \delta_{i3} - C_{ij}^H q_j, \quad i,j = 1,2,\ldots,6,$$

where ρ is the density of water (1025.0 kg/m^3), g is the local acceleration due to gravity (9.80665 m/s^2), V_o is the displaced volume in the undisplaced position, δ_{i3} is the Kronecker delta, q_j are the six rigid-body DOF located at the waterline and C_{ij}^H is

$$\boldsymbol{C}^H = \begin{bmatrix} 0 & 0 & 0 & 0 & 0 & 0 \\ 0 & 0 & 0 & 0 & 0 & 0 \\ 0 & 0 & 3.836\ N/m & 0 & 0 & 0 \\ 0 & 0 & 0 & -377.6\ Nm/rad & 0 & 0 \\ 0 & 0 & 0 & 0 & -377.6\ Nm/rad & 0 \\ 0 & 0 & 0 & 0 & 0 & 0 \end{bmatrix} \times 10^6.$$

The diffraction forcing, which considers the hydrodynamic loads associated with incident waves, is characterized by wave frequency- and direction-dependent first-order transfer functions, $X_i(\omega,\beta)$, where ω is the wave frequency and β is the wave direction. The complex valued $X_i(\omega,\beta)$ vector contains the platform forces and moments per unit wave amplitude and the interplay of the real and imaginary components determine the phase lag between the wave crest and the peak forces. A plot of the first-order transfer function magnitudes and phase angles for a zero degree wave heading is given in Figure 74.

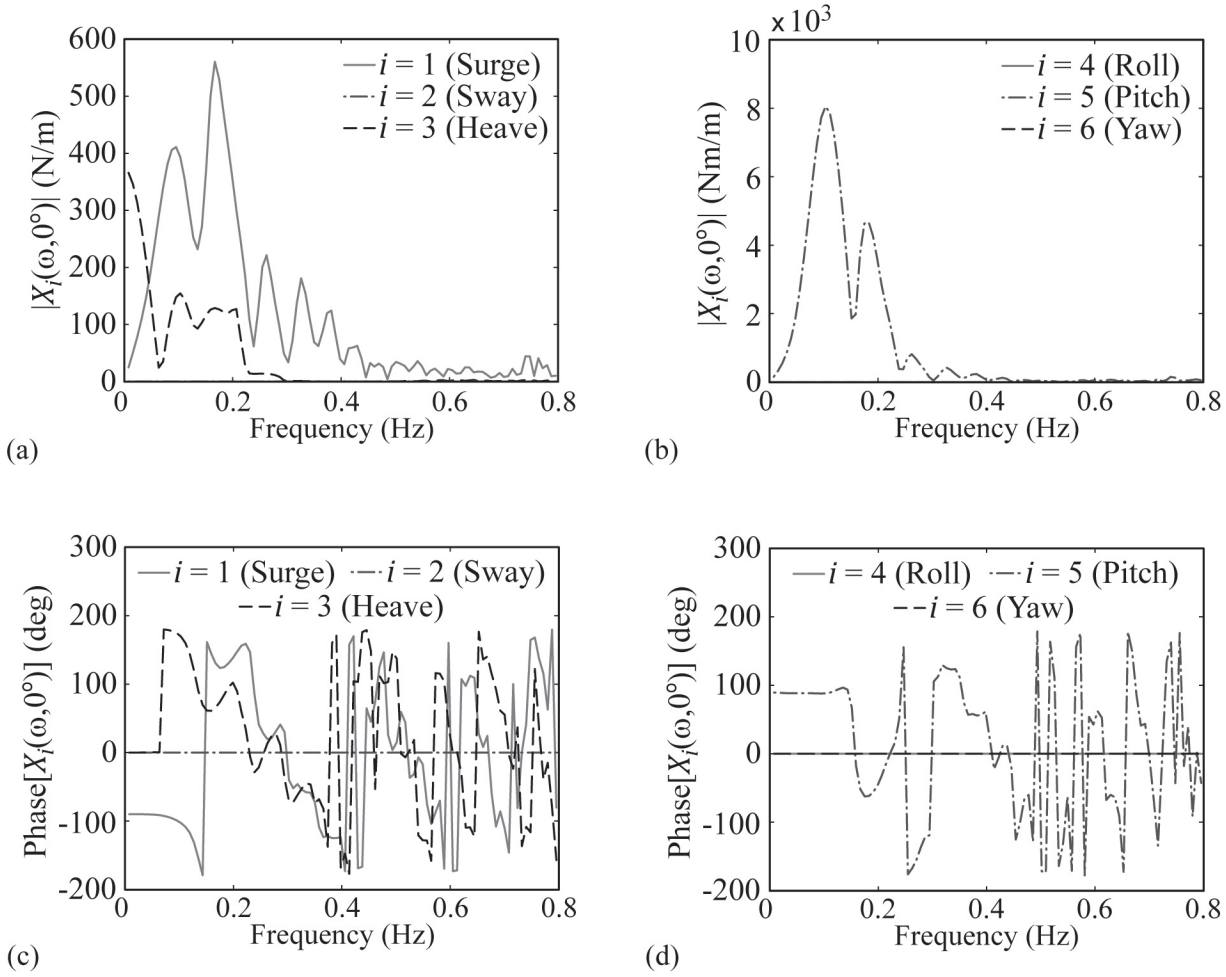

Figure 74: Plots of first-order transfer functions at a zero-degree wave heading for (a) forces and (b) moments, along with phase lag angles for forces and moments in (c) and (d), respectively, as a function of frequency.

The last hydrodynamic force considered in the linear implementation is the radiation force that accounts for platform forces associated with the oscillation of the platform. To compute forces associated with radiation in the time domain, FAST requires knowledge of the infinite-frequency, added-mass matrix, $A_{ij}(\infty)$, and the oscillation-frequency-dependent damping matrix, $B_{ij}(\omega)$ (Jonkman, 2007). The WAMIT-derived, infinite-frequency, added-mass matrix for the DeepCwind semi-submersible platform is

$$\boldsymbol{A}(\infty) = \begin{bmatrix} 6.504 & 0 & 0 & 0 & -85.44\,m & 0 \\ 0 & 6.504 & 0 & 85.44\,m & 0 & 0 \\ 0 & 0 & 14.71 & 0 & 0 & 0 \\ 0 & 85.44\,m & 0 & 7257\,m^2 & 0 & 0 \\ -85.44\,m & 0 & 0 & 0 & 7257\,m^2 & 0 \\ 0 & 0 & 0 & 0 & 0 & 4894\,m^2 \end{bmatrix} \times 10^6\ kg. \qquad (3)$$

Plots of the non-zero damping-matrix components for the DeepCwind semi-submersible platform as a function of frequency are given in Figure 75.

In addition to linear hydrodynamic forces, a quadratic drag model is implemented in this work to account for flow-separation-induced drag. FAST has the ability to compute drag forces using Morison's equation for the main column; however, the formulation does not permit inclusion of all the members of the semi-submersible platform. Therefore, the coefficients employed in this quadratic drag model are determined from experimental data to represent the additional damping present in the system. A discussion of the quadratic drag model and derivation of coefficients is presented in the subsequent calibration section.

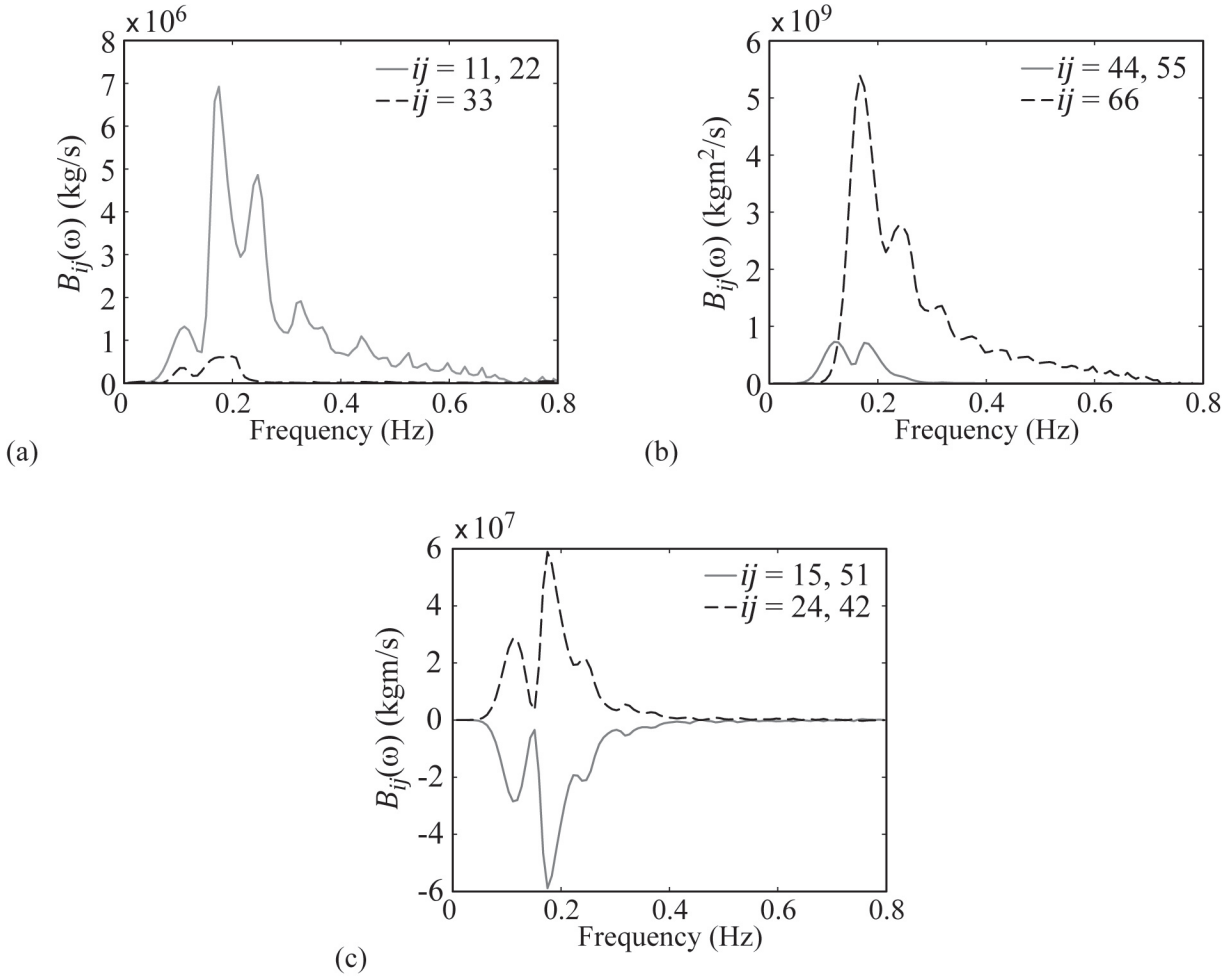

Figure 75: Plots of the nonzero entries of the damping matrix as a function of frequency for the (a) translational modes, (b) rotational modes, and (c) coupled translation-rotation modes.

5.1.1.4 Mooring System

The mooring system for the DeepCwind semi-submersible platform consists of three slack, catenary lines that provide the primary global restoring forces for motion in surge, sway, and yaw, and additional, albeit marginal, global restoring forces for heave, roll, and pitch motion. The default quasi-static mooring module from FAST is employed in this work, and the details of how the non-linear catenary equations are solved can be found in (Jonkman, 2007). The relevant information for the mooring system is found in Table 36. The three mooring lines are orientated at 60°, 180°, and 300° (lines 1, 2, and 3 respectively) about the heave axis with 0° being aligned with the surge axis. A comparison of the numerical model and the tuned physical mooring system employed for testing is covered in the calibration section.

Table 36: Mooring system properties

Number of Mooring Lines	3
Angle Between Adjacent Lines	120°
Depth to Anchors Below SWL (Water Depth)	200 m
Depth to Fairleads Below SWL	14 m
Radius to Anchors from Platform Centerline	837.6 m
Radius to Fairleads from Platform Centerline	40.868 m
Unstretched Mooring Line Length	835.5 m
Mooring Line Diameter	0.0766 m
Equivalent Mooring Line Mass Density	113.35 kg/m
Equivalent Mooring Line Mass in Water	108.63 kg/m
Equivalent Mooring Line Extensional Stiffness	753.6×10^6 N

5.1.2 Model Calibration

In this section, the calibration of various tunable aspects of the wind turbine model is presented. These tunable aspects rely on test information from simple, fundamental tests of the floating wind turbine that focus on characterizing a particular facet of system behavior. These tests, called system identification tests, are used to tune the FAST wind turbine aerodynamics, first tower-bending mode frequencies, and viscous damping parameters. The tests also verify the system restoring forces provided by the mooring system. The data employed for use in the calibration process can be found in (Koo *et al*., 2012). This step is necessary because of unknown testing parameters and some imperfections in the numerical model.

5.1.2.1 Wind Turbine Performance

During model testing, the low wind speeds of the Froude-scale environment created Reynolds numbers that were nearly three orders of magnitude lower than full-scale. This resulted in altered airfoil lift and drag performance with overall lower thrust loads and power production relative to the full-scale NREL 5-MW reference wind turbine for a given wind speed. Because thrust loading is the major aerodynamic driver for global motion of the system, higher wind speeds were selected for testing, which yielded proper, Froude-scale rotor thrust values. The details of the wind turbine performance deficiency and accompanying adjustments are discussed in (Martin *et al*., 2012).

For completeness, it is noted that a high-quality wind environment was generated in MARIN's offshore basin using a suspended rectangular rack with 35 fans, a series of screens, and an elliptically shaped nozzle. The nozzle outlet used was 200 m wide and 150 m tall (full scale), this being larger than the rotor swept area. Turbulence intensity at the hub location was measured to be 4% and modestly higher at the boundaries of the outlet nozzle. Swirl in the flow field was less than 1% of the free stream velocity. A more thorough description of the wind generation machine can be found in (Goupee *et al*., 2012 OTC).

For numerical modeling in FAST, the altered performance of the wind turbine necessitated a new aerodynamic model because the one associated with the standard NREL 5-MW reference wind turbine was no longer applicable. To begin the process, new coefficients of lift and drag for the airfoils of Table 31 at various angles of attack were generated by building a model of the airfoils in XFOIL, a high-order, viscous-analysis panel code (Drela 1989). The resulting lift and drag curves were then processed using NREL's AirfoilPrep tool (Hansen, 2012) to expand the data over the entire 360° range of possible angles of attack required by FAST. This produced simulation results that correlated poorly to model test data because of the questionable applicability of XFOIL solutions for the separated flows experienced in the

tested model wind turbine. Hence, the XFOIL lift and drag curves for the airfoils were parameterized and tuned using multi-objective genetic algorithm optimization techniques (e.g. see (Deb, 2001)) to simultaneously minimize the error between FAST simulations and test data curves for the wind turbine thrust and power as a function of rotor speed under a steady hub height wind speed of 21.80 m/s. Options utilized in FAST for the optimization included disabled dynamic stall, elimination of the pitching moment model, selection of the swirl equilibrium inflow model, and selection of the Prandtl tip- and hub-loss models.[1] The air density was taken to be 1.225 kg/m^3. The wind profile generated in the wind/wave basin used a simple wind file, which contained one hub-height wind speed for steady winds and a time-series of varying wind speeds for dynamic winds studied later in this work. To best represent this wind profile, the measured hub height wind speed was multiplied by a factor of 0.952 and a vertical power law wind shear exponent of 0.0912 was employed. These parameters yielded the best comparison between measured hub-height wind speeds and information gleaned from spatial surveys of the wind generation machine output used for testing. Details of the wind machine surveys can be found in (Goupee *et al*., 2012 OTC) and (Koo *et al*., 2012. Regarding parameterization of the airfoil coefficients, variables were introduced that permitted perturbations of lift curve slope and zero-lift angle of attack, as well as more moderate alterations of the lift curve stall point, lift curve post-stall behavior, and general nature of the drag coefficients. Because the multi-objective optimization generated several pareto-optimal solutions, a solution was chosen for use in the numerical model that exhibited nearly identical thrust behavior to the test model and a reasonably fair prediction of wind turbine power. This bias towards more accurately capturing the thrust response is due to the aforementioned fact that wind turbine thrust is the aerodynamic driver in global motion and load response.

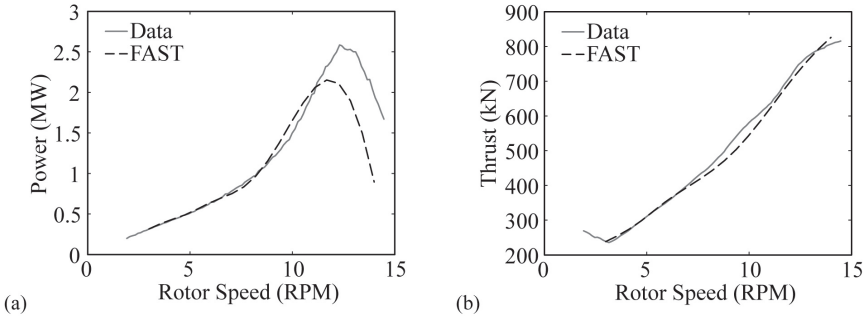

Figure 76: Comparison of calibrated FAST and tested wind turbine performance as a function of rotor speed for (a) rotor power and (b) thrust under steady 21.80-m/s winds.

Table 37: Comparison of calibrated FAST model and tested wind turbine thrust

Mean Wind Speed (m/s)	Rotor Speed (RPM)	Tested Thrust (kN)	FAST Thrust (kN)
7.32	4.95	126.1	102.6
8.94	5.66	156.9	143.4
11.23	7.78	202.7	247.2
16.11	9.19	381.7	413.0
21.80	12.73	749.8	779.3
30.50	0	156.8	153.2

A comparison of the calibrated FAST and model test wind turbine performance is given in Figure 76. In addition, Table 37 shows the thrust values corresponding to the steady wind cases of Table 32. As can be seen in Figure 76 and Table 37, the thrust behavior that is critical for properly simulating global response

is captured very well by the calibrated FAST wind turbine model. In addition, the range of thrust values captured during testing is very similar to the true NREL 5-MW reference wind turbine with peak thrust loads in the neighborhood of 800 kN, as shown in Table 37. It should be noted that the peak thrust load occurs at a different wind speed for model-scale compared to an ideal full-scale wind turbine because of the inherently low Reynolds numbers seen at model-scale. The aerodynamic lift (C_L) and drag (C_D) coefficients corresponding to the calibrated wind turbine model for the airfoil sections noted in Table 31 are given in Figure 77. For the Cylinder section, the lift coefficient was set to 0.0 and the drag coefficient to 1.0 for all angles of attack.

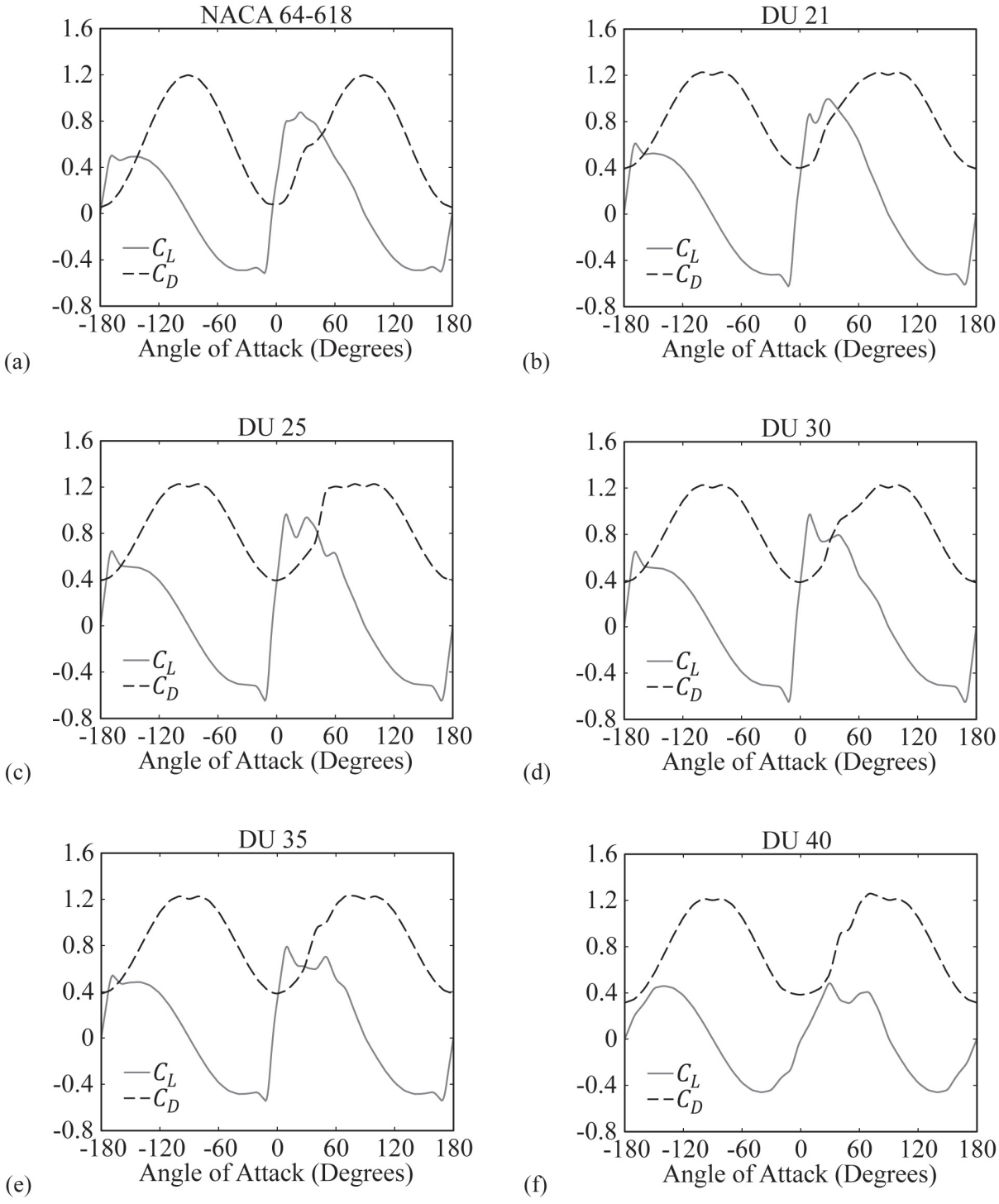

Figure 77: Plots of airfoil lift and drag coefficients at low Reynolds number for (a) NACA 64-618, (b) DU 21, (c) DU 25, (d) DU 30, (e) DU 35 and (f) DU 40 airfoils for the tuned FAST aerodynamic model.

5.1.2.2 Tower Mode Shapes and Frequencies

To model tower flexibility, FAST's modal representation requires the first two elastic bending mode shapes for both the fore-aft and side-side tower-bending DOF. Factors that influence the tower vibration mode shapes include distributed tower mass and stiffness properties, tower-top mass properties, gravity, floating foundation mass, added-mass, hydrostatic stiffness, and mooring stiffness properties.

To estimate these mode shapes, a simple custom finite-element tool was developed that employed three-dimensional Euler-Bernoulli beam elements (e.g., see (Cook *et* al., 2002)) to discretize the tower. After inputting the aforementioned distributed tower, turbine mass, platform mass, and stiffness properties, the finite-element system mass and stiffness matrices were constructed and the eigenvalue problem was solved using standard techniques. The appropriate first and second bending mode shapes for the fore-aft and side-side tower-bending DOF were extracted, and normalized ninth-order mode shapes were constructed for input into FAST. The mode shapes are plotted in Figure 78. The higher-order polynomials were employed because the standard sixth- order polynomials do not accurately capture the finite-element-estimated mode shapes resulting from the multiple discontinuities in the distributed tower properties.

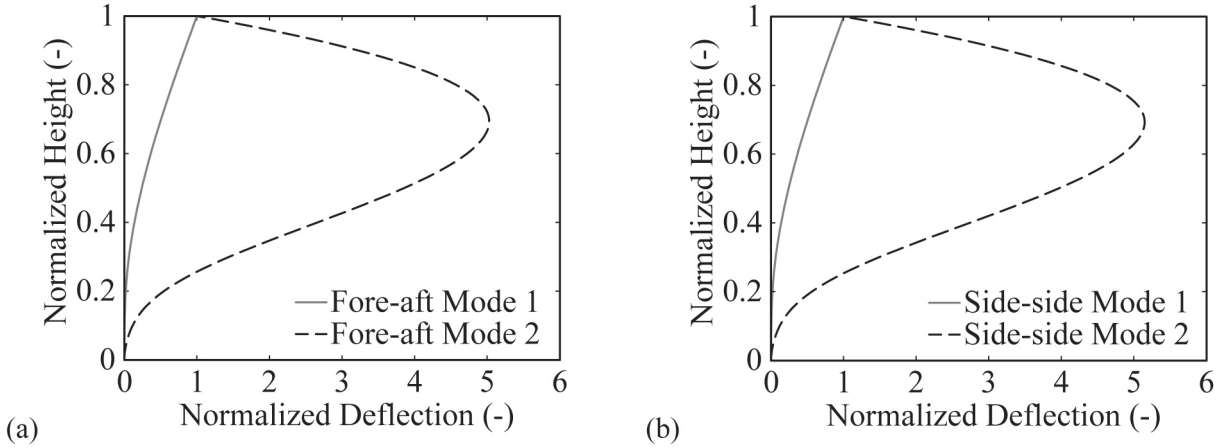

Figure 78: Plots of the FAST normalized ninth-order tower mode shapes for (a) fore-aft and (b) side-side bending DOF.

Upon inserting the mode shapes into the FAST model and running a linearization analysis to determine the tower-bending frequencies (Jonkman and Buhl, 2005), it was found that the finite element and FAST tower frequencies were in relative agreement. However, the FAST fundamental tower-bending frequencies were approximately 10% higher than measured from hammer tests conducted on the DeepCwind semi-submersible. While it is unknown why the discrepancy occurred, it could be due to, for example, a greater compliance between the tower base and floating platform connection for the DeepCwind semi-submersible. Another possibility is that the DeepCwind semi-submersible was the last specimen tested and that the base, mid-tower, and top joints on the tower could have relaxed or loosened slightly after weeks of double-shift, repeated testing. In any event, the tower stiffness properties of Table 34 were reduced by 21.0% to better match the test data. The individual fore-aft and side-side fundamental tower-bending natural frequencies were fine tuned to match test data by adjusting FAST's modal stiffness tuners. The final stiffness tuner values used in fore-aft and side-side DOFs were 0.905 and 1.049, respectively. After final calibration of the tower stiffness, the FAST fore-aft and side-side tower-bending frequencies match experimental measurements and are 0.35 Hz and 0.38 Hz respectively.

In addition to mode shapes, FAST also requires damping ratios for each of the tower bending modes. The damping ratios of the tower-bending modes were estimated using the half-power bandwidth method (e.g., see (Bendat and Piersol, 1980)) in conjunction with acceleration records from hammer tests. A value of 2.1% was determined for first mode fore-aft and side-side structural damping, and a value of 1.5% was determined for second mode fore-aft and side-side structural damping.

5.1.2.3 Hydrodynamic Viscous Damping

For the DeepCwind semi-submersible platform, flow-separation-induced drag is a large component of the total hydrodynamic damping. As such, the linear time-domain radiation damping included in FAST was augmented with a quadratic damping model that captures the effects of this viscous damping. The platform viscous damping forces and moments, F_i^v, are computed as

$$F_i^v = -B_{ij}^v \dot{q}_j \left|\dot{q}_j\right|, \quad i,j = 1,2,\ldots,6,$$

where B_{ij}^v are the quadratic damping coefficients, q_j are the six rigid-body DOF located at the waterline, and a superimposed dot indicates the first time derivative. This model assumes no directional coupling of drag terms, so only diagonal terms of B_{ij}^v are nonzero.

The coefficients B_{ij}^v were determined using the rigid-body motion free-decay tests conducted in the wind/wave basin. Simulation free-decay results for each of the six platform degrees of freedom were tuned by varying B_{ij}^v for each DOF until fair agreement existed between FAST and the test data. The free-decay test data was also employed to estimate the additional global surge stiffness provided by the cable bundle shown in Figure 72. The computed additional surge stiffness is 7.39 kN/m and was employed in all subsequent numerical experiments. The derived global drag coefficients are given in Table 38. A comparison of the FAST predictions and test data for free-decay damping ratio response is given in Figure 79 for platform surge, heave, and pitch DOF. The free-decay damping ratios are presented as the damping ratio over one cycle as a function of initial cycle amplitude. As can be seen in the figure, the overall nonlinear hydrodynamic damping behavior is captured very well for small to moderate amplitude oscillations. For large amplitudes, the quadratic damping model employed here over-predicts heave and pitch damping and under-predicts surge damping.

Table 38: Platform quadratic drag coefficients.

DOF	Global Quadratic Coefficient
Surge	1.25×10^{6} Ns^2/m^2
Sway	0.95×10^{6} Ns^2/m^2
Heave	3.88×10^{6} Ns^2/m^2
Roll	3.35×10^{10} Nms^2/rad^2
Pitch	3.35×10^{10} Nms^2/rad^2
Yaw	1.15×10^{10} Nms^2/rad^2

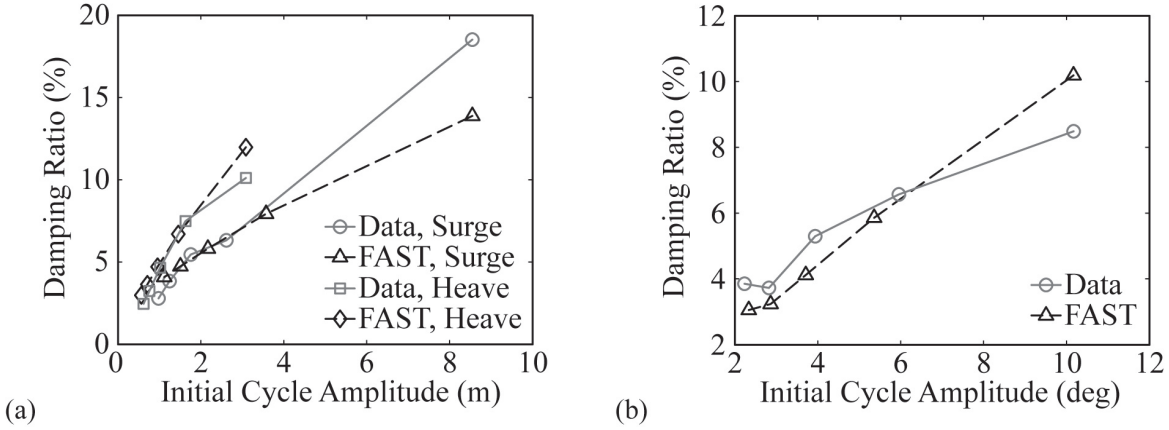

Figure 79: Comparisons for FAST prediction and test data free-decay damping ratios for (a) surge and heave as well as (b) pitch DOF.

5.1.2.3 Mooring Restoring Forces

Unlike the previously discussed quantities in this calibration section, the mooring system parameters were not tuned in order to reconcile differences in system restoring forces between FAST and the test data. In fact, the mooring module in FAST was utilized to set the target global restoring forces for the model test, and the physical model was tuned to reach these targets. The physical mooring system that was tested, which was full length and not truncated, utilized chain that yielded the correct mooring line wet weight with carefully selected springs placed at the anchors to capture the appropriate extensional stiffness of the mooring line. A comparison of mooring restoring in surge and sway DOF for both FAST simulations and test results are given in Figure 80. As can be seen in the figure, there is excellent agreement between the simulation and test data. There is further evidence that the numerical model mooring system stiffness is correct; in addition to hydrostatic stiffness, system mass, and added-mass, a comparison of FAST simulation and tested rigid-body motion natural periods is given in Table 39. As the table shows, the agreement between the simulation and test data is excellent.

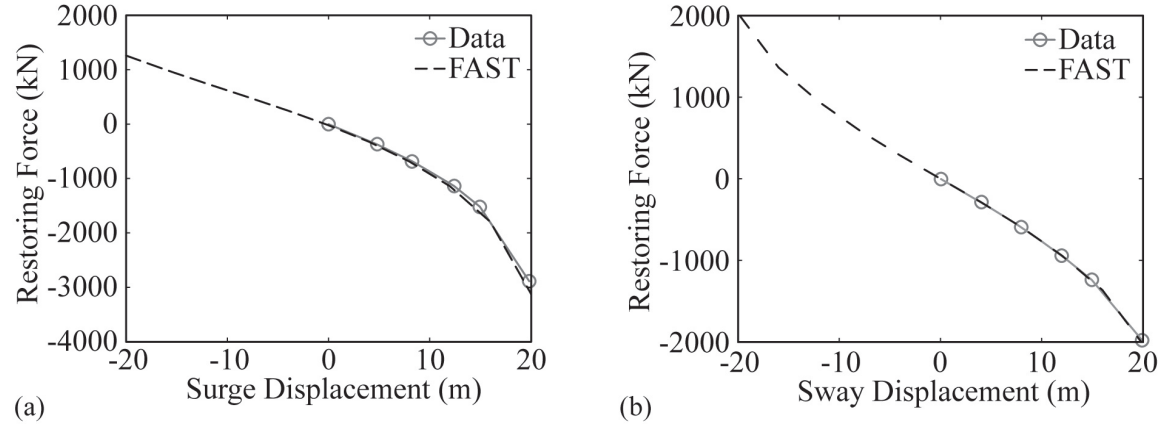

Figure 80: Comparisons for FAST prediction and test data for (a) surge mooring restoring force and (b) sway mooring restoring force.

Table 39: Comparison of FAST prediction and test data for the six rigid-body motion natural periods.

DOF	FAST (s)	Data (s)
Surge	107	107
Sway	113	112
Heave	17.3	17.5
Roll	26.7	26.9
Pitch	26.8	26.8
Yaw	82.7	82.3

5.1.3 Model Validation

In this section, the output of the calibrated FAST model from Section II will be compared to wind/wave basin model test data for the DeepCwind semi-submersible. Cases that are considered include steady wind only, dynamic wind only, free-decay under steady wind, regular waves only, irregular white noise waves only, and lastly, combined dynamic wind and irregular wave conditions. This systematic approach allows for an easier identification of root causes for discrepancies between test data and FAST simulations. This noted, the results highlight the many merits of FAST's predictive capabilities in addition to potential shortcomings in the test data, as well as possible areas of improvement for FAST. Lastly, it should be noted that all the relevant global motion results presented in subsequent sections are given with respect to the center of gravity of the total system. The FAST global motions results are initially obtained at the waterline and have been transformed accordingly.

5.1.3.1 Steady Wind Only

Simulations of the DeepCwind semi-submersible platform subjected to the six steady wind environments noted in Table 32 were conducted and compared to model test data. All winds were directed along the positive surge direction. As was done in the calibration portion for tuning wind turbine aerodynamics, the steady wind files required for simulation were produced by multiplying the mean hub height wind speed of Table 32 by 0.952 and using a wind shear coefficient of 0.0912. The metric targeted for comparison between simulation and test data was the steady-state solution. While the model test cases were run for one hour, the FAST simulations results were terminated at 2000 seconds because any significant transient global motions had diminished well in advance of this time.

For these particular loading scenarios, responses associated with surge and pitch motion receive the most excitation. As such, the mean platform surge and pitch angle are presented in Figure 81, as are the tower base fore-aft bending moment and mooring line 2 fairlead tension. As can be seen in the figure, the comparison between the simulation and test data is quite favorable. One obvious trend shown in the figure is that FAST appears to under-predict the mean surge offset with the largest discrepancies, from a percentage point of view, occurring at low operational winds and at the highest wind speed where the blades are feathered and the rotor is parked. For these aforementioned conditions, the thrust load on the rotor is low and aerodynamic drag loads on the tower, floating platform, and instrumentation cable bundle, which are not included in this FAST model, may be contributing a substantial portion to the total overall system surge force. Because the comparison between FAST and the test data is quite good with regard to tower-base fore-aft bending moment, it is likely that the largest contribution is additional aerodynamic drag on the platform.

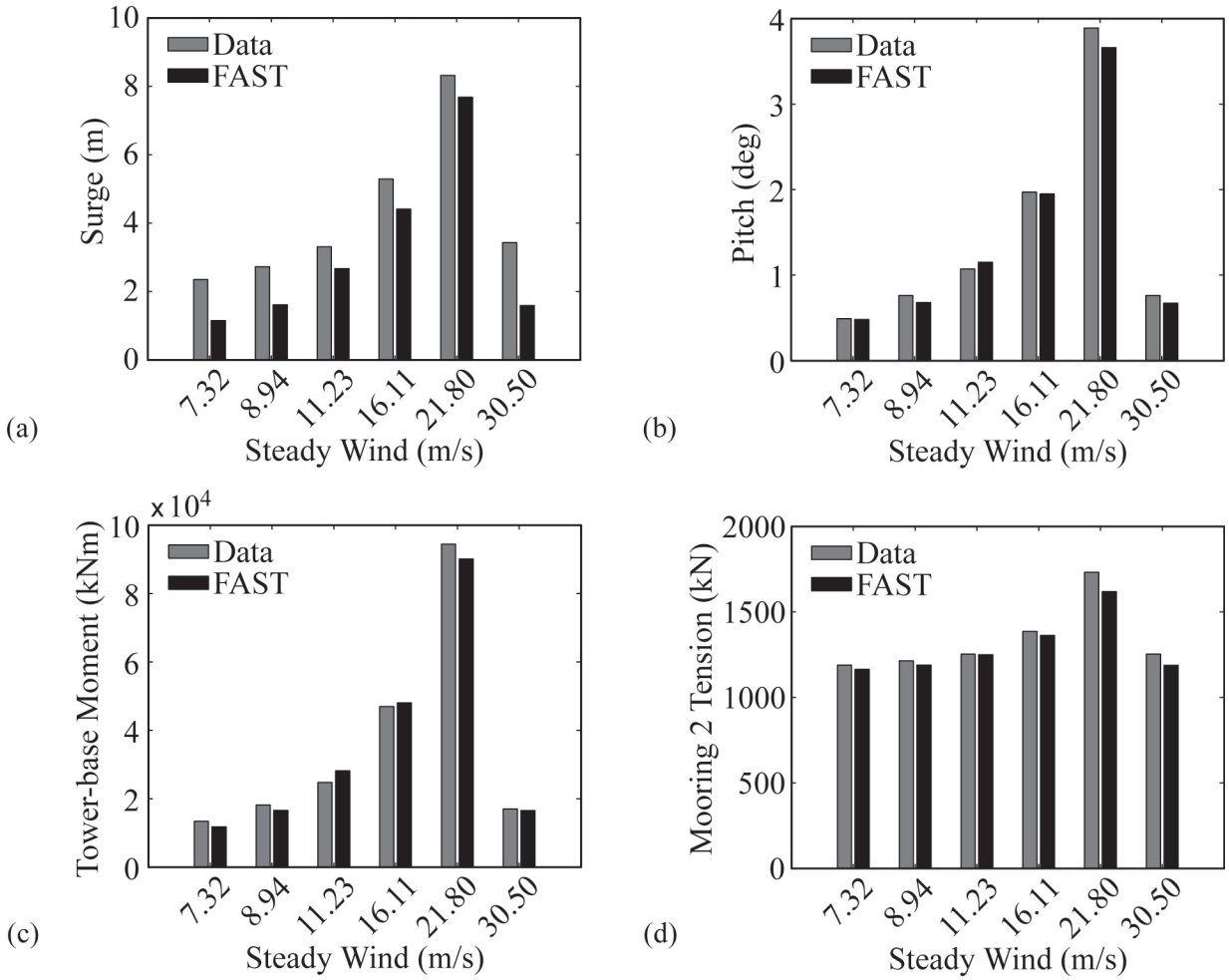

Figure 81: Comparison of simulation and test data steady-state response under steady winds for (a) surge, (b) pitch, (c) tower-base fore-aft bending moment and (d) mooring line 2 fairlead tension.

In addition, this situation is exacerbated by the fact that the low rotor thrust coefficient, resulting from poor airfoil performance (Martin *et* al., 2012) at the low test Reynolds numbers, required higher wind speeds to produce an equivalent full-scale rotor thrust, thus creating greater drag on non-rotor structures (e.g., the platform) than would be seen in a true full-scale system. Lastly, the surge-restoring stiffness is in general quite low, yielding significant discrepancies in surge position despite only small differences in total system surge loading. As an example, even in the 30.5-m/s case where the worst discrepancy occurs, the 1.84-m difference in predicted surge position is caused by a relatively small 140-kN difference in overall system surge loading. Unlike the total system surge loading, the system overturning moment leading to pitch and tower bending moment response is dominated by the rotor, because it is higher above the SWL than the center of pressure for the tower, cable bundle, or platform. The FAST rotor thrust is fairly well predicted as a result of the calibration shown in Figure 76, so it stands to reason that the simulation and test data pitch responses are very similar in Figure 81. In addition, while the agreement for mean pitch offset is good, there is an under-prediction by FAST that is consistent with the simulation, ignoring the aforementioned, additional aerodynamic drag loads.

5.1.3.2 Steady Wind Free-decay

As the second phase of model validation, the ability of FAST to capture the wind turbine rotor's aerodynamic damping forces is assessed. This was evaluated by simulating free-decay while the wind turbine was operating in a steady wind, with no waves, and comparing the motion response between FAST simulations and test data. The surge and pitch platform DOF, which are most affected by aerodynamic forces on the wind turbine, are the focus of this section.

For the two free-decay scenarios investigated, the wind turbine was subjected to the third smallest steady wind from Table 32. Consistent with the treatment of the wind in previous simulations, the steady wind file was generated by multiplying the experimentally measured 11.23-m/s wind by 0.952 and utilizing a 0.0912 wind shear exponent. Recall that this was done to best replicate the experimental wind velocity distribution using only a single, steady wind file. A comparison of the simulation and test data surge and pitch motion damping ratios as a function of initial cycle amplitude is given in Figure 82 for the no-wind and 11.23-m/s wind cases.

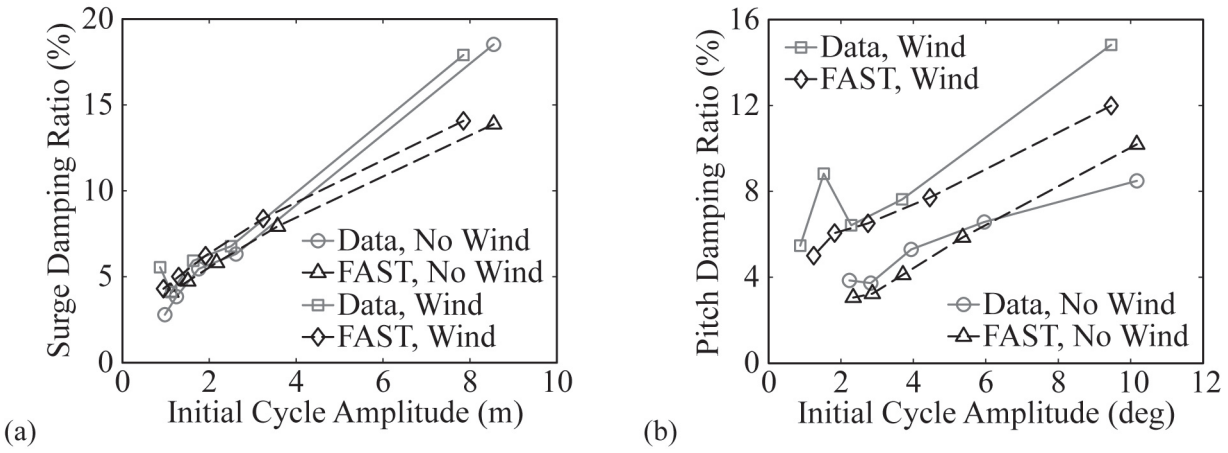

Figure 82: Comparison of simulation and test data damping ratios for (a) surge and (b) pitch motion for no wind and 11.23-m/s steady wind cases.

For both surge and pitch free-decay, regardless of the wind condition, the comparison between FAST and the test data is quite good overall, especially for small to moderate motion amplitudes. More importantly, FAST accurately captures the additional motion damping, approximately 1% in surge and 3% in pitch for this scenario, provided by the operating wind turbine in steady winds.

5.1.3.3 Dynamic Wind Only

To complete the wind only comparisons, the response of the DeepCwind semi-submersible subjected to a strong, dynamic wind in the absence of waves was simulated and compared to experimental data. The wind field, which was temporally dynamic, followed a National Petroleum Directorate (NPD) spectrum (API, 200) and was oriented along the positive surge direction. In the wind/wave basin, the temporally dynamic NPD wind possessed a mean wind speed at hub height of 20.6 m/s, a standard deviation of 2.04 m/s, a maximum wind speed of 28.7 m/s, and a minimum wind speed of 12.9 m/s. A power spectral density (PSD) plot of the wind time-series, which was three hours in length, is given in Figure 83.

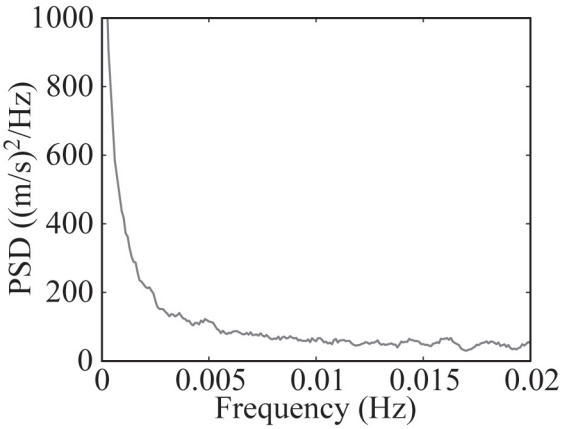

Figure 83: PSD plot for NPD wind spectrum with mean wind speed of 20.6 m/s at 90 m above SWL.

For simulation, a dynamic wind file was created in the usual manner by multiplying the recorded hub height wind velocity time history by 0.952 and utilizing a wind shear exponent of 0.0912 to better represent the measured spatial distribution of wind generated during testing. This yielded winds for simulation with a mean of 19.6 m/s, a standard deviation of 1.94 m/s, a maximum of 27.4 m/s, and a minimum of 12.3 m/s at the hub-height location (90 m above SWL).

A comparison of the FAST predictions and experimental data for platform pitch and mooring line 2 fairlead tension is given in Figure 84 and Figure 85. Figure 84 provides comparisons via PSDs, while Figure 85 displays sample time-series comparisons. As can be seen in Figure 84, the PSD comparison is fair for platform pitch with similar total energy; however, the FAST response is more peaked at the platform natural pitch frequency (0.037 Hz) with less response at frequencies immediately above this particular point. Despite this difference in platform-pitch PSD response, Figure 85 shows good agreement between the FAST simulation and test data time-series consistent with the steady state offset findings in Figure 81.

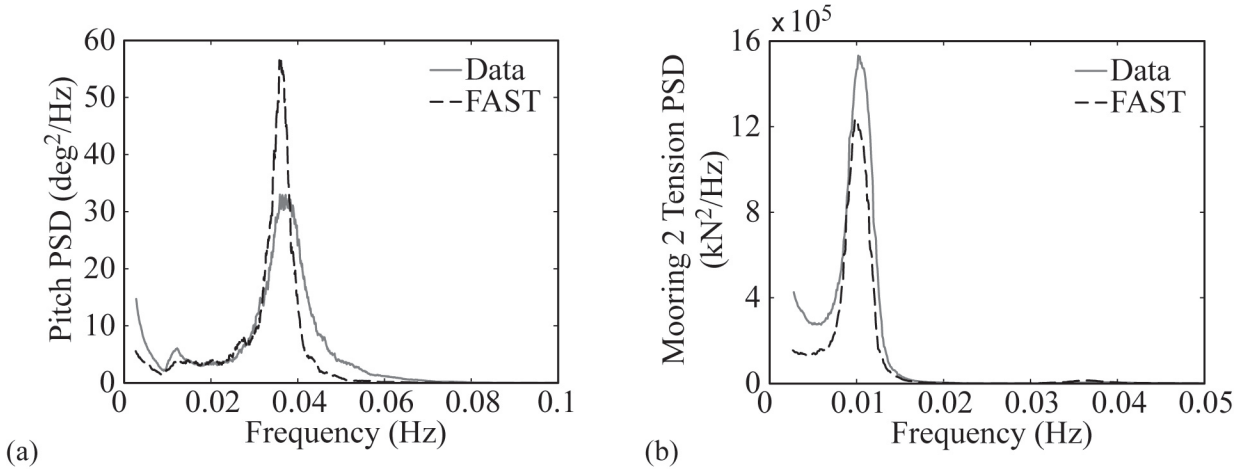

Figure 84: Comparisons of PSDs from FAST and test data for (a) pitch and (b) mooring line 2 fairlead tension for a dynamic wind-only case with a mean hub-height wind speed of 20.6 m/s.

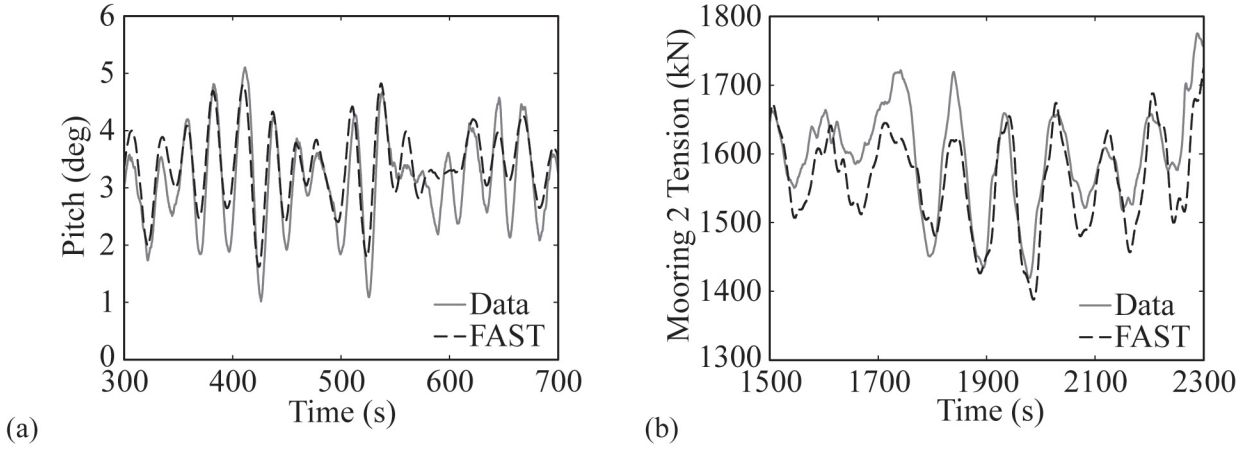

Figure 85: Comparisons of time-series from FAST and test data for (a) pitch and (b) mooring line 2 fairlead tension for a dynamic wind-only case with a mean hub-height wind speed of 20.6 m/s.

Regarding the mooring line 2 fairlead tension, the PSD and time-series comparisons given in Figure 84 and Figure 85, respectively, are also quite favorable. While there was good agreement, FAST generally produces slightly less response for both the PSD and time-series.

In addition to sample PSD and time-series, Table 40 provides statistical comparisons of the FAST simulation and test data for field variables that experience significant excitation for this dynamic wind-only condition. After a review of Table 40, it is clear that the surge, pitch, tower-base bending moment and mooring line 2 fairlead tension statistics are in very good agreement between FAST and the test data. Of all the comparisons provided, the largest difference is for the platform surge with FAST predicting the maximum value to be 8.54% smaller than the true value. However, the mean platform surge is accurately predicted.

Table 40: Comparison of FAST prediction and test data statistics for a dynamic wind-only case with a mean hub height wind speed of 20.6 m/s

DOF	Source	Mean	Std. Dev.	Maximum	Minimum
Surge (m)	FAST	7.22	0.93	9.96	4.07
	Data	7.26	1.18	10.89	3.64
Pitch (deg)	FAST	3.43	0.69	5.45	0.97
	Data	3.34	0.67	5.65	1.04
Fore-Aft Bending (kNm)	FAST	8.45×10^4	1.12×10^4	12.21×10^4	3.66×10^4
	Data	8.09×10^4	1.17×10^4	11.84×10^4	4.03×10^4
Fairlead 2 Tension (kN)	FAST	1.58×10^3	0.075×10^3	1.83×10^3	1.35×10^3
	Data	1.64×10^3	0.094×10^3	1.96×10^3	1.36×10^3

5.1.3.4 Regular Waves Only

To begin the validation of FAST to test data due to wave excitation, the response of the DeepCwind semi-submersible platform to regular waves in the absence of wind was investigated. Since there was no wind, the blades were feathered and the rotor was parked. Seven different regular waves were considered, the amplitudes and periods of which are given in Table 41. All waves propagated in the positive surge direction.

Table 41: Regular wave amplitudes and natural periods

Amplitude (m)	Period (s)
0.96	7.5
3.79	12.1
3.57	14.3
3.79	20.0
5.15	12.1
5.37	14.3
5.56	20.0

It should be noted that two distinct amplitudes were investigated for periods of 12.1, 14.3, and 20.0 seconds for the purpose of assessing any nonlinearity in system response. The DeepCwind semi-submersible platform performance in the presence of regular waves is characterized by response amplitude operators (RAO) magnitudes, which normalize the amplitude of a periodic response of a field variable by the amplitude of the regular wave. In both the time-domain simulation and model test, the RAO values were computed from the nearly harmonic, steady-state response. For FAST, simulations were run for 1600 seconds to achieve the desired steady-state result.

The RAO magnitudes for surge, heave, pitch, tower-base fore-aft bending moment, and fairlead tension for mooring lines 1 and 2 are given in Figure 86 for the seven regular waves investigated. Many of the comparisons in Figure 86 are quite good, as evidenced by FAST's ability to capture the increase in normalized pitch response for a given wave period with increasing wave amplitude. However, there are some notable discrepancies between the FAST simulation and test data. First, the FAST simulation modestly under-predicts the heave RAO for the two 20.0-s cases investigated. Because this period is in close proximity to the DeepCwind semi-submersible's heave natural period (causing some resonance), the normalized response will be sensitive to system damping. The discrepancy is likely a result of the quadratic damping model employed in this study, which over-predicts the damping in large amplitude heave scenarios at the expense of properly modeling the damping for small to moderate motions. The second discrepancy, which is very significant, is the mooring line fairlead tensions, especially for mooring line 2, which is aligned with the wave propagation direction. For the worst scenario, the 5.56-m amplitude, 20.0-s regular wave, the FAST mooring line 2 fairlead tension RAO is only 13.4% of the test data value. It is suspected that this is caused by the exclusion of dynamic mooring line effects in the simulation, because FAST employs a quasi-static mooring solver. Further investigation would be required to confirm this hypothesis.

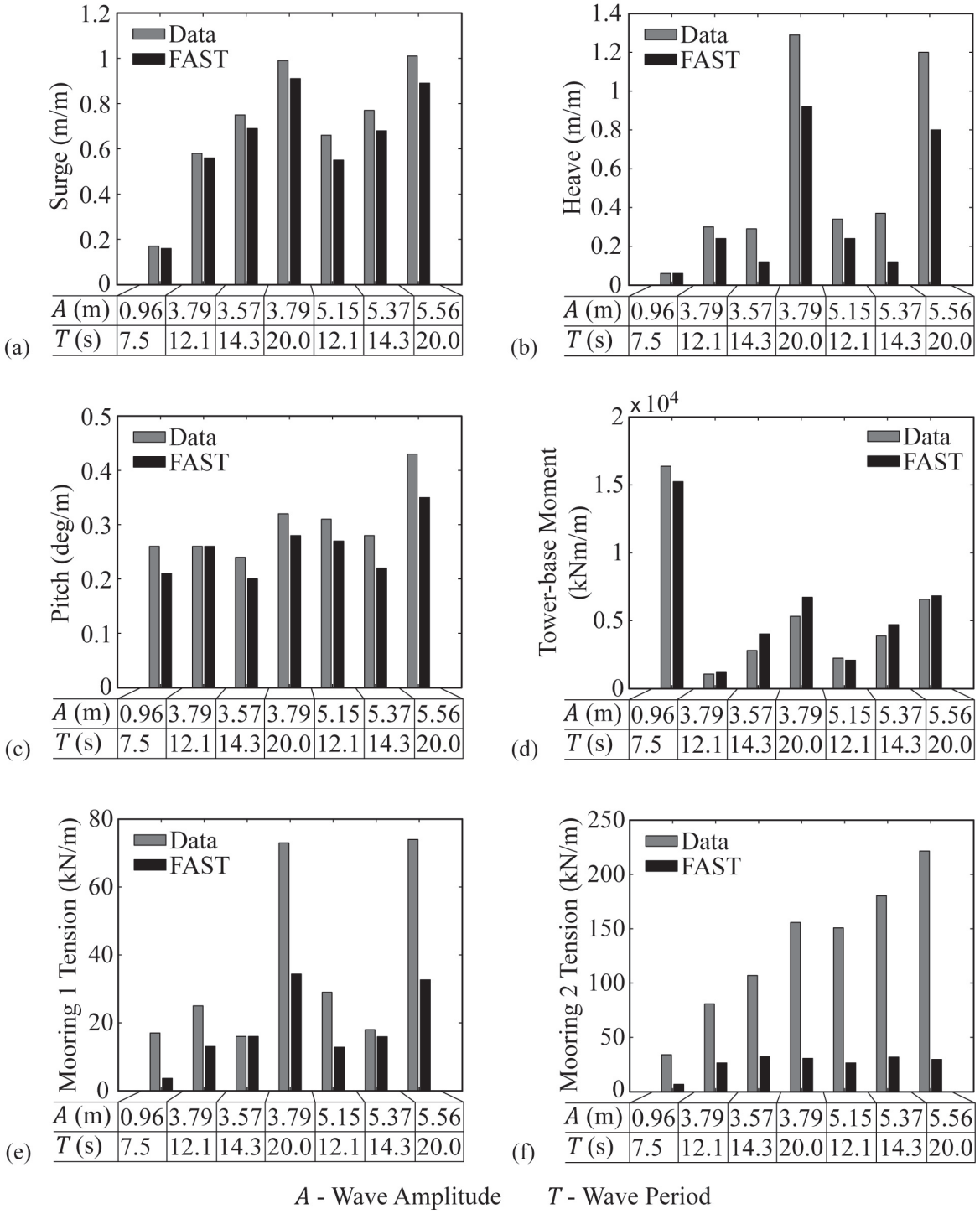

Figure 86: Comparisons of RAOs from FAST and test data for (a) surge, (b) heave, (c) pitch, (d) tower base fore-aft bending moment, (e) mooring line 1 fairlead tension and (f) mooring line 2 fairlead tension.

5.1.3.5 Irregular Waves Only

To continue the validation study, the behavior of the DeepCwind semi-submersible platform subjected to a severe irregular wave in the absence of wind was simulated with the calibrated FAST model, and the simulation results were compared to test data. There was no wind, so the blades were feathered and the rotor was parked. The wave that was investigated possessed a broad-band, white noise spectrum, shown in Figure 87, with a significant wave height of 11.3 m.

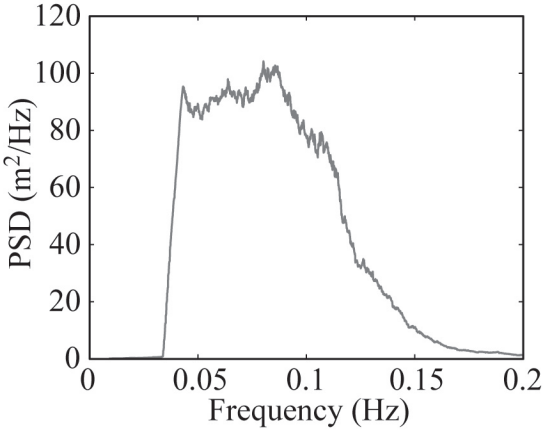

Figure 87: PSD for 11.3 m significant wave height white noise wave.

This significant wave height is in excess of that corresponding to a 100-year event in the Gulf of Maine (University of Maine, 2011). The wave propagated along the positive surge direction. For the 3-hr wave, the maximum crest was 12.8 m, the minimum trough was -11.0 m, and the maximum wave height was 21.5 m. The broad-band spectrum utilized here is advantageous for computing RAOs as well as for amplifying, and thus highlighting, the floating wind turbine's response to second-order wave diffraction forces (e.g., see (Kim and Yue, 1991)). To make the comparison between FAST and the model test data a fair one, a modified version of FAST was employed that could compute the linear wave diffraction forces directly from the tested wave-elevation time-series.

The first results shown are the FAST simulation and test data RAO magnitude and phase angles for the surge, heave, and pitch DOF in the wave energy range (5 to 25 seconds). The plots, given in Figure 88, show that the motion RAO magnitudes are for the most part quite good. The same cannot be said, however, of the phase angles in general. This could be a result of the wave measurement, which was located at the un-displaced position, not coinciding with the true position of the platform as a result of mean drift forces. Regarding the RAO magnitudes, the worst discrepancy between FAST and the test data occurs in the heave DOF for periods near the resonant system heave period of 17.5 seconds, with FAST modestly under-predicting the heave response. This observation is consistent with those made for the regular waves investigated.

To further assess FAST's hydrodynamics abilities, PSD comparisons are presented in Figure 89 for surge, heave, tower-base fore-aft bending moment, and mooring line 2 fairlead tension. Referring to the surge comparison in Figure 89, it is clear that FAST accurately captures the response in the wave energy range (0.04 to 0.15 Hz); however, the prediction of the second-order difference-frequency associated response at the surge natural period of 0.0093 Hz is very poor. This is understandable because FAST neglects this aspect of the wave loading.

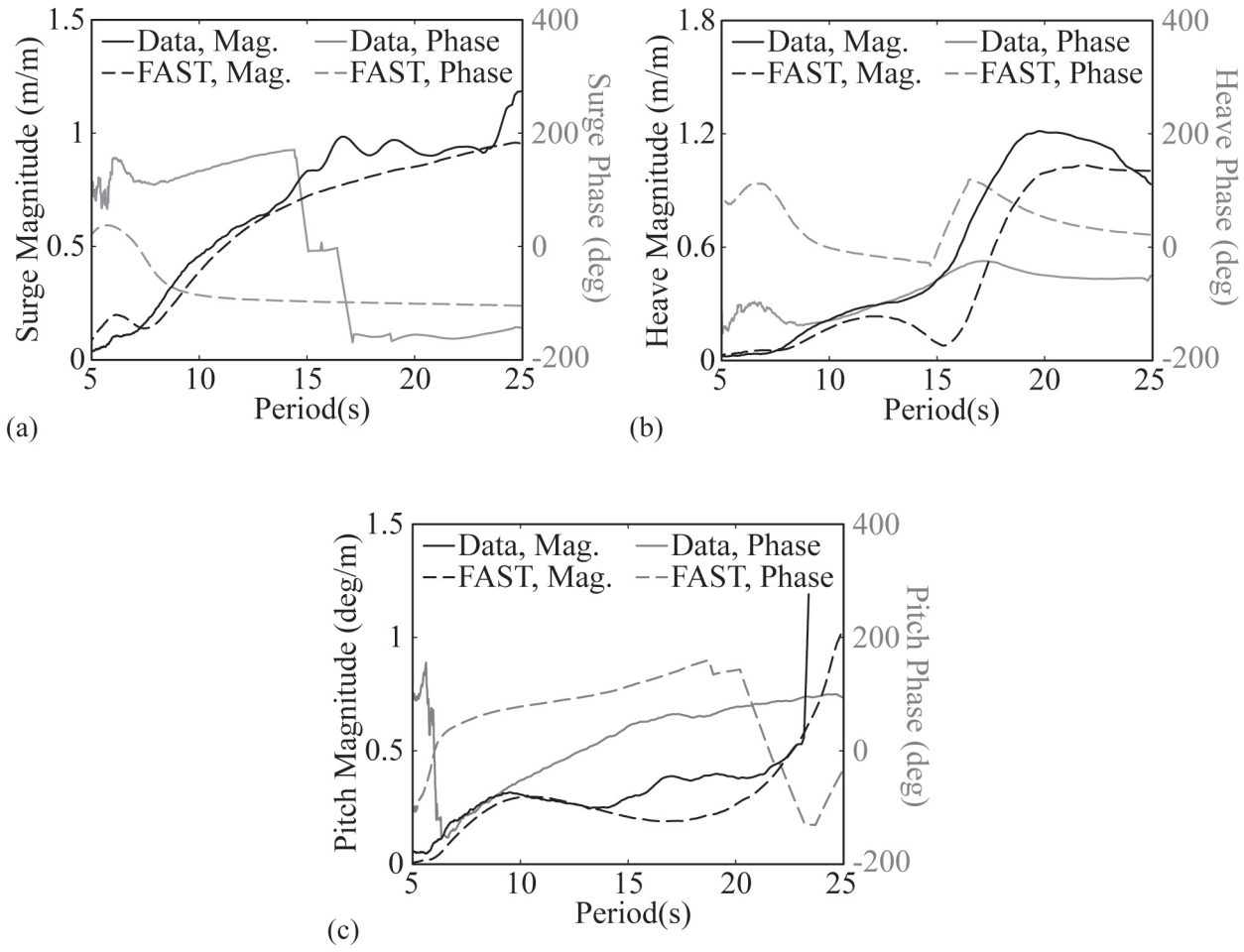

Figure 88: Comparison of RAO magnitudes and phase angles from FAST and test data for (a) surge, (b) heave, and (c) pitch.

Moving to the PSD of the tower-base fore-aft bending moment, it can be seen in Figure 89 that the comparison is fairly good between the FAST simulation and test data. FAST captures the large response at the platform-pitch natural period of 0.037 Hz, as well as the response in the wave-energy range. This stated, the response at the fore-aft fundamental tower bending frequency of 0.35 Hz is severely under-predicted. If the tower modal damping is reduced to negligible levels, the comparison between FAST and the test data at this frequency improves, capturing nearly one third of the measured response as opposed to less than 10% for the calibrated FAST model. Thus, a partial explanation for the difference may be a poor calibration of the tower modal damping. Another explanation is that second-order sum-frequency wave loads, neglected in FAST, may be sufficient to excite tower motion near the fundamental bending frequency. A further explanation for the large difference may be that dynamic loads from the instrumentation cables, which were attached to an automated following system, may be providing additional excitation of the tower that would not exist for commercial, field-deployed systems, and is not accounted for in this FAST model. The final PSD considered, the mooring line 2 fairlead tension, shows a large discrepancy between the FAST simulation test data over a broad range of frequencies.

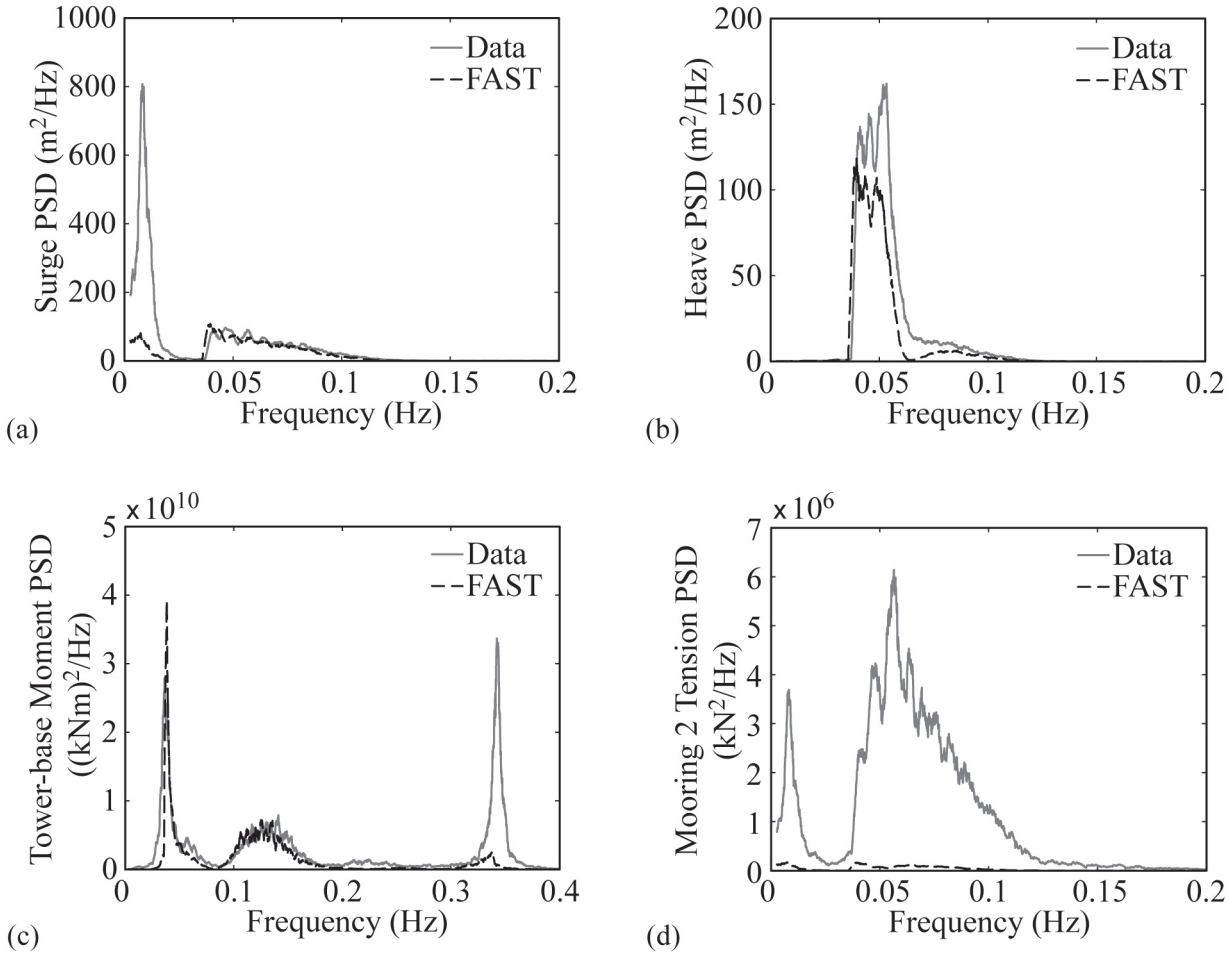

Figure 89: Comparisons of PSDs from FAST and test data for (a) surge, (b) heave, (c) tower-base fore-aft bending moment and (d) mooring line 2 fairlead tension for an irregular white noise wave only case with a significant wave height of 11.3 m.

As can be seen by comparing the surge and mooring tension PSDs in Figure 89, the relative difference between the FAST simulation and test data are nearly identical in the vicinity of the surge natural frequency of 0.0093 Hz.

This indicates that if FAST was able to account for the second-order, difference-frequency associated surge motion, it is likely that FAST's quasi-static catenary mooring line solver could capture the mooring tension behavior associated with slowly-varying drift motion. However, FAST's admirable performance with regard to emulating the correct surge motion response in the wave-energy range does not translate into accurate prediction of mooring tensions in the wave energy frequency range. As can be seen in Figure 89, the mooring line 2 fairlead tension dynamic response is grossly under-predicted by FAST. This clearly demonstrates that mooring line tension is not arising from platform motion alone and the sharp increase in mooring line 2 fairlead tension response in the wave energy frequency range is likely the result of dynamic mooring effects that are excluded in the FAST simulation. It is suspected that the inclusion of a more sophisticated, finite-element-method based dynamic mooring module (e.g., see (Garrett, 1982; Paulling and Webster, 1986)) into FAST might rectify much of the discrepancy between FAST and the test data for mooring tension response in the wave-energy frequency range.

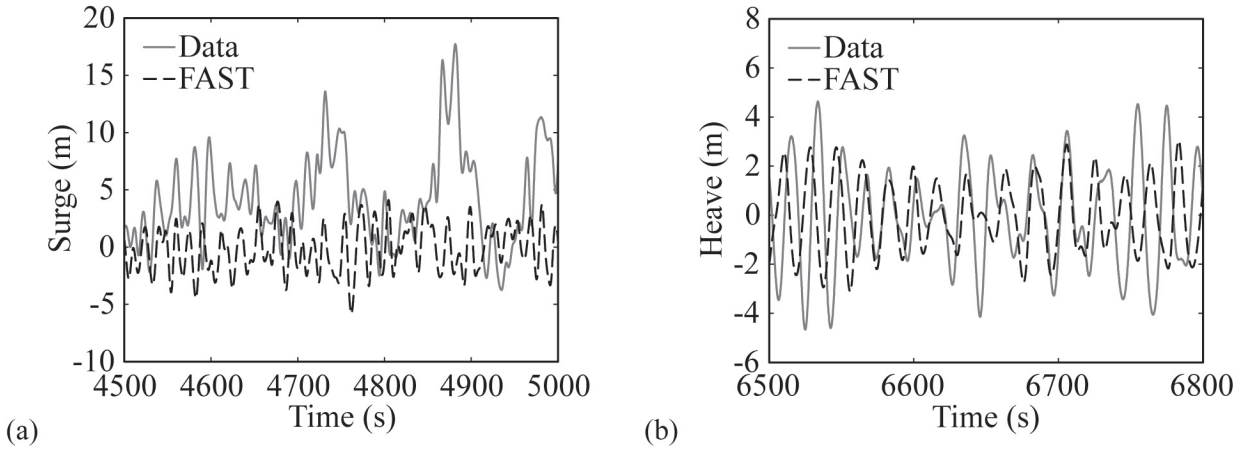

Figure 90: Comparisons of time-series from FAST and test data for (a) surge and (b) heave for an irregular white noise wave only case with a significant wave height of 11.3 m.

To complement previous results in the section, a comparison of FAST simulation and test data time-series for surge and heave motion is given in Figure 90. Turning to the surge time-series, it is clear that the higher frequency wave response is captured commendably by FAST; however, the mean drift and slowly-varying response of the real system is visibly ignored. This observation, consistent with previous statements, indicates that the inclusion of mean drift and second-order difference-frequency wave diffraction models into FAST would likely yield high quality hydrodynamic simulations. Moving to the second comparison, the heave time-series are similar in nature, with FAST occasionally under-predicting the magnitude of the heave motion excursion. This is consistent with the heave motion RAO and PSD previously presented. As noted earlier, this is most likely due to too much damping in the FAST model for heave motions with large amplitudes.

To complete this section, a comparison of the simulated and measured statistics for surge, heave, pitch, tower-base fore-aft bending moment, and mooring line 1 and 2 fairlead tensions is given in Table 42. It is observed from Table 42 that FAST under-predicts the standard deviation and range for the six field variables presented. Other key points worth noting include FAST's inability to predict the surge mean drift position and a maximum mooring line 2 fairlead tension that is only 26.7% of the measured value. This last discrepancy is in part due to FAST estimating insufficient surge motion, with the remainder likely due to a neglect of dynamic mooring effects. Nonetheless, many of the statistical comparisons are fair and differences between the FAST simulation and test data are in keeping with previous observations in this section.

Table 42: Comparison of FAST prediction and test data statistics for an irregular white noise wave only case with a significant wave height of 11.3 m

DOF	Source	Mean	Std. Dev.	Maximum	Minimum
Surge (m)	FAST	-0.14	2.01	8.09	-6.79
	Data	3.78	2.99	18.01	-4.41
Heave (m)	FAST	0.00	1.42	4.27	-4.17
	Data	-0.07	1.73	5.87	-6.50
Pitch (deg)	FAST	-0.01	1.20	4.83	-3.75
	Data	-0.02	1.55	6.94	-6.09
Fore-Aft Bending (kNm)	FAST	0.0×10^4	2.40×10^4	9.36×10^4	-10.53×10^4
	Data	0.16×10^4	3.31×10^4	19.89×10^4	-19.49×10^4
Fairlead 1 Tension (kN)	FAST	1111	60.05	1338	918.6
	Data	990.6	91.91	1403	431.8
Fairlead 2 Tension (kN)	FAST	1105	82.68	1541	879.5
	Data	1344	468.0	5774	95.25

5.1.3.6 Combined Dynamic Wind and Irregular Wave

To complete this validation study, a combined dynamic wind and irregular wave case of three hours in length was studied. The wave and wind were aligned and directed along the positive surge direction. The dynamic wind was the same as that described in Section IV, Subsection C. The wave considered was a 10.5-m significant wave height, 14.3-s peak spectral period wave based on a JONSWAP (IEC, 2009) spectrum, shown in Figure 91, with a shape parameter of 3.0.

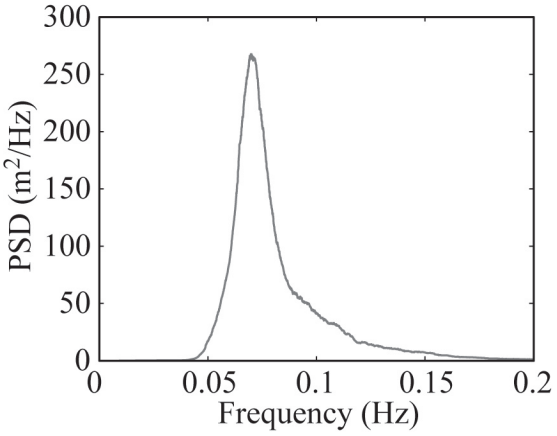

Figure 91: PSD for 10.5-m significant wave height JONSWAP wave condition.

This wave corresponds to a 100-year event in the Gulf of Maine (University of Maine, 2011). The wave condition possessed a maximum crest of 13.6 m, a minimum trough of -9.6 m, and a maximum wave height of 22.0 m. Unlike the white noise spectrum wave studied in the previous section, the JONSWAP wave considered here is more representative of a real sea condition. For comparison purposes, the custom FAST tool was again employed such that the wave diffraction forces could be computed based on the wave produced in the wind/wave basin during model testing. It is worth noting that while a sea condition of this magnitude would likely be encountered with much more severe winds that would necessitate a parked or idling turbine, the combination studied here of an operating wind turbine in a severe wave environment is still of interest because it is representative of an IEC design load case (IEC, 2009) (DLC 1.6a).

For comparison, this section will focus primarily on the tower-base fore-aft bending moment; however, statistics will also be given for surge, pitch, and mooring line 2 fairlead tension. The response of the fore-aft bending moment is influenced by most of the relevant physics of interest, including wind, waves, tower structural vibration frequencies, and lastly, second-order difference-frequency diffraction wave forcing. Regarding this last effect and its influence on tower-bending, it should be noted that all platform pitch motion, whether as a result of wind, linear wave, or second-order wave forcing, creates tower-base bending moments as a result of supporting the weight of the heavy wind turbine atop a tilted tower. In addition to comparing FAST and the test data for the combined wind and wave case, the bending moment comparison will also be presented for the dynamic wind only and the JONSWAP wave only. This will permit assessment of the importance of a few of the wind-only or wave-only deficiencies noted previously, and whether or not they are still present in the combined wind and wave case.

The PSDs of the tower-base fore-aft bending moment for the dynamic wind only, irregular wave only, and combined dynamic wind and irregular wave case are given in Figure 92. For the dynamic wind only condition, the comparison is very good, with FAST accurately predicting the increase in response resulting from wind-induced system pitch motion (0.037 Hz). Both the FAST and test data show some minor response at the tower fore-aft fundamental bending frequency of 0.35 Hz, with FAST marginally over-predicting the response. Note that Figure 84 and Figure 85 and Table 40 contain additional plotted results and statistics, respectively, for the dynamic wind only condition used in the combined case.

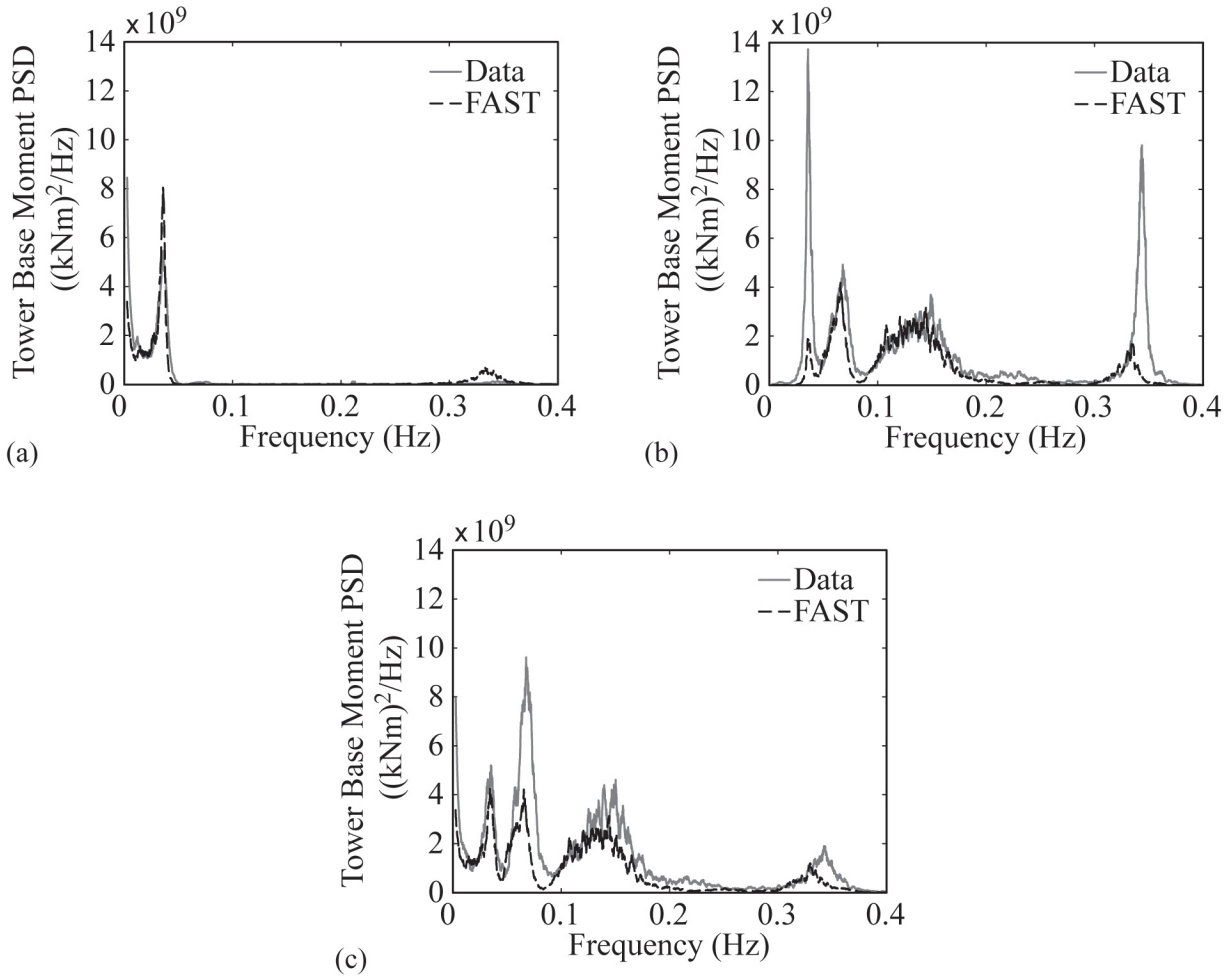

Figure 92: Comparisons of tower-base fore-aft bending moment PSDs from FAST and test data for (a) 20.6 m/s mean wind speed dynamic wind only, (b) 10.5-m significant wave height irregular wave only and (c) combined dynamic wind and wave cases.

Moving to the wave-only bending moment PSD, the comparison is fairly good in the wave-energy range (0.05 to 0.2 Hz), but less so outside of these bounds. FAST poorly predicts the sharp rise in bending moment response associated with platform-pitch motion resulting from second-order difference-frequency wave diffraction forces at 0.037 Hz. The response at the fore-aft fundamental bending frequency is also severely under-predicted by FAST, the possible reasons being highlighted in the previous subsection. On a positive note, the strong correlation between FAST and test data in the wave-energy range is very encouraging because the response for the tower-base fore-aft bending moment is rather complex. Note that in Figure 92 there is a marked decrease in response near 0.08 Hz, despite the fact that the peak wave energy occurs at 0.07 Hz. This results from the unique platform motion of this system for this particular sea. Despite significant platform motion, the nacelle motion is very low. This results in lower inertial forces at the tower-top and hence, lower tower-base bending moments. As Figure 92 clearly shows, this behavior is accurately captured by FAST. To continue the discussion of wave-only response to the JONSWAP wave, Table 43 below shows statistics for the field variables of interest. The results comparison is fair, with similar discrepancies and possible explanations as those given for the irregular wave-only study with the 11.3-m significant wave height white noise wave.

Table 43: Comparison of FAST prediction and test data statistics for an irregular wave-only case with a significant wave height of 10.5 m

DOF	Source	Mean	Std. Dev.	Maximum	Minimum
Surge (m)	FAST	-0.08	1.75	6.89	-7.37
	Data	2.35	2.37	16.29	-4.98
Pitch (deg)	FAST	0.00	0.68	3.15	-3.10
	Data	-0.06	1.08	4.50	-4.15
Fore-Aft Bending (kNm)	FAST	0.0×10^4	1.61×10^4	7.69×10^4	-6.83×10^4
	Data	0.13×10^4	2.14×10^4	17.85×10^4	-13.55×10^4
Fairlead 2 Tension (kN)	FAST	1106	75.41	1487	862.0
	Data	1256	406.9	5469	36.05

Moving to the combined dynamic wind and irregular wave condition of Figure 92, the comparison between FAST and the test data shows a fairly good agreement over the entire range of frequencies investigated. The figure indicates that the tower-base fore-aft bending moment response at the platform-pitch (0.037 Hz) and fundamental tower-bending (0.35 Hz) frequencies is dominated by wind rather than second-order wave diffraction or other effects and is therefore predicted very well by FAST. Over the wave-energy range of 0.05 to 0.2 Hz, FAST captures the appropriate trend in the response, albeit with less energy than measured during testing. Because the measured response in the wave-energy frequency range is greater for the combined wind and wave condition than just for waves alone, the data suggests that the combined case yields additional excitation to the system. This could be caused by wave-induced motion creating additional aerodynamic loads as a result of altering the wind turbine rotor relative velocity at frequencies in the wave energy range. It is possible that this calibrated model of FAST may be unable to capture these higher frequency changes in rotor aerodynamic load as a result of choosing simplistic aerodynamic calculation options, for example, by eliminating the dynamic stall model. By employing a wind turbine model that exploits the full features of FAST's aerodynamic calculation abilities, a better comparison in the wave-energy range could result for the tower-base fore-aft bending moment for the combined dynamic wind and irregular wave case.

Table 44: Comparison of FAST prediction and test data statistics for the combined case consisting of an irregular wave with a significant wave height of 10.5 m and a dynamic wind with a mean hub height wind speed of 20.6 m/s

DOF	Source	Mean	Std. Dev.	Maximum	Minimum
Surge (m)	FAST	7.13	1.81	13.87	0.28
	Data	9.28	2.29	22.26	2.33
Pitch (deg)	FAST	3.42	0.89	6.70	-0.05
	Data	3.49	1.23	8.66	-1.33
Fore-Aft Bending (kNm)	FAST	8.44×10^4	1.85×10^4	16.16×10^5	1.76×10^4
	Data	8.45×10^4	2.42×10^4	21.70×10^4	-5.01×10^4
Fairlead 2 Tension (kN)	FAST	1580	135.1	2231	1173
	Data	1825	697.6	8109	23.42

That aside, this case is much more realistic because it is unlikely the system would see either a high wave or wind loading alone; they would be expected to occur simultaneously. To finish the comparison, Table 44 presents the statistics for the combined wind and wave case. While discrepancies are still present for the field variables shown, the presence of the wind loads reduces some of the error compared to the wave-only case. The surge response compares much better in this case, with FAST capturing 76.8% of the mean offset without the inclusion of any second-order wave forcing. The discrepancies in the predicted ranges

of the surge, pitch, and tension in mooring line 2 responses are similar to the wave-only case, and the predicted range of tower-base bending moments is improved. Overall, FAST demonstrates a fair prediction in this combined wind and wave loading scenario, which is promising.

5.2 Calibration and Validation of a Tension-leg Platform Floating Wind Turbine Model

This section will focus on the calibration and validation of the UMaine-designed TLP. This TLP design was inspired by the Glosten Associates' design (Moon and Nordstrom, 2010). The simulation tool used in this research to create the model of the TLP experiment was FAST. FAST is a coupled aero-hydro-servo-elastic code that simulates the dynamics of wind turbines in the time domain (Jonkman, 2007). It uses Blade-Element/Momentum theory (BEM) or Generalized Dynamic Wake (GDW) theory with static or dynamic stall to calculate aerodynamic loads, a combined nonlinear multibody dynamics and modal superposition formulation for structural components, a quasi-static mooring line model based on continuous cable theory with stretching, turbine control algorithms, and a hydrodynamic module that calculates wave loading on the platform based on linear radiation and diffraction as well as nonlinear viscous drag for offshore applications.

5.2.1 Model Description

Floating platforms lose the stiffness associated with the fixed-ground foundations, and gain new degrees of freedom (DOF). The naming convention for the floating platforms' DOF used for the TLP study can be seen in Figure 93. The wind turbine used in the MARIN tests was modeled after the NREL 5-megawatt (MW) reference turbine (Jonkman et al., 2009). Froude scaling is used both to provide the geometry and other properties of the 1/50th-scale experiment as well as the scaling of the output data from the tests. All of the analysis in this TLP section was done using data and modeling at full scale. For the test data, this means that it must be scaled up to full scale before comparisons are made. Figure 94 shows a diagram of the TLP used in the experiments, including sensor locations. Table 45 describes the full-scale physical dimensions of the TLP. The experimental apparatus includes accelerometers in the nacelle and three locations along the tower. There is also an optical displacement sensor located near the tower base, labeled "Motions" in Figure 94. Load cells are installed between the tower and the platform, between the tower and the nacelle, and on the mooring line fairleads to provide mooring line tension data. The goal of this research was to create, calibrate, and validate a full-scale FAST model of this TLP. The calibration step involved tuning the platform, tower, and aerodynamic parameters in the simulation of the wind turbine to match the data produced by the static equilibrium, decay, regular wave tests, and tests with only aerodynamic loading. The calibrated model was then used to compare to the combined wind and wave tests in an effort to validate FAST as a modeling tool for floating wind turbines.

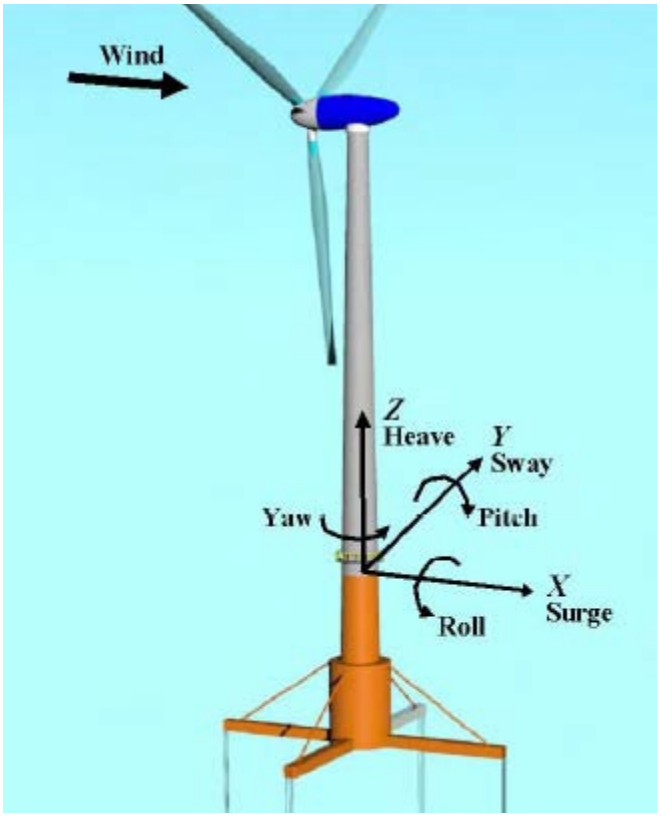

Figure 93: DOF terminology (Jonkman 2007).

Table 45: Physical Properties of the TLP

TLP Dimensions	
Mass with Turbine (metric ton (mt))	1,361
Displacement (mt)	2,840
Draft (m)	30.0
Center of Mass above Keel (m)	64.1
Mooring Spread Diameter (m)	60.0
Roll Radius of Gyration (m)	52.6
Pitch Radius of Gyration (m)	52.7

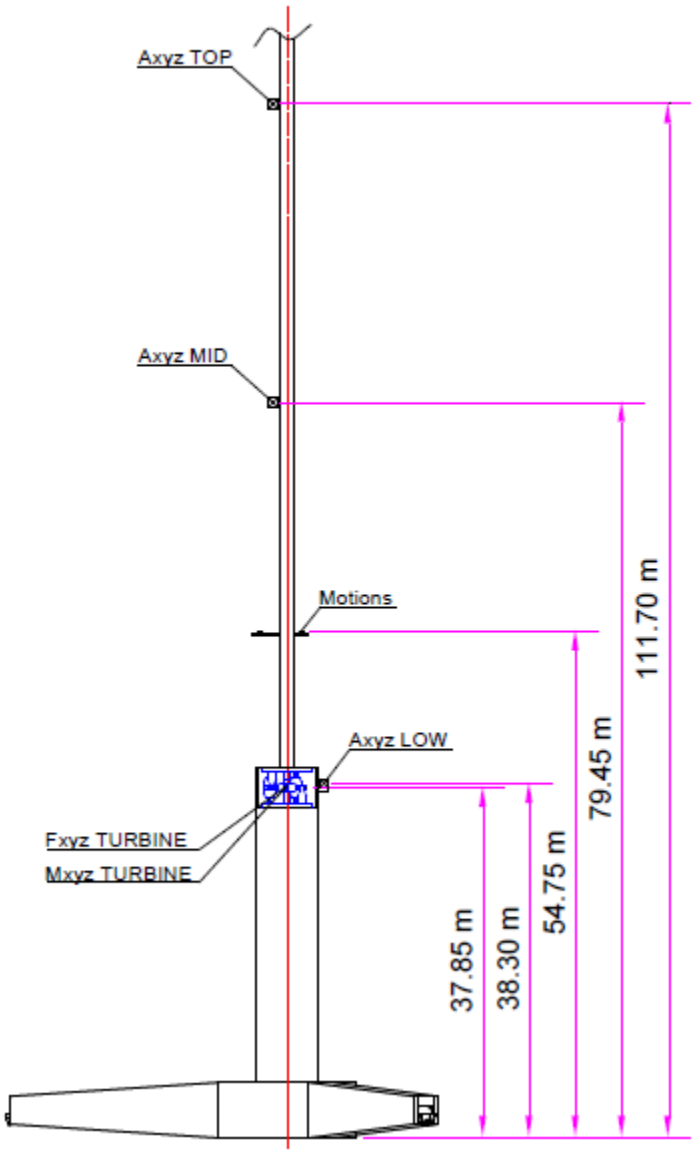

Figure 94: Sensor location on experimental TLP.

5.2.2 Model Calibration

5.2.2.1 Wind Turbine Geometry and Mass Properties

The horizontal-axis wind turbine chosen for scale-model construction is the fictitious, albeit extensively studied, NREL 5-MW reference wind turbine (Jonkman et al., 2009). The wind turbine possesses a 126-m rotor diameter and a hub height of 90 m above the still water line (SWL). The flexible tower, which begins 10 m above the SWL, is designed to emulate the mass and stiffness of the OC3-Hywind tower (Jonkman, 2010). The scale-model wind turbine deviates from the standard NREL 5-MW reference wind turbine in a few notable areas. For the model wind turbine, the shaft tilt is 0°, the blade precone is 0°, and the blades are essentially rigid, which is a reasonable approximation of the actual model. The total mass

of the rotor inclusive of the hub and three blades is a full-scale equivalent of 122,220 kilograms (kg). All values reported in this TLP section are full-scale-equivalent values. The nacelle mass is 274,940 kg.

For the physical model, instrumentation cables used for recording all of the wind turbine response data, as well as nacelle accelerations and tower-top forces, were affixed to approximately the upper two-thirds of the model tower before being looped away to run to the data acquisition system. In FAST, this instrumentation cable is not modeled directly. Instead, the apparent additional weight the platform had to support due to the cables was smeared evenly over the length of the tower for numerical modeling. The distributed stiffness of the tower was assumed to be unaltered by the presence of the cables. Therefore, the distributed bending stiffness for the tower employed for the numerical model was taken directly from the product of the tower material Young's modulus and distributed area moment of inertia. The tower area moment of inertia did not vary smoothly along the length of the tower, with the lower 11.3 m of the tower having a larger outer diameter than the remainder of the tower. The total tower mass, including the additional cable mass, was 302,240 kg. The sensor cable accounts for 137,650 kg of this tower mass. The total topside mass, which included the wind turbine and tower, was 699,400 kg. This value is 16.6% larger than the standard specifications for the combined NREL 5-MW reference turbine and OC3-Hywind tower.

5.2.2.2 Blade Aerodynamic Properties

Due to the low Reynolds numbers experienced during Froude-scale wind/wave basin testing, the aerodynamic performance of the wind turbine blade airfoil sections (which were geometrically scaled) was significantly altered. To generate the airfoil data required for numerical modeling calibration and validation studies, analyses of the airfoil sections were performed at the low Reynolds numbers for small positive angles of attack using the high-order viscous airfoil analysis panel code XFoil (Drela 1989). However, the analyses were incredibly sensitive to the particular Reynolds number and laminar-to-turbulent transition parameters. Despite the fact that the analysis replicated the general change in performance seen during the testing, the generated lift and drag coefficient curves did not accurately reproduce the model-testing-derived coefficient of thrust and coefficient of performance curves for the wind turbine when utilized in FAST. Therefore, the XFoil curves were used as a guide to create a parameterized set of curves that permitted variations in key lift and drag coefficient parameters, such as lift coefficient stall points and minimum drag coefficients. The parameterized curves were extrapolated for all angles of attack via the Viterna Method (Hansen, 2010). A multi-objective genetic algorithm (e.g. see Deb, 2001) was used to search for the lift and drag coefficient parameters that minimized the error between the FAST predictions and wind-only model test data for the wind turbine coefficient of thrust and coefficient of performance curves simultaneously.

Of the various Pareto-optimal solutions found, the result selected was one which favored a solution that achieved minimal error in the thrust coefficient curve (Ct) while still maintaining some semblance of the measured performance coefficient (Cp). This preference of matching the thrust performance was undertaken because the wind turbine thrust force, and not the rotor torque, is the key driver in the global motions of the floating wind turbine under combined wind and wave loadings. A comparison between the FAST prediction and the test data is shown in Figure 95.

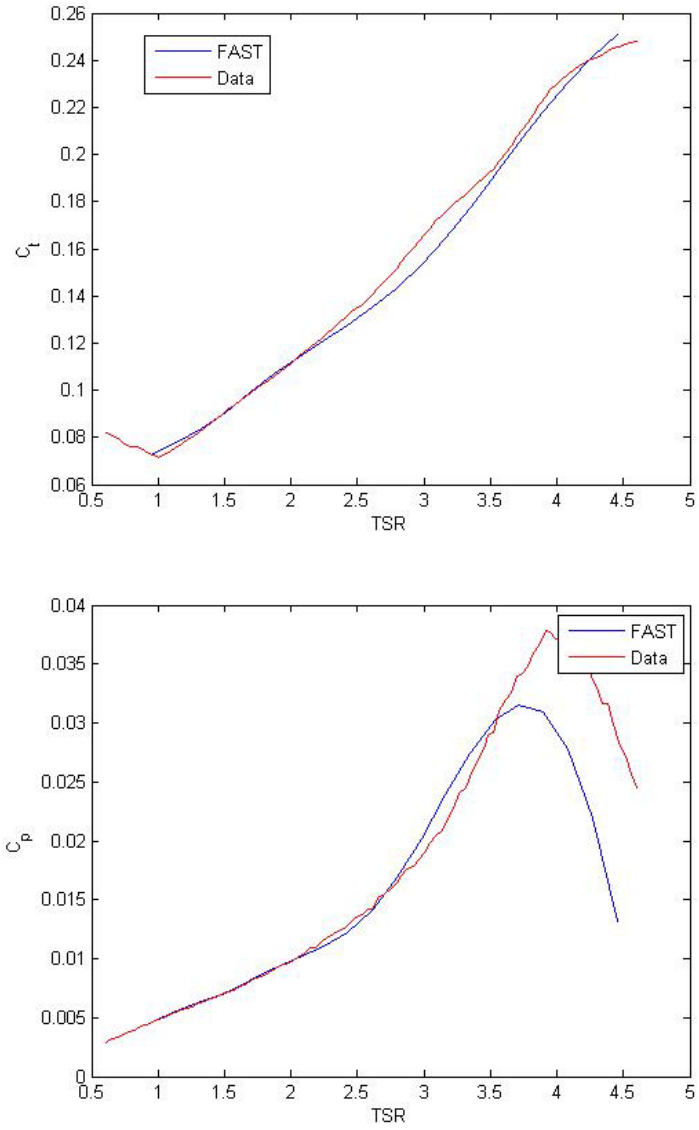

Figure 95: Comparison of model test data and aerodynamic model for coefficients of thrust and performance versus tip-speed ratio (TSR).

The FAST results in Figure 95 were generated with no aerodynamic pitching-moment coefficients. As can be seen in Figure 95, the thrust, and especially the performance coefficients are significantly lower than the NREL 5-MW reference wind turbine. The reason for this, discussed in detail in Martin (2011), is due primarily to laminar separation of the airfoil sections that drastically reduces lift and increases drag. This is especially true for the numerous thick airfoil sections found on the NREL 5-MW blade.

Figure 96: UMaine TLP model.

5.2.2.3 Initial Model and Static Equilibrium Comparison

Static equilibrium simulations were carried out in FAST with this initial model to check the global characteristics of the model. It was found that, by using the platform volumetric displacement given by MARIN, there was substantial platform heave ringing. When the platform displacement value was reduced by approximately 1% of the original value, the magnitude of this heave ringing was reduced to negligible values. Once this heave motion was eliminated, the tension values in the mooring cables were compared to the experimental values and were found to be in good agreement.

5.2.2.4 Free-decay Tests

Free-decay tests were conducted on the experimental TLP by introducing a displacement to a platform DOF and allowing the system to come to rest. Specifically, these tests were conducted to determine the natural frequencies and damping ratios of the various DOFs. Ideally, only one DOF is excited by these tests, but in practice, the tests usually excited more than one DOF. By reviewing the experimental time series, the initial displacements could be extracted and applied to the FAST model.

The data from the optical displacement sensor was found to be inaccurate for the rotational DOFs (pitch, roll, and yaw). This is most likely due to the relatively small displacement of the TLP in these DOFs compared to the rotational sensing accuracy. For this reason, the acceleration data was used instead of the displacement data as a basis for comparison between FAST and the tests.

To tune the natural frequencies and damping ratios of the platform DOFs in FAST, an additional FAST input file was created that gives the user the capability of adding stiffness and damping to each platform DOF. Using this addition, the natural frequencies and damping ratios were iteratively tuned to match the values found in the decay tests. This was done using a frequency-domain analysis of the test data and the FAST output. The stiffness and damping parameters were tuned by hand using a visual comparison of the frequency response of the experiment to the simulation.

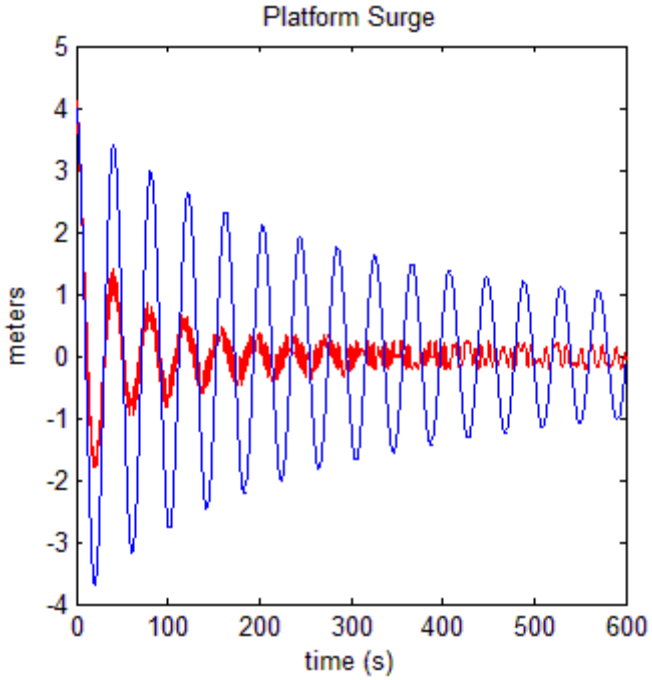

Figure 97: Un-tuned surge decay test surge displacements

5.2.2.4.1 Surge Decay Test

For the surge decay test, the comparison of the surge DOF displacement from the un-tuned FAST model and the test can be seen in Figure 97. In this test, the platform was displaced the full-scale equivalent of 4 m in the surge direction. Figure 98 and Figure 99 show the acceleration and acceleration power spectral density (PSD) of the surge DOF, respectively.

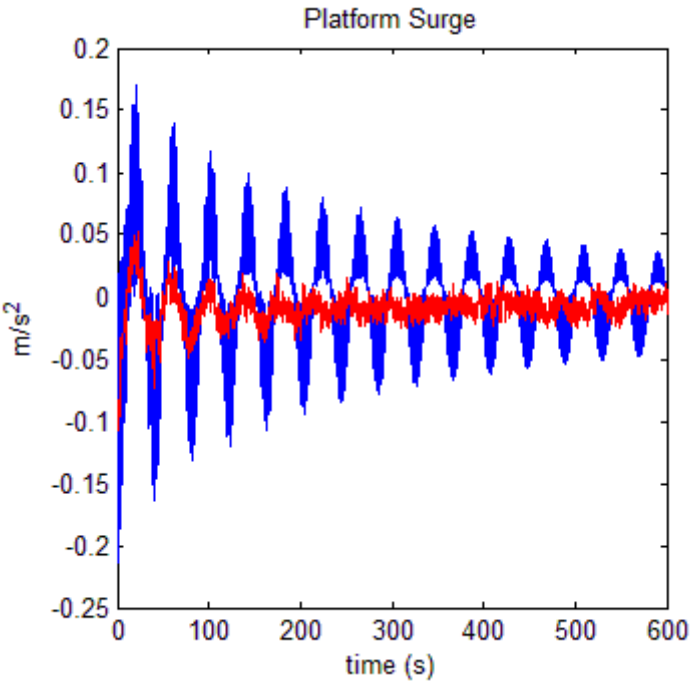

Figure 98: Un-tuned surge decay acceleration.

Figure 97, Figure 98, and Figure 99 show that the FAST model is producing a surge frequency that closely matches the test data, but the FAST simulation model is under-damped for this DOF. In addition, it can be seen in Figure 99 that the heave DOF is highly under-damped in the FAST model as well. This is most likely due to the effect of the sensor cable bundle mentioned earlier, as well as possible under-predictions of damping due to the neglecting of viscous drag in the numerical model. The simulation shows large peaks due to the coupling of the heave, pitch, and tower-bending DOFs with the surge DOF that do not show up in the test. As there is no excitation in the sway, roll, or yaw DOFs, these DOFs can be ignored for this test.

Figure 100 shows the PSD of the platform acceleration with additional damping implemented for the surge and heave DOFs. The surge damping has been increased by 1x105 Ns/m, increasing the damping ratio from 0.01 in the un-tuned case to approximately 0.094. The heave damping ratio has been changed from near zero in the un-tuned case to 0.57.

One issue with the tuned model can be seen in Figure 101. The data from the experiment indicates non-linear, amplitude-dependent damping. In other words, the value of the damping constant for the experiment is larger for larger amplitude motion, and reduces as the motion damps out. This phenomenon could be a result of the sensor cable bundle, or more likely viscous drag, where damping is proportional to velocity squared, and should be investigated in future work. For the scope of this study, the damping is approximated as linear in FAST.

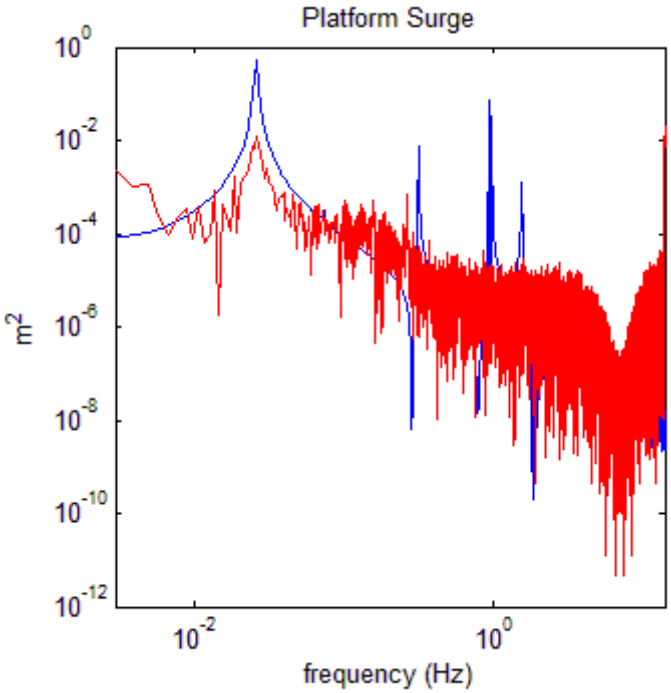

Figure 99: Un-tuned surge decay acceleration PSD.

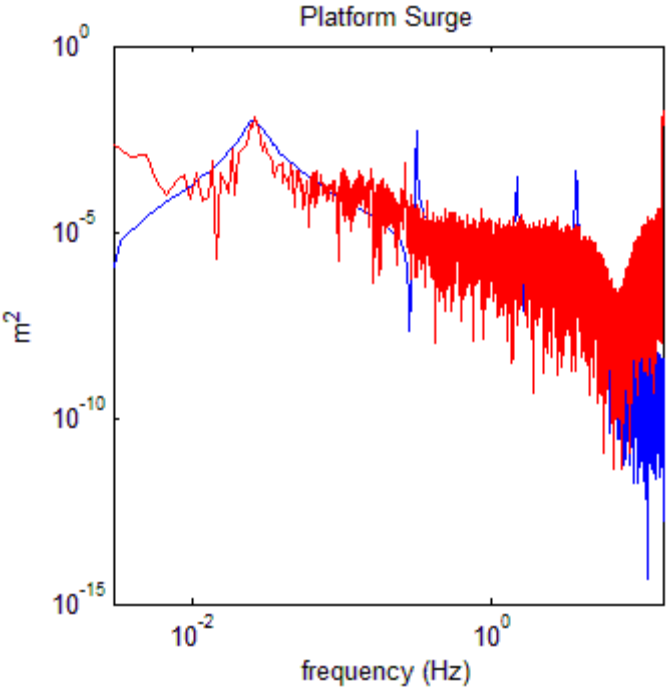

Figure 100: Tuned surge acceleration PSD.

5.2.2.4.2 Further Decay Tests

This method of tuning was carried out for the other DOF decay tests. Due to difficulties in determining the exact initial conditions of each test, only approximate constants could be determined from the decay tests. For example, one of the pitch-decay tests was conducted by pushing the top of the tower in the pitch direction. This method of excitation produces a substantial amount of initial tower bending which is hard to quantify from the test data. The other pitch-decay test was conducted by pushing on the leg of the TLP to impart an initial pitch. Because of these inaccuracies with the free-decay tests, the plane-progressive (regular) wave tests were used for further calibration.

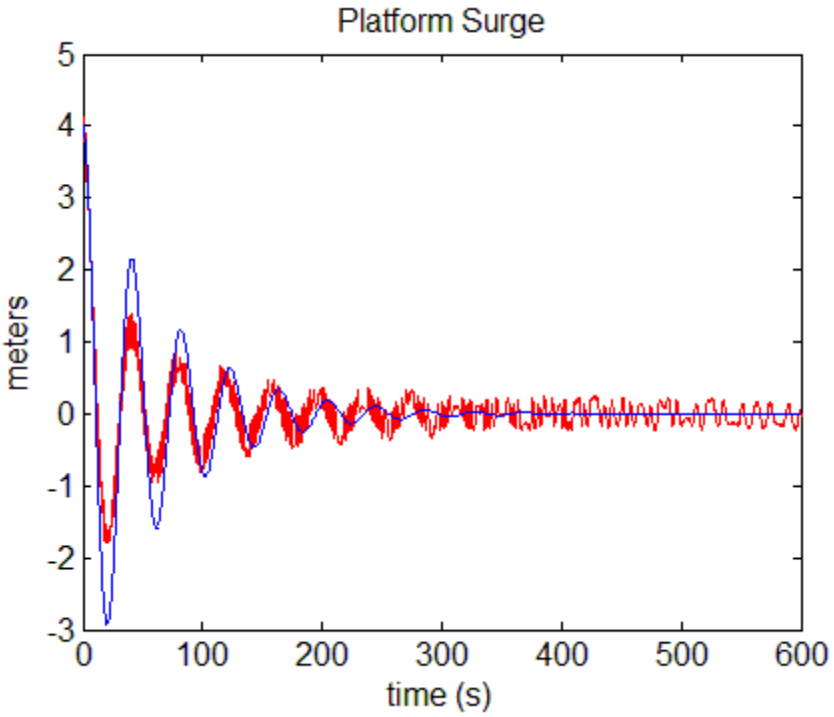

Figure 101: Tuned surge DOF displacement.

5.2.2.5 Regular Wave Tests

The tests conducted in the wave basin included seven regular wave tests with no wind excitation. These tests used a single-frequency long-crested wave input. FAST has the capability to generate these types of waves, so the inputs for the experiment and model were very similar; resulting in a stronger comparison than the decay tests. Figure 1020 shows the surge displacement for one of the regular wave tests and includes the surge damping tuning from the surge decay test. Due to the inaccuracies in the free-decay tests, some of the platform parameters were further tuned using the frequency response of one of the regular wave tests. Figure 103 shows a plot of the acceleration frequency response for all six DOFs, after tuning. In the upper left graph of the platform-surge frequency response, the simulation-surge response at the wave frequency agrees with the experiment well, and the response at the first tower-bending mode agrees as well.

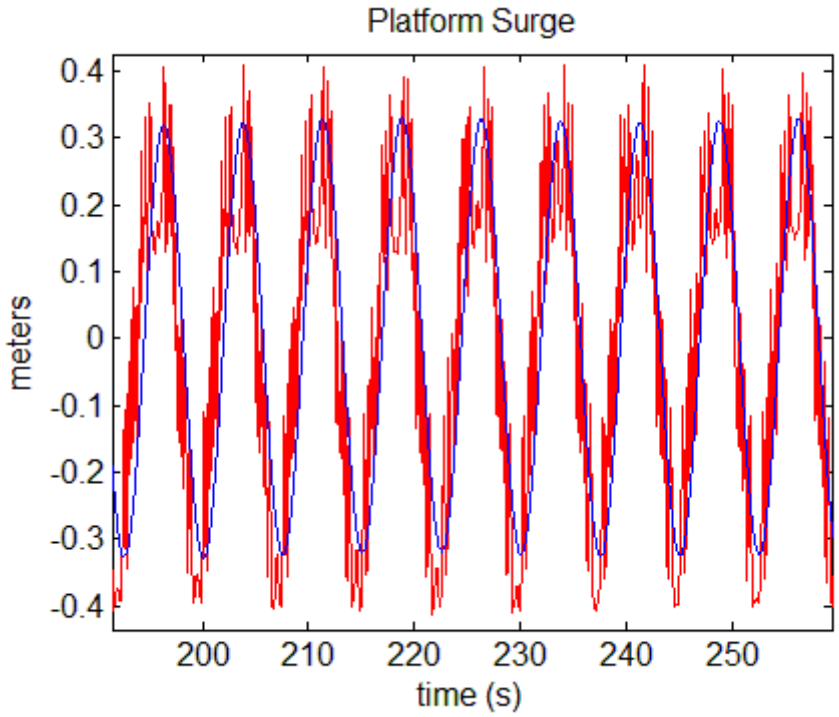

Figure 102: Surge displacement for regular wave test with Height = 1.92 m, Period = 7.5 s.

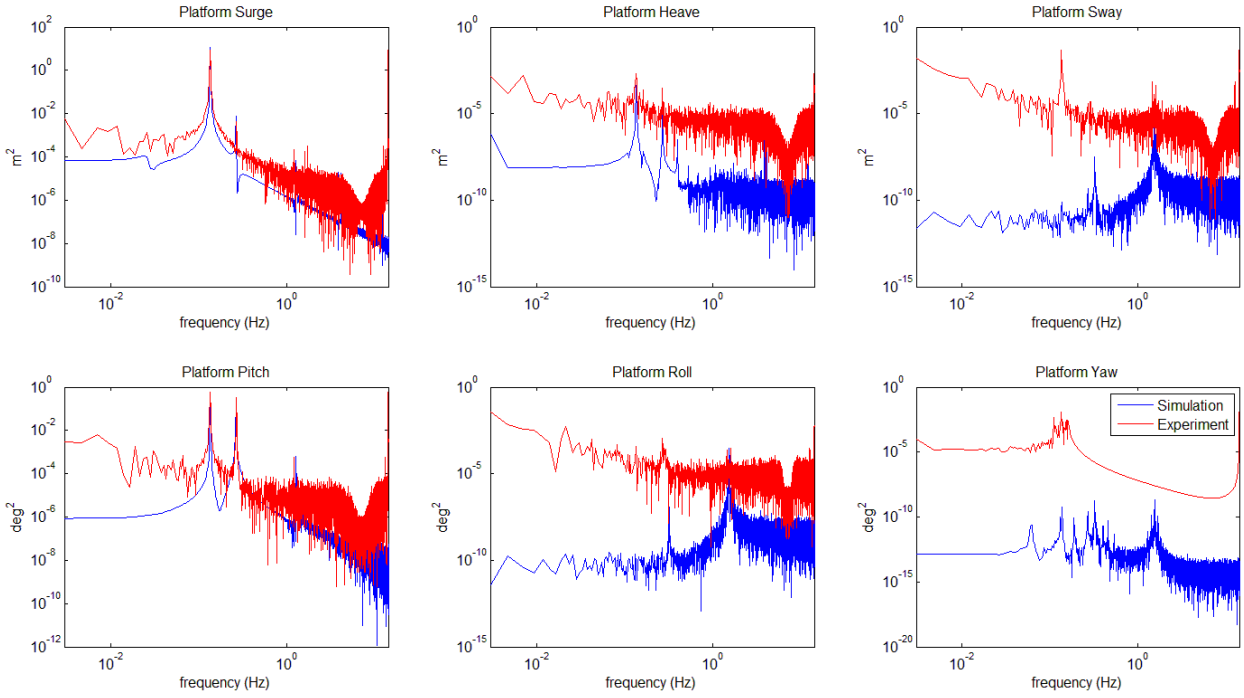

Figure 103: Acceleration frequency response for regular wave test.

In the plot of the pitch-acceleration frequency response (lower left), the wave frequency, the first tower-bending mode, and the pitching frequency are indicated. Tuning the pitch and tower-bending frequency proved to be a challenge. The mode shapes of the tower were initially determined by the University of Maine using an in-house finite-element method (FEM) code, and as confirmation, an analysis was conducted using BModes, an NREL FEM mode shape software (Bir 2008). The difficulty with this procedure is that the tower-bending mode and the pitch mode are highly coupled. In order to find the proper mode shapes, an iterative process was conducted with BModes by reducing the pitch stiffness from 5.8x1010 Newton-meters/radian (Nm/rad) to 2.6x1010 Nm/rad until both the pitch and tower-bending frequencies aligned with the tests. The other four DOFs, heave, sway, roll, and yaw, were excited more by the waves in the experiment than in the simulations. Of note is that the magnitude of these DOFs is much smaller than the surge and pitch magnitudes. These discrepancies are most likely due to experimental imbalances in the mooring lines or in the mass symmetry of the experimental TLP.

5.2.2.6 Summary of Model Calibration

A summary of the changes to the DOF damping ratios and frequencies can be seen in Table 46. In addition to the changes seen in the table, the tower mode shapes were changed, which caused the change in tower frequency seen in the table.

Table 46: Summary of Calibration

	Nat. Freq. (Hz)	Tuned Nat. Freq. (Hz)	Original Damping Ratio	Tuned Damping Ratio
Surge	0.025	0.025	0.01	0.098
Sway	0.025	0.025	0.01	0.098
Heave	0.96	0.96	5.1e-7	0.57
Roll	1.52	1.52	0.0050	0.0050
Pitch	1.56	1.27	0.0051	0.0050
Yaw	0.058	0.058	0.047	0.047
First Tower Fore-Aft	0.32	0.26	0.006	0.006
First Tower Side-Side	0.32	0.26	0.006	0.006

5.2.3 Model Validation

In this section, the simulations that were run to date for the model validation step are presented. Two experiments with constant wind and operational waves were simulated in FAST. More simulations will be conducted in future work on this project. In these tests, the time series of the wave input was not replicated directly, but the spectrum of the wave input was the same as the experiment. The first experiment that was simulated used a 7-m/s wind speed, and a wave spectrum with a 2- m significant height, a 7.5-s peak-spectral period, and a peak shape parameter of 2.0. The pitch of the blades was held at a constant 6.4 degrees, and the rotor was held at a constant speed of 4.95 revolutions per minute (RPM) in both the simulation and the experiment. The values for pitch and rotor speed differed from the normal NREL 5-MW specification as these values were chosen to match simulated rotor thrust with the augmented aerodynamic performance of the 1/50th-scale model.

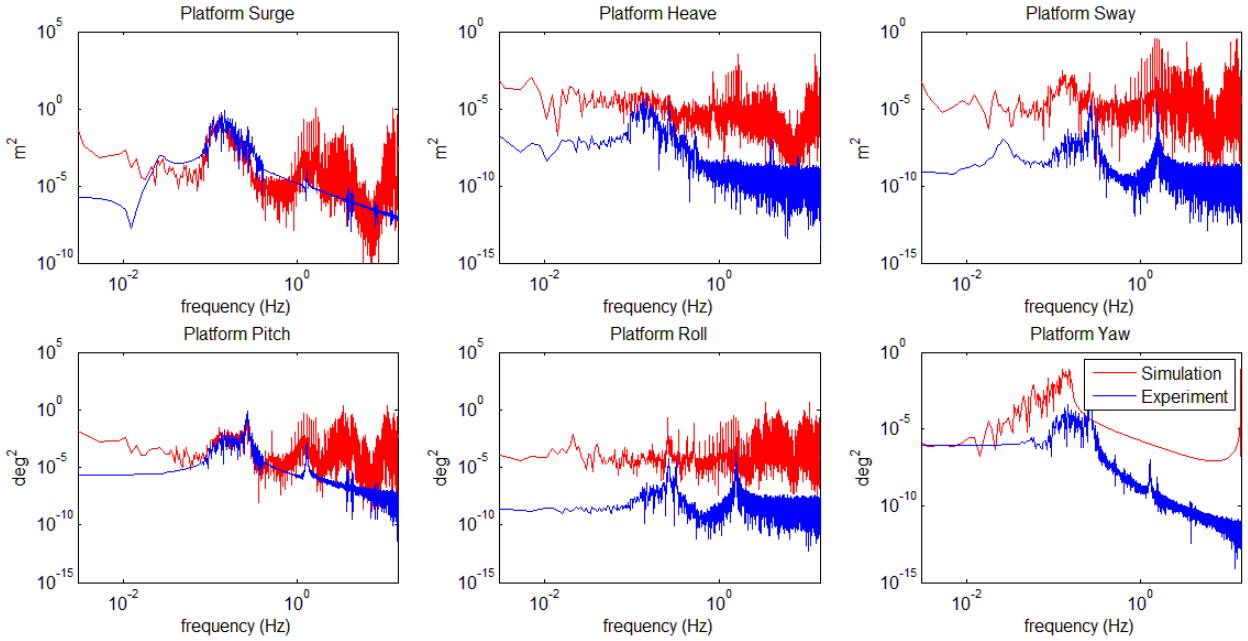

Figure 104: Acceleration frequency response for low operational wave test and steady 7 m/s wind.

Figure 104 shows the frequency response of the acceleration of the DOFs for this first validation case. The discrepancies in the frequency range lower than the wave frequencies were most likely due to fluctuations in the experimental wind speed. Similar to the regular wave response, the lower frequency modes were captured well by the simulation, but the simulation diverged from the experiment for higher frequency modes.

The difference in energy between the experiments and the simulations at these higher frequencies could mean that the FAST model needs higher frequency modes, that the simulation model was improperly calibrated, or that the sensors used in the experiments had errors or noise at these high frequencies. Further research is required to determine what combination of these three options is present.

In the pitch frequency response in Figure 104, the experiment shows a peak at the rotor frequency (1P). The FAST simulation shows no pitch excitation at this frequency. Causes of 1P excitation are indicative of a rotor imbalance in the experiment, which was not simulated in FAST. Future models may address this issue of rotor imbalance.

The second case that was simulated was an experiment with much higher wind and wave loading. The steady wind speed for this test was 21 m/s, the wave height was 7.1 m, the peak-spectral period was 12.1 s, and the shape factor was 2.2.

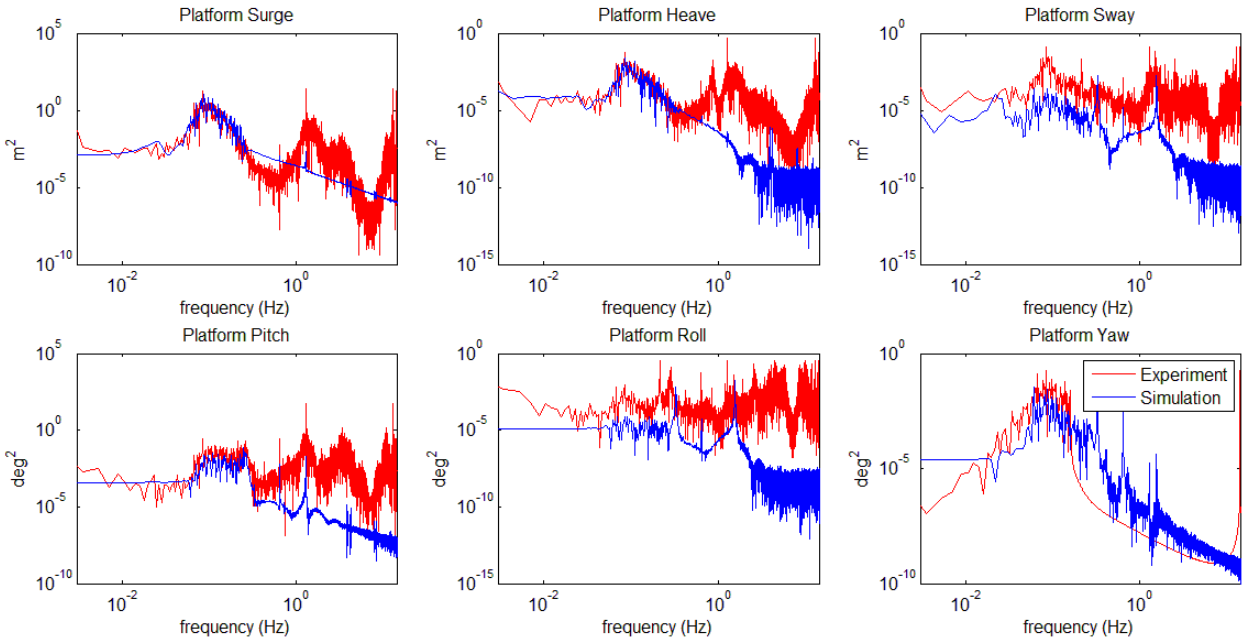

Figure 105: Acceleration frequency response for high operational wave test and steady 21 m/s wind.

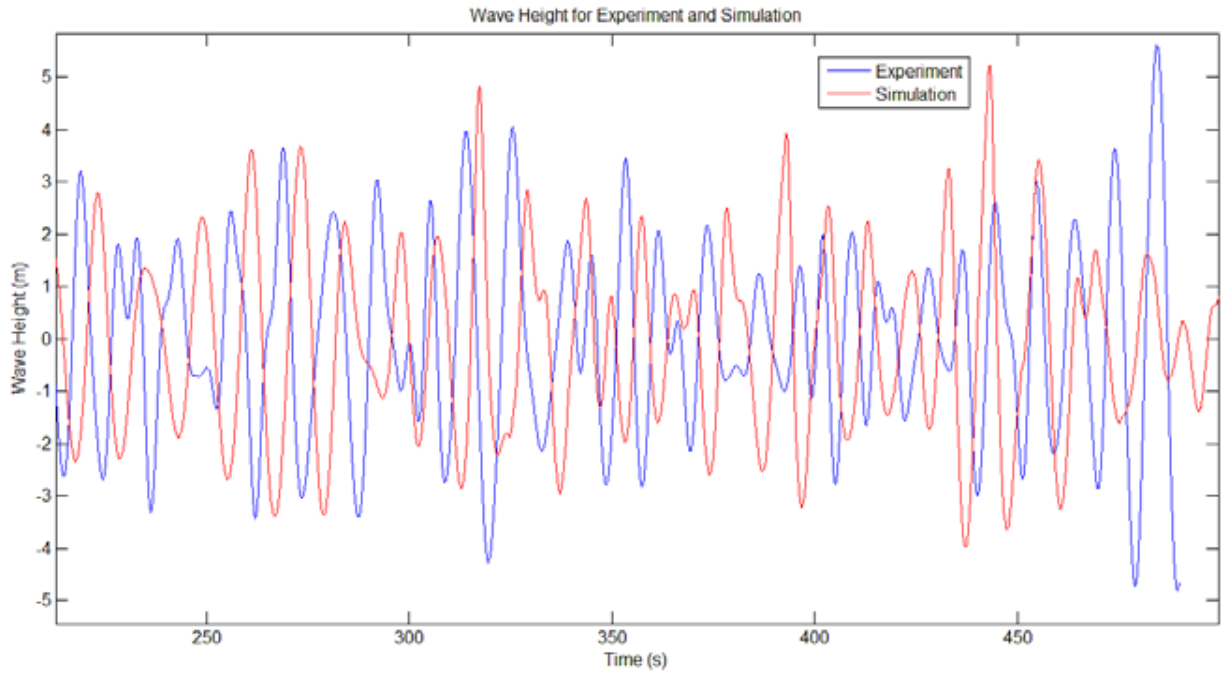

Figure 106: Wave time series

In Figure 105, there is reasonable agreement between the response of the experiment and the response of the simulation. This case produced the most consistent results seen to date for the sway, heave, roll, and yaw DOFs and could be caused by a phenomenon similar to the non-linear damping seen in Figure 101.

As the amplitude of motion becomes higher, the damping values of various degrees of freedom may increase in the experiment, which is closer to what the simulation is showing.

With the higher wind speed of this experiment, the 1P excitation is showing up in the FAST simulation, as indicated in the pitch response in Figure 105. The cause of this 1P excitation is being investigated. Figure 105 shows the acceleration frequency response in each DOF. Due to the high wind and wave loading, the simulated TLP exhibited an excessive increase in pitch angle magnitude during a large wave event, causing the simulation to end prematurely. Figure 106 shows a plot of the experimental and simulated wave heights. The simulation crashed after the large wave seen at the end of the time series. Because the blade pitch was constant in all of these tests, the rotor thrust produced by the 21-m/s wind was enough to cause a 12-m surge. These factors combined to cause excessive pitch motion. The amplitude of the pitch motion leads to a slack-line event in FAST, in which the tension in the rear mooring line goes to zero. This phenomenon was seen in the experiment as well, which is an encouraging sign for modeling accuracy.

5.3 Calibration and Validation of Spar-buoy Floating Wind Turbine Model

This section focuses on an effort to use the DeepCwind 1/50th-scale test data to calibrate and validate a FAST turbine model of a spar buoy floating wind turbine. FAST is a nonlinear time-domain simulation tool that is capable of modeling the coupled aero-hydro-servo-elastic response of floating offshore systems that are operating in an environment with combined wind and wave loading. Rotor aerodynamics are calculated using the AeroDyn software library—which relies on blade-element/momentum theory or generalized dynamic wake theory for the calculation of wake effects—and the Beddoes-Leishman model for calculation of dynamic stall, and provides the user with the option of incorporating the effects of tip losses and hub losses (Hansen and Moriarty, 2005). Structural components of the turbine are modeled as a combination of coupled rigid and flexible bodies. Flexible bodies include the blades, tower, and drive shaft (Jonkman, 2012; Jonkman and Buhl, 2005). Time-domain hydrodynamics include the effects of hydrostatic restoring, viscous drag from waves and turbine motion, added mass and damping from wave radiation, and linear wave diffraction. Mooring lines are modeled as quasi-static taut or catenary lines and include the effects of stretching, mass density, buoyancy, geometric nonlinearity, and seabed interactions. Dynamic mooring line effects and mooring line drag are not included in the model (Jonkman, 2007).

5.3.1 Model Description

The degrees of freedom (DOF) of the complete wind turbine and floating platform FAST model include edgewise and flapwise blade motions, rotor rotation, driveshaft torsion, nacelle/rotor yaw, first and second modal tower-bending motions (both side-to-side and fore-aft), as well as six degrees of platform motions, including surge, sway, heave, roll, pitch, and platform yaw. Surge, sway, and heave are translations in the X, Y, and Z directions, respectively; whereas roll, pitch, and yaw are rotations about the X, Y, and Z axes, respectively. Coordinate systems and platform DOF definitions used in this study are illustrated in Figure 107.

5.3.1.1 The Spar-type Floating Wind Turbine

The Maritime Research Institute Netherlands (MARIN)/University of Maine (UMaine) scale test model and FAST full-scale, three-bladed horizontal-axis wind turbine model are based on the National Renewable Energy Laboratory's (NREL's) offshore 5-megawatt (MW) baseline wind turbine (Jonkman *et al.*, 2009). The turbine was attached to a spar buoy platform that was adapted from a spar design developed for Phase IV of the Offshore Code Comparison Collaboration (OC3), which is based on Statoil's Hywind spar (Jonkman, 2010). The spar has three equally spaced mooring lines in a water depth of 200 meters (m). The UMaine model uses a bridle system for the attachment of the three mooring lines to the spar, providing additional yaw stiffness; whereas the FAST model has a direct attachment to the

spar of each mooring line at a radius of 5.2 m and a draft of 70 m because of FAST mooring line geometrical definition limitations. Pertinent dimensions of the FAST model are given in Table 47.

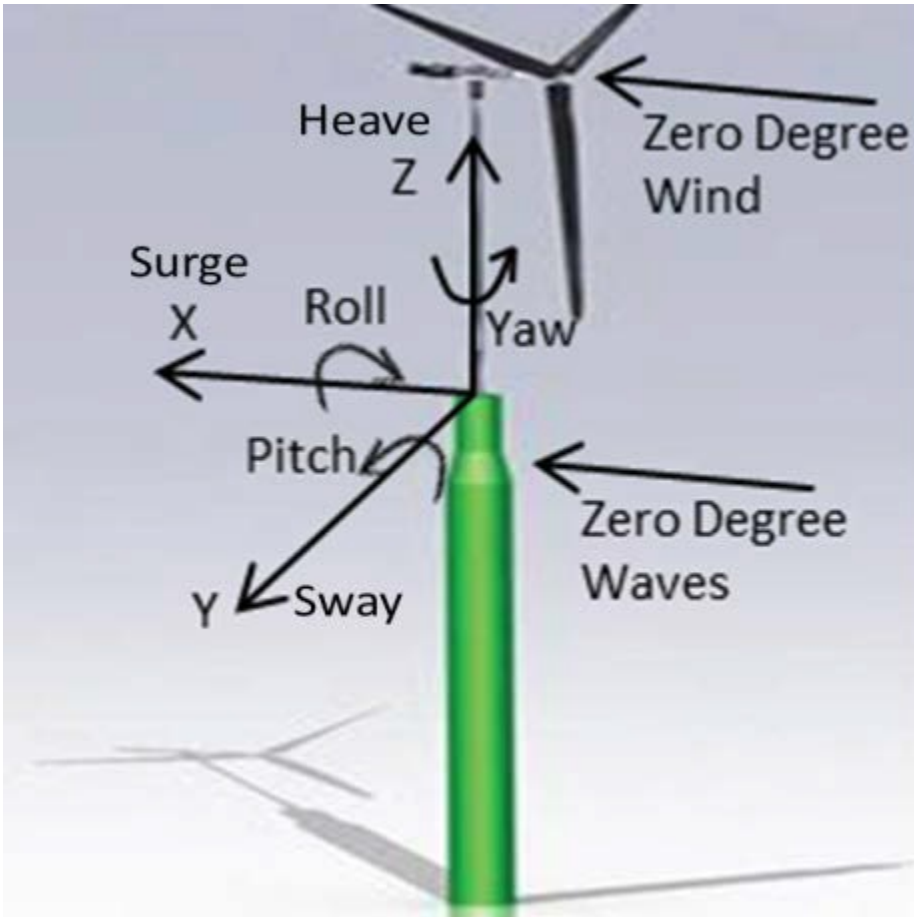

Figure 107: **Coordinate system and definitions for platform DOF used in this spar-buoy study.**

Table 47: **Dimensions of the spar type floating wind turbine model**

Hub Height [m]	90
Flexible Tower Length [m]	77.6
Blade Length [m]	61.5
Tower Top Mass [kg]	394,000
Tower Mass [kg]	303,145
Tower Base Above MSL [m]	10
Spar Length [m]	130
Spar Center of Mass Below MSL [m]	90
Spar Mass [kg]	7,280,000
Displacement Volume [m3]	7,948
Total System Mass [kg]	7,977,33

5.3.1.2 MARIN Wave Tank Testing (1/50th Scale)

Tests were carried out in MARIN's wind/wave basin on a 1/50th Froude-scaled model of the spar system built by UMaine and MARIN (Martin *et al*., 2012). Researchers conducted static offset tests, six DOF decay tests, periodic wave tests with and without wind, and combinations of stochastic wind and wave conditions. In addition, hammer tests were performed on the system to obtain fundamental modal responses. Data recorded during the tests included six platform DOF positions and accelerations; rotor torque and position; accelerations at three locations spanning the tower, forces, and moments at the tower base and tower top; and mooring line tensions. The sampling frequency was 100 hertz (Hz), corresponding to a Froude-scaled sampling frequency at full scale of roughly 14 Hz. All data from the MARIN tests were converted to full scale using Froude scaling prior to analysis (Martin, 2011). All test data provided in this spar-buoy study were presented at full scale, unless otherwise noted.

5.3.1.3 Introduction to Calibration and Validation

The FAST model was calibrated prior to validation to match the UMaine test model as closely as possible by using free-decay and periodic-wave tests (a small subset of the total experimental data available). Parameters in the FAST model were calibrated to match the test model when there was a known potential for discrepancy between the two. These discrepancies took the form of simplifications in the FAST model or simulation algorithms, or uncertainties in the characteristics of the scale test model. Once calibrated, the FAST model was validated by comparing the responses of the FAST model and test model for several tests, again including the free-decay and periodic-wave tests, with the addition of tests with irregular waves and steady wind.

5.3.2 Calibration

The parameters of the FAST model, which were calibrated prior to validation, are included in Table 48, along with a brief justification for calibration. Additionally, prior to this study, the aerodynamic coefficients of the blade were calibrated to match rotor thrust between FAST full-scale simulations and scaled-up test data because of poor aerodynamic performance of the UMaine test model resulting from Reynolds number (Re) dissimilitude (Martin, 2011).

Table 48: **FAST model parameters calibrated prior to validation with a brief reason for calibration**

Calibrated Parameter	*Justification for Calibration*
Mooring Line Mass, Stiffness, and Length	Matching the mooring system tensions in the FAST model caused by horizontal displacement to the UMaine test model; necessary because of a delta connection in the UMaine test model that was not directly modeled in FAST
Tower Stiffness	Matching of first tower vibrational mode in the FAST model to the UMaine test model because of uncertainty in its stiffness, which was altered by sensors and sensor cables
Platform Displacement at Equilibrium	Matching zero heave at equilibrium of the FAST model and the UMaine test model because of uncertainties in mooring line fairlead angle and equilibrium displacement in the test model
Platform Yaw Stiffness	Emulating the added yaw stiffness created by the UMaine mooring system's delta connections in FAST
Heave and Yaw Damping	Fixing discrepancies between the UMaine test model and the FAST model because of FAST viscous drag simplifications

5.3.2.1 Mooring System Calibration

The mooring system used in the MARIN tests consisted of three equally spaced primary mooring lines connected to the spar via delta connections that provided additional platform yaw stiffness than a single (direct) connection. Each of the three primary lines contained an inline linear spring intended to simulate the combined stiffness caused by mooring line axial stiffness and mass density of a full-scale catenary mooring line. Because FAST was not able to simulate the more complex delta connection of the UMaine test model, and because it relied on a quasi-static catenary solution (rather than an inline spring), the FAST mooring model was calibrated, as described in the following paragraph, to mimic the steady-state reaction of the MARIN model to X-direction displacements. Static offset tests were kept constant at the equilibrium value. The length, axial stiffness, and mass density of the FAST mooring lines were tuned until lines 1 and 2, at 120 and 240 degrees from the X-axis, respectively, and line 3, at zero degrees from the X-axis, matched the MARIN results for line tension at offsets of 12.4 m and at equilibrium (i.e., zero offset for all platform degrees of freedom). The anchor locations were kept fixed at a radius of 445 m for both models. The resulting line tensions at the spar connection for several offsets for the FAST model and UMaine test model are shown in Figure 108. The two models were in agreement for all offsets, with the largest discrepancy of 39 kN occurring for line 2 at an offset of 9.9 m.

5.3.2.2 Tower Calibration

The as-tested UMaine test model included an instrument cable attached to the tower and a force and moment sensor at the base of the tower of unknown stiffness. To represent the interaction of the cable and

the sensor with the structure, a single stiffness multiplier was used at all FAST tower nodes to decrease the stiffness from nominal UMaine test model design specifications. The multiplier was calibrated so that the tower's first fore-aft frequency mode matched between MARIN and FAST, as measured by a fast Fourier transform (FFT) of tower-top acceleration with the turbine operating in periodic waves. The multiplier decreased the FAST model's first tower-bending mode from 0.49 Hz to 0.42 Hz.

5.3.2.3 Platform Displacement, DOF Stiffness and Damping Calibration

Platform yaw stiffness was added to the FAST model until the yaw natural frequency matched that of the MARIN tests. The first natural frequencies in yaw for both models were measured using an FFT of a time series from a yaw decay test.

The platform draft at zero heave was reduced from the design specification value of 8,029 m3 to 7,948 m3 so that the model would float at zero heave in its equilibrium state with the calibrated mooring system.

FAST includes the capability of modeling nonlinear viscous drag on the platform in the X and Y directions via a user-specified coefficient of drag and varying platform diameter. The coefficient of drag (Cd) for the FAST spar model was calculated as the coefficient of drag for an infinite cylinder, which was determined based on the oscillatory Re of the relative water flow (Newman, 1977). Re, however, does not scale consistently with Froude scaling. Because the goal was to model the test model, the range of Re values used for calculating the appropriate Cd were based on the 1/50th-scale test data rather than the full-scale data. It was found that the likely range of Re for the scaled data corresponded to an area of low slope in a Cd versus Re curve, with a mean value of approximately 1.0. Therefore, a value of 1.0 was used for Cd in the FAST model. It should be noted that the maximum Re expected from full-scale test data (using Froude scaling) was roughly 106, corresponding to a Cd of approximately 0.6 for an infinite cylinder, thereby illustrating the importance of using Re from scale test data when approximating Cd for viscous drag for the purposes of simulating the behavior of a model-scale system.

Because viscous drag in FAST was calculated only in the X and Y directions, it had a damping effect on the surge, sway, pitch, and roll motions of the spar platform. Additional linear damping was added to the heave and yaw DOFs in the FAST model to account for damping characteristics that are currently not modeled in FAST—such as skin friction, drag on mooring lines, and the drag caused by the abrupt edge at the bottom of the spar—that would be present in the MARIN tests. During calibration, 71.0×103 N/(m/s) and 10.1×106 N·m/(rad/s) of damping were added to heave and yaw, respectively, so that the average damping ratio over several peaks from the time series of heave and yaw decay tests were consistent between FAST simulations and MARIN tests.

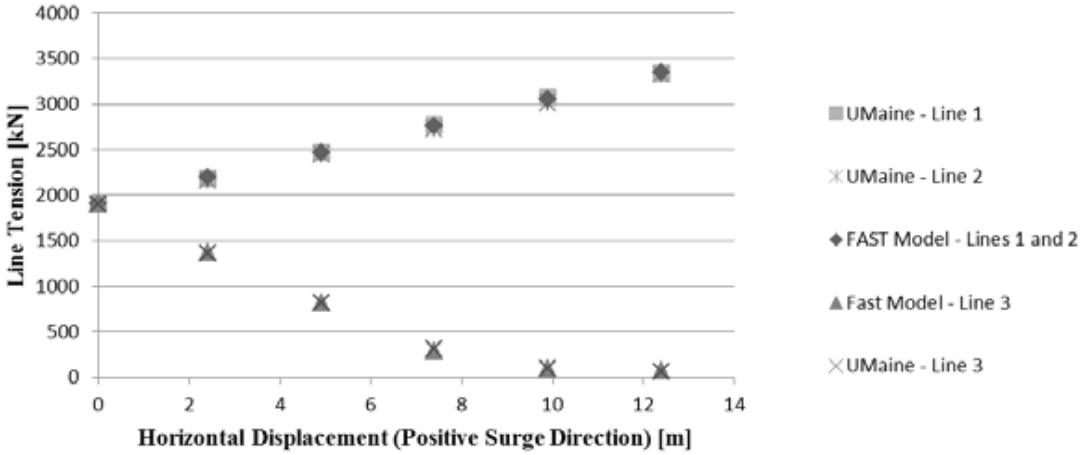

Figure 108: **Mooring line tensions at the spar connection for the FAST model and UMaine test model.**

5.3.3 Validation

After calibrating the FAST model to account for any known discrepancies between it and the UMaine test model, the FAST model was validated by comparing the results between the simulation and test for a series of tests, including free-decay tests, periodic-wave tests with no wind, and irregular-wave tests [Joint North Sea Wave Project (JONSWAP) waves] with wind.

5.3.3.1 Free-decay Tests

After calibration, damping properties and natural frequencies for the six platform DOFs were compared between the FAST model and the UMaine test model via decay tests. The tests were performed by translating or rotating the model in the direction of each of the platform DOFs and letting the model return to equilibrium. The tests were performed with no incident waves or wind and a stationary rotor. Natural frequencies were calculated by locating the dominant frequency in the FFT of the resulting free-decay time series. Figure 109 shows the resulting natural frequencies for the FAST model and UMaine test model. As described, yaw stiffness and damping, as well as heave damping, were added to the FAST model during calibration. All frequencies matched well between FAST and the UMaine test model with the exception of pitch and roll, for which FAST exhibited a noticeably lower frequency response than the MARIN test data (0.0290 Hz and 0.0315 Hz for FAST and MARIN, respectively). This lower frequency response may have been because of incorrect placement of mass along the tower during the tower mass calibration process, which would have resulted in an incorrect moment of inertia for the system and incorrect pitch and roll restoring associated with the system center of mass.

The damping ratio for the platform motions were calculated from the average ratio of successive peaks using peaks 2−9 and peaks 9−16 from the decay tests. Averages of two ranges of time series peaks were used because the FAST model included nonlinear viscous drag, which increased with the higher platform velocities that occurred with high-amplitude oscillations; whereas damping during lower amplitude oscillation was primarily because of radiation damping. The damping ratios are presented in Figure 110. Heave and yaw were consistent between FAST and the UMaine test model for peaks 9−16. The MARIN surge damping ratio increased for lower amplitude oscillations, which may have been caused by a problem with the test procedure or the average successive peak ratio analysis procedure. FAST showed self-consistency between surge and sway (small variations were caused by different initial offset values to match MARIN tests as well as the greater influence of rotor drag in the surge direction) but did not match

the MARIN test values. This inconsistency may be explained by large displacements of the mooring systems in surge and sway, leading to nonlinearities and differing behavior of the mooring systems in the FAST model and UMaine test model. This explanation would also account for the lack of self-consistency in the MARIN test data for surge and sway because the initial offset for sway was significantly larger than for surge, at 10 m and 4 m, respectively. In general, the FAST model appeared to have greater damping in surge and sway and less damping in pitch and roll relative to the UMaine model. Drag on the mooring lines was not modeled in the current version of FAST, which may have accounted for some of the discrepancy in surge and sway.

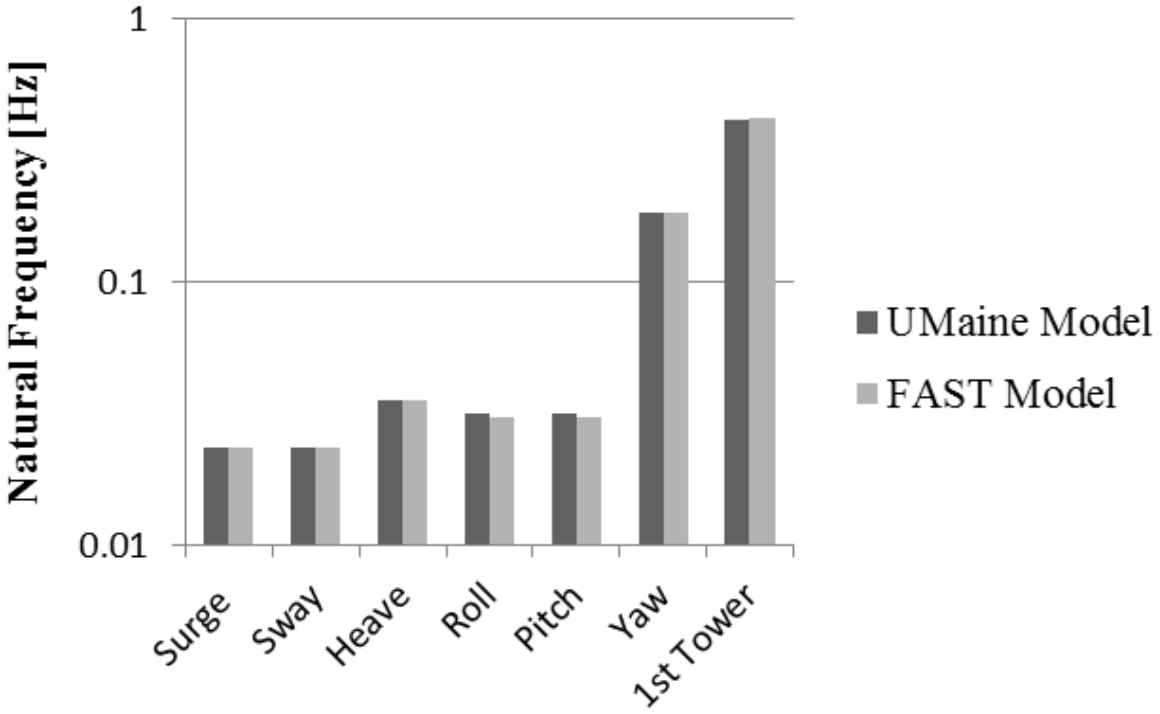

Figure 109: **Natural frequencies of platform motions for the UMaine test model and FAST model.**

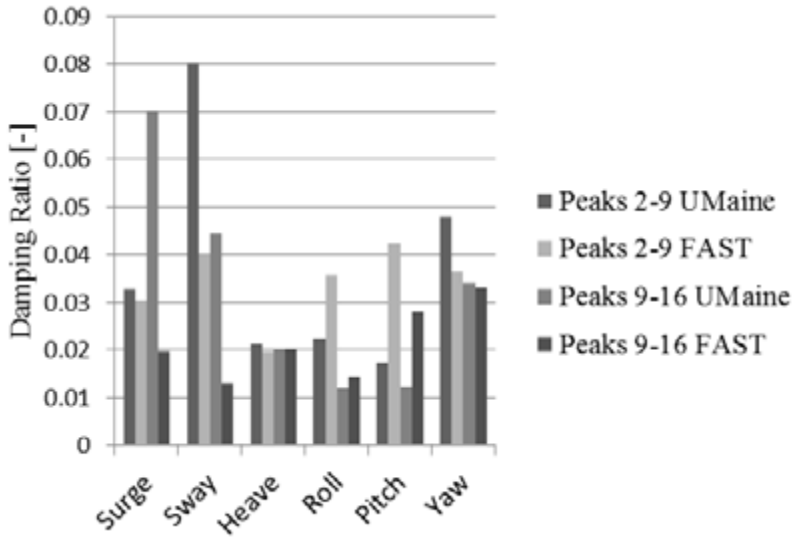

Figure 110: Average damping ratios from peaks 2−9 and peaks 9−16 of platform DOF decay tests.

5.3.3.2 Periodic Wave Tests

The results of two periodic wave tests, with wave heights of 1.92 and 7.14 m and wave periods of 7.5 and 14.3 s, were compared between the FAST model and the UMaine test model to validate the system response to a relatively simple sea state. These tests were run with no wind, a stationary rotor, and waves propagating along the positive X-axis (i.e., toward the rotor in the direction of platform surge).

Figure 111 shows the resulting power-spectral densities (PSDs) of the response to a periodic wave test with low-height (1.92 m) and low-period (7.9 s, 0.13 Hz) waves. Both heave and tower-top acceleration response at the wave frequency was consistent between the MARIN experiment and FAST simulation. The response of the tower top at the pitch frequency as well as the heave response at the heave natural frequency was stronger for the simulation than the experiment. The difference in heave response at the natural heave frequency suggested insufficient heave damping in the FAST model. However, the damping ratios in Figure 110 indicated agreement for the heave DOF. Similarly, Figure 110 indicates that pitch had greater damping in FAST than the experiment for both of the large displacements. This fails to explain the greater response of the tower top in the FAST model at the natural pitch frequency.

The PSD of the tower top X-acceleration for the experimental data showed a strong response at 0.26 Hz, which was twice the wave frequency. This could have been caused by second-order hydrodynamic excitation. The simulation did not show that this response was likely because it was not capable of modeling second-order hydrodynamic loading.

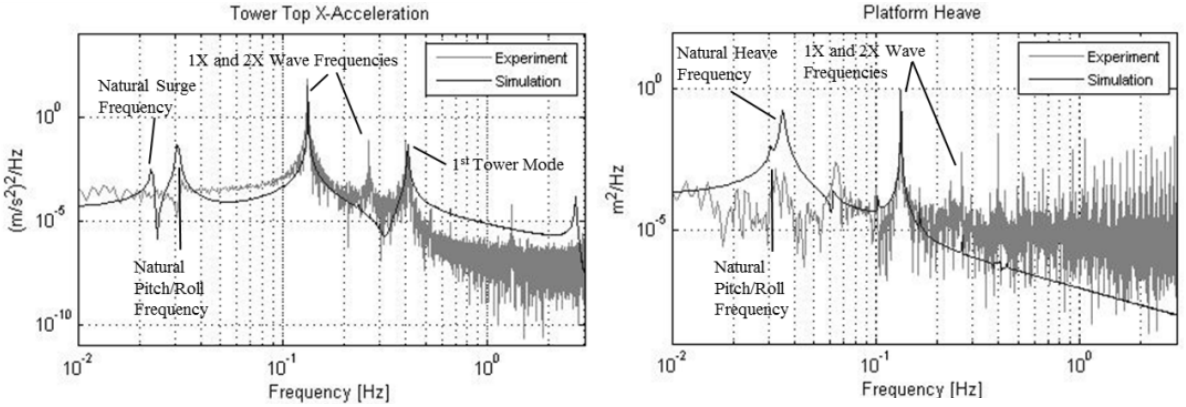

Figure 111: **Tower-top X-direction acceleration response and platform-heave response of the UMaine test model and FAST model in periodic waves with a height of 1.92 m and a wave period of 7.5 s.**

PSDs from a periodic wave test with a wave height of 7.15 m and a period of 14.3 s (0.070 Hz frequency) are shown in Figure 112. Response of both platform-heave and tower-top acceleration at the wave frequency was fairly consistent between the simulation and the experiment. However, the simulation resulted in a significantly greater tower-top response at the platform-pitch frequency than the experiment, as well as greater heave response at the heave frequency than the experiment. Again, this outcome may point toward differences in damping between the two systems that are still occurring with larger waves and platform motions and may be partially explained by damping in the UMaine test model that was caused by nonlinear drag of the mooring lines (not modeled in FAST). The MARIN test data showed large responses at two and three times the wave frequency, 0.14 Hz and 0.21 Hz, respectively; whereas the simulation showed only the 0.14 Hz response. This response was likely because of the quadratic viscous damping term in FAST, which caused a pronounced response at twice the regular wave frequency when subjected to higher waves and greater motions.

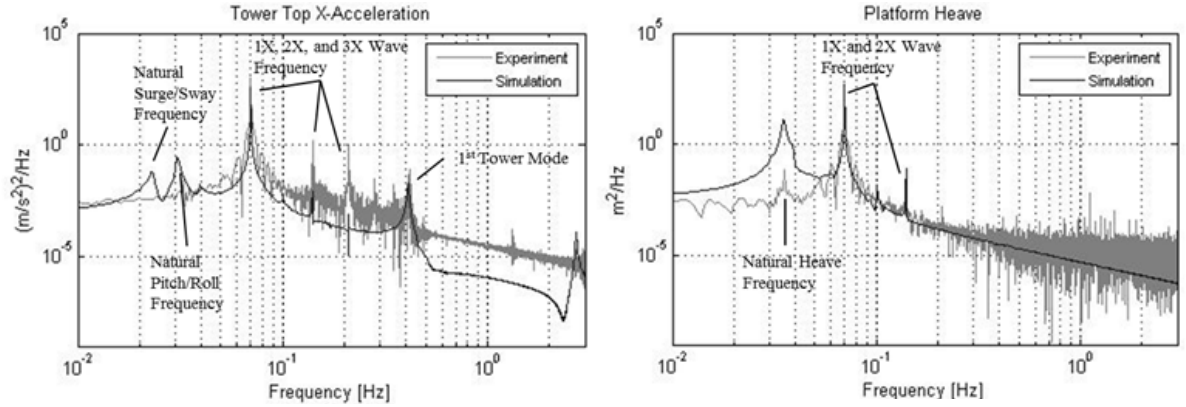

Figure 112: **Tower-top X-direction acceleration response and platform heave response of the UMaine test model and FAST models in periodic waves with a height of 7.14 m and a wave period of 14.3 s.**

5.3.3.3 Irregular Wave Tests

The MARIN spar model was tested under a variety of metocean conditions with irregular waves and steady wind. Waves in both the experiment and simulation were based on JONSWAP spectra (Jonkman,

2007). The recorded wave parameters in the experiment and wave spectra parameters in FAST were the same, and included significant wave height, peak-spectral period, peak shape factor, and propagation direction. The FAST simulation used these four parameters to produce a wave height time series that was based on the JONSWAP spectrum, which was then used in the simulation. This method resulted in sea surface elevations that were not identical in time, but had more consistent spectra than the MARIN tests.

The first irregular wave test used for validating the FAST model consisted of a significant wave height of 2 m, a peak-spectral period of 7.5 s (0.133 Hz), and a shape factor of 2.0. The steady horizontal wind speed was 11.23 meters per second (m/s) and the rotor was kept at a constant speed of 7.8 rpm (0.13 Hz). The wave direction was zero degrees (i.e., propagation was toward the downwind side of the turbine). Figure 113 shows PSDs of the moment about the Y-axis at the base of the tower, and the tower-top acceleration in the X direction. Both plots show a similar response shape within the region of the JONSWAP wave frequencies (roughly 0.009 to 0.035 Hz) between both measurements and between the experiment and simulation, as expected because of the influence of the tower-top motions on the tower-base moments. The response of the tower-top acceleration at the platform-pitch frequency was also similar between the experiment and simulation. It would be expected that similar tower-top motion spectra in the vicinity of the platform-pitch frequency would translate into similar tower-base moment spectra in that frequency range. However, it can be seen in Figure 113 that the magnitude of the tower-base moment response was somewhat larger for the FAST simulation than the experiment at the platform-pitch frequency (0.030 Hz). This outcome may have been caused by an incorrect tower/nacelle/rotor system rotational inertia, and thus a larger moment at the base for a given tower-top acceleration. This would also account for the lower pitch natural frequency for the FAST model than in the MARIN experimental model previously noted.

In both spectra, the experimental data showed prominent peaks at the blade-passing frequency (3P) of 0.39 Hz, as well as the first two blade-passing frequency harmonics (6P and 9P). Although an effort was made to produce a low turbulence and constant wind field over the rotor area for the experiments, wind calibration results showed both vertical and horizontal variation in wind velocity, with a minimum wind speed measured across the rotor of roughly 70% of the maximum. The prominent 3P, 6P, and 9P peaks may be because of these inconsistencies in wind velocity over the rotor. In comparison, the FAST simulations (for these tests) modeled wind velocity as a constant wind field over the rotor area; thus, for this experiment, the spectra did not exhibit pronounced peaks at the blade-passing frequency or its harmonics. FAST does include the capability for modeling wind fields with horizontal and vertical shear. These effects may be examined in the future.

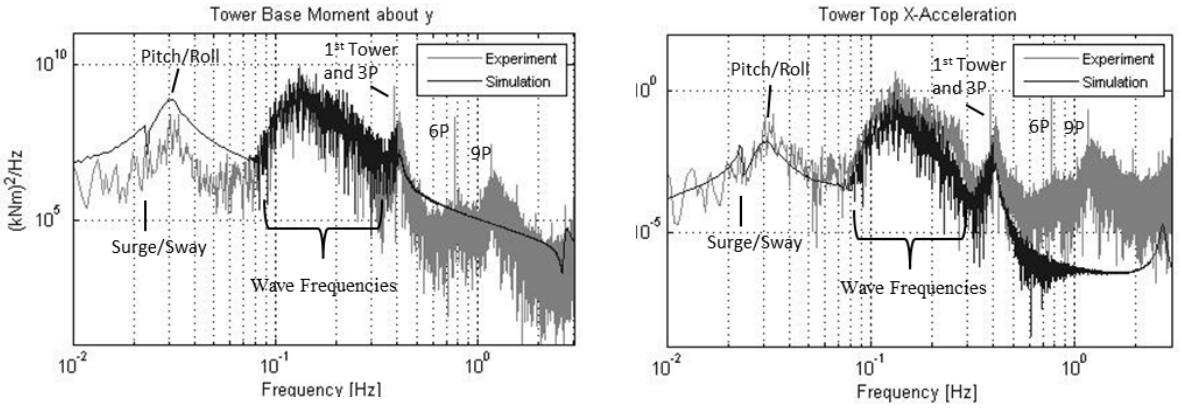

Figure 113: **Response in irregular waves of significant wave height, peak-spectral period, and shape factor of 2 m, 7.5 s, and 2.0, respectively. The horizontal wind speed was 11.23 m/s and the rotor speed was 7.8 rpm.**

The next irregular wave test used for validation consisted of an increased wave height and peak-spectral period of 7.1 m and 12.1 s (0.083 Hz), respectively. The shape factor increased to 2.2 and the wind velocity and rotor speed were kept the same as the previous test, at 11.23 m/s and 7.8 rpm (0.13 Hz). As pitching motions increased, it was expected that yaw-pitch coupling would be present because of rotor gyroscopic forces. Figure 114 shows that the tower-top X-accelerations increased with the higher height and longer period waves relative to the previous test shown in Figure 113. As shown in the PSD of the yaw response, the simulation data showed the expected pronounced peak corresponding to the model's natural platform-pitch frequency. However, rather than having a peak at the pitch frequency, the experimental data has a peak that corresponds with the natural heave frequency of 0.036 Hz. Another clear discrepancy was in the experimental peak yaw response at 0.08 Hz, or roughly the peak spectral wave frequency, which shifted to the right for the simulation response. The reason for these discrepancies is currently unknown. FAST currently utilizes the Massel wave cut-off frequency criterion, for which the JONSWAP wave spectra is truncated at three times the peak-spectral frequency (Jonkman, 2007).

An irregular wave test designed to emulate a survival condition was performed. The wave height and period were increased to 10.5 m and 14.3 s (0.070 Hz), respectively. Constant horizontal wind velocity was increased to 21.8 m/s and the rotor speed was increased to 12.7 rpm (0.21 Hz). The waves propagated at a 45-degree angle to the X-axis; the wind direction stayed at zero degrees.

The X and Y tower-top accelerations, shown on the left-hand side of Figure 115, showed agreement between them as well as between the experimental and simulation data. Unlike previous tests, a distinct peak was present at the 3P frequency for both the experiment and the simulation in both the X- and Y-acceleration plots. The presence of this 3P response in the simulation may have originated from the oblique 45-degree wave propagation direction. A noticeable discrepancy between the experiment and the simulation was the large 6P peaks in the X- and Y-acceleration PSDs that occurred only for the experimental data. Again, this discrepancy was likely caused by variations in wind speed over the rotor for the UMaine test model. Pure vertical shear produces 3P excitations because each blade passes through a high and low wind speed region of the rotor plane once per revolution. Other non-uniformities in the wind field will result in 6P excitations. More complex variations, as were observed during the wind calibration process at MARIN, could result in a noticeable response at higher order multiples of 3P. Although 3P response may occur in the simulation data because of platform pitching and the resulting misalignment between the rotor plane and the wind vectors, higher order responses will not be present because of the constant wind field modeled in the simulation.

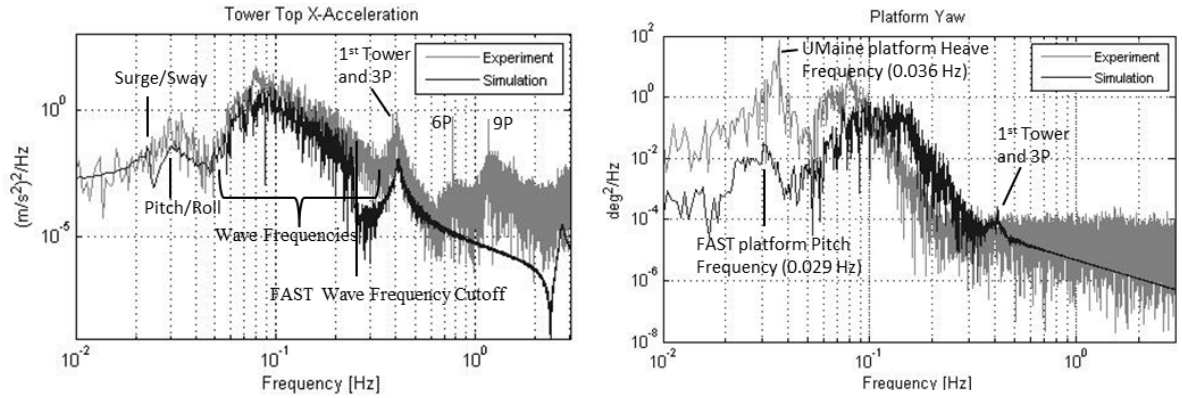

Figure 114: **Response in irregular waves of significant wave height, peak-spectral period, and shape factor of 7.1 m, 12.1 s, and 2.2, respectively. The horizontal wind speed was 11.23 m/s and the rotor speed was 7.8 rpm.**

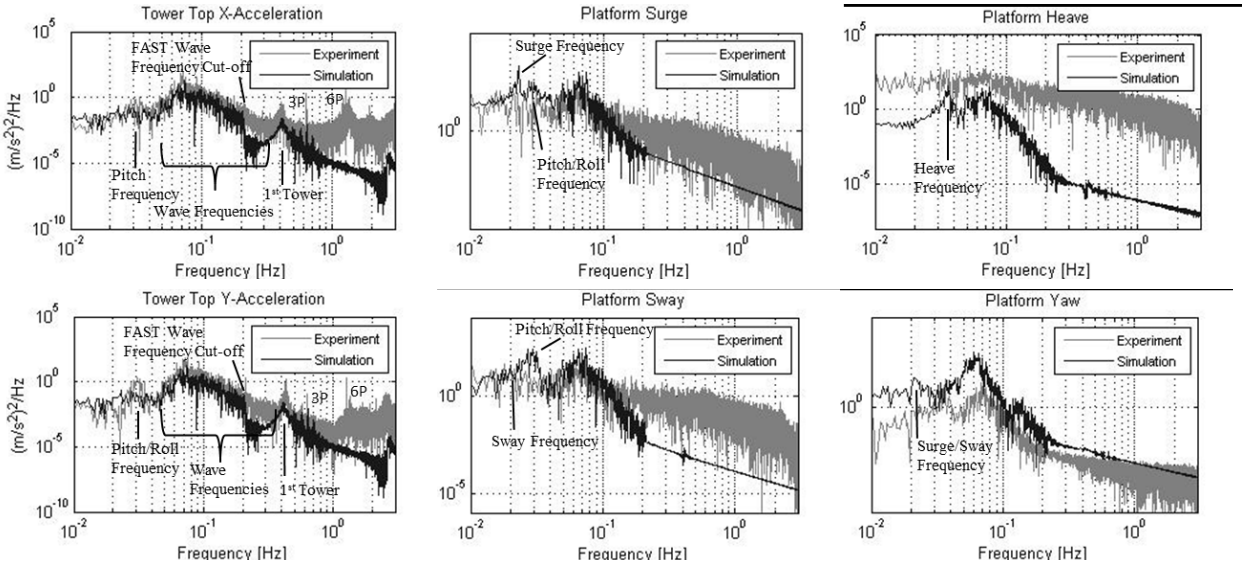

Figure 115: **Response in irregular waves of significant wave height, peak-spectral period, and shape factor of 10.5 m, 14.3 s, and 3.0, respectively. The horizontal wind speed was 21.8 m/s and the rotor speed was 12.7 rpm.**

As with the X and Y tower-top accelerations, surge and sway responses in Figure 115 show agreement between them as well as between the two experimental and simulation data in the range of wave frequencies. However, the simulation data has a distinct peak in surge response, at 0.023 Hz, and in sway, at 0.028 Hz, neither of which were apparent in the experimental data. The 0.023-Hz surge response was easily identified as the FAST model surge/sway natural frequency.

The UMaine test model demonstrated significantly greater response than the FAST model in the region of wave frequencies for heave; the opposite was true for yaw response.

5.4 Improvement of FAST Simulations

In addition to the calibration and validation work shown in the previous sections, further FAST validation of the TLP floating wind turbine system has been performed and is documented in (Prowell *et al.*, 2013). Aside from this continued FAST validation effort, improved and alternate versions of FAST have also been studied. These studies invariably investigate either improved hydrodynamic or mooring capabilities for FAST as these areas possess the most room for improvement. In (Koo *et al.*, 2013), FAST is coupled with Technip's MLTSIM hydrodynamics and dynamic mooring code to perform analysis of the TLP floating wind turbine yielding improved correlation with experimental data. In (Masciola et al., 2013), FAST is linked with the commercial floating structure code OrcaFlex and the semi-submersible system is analyzed. The results show improved correlation, particularly for mooring line tensions, when comparing the simulation and test data. In the next sections, another study investigating improvements to FAST is investigated. This study revisits the semi-submersible validation work given in previous sections and includes the second-order wave-diffraction forces neglected in the standard version of FAST to investigate the importance of including these effects for the purposes of obtaining quality simulation results.

5.4.1 Model Description

In this section, a brief description of the DeepCwind semi-submersible floating wind turbine is presented. In addition, a short discussion on tuning the FAST model with key pieces of test data is also given. This

tuning is required to account for unknown test parameters and some imperfections in the numerical model. Figure 116 depicts the degrees of freedom (DOF) and the general wind and wave orientations used in this study.

Froude scaling (e.g. see (Chakrabarti, 1994)) was employed to create a 1/50th-scale model of the DeepCwind semi-submersible, shown in Figure 117, in addition to an assortment of scaled environmental conditions, for testing in the Maritime Research Institute Netherlands (MARIN) offshore basin. The properties of the DeepCwind semi-submersible, and the corresponding test results discussed in this study, are all presented at full scale. More information on the specific scaling methods employed for the DeepCwind tests can be found in (Martin *et al.*, 2012; Jain *et al.*, 2012).

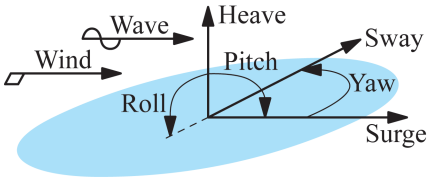

Figure 116: Depiction of degrees of freedom, wind orientations and wave orientations.

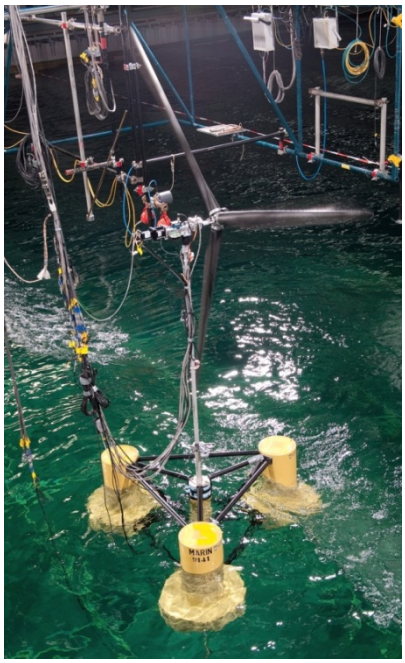

Figure 117: Image of 1/50th-scale model of the DeepCwind semi-submersible floating wind turbine.

As illustrated in Figure 117, the DeepCwind semi-submersible floating platform consists of three outer columns connected through a series of slender pontoons and braces to a central column. The platform, which was designed to be rigid, supports a modified version of the NREL 5-MW reference wind turbine (Jonkman *et al.*, 2007). The wind turbine modifications include zero blade precone, zero shaft-tilt, a slightly larger mass, and finally, rigid blades to eliminate the aero-elastic complexities of flexible blades during testing. The wind turbine is connected to the platform via a flexible tower. The entire system is moored via three slack, catenary lines attached to the outer columns. An overview of key system properties is given in Table 49, Table 50 and Table 51. Wind turbine and tower properties are given in Table 49, floating platform properties in Table 50, and mooring properties in Table 51. Additional information on system properties, such as platform geometry, hydrodynamic parameters, and mooring

restoring forces, can be found in (Coulling *et al.*, 2013; Koo *et al.*, 2012). Information on the model wind turbine performance is detailed in (Coulling *et al.*, 2013; Martin *et al.*, 2012).

Table 49: Wind turbine and tower gross properties

Rotor Orientation, Configuration	Upwind, 3 Blades
Rotor, Hub Diameter	126.0 m, 3.0 m
Hub Height Above Still-water Line (SWL)	90.0 m
Height of Tower-Top Flange Above SWL	87.6 m
Overhang, Shaft Tilt, Precone	10.58 m, 0°, 0°
Vertical Distance Along Tower Centerline Between Tower Top and Shaft	2.4 m
Total Tower-Top Mass	397,160 kg
Tower Height	77.6 m
Tower-Base Elevation Above SWL	10.0 m
Total Tower Mass	302,240 kg

Table 50: Floating platform gross properties

Total Draft	20.0 m
Elevation to Platform Top (Tower Base) Above SWL	10.0 m
Platform Mass, Including Ballast	13,444,000 kg
Displacement	13,986.8 m^3
Center of Mass (CM) Location Below SWL Along Platform Centerline	14.4 m
Platform Roll Inertia About CM	8.011×10^9 kgm^2
Platform Pitch Inertia About CM	8.011×10^9 kgm^2
Platform Yaw Inertia About Platform Centerline	1.391×10^{10} kgm^2

Table 51: Mooring system properties

Number of Mooring Lines	3
Angle Between Adjacent Lines	120°
Depth to Anchors Below SWL (Water Depth)	200.0 m
Depth to Fairleads Below SWL	14.0 m
Radius to Anchors from Platform Centerline	837.6 m
Radius to Fairleads from Platform Centerline	40.868 m
Unstretched Mooring Line Length	835.5 m
Equivalent Mooring Line Mass in Water	108.63 kg/m
Equivalent Mooring Line Cross Section Extensional Stiffness	753.6×10^6 N

As a final step in the completion of the FAST floating wind turbine model, certain aspects of the model must be tuned. These include wind turbine aerodynamics, tower-bending dynamics, and platform hydrodynamic damping. Tuning of the wind turbine aerodynamics is required to emulate the correct wind turbine torque, and more importantly, the thrust because this is the major aerodynamic global response

driver, under multiple tip-speed ratios. The tuning is performed through a numerical optimization procedure that tailors the wind blade airfoil section lift and drag coefficients, initially created with XFOIL (Drela, 1989), to match the experimentally measured wind turbine performance. A comparison of the measured and tuned wind turbine thrust curves for a steady hub-height wind speed of 21.80 m/s is given in Figure 118. A complete summary of the wind turbine performance tuning is covered in (Stewart *et al.*, 2012; Coulling *et al.*, 2013).

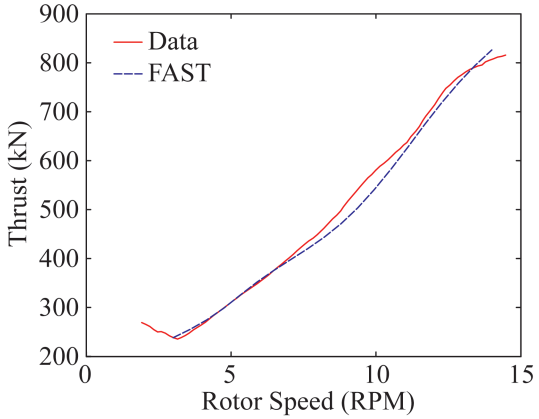

Figure 118: Comparison of wind turbine thrust data and calibrated FAST results under a steady wind of 21.80 m/s.

Next, the tuning of the FAST tower inputs is discussed. After generating and inputting the distributed tower properties and finite-element-method-generated tower mode shapes required for FAST simulations, FAST's modal stiffness tuners (Jonkman and Buhl, 2005) were altered to match the experimentally measured, fundamental tower-bending frequencies. This process, detailed in (Coulling *et al.*, 2013), yields fundamental tower-bending frequencies in the fore-aft and side-side directions of 0.35 Hz and 0.38 Hz respectively.

To complete the tuning of the FAST model, a quadratic hydrodynamic drag damping model is added to the FAST model to account for the omitted viscous drag, and the coefficients are tuned to emulate rigid-body motion, free-decay experimental results. The tuning of the drag model, which augments the radiation damping found in the standard version of FAST, is documented in (Coulling *et al.*, 2013). Because the surge response is of primary concern in this work, a comparison of the surge DOF damping ratio as a function of amplitude from experiments and the tuned FAST model is given in Figure 119. The surge quadratic-drag damping coefficient employed in (Coulling *et al.*, 2013) (1.25×10^6 Ns^2/m^2) corresponds to the simulation in Figure 119, which correlates well with the test data for modest surge amplitude motions (1.5 to 3.5 m). In this work, as will be discussed in a later section, a mild, operational sea state is considered wherein the quadratic-drag damping coefficient used in (Coulling *et al.*, 2013) tends to over-predict the surge damping for the small surge motions the sea produces. Therefore, a second surge quadratic-drag damping coefficient will be investigated that is 10% of that used in (Coulling *et al.*, 2013) (1.25×10^5 Ns^2/m^2). The free decay simulation corresponding to this reduced surge drag damping coefficient is also shown in Figure 119. As can be seen in the figure, the reduced quadratic-drag coefficient produces a better fit to the experimental data for surge amplitudes of 1 m or less.

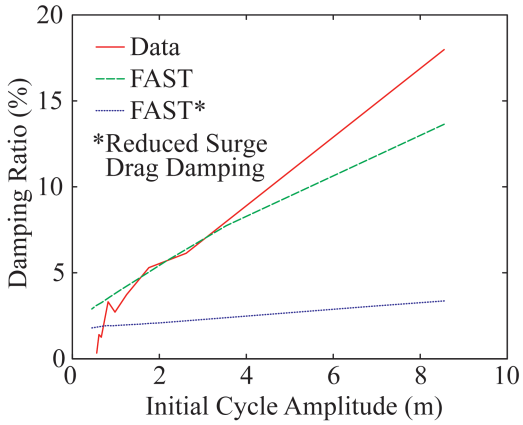

Figure 119: Comparison of surge free-decay damping response from test data and FAST simulations.

To complete this section, a comparison of the rigid-body natural periods as obtained from test data and FAST simulations is given in Table 52. As the table shows, there is good agreement between the test data and FAST predictions.

Table 52: Rigid-body natural periods obtained from test data and FAST simulations.

DOF	Data (s)	FAST (s)
Surge	107	107
Sway	112	113
Heave	17.5	17.3
Roll	26.9	26.7
Pitch	26.8	26.8
Yaw	82.3	82.7

5.4.1 Second-order Difference-Frequency Wave-diffraction Force Formulation

In the current standard version of FAST, the true linear time-domain hydrodynamics are implemented (Jonkman and Buhl, 2005). This formulation, however, omits the nonlinear, second-order wave diffraction effects that occur at the sum and difference of the frequency components in the incident waves (e.g., see (Kim and Yue, 1991)). As observed in (Goupee *et al.*, 2012 OTC; Koo *et al.*, 2012; Goupee *et al.*, 2012), the second-order difference-frequency wave-diffraction forces are important for properly simulating the global response of the DeepCwind semi-submersible. In this study, these second-order wave-diffraction forces are included in the custom FAST tool in order to assess the importance of including these effects in validating the DeepCwind semi-submersible numerical model. The remainder of this section outlines the formulation of the second-order wave-diffraction force implementation that is employed in the custom FAST tool.

To begin, we note that the time-varying wave-surface elevation $h(t)$ can be written as the sum of its wave frequency components in the form

$$h(t) = Re \sum_{n=1}^{N} a_n e^{i\omega_n t},$$

where N is the number of frequency components, a_n is the n^{th} complex-valued wave component amplitude (including phase), ω_n is the n^{th} wave component frequency, t is time and i is imaginary unity.

With the coefficients a_n in the above equation obtained from a simple discrete Fourier transform analysis of the experimentally measured calibrated wave-elevation time series, the second-order difference-frequency wave diffraction force $F_j^D(t)$ can be computed with the equation (e.g., see (Langley, 1986))

$$F_j^D(t) = Re \sum_{n=1}^{N} \sum_{m=1}^{N} a_n a_m^* D_{nm}^{(j)} e^{i(\omega_n - \omega_m)t},$$

where $D_{nm}^{(j)}$ is the complex difference-frequency second-order transfer function for the j^{th} DOF and the superscript * denotes the complex conjugate. As shown in (Langley, 2012), the above equation is often separated into terms that are constant (mean-drift force) and those that are not (slowly-varying force). This is accomplished by first separating the preceding equation into three regions: $n = m$, $n > m$, and $n < m$. Upon setting $k = n - m$, noting that $D_{nm}^{*(j)} = D_{mn}^{(j)}$, and performing a series of straightforward manipulations, the desired result is produced:

$$F_j^D(t) = \sum_{n=1}^{N} |a_n|^2 D_{nn}^{(j)} + Re \sum_{k=1}^{N-1} X_k^{(j)} e^{i\omega_k t},$$

where the first term is the mean-drift force, the second is the slowly varying force and $X_k^{(j)}$ is computed as

$$X_k^{(j)} = 2 \sum_{m=1}^{N-k} a_{m+k} a_m^* D_{m+k,m}^{(j)} e^{i\omega_k t}.$$

For implementation in the custom FAST tool, only those second-order wave diffraction forces associated with the surge DOF ($j = 1$) are included because they are the most prominent second-order wave-diffraction forces for the DeepCwind semi-submersible.

To carry out the calculation of $F_j^D(t)$, the quantities $D_{nm}^{(j)}$ must be obtained. To determine the coefficients $D_{nm}^{(j)}$, use is made of the mean-drift coefficients $D_{nn}^{(j)}$ derived from a first-order WAMIT analysis (Lee and Newman, 2006) in conjunction with Newman's approximation (Newman, 1974). The particular formulation used is that developed in (Standing *et al*., 1987), which approximates $D_{nm}^{(j)}$ from $D_{nn}^{(j)}$ using the relation

$$D_{nm}^{(j)} =$$

$$\begin{cases} sgn\left(D_{nn}^{(j)}\right)\sqrt{\left|D_{nn}^{(j)} D_{mm}^{(j)}\right|} \; if \; sgn\left(D_{nn}^{(j)}\right) = sgn\left(D_{mm}^{(j)}\right) \\ 0 \; if \; sgn\left(D_{nn}^{(j)}\right) \neq sgn\left(D_{mm}^{(j)}\right) \end{cases},$$

where $sgn(\cdot)$ indicates the sign (either positive or negative) of the argument. It is worth stating that it would be best if $D_{nm}^{(j)}$ were computed from a second-order WAMIT analysis. However, Newman's approximation is justified for this work for the following two reasons:

1. Performing the second-order WAMIT analysis requires significant computational expense, whereas computing the coefficients $D_{nn}^{(j)}$ requires solution of only the first-order wave-diffraction problem.

2. Assuming that the second-order transfer function $D_{nm}^{(j)}$ is continuous, and also assuming that only slowly-varying loads associated with resonance of the surge DOF (natural frequency of 0.0093 Hz) are important (i.e., only $D_{nm}^{(j)}$ near the diagonal $D_{nn}^{(j)}$ terms need be approximated accurately).

Therefore, Newman's approximation should yield suitable results for the DeepCwind semi-submersible study conducted here.

To complete this section, the magnitude of the approximated second-order transfer function $D_{nm}^{(1)} = D^{(1)}(\omega_1, \omega_2)$ is shown via a surface plot in Figure 120.

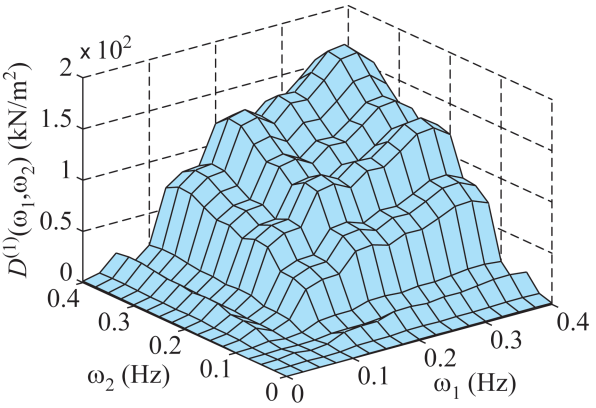

Figure 120: Surface plot of the $D^{(1)}(\omega_1, \omega_2)$ second-order difference-frequency transfer function.

5.4.2 Environmental Conditions

To investigate the impact of including second-order difference-frequency wave-diffraction forcing in FAST for analyzing the DeepCwind semi-submersible, a particular wind and wave condition is chosen. The details of these environmental conditions comprise the remainder of this section.

In this analysis, the chosen wind condition is temporally dynamic and follows a Norwegian Petroleum Directorate (NPD) (API, 2000) spectrum. In the basin, the mean wind speed at the hub height was U_m = 20.6 m/s, the standard deviation was 2.04 m/s, the maximum wind speed was 28.7 m/s, and the minimum wind speed was 12.9 m/s. This wind is chosen because it produces thrust loads similar to those experienced in the rated wind speed condition of the NREL 5-MW reference wind turbine when paired with the low thrust coefficient turbine employed in the wind/wave basin tests (Martin *et al*., 2012).

For the purposes of simulation, FAST hub-height wind files are employed which possess a constant spatial variation in wind profile, albeit, wind speed magnitudes that are time-varying. Based on surveys of the wind-generation machine output, which were recorded in the wind/wave basin (Goupee *et al*., 2012 OTC; Koo *et al*., 2012), the FAST hub-height wind file is created by multiplying the measured hub-height velocity by 0.952 and employing a wind shear exponent of 0.0912. The tested wind field possessed some spatial variation in wind speed. Hence, these hub-height wind file choices yielded the best possible representation of the wind field utilized during testing, using only the simple hub-height wind file option in the FAST simulations. The spectrum of the NPD wind used in this study is given in Figure 121.

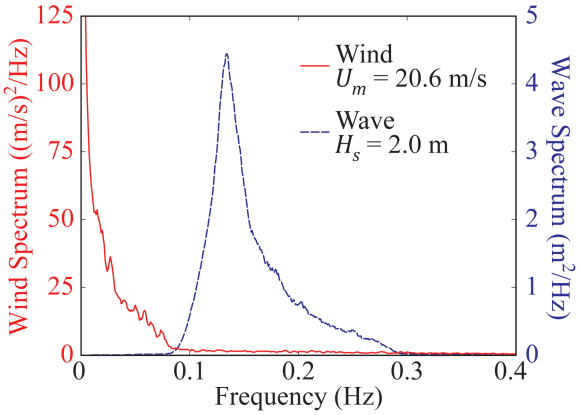

Figure 121: Spectra for the U_m = 20.6 m/s NPD dynamic wind and H_s = 2.0 m JONSWAP wave conditions.

Regarding the wave condition, an operational sea with a significant wave height of H_s = 2.0 m and a peak-spectral period of T_p = 7.5 s following a Joint North Sea Wave Project (JONSWAP) (IEC, 2009) spectrum is chosen for this work. This condition is selected because it produced large responses associated with the second-order difference-frequency wave-diffraction forces relative to those caused by the linear wave forces. In addition, this sea state will produce wave loadings that are in decent proportion to the wind loads expected with the chosen wind, based on typical joint probabilities (e.g., see (Jonkman, 2007)). For the waves tested in the basin, the wave-elevation standard deviation was 0.49 m, the maximum crest 2.14 m, the minimum trough 1.87 m and the maximum wave height 3.64 m. The spectrum of the JONSWAP wave considered here is given in Figure 121.

5.4.3 Wave-only Comparisons

In this section, the calibrated FAST model is used to simulate the response of the DeepCwind semi-submersible subjected to the H_s = 2.0 m sea state in the absence of wind. Because there is no wind, the wind turbine rotor is parked (0 rpm) and the blades are feathered. Simulations are conducted with and without the inclusion of the second-order difference-frequency wave-diffraction forces and compared to test data. All simulations are 3 hr. in length with 1000 s of additional settling-in time prior to recording data. This timing is similar to the actual model tests, which were 3 hr. in length with 1800 s of settling-in time.

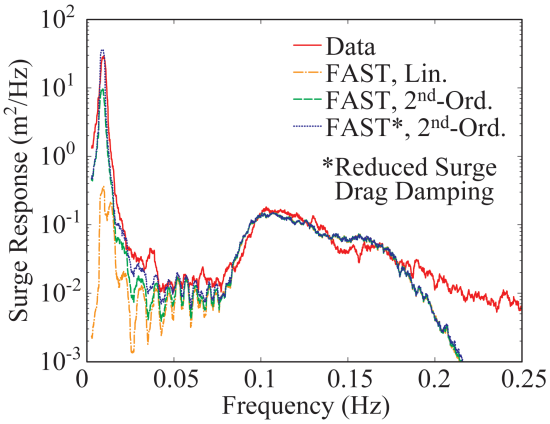

Figure 122: Comparison of surge frequency-domain response from test data and three different FAST simulations.

A comparison of the surge frequency-domain response, computed as a power spectral density, is given in Figure 122 for the test data and three different FAST simulations. The FAST simulations consist of a standard analysis with linear wave-diffraction wave forces, an analysis including the second-order difference-frequency wave-diffraction forces, and lastly, another analysis including the second-order wave forces, albeit with a reduction in the surge quadratic-drag model coefficient to 10% of the initial calibrated value from (Coulling *et al*., 2013). Noting that the ordinate axis is displayed on a logarithmic scale, it is clearly seen by the test data shown in Figure 122 that the low-frequency response at the rigid-body surge natural frequency (0.0093 Hz) dominates the entire surge response of the system. When comparing the test data to the FAST analyses, it is evident that the FAST model that uses only linear wave-diffraction forcing severely under-predicts the low-frequency response of the system. Including the second-order difference-frequency wave-diffraction forces improves the correlation between the simulation and test data significantly, as seen in Figure 122. However, because the large response is created via resonance with relatively small second-order wave loads, the magnitude of the response at the surge natural frequency is highly dependent on the damping employed in the FAST model. As seen in Figure 122, the model using the calibrated surge drag model coefficient of (Coulling *et al*., 2013)under-predicts the response near surge resonance. Utilization of the reduced quadratic-drag model damping coefficient, which was discussed in the Model Description section, yields simulation results that compare much better with experimental values, as shown in Figure 122. The final observation to be made from Figure 122 is that the test data and all simulations correspond well with one another in the wave-energy frequency range (approximately 0.1 Hz to 0.3 Hz shown in Figure 121). Although there is some discrepancy at frequencies higher than 0.2 Hz, the magnitude of the response is much lower and the error appears larger due to the log scaling.

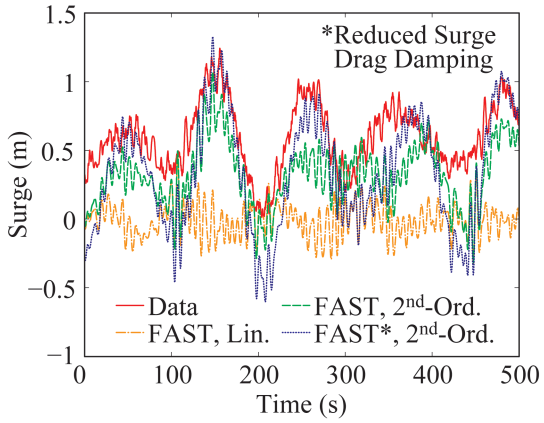

Figure 123: Comparison of surge time-series response for 0 to 500 s from test data and three different FAST simulations.

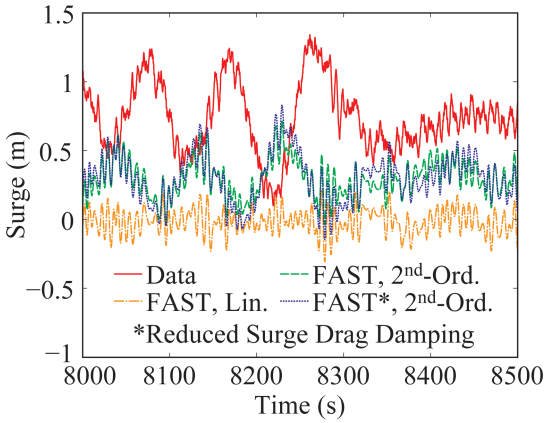

Figure 124: Comparison of surge time-series response for 8000 to 8500 s from test data and three different FAST simulations.

To continue the wave-only comparison, Figure 123 and Figure 124 show two examples of surge response time-series comparisons between the test data and various FAST simulations for the same H_s = 2.0 m sea state. As can be seen in the figures, the inclusion of the second-order difference-frequency forces greatly improves the correlation between the test data and simulations. This stated, the simulations that include the second-order wave-diffraction effects using Newman's approximation do not always capture the appropriate local time-domain response that is measured in the basin. As can be seen in Figure 123, the FAST simulation over-predicts the amplitude of the second-order response in the noted time range 0 to 500 s, and in Figure 124, the FAST simulation under-predicts the second-order wave-diffraction-associated response and predicts the incorrect phase of this response in another time range (8000 to 8500 s) of the same simulation.

As a next step in this wave-only simulation discussion, the statistics for the surge response from the test data and three simulations is given in Table 53. As shown in the table, without inclusion of the second-order difference-frequency wave-diffraction forces, very poor predictions of the surge behavior are obtained.

Table 53: Surge motion statistics for the wave-only case.

Statistic	Data	Linear	2nd-Ord.	2nd-Ord.*
Mean (m)	0.735	0.000	0.307	0.307
Std. Dev. (m)	0.354	0.103	0.218	0.343
Max. (m)	2.200	0.486	1.137	1.385
Min. (m)	-0.507	-0.382	-0.378	-0.711
Range (m)	2.707	0.868	1.515	2.096

*Reduced Surge Drag Damping

For the simulation using only linear wave-diffraction forces, the mean surge is zero, and the standard deviation and range of the surge DOF over the simulation are only 29.1% and 32.1% of those measured from the test. For the best simulation, which includes the reduced surge quadratic-drag damping coefficient, the surge mean, standard deviation, and range are 42.3%, 96.9%, and 77.4% of the experimental values, respectively.

To complete the wave-only comparison, the response of the upwind mooring line (which lies along the negative surge axis) fairlead tension is investigated. Figure 125 compares the test data and the three FAST simulations for the fairlead tension in the frequency domain. Table 54 compares the fairlead tension statistics of the test data and three simulations. As can be seen in Figure 125, the frequency-domain fairlead tension comparison is similar to the surge comparison at low frequencies.

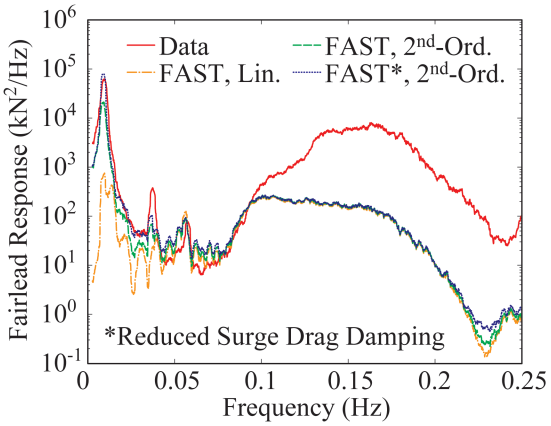

Figure 125: Comparison of upwind mooring line fairlead tension response from test data and three different FAST simulations.

Table 54: Upwind fairlead tension force statistics for the wave only case.

Statistic	Data	Linear	2nd-Ord.	2nd-Ord.*
Mean (kN)	1161	1105	1120	1120
Std. Dev. (kN)	18.6	4.7	10.1	16.0
Max. (kN)	1247	1128	1160	1173
Min. (kN)	1097	1089	1090	1075
Range (kN)	150.0	39.0	70.0	98.0

*Reduced Surge Drag Damping

This indicates that the mooring tension response is accurately predicted for the DeepCwind semi-submersible at low frequencies if the second-order difference-frequency wave-diffraction forces are

included. However, the fairlead tension response in the linear wave-energy frequency range is significantly under-predicted. This is theorized to be a product of using a quasi-static catenary line solver in FAST (Jonkman, 2007), which ignores mooring line dynamics and direct wave particle excitation. The interplay of improved low-frequency prediction and poor linear wave-energy frequency range simulation is captured in the statistics of Table 54. For the best simulation, which includes second-order wave-diffraction loads and a reduced quadratic-drag damping coefficient, the standard deviation and range are 86.0% and 65.3%, respectively, of the experimental values. While these are improvements compared to the simulation that includes only linear wave loads, these improvements are less than what was found for the surge response earlier in this section.

5.4.4 Combined Wind/Wave Comparisons

With the wave-only comparisons complete, this section describes the investigation of the interaction of the dynamic wind and second-order difference-frequency wave-diffraction loads, both of which influence the global response of the floating structure at low frequencies. The investigation will be conducted by comparing the response of the DeepCwind semi-submersible subjected to the following conditions: NPD wind-only, the irregular wave-only, and the simultaneous application of the wind and wave. Note that the U_m = 20.6 m/s dynamic wind and H_s = 2.0 m irregular wave are detailed in the Environmental Conditions section. For tests and simulations with wind, the rotor blade pitch is fixed in the operational position and the rotor speed is held constant at 12.7 rpm. For the test and simulations without wind, the blades are feathered and the rotor is parked. Finally, all simulations use the reduced surge quadratic-drag damping coefficient of 1.25×10^5 Ns^2/m^2.

Figure 126 depicts the frequency-domain surge response of the wind-only, wave-only and combined wind and wave case as computed from the model test data. As can be seen by comparing the combined condition case to the other two scenarios in the figure, the dynamic wind loads control the response of the DeepCwind semi-submersible for frequencies less than 0.05 Hz, not the second-order wave-diffraction loads for the environments considered here. For frequencies between 0.05 to 0.25 Hz, the linear wave loads understandably control the response of the system.

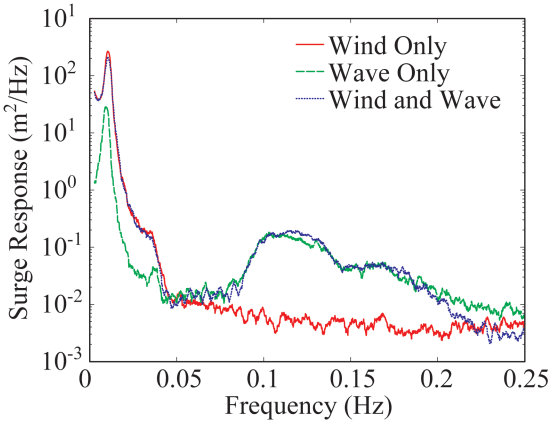

Figure 126: Comparison of model test data surge response from wind-only, wave-only, and combined wind and wave conditions.

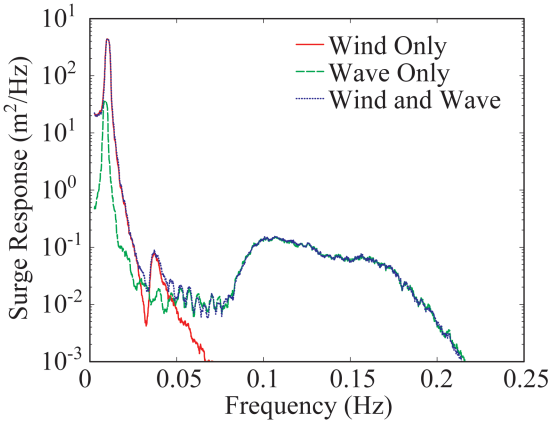

Figure 127: Comparison of FAST simulation surge response from wind-only, wave-only and combined wind and wave conditions.

With the comparative responses and trends established from model test data, the same three identical cases are simulated using the custom FAST tool. The frequency-domain surge response for the three cases, as computed from FAST simulations, is given in Figure 127. As can be seen by comparing Figure 126 and Figure 127, it is clear that FAST captures the same trends observed in the model test data. For low frequencies, the dynamic wind loads control the response of the system, and for frequencies above 0.05 Hz, the linear wave loads dictate the DeepCwind semi-submersible surge response. To further emphasize the correlation between the combined wind and wave case and the model test data and simulation, the surge motion statistics for the combined environment cases are given in Table 55. Table 55 clearly shows a fair agreement between the test data and the simulation including second-order wave-diffraction forces for this condition. However, comparing the values in Table 53 and Table 55 indicates that most of the response in the combined wind and wave case is driven by the wind loads because the mean, standard deviation, and maximum values are all much larger when the wind loads are present.

Table 55: Surge motion statistics for the combined wind and wave case.

Statistic	Data	Linear	2nd-Ord.*
Mean (m)	8.153	7.208	7.436
Std. Dev. (m)	1.131	1.221	1.232
Max. (m)	11.54	11.06	10.99
Min. (m)	4.281	3.073	2.882
Range (m)	7.259	7.987	8.108

*Reduced Surge Drag Damping

To complete this section, an additional simulation is performed for the combined wind and wave case, including only the linear wave-diffraction forces. The surge response statistics for this case are also given in Table 55, alongside the test data and simulation with second-order difference-frequency wave-diffraction forcing. As the table clearly shows, neglecting the second-order wave-diffraction forcing for the combined wind and wave case studied here is not of significant concern for the DeepCwind semi-submersible. Excluding the second-order difference-frequency wave-diffraction forces in the simulation results in reductions of only 3.1% for the mean surge, 0.9% for the surge standard deviation, and 1.5% for the surge range.

6 Development of Improved Wind Turbine Designs for Model Testing of Floating Wind Turbines

As shown earlier in this report, there are difficulties associated with performing Froude-scale wind wave basin tests since the low Reynolds numbers make for very poor performing wind turbines if the blade geometry is preserved as is customary for such experiments. In this section, the option of redesigning the wind turbine geometry to preserve wind turbine thrust is investigated. This is ideal as the correct environments and rotor speeds can be used. In addition, an improved wind turbine design can yield significantly more power production during the model tests permitting possibilities such as utilizing realistic blade pitch control to control power output in post-rated wind speed regions as would be done in a real floating wind turbine. In the next sections, the design methodology and testing of a redesigned rotor for Froude-scale model testing of floating wind turbines is presented.

6.1 Design Methodology

In this section, a brief discussion of the design methodologies employed for designing improved performance wind turbine blades for Froude model-scale testing is given. Along with outlining the objectives and techniques used for designing a suitable model-scale wind turbine for wind/wave basin testing, an overview of the numerical tools employed in the design of the blades is also presented. A review of Froude scaling relationships from prototype to model scale for floating wind turbines is given in (Martin *et al*., 2012; Jain *et al*., 2012).

As noted in (Martin *et al*., 2012), proper emulation of the prototype thrust in the Froude-scale experiment is most important as it drives most of the wind-induced global response of a floating wind turbine. This is due the fact that the floating wind turbine overturning moment due to thrust is more than an order of magnitude larger than that caused by the rotor torque. Therefore, the first objective of redesigning a wind turbine blade considered here is matching the thrust coefficient C_T for the low-Reynolds number, Froude-scale conditions encountered in the wind/wave basin. The thrust coefficient is defined as

$$C_T = \frac{T}{\frac{1}{2}\rho A U^2},$$

where T is the rotor thrust, ρ is the density of air, A is the swept area of the rotor and U is the mean wind speed. More specifically, it is desirable to reproduce the thrust coefficient of the prototype turbine over a larger number of tip-speed ratios TSR. The tip-speed ratio is a non-dimensional measure of rotor angular speed and is defined as

$$TSR = \frac{\omega R}{U},$$

where ω is the rotor angular speed and R is the wind turbine rotor radius.

The second objective is to improve the rotor performance coefficient C_P as much as possible in hopes of approaching the prototype non-dimensional power (and hence torque) specification. Matching the performance coefficient of the prototype over a range of operational TSR values is likely not achievable due to the elevated airfoil drag coefficients at the low Froude-scale Reynolds numbers (Martin *et al*., 2012; Jain *et al*., 2012). However, model wind turbines which exhibit C_P values closer to the prototype value will permit a much broader and more useful class of wind/wave basin model tests for floating wind turbines by permitting studies investigating the interplay of wind turbine controls, global system motion behavior and rotor power production. The performance coefficient is computed as

$$C_P = \frac{P}{\frac{1}{2}\rho A U^3},$$

where P is rotor power.

With the basic objectives defined, a discussion of the wind blade variables targeted for tuning the performance of the rotor at low Reynolds numbers is now given. Variables which are held constant include blade length, gross blade mass properties and rotor operational speeds. Maintaining these quantities will yield a rotor that produces the correct gyroscopic moments during motion of the floating platform as well as maintain the correct Froude-scale TSR values when the model is subjected to proper Froude-scale winds. As discussed in (Martin *et al*., 2012), variables which are considered for alteration for the purposes of meeting the aforementioned C_T and C_P objectives include airfoil type, airfoil section chord length and airfoil section blade twist. For the purposes of this work, the blades were designed to be rigid in order to reduce aeroelastic effects. Flexible blade effects could be incorporated into the procedures discussed, but would require more sophisticated modeling and instrumentation to deal with the aeroelastic effects.

Regarding the first variable, airfoil type, airfoil sections are selected which are generally thinner than those found in commercial wind turbines with preference given to sections designed to perform at low Reynolds numbers (e.g., the Drela AG04 airfoil selected in (Martin *et al*., 2012)). In addition, the thick shapes located near the root of commercial wind turbine blades, whose shapes are dictated by structural factors more than aerodynamic performance, are eliminated and replaced with the previously mentioned thin airfoil sections. The remaining two variables, chord length and blade twist, permit sufficient flexibility to closely emulate the $C_T(TSR)$ behavior of the prototype over a range of desired TSR values. Ideally, this will be performed in a manner that matches the $C_T(TSR)$ behavior of the prototype while producing $C_P(TSR)$ trends that are a fair representation of the prototype.

To ensure a robust design that will not be prone to laminar separation at model scale, the target airfoil section lift coefficients at the design condition should be much less than are used for full-scale wind turbine designs. For example, the blade lift coefficients for the design condition of the model-scale rotor may be only 0.5 or less, whereas the prototype values for the commercial wind turbine may be closer to 1.0. By choosing lower lift coefficients for the model-scale wind turbine, the probability that the physical model-scale wind turbine will avoid laminar stall issues and perform as intended is much higher. This, however, necessitates larger chords for the model-scale wind turbine than would be expected based on Froude scaling.

To execute such a design, one must couple a wind turbine aerodynamic simulation tool with a numerical optimization technique that tailors parameterized features of the wind turbine blade, e.g. blade twist and chord distribution details. For example, the design detailed in a subsequent section was created by coupling NREL's WT_Perf analysis tool (Buhl, 2004) with a custom multi-objective genetic algorithm optimization code (e.g. see (Deb 2001)). With the numerical tools in place, a possible optimization problem with objectives f_i and constraints g_i to be considered for creating the desired model-scale wind blade is as follows:

$$\begin{aligned}
&\text{Find} && \theta(r), \quad 0 \le r \le R, \\
& && c(r), \quad 0 \le r \le R, \\
&\text{Minimize} && f_1(\theta, c) = \int_{TSR_L}^{TSR_U} \left| C_T(TSR) - C_T^{pr}(TSR) \right| dTSR,
\end{aligned}$$

$$f_2(\theta, c) = \int_{TSR_L}^{TSR_U} \left| C_P(TSR) - C_P^{pr}(TSR) \right| dTSR,$$

$$\text{Subject to} \quad g_1(\theta, c) = C_L(r, TSR^*) \leq C_L^{max}, \;\; 0 \leq r \leq R,$$
$$\theta_L(r) \leq \theta(r) \leq \theta_U(r),$$
$$c_L(r) \leq c(r) \leq c_U(r),$$

where r is the blade radial coordinate, R is the blade radius, $\theta(r)$ is the blade twist distribution, $c(r)$ is the chord distribution, TSR_L and TSR_U define the TSR range over which the thrust and performance coefficients are to be matched, $C_T^{pr}(TSR)$ and $C_P^{pr}(TSR)$ are the full-scale prototype target behaviors, $C_L(r, TSR^*)$ is the blade lift coefficient distribution at the design tip-speed ratio TSR^*, C_L^{max} is the prescribed maximum lift coefficient at TSR^*, $\theta_L(r)$ and $\theta_U(r)$ define the lower and upper bounds, respectively, of the twist distribution and $c_L(r)$ and $c_U(r)$ are the lower and upper bounds, respectively, of the chord distribution. There are several options for parameterizing the design variables $\theta(r)$ and $c(r)$ in addition to some leeway in the choice of TSR_L, TSR_U, TSR^*, C_L^{max}, $\theta_L(r)$, $\theta_U(r)$, $c_L(r)$ and $c_U(r)$. An obvious choice for parameterizing the design variables is to tailor the blade twist and chord lengths at the discrete locations used in typical blade element momentum theory numerical analysis. The choice of the integration limits TSR_L and TSR_U will be dictated by the range of TSR values expected in the test matrix of the model test program. C_L^{max} should be less than the full scale design (e.g., 0.5 or less) and TSR^* should be selected near the operating TSR of the wind turbine. Regarding the choice of the remaining bounds on blade twist and chord design variables, sufficient latitude should be given to search the design space. This stated, searches should occur in the neighborhood of optimal twist and chord distributions (e.g. see (Manwell *et al*., 2009) with the chords in the power-producing outer portions of the blade being at a minimum slightly larger than the Froude-scale values. Lastly, the previous problem statement structured as a multi-objective optimization problem which will produce multiple Pareto-optimal solutions to choose from. The final choice should favor designs that minimize the discrepancy between the model and prototype thrust behaviors as these will be the best choice for Froude-scale, floating wind turbine global performance wind/wave model tests.

6.2 Wind Blade Design Specifications

In this section, the blade designs considered in this work are presented. The first is the 1/50th-scale, geometrically-similar NREL 5 MW reference wind turbine blade originally presented in **Error! Reference source not found.**. The second design is based on the Drela AG24 airfoil, which is of the same family of low-Reynolds number airfoils as the Drela AG04 proposed in (Martin *et al*., 2012). It should be noted that the aerodynamic performance of the rotors is the primary concern in this work and that no attempt has been made to maintain the aforementioned distributed blade mass properties as suggested in the design methodology section of this work. Once a design has been proven, appropriate blade mass properties can be obtained utilizing the light-weight materials and manufacturing methods that have been demonstrated in **Error! Reference source not found.**.

First, select details concerning the geometrically-scaled NREL 5 MW reference wind turbine blade are presented. For brevity, only an overview of the specifications is presented. An exhaustive description of the design can be found in **Error! Reference source not found.**. To begin, an image of the geometrically-scaled NREL 5 MW reference wind turbine blade is shown in Figure 128. The blade

Figure 128: Images of a) redesigned, thrust-matched blade and b) original geometrically-scaled, NREL 5 MW reference wind turbine blade.

possesses a chord at 70% radius that is 4.8% of the blade radius. The thickness of the airfoil sections, which are comprised of the NACA 64-618 airfoil for the outer 30% of the blade and various Delft University and Cylindrical sections for the remainder of the blade, range in thickness from 18% to 100%.

With an overview of the model-scale NREL 5 MW reference wind turbine blade given, the details of the redesigned blade considered in this work are now presented. To design the blade, the low-Reynolds number Drela AG24 airfoil was chosen. Optimization of the airfoil selection procedure is possible, but beyond the scope of this work. This aside, the Drela AG24 design was chosen in lieu of the Drela AG04 utilized in (Martin *et al*., 2012) as it offers a larger thickness which yields greater structural stiffness for the small model-scale components fabricated for testing. An image of the airfoil section, which is 8.4% thick, is given in Figure 129.

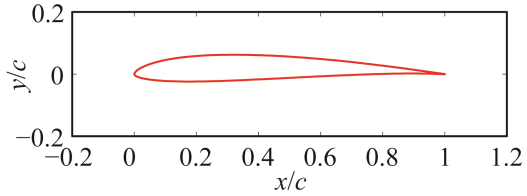

Figure 129: Image of normalized Drela AG24 airfoil section

This section was employed throughout the entire thrust-matched wind turbine design with the exception being near the root of the blade, where cylindrical sections were utilized as strength was required for the physical blade-to-hub connection. The airfoil lift and drag coefficients required for analysis with WT_Perf for the Drela AG24 section were created using XFOIL (Drela, 1989) and NREL's AirfoilPrep tool (Hansen, 2012). The XFOIL analysis, performed at comparable model-scale Reynolds numbers, provided the lift and drag curves for small angles of attack α. The AirfoilPrep tool was then used to extend results for all possible angles of attack in addition to including rotational augmentation corrections. The obtained lift coefficients C_L and drag coefficients C_D are given in Figure 130. All cylindrical sections in the WT_Perf analyses used C_L = 0.0 and C_D = 1.0.

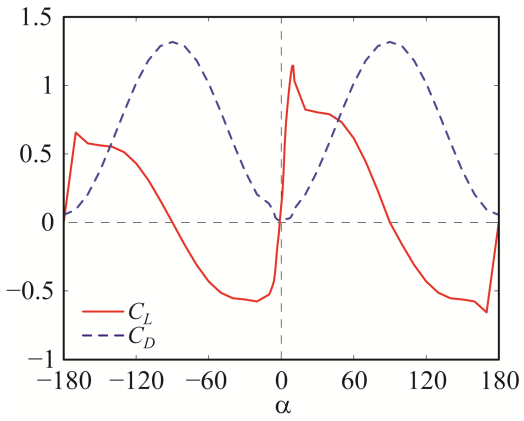

Figure 130: Lift and drag coefficients for the Drela AG24 airfoil.

To create the design, the aforementioned optimization methodology was undertaken using the performance of the full-scale, NREL 5 MW reference wind turbine as the design target. As the TSR of the NREL 5 MW reference wind turbine at the rated wind speed condition is 7, and since the NREL turbine operates near this TSR for most below-rated wind speeds due to its variable-speed design, the optimization focused on matching the performance of this design in the neighborhood of this particular TSR. In addition, a value of $C_L^{max} = 0.3$ was chosen at $TSR^* = 7$ to produce a conservative design. The optimization was directed to search for solutions which consisted of blade twist and chord distributions near the classic optimal distributions (e.g. see (Manwell *et al*., 2009)). An image of the blade chosen from the set of Pareto-optimal designs for testing is shown in Figure 128. A non-dimensional description of the blade geometry is given in Table 56. As seen in Table 56, the chord at 70% radius is much thicker than the original geometrically-scaled design. Specifically, the chord is 14.4% of the radius at this point, a value which is three times larger than the geometrically-scaled NREL 5 reference wind turbine.

Table 56: Non-dimensional geometry of the thrust-matched wind turbine blade

r/R	θ (deg)	c/R	Foil Type
0.046	37.18	0.058	Cylinder
0.140	37.18	0.058	Cylinder
0.148	35.84	0.244	Drela AG24
0.187	30.81	0.237	Drela AG24
0.252	23.74	0.226	Drela AG24
0.317	18.66	0.214	Drela AG24
0.382	15.02	0.202	Drela AG24
0.447	12.30	0.191	Drela AG24
0.512	10.34	0.178	Drela AG24
0.577	8.86	0.167	Drela AG24
0.642	7.69	0.155	Drela AG24
0.707	6.63	0.143	Drela AG24
0.772	5.82	0.132	Drela AG24
0.837	5.03	0.120	Drela AG24
0.892	4.36	0.110	Drela AG24
0.935	3.87	0.099	Drela AG24
0.978	3.61	0.068	Drela AG24

6.3 Laboratory Test Set-up

In this section, an overview of the laboratory test set-up used to collect the wind turbine performance data is given. The tests were performed at the University of Maine Advanced Structures and Composites Center using 1/130th-scale wind turbine components. That stated, all tests were performed at Reynolds numbers expected in a 1/50th Froude-scale experiment.

For the experiments, data acquisition and control was handled using a National Instruments CompactDAQ (cDAQ) system with analog input and output cards. The turbine motor was controlled using a Copley Xenus XTL motor controller which received rotor speed set points via a control voltage from the cDAQ. Labview software was used to interface with the cDAQ and collect data as well as control the fan speed and turbine rotor speed. The test turbine was instrumented to collect the necessary data. Thrust force, rotor torque, and rotor rotational speed were collected for this work. Thrust force was measured using an Advanced Mechanical Testing Inc. FS6 6-axis force and moment sensor located at the tower/nacelle interface. Torque was measured using an Interface Inc. T2 precision rotary torque transducer located in-line with the turbine drive shaft. Rotor position and speed were measured using a US Digital analog encoder geared to the turbine drive shaft. All data was sent to the cDAQ as analog voltage signals and recorded with a sample rate of 500 Hz. An image of the test wind turbine is shown in Figure 131. The wind generation machine, used for creating the wind environment required for wind turbine performance testing, consisted of an aluminum frame structure which housed 6 Multi-fan industrial fans with analog speed. A honeycomb flow straightener was located at the exit of the fan chamber to eliminate swirl in the flow field. Upon exiting the honeycomb, the wind flow passed through a fine screen to further improve spatial wind speed uniformity and reduce the wind field turbulence intensity.

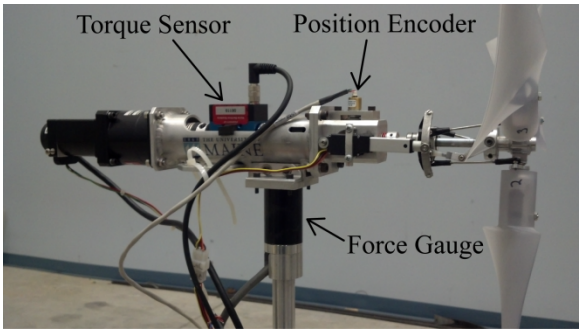

Figure 131: Image of wind test wind turbine showing the torque sensor, position encoder and force gauge.

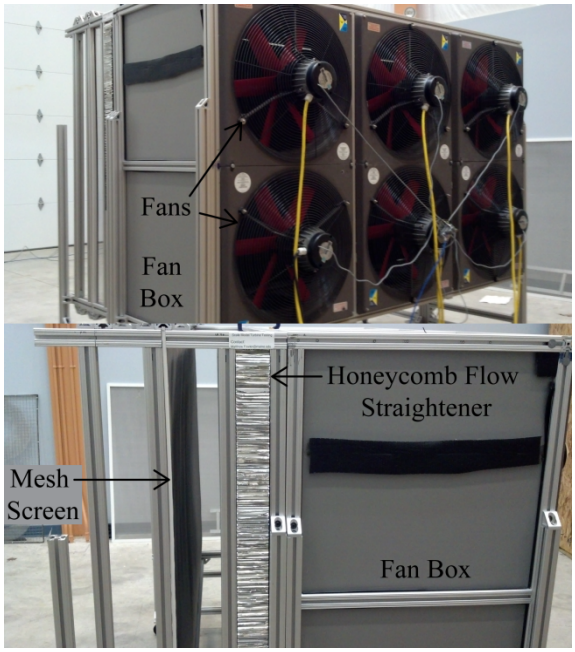

Figure 132: Images of the wind generation system showing fans, flow straighteners and mesh screen.

The wind generation system is shown in Figure 132. An image of the wind turbine being tested behind the wind machine is shown in Figure 133. The wind generation machine, which is typical of the configuration to be expected in a coupled wind/wave basin model test, utilizes an open jet configuration. This configuration mitigates wall effects present in a closed tunnel and permits the use of a more compact wind machine. A closed section tunnel would require a test section of three times the size of this open jet tunnel. The open jet allows the outer streamlines to bend more freely, which simulates the effects of an infinite free stream. Since the wake effects on turbine performance diminish rapidly downstream, it is most important to simulate the near wake effects properly. An open jet tunnel achieves this with a fairly compact and cost effective size.

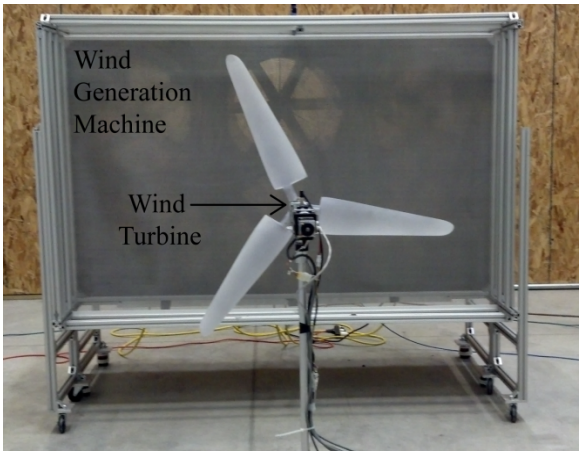

Figure 133: Image of the test wind turbine being tested behind the wind generation machine.

Prior to testing, the wind machine output was surveyed and characterized. The characterization was performed using a vertical traverse carrying a hot film wind probe. The probe had a 10 mm spatial resolution and a frequency response of about 1 ms in the range of the measurements. This is sufficient to capture the turbulence scales of the wind machine. The traverse was located such that the wind probe was in the plane of the turbine rotor and wind speed data was collected using a series of vertical profile cuts. Upon completion of the wind turbine output survey, the spatial variation of mean wind speed and turbulence intensity was obtained. A survey of the system mean wind speed, normalized relative to the maximum speed recorded, is given in Figure 134. Note that x is the horizontal distance and z is the vertical distance. This stated, the coefficient of variation of the mean wind speed over the rotor swept area is 8.5%. This is visually illustrated in Figure 135. Figure 135 displays the vertical wind profile cuts at the centerline, first cut to starboard, and the first cut to port as well as vertical lines illustrating the rotor swept area average and corresponding standard deviation. As can be seen in the figure, the spatial uniformity of the wind environment is fair. To complete the wind turbine characterization, the spatial survey of local relative wind turbine intensity is shown in Figure 136. The wind turbine intensity is defined as the temporal standard deviation in the wind speed divided by the mean. As shown in the figure, the turbulence intensity of the wind generation machine output is very good, with an average of only a few percent over most of the rotor swept area.

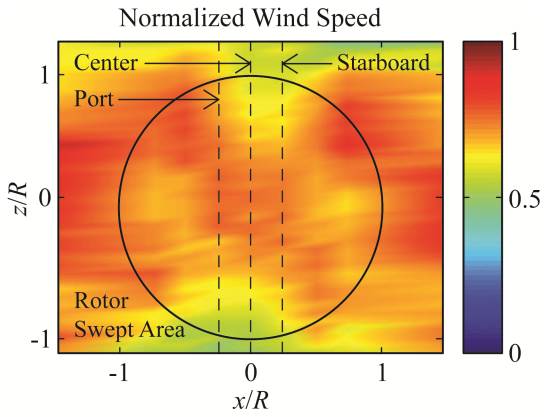

Figure 134: Spatial survey of wind generation machine mean wind speed and select vertical cut locations.

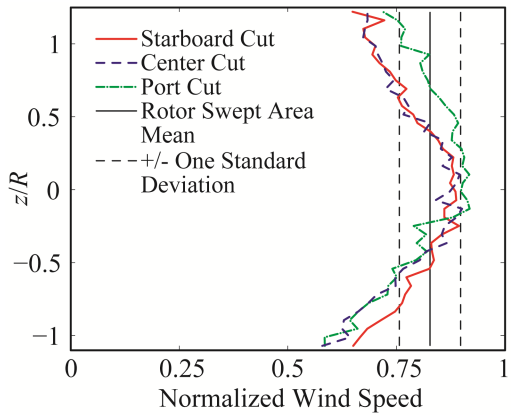

Figure 135: Vertical wind speed profiles across the first cut to starboard, center cut and first cut to port normalized to the maximum mean wind speed observed in the rotor swept area.

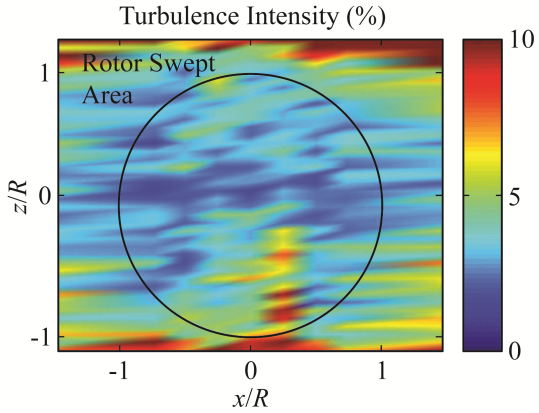

Figure 136: Spatial survey of wind generation machine turbulence intensity.

6.4 Wind Turbine Performance Results

In this section, results are presented for the wind blades considered in this work. In addition to comparisons between simulations and test data, parametric studies investigating blade pitch angle and Reynolds number are also offered.

To begin this results section, a comparison of the full-scale prototype NREL 5 MW reference wind turbine target, geometrically similar model-scale test data, redesigned thrust-matched wind turbine simulation and thrust-matched wind turbine test data is given. The curves for the thrust coefficient and performance coefficient as a function of tip-speed ratio for the aforementioned cases are given in Figure 137 and Figure 138, respectively. The prototype targets in Figure 137 and Figure 138 were obtained from a WT_Perf analysis of the full-scale, NREL 5 MW reference wind turbine. For the geometrically-similar model test data, the Reynolds number at 70% radius based on chord length at a TSR of 7 was 32.1×10^3.

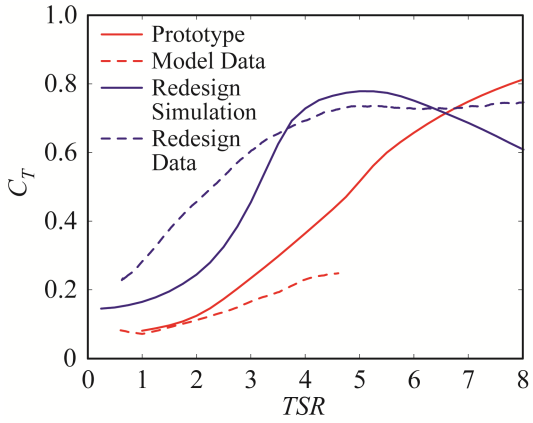

Figure 137: Comparison of thrust coefficient behavior for the prototype target, tested geometrically-similar model and redesigned thrust-matched wind turbine as obtained from simulations and test data.

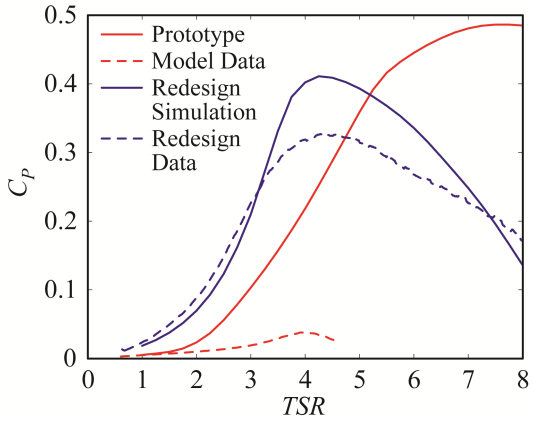

Figure 138: Comparison of performance coefficient behavior for the prototype target, tested geometrically-similar model and redesigned thrust-matched wind turbine as obtained from simulations and test data.

For the thrust-matched wind turbine, Figure 137 and Figure 138 show results of the optimal solution as computed from WT_Perf in addition to test data corresponding to a 70% radius Reynolds number at $TSR = 7$ of 88.8×10^3. As the chord length for the thrust-matched design is about three times that of the geometrically-similar design, it is expected that the Reynolds numbers be approximately three times higher for the thrust-matched design for the same test condition. That aside, Figure 137 and Figure 138 clearly show that the geometrically-similar design performs extremely poorly in replicating the full-scale prototype target performance. The thrust-matched design, on the other hand, is a fair match to the target with regard to thrust coefficient near the rated wind speed operational TSR of approximately 7. More specifically, the thrust-matched design possesses a C_T at this TSR that is 98.1% of the desired prototype value. However, it should be noted that the slope of curve differs greatly between the model and prototype. This is discussed further in the next section. Also, the peak performance coefficient, 0.33, is much greater than the tested geometrically-scaled model value of only 0.04. As evidenced by the results of these two figures, the proposed redesigned, thrust-matched wind turbine would be adequate for a Froude-scale model test as it would produce the correct thrust forces when subjected to Froude-scale winds and would also yield significantly more power than a geometrically-similar design. A final point concerning Figure 137 and Figure 138 is that the comparison between the projected performance from the

simulation of the optimized design and test data for the redesigned thrust-matched wind turbine is fairly good. The tested performance coefficient curve follows the simulation except in the neighborhood of the peak performance. A likely reason for the discrepancy is that the drag coefficients maybe somewhat higher at low angles of attack than was used in the simulation. It is worth noting that the multi-objective optimization produced designs with a peak C_P closer to the design TSR, however, the primary objective was matching C_T at the design TSR. Concerning the comparison of the thrust curve simulation and test data, the shapes are not identical but the basic trend is similar between the two.

In this next phase of this results section, the tested performance at various blade pitch angle settings is presented for the thrust-matched design. The results will be useful for demonstrating the sensitivity of the redesigned wind turbine performance to blade pitch angle, and in turn, the usefulness of the design for emulating the behavior of typical commercial-scale pitch-to-feather post-rated wind speed blade pitch control schemes. Four blade pitch offsets are considered here with the blade pitch identified as the angle of the blade tip chord relative to the rotor plane, and the offsets normalized such that the offset at the design blade pitch is 0.0°. Note that positive pitch angle offsets indicate a more feathered rotor blade with the trailing edge of the blade moving towards the downwind direction. For all results in this blade-pitch sensitivity study, the Reynolds number at 70% chord at a TSR of 7 is 88.8×10^3. The first blade pitch sensitivity result is given in Figure 139. The figure illustrates thrust coefficient performance and considers blade pitch offsets of -3.5, 0.0 (the design setting of 3.5 degrees), +3.5 and +6.5 degrees. As observed in the figure, there is a broad variation in thrust coefficient for moderate to large TSR values with -3.5 degrees producing the most thrust and +6.5 degrees the least for the configurations tested. Next, the performance coefficient curves for the same four blade pitch settings of the redesigned wind turbine are shown in Figure 140. As observed in Figure 140, the design setting produces the best performance. The performance of the turbine is slightly less at the settings of -3.5 and +3.5 degrees with the performance significantly less at the most feathered blade pitch tested, +6.5 degrees.

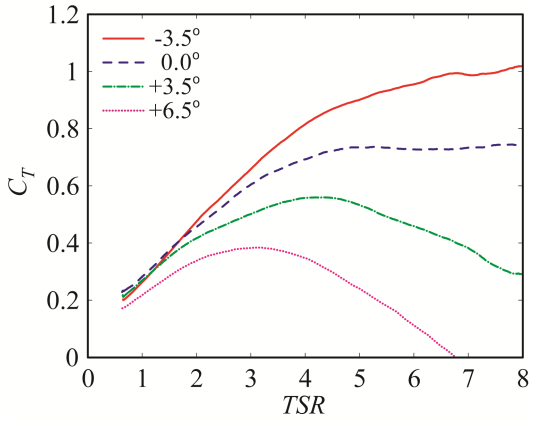

Figure 139: 12 Tested thrust-matched wind turbine thrust coefficient at four blade pitch settings.

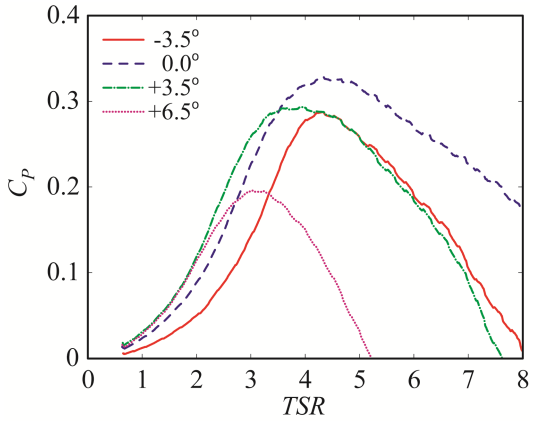

Figure 140: Tested thrust-matched wind turbine performance coefficient at four blade pitch settings.

For the purposes of comparison, the C_T and C_P trends for the full-scale NREL 5 MW reference wind turbine at the same four blade pitch settings as computed from WT_Perf are shown in Figure 141 and Figure 142, respectively. As seen from comparing Figure 139 and Figure 141, it is clear that very similar trends exist in the sensitivity of the thrust coefficient behavior between the full-scale prototype and the model-scale thrust- matched wind turbine. And while the change in C_T with blade pitch angle may not emulate the full-scale prototype directly, it is quite likely that a reasonable mapping between the two configurations can be constructed for the purposes of implementing the desired full-scale target blade pitch-to-feather control global forcing effects in a Froude-scale model test of a floating wind turbine. Comparing Figure 140 and Figure 142, it is observed that the thrust-matched design does not produce the same performance coefficient variation as the full-scale prototype. Both scenarios do, however, share a reduction in peak performance once the blade pitch setting is altered from the design setting. Nonetheless, it is likely that some care will be required for implementing blade pitch control schemes in post-rated wind speed conditions as the primary focus is the regulation of power production.

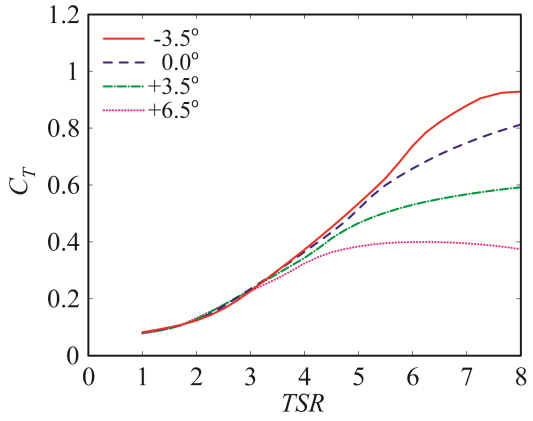

Figure 141: Full-scale NREL 5 MW reference wind turbine thrust coefficient at four different blade pitch settings.

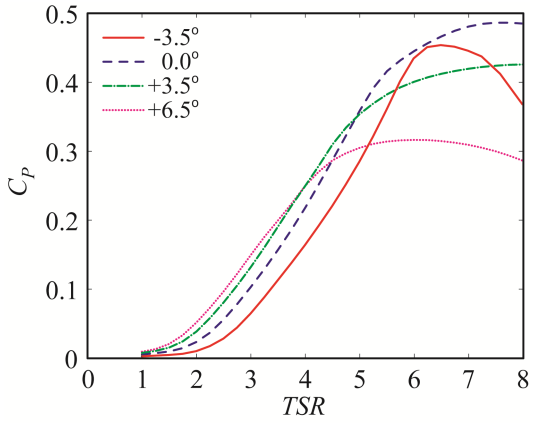

Figure 142: Full-scale NREL 5 MW reference wind turbine performance coefficient at four different blade pitch settings.

For floating wind turbines, however, this is not always the case as often control of the global motion of the floating structure is sought by devising blade pitch commands which use motion inputs, such as tower-top acceleration (e.g. see Jonkman, 2008).

To complete the results section, the sensitivity of the thrust-matched wind turbine performance to Reynolds number is investigated. Three tests are conducted with varying wind speeds to produce a range of Reynolds number conditions. The test conditions utilized produce Reynolds numbers at 70% blade radius and $TSR = 7$ of $Re = 44.4 \times 10^3$, 66.6×10^3 and 88.8×10^3. The first curves presented, shown in Figure 143, are the thrust coefficient results. As shown in the figure, the thrust performance sensitivity to Reynolds number is not very strong. In fact, the results of Figure 143 indicate that for the range of Reynolds numbers considered here, there is little change in the thrust coefficient as the Reynolds number is reduced. In other words, the thrust-matched design created in this work should perform well with regard to producing the primary wind turbine load, thrust, for Froude-scale model tests quite a bit smaller than 1/50th scale. The same cannot be said of the performance coefficient results, shown in Figure 144. As shown in the figure, the performance degrades slightly at the middle Reynolds number investigated and degrades significantly more at the lowest Reynolds number tested. Noting that the behavior for the largest Reynolds number studied is representative of 1/50th Froude-scale conditions, it is clear that the power produced by this design will begin to falter if the Froude scale chose for testing is much smaller than 1/50th scale.

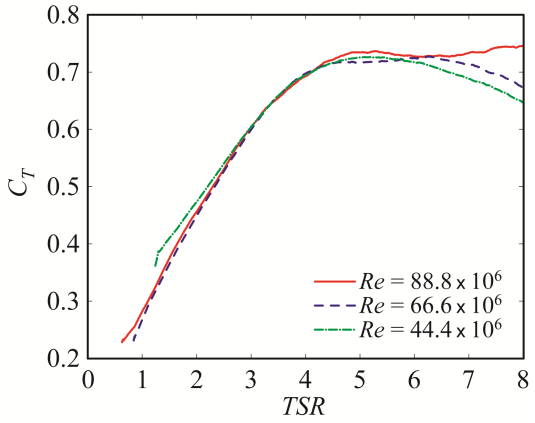

Figure 143: Tested thrust-matched wind turbine thrust coefficient for three different Reynolds number conditions.

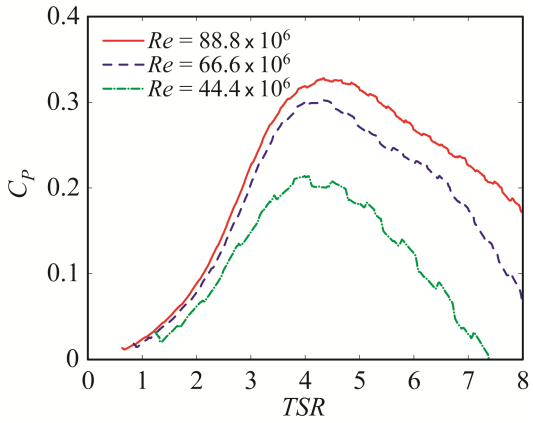

Figure 144: Tested thrust-matched wind turbine performance coefficient for three different Reynolds number conditions.

7 Conclusions and Future Work

In this final section, the conclusions for the various portions of this report will be covered. The topics will include scaling methods, model test experimental results, FAST calibration and validation and redesigned model test wind turbine. Subsequently, a brief discussion of future work will also be given.

7.1 Scaling Methods Conclusions

A methodology has been presented for model testing of floating wind turbines under Froude scale conditions. The scaling relationships for all of the field variables are established with particular emphasis on the unique aspects of such testing, namely the wind turbine design, operation and accompanying wind environment. Model test data is used to demonstrate the difficulty of capturing the correct prototype aerodynamic forces as a result of Reynolds number dissimilitude, namely the thrust force which is the most critical to emulate properly for a wind/wave basin test of a floating wind turbine. Analysis reveals that the thick airfoil sections employed on commercial scale wind blades exhibit low lift and high drag forces at the low Reynolds numbers of a Froude scale experiment, in turn producing poor rotor aerodynamic performance. Corrective measures are suggested, these being to increase the wind inflow speed to compensate for low wind turbine thrust coefficients, roughen the leading edge of the blade to trip the boundary layer transition to turbulence, or lastly, to design a low-Reynolds number specific wind turbine. Test data and simulations indicate that increasing the wind speed to compensate for poor turbine performance does not greatly affect the wind turbine damping resulting from a fixed blade rotor. This method, however, may not capture all wind turbine damping effects correctly. Leading edge roughness applied to the wind turbine blades can greatly improve the performance of thick airfoil sections at low Reynolds numbers, but may result in erratic wind turbine rotor behavior. It is suggested that this technique be used more as a fine tuning adjustment than be solely relied upon to solve all model wind turbine aerodynamic performance issues. The last recommendation, a low-Reynolds number specific blade design, allows one to match thrust forces with unaltered Froude scale winds, will better capture wind turbine damping effects, and is best suited to experiments where the impact of active blade pitch control on global motions are of interest. Therefore, if possible, a redesigned rotor is the best option with the other two thrust matching techniques being used sparingly to fine tune the model thrust forces.

7.2 Floating Wind Turbine Experimental Comparison Conclusions

This report presented experimental performance results from wind/wave basin model testing of three floating wind turbine concepts. The three platform concepts, each supporting the same horizontal axis NREL 5 MW Reference Wind Turbine, consisted of a TLP, a spar-buoy and a semi-submersible. Results were presented for a number of wind and wave environments with an emphasis on global motions, wind excitation and damping effects, nacelle acceleration and system tower and mooring loads. It should be noted that the following conclusions are specific to the load cases evaluated in this report, as well as to the specific designs tested. As such, the conclusions herein are not intended to be generalized to other TLP, spar-buoy and semi-submersible designs, nor to their response under load cases not considered herein.

7.2.1 Wave Only Performance

The results of the wave only cases indicate that the spar-buoy tested possesses the smallest surge response in irregular seas, while the TLP system tested exhibits the smallest pitch response of any of the systems. The semi-submersible response for both DOF studied is typically in between that of the TLP and spar-buoy in the wave energy frequency range, however, the semi-submersible exhibits by far the greatest second-order difference-frequency associated motion response.

7.2.2 Effect of Wind on Global Motions

Regarding the effect of wind, the difference in response for all three systems without wind or with a parked rotor with feathered blades in a severe dynamic wind is very similar. This indicates that feathering the rotor blades is an effective means of minimizing the impact of wind loads on the system. Unlike the feathered case, an operating wind turbine in moderate winds modifies the global motion response of the floating wind turbine. For a TLP floating wind turbine, the wind loading significantly increases the pitch response of the system, however, the pitch response energy as a whole is still quite small. For the spar-buoy and semi-submersible designs, the operating wind turbine significantly damps the second-order difference-frequency pitch response of the structures, and in the case of the semi-submersible, also damps the second-order surge response.

7.2.3 Nacelle Acceleration

The nacelle surge acceleration for the TLP at low energy sea states possesses significant response near the coupled platform pitch/tower bending frequency, whereas the other two systems do not. For intermediate sea states, the unique motion characteristics of the semi-submersible platform yield a near net zero motion of the 90 m hub height wind turbine, minimizing nacelle motion and the accompanying inertial loads.

7.2.4 Tower and Mooring Loads

The tower base bending moment for all three systems at low sea states is characterized by significant response at the platform pitch frequencies, this being above the wave energy frequency for the TLP and below it for the spar-buoy and semi-submersible. For severe sea state conditions, the tower bending moment response for all three systems is dominated by the wave and not the platform pitch frequencies. On the topic of moorings, the TLP mooring load response in the frequency domain is approximately an order of magnitude greater than for the spar-buoy and semi-submersible floating wind turbine designs. In addition, the spar-buoy and semi-submersible response is primarily located at the system surge natural frequencies whereas the TLP mooring load response is substantial in the wind energy, wave energy and coupled platform pitch/tower bending natural frequencies.

7.3 FAST Calibration and Validation Conclusions

7.3.1 Semi-submersible

This work presented the validation of a FAST numerical model of the DeepCwind semi-submersible floating wind turbine system, which supported a slightly altered version of the NREL 5-MW horizontal-axis reference wind turbine using 1/50th-scale model wind/wave basin test data collected at MARIN. Details required for construction of the model are discussed, including system mass, elastic, aerodynamic, and hydrodynamic properties. The calibration procedure is also presented, and includes tuning of the aerodynamics, tower-bending frequencies, and hydrodynamic damping using system identification test data. With the calibrated FAST model complete, a validation study was undertaken comparing FAST predictions to measured test data. Conditions studied included steady and dynamic wind-only cases, platform free-decay motion under steady winds, regular and irregular wave-only conditions, and finally, a combined dynamic wind and irregular wave case. The load cases examined are representative of specific operational and extreme conditions for the Gulf of Maine.

Upon completion of the validation study, a number of important observations were made. For wind-only loading, whether steady or dynamic, FAST predictions agree very well with experimental data, producing similar statistics, PSDs, and time-series. For wave-only cases, FAST simulations captured the linear wave energy frequency response of the DeepCwind semi-submersible well. The mean drift and second-order difference-frequency responses present in the test data, which were occasionally quite strong, were not captured by FAST. Another deficiency discovered included the significant under-prediction of the mooring line fairlead tensions by FAST's quasi-static mooring module. A portion of this deficiency was likely caused in part by the neglect of platform mean and slowly-varying drift forces; however, much of the deficiency was probably caused by dynamic mooring effects, which FAST is unable to account for. In combined dynamic wind and wave cases, the test data indicated that wind forcing dominated second-order wave and tower-bending frequency effects. Because FAST performed admirably in predicting wind-induced response, the combined wind and wave case studied showed a fairly good agreement between the simulation and test data. This finding signifies that FAST's neglect of second-order wave diffraction effects may only be important in extreme events when the wind turbine blades are feathered and the rotor is parked or idling. A further observation is that a more sophisticated damping model could reduce some discrepancies in the validation studies presented here. One way to achieve this in such a model would be to represent the individual components of the submerged portion of the platform with Morison elements rather than just assigning global damping coefficients to the model.

Aside from possible improvements for the numerical model, the validation studies also revealed potential areas of improvement for experimental set-up and procedures. The cable bundle used to transmit data from the model to the computers added stiffness to both the tower and the surge motion DOF that would never exist in a full-scale, commercial system. Wireless data transmission would eliminate the need for this cable bundle altogether. The tower could also be improved because the one used here was composed of multiple cross sections. It would be more desirable to have a uniform or linearly tapered cross section along the length of the tower to make distributed properties continuous (both mass and elastic) and hence easier to quantify and model. Another experimental improvement would be to modify the wind turbine so the rotor thrust is correct at properly scaled wind speeds. One way this could be addressed is through the use of different wind blade designs that perform better in lower Reynolds number regimes. Not having to increase wind speeds to achieve proper thrust values would also reduce the aerodynamic drag on the tower and support structure that is currently ignored by FAST; this would yield better comparisons.

In conclusion, this validation study has found FAST to perform well in predicting the coupled aero-hydro-elastic response of the DeepCwind semi-submersible floating wind turbine. The results indicate that the inclusion of second-order wave diffraction and mooring dynamic physics into FAST, the

formulations and implementations for which are readily available, would create an accurate and powerful tool for the design and analysis of floating wind turbines.

7.3.2 TLP

This report presents a calibrated FAST model built to represent a scaled model of a floating wind turbine mounted on a TLP. A preliminary validation study of this model was also conducted. After calibrating the FAST model, the comparison between the simulations and experiment was very good in the wave-excitation frequency range in the DOFs that were directly forced by the wind and waves. Discrepancies between the simulations and experiment were seen in other areas, however. As a result, more research is needed in order to determine if the differences between the model and experiment are due to errors in model calibration, sensor error, test errors, or true underperformance of the simulation tool.

7.3.3 Spar-buoy

conditions were compared to results of tank tests of a 1/50th Froude-scaled model of the same system for the purposes of calibration and validation of the FAST model. The FAST model was calibrated to account for differences in mooring systems between the FAST model and UMaine test model and simplifications in the modeling of nonlinear viscous damping. Once calibrated, the natural frequencies of the platform DOFs, as well as the first tower mode, were mostly consistent between the experiment and the simulation, with a roughly 3% inconsistency in pitch and roll. Damping of the platform, as measured by the damping ratio from free-decay tests, was reasonably consistent between the simulation and experiment for heave and yaw decay (particularly for lower height motions), but was inconsistent for surge, sway, pitch, and roll. FAST surge and sway appeared to be less damped than the UMaine model; whereas pitch and roll appeared to have increased damping relative to the UMaine model.

The response of the two systems to periodic waves and zero wind compared well at the wave frequency and fundamental tower frequency, but the FAST model tended toward a greater response at the natural frequencies of platform DOFs. In addition, the experimental data showed greater responses at the first and second harmonics of the wave frequency than the simulation. A quadratic effect was noticeable at twice the wave frequency in the simulation data for higher waves, but was not present for lower waves.

Several irregular wave tests with wind were compared. The response of the two models was generally consistent at frequencies corresponding to the wave spectra. At lower wind velocities, the experimental data showed a 3P response that was not apparent in the FAST simulations until wind speeds were increased to 21.8 m/s, at which point the 3P FAST response exceeded that of the experiment, indicating an increased 3P simulation response with higher platform pitching and increased rotor loads. Responses of 6P and 9P were present in the test data but not in the simulation data. A yaw response at the heave natural frequency was present in the test data but not in the simulation. The response of the two systems in the pitch/roll and surge/sway frequency range was more consistent for simulations including wind, indicating that wind effects dominated in these lower-frequency ranges.

In general, the responses compared well between the experiment and the simulation, particularly in the region of the wave-spectra frequencies. However, differences existed in the responses to periodic and irregular waves, which may be important for full-scale turbine design. More research is needed to understand the discrepancies between the simulation and experiment before an assessment of FAST's ability to accurately model floating wind turbines can be made. In particular, there appears to be significant discrepancies in damping behavior between the experiment and the FAST simulation.

7.3.4 Redesigned Model Wind Turbine Conclusions

In this work, a numerical model of the DeepCwind semi-submersible floating wind turbine was created in the open-source coupled aero-hydro-servo-elastic CAE tool FAST. The model was calibrated using select

DeepCwind model test data, and subsequently, was used to simulate wave-only and combined wind and wave cases from the model test program. Second-order difference-frequency wave-diffraction forcing played a significant role in the global response of the DeepCwind semi-submersible based on the analysis of model test data. This study included these forces in the FAST CAE simulator via Newman's approximation in an effort to understand the importance of including these effects.

For wave-only simulations, the inclusion of second-order difference-frequency wave-diffraction forces greatly improved the frequency-domain and statistical correlation between the simulation output and test data for surge and mooring fairlead tension response. To best capture the low-frequency response near the surge resonance frequency, the coefficients employed for the quadratic surge damping model had to be tailored to suit the small amplitude motions created by the operational H_s = 2.0 m sea state. This situation stemmed from two factors. First, the low-frequency resonant surge response is sensitive to the quadratic-drag damping coefficient used in the simulation. Second, the quadratic-drag damping model employed here is unable to capture the damping characteristics of the DeepCwind semi-submersible over a large range of surge amplitudes, and can at best capture the damping response of the system over a limited range of motion amplitudes. It was also found that the Newman's approximation implementation utilized here yielded improvements in the time-series comparisons of the surge response; however, the amplitudes and phases of the low-frequency response were often not in great agreement. In addition, while the inclusion of the second-order wave-diffraction forces improved the low-frequency correlation of the fairlead tension response, a significant discrepancy between the simulation and test data still persisted in the wave-energy frequency range, likely due to the hydrodynamic loading of the mooring line and mooring line dynamics that are currently excluded in the FAST CAE tool.

Upon completion of the wave-only portion of the study, simulations of a combined wind and wave environment were performed and compared to the test data. For the case studied, where the relationship of wind and wave environmental loads was considered to be representative of a realistic operating condition, the dynamic wind loads dominated the low-frequency surge response of the system, as opposed to the second-order difference-frequency wave-diffraction forces. This was confirmed by comparing FAST simulations with and without the second-order wave-diffraction forces. Excluding the second-order wave-diffraction forces for the combined wind and wave case resulted in a small 3.1% reduction in the mean surge value, and even smaller reductions in the surge standard deviation and range. These small reductions indicate that excluding the second-order wave forces, as is done in the current version of FAST, is likely a reasonable approach when simulating floating wind turbines subjected to simultaneous wind and wave loading. However, for instances where the rotor is parked/idling, and the rotor blades are feathered to reduce the rotor thrust coefficient, the response is driven by the wave loads with negligible influence of the wind loads, even in large winds. This conclusion is based on previous analysis of the DeepCwind semi-submersible test data. In other words, this turbine configuration leads to responses very similar to a wave-only condition. Therefore, neglecting the second-order wave-diffraction forces may no longer be advisable for parked/idling turbine scenarios, as supported by the results obtained from the wave-only analyses conducted in this work.

7.4 Redesigned Model Wind Turbine Conclusions

In this effort, the groundwork laid by Martin et al. for producing a wind turbine model which properly emulates the full scale thrust behavior in a manner suitable for coupled wind/wave Froude-scale model testing of floating wind turbines was extended and validated through physical testing. A more thorough description of the numerical design procedure was presented and the method was employed to produce a design for physical testing and validation in the University of Maine Advanced Structures and Composites Center.

After performing the physical testing at equivalent Froude-scale Reynolds numbers, it was shown that the thrust-matched design performed almost as predicted by the numerical simulation procedure. And unlike the geometrically-similar model, the improved, thrust-matched design replicated the thrust coefficient of the target, NREL 5 MW reference wind turbine target at the design tip-speed ratio in addition to producing significantly more power. Additional findings gathered through testing included adequate thrust coefficient variation with blade pitch angle, a property that will enable realistic pitch-to-feather control schemes for post-rated wind speed conditions during Froude-scale model tests of floating wind turbines. A final observation from laboratory testing was that the thrust-matched design will produce appropriate thrust behavior at Reynolds numbers corresponding to Froude-scale tests significantly less than $1/50^{th}$ scale. However, the performance coefficient of the proposed design degrades sharply for Froude scales much less than 1 to 50.

Future improvements to the design of the thrust-matched wind turbine include a blade redesign to move the peak C_P closer to the design TSR of 7. This would improve the torque simulation of the model and, if done properly, should not degrade the ability to match prototype thrust which is most important for Froude-scale model testing. In addition, the authors are also focused on improving the wind quality of the wind machine for future tests using a conditioning nozzle, individual fan speed tuning and refined screens to improve the flow uniformity.

7.5 Future Work

The efforts put forth in this report have revealed a great deal about testing methods for floating wind turbines, the dynamic behavior of floating wind turbines and the accuracy of the popular floating wind turbine simulator, FAST. This stated, there is still much left to do in this research arena. First, efforts should, and will be, undertaken to quantify the value of the current DeepCwind data set as the tests utilized an under-performing wind turbine. This will be executed by retesting select cases for the semi-submersible using a redesigned, thrust-matched wind turbine in MARIN's offshore basin over the last week of May 2013. Other research will look to add an important level of wind turbine control realism absent from the current DeepCwind data set, namely, variable generator speed and blade pitch control. Efforts will be taken in the near future to add these elements to floating wind turbine model test campaigns. This data will be invaluable for better assessing the ability of numerical tools to capture the full spectrum of coupled aero-hydro-servo-elastic response behaviors that a floating wind turbine can produce.

Another significant area of future work is utilizing the lessons learned and improved numerical simulation techniques in the design and execution of field-scale experiments, and ultimately, commercial demonstration projects. This will come to fruition in the design, construction and deployment of the $1/8^{th}$ scale VolturnUS system in Castine, ME in May of 2013 in addition to the design efforts for the Department of Energy-funded 50% design phase of the Aqua Ventus I project currently being performed over the 2013 year.

8 References

API Recommended Practice 2A-WSD, 21st Edition, Recommended Practice for Planning, Designing and Constructing Fixed Offshore Platforms – Working Stress Design, 2000.

Aubault, A., Cermelli, C. and Roddier, D., 2009. WindFloat: A Floating Foundation for Offshore Wind Turbines Part III: Structural Analysis, OMAE 2009 1: 213-220.

J.S. Bendat and A.G. Piersol, Engineering Applications of Correlation and Spectral Analysis (John Wiley & Sons, New York, New York, USA 1980).

NWTC Design Codes (BModes by Gunjit Bir). http://wind.nrel.gov/designcodes/preprocessors/bmodes/. Last modified 20-March-2008; accessed 20-March-2008.

Buhl Jr., M.L., 2004, "WT_Perf User's Guide", National Renewable Energy Laboratory.

Cermelli, C., Roddier, D. and Aubault, A., 2009. WindFloat: A Floating Foundation for Offshore Wind Turbines Part II: Hydronamics Analysis, OMAE 2009 4: 135-143.

Chakrabarti, S.K., 1994. Offshore Structure Modeling. Singapore: World Scientific Publishing Co. Pte. Ltd.

R.D. Cook, D.S. Malkus, M.E. Plesha and R.J. Witt, Concepts and Applications of Finite Element Analysis, 4th Edition (John Wiley & Sons, Hoboken, New Jersey, USA, 2002).

A.J. Coulling, A.J. Goupee, A.N. Robertson, J.M. Jonkman and H.J. Dagher, 2013, Validation of a FAST semi-submersible floating wind turbine model with DeepCwind test data, Journal of Renewable and Sustainable Energy 5, 023116.

Deb, K., 2001, Multi-objective Optimization Using Evolutionary Algorithms, John Wiley & Sons, Chichester.

Drela M., 1989, XFOIL: An analysis and design system for low Reynolds number airfoils, Conference on Low Reynolds Number Airfoil Aerodynamics, University of Notre Dame.

Drela M., Giles M.B., 1987, Viscous-inviscid analysis of transonic and low Reynolds number airfoils, AIAA Journal 25(10).

US Energy Information Administration, 2011, Annual Energy Review 2010, Technical Report DOE/EIA-0384(2010).

O.M. Faltinsen, Sea Loads on Ships and Offshore Structures (Cambridge University Press, Cambridge, United Kingdom, 1990).

D.L. Garrett, "Dynamic analysis of slender rods," Journal of Energy Resource Technology 104, 302-306 (1982).

Glauert H., 1926, The Elements of Aerofoil and Airscrew Theory, Cambridge University Press, Cambridge.

A.J. Goupee, B.J. Koo, K. Lambrakos and R.W. Kimball, "Model tests for three floating wind turbine concepts," Proceedings of the 2012 Offshore Technology Conference, Houston, Texas, USA, 30 April-3 May 2012.

Goupee, A.J., Koo, B, Kimball, R.W., Lambrakos, K.F. and Dagher, H.J., " Experimental Comparison of Three Floating Wind Turbine Concepts," Proc. 31st ASME International Conference on Offshore Mechanics and Arctic Engineering, Rio de Janeiro, Brazil.

C. Hansen, NWTC Design Codes: AirfoilPrep, http://wind.nrel.gov/designcodes/preprocessors/airfoilprep/, accessed August 6, 2012.

Hansen A C and Moriarty P J 2005 AeroDyn Theory Manual NREL Technical Report NREL/TP-500-36881 National Renewable Laboratory Golden Colorado United States

IEC 61400-3, 2009, Wind Turbines - Part 3: Design Requirements for Offshore Wind Turbines, International Electrotechnical Commission (IEC).

A. Jain, A.N. Robertson, J.M. Jonkman, A.J. Goupee and R.W. Swift, "FAST code verification of scaling laws for DeepCwind floating wind system tests," Proceedings of the 22nd International Offshore and Polar Engineering Conference, Rhodes, Greece, 17-22 June 2012, pp. 355-365.

Jonkman, B. J. (2009). TurbSim User's Guide: Version 1.50, National Renewable Energy Laboratory, Golden, Colorado, USA, Technical Report: NREL/TP-500-46198.

Jonkman, J.M., 2007. Dynamics Modeling and Loads Analysis of Offshore Floating Wind Turbines. NREL Technical Report NREL/TP-500-38060.

Jonkman, J.M., 2010. Definition of the Floating System for Phase IV of OC3. NREL Technical Report NREL/TP-500-47535.

Jonkman, J.M. and Buhl Jr., M.L., 2005. FAST User's Guide. NREL Technical Report NREL/EL-500-38230.

Jonkman, J.M., Butterfield, S., Musial, W. and Scott, G., 2009. Definition of a 5-MW Reference Wind Turbine for Offshore System Development. NREL Technical Report NREL/TP-500-38060.

M.H. Kim and D.K.P. Yue, "Sum- and difference-frequency wave loads on a body in unidirectional Gaussian seas," Journal of Ship Research 35(2), 127-140 (1991).

B. Koo, A.J. Goupee, K. Lambrakos and R.W. Kimball, "Model tests for a floating wind turbine on three different floaters," Proceedings of the 31st ASME International Conference on Offshore Mechanics and Arctic Engineering, Rio de Janeiro, Brazil, 1-6 July, 2012.

B. Koo, A.J. Goupee, K. Lambrakos and H.-J. Lim, 2013, Model test correlation study for a floating wind turbine on a tension leg platform, Proceedings of OMAE 2013, ASME 32nd International Conference on Offshore Mechanics and Arctic Engineering, Nantes, France, June 9-14, 2013, accepted for publication.

Langley, R.S., 1986, "On the Time Domain Simulation of Second Order Wave Forces and Induced Responses," AppliedOcean Research 8(3), pp. 134-144.

C.H. Lee and J.N. Newman, WAMIT® User Manual, Versions 6.4, 6.4PC, 6.3S, 6.3S-PC (WAMIT, Inc., Chestnut Hill, Massachusetts, USA 2006).

Leishman J.G., 2000, Principles of Helicopter Aerodynamics, Cambridge University Press, Cambridge.

Manwell J.F., McGowan J.G., Rogers A.L., 2009, Wind Energy Explained: Theory, Design and Applications 2nd Ed., John Wiley & Sons Ltd., West Sussex.

Martin H., 2011, Development of a Scale model Wind Turbine for Testing of Offshore Floating Wind Turbine Systems, M.S. Thesis, University of Maine.

H.R. Martin, R.W. Kimball, A.M. Viselli and A.J. Goupee, "Methodology for wind/wave basin testing of floating offshore wind turbines," Proceedings of the 31st ASME International Conference on Offshore Mechanics and Arctic Engineering, Rio de Janeiro, Brazil, 1-6 July, 2012.

M. Masciola, A. Robertson, J. Jonkman, A. Coulling and A. Goupee, 2013, Assessment of the importance of mooring dynamics on the global response of the DeepCwind floating semi-submersible offshore wind turbine,Proceedings of ISOPE 2013, The 23rd International Ocean and Polar Engineering Conference, June 30-July 5, 2013, accepted for publication.

Matha, D. (2010). Model Development and Loads Analysis of anOffshore Wind Turbine on a Tension Leg platform, with aComparison to Other Floating Turbine Concepts, National Renewable Energy Laboratory, Golden, Colorado, USA, Subcontract Report: NREL/SR-500-45891.

Moon III, WL, Nordstrom, CJ, (2010) "Tension leg platform turbine: A unique integration of mature technologies," Proceedings of the 16th Offshore Symposium, Houston, Texas Section of the Society of Naval Architects and Marine Engineers.

Multisurf 8.0, Version 8.0 (AeroHydro, Inc., Southwest Harbor, Maine, USA 2011).

Musial W., 2008, Status of Wave and Tidal Power Technologies for the United States, Technical Report NREL/TP-500-43240.

Musial W., Ram B., 2010, Large-Scale Offshore Wind Power in the United States, Technical Report NREL/TP-500-40745.

Neville, A., 2009. Hywind Floating Wind Turbine, North Sea, Norway. POWER 153(12): 40.

Newman, J.N., 1974, "Second-order, Slowly-varying Forces on Vessels in Irregular Waves," Proc. Dynamics of Marine Vehicles and Structures in Waves, pp. 193-197.

J.N. Newman, Marine Hydrodynamics (The MIT Press, Cambridge, Massachusetts, USA, 1977).

The Norwegian Petroleum Directorate (NPD), 1992, Guidelines Concerning Load Effects to Regulations Concerning Load Bearing Structures in the Petroleum Activities.

J.R. Paulling and W.C. Webster, "A consistent, large-amplitude analysis of the coupled response of a TLP and tendon system," Proceedings of the 5th ASME International Conference on Offshore Mechanics and Arctic Engineering, Tokyo, Japan, 13-18 April, 1986, pp. 126-133.

Peters D.A., He C.J., 1991, Correlation of measured induced velocities with a finite-state wake model, Journal of the American Helicopter Society 36(3).

I. Prowell, A. Robertson, J. Jonkman, G.M. Stewart and A.J. Goupee, 2013, Numerical prediction of experimentally observed behavior of a scale model of an offshore wind turbine supported by a tension-leg platform, Proceedings of the Offshore Technology Conference (OTC 2013), Houston, Texas, USA, May 6-9, 2013, accepted for publication.

Roddier, D., Cermelli, C. and Weinstein, A., 2009. WindFloat: A Floating Foundation for Offshore Wind Turbines Part I: Design Basis and Qualification Process, OMAE 2009 4: 845-853.

Roddier, D., Cermelli, C., Aubault. A. and Weinstin. A., 2010. WindFloat: A floating foundation for offshore wind turbines. Journal of Renewable and Sustainable Energy 2: 033104.

Skaare. B., Hanson, T.D., Nielsen, F.G., Yttervik, R., Hansen, A.M., Thomesn, K. and Larsen, T.J., 2007. Integrated Dynamic Analysis of Floating Offshore Wind Turbines. Paper presented at the European Wind Energy Conference and Exhibition, Milan, 7-10 May.

Standing, R.G., Brendling, W.J. and Wilson, D., 1987, "Recent Developments in the Analysis of Wave Drift Forces, Low-Frequency Damping and Response," Proc. 1987 Offshore Technology Conference, Houston, Texas.

Stewart, G., Lackner, M., Robertson, A., Jonkman, J. and Goupee, A., 2012, "Calibration and Validation of a FAST Floating Wind Turbine Model of the DeepCwind Scaled Tension-leg Platform," Proc. 22nd International Offshore and Polar Engineering Conference, Rhodes, Greece, pp. 380-387.

University of Maine and James W. Sewall Company, "Maine deepwater offshore wind report," February 2011.

van Walree, F., Yamaguchi, K., 1993, Hydrofoil research: model tests and computations, FAST '93, 2nd International Conference on Fast Sea Transportation, Yokohama, Japan.

WAMIT USER MANUAL (1998-2006): Versions 6.4, 6.4PC, 6.3S,6.3S-PC, WAMIT Inc., USA.

http://www.windsea.no/, accessed January 2012.

THE UNIVERSITY OF MAINE

ADVANCED STRUCTURES & composites center

DE-EE0002891

FINAL TECHNICAL REPORT

VOLUME 3: COMPOSITE MATERIALS

DeepCwind Consortium Research Program

January 15, 2010 – March 31, 2013

Habib J. Dagher, Ph.D., P.E., University of Maine
Jade Chung, University of Maine
Andrew Goupee, Ph.D., University of Maine
Dustin Jalbert, University of Maine
Matthew Lankowski, University of Maine
Thomas Snape, University of Maine
Anthony M. Viselli, P.E., University of Maine

DE-EE0002891 Final Technical Report

Volume 3: Composite Materials

The entirety of this volume has been redacted as it contains proprietary data.

Contact:
Dr. Habib Dagher, P.E.
UMaine Composites Center
(207) 581-2123